

James De Clerck *Editor*

Topics in Modal Analysis I, Volume 7

Proceedings of the 32nd IMAC, A Conference and Exposition
on Structural Dynamics, 2014



Conference Proceedings of the Society for Experimental Mechanics Series

Series Editor

Tom Proulx
Society for Experimental Mechanics, Inc.,
Bethel, CT, USA

For further volumes:
<http://www.springer.com/series/8922>

James De Clerck

Editor

Topics in Modal Analysis I, Volume 7

Proceedings of the 32nd IMAC, A Conference and Exposition
on Structural Dynamics, 2014

Editor

James De Clerck
The Enterprise Program
Michigan Technological University
Houghton, MI, USA

ISSN 2191-5644 ISSN 2191-5652 (electronic)
ISBN 978-3-319-04752-2 ISBN 978-3-319-04753-9 (eBook)
DOI 10.1007/978-3-319-04753-9
Springer Cham Heidelberg New York Dordrecht London

Library of Congress Control Number: 2014931510

© The Society for Experimental Mechanics, Inc. 2014

This work is subject to copyright. All rights are reserved by the Publisher, whether the whole or part of the material is concerned, specifically the rights of translation, reprinting, reuse of illustrations, recitation, broadcasting, reproduction on microfilms or in any other physical way, and transmission or information storage and retrieval, electronic adaptation, computer software, or by similar or dissimilar methodology now known or hereafter developed. Exempted from this legal reservation are brief excerpts in connection with reviews or scholarly analysis or material supplied specifically for the purpose of being entered and executed on a computer system, for exclusive use by the purchaser of the work. Duplication of this publication or parts thereof is permitted only under the provisions of the Copyright Law of the Publisher's location, in its current version, and permission for use must always be obtained from Springer. Permissions for use may be obtained through RightsLink at the Copyright Clearance Center. Violations are liable to prosecution under the respective Copyright Law.

The use of general descriptive names, registered names, trademarks, service marks, etc. in this publication does not imply, even in the absence of a specific statement, that such names are exempt from the relevant protective laws and regulations and therefore free for general use.

While the advice and information in this book are believed to be true and accurate at the date of publication, neither the authors nor the editors nor the publisher can accept any legal responsibility for any errors or omissions that may be made. The publisher makes no warranty, express or implied, with respect to the material contained herein.

Printed on acid-free paper

Springer is part of Springer Science+Business Media (www.springer.com)

Preface

Topics in Modal Analysis I, Volume 7 represents one of the eight volumes of technical papers presented at the 32nd IMAC, A Conference and Exposition on Structural Dynamics, 2014, organized by the Society for Experimental Mechanics, and held in Orlando, Florida, February 3–6, 2014. The full proceedings also include volumes on Dynamics of Coupled Structures; Nonlinear Dynamics; Model Validation and Uncertainty Quantification; Dynamics of Civil Structures; Structural Health Monitoring; Special Topics in Structural Dynamics; and Topics in Modal Analysis II.

Each collection presents early findings from experimental and computational investigations on an important area within structural dynamics. *Topics in Modal Analysis I* represents papers on enabling technologies for modal analysis measurements such as sensors and instrumentation, and applications of modal analysis in specific application areas. Topics in this volume include:

- Experimental techniques
- Processing modal data
- Rotating machinery
- Acoustics
- Adaptive structures
- Biodynamics
- Damping

The organizers would like to thank the authors, presenters, session organizers, and session chairs for their participation in this track.

Houghton, MS

J. De Clerck

Contents

1	Infant Brain Response Against Shaking Vibration Using Finite Element Analysis	1
	Takayuki Koizumi, Nobutaka Tsujiuchi, and Keisuke Hara	
2	Integrity Assessment of Pickup Vehicle Occupants in Rollover Situation Considering Internal ROPS Device: A Numerical Approach	13
	Maria Alzira de Araújo Nunes, Rita de Cássia Silva, and Alessandro Borges da Silva Oliveira	
3	Rated Life Calculation Potential of Gearbox Model Based Force Estimates	23
	Jan Helsen, Daniele Brandolisio, Bart Peeters, Frederik Vanhollebeke, Joris Peeters, David Moens, and Wim Desmet	
4	Electromechanical Impedance Based Crack Detection for a Rotating Machine	31
	Aldemir Ap Cavalini Jr, Roberto Mendes Finzi Neto, and Valder Steffen Jr	
5	Wind Turbine Gearbox Dynamic Characterization Using Operational Modal Analysis	41
	E. Di Lorenzo, S. Manzato, J. Houben, F. Vanhollebeke, S. Goris, and B. Peeters	
6	Mode Classification and Dynamic Analysis of Coupled “Motor-Compressor-Flexible-Foundation” Structures	53
	Sumit Singhal, Neal Birchfield, and Kumar Vikram Singh	
7	Reconstructing Forces from Continuous Connections Using SWAT	65
	Tyler F. Schoenherr	
8	Modal Analysis of Rotating Wind Turbine Using Multiblade Coordinate Transformation and Harmonic Power Spectrum	77
	Shifei Yang, Dmitri Tcherniak, and Matthew S. Allen	
9	Lateral Vibrations in High Speed Over Critical Drive Train Systems	93
	Sumit Singhal	
10	Vibration Energy Trending and Speed-Frequency Transformation in Run-Up/Coast-Down Tests	101
	Nader Sawalhi and Suri Ganeriwala	
11	Vibration Mitigation on Engine Test Stands Using Conventional Analysis Techniques	109
	B. Swaminathan	
12	Dynamic Modeling and Vibration Analysis of Oilwell Drillstring During Backreaming Operation	123
	Cristiano Eduardo Agostini and Rodrigo Nicoletti	
13	Torsional Damping Identification in Rotating Machinery	133
	Bram Vervisch, Kurt Stockman, and Mia Loccufier	
14	Numerical and Experimental Dynamic System Identification for the Development of Operational Modal Analysis in a Physics-Based Diagnostic/Prognostic Model	141
	Suri Ganeriwala and Nader Sawalhi	

15	The Influence of Loading Conditions on the Static Coefficient of Friction: A Study on Brake Creep Groan	149
	Sebastian Kruse, Bernhard Stingl, Jakob Hieke, Antonio Papangelo, Merten Tiedemann, Norbert Hoffmann, and Michele Ciavarella	
16	Linear Superposition and Modal Participation	161
	Brian J. Schwarz and Mark H. Richardson	
17	Un-weighted and Weighted Versions of the Modal Assurance Criterion (MAC) for Evaluation of Modal Vector Contamination	173
	R.J. Allemang and A.W. Phillips	
18	Modal Properties of Rotating Shafts with Order-Tuned Absorbers	181
	Steven W. Shaw, Mustafa Ali Acar, Brian F. Feeny, and Bruce K. Geist	
19	Structural Modal Identification Through High Speed Camera Video: Motion Magnification	191
	Justin G. Chen, Neal Wadhwa, Young-Jin Cha, Frédo Durand, William T. Freeman, and Oral Buyukozturk	
20	Operational Modal Analysis with Photo Images from Low Speed Digital Camera	199
	Marcos Tan Endo, Arlindo Neto Montagnoli, and Rodrigo Nicoletti	
21	Recovery of Mode Shapes from Continuous Scanning Laser Doppler Vibration Data: A Mode Matching Frequency Domain Approach	207
	P. Chiariotti, P. Castellini, and M. Martarelli	
22	A Compact Device for Measuring Rigid-Body Properties Based on Five Unscaled Modes	215
	Robert Kloepper, Masaaki Okuma, and Joerg Bienert	
23	Three-Dimensional Modal Parameters of Tire	225
	Jianfeng Qiao, Yongchang Du, and Peng Zhao	
24	Hybrid EMA/OMA Data Collection/Reduction for Improved Modal Characterization	231
	Sergio E. Obando and Peter Avitabile	
25	Numerical and Experimental Determination of Nonlinear Normal Modes of a Circular Perforated Plate	239
	David A. Ehrhardt, Ryan B. Harris, and Matthew S. Allen	
26	Experimental Identification of a System Containing Geometric Nonlinearities	253
	Julian M. Londono and Jonathan E. Cooper	
27	Experiment of Vibration Isolation Characteristics of a Periodic Curved Beam	261
	Xiuzhong Xu, Zhiyi Zhang, Xiong Hu, Congxiao Zhou, and Long Liu	
28	Investigation on Damping of a Host Structure Induced by Attached Cables	269
	Jiduck Choi and Daniel J. Inman	
29	Effect of Structural Damping on Vibrations Transmitted to Road Cyclists	283
	Jean-Philippe Pelland-Leblanc, Julien Lépine, Yvan Champoux, and Jean-Marc Drouet	
30	Statistical Approach for Active Buckling Control with Uncertainty	291
	Georg C. Enss and Roland Platz	
31	An Overview of the Technology, History, and Application of Vibro-Acoustic Coupling	299
	Kurt G. Schneider	
32	EMA-BEM-NAH-SEA Path to a Dynamic Filter Model for Violin Radiativity	307
	George Bissinger	
33	Coupled Vibro-Acoustic Model of the <i>Titian</i> Stradivari Violin	317
	Michael A. Pyrkosz and Chuck Van Karsen	

34	Vibrational Response of Elastic Membranes Coupled to Acoustic Fluids Using a BEM-BEM Formulation	333
	Jairo Useche and Alexander Narvaez	
35	Parametric Study of a Continuous Scanning Method Used to Characterize an Acoustic Field	341
	V.V.N. Sriram Malladi, Kevin L. Lefeave, and Pablo A. Tarazaga	

Chapter 1

Infant Brain Response Against Shaking Vibration Using Finite Element Analysis

Takayuki Koizumi, Nobutaka Tsujiuchi, and Keisuke Hara

Abstract The most serious head injury resulting from shaken baby syndrome (infant brain injuries resulting from violent shaking attributed to child abuse) is acute subdural hematoma (ASDH). ASDH in infants has a high mortality rate and results in serious permanent injury. It is difficult gather accurate evidence from third parties since this abuse occurs mainly in the home mainly. As the result, medical practitioners rely on experience and intuition to determine the cause of infant head injuries. Therefore, in this study, we conducted simulation analysis that reproduced the shaking action—using a finite element model of an infant’s head to provide a scientific basis for the determination of shaken baby syndrome. We used a model head of a 6-month-old that was constructed from adult head models and CT scan images of an infant head. The input value was defined as the angular velocity and head displacement obtained from the vibration experiments using a 6-month-old-infant dummy. ASDH is caused by the relative rotational motion between the skull and the brain with a rupture of the bridging veins that connect the skull and brain. Accordingly, we evaluated the relative movement between the skull and brain and measured the stretch ratio of the bridging veins. We then compared this ratio with the threshold, which is the rupture value. As a result, the violent shaking action regarded as shaken baby syndrome abuse results in ASDH when the bridging veins rupture. As the brain movement follows the skull, the bridging veins are stretched greatly depending on the forced skull movement and the brain’s inertia.

Keywords Acute subdural hematoma (ASDH) • Finite element analysis • Shaken baby syndrome • Bridging veins rupture • Frequency

1.1 Introduction

Infant head trauma caused not by falling or other accidents, but by abuse such as dangerous shaking (shaken baby syndrome: SBS) has been reported [1]. Among severe cases of infant head trauma classified as SBS, acute subdural hematoma (ASDH) is prominent. The mortality rate due to ASDH is high and the survivors suffer substantial permanent damage. When assessing ASDH, it is difficult to obtain accurate testimony from third parties because such child abuse mainly occurs in the home. Therefore, a determination by medical authorities as to whether the injuries are the result of abuse or accident must be made based on experience and intuition, and thus lacks a scientific basis. Consequently, a means of clarifying the generating mechanism of ASDH in infants is necessary to provide a scientific basis for making such a judgment.

In this article, we perform experiments to evaluate the behavior of a dummy’s head and what happens in the interior of the skull after vibration input to identify which vibration is a high risk for SBS injury. In the experiment, we used a 6-month-old dummy with a transparent skull head model and a vibration exciter to reproduce the shaking action. We also simulated the shaking action with a finite element model of a 6-month-old head. The finite element model was constructed using CT images and an existing adult head model. The input value is the displacement data and angle data obtained by the vibration experiments.

T. Koizumi • N. Tsujiuchi • K. Hara (✉)

Department of Mechanical Engineering, Doshisha University, 1-3 Tataramiyakodani, Kyotanabe-City, Kyoto 610-0321, Japan
e-mail: ksk.hara0511@gmail.com

ASDH occurs as a result of relative rotational motion between the skull and the brain with a subsequent rupture of the bridging veins. Accordingly, we evaluated the stretch of the bridging vein model and relative rotational motion between the brain model and the skull model. We then evaluated the effect of the shaking vibration on the infant head and the resulting risk through comparative verification with the threshold, which resulted in a bridging vein rupture at a stretch ratio of 1.4 [2].

1.2 Threshold of Bridging-Vein-Rupture Stretch Ratio

Maw-Chang Lee et al. performed a tensile test using human bridging veins that were harvested from eight unembalmed cadavers aged 62–85 years. To evaluate bridging vein rupture, they used stretch ratio λ defined by the following equation:

$$\lambda = \frac{l}{l_0} \quad (1.1)$$

l_0 is the initial length of the bridging vein and l is the length during tensile strain.

Their reported maximum stretch ratio was approximately 1.5 at a strain rate of 200 s^{-1} . They also reported that the maximum value does not depend on the strain rate; the mean stretch ratio was 1.51 ± 0.24 and the mean load was $1.02 \pm 0.92 \text{ N}$ at a strain rate of 0.17 s^{-1} , and the mean stretch ratio was 1.55 ± 0.15 and the mean load was $0.99 \pm 0.5 \text{ N}$ at a strain rate of 170 s^{-1} .

In this study, we define the rupture value as 1.4, which is the minimum value at strain rate 170 s^{-1} because we assume the strain rate is higher during shaking.

1.3 Vibration Experiment Using 6-Month-Old Dummy

The shaking vibration produced by humans is not consistent. Therefore, we performed our experiments using a vibration exciter to set input parameters such as frequency and amplitude.

1.3.1 Six-Month-Old Anthropometric Test Dummy

We used a 6-month-old CRABI (client restraint/airbag interaction) dummy with a height of 67 cm and weight of 7.8 kg. This dummy has a transparent head model to visualize brain behavior in the skull. The x axis is aligned in the anterior-posterior direction with positive x indicating the anterior direction. The y axis is aligned in the lateral direction, with positive y indicating the dummy's left side. The z axis is aligned in the superior-inferior direction, with positive z indicating the superior direction. Photographs of the dummy are shown in Fig. 1.1.

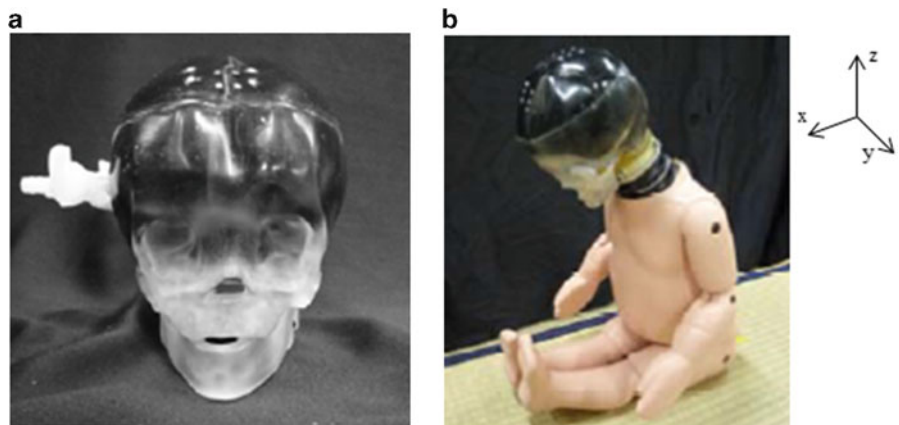


Fig. 1.1 CRABI 6 month-old.
(a) Head model and (b) dummy

Fig. 1.2 Shaking experiment using vibration exciter

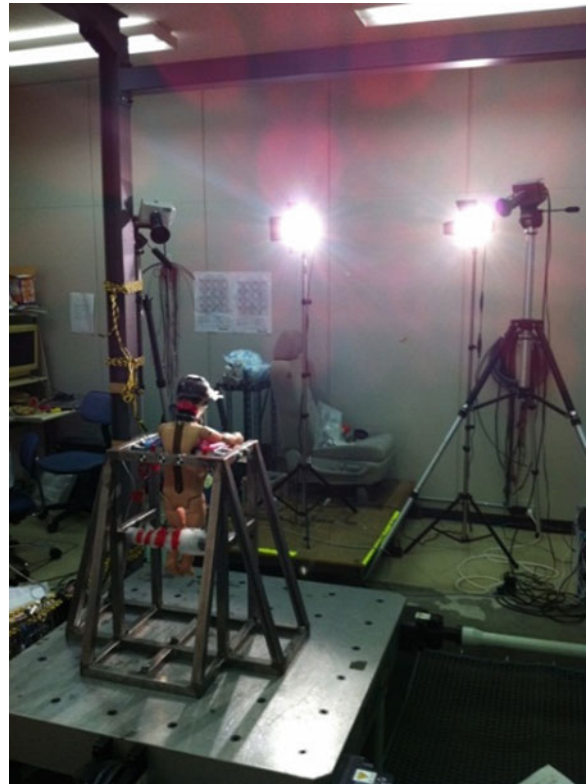
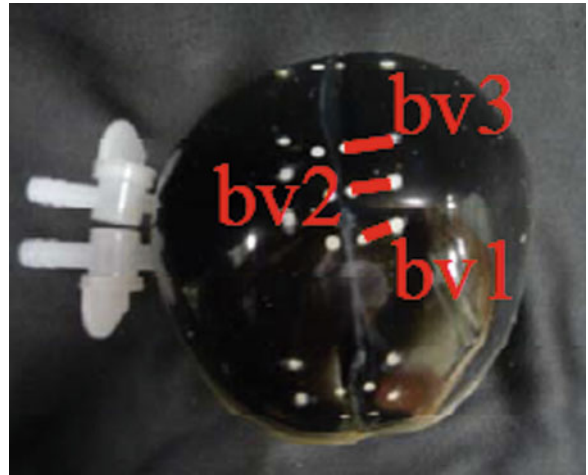


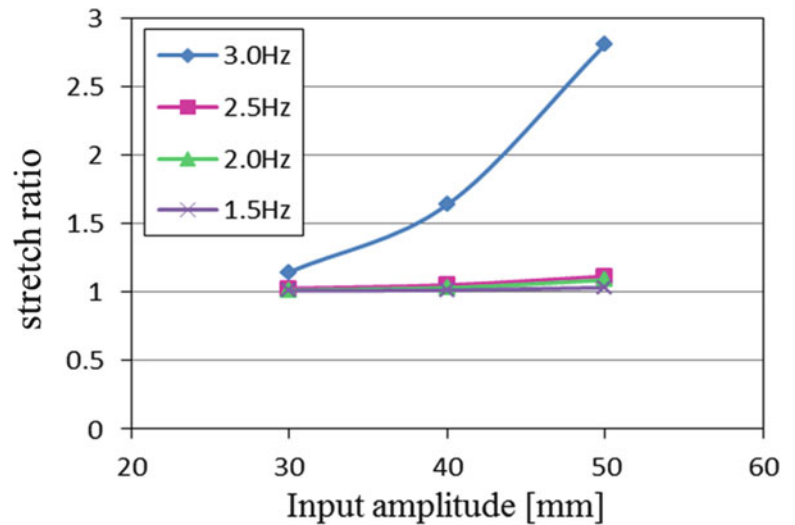
Fig. 1.3 Marker positions



1.3.2 Methods

The experiment model is shown in Fig. 1.2. The dummy was affixed on a board to transmit vibrations from the vibration exciter to the chest. We set up an angular velocity sensor and acceleration sensors to the dummy's head and attached an acceleration sensor to the chest. We then measured the acceleration and angular velocity. We applied white markers to the inner surface of the skull and the brain surface to measure the relative movement between the skull and brain. We set each combinations of brain and skull markers assumed to be the bridging veins as bv1–bv3. Figure 1.3 shows the marker combinations of brain and skull. Head behavior was taken at a sampling rate of 500 or 200 fps with two high-speed cameras (D-III: Detect). We then measured the relative displacement of the bv1–bv3 markers by converting the three-dimensional displacement method using the direct linear transformation (DLT) method. We calculated stretch ratio λ between two points as the evaluation strain parameters of the bridging veins. We used Eq. (1.1) to calculate the ratio, using distance l_0 of the bv1–bv3 in the video frame and distance l of bv1–bv3 in the initial position. We then evaluated the relative displacement between the brain and the skull.

Fig. 1.4 Maximum stretch ratio responses via high-speed camera images



1.3.3 Input Vibration

We performed experiments for only the x axial, which is the main component of the shaking vibration. In addition, we ignored vertical vibration in error of less than 5 % compared with the two-axis coupled vibration. The input values were a total of 12 patterns, combining three amplitude patterns (± 30.0 , ± 40.0 , and ± 50.0 mm) in the x axial with four frequency patterns (1.5, 2.0, 2.5, and 3.0 Hz). To reproduce the human act of shaking an infant, the input amplitudes were set to the value close to the one at which people shook the infant dummy. In addition, the input frequencies were set at a lower value than the maximum high-risk frequency (around 3.0 Hz) obtained by a previous study. In the previous study, the dummy's head, which was a rigid model, was swung most at the 3.0-Hz frequency.

1.3.4 Results and Discussion

Our results are reported in Fig. 1.4 in terms of the maximum bridging-vein stretch ratio and the amplitudes for each condition. The maximum of the bridging-vein stretch ratio tends to increase with increasing amplitude at any frequency, as shown in Fig. 1.4. Therefore, the breaking risk for the bridging veins becomes higher as amplitude increases. For a ± 40 mm or more amplitude at the 3.0-Hz frequency, the stretch ratio between two points shows as large value and is significantly higher for ± 50.0 mm amplitude. Therefore, there is a possibility that the bridging veins will rupture at this vibration. On the other hand, the value shows a small shift at any amplitude of 2.5 Hz and under. In other words, the bridging veins do not break at 2.5 Hz or under. Therefore, we can conclude that ASDH due to rupture of the bridging veins does not occur with vibrations caused during cradling.

1.4 Simulation Analysis Using 6-Month-Old Finite Element Model

We performed finite element analysis of shaking action using with the 6-month-old head model using the same method as in the experiments. We used PAM-CRASH (ESI Group) as the dynamic explicit analysis solver.

1.4.1 Original Finite Element Model of 6-Month-Old Head

A highly accurate infant head model cannot be constructed because the characteristics of skull shape are different for infants and adults. Therefore, scaling down an adult head model to a finite element model of the infant head is not appropriate. In this study, we used the finite element model of a newly constructed 6-month-old head based on three-dimensional shape

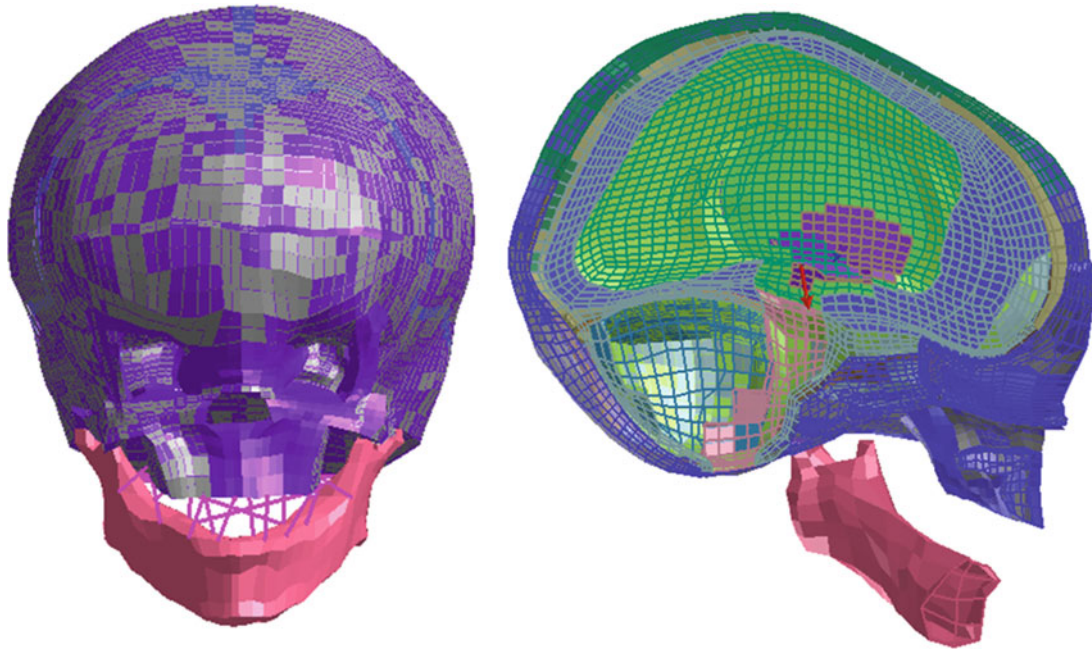


Fig. 1.5 Finite element original model of 6-month-old head

Table 1.1 Dimension of 6-month-old head (mm)

Length	Breadth	Height
154.9	119.4	147.3

data of the head obtained from CT images of a particular 4-month-old head. The shape of the finite element model of an adult head was then converted into the 4-month-old head model based on the shape data using the free-form deformation (FFD) method. The 6-month-old infant head finite element model was constructed by scaling the dimensions of the 4-month-old head that had been converted to the shape of the 6 month-old CRABI head. The original head model is composed of a skull including structure and anterior fontanel, cerebrospinal fluid (CSF), brain (left and right cerebrum, cerebellum, and brainstem), membrane (dura mater, pia mater, flax, and tentorium), and bridging veins. The total number of nodes is 121.561 and the total number of elements is 151.720. Figure 1.5 illustrates the original model and Table 1.1 shows the main dimensions.

1.4.2 Reducing Original Finite Element Model of 6-Month-Old Head

The original model required a substantial amount of computation time, as each node has 6° of freedom. Therefore, in this study, we reduced the original finite element model of the 6-month-old head without changing the shape of the skull model, brain model, and bridging model, which are important objects. The adult skull has three layers, an inner table, outer table, and skull dipole, and the structure and anterior fontanel are closed for completing ossification. On the other hand, the infant skull has a single layer without an inner and outer table, and the structure and anterior fontanel exist because of incomplete ossification. In addition, the skull model is regarded as a rigid body for high strength and high density compared to the inside of the skull. On this basis, we simplified the skull and structure as Shell elements and defined their rigid bodies. Moreover, the original model has microelements of a partially asymmetrical and complicated shape. This analysis tool, which decides the time step for the distance of nodes, requires a substantial amount of computation time. Therefore, we re-built each part symmetrically centered at the X–Z plane. We also united the left and right cerebrum, cerebellum, and brainstem as a brain group having the same material properties. The CSF was constructed as a smoothed particle hydrodynamics (SPH) model,

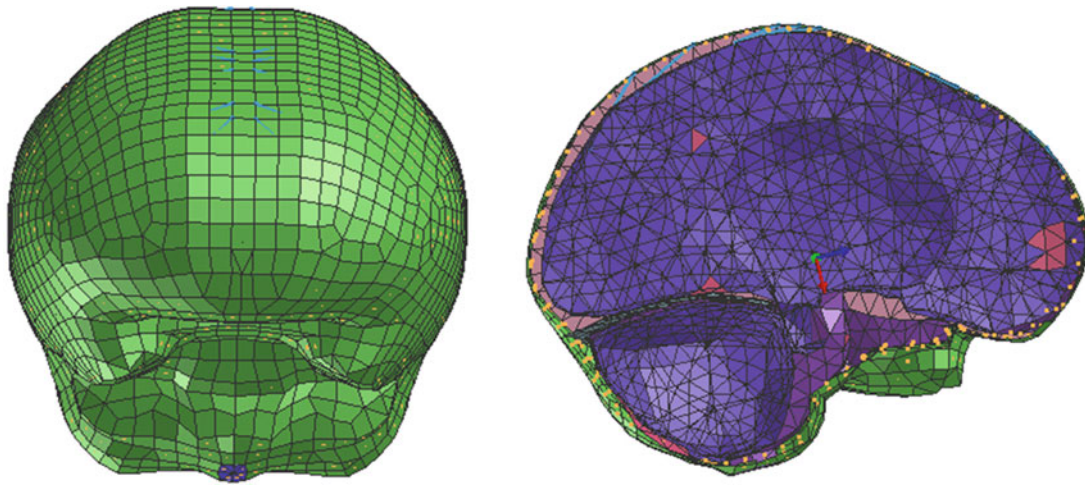
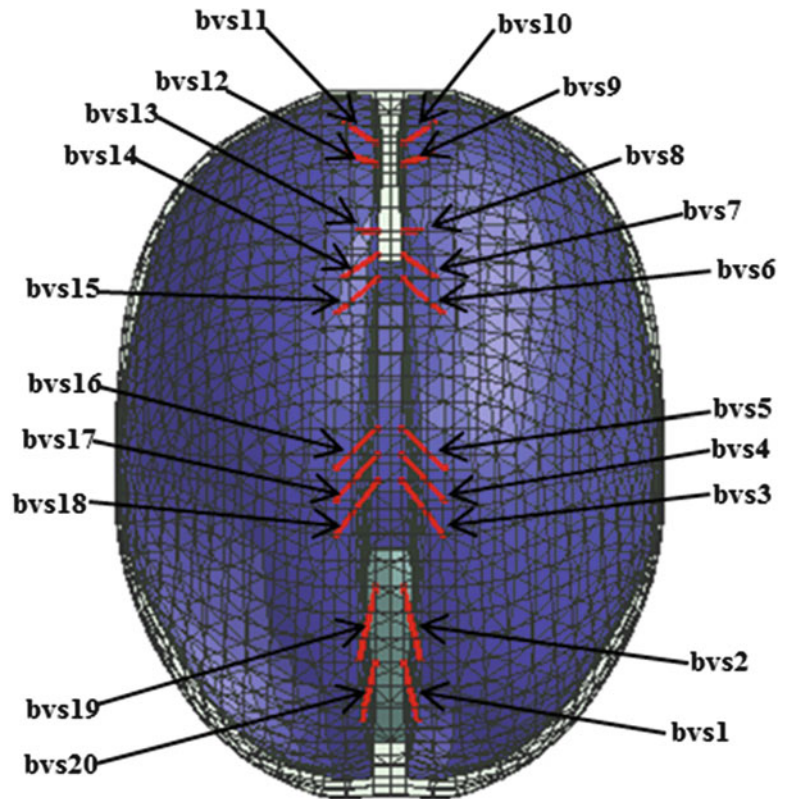


Fig. 1.6 Finite element model of the 6-month-old infant head

Fig. 1.7 Bridging veins of the finite element model



which enables calculation of large deformation for the continuum analysis method of a compressible fluid model. The bridging veins were constructed 20 models connecting the pia matter and dura matter at the sagittal plane where ASDH is likely to occur. We consulted Zhou et al. [3] and Oka et al. [4] to obtain their connecting location and angle. Figure 1.6 shows our finite element 6-month-old head model. Figure 1.7 shows the bridging veins (bvs1–bvs20). The model is composed of a rigid skull, CSF, the brain group, membrane (dura mater, pia mater, flax, and tentorium), and bridging veins. The brain group model is Solid, the rigid skull model and membrane models are Shell, the CSF model is SPH, and the bridging vein model is Beam. The total number of nodes is 10,516 and the total number of elements is 27,872.

Table 1.2 Material properties (1)

Part	Material property	Density, ρ (kg/m ³)	Young's modulus, E (GPa)	Poisson's ratio, ν
Brain group	Linear viscoelastic	1,040	$K = 2.19$	
Pia mater	Elastic	1,133	1.15×10^{-2}	0.45
Dura mater		1,133	3.15×10^{-2}	0.45
Falx		1,133	3.15×10^{-2}	0.45
Tentorium		1,133	3.15×10^{-2}	0.45
Sagittal sinus		1,133	3.15×10^{-2}	0.45
CSF	SPH	1,060	$K = 2.19$	
Structure	Elastic	2,150	4.2×10^{-3}	0.22
Inner table	Elastic	2,723	15	0.21
Bridging vein	Elastic	1,133	9.43×10^{-3}	0.45

Table 1.3 Material properties (2)

Part	Density (kg/m ³)	Bulk modulus (GPa)	Short time shear modulus (GPa)	Long time shear modulus (GPa)	Decay constant (s ⁻¹)
Brain	1,040	2.19	$2,710 \times 10^{-9}$	891×10^{-9}	166

1.4.3 Material Property

The brain group is a viscoelastic model and the deviation response is a dominated Zener model, which is a parallel model using a Maxwell model and a spring model. This shear stress-relaxation behavior, response against step function, is defined by the following equation.

$$G(t) = G_{\infty} + (G_0 - G_{\infty}) e^{-\beta t} \quad (1.2)$$

G is the relaxation modulus, G_0 is the instantaneous modulus, G_{∞} is the equilibrium modulus, β is the decay constant, and t is the duration. Each value was obtained from Fallenstein et al. [5]. The CSF viscous fluid was reproduced using the Monaghan-Gingold method [6] and the material property was water because CSF is very similar to water. The bridging vein model is defined as an elastic body and the material property is obtained from the experiment performed by Lee et al. [2]. They publish bridging veins rupture when the mean strain is 0.5 and the load is 1.0 N. The bridging veins dimension is reported mean length 6.2 mm, mean circumference 4.4 mm, mean thickness 0.05 mm. We calculated Young's modulus (E) 9.43 MPa from these values. And other properties are given the same characteristics as the adult [7–9]. The average head mass of 6-month-old is 2.3 kg. Therefore, we added mass to each part comparing to original model to be the 2.3 kg. Tables 1.2 and 1.3 show the material property of each part.

1.4.4 Simulation of Shaking Vibration

To simulate shaking by a human, we verified the effect of the presence or absence of bridging veins and only rotational motion or only translational motion. The input value was the displacement data and angle data obtained from the vibration experiments. For comparison, we used the experiment data of the ± 50 mm chest amplitude and 3 Hz, which showed the maximum bridging-vein stretch ratio. As we reproduced the exact behavior due to forced displacement, we reduced the noise of the measured experimental data with a low-pass filter. We then calculated the integral to get the displacement data and the angle data. Figure 1.8 shows the displacement data and angle data as the input data. In Fig. 1.8, the input data can be regarded as reasonable because the dummy's head behavior showed approximately ± 130 mm amplitude at 3 Hz in the experiment.

At the start of the simulation, we performed comparative verification of the head behavior between the experiment and the simulation. We extracted the dummy's head trajectory at one cycle every 1/30 s, at which the behavior was stable. Figure 1.9 shows the head trajectory of the experiment. Next, we performed simulation of shaking vibration by setting the input data to the center of gravity. Figure 1.10 shows the input position. We then extracted the head trajectory at one cycle at the same time as in the experiment. Figure 1.11 shows the head trajectory of the simulation. These two trajectories are almost identical.

Second, we calculated the stretch ratio of the bridging vein model using Eq. (1.1).

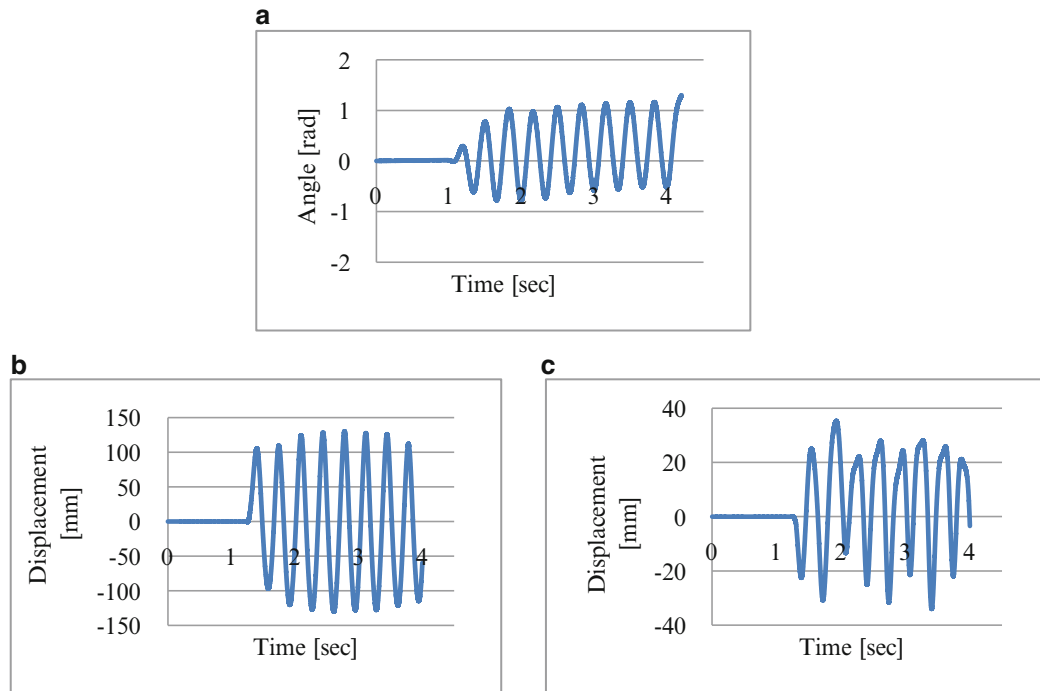


Fig. 1.8 Input condition of analysis. (a) Angular data, (b) displacement data (X axis), and (c) displacement data (Z axis)

Fig. 1.9 Head trajectory of experiment. (a) Toward the front from the back (1/30–5/30 s) and (b) front to back (6/30–10/30 s)

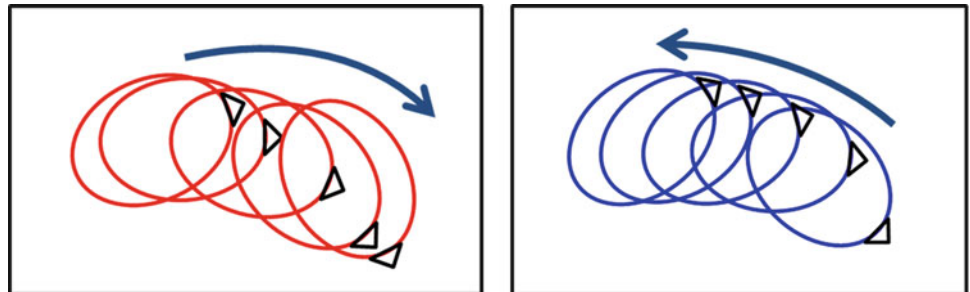


Fig. 1.10 Shaking simulation condition

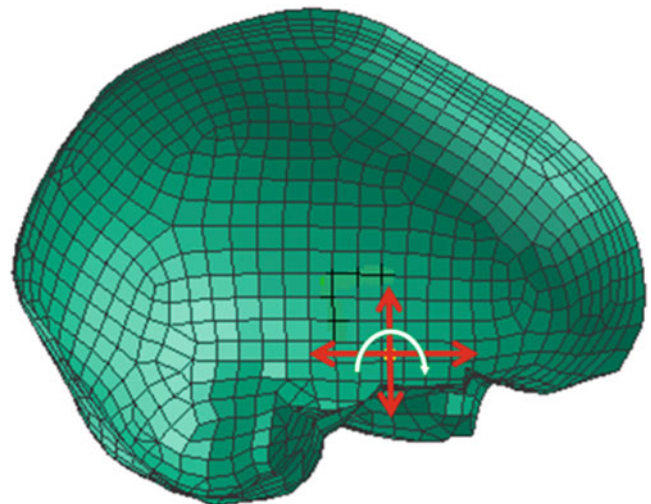


Fig. 1.11 Head trajectory of simulation. (a) Toward the front from the back (1/30–5/30 s) and (b) front to back (6/30–10/30 s)

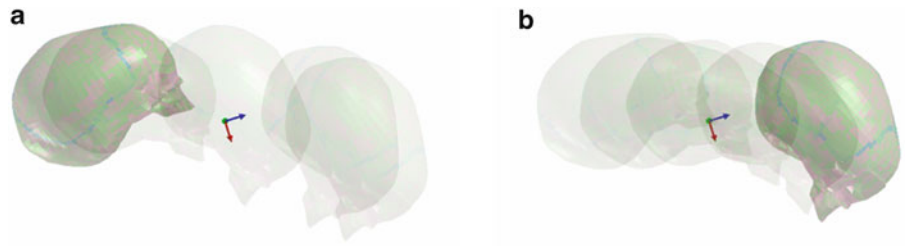


Fig. 1.12 Maximum bridging-vein stretch ratio

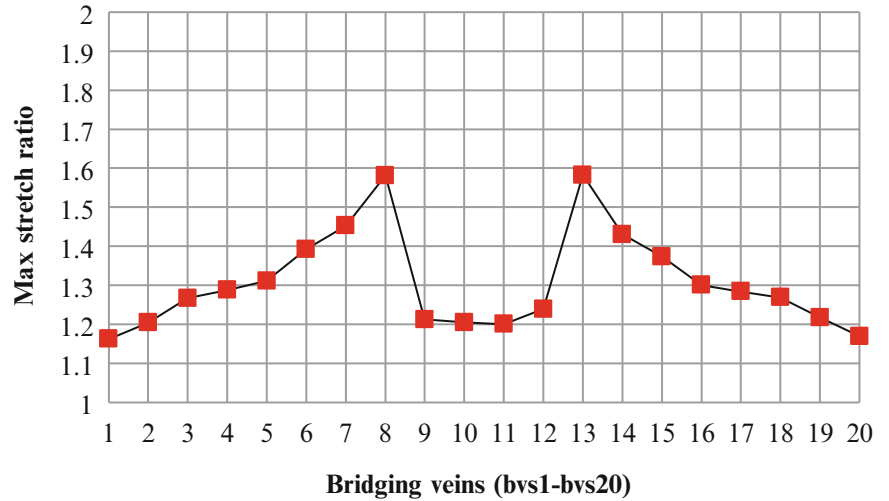
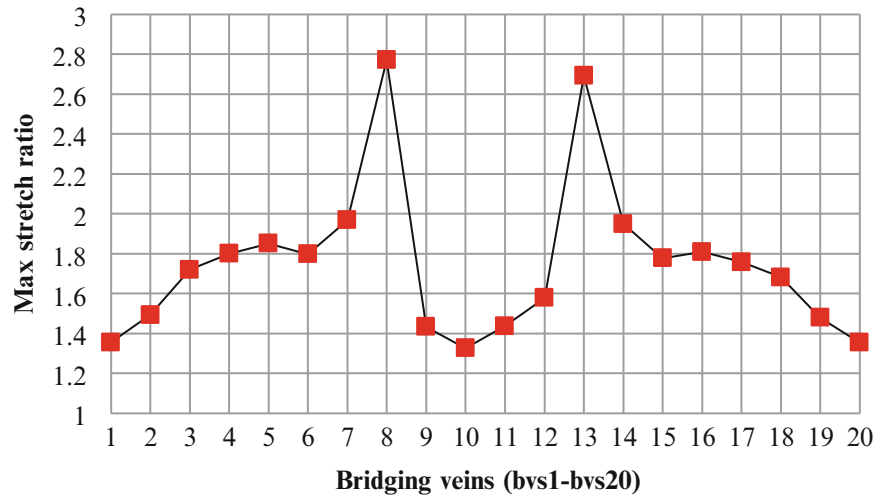


Fig. 1.13 Maximum assumed bridging-vein stretch ratio



1.4.5 Result of Simulation

Figure 1.12 shows the maximum stretch ratio of bvs1–bvs20. In the model without bridging veins, we measured the distance between the nodes assumed to be bridging veins during the simulation. Figure 1.13 shows their maximum stretch ratio. In Fig. 1.13, the peak value is 2.77 for bvs8. In the experiment, the maximum value was 2.8 at the ± 50 mm amplitude and 3 Hz frequency. Therefore, the model is valid. In Fig. 1.12, the peak value is 1.58 of bvs13 over a threshold of 1.4 [2]. Therefore, this represents the violent shaking action regarded as child abuse in which ASDH with the bridging vein rupture occurs.

Moreover, we verified the effect of rotation and translation. Figures 1.14 and 1.15 show the maximum stretch ratio of rotation and translation. The peak value is 1.30 for bvs14 for rotation and 1.54 for bvs8 for translation. For the bridging vein’s stretch, the translation movement has larger brain behavior than rotation. We believe this is caused by the occipital area’s space.

Fig. 1.14 Maximum bridging-vein stretch ratio (rotation)

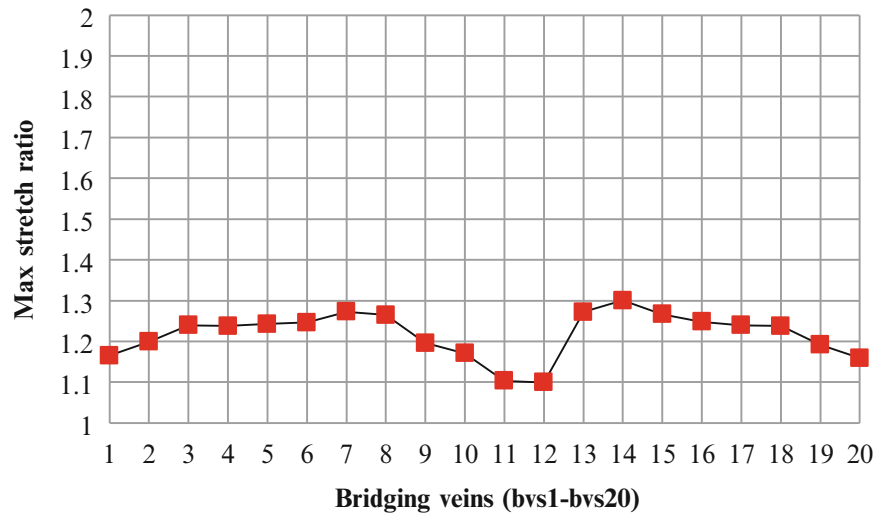
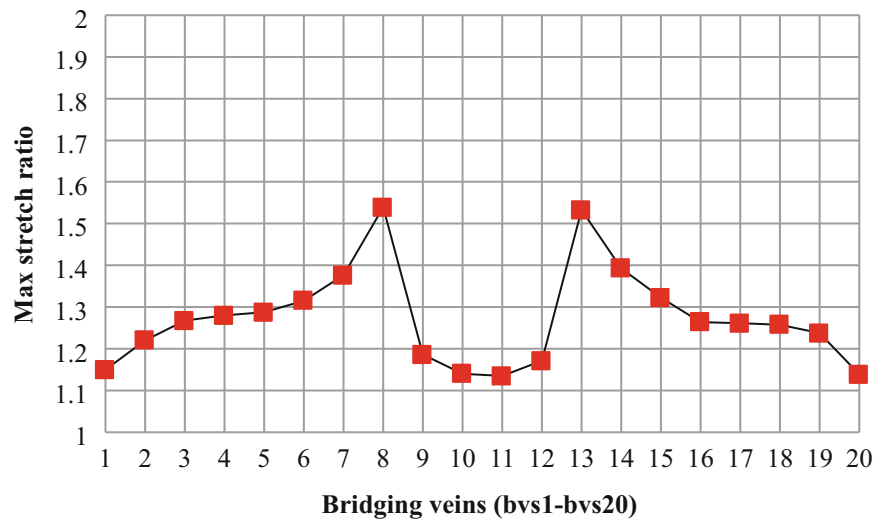


Fig. 1.15 Maximum bridging-vein stretch ratio (translation)



The maximum tension in shaking occurs at the frontal region when the head moves toward the front from the back. This area is relatively consistent with the area where ASDH is likely to occur. The maximum tension occurs when the skull is forced front and the brain's inertia as a result because the brain behavior follows the skull's movement. Therefore, we found that bridging veins rupture due to brain's phase lag against the skull and the possibility of rupture is lower with relative rotational movement due to a difference in vibration frequency.

1.5 Conclusion

1. In the experiment, ASDH is likely to occur for severe vibration such as the frequency is 3.0 Hz and the amplitude is 50.0 mm.
2. In finite element analysis, the model is reasonable since similar results with experiment.
3. For bridging veins stretch, the violent shaking action occur bridging veins rupture and ASDH.
4. As brain move in a phase lag against skull, bridging veins are stretched greatly depending on the skull forced front and the brain's inertia.

Acknowledgments This work was partially supported by Grant-in-Aid for Scientific Research (C) (23560272), Japan Society for the Promotion of Science. And also, this was supported by Associate Professor Yusuke Miyazaki at Tokyo Institute of Technology for 6-month-old dummy and original simulation model. Express our gratitude to write.

References

1. Nagashima T (2011) The infant head injury by abuse, rainbow information training center for children bulletin-(9), pp 1–12 (in Japanese)
2. Lee MC, Haut RC (1989) Insensitivity of tensile failure properties of human bridging veins to strain rate: implications in biomechanics of subdural hematoma. *J Biomech* 22(6/7):537–542
3. Zhou C, Khalil TB, King AI (1995) A new model comparing impact responses of the homogeneous and inhomogeneous human brain. SAE paper 952714, pp 121–137
4. Oka K, Rhoton AL Jr, Barry M, Rodriguez R (1985) Microsurgical anatomy of the superficial veins of the cerebrum. *Neurosurgery* 17(5): 711–748
5. Fallenstein GT, Hulce VD (1969) Dynamic mechanical properties of human brain tissue. *J Biomech* 2(3):217–226
6. Monaghan JJ (2000) SPH without a tensile instability. *J Comput Phys* 159(2):290–311
7. Zhang L, Bae J, Hardy WN, Monson KL, Manley GT, Goldsmith W, Yang KH, King AI (2002) Computational study of the contribution of the vasculature on the dynamic response of the brain. *Stapp Car Crash J* 46:145–164
8. Raul J-S, Baumgartner D, Willinger R, Ludes B (2006) Finite element modeling of human head injuries caused by a fall. *Int J Leg Med* 120(4):212–218
9. Kleivena S, von Holsta H (2002) Consequences of head size following trauma to the human head. *J Biomech* 35(2):135–160

Chapter 2

Integrity Assessment of Pickup Vehicle Occupants in Rollover Situation Considering Internal ROPS Device: A Numerical Approach

Maria Alzira de Araújo Nunes, Rita de Cássia Silva, and Alessandro Borges da Silva Oliveira

Abstract The rollover accidents represent a major cause of injuries and death of vehicle occupants and they are also higher among light trucks than passenger cars. The pickup trucks have important applications in mining scenario where protective structures are required to provide safety in case of a rollover during engineering works. The use of safety devices commonly referred to as ROPS-Rollover Protection System in this kind of vehicle has been shown to be an effective manner to mitigate some of the effects caused by this event, ensuring safety and integrity of passengers. Such device can be constructed using steel bars which constitute a framework to be added into the vehicle, like a cage, in order to minimize the structure intrusion in rollover accidents. In this context, this paper makes up the assessing the integrity of pickup truck occupants in rollover events of a priori designed and proposed ROPS. For this a numerical simulation is carried out based on the experimental Roof Crush Test (FMVSS-216 regulation) using the software LS-Dyna[®] which uses Finite Element Method (FEM). The criteria for neck and head injuries are established in the standard FMVSS-208. The analyses were conducted comparing the vehicle model equipped with and without internal ROPS.

Keywords Rollover • ROPS • Pickup • Integrity • Simulation

2.1 Introduction

According to NHTSA—National Highway Traffic Safety Administration [1], the rollover crashes are responsible for a large number of serious injuries and fatalities compared to other crash modes. Such injuries can cause serious consequences mainly in cervical spine and neck/head [2], thorax and chest [3, 4] and torso region [5]. The risk factors associated to related injuries and to the rollover phenomenon were identified by scientific studies [2, 6] as roof intrusion, the number of quarter turns, far side seating position, vehicle type and occupant physiological characteristics.

Engineering and agricultural machines are vehicles which have large index of rollover accidents, particularly lateral rollover, because of their difficult working conditions, high and unfixed centroid, as well as poor stability [7]. There are international standards [8] which recommends the installation of protective structures, called ROPS, in order to minimize the risk to the driver or operator during a rollover accident.

The Rollover Protective Structures (ROPS) are used in off-highway vehicles to protect operator in case of accidents involving overturning of vehicle. The role of a ROPS is to absorb the energy of Rollover without violating the protected operator zone. The performance of a ROPS is determined by its ability to absorb energy under prescribed loading conditions. The performance depends upon design parameters, such as tube thicknesses, material grades, ROPS tube cross-sections, etc., that define the structure [9].

Special attention must be given to rollover accidents in mining fields. In this environment is usual to have engineering machines, like earth-moving vehicles, and pickup trucks which are used to carry freight and workers through the mine

M.A.A. Nunes (✉) • R.C. Silva • A.B.S. Oliveira
University of Brasília, UnB Gama College, Automotive Engineering, Área Especial de Indústria Projeção A-UnB,
Setor Leste, 72.444-240 Gama, DF, Brazil
e-mail: maanunes@unb.br; ritasilva@unb.br; abso@unb.br

operating on sloping and uneven terrain (above ground and underground). Both vehicles have large probability to suffer rollover accidents due to the described operation conditions. The use of the ROPS in these is highly recommended. Although there are not statistics about human injury considering rollover accidents with these kind of vehicles.

The ROPS design involves two main steps: the mechanical study of the ROPS structure and the integrity evaluation of the vehicle occupants due to the safety system performance. The first one needs to guarantee that the ROPS make a big elastic–plastic deformation, thereby absorbing the kinetic energy generated by the rollover motion. The ROPS must be able to absorb the kinetic energy mainly through a plastic hinge (plastic deformation occurs in particular areas creating weaknesses about which the structure bends) formed in the local area [9]. The second step is performed by dynamic tests in which the biomechanical loads measured by anthropomorphic test devices are compared against injury assessment reference values to predict the level of occupant safety and injury. The tests are performance based and codified into vehicle safety standards [10].

Such dynamic tests commonly utilizes real vehicle in rollover tests which is closest to the actual situation in the rollover accident [11]. This is a basic and intuitive method of comprehensively evaluating vehicle safety performance. However, its repeatability is poor and each test needs large amounts of manpower, money, and time. The static loading test method [12] is less demanding than an actual vehicle rollover test, but it is still costly and time-consuming. In order to avoid the listed disadvantages, a good solution is use computer simulation in combination with experimental tests. In this work a numerical approach is shown.

This paper aims to use simulation analysis methods in order to verify the effectiveness of a designed internal ROPS related to the human injury mechanism during a dynamic rollover accident. The considered vehicle is a pickup truck with four dummies inside it. The numerical simulation is carried out based on the experimental Roof Crush Test [12] using the software LS-Dyna[®]. Prior papers published by the authors [13, 14] describe in detail the finite element (FE) model of the pickup truck and show the numerical validation using impact energy analysis between both rollover models: the dynamic Dolly Rollover test [11] and the quasi-static Roof Crush test [12]. The authors investigated too the rollover accident effect in the dummies when used a external designed ROPS [14]. The roof crush device model is adopted in [14] and in this paper in order to reduce computational time. The criteria for neck and head injuries are established in [10]. The analyses were conducted comparing the vehicle model equipped with and without internal ROPS.

2.2 Roof Crush Numerical Model

The Roof crush test is regulated by the American standard FMVSS-216 [12] which establishes strength requirements for the passenger compartment roof in order to reduce deaths and injuries due to the crushing of the roof into the occupant compartment in rollover crashes. In practice this standard establish a quasi-static test although it simulates experimentally rollover accident. This standard applies to passenger cars, trucks and buses with a gross vehicle weight rating (GVWR) of 2,722 kg or less.

This standard describes the test device like shown in Fig. 2.1. The test device is a rigid unyielding block whose lower surface is a flat rectangle measuring 762 mm × 1,829 mm. It establishes that the lower surface of the test device must not move down more than 127 mm. The applied force in Newton is equal to 1.5 times the unloaded vehicle weight of the vehicle, measured in kilograms and multiplied by 9.8 m/s².

The roof crush setup shown in Fig. 2.1a was modeled by FE method as well the pickup truck model [13, 14]. The pickup base model used in this work is available in the website (<http://www.ncac.gwu.edu/vml/models.html>) of the National Crash Analysis Center (NCAC). The NCAC developed this vehicle finite element model for use with LS-Dyna[®] software. The pickup has the following characteristics: 2007 model year, 1500 2WD pickup truck, 4 door crew cab short box pickup truck; 4.8L V8 engine; 4-speed automatic transmission, tires P245/70R17, wheelbase of 3.664 m. The CG (rearward of front wheel) is 1.664 m and it has a weight of 2,617 kg.

The roof crush numerical model is shown in Fig. 2.1b (measures in millimeters). The original NCAC pickup truck model was re-meshed reducing the number of elements to 153,616 (number of nodes equal 160,057) by increasing the time step from 1×10^{-6} to 2.5×10^{-6} s. The elements have average size of 28×10^{-3} m. In order to evaluate the occupants integrity only the device test setup was based in the FMVSS-216.

The boundary conditions of the simulations (plate mass, translation velocity of the impact device and stored impact energy) was estimated prior using the dolly rollover simulation and impact energy analysis [13]. It emphasizes the aim of this work which consists in to evaluate occupants integrity resulting from roof impact in the ground, using a low cost computational model (roof crush model instead dolly rollover model and reduced FE model). The inputs to the roof crush simulation is: plate mass of $1,500 \times 10^3$ kg, velocity of $6,000 \times 10^{-3}$ m/s, 27×10^3 N m.

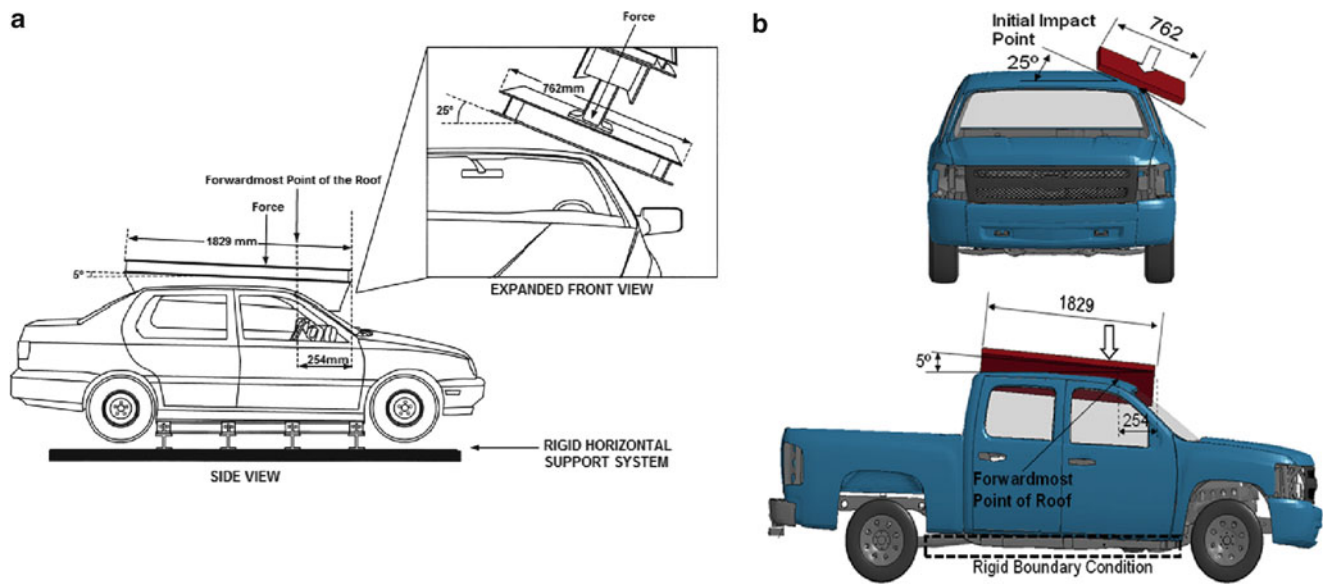


Fig. 2.1 (a) Test device orientation for roof crush test [12]. (b) Roof crush setup used for numerical simulation

In order to insert the dummies in the interior vehicle, the interior components of the vehicle must be considered in the modeling. The plastic components like Dashboard, IP and centre console, were modeled with shell elements. The seats were modeled with solid elements for the foam, beam elements for the headrest bars and shell elements for the rest (frame and foam fabric cover). The interior trimmings will have a direct effect absorbing part of the impact of the roof intrusion to the dummy heads and they were modeled with shell elements of 3×10^{-3} m thickness.

The considered dummies in this work is male Hybrid III 50 % percentile. The dummies position is highly important in this kind of analysis. For the front dummies the established distances were: distance to roof = 185.5×10^{-3} m and distance to roof trimming = 122×10^{-3} m. For the rear dummies the same distances were: distance to roof = 187×10^{-3} m and distance to roof trimming = 104.5×10^{-3} m.

2.2.1 Numerical Model with Internal ROPS

The internal ROPS considered here were design prior using solid mechanics concepts. So the aim of this work is not to focus in the ROPS design. Here the ROPS have already been designed and it will be analyzed in terms of efficiency for safety purposes and occupants integrity. It was modeled using FEM.

From geometry file of the ROPS, the neutral fiber (surface of the part in the middle of the thickness) was used to mesh it in discrete shell elements. The elements size is 18 mm and its thickness is 9 mm. The shell formulation is the Belytschko-Tsay with five integration points. The main material properties are: Modulus of Elasticity = 207 GPa and Poisson's ratio = 0, 3.

Figure 2.2a shows the FE model of the internal ROPS considered. Figure 2.2b shows the roof crush FE model with dummies (drive and co-drive) and the internal ROPS (grey color tubes inside the pickup). In the numerical simulations were considered the four dummies: drive, co-drive, left and right occupants.

2.3 Integrity of Occupants: Head and Neck Injury Criteria

This topic will discuss the criteria involved in respect to damage and injuries involving occupants of vehicles in case of accidents. In this work two body regions will be considered: head and neck. In order to evaluate head injuries the criteria *HIC15* (Head Injury Criteria) and *A3ms* (Head Peak Acceleration at 3 ms) were used. The parameters: Normalized Neck Injury Criteria (N_{ij}), Peak Moment (M_{max}) and Peak Force (F_{max}) were used to evaluate neck injuries. These are based on standard FMVSS 208 [10] with exception of *A3ms* and M_{max} which were removed from the current FMVSS 208 but classical papers [15, 16] show that these two parameters are important to evaluate head and neck injuries. In the next topics each criteria is defined.

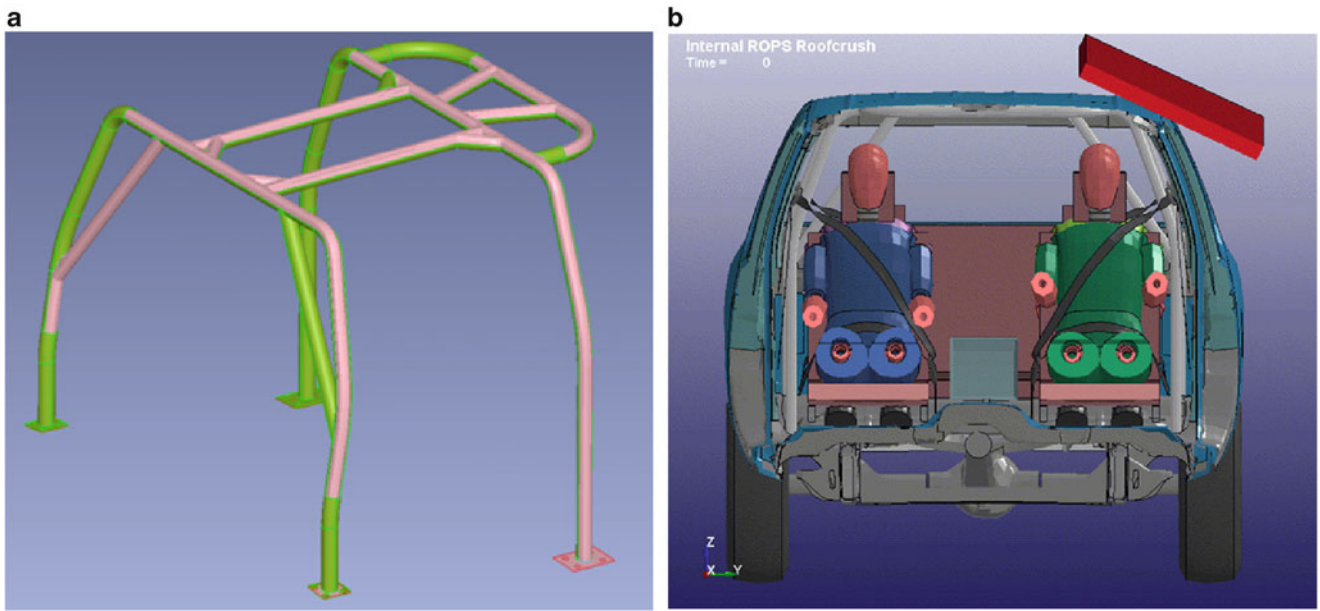


Fig. 2.2 (a) FE model of the internal ROPS. (b) Roof crush FE model with dummies and the internal ROPS

2.3.1 Head Injury Criteria (HIC15)

For any two points in time, t_1 and t_2 , during the accident event, which are separated by not more than a 15 ms time interval and where t_1 is less than t_2 , the *HIC15* shall be determined using the resultant head acceleration (a_r) at the center of gravity of the dummy head, and, expressed as a multiple of the acceleration of gravity and shall be calculated using Eq. (2.1). The maximum calculated *HIC15* value shall not exceed 700 for male Hybrid III 50 % percentile.

$$HIC = (t_2 - t_1) \left[\frac{1}{(t_2 - t_1)} \int_{t_1}^{t_2} a_r(t) dt \right]^{2.5} \quad (2.1)$$

2.3.2 Head Peak Acceleration at 3 ms (A3ms)

According to [15] the resultant head acceleration (a_r) shall not exceed 80 g's (where $g = 9.8 \text{ m/s}^2$) for more than 3 milliseconds (ms). Peak acceleration values must last 3 ms. This requirement has reasons of measurement technique and is supported by the assumption that decelerations of shorter duration do not have any effect on the brain.

2.3.3 Normalized Neck Injury Criteria (N_{ij})

The estimative of N_{ij} is obtained from Eq. (2.2).

$$N_{ij} = \frac{F_z}{F_{zc}} + \frac{M_{ocy}}{M_{yc}} \quad (2.2)$$

where: F_z is the axial force [it can be either in tension (t) or compression (c), corresponding to index i] and M_{ocy} is the occipital condyle bending moment [it can be either in flexion (f) or extension (e), corresponding to index j] which they shall be measured by the dummy upper neck load cell for the duration of the accident event; F_{zc} and M_{yc} are values defined in the

Table 2.1 Maximum values for the considered injuries criteria

Injury criteria	Maximum value
<i>HIC15</i>	700
<i>A3ms</i>	80 g's
N_{ij} (N_{te} , N_{tf} , N_{ce} , N_{cf})	1
F_{max} <i>compression/tension</i>	4,000/4,170
M_{max}	57 N m

standard FMVSS 208 [10]: $F_{zc} = 6,806$ N when F_z is in tension; $F_{zc} = 6,160$ N when F_z is in compression; $M_{yc} = 310$ N m when a flexion moment exists at the occipital condyle; $M_{yc} = 135$ N m when an extension moment exists at the occipital condyle.

At each point in analysis time, only one of the four loading conditions (tension/extension— N_{te} , tension/flexion— N_{tf} , compression/extension— N_{ce} or compression/flexion— N_{cf}) occurs and the N_{ij} value corresponding to that loading condition is computed and the three remaining loading modes shall be considered a value of zero. None of the four N_{ij} values shall exceed 1.0 at any time during the event.

2.3.4 Neck Peak Force (F_{max})

Two conditions is available for this parameter. For the neck under extension the tension force measured at the upper neck load cell shall not exceed 4,170 N at any time. If the neck is under compression force, the measure made in the same place as cited in the prior sentence shall not exceed 4,000 N at any time.

2.3.5 Neck Peak Moment (M_{max})

The maximum occipital condyle extension bending moment measured at the upper neck load cell shall not exceed 57 N m. Tolerance levels for flexion and extension bending moments were based on sled tests conducted on volunteers and cadaver subjects [16]. Volunteer tests provided data up to the pain threshold, and cadaver tests extended the limits for serious injuries. Ligamentous damage occurred in a small stature cadaver subject at an extension moment of 35 ft-lbs. This value was scaled up to an equivalent 50 % male level of 42 ft-lbs (57 N m).

Table 2.1 summarizes the injuries criteria used in this work and their acceptable limits.

2.4 Simulation Results Considering Dummies and Internal Rops

The methodology adopted was: firstly the roof crush simulation was conducted without the ROPS and all five injury criteria described in item 3 were evaluated for each dummy. After, the internal ROPS which was previously designed were inserted in the same pickup truck FE model and the same numeric evaluation was followed. The initial conditions for the roof crush simulation are described in item 2. It is important to highlight that the mechanical design of the internal ROPS was done using CAD software and the principles of solid mechanics as well as material science theory.

From roof crush simulation the Fig. 2.3a, b show the resultant intrusion in the numerical model in the last impact instant considering absence of ROPS (higher intrusion is reached at $t = 100$ ms) and the insertion of the ROPS (higher intrusion is reached at $t = 45$ ms) respectively. Due to the characteristics of the roof crush test the right occupants should have low damage criteria values considering that the roof crush impact occurs on the left. So, it is easy to note that the left occupants (driver and rear left occupant) of Fig. 2.3b suffers less damage when compared with the same occupants of Fig. 2.3a. The influence of the ROPS in these results is clearly visible when we analyze both figures.

In order to estimate the injury criteria of item 3 the software Matlab[®] was used for data pos-processing. The result data were obtained from each virtual sensor settled in the dummies. The estimated results may prove that the left two occupants are the most affected by the impact, which testify this same affirmation based on Fig.2.3 analysis. The results show that the right two occupants have injury criteria values below the limits established by FMVSS 208 considering both situations: without and with ROPS. Due to space constraints in this work will be present the injury criteria values (Table 2.2) for only the two left occupants: driver and rear left occupant. Note that the grey filled cells in Table 2.2 corresponds to parameters that had it value above the limit established in Table 2.1.

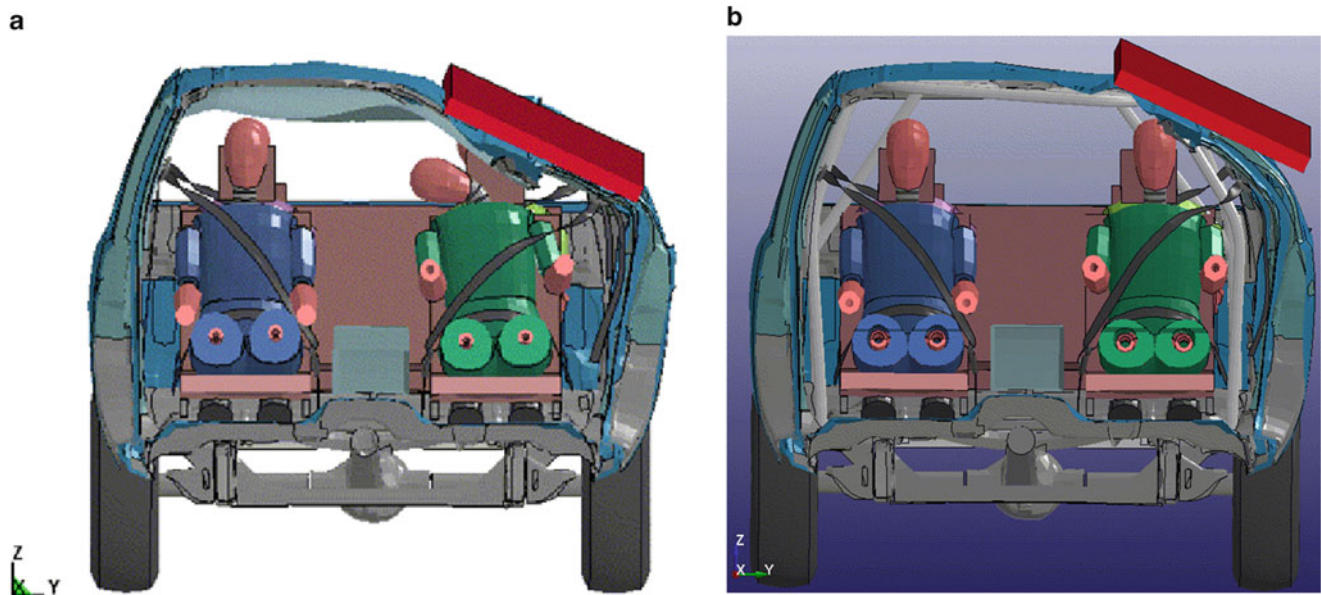


Fig. 2.3 (a) Impact intrusion without ROPS. (b) Impact intrusion considering internal ROPS

Table 2.2 Injury criteria values for driver and rear left occupant

Injury Criteria	Driver		Rear Left Occupant	
	Without ROPS	With ROPS	Without ROPS	With ROPS
HIC15	591	3	664.7	1.6
A3ms	70 g's	9.4 g's	102.6 g's	8.1 g's
N_{te} (plane XZ)	0.3	0.06	0.25	0.04
N_{tr} (plane XZ)	0.3	0.03	0.01	0.02
N_{ce} (plane XZ)	0.2	0.06	0.25	0.07
N_{cf} (plane XZ)	2.8	0.12	1.4	0.11
N_{te} (plane YZ)	0.4	0.03	0.25	0.03
N_{tr} (plane YZ)	0.1	0.02	0.01	0.02
N_{ce} (plane YZ)	0.3	0.14	0.2	0.11
N_{cf} (plane YZ)	3.2	0.10	1.5	0.08
F_{max} Compression	11600 N	457 N	5560 N	411 N
M_{max}	171.7 Nm	12 Nm	81 Nm	11 Nm

From analysis of Fig. 2.3a and Table 2.2 (second column) it is possible to note that the driver suffers an intense impact when the vehicle is not equipped with the ROPS, although the head acceleration ($HIC15$ and $A3ms$) is not over the legal limits, but it is not so far to them. Besides, the neck force (F_{max}) and moment maximum peak limits (M_{max}) exceeded by almost three times the maximum values of Table 2.1. The compression-flexion normalized neck injury criterion (N_{cf} in the plane XZ and YZ) is also almost three times the allowable limit. Due to the rear left passenger is in the impact side so he suffers high damage too when compared with the other occupants. The forces considered in his head and neck (column 4 in Table 2.2) are lower than the suffered by the driver but still quite high, around twice the limits established in Table 2.1. When the results obtained with the inserted ROPS are analyzed (columns 3 and 5 in Table 2.2) we can note that all criteria are below the maximum values of Table 2.1.

In order to analyze the obtained results in time domain the Figs. 2.4 and 2.5, from *a* to *c*, show the three damage parameters: head resultant, neck force resultant and neck moment resultant to the driver and rear left passenger respectively. Note in these figures that the impact time is from 0.022 to 0.048 s. The last figure (Figs. 2.4d and 2.5d) is the intrusion occasioned by the impact device in millimeters. It is the down displacement of the vehicle roof from its application. While the maximum front intrusion is about 200 mm, the maximum rear intrusion is about 175 mm considering the vehicle without ROPS, so it is expectable to obtain more damage in the driver than in the left-rear passenger as the damage criteria showed.

Still analyzing Figs. 2.4d and 2.5d, when the internal ROPS is inserted in the vehicle the maximum front intrusion is reduced to 80 mm and the maximum rear intrusion to 50 mm. It concludes that the design internal ROPS may reduce the intrusion in the driver position about 40 % and in the rear-left about 29 %. The most important aspect is that the internal ROPS keep all injuries criteria below the limits.

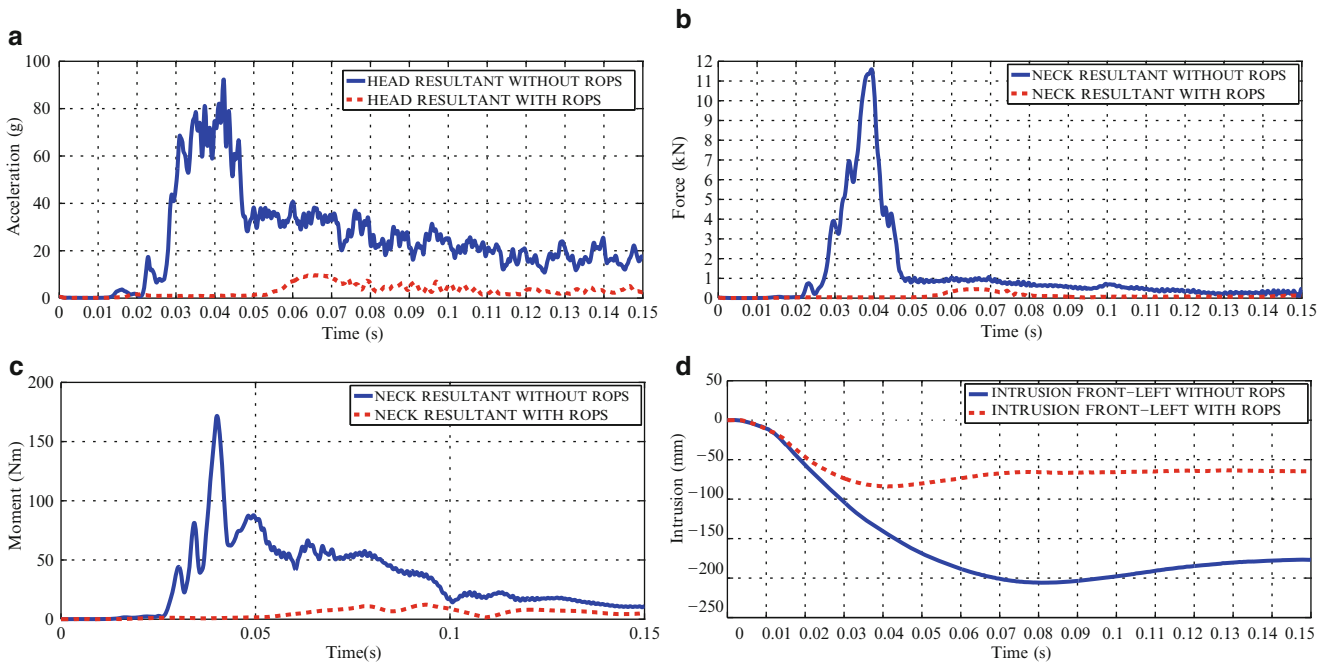


Fig. 2.4 Time evaluation of damage criteria in the driver dummy with and without internal ROPS

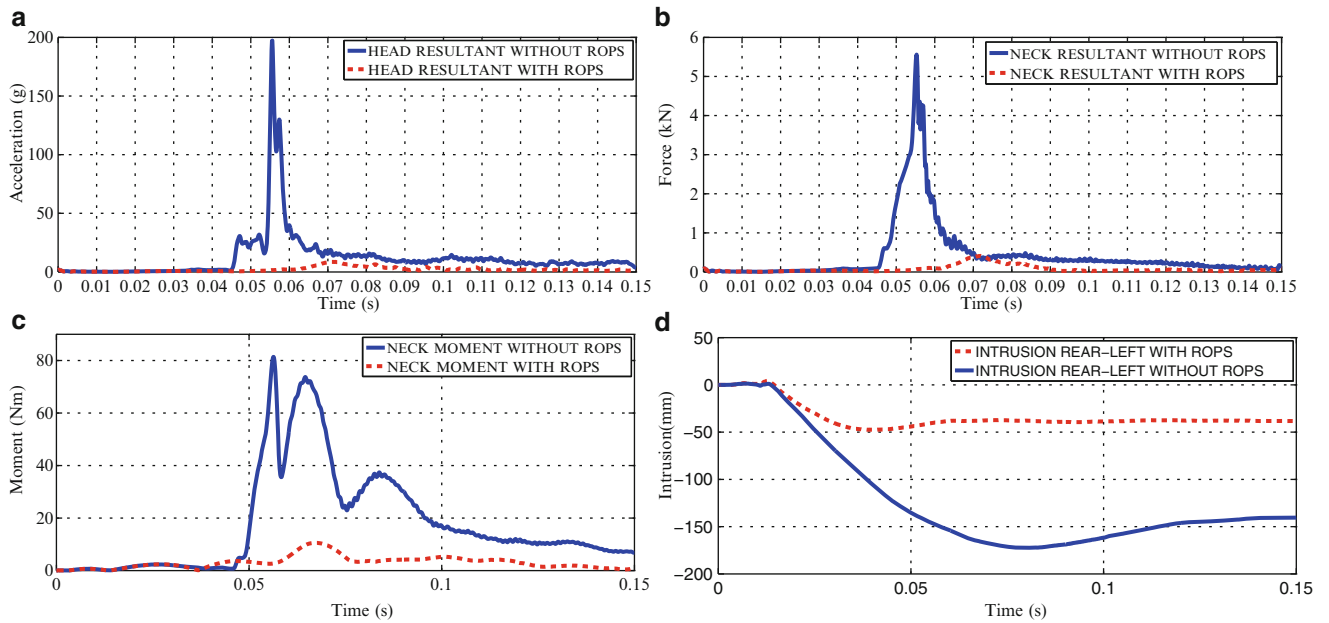
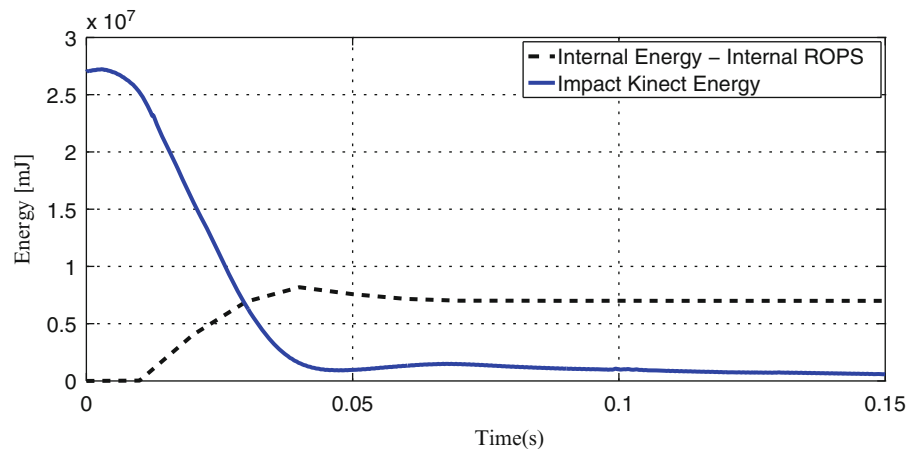


Fig. 2.5 Time evaluation of damage criteria in the rear-left dummy with and without internal ROPS

Figure 2.6 shows the energy behavior during the roof crush simulation in time domain considering the vehicle with the ROPS. There are two curves in this figure: the internal energy and the kinetic energy due to the impact device. The internal energy is caused by the deformation of the ROPS when occurs the impact, it is the absorbed energy. Analyzing Fig. 2.6 we can note that the ROPS internal energy maximum value is 0.82×10^7 mJ at 0.04 s (dashed black curve). It represents the 30 % of the total impacting energy (2.7×10^7 mJ) represented by the blue curve. The remaining impacting energy is absorbed by the vehicle bodywork. There is also some kinetic energy returned to the impact device due to the elastic deformation of the bodywork, justifying why the kinetic energy increases a bit from 0.045 s.

Fig. 2.6 Energy analysis of the internal ROPS



2.5 Conclusions

Comparing the injuries criteria maximum values and these values estimated from numeric roof crush simulation is clear that the proposed internal ROPS has a good performance protecting the vehicle occupants mainly the right side one.

The numeric simulation showed that the driver suffers an intense impact when the vehicle is not equipped with the ROPS. The parameters: F_{max} , M_{max} , N_{cf} exceeded by almost three times the legal limits. The parameters $HIC15$ and $A3ms$ not exceed the maximum values but they is not so far to them. The rear left passenger suffers high damages too due to he is in the same side of the impact in which the head and neck forces are around twice the permitted maximum values. When the ROPS is considered in the numeric simulation the results obtained show that all injury criteria are below the maximum values.

Analyzing the intrusion occasioned by the impact device, the vehicle without the ROPS has the maximum front intrusion about 200 mm and the maximum rear intrusion is about 175 mm. When the internal ROPS is inserted the maximum front intrusion is reduced to 80 mm and the maximum rear intrusion to 50 mm. A intrusion reducing of 40 % is obtained in the driver position and about 29 % in the rear-left occupant. The most important aspect is that the internal ROPS keep all injuries criteria below the limits.

The energy analysis showed that the maximum value of the ROPS internal energy represents the 30 % of the total impacting energy. The remaining impacting energy is absorbed by the vehicle bodywork.

Acknowledgments Authors would like to thank VALE (global mining company) for the financial support; FINATEC for administrative work related to the development of this research and finally, CTAG IDIADA Safety Technology S. L. by the partnership in the development of this work.

References

1. National Highway Traffic Safety Administration (2010) Traffic safety facts: 2008 data, DOT HS 811 368, 12 pp
2. Funk JR, Cormier JM, Manoogian SJ (2012) Comparison of risk factors for cervical spine, head, serious, and fatal injury in rollover crashes. *Accid Anal Prev* 45:67–74
3. Bedewi PG, Godrick DA, Digges KH, Bahouth GT (2003) An investigation of occupant injury in rollover: NASS-CDS analysis of injury severity and source by rollover attributes. In: Proceedings of the 18th international technical conference on the enhanced safety of vehicles (ESV), USA, Paper no. 419
4. Bambach MR, Grzebieta RH, McIntosh AS (2013) Thoracic injuries to contained and restrained occupants in single-vehicle pure rollover crashes. *Accid Anal Prev* 50:115–121
5. Digges KH, Eigen AM, Dahdah S (2005) Injury patterns in rollovers by crash severity. In: Proceedings of the 19th international technical conference on the enhanced safety of vehicles (ESV), USA, Paper no. 355
6. Mandell SP, Kaufman R, Mack CD, Bulger EM (2010) Mortality and injury patterns associated with roof crush in rollover crashes. *Accid Anal Prev* 42(4):1326–1331
7. Chen C, Wang G, Zhang Y, Zhang Y, Si J (2012) Effect of lateral stiffness coefficient of loader ROPS on human injury in a lateral rollover incident. *Biosyst Eng* 113:207–219
8. ISO 3471:1994 (1994) Earth-moving machinery - Roll-over protective structures - Laboratory tests and performance requirements, International Organization for Standardization.
9. Malik M, Kshirsagar S, Barve S (2012) DOE for non linear structural analysis of ROPS (rollover protective structure). SAE Technical Paper 2012-01-1902

10. U.S. Department of Transportation (2008) FMVSS 571.208 Standard No. 208 Occupant crash protection, National Highway Traffic Safety Administration, Federal Motor Vehicle Safety Standards, Washington, DC. Retrieved March, 2014, from <http://www.fmcsa.dot.gov/rules-regulations/administration/fmcsr/fmcsrruletext.aspx?reg=r49CFR571.208>
11. Society of Automotive Engineers (2011) SAE J2114 Dolly Rollover Recommended Test Procedure, USA: Society of Automotive Engineers
12. U.S. Department of Transportation (2008) FMVSS 571.216 Standard No. 216 Roof crush resistance, National Highway Traffic Safety Administration, Federal Motor Vehicle Safety Standards, Washington, DC. Retrieved March, 2014, from <http://www.fmcsa.dot.gov/rules-regulations/administration/fmcsr/fmcsrruletext.aspx?reg=571.216>
13. Nunes MAA, Silva RC, Oliveira ABS (2013) Avaliação da integridade de ocupantes de veículos tipo pick-up em caso de capotamento: uma abordagem numérica. XXI Simpósio Internacional de Engenharia Automotiva, São Paulo
14. Nunes MAA, Silva RC (2013) Computational simulation of a pickup truck rollover test: impact energy analysis. SAE Technical Paper 2013-36-0146
15. Versace J (1971) A review of the severity index, 15th stapp car crash conference. SAE Technical Paper No. 710881, pp 771–796
16. Mertz HJ, Patrick LM (1971) Strength and response of the human neck. In: Proceedings of the fifteenth stapp car crash conference, SAE Paper No. 710855

Chapter 3

Rated Life Calculation Potential of Gearbox Model Based Force Estimates

Jan Helsen, Daniele Brandolisio, Bart Peeters, Frederik Vanhollebeke, Joris Peeters, David Moens, and Wim Desmet

Abstract One main contributor for gearbox rated lifetime estimation is the assessment of bearing loading during predicted operating conditions. This paper investigates an approach to determine input bearing loading by means of a TPA (Transfer Path Analysis) approach. TPA is suggested to retrieve internal bearing forces from acceleration measurements acquired at the outside of the gearbox housing. However, classical TPA methods would require the gearbox to be dismantled during the transfer path determination process. This poses significant practical challenges. To overcome this issue, this paper investigates the possibility of using a flexible multibody simulation model to calculate the different frequency response functions between bearings forces and acceleration sensors. All simulations use a flexible multibody modeling approach, which has been extensively validated. Main results of this validation process have been published by the authors in the past. The paper discusses the results of such analysis on a multi-megawatt wind turbine gearbox. Here, simulated acceleration measurements on the gearbox housing are processed into bearing forces. The feasibility of using these forces for a rating life calculation is investigated.

Keywords Gearbox dynamics • Multibody • Transfer path analysis • Model inversion • L-curve

3.1 Introduction

High reliability and optimized noise and vibration behavior are important aspects of a good wind turbine design [1]. Bearing loading during operating conditions plays an important role in both fields [2, 3]. Therefore, it is essential to accurately determine these loads. However, direct bearing load measurements pose significant challenges both from a measurement technology point of view as in the practical realization of the instrumentation inside the gearbox. The possible use of sensors on the outside of the gearbox housing such as accelerometers has several advantages: amongst others their easy installation, robustness to external influences and low price in comparison to internal instrumentation. Nonetheless, the challenges are shifted to the determination of the relationships between the different internal quantities and the signals measured on the outside of the system. This paper uses an approach based on transfer path analysis (TPA). However, classical TPA methods would require the gearbox to be dismantled during the transfer path determination process. This poses significant practical challenges. To overcome this issue, this paper investigates the possibility of using a flexible multibody simulation model to generate the necessary input information for the transfer path calculations.

J. Helsen (✉) • D. Brandolisio • W. Desmet
Mechanical Engineering Department, KU Leuven, Celestijnenlaan 300b bus 2420, Leuven, Belgium
e-mail: jan.helsen@mech.kuleuven.be

B. Peeters
LMS International, Interleuvenlaan 68, Leuven, Belgium

F. Vanhollebeke • J. Peeters
ZF Wind Power NV, Ottergemsesteenweg 439, Ghent, Belgium

D. Moens
Department of Applied Engineering, Lessius Mechelen – Campus De Nayer, Jan De Nayerlaan 5, 2860 Sint-Katelijne-Waver, Belgium

Different drivers govern wind turbine gearbox behavior in the different frequency ranges of interest [4]. In this work three ranges of interest are defined: the quasi-static range, gearbox rigid dynamic range and gearbox flexible range. The gearbox behavior in the first frequency range is completely defined by the quasi-static response of the drivetrain to quasi-static external loading originating from the rotor and the generator. In the second frequency range the rigid body motions of the gearbox and other wind turbine drivetrain components are the main drivers of the drivetrain dynamics. The third frequency range shows highly complex modal behavior. Local gearbox flexibilities and local modal behavior are significant drivers in this frequency range. Since TPA uses the local gearbox modal behavior to link different quantities within a system this technique is advisable for the third frequency range. Therefore, the approach discussed in this paper will focus on bearing force estimation in the third frequency range. The paper ends with the study of the applicability of the identified loading histories for bearing rated life estimation.

3.2 Methodology

The radial and axial loads acting on the internal bearings are identified during operating conditions by means of a system inversion method: a set of measured external operational response signals are combined with an inverted system model for the calculation of specific bearing forces. The inverted model can be frequency or time domain based. The pure gearbox housing model is used, without the presence of internal components to avoid terms that could result in coupling effects.

3.2.1 Frequency Domain Technique

To estimate the bearing forces a transfer path based approach (TPA) is used to retrieve the internal quantities. The model matrix consists of transfer functions between input bearing forces and output accelerations. Matrix inversion is applied to retrieve the input forces. To overcome the disassembling issue, a flexible multibody simulation model is used to calculate the different frequency response functions between bearings forces and acceleration sensors. The virtual models used in this investigation are based on previously validated models [5–7].

The proposed method consists of the following steps:

1. Select the n bearing force degrees of freedom (DOFs) to investigate.
2. Determine $2 \times n$ optimal acceleration positions on the gearbox housing. $2 \times n$ is suggested based to achieve a better pseudo inverse matrix.
3. Determine FRF matrix H between the bearing forces and chosen acceleration locations of the pure gearbox housing.
4. Calculate the pseudo inverse of the FRF matrix for each frequency of interest.
5. Measure acceleration signals at the selected response locations during operating conditions.
6. Multiply the inverted FRF matrix with the measured accelerations to calculate the bearing forces.

3.2.2 Time Domain Technique

In addition to the analysis in the frequency domain it is possible to perform a time domain based approach. The assumption made in this method is that the full dynamic behavior of the system is linear and fully known since a model is used to describe the system. This implies that a discrete-time state-space model of the system can be defined:

$$\dot{x} = A x + B u \quad (3.1)$$

$$y = C x + D u \quad (3.2)$$

with x_k the vector containing the states of the system, u_k the vector of the externally applied forces and y_k the vector with the resulting system responses. In the gearbox case the external forces applied to the forward model are all bearing and gear forces introduced in the gearbox housing.

Since the system matrices (ABCD) are fully known in the simulation model it is possible to analytically invert the system to obtain the inverse model. Writing this model again in state space notation as a function of a new x_{inv} -vector containing the inverse states and the u_{inv} -vector containing the accelerations on the gearbox housing results in:

$$x_{inv} = (A - B.D^{-1}.C) x_{inv} + (B.D^{-1}) u_{inv} \quad (3.3)$$

$$y_{inv} = D^{-1}.C.x_{inv} + D^{-1}.u_{inv} \quad (3.4)$$

or

$$x_{inv} = A_{inv} x_{inv} + B_{inv} u_{inv} \quad (3.5)$$

$$y_{inv} = C_{inv} x_{inv} + D_{inv} u_{inv} \quad (3.6)$$

Time simulation using acceleration signals as input vector u_k allows the calculating the force response vector at the bearing and gear force locations.

3.3 Accuracy Considerations

Three main drivers determine the accuracy of both the frequency and the time domain approach: the system model accuracy, the model inversion error and the system observability corresponding to the used sensor set-up. The ability of the reduced model, in this case the gearbox housing, to describe the system dynamics determines the model accuracy. If experimental FRFs are used the main error sources are measurement errors. In the case of a model-based approach the quality of the experimental model update is the defining factor. Since the forward model linking accelerations to input forces is used, errors will be introduced by matrix inversion of the FRF matrix in case of the frequency based approach and D-matrix inversion for the time based approach. The third source of error is due to measuring only a reduced set of response points, which could result in bad observability of certain dynamic content of the system. The following paragraphs define an optimization approach for improving the quality of the matrix inversion and discuss the observability challenges.

3.3.1 Observability and Optimal Sensor Locations

The dynamic response of the system is measured by means of acceleration sensors placed on the gearbox housing. If one is considering the state-space equations the state-space vector contains the number of independent variables needed to fully describe the state of the system. In practice however it is not possible to monitor all degrees of freedom. Therefore the vibration sensors should be placed on those locations that result in maximal observability. This paper suggests the use of the condition number of the system FRF matrix to choose the most optimal sensor locations. The condition number of a matrix is the ratio of the largest singular value to the smallest singular value of the matrix. It is a measure of the ill conditioning of the matrix. Reduction of condition numbers usually results in an improved force determination [8]. Literature review revealed that it is suggested to use at least twice the number of forces to estimate as number of response points [9]. This paper suggests a bootstrapping approach to choose the optimal locations. A net of virtual accelerometers is created on the surface of the gearbox housing. An initial accelerometer location needs to be selected from the virtual accelerometer net. Subsequently the algorithm adds additional accelerometers one by one until the total number of requested accelerometers is reached. For each time an accelerometer is added the influence of all virtual accelerometers on the total FRF matrix condition number is tested. All accelerometers of the virtual net are added one by one and the corresponding condition number of the FRF matrix recorded. The accelerometer corresponding to the minimum condition number is chosen as additional accelerometer and added to the set.

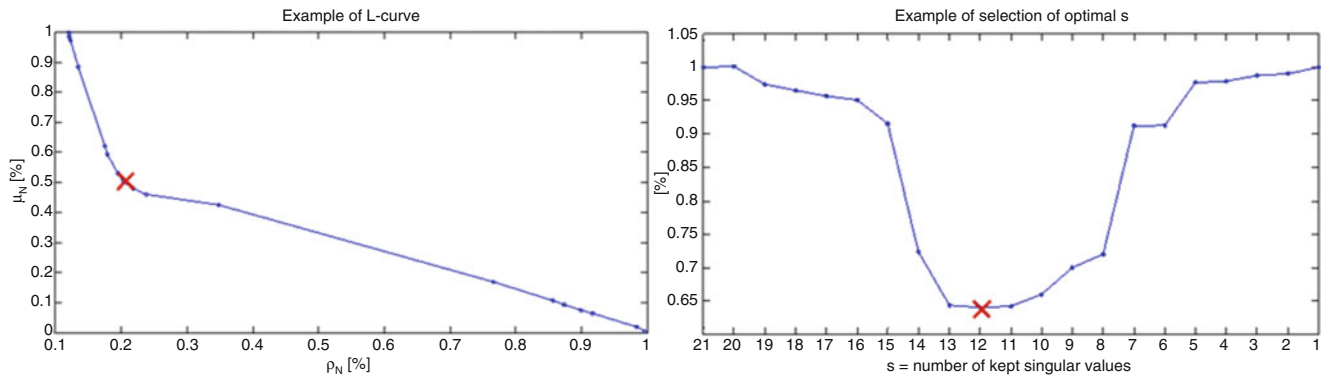


Fig. 3.1 Example of L-curve and corresponding parametric curve

3.3.2 Pseudo-Inverse Matrix Calculation

A critical step in both the frequency and time based approach is the inversion of the FRF matrix or system D matrix. Traditionally a pseudo inverse is calculated. The classical least-squares approach is used to calculate the pseudo inverse of the FRF matrix. Good conditioning of the FRF matrix is essential for high quality inversion. There are several influence factors for ill conditioning. Two or more excitations can be too close and are therefore difficult to separate due to too equivalent response. Another possibility is poor modal participation of the response particularly in low frequency or in the vicinity of lightly damped resonant frequencies of the structure. The number of modes significantly participating to the response has to be at least equal to the number of unknown forces. In the case of ill-conditioning some linear dependencies are introduced between columns of the transfer matrix. Several linear combinations exist, which could generate the measured deflection shapes with equivalent residual quantities. Therefore one of these solutions has to be chosen. The strict application of the classical least-squares approach would lead to the selection of the solution with the smallest residue, but the magnitude of this solution is often too large to be realistic [8, 10]. Many solutions with significantly higher residue are far more realistic. Different methods exist. The most popular regularization methods are truncated singular value decomposition (TSVD) and Tikhonov [10]. These methods are based on the adjustment of a regularization parameter, that changes the importance given to the minimization of the residue norm on the one hand and the solution norm on the other hand. Many variants of this method are available. This document discusses an approach based on the L-curve principle [11]. The L-curve principle is combined with a TSVD regularization, based on the singular value decomposition of the transfer matrix:

$$[H]_{mn} = [U]_{mn}[S]_{nn}[V]_{nn}^* \quad (3.7)$$

With:

- H: FRF Matrix
- M: number of outputs (response points)
- N: number of inputs
- S: diagonal matrix of singular values sorted in descending order
- V: unitary matrix
- U: matrix such that $U^* \cdot U = I$

The TSVD is based on an approach to regularize the matrix $[S]_{nn}^{-1}$ by zeroing the last elements of the diagonal matrix. A regularizing parameter s corresponding to the number of kept singular values is defined. $(n-s)$ singular values are set to zero in this approach. Since the elements of S are arranged in descending order this corresponds to the $(n-s)$ smallest singular values. The regularized pseudo-inverse of the transfer matrix based on the chosen s number can be written as follows:

$$[H]_{mn}^+ = [V]_{nn} \begin{bmatrix} [S]_{ss}^{-1} & 0 \\ 0 & 0 \end{bmatrix} [U]_{mn}^* \quad (3.8)$$

The parameter s is the artificial rank given to the transfer matrix. In case the system matrix is rank deficient the parameters s should be chosen such that the solution of the above equation is of minimal norm. The selection is done based on the L-curve principle adapted for TSVD discussed in [10]. The selection is based on the parametric curve with the residue norm (ρ) on the x-axis and the solution norm (η) on the y-axis in function of the regularization parameter s . Figure 3.1 shows an example of such an L-curve.

The inputs for the L-curve are defined by:

$$\rho_N(s) = \frac{\|X - [H] F\|}{\|X\|} \quad (3.9)$$

$$\mu_N(s) = \frac{\mu(s)}{\mu(n)} \quad (3.10)$$

$\rho_N(s)$ and $\mu_N(s)$ are the values of the solution norm and the normalized residue norm for $s = n$. This is the case of no regularization. The equation below uses these parameters to determine the optimal point on the L-curve [10]:

$$\varepsilon(s) = \rho_N(s) + \mu_N(s) (1 - \rho_N(n)) \quad (3.11)$$

The optimal point of the L-curve is its angle for which the decrease of s has caused an important diminution of the solution norm η without a significant growth of the residue norm ρ . For the L-curve shown in the figure above the red cross marks the optimal point.

3.4 Virtual Models

A representative multi-megawatt wind turbine gearbox is chosen for the feasibility study. Two models are used: a full gearbox flexible multibody model and a gearbox housing Craig Bampton Reduced finite element model. The former model is used to generate reference signals, whereas the latter model is used in the actual TPA calculations. Figure 3.2 shows the layout of the flexible multibody model of the entire wind turbine gearbox. The bearings under investigation are highlighted. The gearbox consists of three stages: a High Speed Stage containing the High Speed Shaft (HSS) with bearings HSS_B1 and HSS_B2, and the Low Speed Shaft (LSS) with bearings LSS_B1 and LSS_B2; A planetary Intermediate Speed Stage with one bearing PS2_B1; A planetary Low Speed Stage with bearings PS1_B1 and PS1_B2.

On the outer surface of the gearbox model, 205 virtual tri-axial accelerometers are placed in a grid pattern, thus to cover the entire surface of the housing and capture the most information to allow for a future observability study.

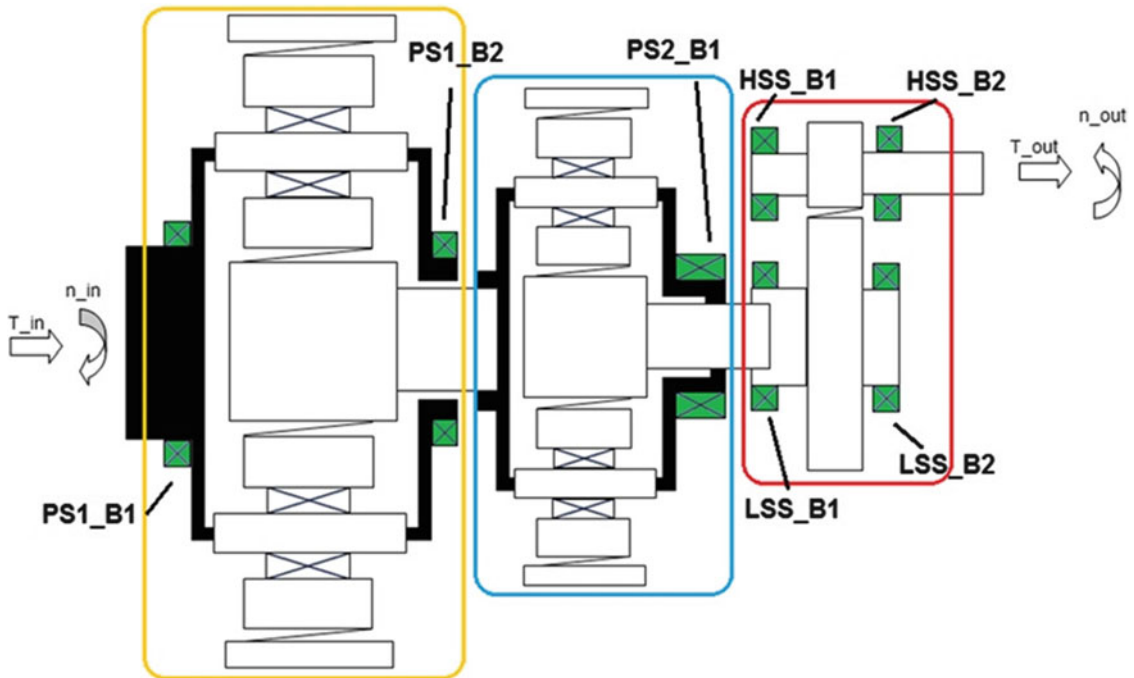


Fig. 3.2 Gearbox scheme and bearings locations (green) (Color figure online)

3.5 Virtual Experiment

To assess the potential of the time and frequency based TPA method a virtual experiment is conducted. For brevity reasons only the frequency based approach is discussed. The full gearbox model is used to generate time signals for all bearing forces of interest and accelerometers of the virtual accelerometer net. Nominal torque is applied to the planet carrier at the gearbox input. A rotational damper at the HSS output shaft creates steady state conditions after an initial run-up. Dynamic excitation is originating from the gear meshing at the different gear stages. Two seconds of signal length are cut from these steady state conditions and used as input for the TPA calculations. The input acceleration signals for the TPA are a subset of 63 acceleration signals. This number of sensor signals is equal to three times the number of bearing forces to estimate. Figure 3.3 shows an example bearing force frequency spectrum for TPA estimation and full gearbox model time simulation. Forces are compared at the different gear meshing frequencies, since excitation is necessary to result in a representative acceleration signal on the housing. In general it can be concluded that estimate quality changes over frequency. The errors can be due to observability and model inversion issues. Estimation tended to be worse at lower frequencies, which is in line with the higher condition numbers found in the low frequency range. Strain signals could be added to the measurement set to improve this low frequency behavior. Further investigations will focus on improving these condition numbers and trying to optimize observability.

3.5.1 Potential for Bearing Rated Life Calculations

A common calculation method for rated life of bearings is the L_{10} -approach. Bearing life is expressed as the number of revolutions a bearing can achieve with 10 % failure probability [12]. The input for these calculations is a bearing force time signal for the axial and two radial DOFs. In a first step these forces are classified in load bins depending on their value. These bin values for axial and radial DOFs are used as input to determine the total loads in the different DOFs and combine these loads into a total equivalent load:

$$P_{eq} = XF_r + YF_a \quad (3.12)$$

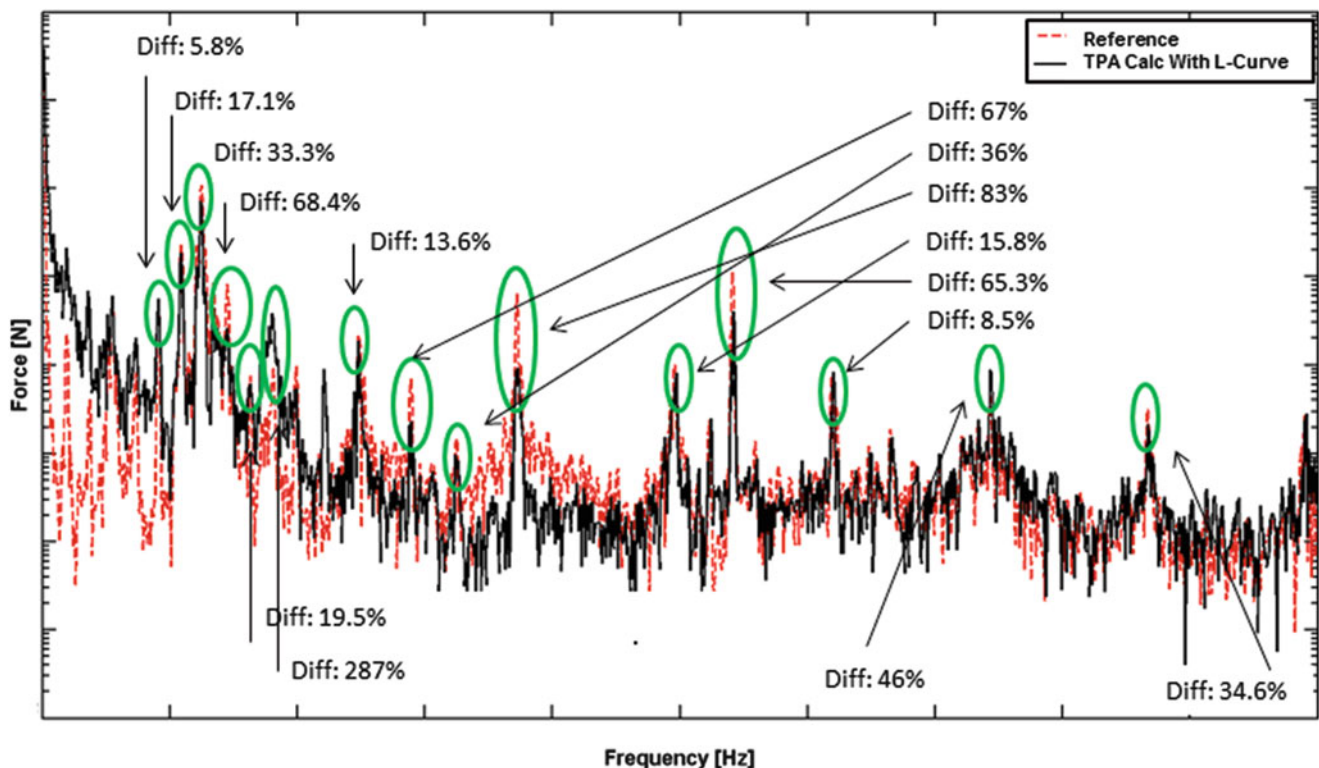


Fig. 3.3 Example of estimated bearing forces

with:

- F_r : Radial force
- F_a : Axial force
- X, Y : Specific bearing coefficients from catalogue
- P_{eq} = equivalent dynamic bearing load

Including all equivalent bearing loads in the following formula results in an estimate of the rated life:

$$L_{10} = \left(\frac{C_D}{P_{eq}} \right)^p \quad (3.13)$$

with:

- C_D = dynamic load rating (from catalogue)
- $p = 3$ for ball bearings, $10/3$ for roller bearings

There are several challenges with using the L_{10} -approach in combination with the TPA approach. The first is the need for time-based signals. This challenge can be overcome by using the inverse FFT to transform the signals back to the time-domain. Since the bins-approach is used there is no need to save the exact moment in time that a peak occurred. The second main challenge is the quasi-static character of the L_{10} -approach. The dynamic forces shown in the TPA spectra are superimposed on the quasi-static force fluctuations. Due to their low amplitude they are not visible in the force bins. Nonetheless there is a large number of cycles related to these loading conditions. To be able to objectively include their influence on the overall rated bearing life it would however be necessary to adjust the L_{10} approach. Since the TPA approach delivers the full frequency spectrum this extension is needed in order to fully use the potential of the TPA.

3.6 Conclusions

This paper discussed a TPA based approach to determine bearing forces of a wind turbine gearbox by means of external acceleration measurements on the housing. The different challenges related to the estimation were suggested and a full method was described. The compatibility of this approach with classical L_{10} rated bearing life discussed and concluded that an extension of the classic formulae is needed if the non-quasi static forces identified by the TPA want to be included.

Acknowledgements The IWT Flanders within the ALARM, Prognostics for Optimal Maintenance 2 and OptiWind projects. The IWT Flanders PROTEUS mandate of Jan Helsen.

References

1. Aberrazq MA, Hahn B (2006) Analysis of the wind turbine standstill for a grid connected wind farm (case study). *Renew Energ* 33:89–104
2. Errichello R, Muller J (2011) Gearbox reliability collaborative gearbox 1 failure analysis report. NREL report, NREL/SR-5000-53062
3. Guo Y, Keller J, LaCava W (2012) Combined effects of gravity, bending moment, bearing clearance and input torque on wind turbine planetary gear load sharing. In: AGMA fall technical meeting, Dearborn
4. Helsen J, Marrant B, Vanhollebeke F, De Coninck F, Berckmans D, Vandepitte D, Desmet W (2013) Assessment of excitation mechanisms and structural flexibility influence in excitation propagation in multi-megawatt wind turbine gearboxes: experiments and flexible multibody model optimization. *Mech Syst Signal Process* 40(1):114–135
5. Peeters J (2006) Simulation of dynamic drive train loads in a wind turbine. PhD dissertation, KU Leuven, Belgium. <https://repository.libis.kuleuven.be/dspace/handle/1979/344>
6. Vanhollebeke F, Helsen J, Peeters J, Vandepitte D, Desmet W (2012) Combining multibody and acoustic simulation models for wind turbine gearbox NVH optimisation. In: Proceedings of ISMA 2012, Leuven
7. Helsen J (2012) The dynamics of high power density gear units with focus on the wind turbine application. PhD dissertation, KU Leuven, Belgium. <https://lirias.kuleuven.be/handle/123456789/337483>
8. Thite AN, Thompson DJ (2006) Selection of response measurement locations to improve inverse force determination. *Appl Acoust* 67:797–818
9. Gajdatsy PA (2011) Advanced transfer path analysis methods. Dissertation, KU Leuven, Belgium. <https://lirias.kuleuven.be/handle/123456789/289454>
10. Leclère Q, Pezerat C, Laulagnet B, Polac L (2005) Indirect measurement of main bearing loads in an operating diesel engine. *J Sound Vib* 286:341–361
11. Hansen PC (2000) The l-curve and its use in the numerical treatment of inverse problems. <http://citeseer.nj.nec.com/196586.html>
12. ISO 281: Rolling bearings – Dynamic load ratings and rating life, International organization for standardization

Chapter 4

Electromechanical Impedance Based Crack Detection for a Rotating Machine

Aldemir Ap Cavalini Jr, Roberto Mendes Finzi Neto, and Valder Steffen Jr

Abstract Visual examination, ultrasonic tests, and dye penetrant inspection, are some examples of nondestructive techniques widely used for crack detection in rotors. These methods have proved to be costly, since satisfactory results rely on detailed and periodic inspections. Significant research effort has been directed in recent years to online monitoring techniques, i.e., based on vibration signals measured during rotor operation. However, most of them are able to only detect deep cracks. The uniqueness of this paper relies on the detection of incipient transverse cracks in rotating shafts by using the so-called, electromechanical impedance method. This method has become a promising tool for structural health monitoring of machines due to its sensitivity to small local damage. Basically, the method monitors changes in the electric impedance of piezoelectric transducers, bonded to (or embedded into) the host structure, through specific mathematic functions, the so-called damage metrics, to detect damage. This is possible because the transducer's impedance is directly related to the mechanical impedance of the structure. In this context, successful experimental tests were performed in a horizontal rotor supported by roller bearings. PZT patches were bonded along the rotor's shaft, in which transverse cracks were introduced. The technique was validated under different unbalance conditions.

Keywords SHM technique • Rotating machine • Crack detection • Electromechanical impedance method • Catastrophic failures

4.1 Introduction

According to [1], shaft crack detection is a very serious matter, and machines that are suspected of having a crack must be treated with the upmost respect. The importance attributed to this problem is addressed to the serious consequences when cracks are not early identified in rotating systems. In 1987 [2], Allianz, a consolidated insurance company, organized a conference about the prevention of catastrophic failures in rotating machinery. During this event, 37 cases of crack detection were reported to have occurred only in Europe after 1967. Additionally, 16 cases of catastrophic failure were presented, being some of them credited to the presence and propagation of transverse cracks. Accidents of this magnitude are usually kept in secret by the manufacturers. However, documented information shows that cracks have been detected continuously in steam turbines, generators, and pumps of industrial plants in Europe, North America, etc.

Although there are no statistical studies that account for the exact dimension of the damage caused by cracks in rotating shafts, the Electric Power Research Institute estimates that approximately \$1 billion were expended in repairs, exchanges, loss of production, etc., in electrical industries, nuclear, and conventional, since the 1970s [3]. Thus, manufacturers have adopted design concepts (shafts manufactured with materials that have high values of fracture toughness on the operation temperature), as well as, special procedures for startup, operation, monitoring, and maintenance, in order to minimize the appearance and grown of cracks in different rotors, such as, steam turbines, centrifugal compressors, and generator units found in hydroelectric plants.

A.A. Cavalini Jr (✉) • R.M. Finzi Neto • V. Steffen Jr
LMEst - Structural Mechanics Laboratory, INCT (EIE) - National Institute of Science and Technology, Federal University of Uberlândia, School of Mechanical Engineering, Av. João Naves de Ávila 2121, Uberlândia, MG 38408-196, Brazil
e-mail: aacjunior@mecanica.ufu.br

There are several structural monitoring techniques, the so-called SHM techniques, proposed in the literature for crack detection in rotating machines. Among them, the ones based on vibration measurements are recognized as useful tools because they lead to satisfactory results even when the damage location is not accessible or even unknown [4]. About these kind of techniques, two accepted rules are employed for detecting a crack. The first one is based on the monitoring of the synchronous vibration amplitude and phase. According to [1], changes in $1\times$ amplitude and phase are the primary indicators of crack presence. The second rule relies on $2\times$ vibrations, where [1] states that if a cracked rotor has a steady unidirectional radial load, then a strong $2\times$ response may appear when the rotor is turning at half of any balance resonance speed. However, although widely used in industry, when applied in non-ideal conditions such techniques can detect cracks that eventually have already spread significantly by the cross section of the shaft, usually above 40 % of its diameter. Therefore, currently, the researchers' attention is turning to more sophisticated methods capable of identifying incipient cracks (cracks that spread up to 25 % of shaft diameter), which represent a type of damage that are hardly observable in vibration analysis.

In this context, the aim of this paper relies on the detection of incipient transverse cracks in rotating shafts by using the so-called electromechanical impedance method. This technique measures the electromechanical impedance of the structure by using patches of piezoelectric material (PZT patches) bonded on the surface of the structure (or embedded into it). Through the PZT sensor-actuators, the electromechanical impedance, which is directly related to the mechanical impedance of the structure, is obtained. Based on changes of the impedance signals (e.g., due to the growing crack), the damage can be detected. Damage metrics are normally used to quantify the severity of the failure [5]. The electromechanical impedance method has advantages over other SHM techniques [6]. The mathematical model of the structure is not required, which allows the application of the proposed technique in complex systems. Additionally, the results generated by the technique are easily to interpret and they are prone to be adapted to continuous monitoring. This SHM technique operates at high frequencies as compared to the range of frequencies that are normally used in modal analysis (sensitive to incipient damage). The PZT patches have a wide linearity range, being lightweight and durable. Consequently, this method is extensively applied to damage detection, particularly in aircraft structures. In [7], an extensive literature review is available regarding various applications of this technique.

It is important to point out that no reports were found in the available databases on the application of the electromechanical impedance method in rotating systems, which makes this proposal quite unique in the area of rotor dynamics. There are particularities specific to the application of the method in rotor systems. For example, the rotor is dynamically excited. In most studies about crack detection by using the electromechanical impedance method, the impedance signatures are measured with the structure at rest. Another particularity is related to the device that enables the acquisition of the impedance signal when the rotor is in operation. Clearly, in this type of application electrical signals have to be transmitted by electric cables from the rotating shaft to a fixed measurement system (and vice versa) with little interference of noise even when the rotor is operating at high speeds. These special features will be discussed along this work.

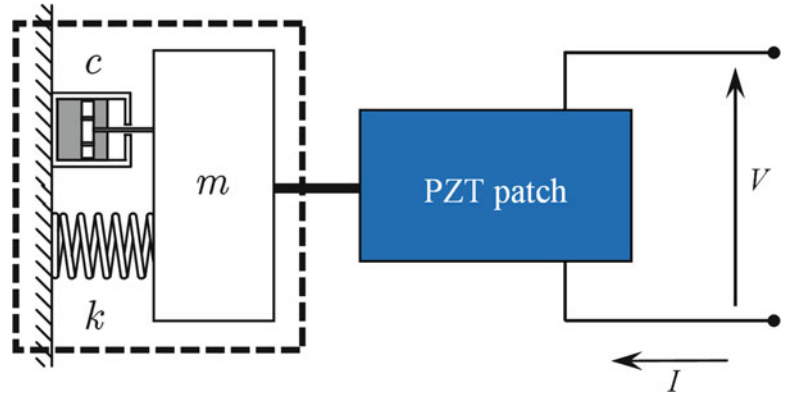
4.2 Impedance Based Structural Health Monitoring

The impedance based SHM technique was first proposed by [8], and subsequently the method was extended by many other researches [9–15]. As mentioned, this technique uses small PZT patches (impedance sensors) to monitor changes in the structure that may occur due to the appearing of damage (changes in stiffness, damping, and mass). When the PZT is bonded to the structure and a low electric voltage is applied, generally 1V [16], a strain is produced. Using a high excitation frequency (in terms of typical modal analysis testing), the dynamic response of the structure will represent only the local area around the sensor. The dynamic response of the induced mechanical vibrations is transmitted by the same PZT patch as an electrical signal. Thus, if an incipient damage was grown in the system, changes can be observed in the electric response measured by the PZT (dynamic response that leads to an impedance signature). The electromechanical model that quantifies and describes the measurement process is illustrated in Fig. 4.1 for a single degree of freedom system (mass m , stiffness k , and damping c ; V and I are the voltage and current, respectively).

For this system, [8] demonstrated that the admittance $Y_a(\omega)$ (inverse of the impedance) of the PZT patch can be written as a function of the combined PZT actuator and structure mechanical impedances, $Z_{ma}(\omega)$ and $Z_{me}(\omega)$, respectively, as given by Eq. (4.1):

$$Y_a(\omega) = I(\omega) \omega a \left\{ \varepsilon_{33}^T [1 - I(\omega) \delta] - \frac{Z_{ma}(\omega)}{Z_{ma}(\omega) - Z_{me}(\omega)} d_{3x}^2 \hat{Y}_{xx}^E \right\} \quad (4.1)$$

Fig. 4.1 Electromechanical model that describes the process of measuring the impedance signature



where \hat{Y}_{xx}^E is the complex Young's modulus of the PZT with zero electric field, d_{3x} is the piezoelectric coupling constant in the arbitrary x direction at zero electric field, ε_{33}^T is the dielectric constant at zero stress, δ is the dielectric loss tangent to the PZT, a is a geometric constant of the PZT, and is ω the frequency. Assuming that the mechanical properties of PZT do not vary over time used for monitoring, Eq. (4.1) shows that the electrical impedance of the PZT patch is directly related to the structure's impedance (damages cause changes in the structure's mechanical impedance). As shown in Eq. (4.1), the impedance is a complex function of the frequency having real and imaginary parts. The real part is more sensitive to structural changes, i.e., it is the most suitable for the detection of damage [17].

Extensively applied in different structures, particularly in aircrafts, the electromechanical impedance method operates at high frequencies (typically ranging from 30 to 250 kHz, determined by a trial and error method) and has an accurate sensitivity to incipient damage [18]. According to [7], for a simple PZT patch, a damage located at a distance up to 0.4 m can be identified in composite materials and up to 2 m in bars consisting of a single metal. The impedance signature is determined by means an impedance analyzer. The structural integrity assessment is made based on the comparison of impedance signatures measured before and after the occurrence of a possible damage. A visual comparison is not enough, being necessary to use quantitative criteria. In this sense, the so-called damage metrics is defined, which is represented by scalar parameters that are able to represent numerically the difference between two measurements. Among the various damage metrics proposed, the root mean square (RMS), the deviation of the root mean square (RMSD), and the deviation of the correlation coefficient (CCD), are the mostly used.

As the first damage metric, Eq. (4.2) defines the root mean square (RMS).

$$RMS = \left\{ \sum_{i=1}^n \frac{[\text{Re}(Z_{1i}) - \text{Re}(Z_{2i})]^2}{n} \right\}^{1/2} \quad (4.2)$$

where $\text{Re}(Z_{1i})$ is the real part of the impedance signature of the system without damage (reference value: *Baseline*) and $\text{Re}(Z_{2i})$ is the real part of the impedance signature of the system for an unknown structural condition, n is the number of points (frequency vector) of the impedance signal ($i = 1, 2, \dots, n$).

The deviation of the root mean square (RMSD) is given by Eq. (4.3). This metric is not qualitatively affected when applied in impedance signatures obtained from different PZT patches (different amplitude levels).

$$RMSD = \left\{ \sum_{i=1}^n \frac{[\text{Re}(Z_{1i}) - \text{Re}(Z_{2i})]^2}{\text{Re}(Z_{1i})^2} \right\}^{1/2} \quad (4.3)$$

The deviation of the correlation coefficient, CCD, is used to measure and interpret the information found in both data sets considered. The mathematical formulation of this metric is given by the difference between the first scale and the correlation coefficient CC of the signatures obtained from any measurement and its reference [19]. The greater the correlation coefficient, CC , the smaller will be the deviation CCD and smaller are the changes caused by the damage in the system.

$$CCD = 1 - CC = 1 - \frac{1}{n} \sum_{i=1}^n \frac{[\text{Re}(Z_{1i}) - \text{Re}(\bar{Z}_{1i})] - [\text{Re}(Z_{2i}) - \text{Re}(\bar{Z}_{2i})]}{S_{Z1} S_{Z2}} \quad (4.4)$$

where $Z_{1,i}$ is the impedance of the PZT patch measured at healthy conditions, $Z_{2,i}$ is the impedance for the comparison with the *baseline* measurement at frequency interval i . The symbols \bar{Z}_{1i} and \bar{Z}_{2i} represent mean values, while S_{Z1} and S_{Z2} represent standard deviations.

4.3 Experimental Results

Figure 4.2 shows the test rig used in the application of the SHM technique proposed by this work, i.e., the detection of incipient transverse cracks in rotating shafts by using the electromechanical impedance method. This machine is composed by a flexible steel shaft with 860 mm length and 17 mm diameter, and two rigid discs, both of steel with 150 mm diameter and 20 mm thickness (approximately 2.65 kg each). The shaft is supported by two roller bearings, one of them is a hybrid bearing with electromagnetic actuators (not used in the present contribution). The system is driven by a DC electric motor of 0.5 CV (*Varimot*[®] model BN90M). Its angular position is monitored by means of an encoder (coupled to the free end of the DC electric motor), which is able to produce 1 or 720 pulses per revolution of the shaft (*Suprasonic*[®] model CSS58C-6). The interaction between the electric motor and the shaft is minimized by means of a special coupling named *Lami-Torq* (*Acoplast*[®] model GTG 402 100). From a representative mathematical model of the rotor (finite element model), the first two critical speeds were determined, being approximately: 1,685 rev/min (28.1 Hz) and 5,430 rev/min (90.5 Hz).

As mentioned, the electromechanical impedance method is able to detecting the presence of structural defects at a distance up to 2 m from the PZT patch (simple beam metal without barriers). Clearly, this is not the case of the rotor shown in Fig. 4.2 (three sections limited by the discs). Thus, four PZT patches (12×6 mm) were distributed along the shaft placed at 90° from each other to cover the largest possible surface for detection. For this aim, four machining processes as show in Fig. 4.3 were performed.

An extra PZT (15×15 mm) was coupled to the side of one disc to investigate if sensors orthogonal to the damage are able to detect the failures. This becomes interesting because, if successful, it would not be necessary to perform the machining on the shaft surface. Of course, the above machining process is a drawback of the method (e.g. in industrial machines the PZT patch may be coupled to pulleys). The PZT coupling was performed by using the glue *REPSOL*[®], selected for its good adhesion (piezoelectric patches to steel structures). Figure 4.4 shows a schematic arrangement with each of the five patches bonded to the system, namely PZT-1, PZT-2, PZT-3, PZT-4, and PZT-D (numbered starting from the hybrid bearing; B_1 in Fig. 4.3).

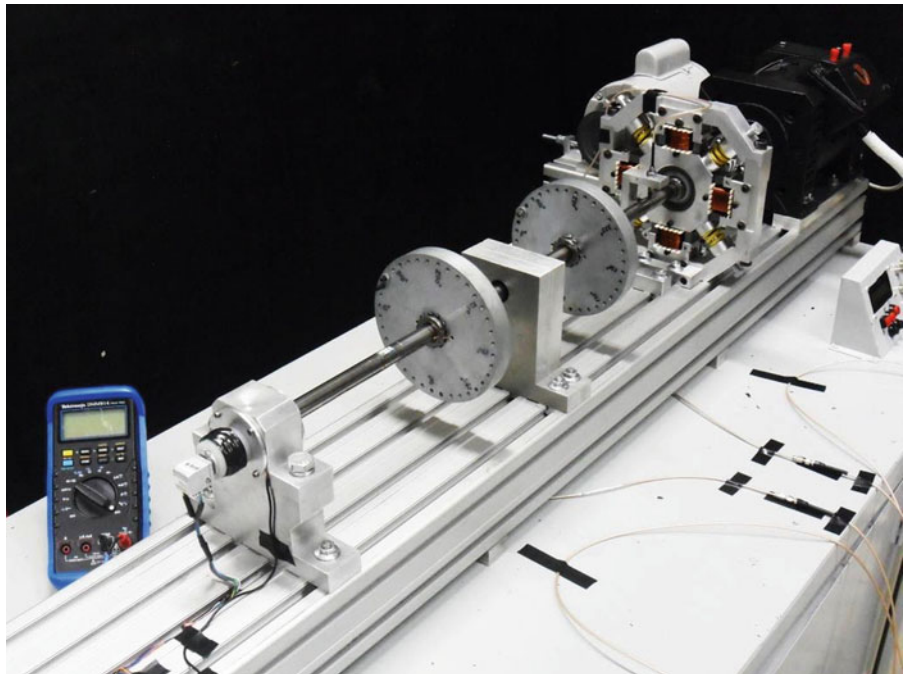


Fig. 4.2 Test rig used in the application of the electromechanical impedance method

Fig. 4.3 Machining process performed on the shaft surface to allow the coupling of the PZT patches



Fig. 4.4 Distribution of the PZT patches along the shaft and on the face of the disc (dimension in mm; note that this scheme is reversed from the picture of Fig. 4.2)

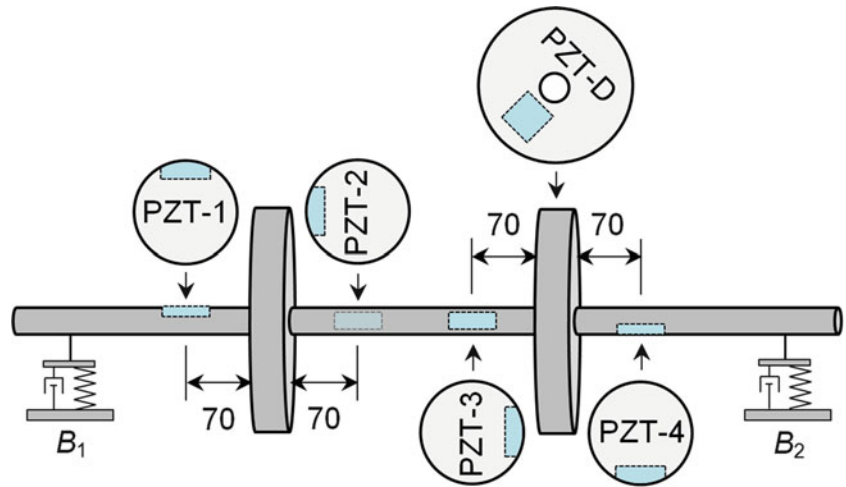
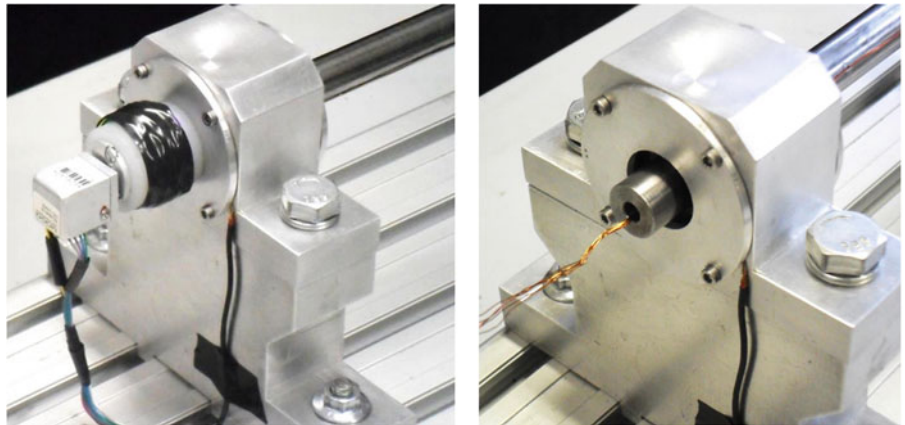


Fig. 4.5 Slip ring connected to the shaft end through the nylon device



For the measurement of the impedance signatures of the PZT patches with the test rig under operation condition (sending excitation signals to the PZT patches and acquiring the responses), a slip ring was used (*MOOG*[®] model EC3848-10). This device is able to transfer electrical signals from fixed to rotating parts (and vice-versa) with low noise interference, even with the rotor operating at high speeds (according to the manufactures, the device is able to transfer electrical signals from accelerometers with the rotor operating in a range of 0–10,000 rev/min). Figure 4.5 shows the slip ring connected to one of the shaft ends. Note that a nylon device was used for coupling the parts. Also, for the sake of clarity, a figure showing the slip ring before assemblage to the shaft can be seen.

Using a low-cost impedance measurement system [20], with the rotor at rest, a frequency sweep was applied to each PZT patch in the range between 0 and 200 kHz for determining the regions with the greatest number of peaks in the impedance signature. Only two evident peaks were found in the impedance signature of the sensors coupled to the shaft (signatures

Table 4.1 Frequency bandwidths used for each one of the five PZT patches

PZT	Frequency bandwidth (kHz)	
	From	To
1	169.1	170.2
2	168.6	169.8
3	168.6	169.8
4	168.7	170.2
D	170	180

Fig. 4.6 Details about the position of DAMAGE-1 in the shaft

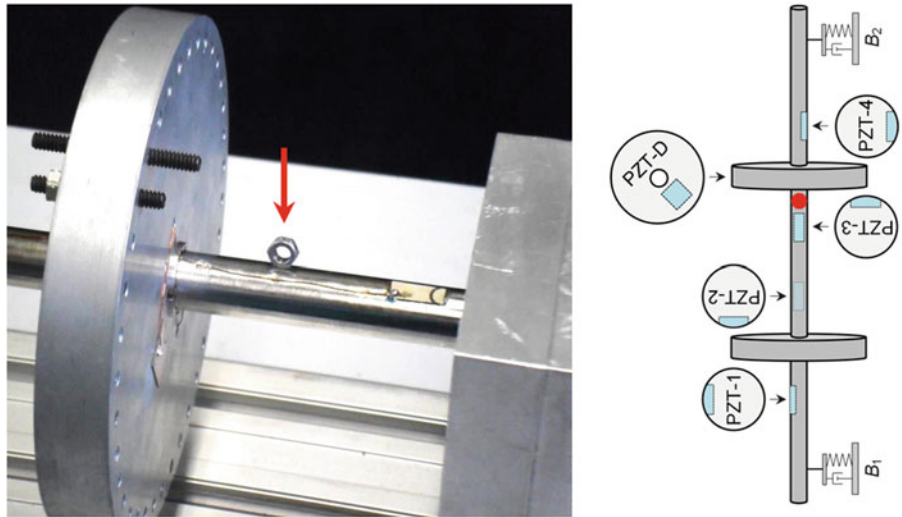
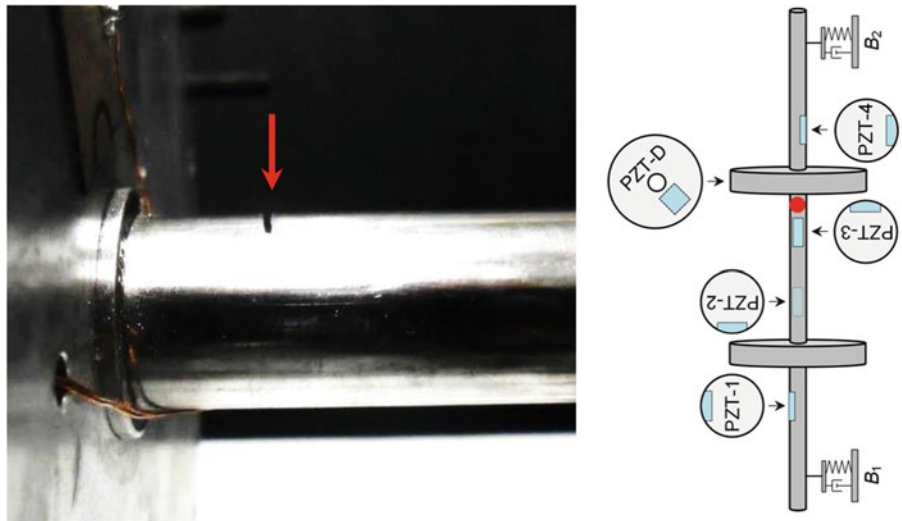


Fig. 4.7 Details of the saw cut performed on the shaft to simulate the crack (DAMAGE-2)

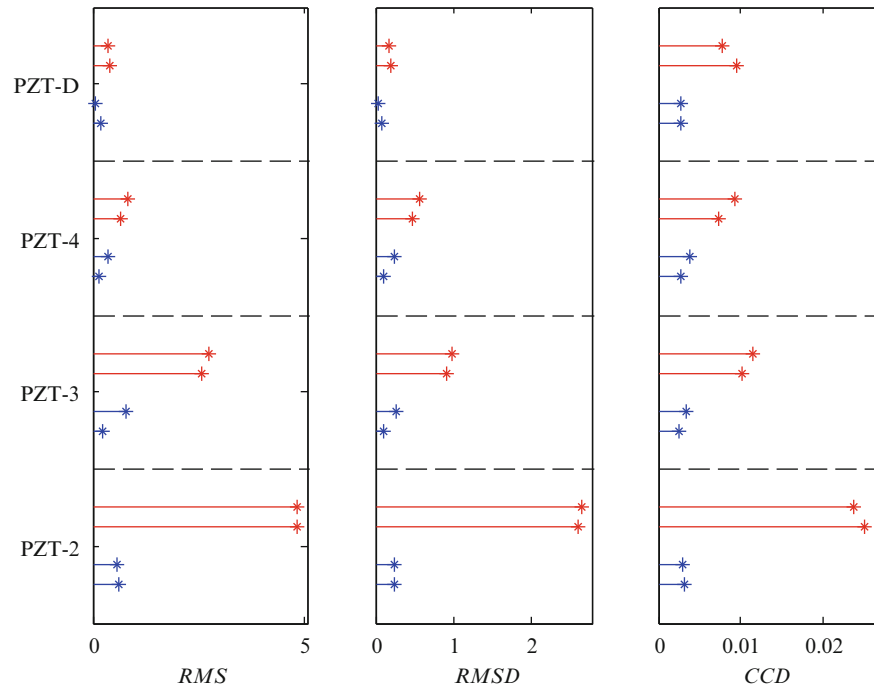


with 401 frequency points). Only the PZT attached to the disc showed more peaks, a result that is typically found in thick plates. Table 4.1 shows the frequency bandwidths determined. Note that the bands are delimited at high frequencies, which, as previously mentioned, allows for detecting incipient damage.

The tests with the proposed methodology included the analysis of two incipient structural damages. In the first one (DAMAGE-1), a steel nut was bonded on the shaft surface (mass of 1.06 g) at approximately 30 mm from one of the discs (40 mm from PZT-3; region delimited by the discs). This nondestructive damage (structural modification) was inserted to perform a preliminary evaluation of the proposed technique. Figure 4.6 shows the positions of PZT-3 and PZT-D, concerning the damage DAMAGE-1.

The second analysis, DAMAGE-2, is a destructive damage. In this case, a saw cut was performed along the shaft cross-section by using a thin machining disc to simulate a crack. This was done about 15 mm from one of the discs (55 mm from PZT-3; region delimited by the discs). The machining work led in a “crack” of approximately 0.5 mm thick and 2.5 mm depth (about 15 % over the shaft diameter), as shown in Fig. 4.7.

Fig. 4.8 Damage metric values obtained with the rotor balanced and operating at 1,200 rev/min for two different structural conditions: undamaged (blue line) and DAMAGE-1 (red line) (Color figure online)



In the analysis of both presented damages, the rotor was kept under 1,200 rev/min. However, two different unbalanced conditions were considered: balanced rotor (balancing performed by using the method of influence coefficients) and unbalanced rotor by 306 g mm/ -50° inserted on both discs (identical unbalances in both disks). Different operating speeds were evaluated, leading to similar results (not presented here). The impedance signals were calculated from an average of 10,000 measurements. In addition, a total time of 0.46154 s was used to measure the 10,000 signals related to each one of the 401 frequencies comprising the impedance signatures. This high number of measurements actually reduces the incidence of “noise” that arises from the dynamic behavior of the rotor (together with some electrical effects).

It is known that the variation of temperature may prejudice the results obtained by the electromechanical impedance method. In addition to the environmental temperature effects, specifically for this application, a temperature variation occurs due to the operation of the rotating machine. These effects are more pronounced in the regions close to the bearings (bearings acting as sources of friction). Of course, the temperature varies until stabilization (temperature increases with the rotational speed of the rotor). To minimize this problem, at each round of testing the rotor was kept under the same operation conditions for 60 min before initiating the measurement procedure. In both tests, the room temperature was controlled in the range between 18 and 21 °C.

Figure 4.8 shows the damage metrics obtained for the structural conditions of the rotor without damage and DAMAGE-1, considering the rotor balanced (remember that in all tests the rotor was in operation at 1,200 rev/min). Note that for all the damage metrics analyzed (*RMS*, *RMSD* or *CCD*), the sensors PZT-2 and PZT-3 were the best to detect DAMAGE-1. The PZT-D was not able to detect clearly the imposed damage. It is possible to observe that even PZT-4 was able to detect DAMAGE-1 (PZT apart from the damage by one disc). The results obtained from PZT-1 were discarded because this sensor presented incoherent results during the tests. Figure 4.9 shows the damage metrics determined when the conditions without damage were analyzed (the same results shown in Fig. 4.8) and the damage DAMAGE-2 (saw cut performed on the shaft surface; Fig. 4.7), considering the rotor balanced. Note that in all cases the damages could be detected satisfactorily. Analyzing Fig. 4.9, it can be seen that PZT-3 showed smaller variation from the *baseline* (reference condition; rotor without damage) than PZT-2, which are closer to the DAMAGE-2 (see Fig. 4.7). This leads to the conclusion that there is a difference involving the electromechanical coupling of these PZT patches with the shaft (probably due to the glue adhesion).

Figure 4.10 shows the impedance signatures measured by the PZT-3 determined for the rotor operating under each structural condition (according to the results shown in Figs. 4.8 and 4.9). Note that the largest deviation from the reference curve (*baseline*) occurs for the signature related with DAMAGE-1. The variation caused by the saw cut (DAMAGE-2) is small, an effect confirmed by the damage metrics shown in Fig. 4.9 (compare with Fig. 4.8). The impedance signatures obtained from other PZTs exhibit similar behavior.

Fig. 4.9 Damage metric values obtained with the rotor balanced and operating at 1,200 rev/min for two different structural conditions: undamaged (blue line) and DAMAGE-2 (green line) (Color figure online)

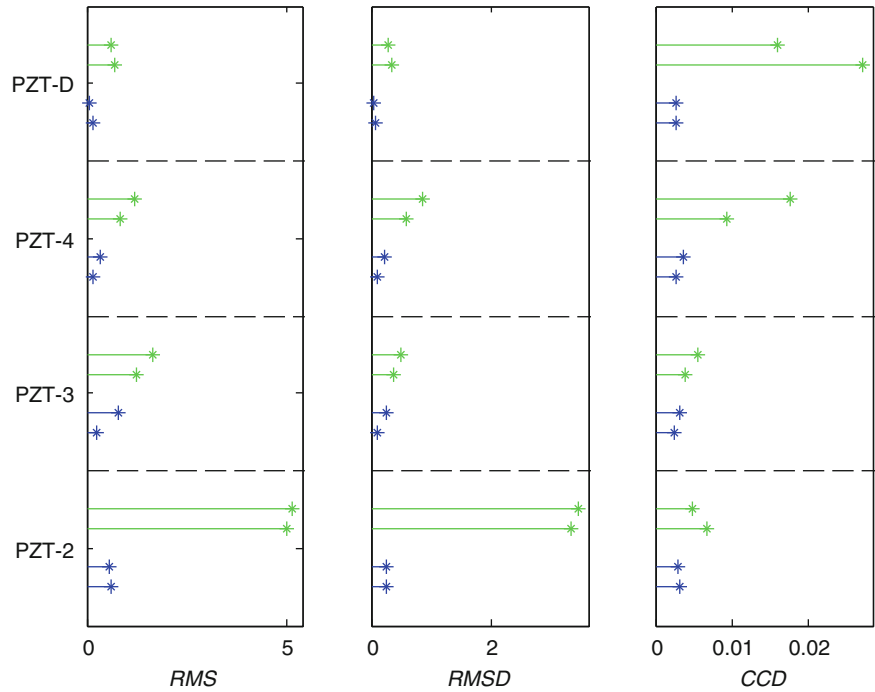
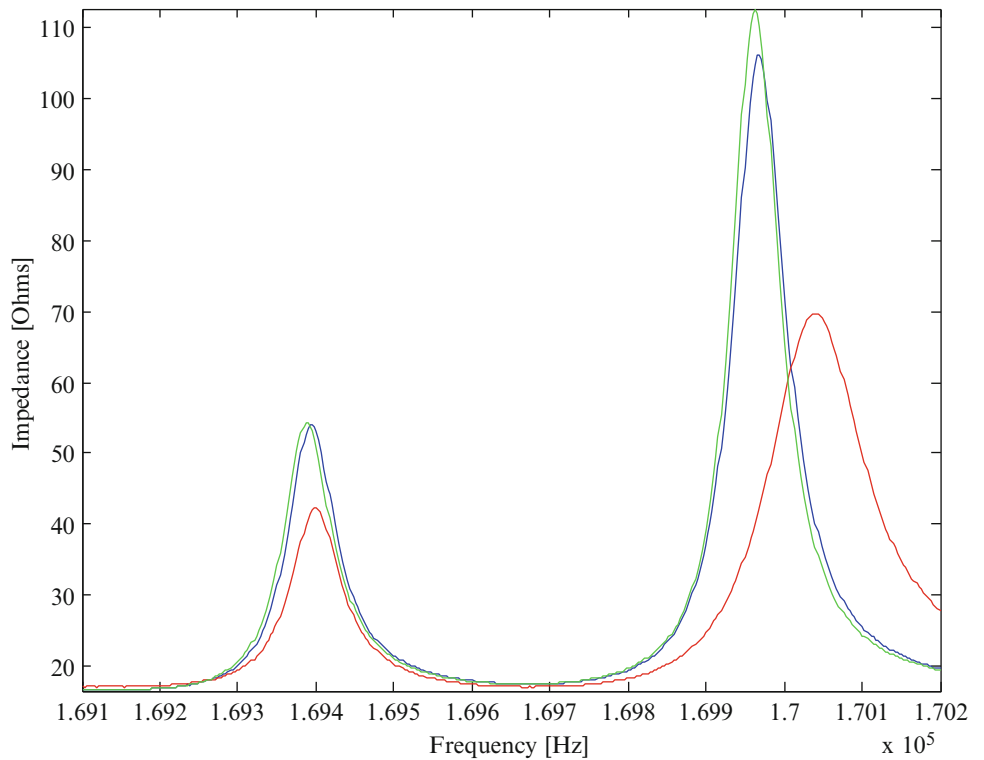


Fig. 4.10 Impedance signatures acquired by the PZT-3 with the rotor balanced and operating at 1,200 rev/min for all structural conditions: undamaged (blue line), DAMAGE-1 (red line), and DAMAGE-2 (green line) (Color figure online)



However, an interesting result was obtained for the rotor under the unbalanced condition (unbalance masses added to the two discs). The PZT-D began to detect more efficiently the saw cut (DAMAGE-2). Figure 4.11 shows the damage metrics found when the structural conditions of the rotor without damage and DAMAGE-2 were evaluated.

Note the difference in the indices obtained from the PZT-D (mainly for the CCD metric) in this operating condition, with respect to the results presented for the rotor under a balanced condition (Fig. 4.9). This result is addressed to the increasing

Fig. 4.11 Damage metric values obtained for the rotor unbalanced and operating at 1,200 rev/min for two different structural conditions: undamaged (*blue line*) and DAMAGE-2 (*green line*) (Color figure online)

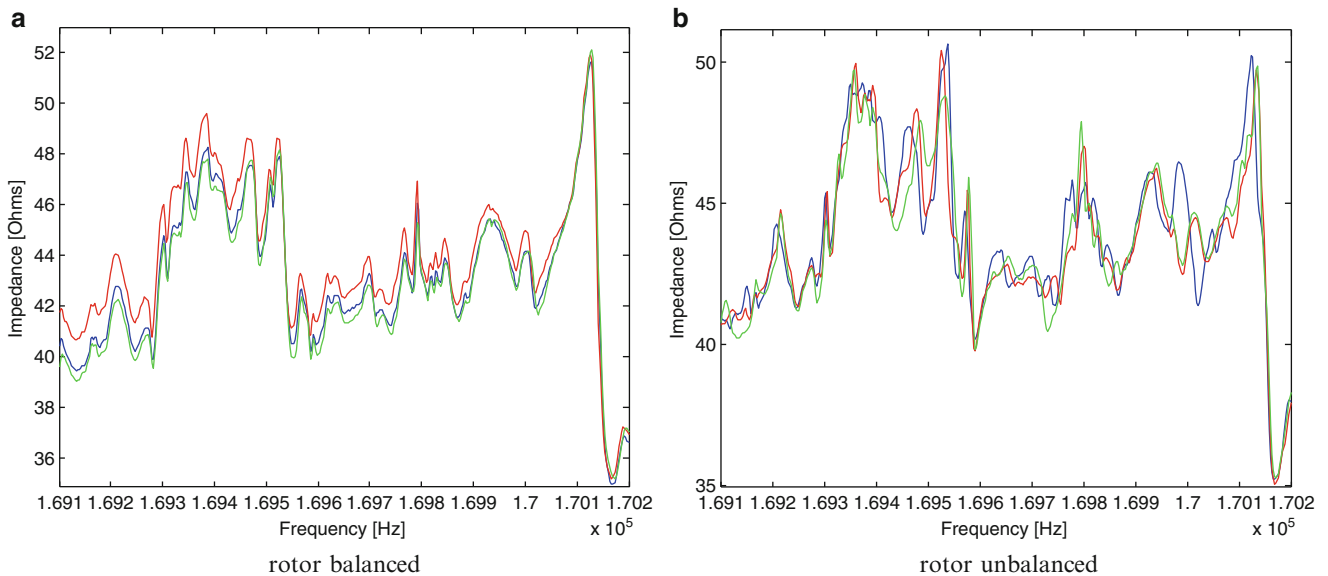
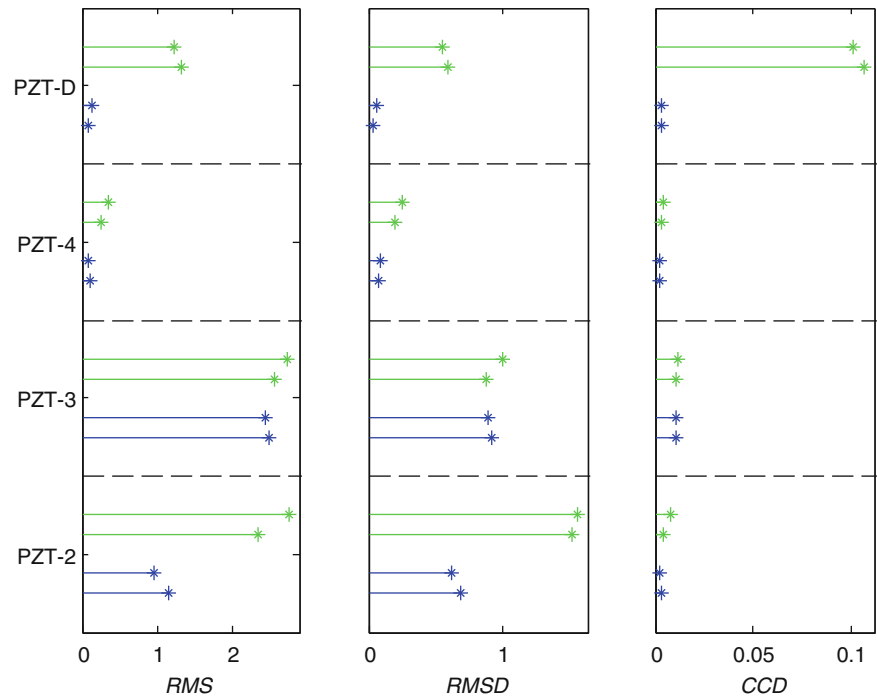


Fig. 4.12 Impedance signatures acquired by the PZT-D for the rotor at 1,200 rev/min for all structural conditions: undamaged (*blue line*), DAMAGE-1 (*red line*), and DAMAGE-2 (*green line*) (Color figure online)

of the vibration of the rotor with the unbalance (the dynamic behavior of the system becomes more significant). Also, note that the results obtained from the other PZT patches are similar to the ones determined for the balanced rotor condition. The DAMAGE-1 was again detected by all the sensors (results not shown here).

Figure 4.12 shows the impedance signatures measured by PZT-D with the rotor balanced (Fig. 4.12a; refers to Figs. 4.8 and 4.9) and unbalanced (Fig. 4.12b; refers to Fig. 4.11) for the three structural conditions. Comparing the curves, one can observe that the changes found in the impedance signatures with damage are more important for the case in which the rotor is unbalanced. This result is also demonstrated by the damage metrics shown in Figs. 4.9 and 4.11.

4.4 Conclusion

The results shown in the present contribution demonstrate the efficiency of the electromechanical impedance method for the detection of incipient cracks in transverse rotating shafts. As seen, the proposed SHM technique was evaluated for the rotor under operation, leading to satisfactory results. The rotordynamic applications were made possible by the use of a special device, the slip ring. In addition, a saw cut was performed on the shaft in order to simulate a crack (procedure adopted by many authors). Attempting to use PZT sensors coupled orthogonally to the shaft (e.g., in pulleys) found limited success. Good results were obtained for the cases in which unbalanced rotors were considered. The effect on the detection capability presented by PZT-D with the increase of the level of unbalance is interesting. Apparently, the variation of local stiffness imposed by the cut is detected more easily when the levels of imbalance are higher, i.e., when the mechanical stresses on the shaft are larger. The high frequency band is an advantage of the method since it permits the detection of incipient damage even in regions of small deflection of the shaft. Most SHM techniques devoted to the detection of cracks in rotors have this limitation. The coupling of the PZT patches to the shaft was made from a machining process, clearly a disadvantage of this application. Thus, in further research work on this topic the use of more flexible piezoelectric sensors is intended (such as Micro Fiber Composites—MFC).

Acknowledgments The authors are thankful to the Brazilian Research Agencies FAPEMIG and CNPq (INCT-EIE) and also to CAPES for the financial support provided for this research effort.

References

1. Bently DE, Hatch CT (2002) Fundamentals of rotating machinery diagnostics. Bently Pressurized Bearing Company, Minden
2. Bachschmid N, Pennacchi P, Tanzi E (2010) Cracked rotors: a survey on static and dynamic behaviour including modelling and diagnosis. Springer, Berlin
3. Sabinavis G, Kirk RG, Kasarda M, Quinn D (2004) Cracked shaft detection and diagnosis. *Shock Vib Dig* 36(4):287–296
4. Carden EP, Fanning P (2004) Vibration based condition monitoring: a review. *Struct Health Monit* 3(5):355–377
5. Palomino LV, Steffen V Jr (2009) Damage metrics associated with electromechanical impedance technique for SHM applied to a riveted structure. In: Proceedings of COBEM2009: 20th international congress of mechanical engineering, Gramado-RS
6. Park G, Inman DJ (2005) Impedance-based structural health monitoring. Damage prognosis for aerospace, civil and mechanical system. Wiley, England, pp 1–12
7. Park G, Sohn H, Farrar CR, Inman DJ (2003) Overview of piezoelectric impedance-based health monitoring and path forward. *Shock Vib Dig* 35(6):451–463
8. Liang C, Sun FP, Rogers CA (1994) Coupled electromechanical analysis of adaptive material systems: determination of the actuator power consumption and system energy transfer. *J Intell Mater Syst Struct* 5:12–20
9. Chaudhry Z, Joseph T, Sun F, Rogers C (1995) Local-area health monitoring of aircraft via piezoelectric actuator-sensor patches. In: Proceedings of the SPIE: SPIE conference, smart structures and integrated systems, vol 2443, San Diego
10. Sun FP, Chaudhry Z, Liang C, Rogers CA (1995) Truss structure integrity identification using PZT sensor-actuator. *J Intell Mater Syst Struct* 6:134–139
11. Park G, Cudney H, Inman DJ (2000) An integrated health monitoring technique using structural impedance sensors. *J Intell Mater Syst Struct* 11(6):448–455
12. Giurgiutiu V, Zagrai A (2000) Characterization of piezoelectric wafer active sensors. *J Intell Mater Syst Struct* 11:959–976
13. Giurgiutiu V, Zagrai AN, Bao J, Redmond J, Roach D, Rackow K (2003) Active sensors for health monitoring of aging aerospace structures. *Int J Cond Monit Diagn Eng Manag* 6(1):3–21
14. Moura JRV Jr, Steffen V Jr (2004) Impedance-based health monitoring: frequency band evaluation. In: XXII IMAC, Dearborn
15. Peairs DM (2006) High frequency modeling and experimental analysis for implementation of impedance-based structural health monitoring. PhD thesis, Virginia Polytechnic Institute and State University, Virginia, 150 pp
16. Raju V (1997) Implementing impedance-based health monitoring. PhD thesis, Virginia Polytechnic Institute and State University, Virginia, 224 pp
17. Park G, Kabeya K, Cudney HH, Inman DJ (1999) Impedance-based structural health monitoring for temperature varying applications. *JSME Int J* 42(2):249–258
18. Inman DJ, Farrar CR, Lopes V Jr, Steffen V Jr (2005) Damage prognosis: for aerospace, civil and mechanical systems. Wiley, England
19. Giurgiutiu V, Zagrai A (2005) Damage detection in thin plates and aerospace structure with the electro-mechanical impedance method. *Struct Health Monit* 4(2):99–118
20. Neto RMF, Steffen V Jr, Rade DA, Gallo CA, Palomino LV (2011) A low-cost electromechanical impedance-based SHM architecture for multiplexed piezoceramic actuators. *Struct Health Monit* 10(4):391–402

Chapter 5

Wind Turbine Gearbox Dynamic Characterization Using Operational Modal Analysis

E. Di Lorenzo, S. Manzato, J. Houben, F. Vanhollebeke, S. Goris, and B. Peeters

Abstract The aim of this paper is to characterize the dynamic behavior of a wind turbine gearbox installed on a dynamic test rig to replicate operational conditions. Wind turbines and gearboxes operate under very dynamic and complex conditions, caused by turbulent wind, fluctuations in the electricity grid etc. In those conditions, structural nonlinearities in bearings and gears cause natural frequencies to be significantly influenced by the operational conditions. To verify the dynamic response of a multi-megawatt gearbox, a comprehensive test campaign has been performed in the context of the European project ALARM at the ZF Wind Power test rig. Accelerations have been measured at more than 250 locations on the test rig and for different load levels and operating conditions. This paper focuses on the influence of the torque levels on the identified modal parameters. The acquired time histories during run-ups have been processed using different Operational Modal Analysis techniques. The aim is to provide a modal model that can be used for correlation and updating of a flexible nonlinear multibody model of the whole test rig as well as vibration levels to estimate structure-borne noise in the different operating conditions.

Keywords Operational modal analysis • Wind turbine gearbox • Test campaign • Gearbox test rig • Modal parameters

5.1 Introduction

The gearbox is one of the key subsystems in a geared wind turbine providing the task to transfer power from the low speed shaft connected to the rotor to the high speed shaft connected to the generator. As turbines become larger, more power is demanded and gearboxes with higher load capacity need to be designed. A deep knowledge into gearbox dynamics becomes of fundamental importance and noise and vibration measurements are demanded [1].

These measurements are mainly quality estimation methods for gear mesh vibrations and overall sound power levels. They are based on standard techniques for the estimation of dynamic characteristic in general applications and not focusing on the wind turbine gearbox case. Since several components properties depend on the applied torque and on the rotational shaft speed, a validation in operational conditions needs to be performed. Building on existing techniques such as “Order Tracking” and “Operational Modal Analysis,” a dedicated methodology will be developed for the analysis of operational gearbox dynamic behavior. Particular attention will be reserved to the separation between structural resonances and excitation orders.

Operational Modal Analysis (OMA) is used to derive an experimental dynamics model from vibration measurements in operational conditions. It cannot be applied in a straightforward way due to the self-induced vibrations at several rpm-dependent frequencies (gear meshing orders). These frequencies with high vibration levels can be wrongly considered

E. Di Lorenzo (✉) • S. Manzato • B. Peeters
LMS International, RTD Test Division, Interleuvenlaan 68, 3000 Leuven, Belgium
e-mail: emilio.dilorenzo@lmsintl.com

J. Houben • F. Vanhollebeke • S. Goris
ZF Wind Power Antwerpen NV, Gerard Mercatorstraat 40, 3920 Lommel, Belgium

resonance frequencies of the system. In order to face these problems, an extensive measurement campaign has been performed at ZF Wind Power on a 13.2 MW test rig facility. Accelerations have been measured at more than 250 locations on the test rig and for different load levels and operating conditions.

For stationary conditions, that means at constant rpm, the gear meshing orders will give a component at discrete constant frequencies that need to be filtered out from the signal in order to determine the resonances. Run-up tests can be considered as a multi-sine sweep excitation and the resonances can be identified combining advanced order tracking methods with operational modal analysis.

5.2 Test Rig Description

ZF Wind Power's dynamic gearbox test rig is one of the world's largest test facilities in its kind matching the wind turbine power growth in the market [2]. Gearboxes can be tested under representative loading conditions using parameterized load cases that can be programmed into the controller. Potential technical risk can be identified well in advance accelerating the life testing so that it is possible to improve gearbox reliability [3].

The "wind & rotor" side is composed of an electrical machine (motor 1), an optional speed reducer (3:1 gearbox) and a wind turbine gearbox (GB1). The "grid & generator" side is composed of an electrical machine (motor 2) and an optional speed reducer. Analogous to the operation of a wind turbine, the wind side of the test rig is speed controlled, while the generator side is torque controlled. Test gearbox 2 (GB2) is driven at a certain time varying speed corresponding to variable wind speeds and loaded with a certain time varying torque by the generator corresponding to the loading from the grid and thus experiences test conditions very similar to wind turbine behavior [4].

It has a nominal power of 13.2 MW and a peak power capacity of 16.8 MW. The complexity of applying dynamics is tackled by the concept of load cases [5]. Each load case represents a specific part or phenomenon in the wind turbine behavior. An overview of the test rig is shown in Fig. 5.1.

5.3 Measurement Campaign

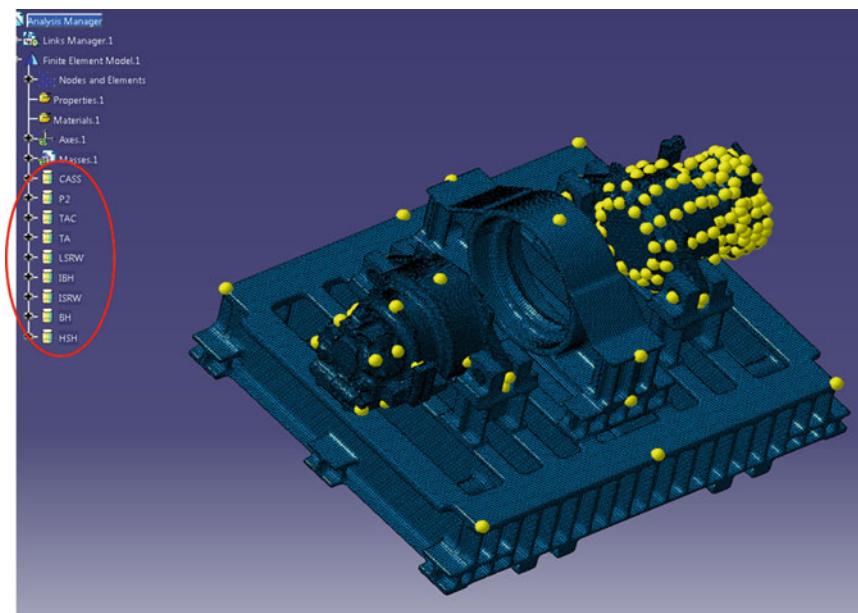
The measurement campaign took place on the 13.2 MW dynamic test rig where a 3.2 MW and a 3 MW prototype gearboxes were placed in a back-to-back configuration with one gearbox (P3) in "generator mode" as in the wind turbine and the other (P2) in "motor mode." The two gearboxes have a slightly different gear ratio so that the motor mode gearbox does not run at nominal speed when the generator mode gearbox is being tested. The measurement campaign was comprised of over 250 measurement points and it included several conditions (constant speed, run up, shaker measurements) at different levels of torque, as shown in Table 5.1.



Fig. 5.1 ZF wind power test rig

Table 5.1 Measurements load cases

Step	Load (%)	Speed
1	0	Standstill (shaker)
2	33	Run up, 200–1,500 rpm (5 rpm/s)
3	33	Constant speed, 1,200 rpm
4	33	Constant speed, 800 rpm
5	66	Run up, 200–1,500 rpm (5 rpm/s)
6	66	Constant speed, 1,200 rpm
7	66	Constant speed, 800 rpm
8	100	Run up, 200–1,500 rpm (5 rpm/s)
9	100	Constant speed, 1,200 rpm
10	100	Constant speed, 800 rpm

Fig. 5.2 Test rig FE model

In order to cover all the measurement points in three directions, seven batches for each configuration were performed because of the limited number of available measurement channels. A global overview of the chosen sensor locations in the FE model is reported in Fig. 5.2, whereas in Fig. 5.3 the test configuration used in LMS Test.Lab is shown. The points were defined under different groups depending on the component as stated in Table 5.2.

The X global axis goes from the Low Speed Shaft (LSS) to the High Speed Shaft (HSS) of the main tested gearbox (P3) that means from P2 to P3 in Fig. 5.3; Z axis point vertically up, while Y axis is defined to get a consistent axis system (Figs. 5.4, 5.5, and 5.6).

5.4 Operational Modal Analysis

Operational Modal Analysis (OMA) technique, also known as output-only modal analysis, allows identifying modal parameters by using operational measurement such as accelerations measured on several points attached to the structure [6]. OMA technique is applied when the input forces cannot be measured and when the system complies with three main assumptions. It must be linear time invariant, the excitation forces must be represented by a flat white noise spectrum in the band of interest and the forces acting on the structure must be uniformly distributed and uncorrelated both temporally and spatially. The better these assumptions are fulfilled, the better the quality of the estimated modal parameters [7]. The identification technique is similar to the classical input–output modal analysis with the substantial difference that, instead than impulse and frequency responses, it uses auto- and cross-correlation and auto- and cross-powers between signals measured simultaneously at different locations. So, there is the need to identify several reference signals that should be as less noisy as possible and that should be able to identify as many modes as possible. Operational PolyMAX [8] and Stochastic Subspace Identification techniques have been applied to the gearbox data for identifying natural frequencies, damping ratios and mode shapes.

Fig. 5.3 Test rig measurement points

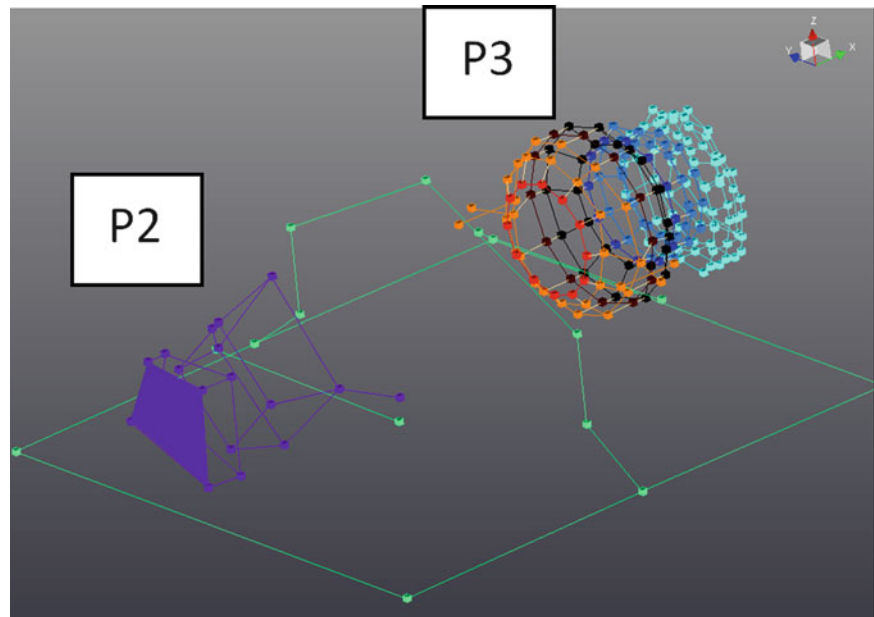
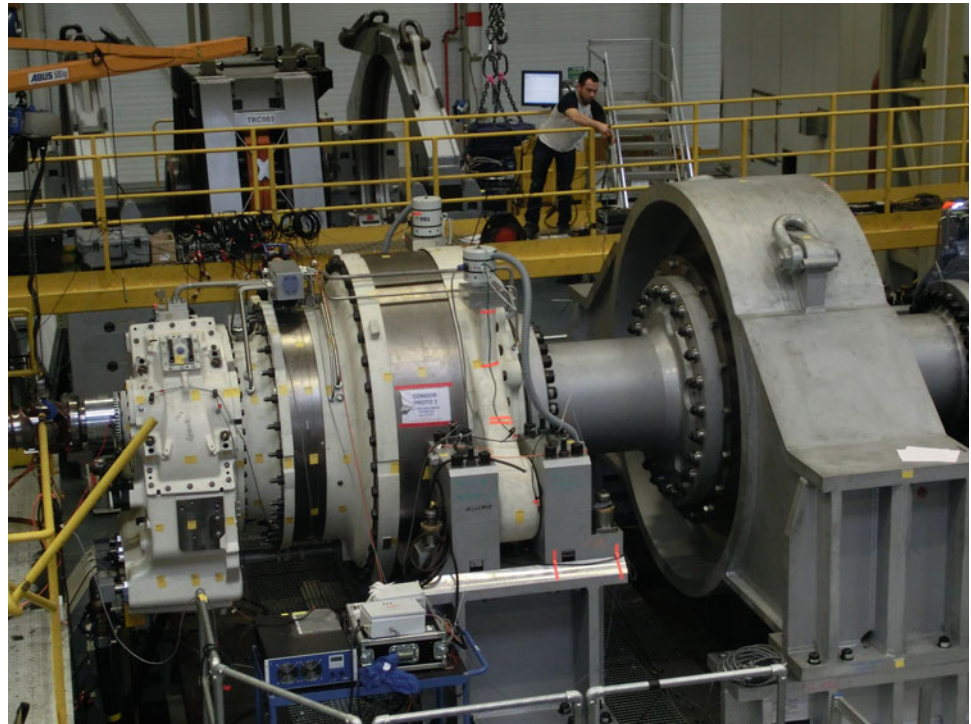
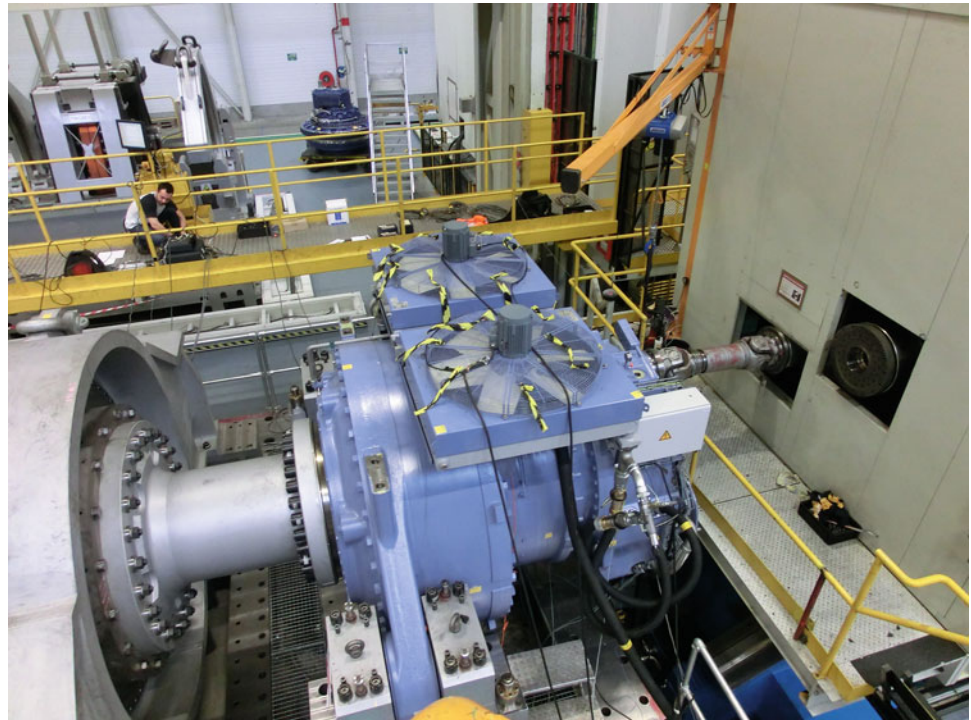


Table 5.2 Measurement points list

Component	Abbreviation	Number of measurement locations
Tested gearbox (gearbox 1) = P3		
Torque arm cover	TAC	12
Torque arm	TA	30
Low speed stage ring wheel	LSRW	12
Intermediate bearing housing	IBH	24
Intermediate speed stage ring wheel	ISRW	12
Bearing housing	BH	36
High speed stage housing	HSH	76
	Total for P3	202
Counter gearbox (gearbox 2) = P2		
	P2	27
Test rig		
Cassette + motor 1 (tested gearbox, P3) + motor 2 (counter gearbox, P2)	CASS	27
	Grand total	256

In our case, the “natural” flat spectrum excitation provided by the rotation of the shafts inside the gearbox can be used as source. In order to fulfill the white noise spectrum hypothesis, the run up case is considered. In fact, the harmonics (orders), related to the number of revolutions, are sweeping through a broad frequency band and they are useful excitation for estimating the modal parameters. According to Table 5.1, the gearbox is rotating from 200 to 1,500 rpm, with a speed run up rate equal to 5 rpm/s, which is a huge part of its operational rotation speed range so that the need for white noise excitation is well approximated [9]. During the measurements, the same run up case was performed at three different torque levels (33, 66 and 100 %) that correspond to step 2, 5 and 8 reported in Table 5.1.

Accelerations were collected by means of tri-axial accelerometers at a quite high sampling frequency (16,384 Hz), so the first step in the data processing is a data down sampling to 1,500 Hz in order to focus the attention in a narrow frequency band (0–500 Hz). While the most part of accelerometers were moved between a batch and the following one in order to cover all the measurement points, eight accelerometers were kept at the same position during all the measurement campaign. Those accelerometers can, then, be used as reference channels in the calculation of cross-powers. Two points (named point 5 and point 8), which location is shown in Figs. 5.7 and 5.8, are considered as the most suitable reference channels since their spectra have a quite good repeatability along the different batches, as shown in Fig. 5.9 for point 8. The smaller the differences, the better the estimation of the modal parameters is. For performing Operational Modal Analysis,

Fig. 5.4 P3 gearbox**Fig. 5.5** P2 gearbox

a pre-processing is necessary to convert time data to auto- and cross-powers. First of all, auto- and cross-correlation functions are calculated and an exponential window is usually required before computing the FFT algorithm. The exponential window reduces the effect of leakage and the influence of the high time lags, which have a large variance [10].

Some pictures of the test rig configuration are shown in Fig. 5.4 (P3 gearbox), Fig. 5.5 (P2 gearbox) and Fig. 5.6 (whole test rig).

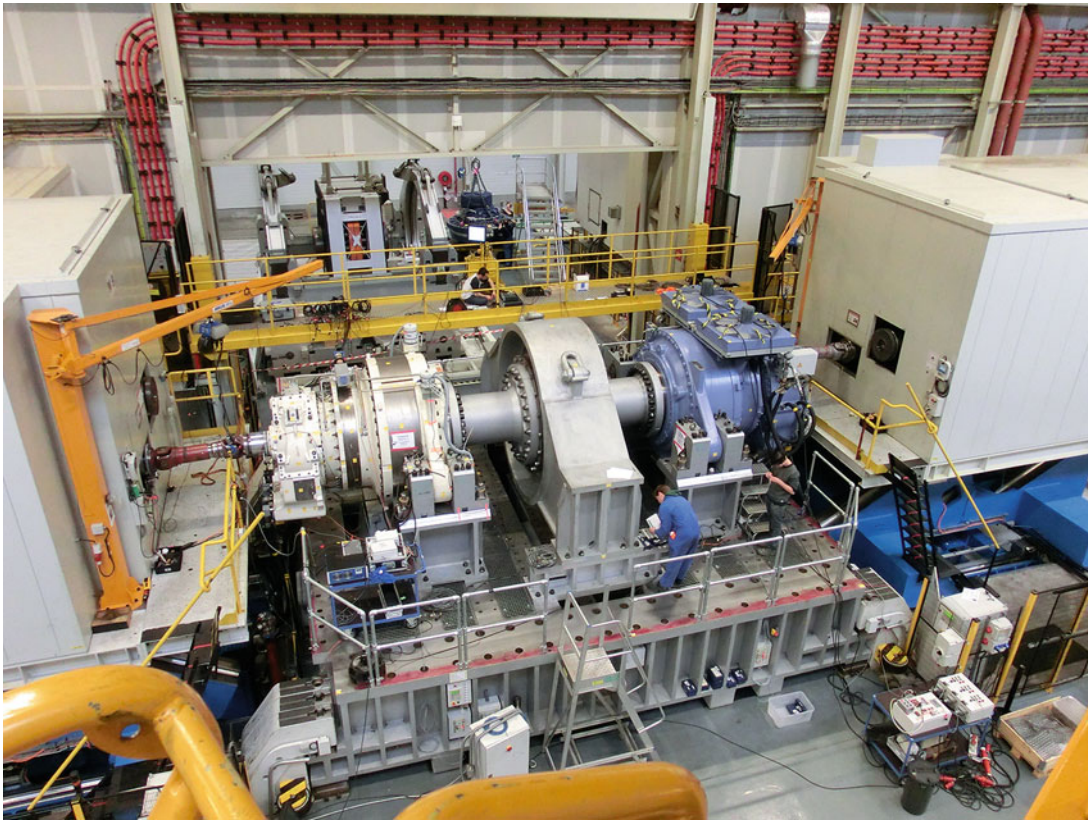
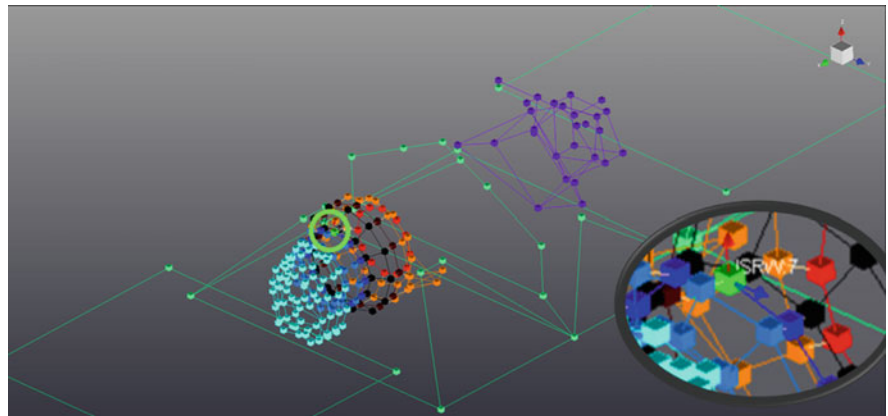


Fig. 5.6 Whole test rig

Fig. 5.7 Reference point 8



5.5 Data Analysis

The main gearbox under test (P3) is the one in which more measurement points were considered but, in order to have a better knowledge of the system, the first part of the analysis focuses on the P2 gearbox with only 18 measurement points even if all the reference channels were placed on the other side of the overall system. The different batches are analyzed separately and then they are merged together by a so-called multi-run analysis in which partial mode shapes are combined to get the global mode shapes. The partial mode shapes are scaled with respect to the common degrees of freedom and the poles are evaluated as averaged poles between the poles coming from the different batches.

Natural frequencies and damping ratios were calculated for the three different torque levels and the results are compared in Tables 5.3 and 5.4.

Fig. 5.8 Reference point 5

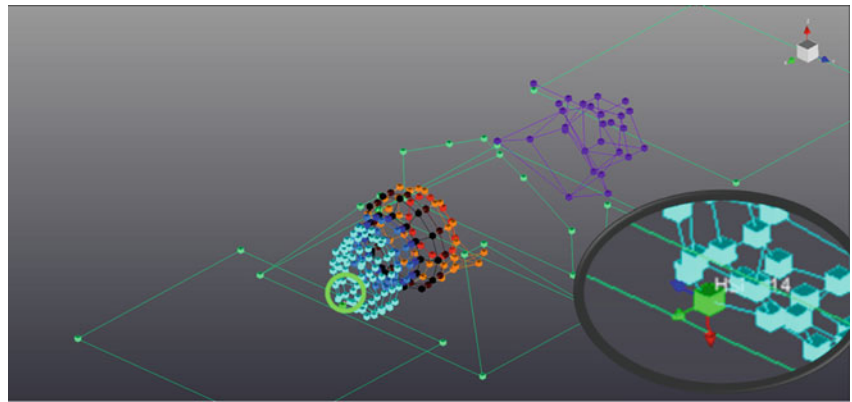


Fig. 5.9 PSD point 8 for several batches at the same load case

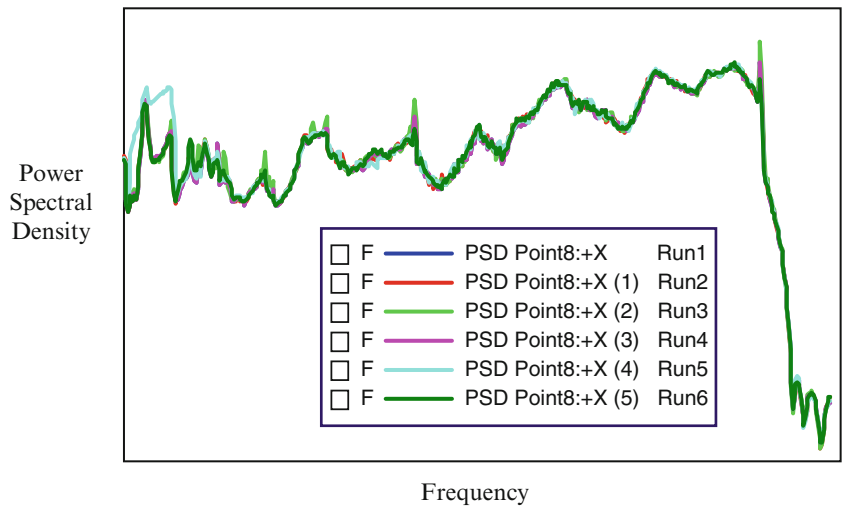


Table 5.3 Natural frequencies comparison for P2 gearbox at different torque levels

Natural frequencies comparison					
	33 % torque (Hz)		66 % torque (% variation)		100 % torque (% variation)
1	[40–80]	↓	−0.32	↑	1.77
2	[40–80]	↑	0.75	↑	5.99
3	[60–100]	↑	0.25	↑	0.26
4	[60–100]	↑	0.71	↑	0.82
5	[80–120]	↑	0	↓	−0.60
6	–	–	[80–120]	↓	−0.37
7	[100–140]	↑	–	–	0.25
8	[130–170]	↑	1.62	–	–
9	[160–200]	↑	3.16	↓	2.83
10	[180–220]	↑	0.35	↑	2.14

The percentage values are referred to the values in the square brackets

After the P2 is fully analyzed at the different torque conditions and its modal parameters are estimated and compared, the overall system can then be analyzed following the same procedure and including all the measurement points.

The accelerometers placed on the auxiliaries are not included in the analysis. While a shift toward higher natural frequencies (upward arrow) can be seen when the torque is increasing, the same is not always true for the damping ratio that is known to be a parameter which is estimated with more uncertainties [11].

When the full system is considered, not all the modes are identified considering only one reference channel so that two different channels need to be considered at the same time. Figure 5.10 shows a typical stabilization diagram used to estimate the modal parameters selecting the stabilized poles while increasing the model size.

Table 5.4 Damping ratios comparison for P2 gearbox at different torque levels

Damping ratios comparison					
	33 % torque (%)		66 % torque (% variation)		100 % torque (% variation)
1	[0.5–1.1]	↑	151.81	↓	142.17
2	[1.7–2.3]	↓	–27.15	↑	–20.26
3	[0–0.5]	↓	–22.22	↑	85.19
4	[1.5–2.1]	↑	4.97	↓	–20.99
5	[0–0.5]	↑	40.00	↑	440.00
6		–	[0.5–1.1]	↓	–38.82
7	[1–1.6]	↓	–	–	–25.00
8	[0–0.5]	↑	127.78	–	–
9	[0.5–1.1]	↓	–40.45	↑	13.48
10	[0–0.5]	↑	56.67	↑	93.33

The percentage values are referred to the values in the square brackets

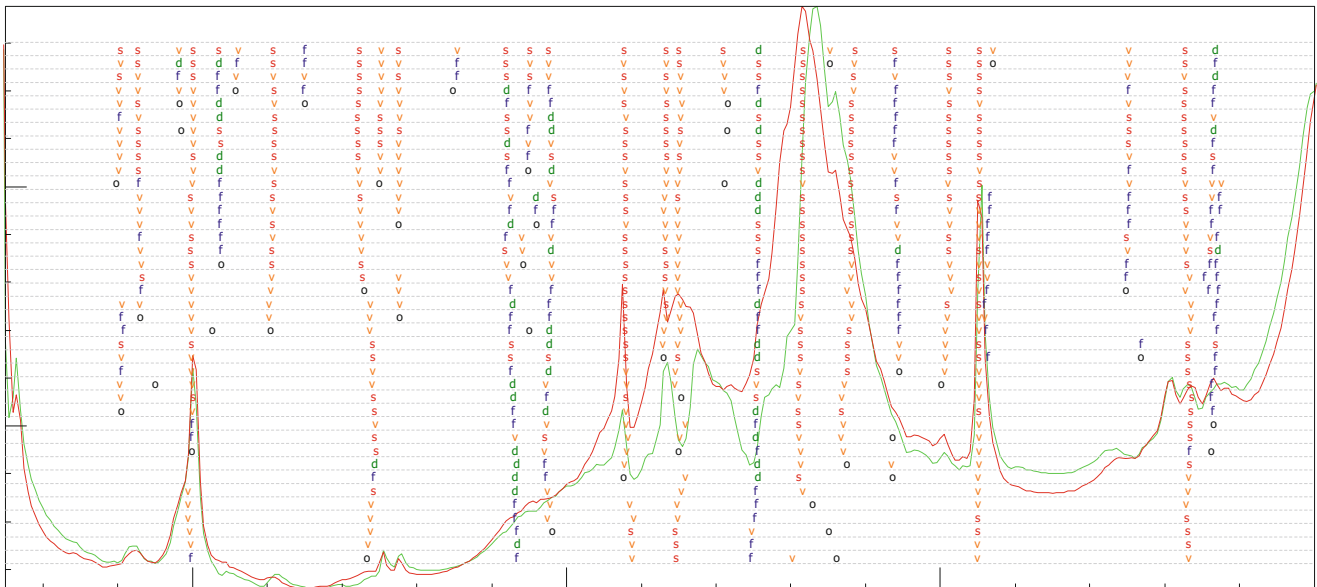


Fig. 5.10 Stabilization diagram using operational PolyMAX

Table 5.5 Natural frequencies comparison for the full system using different reference points

Natural frequencies comparison (100 % torque)			
	Point 5 reference (Hz)	Point 8 reference (Hz)	Point 5 + point 8 reference (Hz)
1	[60–100]	1.52	1.64
2	[80–120]	–0.60	–1.20
3	[130–170]	–	–0.60
4	[160–200]	1.42	0.74
5	[180–220]	–0.15	–0.50
6	[200–240]		–0.33
7	[200–240]	–	0.13
8	[240–280]	–	0.19
9	[280–320]	–	0.91
10	[350–400]	–0.90	–1.35

The percentage values are referred to the values in the square brackets

In Table 5.5 a comparison between the natural frequencies identified considering three different reference channel configurations is shown; on the other hand, Fig. 5.11 shows a Modal Assurance Criterion (MAC) comparison between two of the three configurations to show that the identified mode shapes are coherent if two reference channels are considered instead than only one. The frequency resolution is set equal to 2 Hz.

Fig. 5.11 Modal Assurance Criterion (MAC) comparison using different references (point 5 vs. point 5 + point 8)

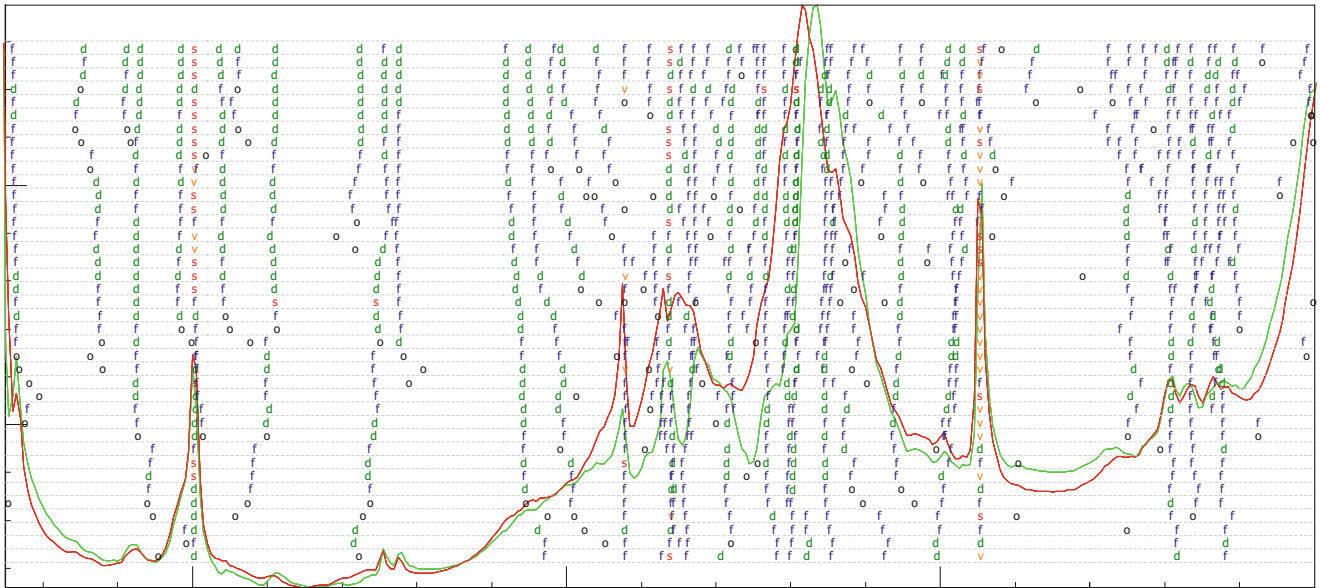
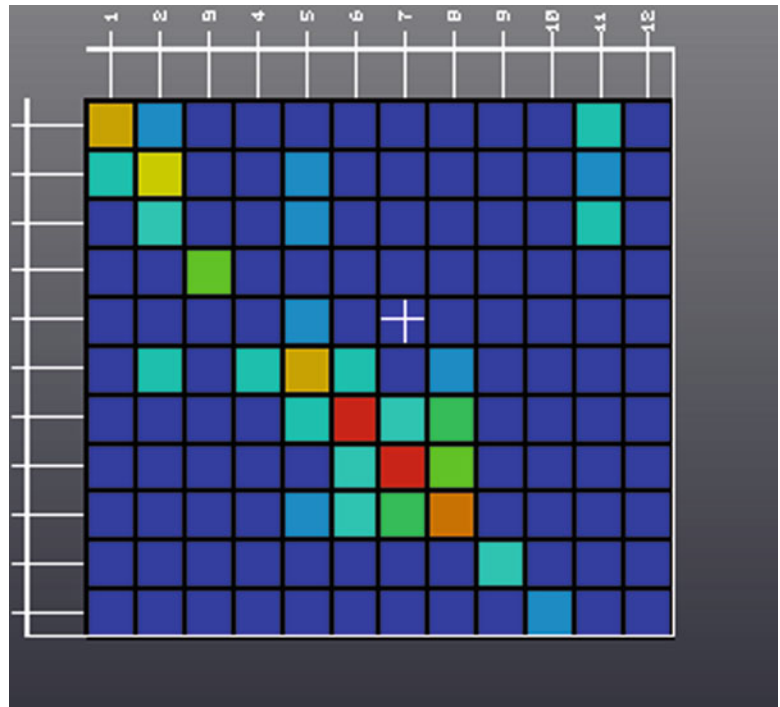


Fig. 5.12 Stabilization diagram using Stochastic Subspace Identification (SSI)

The natural frequencies and the mode shapes are compared using the two different operational modal analysis techniques mentioned in the previous sections: Operational PolyMAX and Stochastic Subspace Identification (SSI) [12].

Figure 5.12 shows the same stabilization diagram of Fig. 5.10, with the only difference that it is obtained using the SSI technique. The stabilized poles are not as clear as they were in the previous one, but a better estimation of the mode shapes is possible (Fig. 5.13).

The natural frequencies and the mode shapes are compared using different torque levels (66 and 100 %) increasing the frequency resolution from 2 to 1 Hz.

A quite good agreement between the two different torque conditions can be underlined both in the natural frequency table and in the MAC comparison which calculates the correlation between two different sets of modes in order to compare different processing. The shift toward slightly high natural frequencies can be seen also for the full system respecting the trend that has been found for the single component, as can be seen from Table 5.6.

Figure 5.14 shows the MAC comparison between the full torque condition (100 %) and the 66 % torque case.

Fig. 5.13 Mode shapes instantaneous picture comparing operational PolyMAX result (*above*) with Stochastic Subspace Identification technique (*below*)

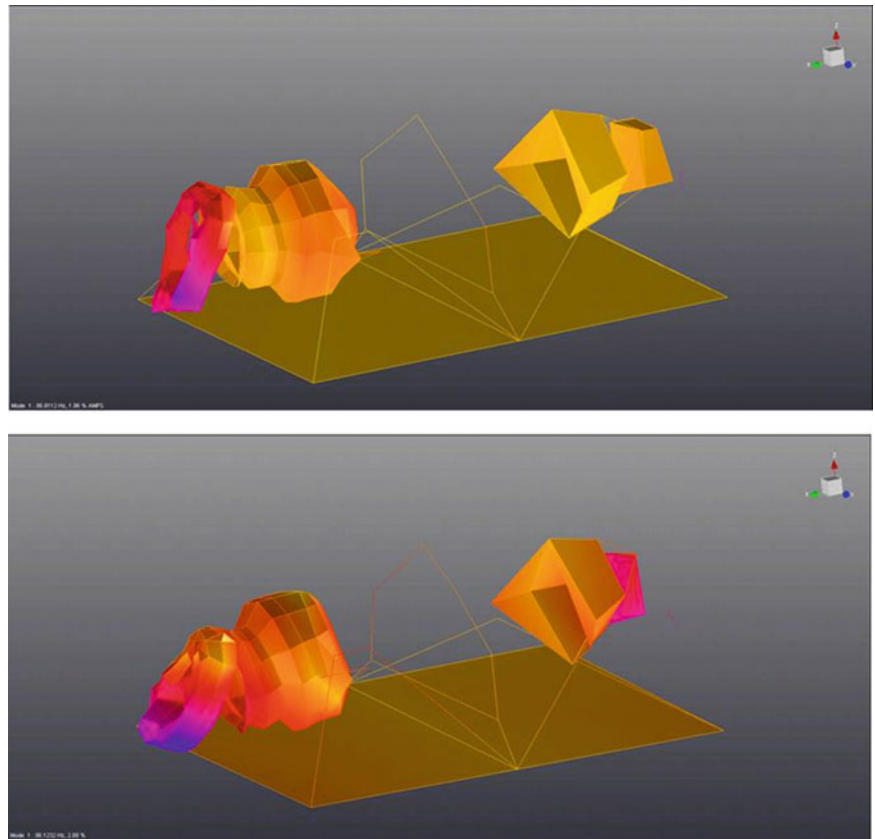


Table 5.6 Natural frequencies comparison at different torque levels (66 % vs. 100 %) at different torque levels

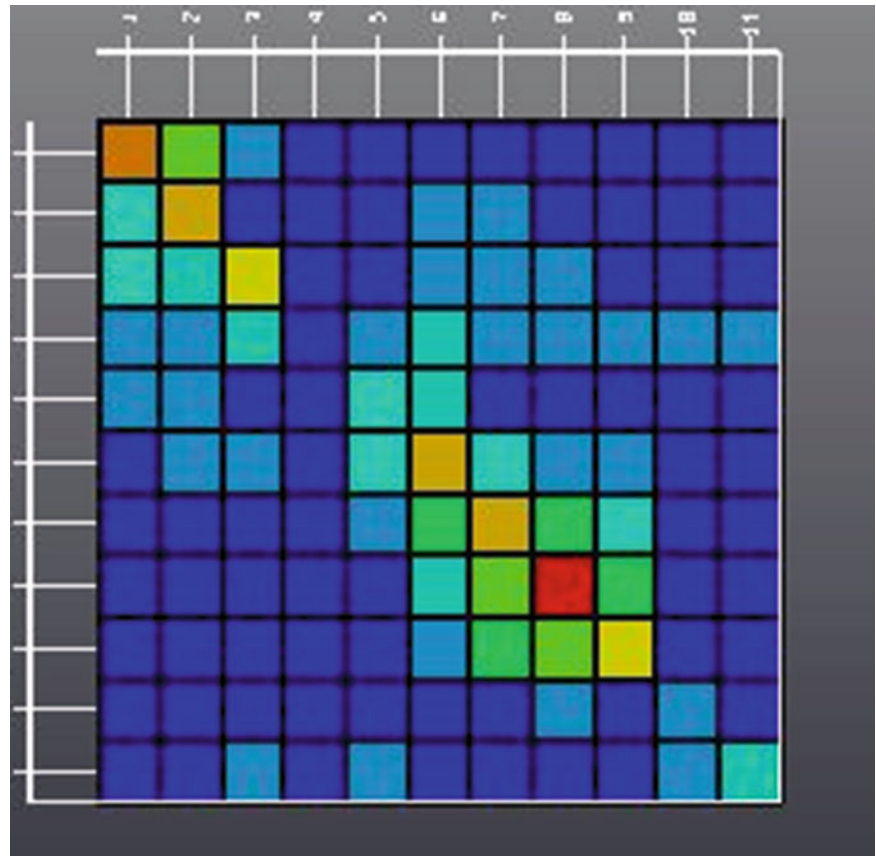
Natural frequencies comparison		
	66 % torque (Hz)	100 % torque (Hz)
1	[60–100]	0.05
2	[80–120]	−0.64
3	[130–170]	−0.09
4	[160–200]	3.30
5	[180–220]	0.48
6	[200–240]	0.03
7	[200–240]	0.40
8	[240–280]	1.22
9	[280–320]	−0.12
10	[340–380]	2.05

5.6 Conclusions

A huge measurement campaign has been performed in order to characterize the gearbox behavior on the test rig. The set up and the test rig are described and, after that, a first analysis has been done and a first modal model has been obtained using OMA techniques and focusing on the run up measurements at different torque values. First of all the analysis has focused on a single component considering a reduced set of measurement points and then the full system has been considered. In both cases, a positive shift toward higher frequencies with an increasing torque is a consistent trend during the different set of measurements. A consistent set of modal parameters such as natural frequencies, damping ratios and mode shapes has been found.

Building further on existing Operational Modal Analysis (OMA) and Order Based Modal Analysis (OBMA) techniques, a dedicated methodology in the presence of rotating machinery will be developed taking into account the separation between excitation orders (rpm dependent) and structural gearbox resonances. In addition the use of Operational Deflection Shapes (ODS) is an added value in order to optimize these techniques.

Fig. 5.14 Modal Assurance Criterion (MAC)



Acknowledgements Emilio Di Lorenzo, first author of this paper, is an Early Stage Researcher under the Marie Curie ITN project 309395 “MARE-WINT” (<http://marewint.eu/>) within the 7th European Community Framework Programme. Furthermore, the research conducted in this paper is supported by following institutions:

- Institute for Promotion of Innovation through Science and Technology in Flanders-Belgium (IWT Vlaanderen).
- German Federal Ministry of Education and Research (BMBF) within the Framework Concept “Research for Tomorrow’s Production” and managed by the Project Management Agency Karlsruhe (PTKA).
- This project is supported by an Eureka label in the framework of international co-operation: www.eurekanetwork.org/project/-/id/7220.

References

1. Helsen J (2012) The dynamics of high power density gear units with focus on the wind turbine application. PhD dissertation, Department of Mechanical Engineering, Katholieke Universiteit Leuven, Belgium
2. Goris S, Vanhollebeke F, Ribbentrop A, Markiewicz M, Schneider L, Wartzack S, Hendrickx W, Desmet W (2013) A validated virtual prototyping approach for avoiding wind turbine tonality. In: Proceedings of 5th international conference on wind turbine noise, Denver
3. Marrant B (2012) Validation of MBS multi-megawatt gearbox models on a 13.2 MW Test Rig. SIMPACK Newsletter Issue (May–June)
4. Peeters J, Leimann D, Huijskens R, Coninck F De (2009) First results of Hansen’s 13 MW test facility for wind turbine gearboxes. In: European offshore wind conference & exhibition, Stockholm
5. De Coninck F, Desmet W, Sas P, Peeters J, Huijskens R, Leimann D (2010) Reproduction of dynamic load cases on a 13.2 MW test facility for wind turbine gearboxes. In: Proceedings of ISMA 2010, Belgium
6. Heylen W, Lammens S, Sas P (2007) Modal analysis theory and testing. PMA, Katholieke Universiteit Leuven, Belgium
7. Peeters B, Van der Auweraer H, Vanhollebeke F, Guillaume P (2007) Operational modal analysis for estimating the dynamic properties of a stadium structure during a football game. *Shock Vib* 14(4):283–303
8. Peeters B, Van der Auweraer H, Guillaume P, Leuridan J (2004) The polymax frequency-domain method: a new standard for modal parameter estimation? *Shock Vib* 11:395–409

9. Peeters B, Gajdatsy P, Aarnoutse P, Janssens K, Desmet W (2009) Vibro-acoustic operational modal analysis using engine run-up data. In: Proceedings of the 3rd international operational modal analysis conference (IOMAC), Ancona
10. LMS International (2013) LMS Test.Lab Rev. 13A. User Manual, Belgium
11. Boeykens R, Van de Vliet J (2010) Operational modal analysis on a state of the art wind turbine gearbox. Master thesis, Department of Werktuigkunde, Belgium
12. Gade S, Schlombs R, Hudeck C, Fenselau C (2009) Operational modal analysis on a wind turbine gearbox. In: Proceedings of the IMAC-XXVII, Orlando

Chapter 6

Mode Classification and Dynamic Analysis of Coupled “Motor-Compressor-Flexible-Foundation” Structures

Sumit Singhal, Neal Birchfield, and Kumar Vikram Singh

Abstract The rotating machine structure along with the flexible foundation is a multibody dynamical system consisting of several coupled flexible elements i.e. rotating shafts, oil film bearings, bearing housing, machine and foundation structure. The interaction among these elements can influence the overall rotor dynamics behaviour of the drive train system. Recently, relationship between the dynamics of rotating machine and its flexible base connected at multiple coupling points are developed. Research is currently underway to extend this analysis to large industrial-scale structures such that they can become the basis for designing the coupling parameters for avoiding excessive vibration due to coupling. In this paper, an industrial-scale-rotor-bearing simulation model is developed. Through numerical simulation, the influence of foundation flexibility and coupling parameters on the coupled modes of rotor dynamic system is obtained. The classification of modes in the coupled system is carried out and the influence of the foundation flexibility on the response of various flexible components is investigated. It is anticipated that such a model will pave a way to seek structural modifications on the foundation or the coupling parameters such that overall vibration can be minimized and desired critical speeds of the coupled system can be designed.

Keywords Rotor dynamics • Structural dynamics • Drive train • Flexible foundation • Structural modification

6.1 Introduction

The rotating machine is a multi body system which consists of a rotor string, non linear oil film bearings, bearing housing, machine structure and foundation structure. In the field of rotor dynamics, the stability of the overall rotor-system is very important because of the inherent capability of the machine to self-excite [1, 2]. The presence of (1) a flexible foundation upon which a rotating system is mounted, and/or (2) a flexible coupling connecting two rotating systems, complicates the overall system dynamics. Foundation structures of rotating machinery can be of different types [1] such as (a) Steel Frame Foundation, (b) Mounted on Foundation Block, and (c) Concrete or Steel Table Foundation, as shown in Fig. 6.1. It is well known that the dynamic behavior of these foundations interacting with the dynamics of rotors changes the overall dynamic behavior (eigen values or critical speeds) of the coupled rotor-system. For example, structural dynamics of a foundation may influence the vibration of a machine structure, bearing housing and rotor vibration of a drive train. The degree of influence of a foundation structural dynamics on the overall vibration level of the drive train depends on the flexibility and mass of the foundation in comparison to the flexibility of housing and rotor systems. With the design trends and requirements is to go towards light weight structures either to reduce cost or operational needs such as in floating oil platform the foundation could be light weight and flexible which leads to greater influence of dynamics of foundation on the drive train rotor dynamics and vibration. On such field conditions large drive train systems on flexible foundation may have to pass through several natural frequencies related to an individual subsystem or of a complete system. Passing or operating at the natural frequencies always

S. Singhal (✉)
Siemens Dynamowerk, Berlin, Germany
e-mail: sumit.singhal@siemens.com

N. Birchfield • K.V. Singh
Mechanical and Manufacturing Engineering Department, Miami University, Oxford, OH, USA

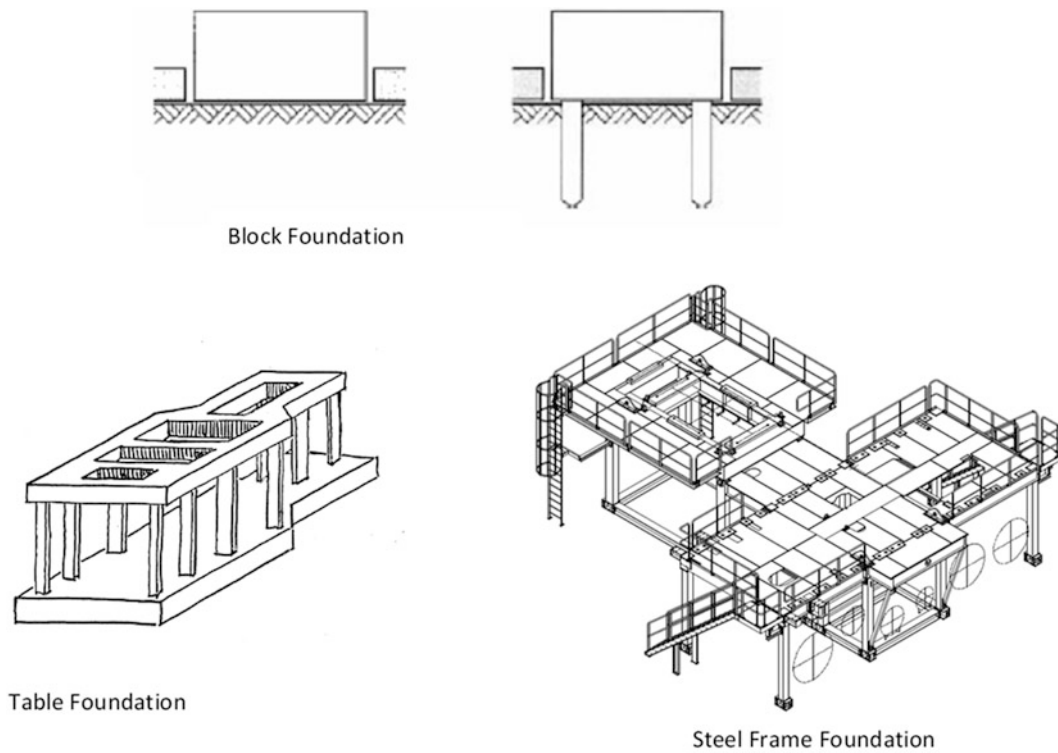


Fig. 6.1 Types of foundation

requires careful examination for the overall mechanical structure integrity and reliability. Long term high vibrations in the system can lead to catastrophic failures of the machine structure. Hence the vibration behaviour of the machine must be calculated and predicted to be as close as to field operating conditions.

In recent years, several studies of the impact of foundation flexibility on the dynamics of rotor-bearing systems have been carried out in the past. For example, the coupling of the subsystems of a rotary system has been shown to be approximated through experimental data for predicting the overall response using the frequency response functions [2, 3]. It has been shown that the impact of the stability of rotor-system is greatly impacted by the flexibility of the supports [4, 5]. It has been shown that through modal analysis data and/or FRF data, a reliable means of predicting this coupling between the systems can be achieved [6]. The major challenges in modeling such coupled system are the errors originating from the several approximation used to define a mathematical model, such as estimation of structural and mass matrices, type and behavior of joints, coupling flexibility and overall damping in structure and well as coupling elements. For example, in order to calculate the vibration characteristics of rotor-bearing systems, a foundation and machine structure is usually assumed to be the rigid bodies and is modelled as a single mass spring system in the rotor dynamics model. Dynamics of foundation represented by a single degree of freedom mass-spring system per plane, where the stiffness is derived from static calculation gives good predictions only when the influence of the foundation on rotor dynamics is small. Also single degree of freedom spring system also represents only one operation deflection shape, in case of flexible structures there are many mixed vibration modes which occurs in the system hence the deflection shape of the foundation may influence the rotor dynamics and vibrations of the rotor bearing. These approximations may lead to inaccurate prediction of the dynamic behavior of the overall system. In practice the rotor and coupling parameters and associated mathematical models of the coupled systems are tuned or updated with the help of some experimental verification. For example, Kang [7] has developed the mathematical model of a foundation structure which was later used to update the coupled rotor-bearing-foundation system. Impedance based models of coupled rotor-bearing-foundation systems were also developed [8, 9]. Identification of rotor-bearing-foundation system by frequency response functions has been done by Chen et.al. as well [10]. Recently the authors have developed relationships among the transfer functions of a rotor dynamic system with various flexible coupling mechanisms interacting at prescribed locations [11, 12]. With the numerical simulations it has been demonstrated that with the knowledge of some transfer functions, the coupling parameters as well as structural modification on the coupling parameters and/or the structure can be estimated to achieve desired dynamic behavior of the coupled system. However, this study was limited to small lab scale structure (GE/Bently Nevada RK4 Rotor kit).

In order (1) to analyze the effect a given foundation flexibility on overall rotor dynamic system, (2) to seek structural modification for prescribed critical speeds as shown in [11, 12], and (3) to validate these coupling interaction through experimentation in future, an accurate model of an industrial scale rotor-foundation system is needed. In this paper at first a generalized formulation of two coupled subsystem is presented in frequency domain. It is shown with discussion of the earlier results in [11, 12] that with selected measurement on rotor-bearing system and flexible foundation separately as well as the knowledge of coupling parameters and its location the dynamic behaviour of the coupled system can be predicted. To realize this approach on an industrial scale structure, a rotor-bearing simulation model is developed which incorporates the details and complexities associated with the real system. This full scale model is coupled to a concrete table foundation. Eigen value analysis of this full scale model is performed and natural frequencies are calculated and mode shapes are computed. The deflection modes are classified depending upon the shape of the deflection. Dynamic response of the complete structure is also calculated and worst case vibration amplitudes are also predicted which can be further used for fatigue and structural strength calculations. The observations of the numerical simulation and future work originating from this analysis are briefly summarized.

6.2 Coupling of Two Flexible Sub-systems at Specified Location

Consider two subsystems A (rotor bearing system) and B (flexible foundation), as shown in Fig. 6.2, defined by $(n_A + p_A)$ and degrees of freedom (DoF). The number of DoF n_A and n_B represents those DoF which are not connected, and p_A and p_B are the degrees of freedom of subsystem A and subsystem B respectively, which are to be joined/coupled together. The joining/connecting co-ordinates of the subsystems are denoted by “ j ” and all other co-ordinates are denoted by “ i .”

$$(n_B + p_B)$$

These two independent substructures may be joined together at multiple points through various mechanical means (e.g. bushing, bolts etc.) which may further influences the behavior of the overall coupled system. Suppose that subsystems A and B are to coupled together to form coupled system C as shown in Fig. 6.2. In the subsequent discussion, subscripts A, B and C will refer to the parameters and degrees of freedom of subsystem A, subsystem B, and of the coupled system C respectively. Subsystem A (rotor-bearing) is defined with p degrees of freedom and subsystem B (flexible foundation) is defined with q degrees of freedom (DoF). Suppose they are also connected with flexible with negligible mass then the overall coupled system can be now defined by $p + q$ DoF.

For the coupled system C, any DOF joining the two substructures will be denoted as $j_{A(DOF)}$ and any DOF from subsystem B will be referred to as $j_{B(DOF)}$. Any joining parameters will then be referred to with subscript $j_{A(DOF),B(DOF)}$, referring to the DOF from each subsystem that is part of the joint. Now by following [13], the equilibrium and compatibility equations at

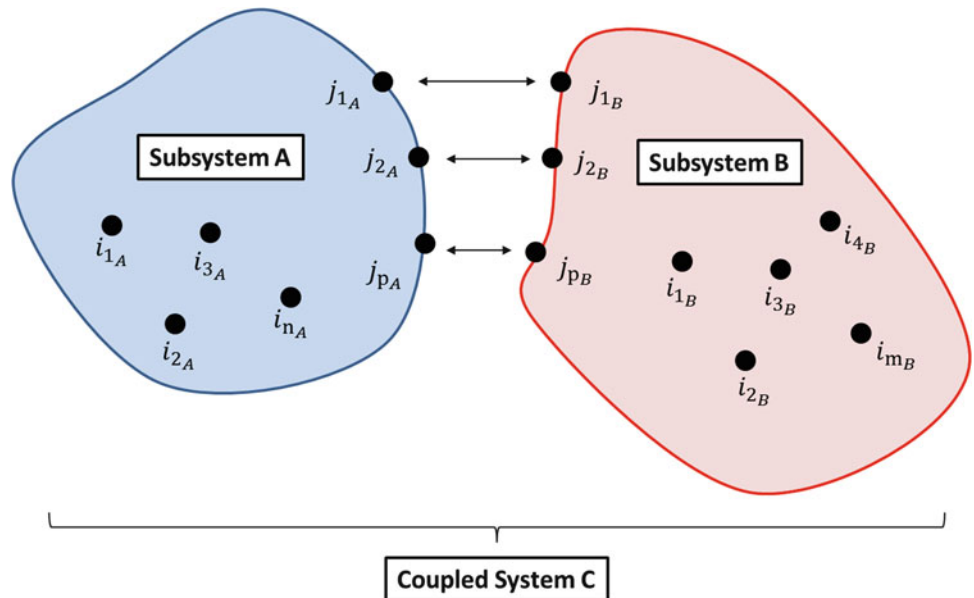


Fig. 6.2 Generic coupling of two subsystems at specified degrees of freedom

the coupling co-ordinates can be obtained and any connection point. For example, the following equilibrium equations are obtained at the coupling DoF j ,

$$\mathbf{F} = \mathbf{f} + \mathbf{f}_j, \quad (6.1)$$

where the force of the coupled system \mathbf{F} is the sum of the forces of the subsystems \mathbf{f} and of the joint \mathbf{f}_j . The force equilibrium equation (6.1) can be now described in terms of force equilibrium of individual subsystems A and B as,

$$\begin{aligned} \mathbf{F}_A &= \mathbf{f}_A + \mathbf{f}_{A(j)} \\ \mathbf{F}_B &= \mathbf{f}_B + \mathbf{f}_{B(j)} \end{aligned} \quad (6.2)$$

Similarly, the condition of compatibility is given by

$$\mathbf{X}_{C(J)} = \mathbf{x}_{c(j)} = \mathbf{x}. \quad (6.3)$$

Note that in (6.3), the uppercase notation for DoF “ J ” refers to the DoF’s after coupling whereas the lowercase notation “ j ” refers to the DoF before coupling and it assumes that the displacement of the assembled structure at the coupling DOF’s, $\mathbf{X}_{C(J)}$ is equal to the displacement of the substructures at the joint, $\mathbf{x}_{c(j)}$, and to the displacement of the joint, \mathbf{x} . By following the steps (6.1) and (6.2) for each subsystem, the relationship (6.3) can be expressed in terms of individual subsystems A and B as

$$\begin{aligned} \mathbf{X}_{C(A(J))} &= \mathbf{x}_{c(A(j))} = \mathbf{x}_A \\ \mathbf{X}_{C(B(J))} &= \mathbf{x}_{c(B(j))} = \mathbf{x}_B \end{aligned} \quad (6.4)$$

With the equilibrium and compatibility equations defined, the system receptance matrix for the coupled system, which consists of FRFs at the joint locations can be given as

$$\mathbf{X}_{C(J)} = \begin{bmatrix} \mathbf{H}_{JI} & \mathbf{H}_{JJ} \end{bmatrix} \begin{bmatrix} \mathbf{F}_I \\ \mathbf{F}_J \end{bmatrix}. \quad (6.5)$$

In Eq. (6.5), the subscript I refers to any non-joint location and J refers to any joint location of the overall coupled system. The receptance matrix \mathbf{H}_{JI} consists of non-located transfer functions obtained at the coupling DoF’s J when excited at a non-coupled DoF’s I , while \mathbf{H}_{JJ} refers to the collocated transfer functions obtained at coupling DoF’s J due to the excitation at J . Similarly, the equation for the uncoupled system (individual subsystems) can be obtained as

$$\mathbf{x}_{c(j)} = \begin{bmatrix} \mathbf{H}_{ji} & \mathbf{H}_{jj} \end{bmatrix} \begin{bmatrix} \mathbf{f}_i \\ \mathbf{f}_j \end{bmatrix}. \quad (6.6)$$

The governing equation of motion associated with the joint (coupling parameter) can be expressed in frequency domain as,

$$\mathbf{Z}\mathbf{x} = \mathbf{f}_j. \quad (6.7)$$

where, \mathbf{Z} refers to dynamic stiffness matrix consisting of the physical parameters describing the joint, such as stiffness and damping, the vector \mathbf{x} refers to the co-ordinates of the joint locations for the system and \mathbf{f}_j is the associated force vector. For this formulation, the equilibrium assumption is that the forces of the coupled system are equal to that of the joint and the substructures, and the condition of compatibility is that the displacement of the coupled degrees of freedom are equal to the summation of the displacement of the substructures and of the joint. Combining Eqs. (6.1), (6.3), and (6.6) into Eq. (6.7), the following expression can be obtained as

$$\mathbf{f} = [\mathbf{I} + \mathbf{Z}\mathbf{H}_{jj}]^{-1} (\mathbf{F}_C - \mathbf{Z}\mathbf{H}_{ji}\mathbf{F}_I), \quad (6.8)$$

where \mathbf{I} is the identity matrix of the same dimension of $\mathbf{Z}\mathbf{H}$. Substituting Eqs. (6.3) and (6.8) into Eq. (6.6) yields

$$\mathbf{X}_{C(J)} = \begin{bmatrix} \mathbf{H}_{ji} - [\mathbf{I} + \mathbf{Z}\mathbf{H}_{jj}]^{-1} \mathbf{Z}\mathbf{H}_{ji} & \mathbf{H}_{jj} [\mathbf{I} + \mathbf{Z}\mathbf{H}_{jj}]^{-1} \end{bmatrix} \begin{bmatrix} \mathbf{F}_I \\ \mathbf{F}_J \end{bmatrix}. \quad (6.9)$$

Comparing Eq. (6.9) with Eq. (6.5), it can easily be seen that by knowing the receptance at the joints of the uncoupled system, the receptance of the overall system at the joints can be found as

$$\mathbf{H}_{JJ} = \mathbf{H}_{jj} [\mathbf{I} + \mathbf{Z}\mathbf{H}_{jj}]^{-1}. \quad (6.10)$$

Equation (6.10) requires only the receptance of all the joints when each of the joints is excited and the joint parameters \mathbf{Z} to calculate the response of the coupled system at the joint locations. The size of the \mathbf{H}_{jj} matrix will depend upon the number of coupling points between the subsystems A and B. For m number of coupling points the \mathbf{H}_{jj} matrix will have the dimension of $(2m \times 2m)$. For example if two points “a” and “b” of the subsystem A is coupled at points “c” and “d” of the subsystem B then the frequency response matrix \mathbf{H}_{jj} of dimension (4×4) has the following form,

$$\mathbf{H}_{jj} = \begin{bmatrix} \mathbf{H}_{A(j)} & \mathbf{0} \\ \mathbf{0} & \mathbf{H}_{B(j)} \end{bmatrix} = \begin{bmatrix} H_{A_a,A_a} & H_{A_a,A_b} & 0 & 0 \\ H_{A_b,A_a} & H_{A_b,A_b} & 0 & 0 \\ 0 & 0 & H_{B_c,B_c} & H_{B_c,B_d} \\ 0 & 0 & H_{B_d,B_c} & H_{B_d,B_d} \end{bmatrix}. \quad (6.11)$$

It is shown with numerical examples in [11, 12] that an overall coupled system, which is composed of simplified Jeffcott rotor model coupled with a fixed-fixed beam at two locations, shifts the critical speeds of the original un-coupled rotor system. Hence instability and excessive vibration may be experienced through the excitation of base as well as the rotor system. It is observed that the structural modes of the base excite the rotor system at speeds that were not expected for uncoupled rotor-bearing system. The modified critical speeds of the coupled system are found to be sensitive to the location of coupling points as well as the dynamic stiffness \mathbf{Z} of the coupling elements (if any). The above formulation became the basis for seeking the structural modification such that coupling points and its dynamic stiffness can be designed in such way that the original dynamic behavior of the rotor system is not influenced due to flexible foundation. Moreover, these coupling points may also be used to our advantage in modifying the critical speeds of the coupled system to desired values for a given operating range.

In order to implement these techniques for a more realistic industrial scale system a finite element model of a Motor-Compressor train mounted on a flexible concrete base is developed in the following section. The overall dynamical behavior of the coupled system is obtained by extracting transmissibility transfer functions at some prescribed locations. In order to design suitable structural modification at the points of coupling, the vibration level at different components for a given unbalance is also obtained through numerical simulations.

6.3 Industrial Scale Rotordynamic System with Flexible Base: Modelling, Simulation and Results

6.3.1 Simulation Model of 65 MW Motor-Compressor Train

In order to study the vibration behaviour of the foundation and rotor system, the coupled structural- rotor bearing FEM simulation model was prepared to represent the complete system as close as possible. With increasing computing power, the rotor-foundation structure model is prepared by considering many nodes and degrees of freedom in order to simulate realistic operating conditions. The motor shaft consists of flexible beam elements based on Timoshenko beam theory, taking into account both bending and shear of the shaft. The rotor-shaft is connected to the bearing housing through a speed dependent linear oil film spring, which represents both the direct and cross coupled oil film stiffness and damping properties. The bearing housing is connected to a main motor-base-frame through a linear translation spring, representing the flexibility of a bearing housing. The motor-base-frame is connected through a linear translational spring, modeling the flexibility of a base frame to the motor mass and inertia in order to distribute the load equally at the supporting locations. The motor mass and inertia is connected to the foundation table top through the linear spring so that the movement of the nodes on the table is transferred to rotor and vice versa the concrete table top and the columns are volume elements containing the mass density and stiffness of steel reinforced concrete. In order to include the effects of the compressor structure, a lumped mass and inertia is created and connected to the foundation table top through linear springs (Fig. 6.3).

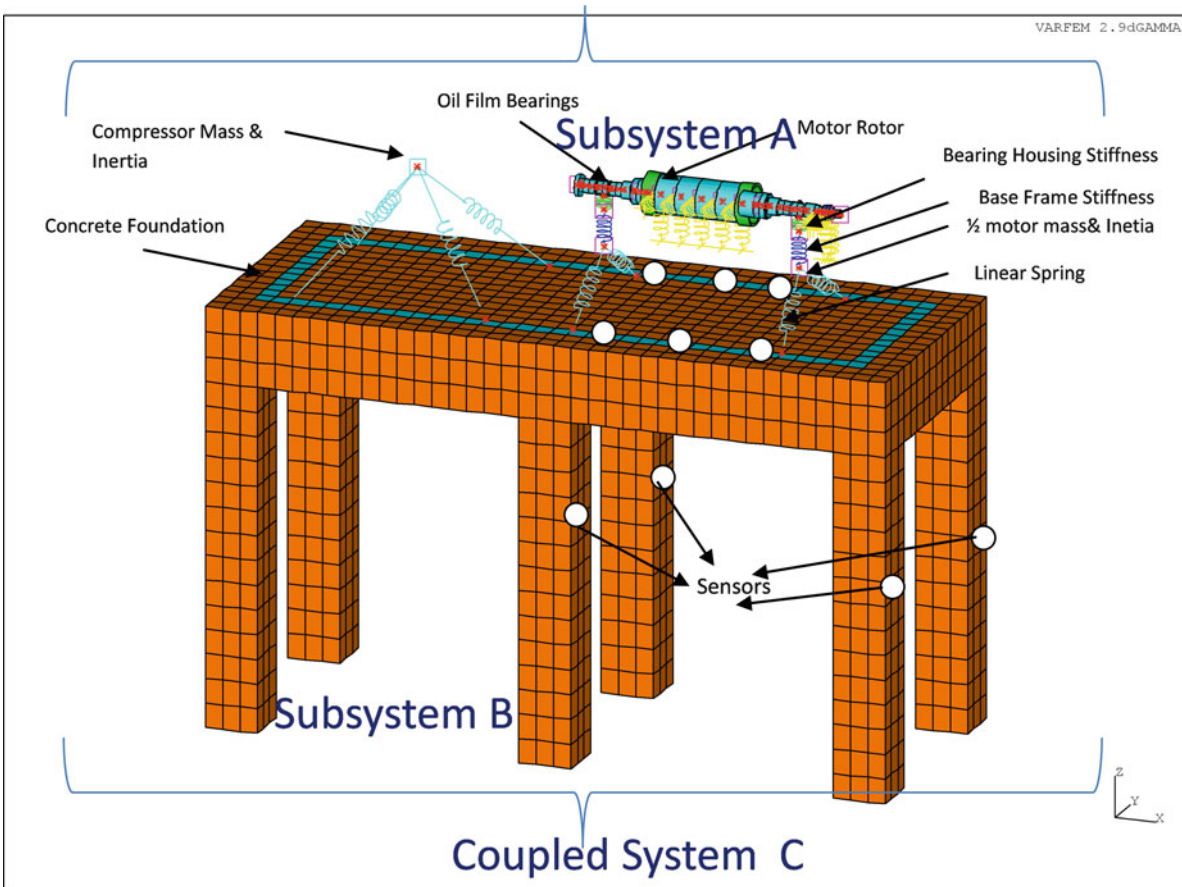


Fig. 6.3 Schematic of simulation model

6.3.2 Classification of Deflection Modes

Vibration calculation with a large number of degrees of freedom leads to many natural frequencies, and in order to evaluate the vibration behaviour, modes of interests must be identified based on the critical mode shapes of the structure or rotor-bearing system. Once identified, these can then be modified for acceptable vibration behaviour. The modes of vibration for foundation-rotor-bearing depending on their deflection shape can be roughly classified in the following forms (Fig. 6.4).

6.3.2.1 Rigid Body

For these vibration modes, the whole structure moves as rigid body, usually the frequencies are much lower than the operating speed range of the typical motor-compressor units. The calculated values depend upon the boundary conditions chosen to fix the structure to the ground (e.g. soil properties, sea floor properties, etc.). Usually these frequencies do not cause vibration issues for the drive train and is of low interest for dynamic calculations. However, special attention should be given if the machine is going to a region that is highly susceptible to earth quakes; such structural modes could be excited by the earth quake forces.

6.3.2.2 Rotor Modes

Rotor modes are the lateral bending modes of drive train rotor. The rotor bending gets excited strongly by the presence of the mass unbalance in the drive train systems. Drive train must be designed so that there are no bending natural frequencies within the operating speed range.

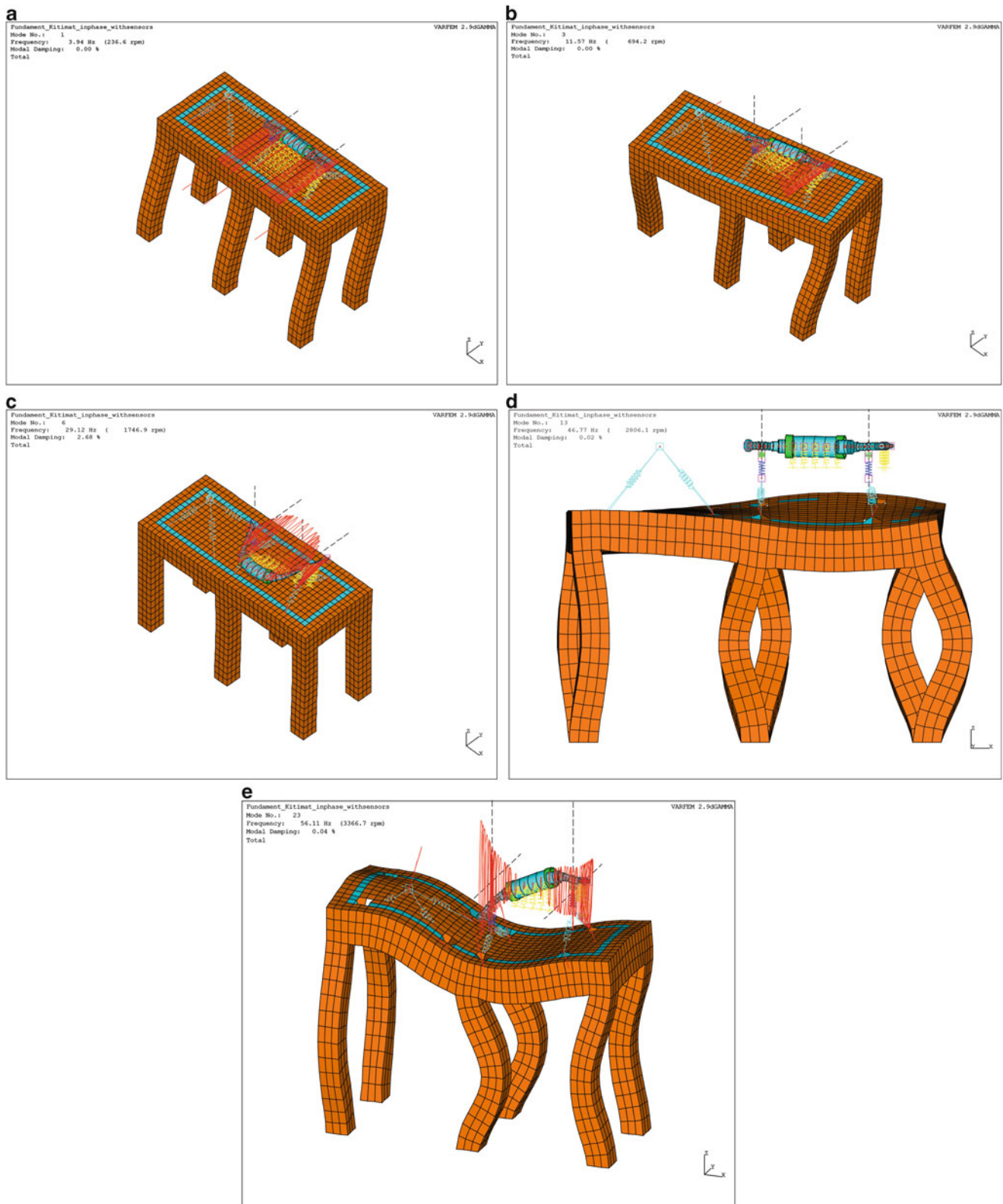


Fig. 6.4 Vibration modes calculated at 3,000 rpm. (a) Rigid body mode $f = 3.94$ Hz, (b) vertical pillar bending mode $f = 11.57$ Hz, (c) rotor lateral bending mode $f = 29.12$ Hz, (d) system mode $f = 46.77$ Hz, (e) system mode $f = 56.11$ Hz

6.3.2.3 Vertical Support Vibrations

A foundation's vertical supports behave like ordinary prismatic beams, having their own bending natural modes caused by axial and lateral loading. However, since it is connected to the table top upon which the rotor system is mounted, it can also cause the bending of the table top, ultimately influencing the drive train shaft vibration. The influence of the vertical support vibrations on the drive train shaft vibration depends upon the flexural stiffness of the vertical beams and the mass and flexibility of the table top.

6.3.2.4 Table Top Vibrations

The table top upon which the drive train structure is mounted behaves like a flat plate, which has its own natural frequencies. The vibration frequency of the table depends upon the mass and the stiffness of the plates, but also the flexibility and the dynamics of the vertical support columns. Vibration of a table bed directly influences the drive train casing and rotor vibration. The natural frequency of table top should not be close to the bending frequencies of the drive train system to prevent any coupling with the rotor dynamics, which can lead to high vibration during start-up of the drive train or passing through the bending critical speeds during machine ramp-up.

6.3.2.5 Systems Modes

The system modes of vibration are caused by the interaction of the various system components. The system modes can only be calculated by considering all the components in the system and will affect the vibration of the complete system.

6.3.3 Calculation of Natural Frequency

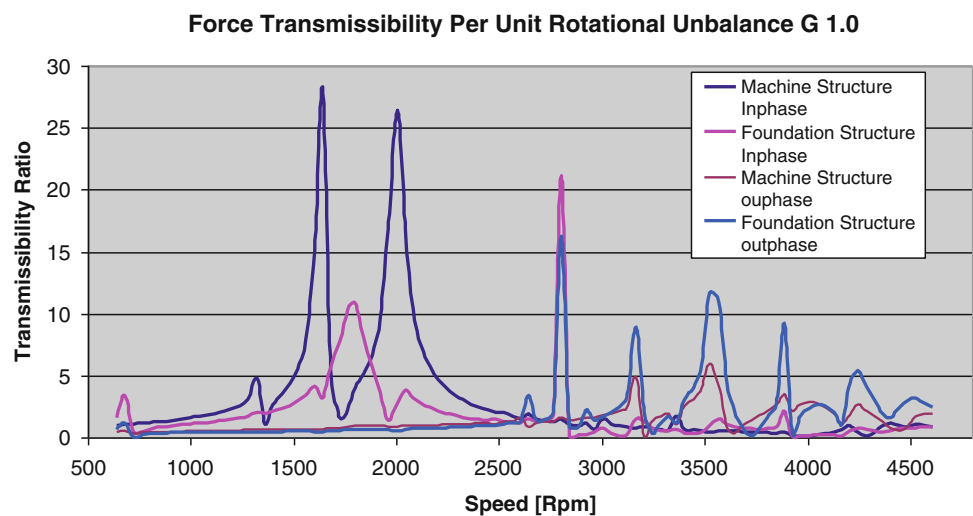
The Eigen values of the complete FEM model were calculated using the MADYN program. For the calculation of the gyroscopic effects and the fluid film bearing stiffness and damping, the rotational speed was held constant at 3,000 rpm. For the worst case vibration design, only the bearing damping is included in the model for eigen frequency calculation. As seen from Table 6.1, there are 27 modes of vibration between frequencies 3 and 69 Hz. Drive train systems with flexible foundations will have to pass through several critical frequencies during operation. The most damaging frequencies to drive train rotor system are the ones which cause the highest relative shaft vibration, as this can cause bearing damage. These frequencies should have sufficient separation margin from the normal operating speed ranges [14]. The most damaging frequencies to the structures and connections are the frequency which causes vibration beyond a certain threshold value, leading to fatigue failure or crack propagation over time. For large rotating equipment mounted on a flexible foundation, as shown in this example, it is not possible to design the system which is free of natural frequencies for the given operating speed range, hence material strength calculations should be performed. Considerable time and experience is required to sort out the modes which may cause vibration issues to the complete system.

6.3.4 Steady State Unbalance Response Calculation for the Complete System

The magnitude of the vibration amplitude at critical modes depends upon the magnitude and distribution of the rotational unbalance in the rotor system and the vibration transmissibility between the various components. Usual source of excitation in rotating machinery is the rotating unbalance forces which are generated whenever the rotational axis of the rotor does not coincide with the center of mass of rotor. In a drive train system, there are always some degree of the residual unbalance forces which are present due to manufacturing tolerances, alignments and thermal expansion of different system components. Distribution of the unbalance in the rotor system provides the excitation forces needed to excite the natural modes. In the present calculation method, the rotor unbalance forces of ISO Grade 1.0 is applied onto the rotor system; half of the unbalance force is distributed at each end of the motor-rotor magnetic core, one in phase and out of phase with the other. In phase unbalance distribution in forces causes the rotor to have a deflection shape similar to the first bending mode of the rotor, while the out of phase unbalance distribution in forces causes the rotor to have a deflection shape similar to second bending mode.

Table 6.1 Natural frequencies at 50 Hz

Mode	Frequency (Hz)	Speed (rpm)	Damping (%)	Mode classification
1	3.94	236	0.001	Rigid body
2	4.28	256	0	Rigid body
3	11.58	694	0.005	Vertical support
4	22.3	1,338	0.058	Rotor bending
5	27	1,620	0.733	Rotor bending
6	29.113	1,746	2.6	Rotor bending
7	32.988	1,979	1.326	Rotor bending
8	41.342	2,480	0.001	Vertical support
9	41.944	2,516	0.008	Vertical support
10	43.770	2,626	0.032	System
11	43.971	2,638	0.011	Vertical support
12	46.15	2,769	0	Vertical
13	46.768	2,806	0.024	System
14	46.896	2,813	0.001	Vertical support
15	47.509	2,850	0	Vertical support
16	47.719	2,863	0.005	Vertical support
17	48.446	2,906	0.003	System
18	48.646	2,918	0.026	System
19	49.781	2,986	0.049	Vertical support
20	50.4	3,024	0.003	Vertical support
21	52.419	3,145	0.02	Table top
22	52.97	3,178	0.16	Table top
23	56.11	3,366	0.041	System
24	58.367	3,502	0.004	Table top
25	59.191	3,551	0.7	Table top
26	64.6	3,891	0.158	Rotor bending
27	68.7	4,121.99	4.86	Rotor bending

Fig. 6.5 Transmissibility due to rotational unbalance forces

The unbalances forces get transmitted from the rotor system to the machine-foundation structure through oil film spring elements, which have both stiffness and damping. Figure 6.5 shows the ratio of force transmitted to the bearing housing and foundation due to rotational unbalances in the drive train system. The force transmitted to the bearing housing and foundation is quite different for different speeds. It can be seen from the system calculations that in phase unbalance distribution transfers higher forces to the bearing housing in the vicinity of the first bending mode of the rotor-bearing system. Also, the force transmitted to the foundation increases significantly near the system natural frequency 46.67 Hz. The transmitted dynamic forces from the rotor unbalance distribution manifest itself as vibration. In order to simulate the vibration behavior for field conditions, the unbalance system response output was calculated for the complete coupled system. The calculated system response is plotted and evaluated for following sensor arrangement.

Fig. 6.6 Unbalance response of shaft vibration relative to bearing housing vibration

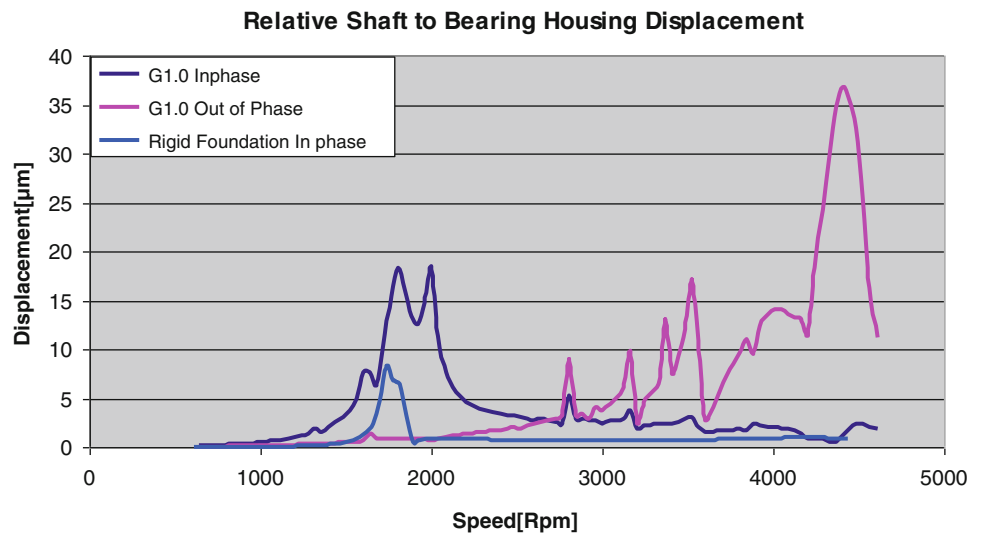
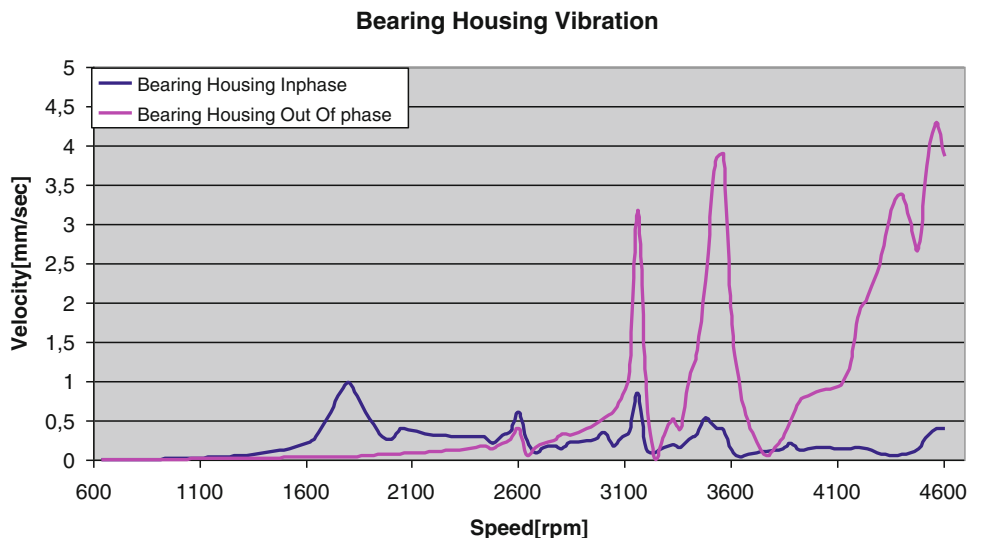


Fig. 6.7 Response of bearing housing vibration to rotational unbalance

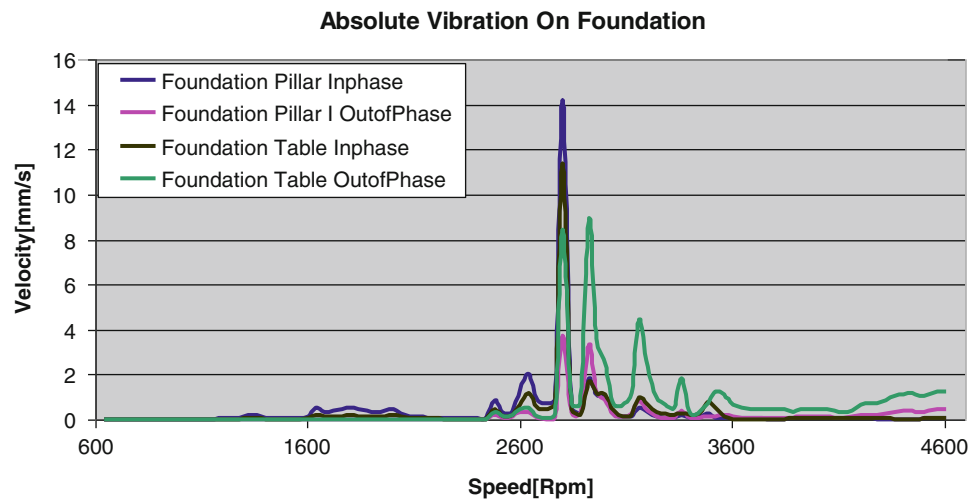


1. Relative displacement between the bearing housing and the shaft vibration (Rotor Bending Vibration)
2. Absolute velocity vibration at bearing housing (Motor Structural Vibration)
3. Absolute velocity vibration at foundation table and vertical pillars (Table Top Modes)

6.3.4.1 Relative Displacement Between Shaft and Bearing Vibration

Figure 6.6 shows the relative shaft vibrations with respect to the bearing housing for the in phase and the out of phase unbalance distribution. As seen from Fig. 6.6 the maximum relative shaft-housing vibration occurs at 1,800 and 2,000 rpm, which corresponds to the first lateral bending mode the motor-rotor systems. This mode is strongly excited by the in phase unbalance distribution. Figure 6.4c gives the corresponding deflection shape for this speed. From Fig. 6.6 it is also seen that the vibration values and the behaviour of the rotor is significantly different when the complete foundation is considered in the rotor dynamics analysis in comparison to rigid foundation. It is also observe that although the location of rotor critical speed is not influenced much but the vibrations amplitudes differ significantly. It can be seen from Figs. 6.7 and 6.8 that the housing and foundation vibration is not the maximum value at this speed and also dynamic force transmitted to foundation is lower. If this mode occurs within the operating speed range then the modification will be required to the rotor-bearing to shift this to acceptable speeds. It can also be observed that the relative shaft vibrations with respect to the bearing housing are quite different for out of phase unbalance distribution in comparison with in phase distribution. New modes get excited at higher speeds which were not observed with the in phase distribution calculation.

Fig. 6.8 Response of foundation and pillars to rotational unbalances



6.3.4.2 Absolute Bearing Housing Vibration

Figure 6.7 shows the absolute vibration at the bearing housing for an in phase and an out of phase unbalance distribution. The maximum vibration for in phase occurs at 1,800 rpm. The peak at 1,800 rpm is caused to the presence of the first lateral bending mode of the rotor-bearing system which was also observed in relative shaft vibrations with respect to bearing housing. The vibration amplification at 2,800 rpm is caused by the presence of system natural frequency. This corresponding high vibration at 2,800 rpm is also observed in shaft vibration foundation table vibration and on vertical support vibration. This is the system natural frequency which may cause potential vibration issues if it lies within the operating speed range. It can also be observed from Fig. 6.7 that absolute vibration of housing is quite different for out of phase unbalance distribution in comparison with in phase distribution. In phase unbalance has higher influences at lower speeds ranges while out of phase unbalance distribution has very strong influences on the housing vibration at higher speed range. In order to have reliable design the fatigue analysis of components should be performed to predict the life of components subjected to the dynamic loads.

6.3.4.3 Absolute Vibration at Vertical Pillar and Foundation Table

Figure 6.6 shows the absolute vibration at the vertical pillar supporting the foundation table for an in phase and an out of phase unbalance distribution. The maximum vibration for in phase occurs at 2,800 rpm. The vibration amplification at 2,800 rpm is strongly excited as visible from vibration response by the in phase unbalance distribution. As observed from Fig. 6.6 the dynamic force transmitted to the foundation is also very high leading to very high vibration in vertical pillars. This high vibration at 2,800 rpm is also observed in shaft vibration, foundation table vibration and on bearing housing leading to the conclusion that this is one of the system resonances. The vibration amplitude for unbalance grade G 1.0 leads to 14 mm/s peak to peak rms vibration in foundation which can cause severe damage to the foundation if this occurs within the speed range. Looking at the deflection shape of this system mode, most of the deflection occurs at foundation table and in the pillars, hence modification to stiffness of the pillars or/and to the mass of foundation table will change the location of this mode.

6.4 Conclusion

Multi-body eigen value analysis of the rotor-bearing system coupled with the flexible foundation structures shows that there are many modes of vibration which exist in the system from the starting frequency to the maximum operating frequency. This shows that a drive train system may have to pass through several natural frequencies related to the rotor, foundation or overall coupled system during startup and shutdown. These additional frequencies calculated from complete foundation model cannot be calculated from a simple model of foundation; hence the system natural frequencies also could not be calculated from simple vibration models. Dynamic forces resulting from unbalance forces can be used to excite the rotor-structure

multi-body system. Dynamic force transmitted to the bearing housing structure and foundation is different for different unbalance distribution in the rotor system. Different unbalance distribution leads to different response of the system. Not all the modes are excited by one unbalance distribution. In phase unbalance distribution has very strong influence on the rotor-bearing bending modes of vibration, while out of phase unbalance has more influence on the higher speed ranges. From the unbalance response analysis, the following can be concluded

1. Dynamic transmissibility of the unbalance forces to the structure increases at the rotor-bearing critical frequencies, which lead to the design criteria that the foundation structures should not have natural frequencies close to the critical frequencies of the rotor-bearing system.
2. Dynamic transmissibility of unbalance forces is very high near the system eigen frequencies. Hence, if system is operating at or near the system frequencies small unbalances can lead to large vibrations.
3. Based on the vibration amplitudes, foundation and machine structural design could be modified to meet the design specifications.

Future research will deal with extracting the numerical transfer functions from the model to construct (6.11) from the subsystems at the coupling location and estimation of dynamic behavior of the coupled system from (6.10) for a given coupling flexibility Z defined by bearing housing stiffness, base frame stiffness and linear springs. Once they are validated against those obtained from full scale model, these small number of FRF's can be used for modifying the stiffness parameters of the coupling flexibility such that vibration of the coupled system is minimized and the vibration modes of flexible foundation do not influence the dynamics of the Motor-Compressor Train.

References

1. Krämer E (1993) Dynamics of rotors and foundations. Springer, Berlin
2. Nicholas JC, Whalen JK, Franklin SD (1986) Improving critical speed calculations using flexible bearing support FRF compliance data. In: Proceedings of the 15th turbomachinery symposium, College Station
3. Vázquez JA, Barrett LE (1999) Transfer function representation of flexible supports and casings of rotating machinery. In: Proceedings of the 17th international modal analysis conference, Kissimmee
4. Vázquez JA, Barrett LE, Flack RD (2001) A flexible rotor on flexible bearing supports: stability and unbalance response. *J Vib Acoust* 123(2):137–144
5. Vázquez JA, Barrett LE, Flack RD (2002) Flexible bearing supports, using experimental data. *ASME J Eng Gas Turb Power* 124:369–374
6. Kruger T, Liberatore S, Knopf E (2013) Complex substructures and their impact on rotordynamics. Berlin
7. Kang Y, Chang Y, Tsai J, Mu L, Chang Y (2000) An investigation in stiffness effects on dynamics of rotor-bearing–foundation systems. *J Sound Vib* 231(2):343–374
8. Bonello P, Brennan M (2001) Modelling the dynamic behaviour of a supercritical rotor on a flexible foundation using the mechanical impedance technique. *J Sound Vib* 239(3):445–466
9. Choi B, Park J (2002) Application of the impedance coupling method and the equivalent rotor model in rotordynamics. *Finite Elem Anal Des* 39(2):93–106
10. Chen Y, Cheng Y, Yang T, Koai K Accurate identification of the frequency response functions for the rotor–bearing–foundation system using the modified. *J Sound Vib* 329(6):644–658
11. Birchfield NS, Singh KV, Singhal S (2013) Dynamical structural modification for rotordynamic application. In: Proceedings of the ASME 2013 international design engineering technical conferences (IDETC 2013), 4–7 August 2013, Portland
12. Birchfield NS (2013) Structural modification of coupled rotordynamic systems from transfer functions. MS thesis, Department of Mechanical and Manufacturing Engineering, Miami University, Oxford
13. Liu W (2000) Structural dynamic analysis and testing of coupled structures. PhD thesis, Imperial College of Science, Technology and Medicine, London
14. API 541 Form-wound squirrel cage induction motors-250 horsepower and larger

Chapter 7

Reconstructing Forces from Continuous Connections Using SWAT

Tyler F. Schoenherr

Sandia National Laboratories is a multi-program laboratory managed and operated by Sandia Corporation, a wholly owned subsidiary of Lockheed Martin Corporation, for the U.S. Department of Energy's National Nuclear Security Administration under contract DE-AC04-94AL85000.

Abstract During an environment, it is desirable to know the forces or inputs on the system of interest. With the inputs, one can directly use a finite element or experimental model to predict responses not measured in a field test. One can attempt to measure point forces using force gauges, however, these gauges are insufficient due to the inability to place a gauge at a forcing interface or to measure a force applied over an area. SWAT (Sum of weighted acceleration technique) is a method that uses mode shapes as a modal filter with measured accelerations and to solve the inverse problem and calculate the forces and moments on the system. This paper will examine an application where the use of a force gauge is impossible due to the external forces being applied over an area. The paper will calculate the sum of the forces and moments imparted on the system and will use a finite element model to check the plausibility of the calculated forces.

Keywords Substructure • Force • Reconstruction • SWAT • Experimental

Nomenclature

ϕ	Mode shape matrix
\bar{F}	Force vector
\bar{x}	Physical displacement
\bar{q}	Modal displacement
\mathbf{M}	Mass matrix
\mathbf{C}	Damping matrix
\mathbf{K}	Stiffness matrix

7.1 Introduction

External forces acting on a system is typically the cause of deformation, vibration and stress. Because of this, the equations of motion can be generated from a dynamic characteristic test such as a modal test and knowledge of the external forces on the system.

T.F. Schoenherr (✉)
Experimental Mechanics, NDE and Model Validation Department, Sandia National Laboratories,
P.O. Box 5800 - MS0557, Albuquerque, NM 87185, USA
e-mail: tfschoe@sandia.gov

Acquiring these external forces on a system are critical to an effective analysis and many have attempted to measure or calculate them. Typically, individuals use force gauges when possible to measure the force on the system. This requires a defined point as a boundary condition. Depending on the application, the force gauge may be bulky or too heavy so that it affects the true measurement.

Besides measuring the forces, forces can be calculated using responses and inverting the frequency response function matrix found through experimentation. Although this is an acceptable method for calculating the forces caused by an environment, several technical difficulties arise when inverting an experimentally found frequency response function.

Some of these difficulties are due to the fact that there are singularities in the inversion of frequency response matrices. This is analogous to the inversion of a single frequency response function in that the anti-resonances become the resonances of the inverted frequency response function. Because of the low response the anti-resonances, noise can corrupt the data and alter the resonances of the inverted frequency response function. Also, the frequency of the anti-resonances are where the sum of all the resonances sum to zero. This means that the location and magnitude of the anti-resonances are dependent on the amplitude and the damping measurements. Both are subject to experimental error.

An algorithm developed by Gregory et al. [2] called SWAT (Sum of Weighted Accelerations Technique) was later used to calculate the input forces on a system by Carne et al. [1]. SWAT uses the mode shapes of the system to act as a modal filter on the acceleration responses of the system under test and computes the sum of the external forces acting on or about the center of gravity of the system. An inversion is still required, however, SWAT inverts the mode shape matrix whose condition can be monitored and controlled by accelerometer placement. The sacrifice of this method is spacial force distribution. If the locations of the forces are known or can be assumed, the forces imparted on the center of gravity can be equated to the sum of the forces at the known external locations.

Although it is a requirement to know the locations of the external forces acting upon the system, it is not always possible due to continuous connections spread over an area where it is not acceptable to assume a point force. This issue is examined as the example given in this paper has such a continuous connection.

This paper first describes the method of SWAT. The paper then describes an application of SWAT on a large pipe as a test article. The laboratory test on the pipe is shown along with respect to the calculation and insight in the quality of the results. The pipe then experiences a mechanical environment in a fixture and the forces during this environment are calculated. These forces are validated by using a calibrated FEM to check the measured responses.

7.2 Formulation of SWAT (Sum of Weighted Acceleration Technique)

The formulation or derivation of the SWAT degrees of freedom and how it was used to calculate external forces begins with the general, linear equations of motion found in Eq. (7.1).

$$\mathbf{M}\ddot{\bar{x}} + \mathbf{C}\dot{\bar{x}} + \mathbf{K}\bar{x} = \bar{F} \quad (7.1)$$

Modal substitution was then used to replace the physical degrees of freedom with modal degrees of freedom as shown in Eqs. (7.2) and (7.3).

$$\phi\bar{q} = \bar{x} \quad (7.2)$$

$$\mathbf{M}\phi\ddot{\bar{q}} + \mathbf{C}\phi\dot{\bar{q}} + \mathbf{K}\phi\bar{q} = \bar{F} \quad (7.3)$$

At this point, the equations of motion were premultiplied by the transpose of the rigid body modes. Because there was no damping or internal stiffness forces for the rigid body degrees of freedom, the resulting damping and stiffness matrices are equal to zero. The resultant of these simplifications can be seen in Eq. (7.4).

$$\begin{aligned} \phi_r^T \mathbf{M} \phi \ddot{\bar{q}} + \phi_r^T \mathbf{C} \phi \dot{\bar{q}} + \phi_r^T \mathbf{K} \phi \bar{q} &= \phi_r^T \bar{F} \\ \phi_r^T \mathbf{C} &= 0 \ \& \ \phi_r^T \mathbf{K} = 0 \\ \phi_r^T \mathbf{M} \phi \ddot{\bar{q}} &= \phi_r^T \bar{F} \\ \phi_r^T \mathbf{M} \ddot{\bar{x}} &= \phi_r^T \bar{F} \end{aligned} \quad (7.4)$$

Equation (7.4) shows that the weighted sum of the measured accelerations can be equated to the sum of the external forces on the test object. These weights were calculated using the orthogonality of the mass matrix and substituted back into Eq. (7.4) as shown in Eq. (7.5).

$$\begin{aligned}\phi_r^T \mathbf{M} \phi_r &= [M_r \ 0] \\ \phi_r^T \mathbf{M} &= [M_r \ 0] \phi_r^+ \\ [M_r \ 0] \phi_r^+ \ddot{x} &= \phi_r^T \bar{F}\end{aligned}\quad (7.5)$$

The results of Eq. (7.5) show that the sum of the weighted accelerations can be used to calculate the sum of the external forces. These forces are the sum of the forces in the three principle translational directions and the three moments around those three principle axes. The weights for the accelerations are the mass properties of the test object multiplied with the rigid body vector components of the pseudo-inverse of the mode shape matrix that includes rigid body and elastic mode shapes.

7.3 Laboratory Test

The purpose of the laboratory test was to measure the mode shapes of the test object so that they could be used to filter out the dynamics of the test object during the environment of interest. A modal hammer was used as the excitation device for the modal test. Modes up to 2,000 Hz were fitted from the test and used to calculate the SWAT weights.

SWAT was performed on the acceleration responses obtained in the modal test. It was compared against the measured force imparted by the modal hammer. The SWAT force shown in the time and frequency domain in Fig. 7.1 shows that the forces match in the frequency domain up to approximately 1,500 Hz and the time domain shows all of the dynamics that were excited beyond 1,500 Hz.

Although modes were fit out to 2,000 Hz, it was apparent from Fig. 7.1 that some modes were either poorly defined, excited, or the accelerometer locations that were selected were inadequate. The acceleration data was filtered to 1,500 Hz to eliminate high frequency response and the forces recomputed. The resultant force in the time and frequency domain can be seen in Fig. 7.2. Figure 7.2 shows that a filter eliminated elastic motion that SWAT does not filter out and that the resulting force was limited to the bandwidth of the filter. It was also noted that the measured hammer force was filtered to 1,500 Hz. This was seen by a shorter peak in the force and a wider pulse in Fig. 7.2.

The laboratory test showed that SWAT has approximately 10% error when comparing the peak force when the signal was filtered at 1,500 Hz.

Another technique derived from SWAT by Mayes called SWAT-TEEM [3] was used on this data. This technique uses the free response acceleration data of a free structure after a force is removed to filter out the elastic motion of the unit under test instead of the mode shapes of the system. Because the accelerations were used to filter out the motion, the frequency limit is based upon the spacial resolution of the accelerometers and if they span the space of the mode shapes within the bandwidth of the forcing function. The force calculated by this technique can be seen in Fig. 7.3.

It was apparent that the reproduced force from SWAT-TEEM shown in Fig. 7.3 was a better fit than the SWAT force. This was due to the fact that the SWAT-TEEM algorithm does not include the error in curve fitting the modal parameters of the system and that the SWAT-TEEM forces only focus on the modes excited at one location while SWAT uses all mode shapes to filter. Also, the laboratory test had high spacial resolution with 132 responses that captured a high number of mode shapes up to a higher frequency than the mode shapes could have been fit. Although SWAT-TEEM was superior in this example, it was not directly applicable to the field test because the force imparted on the system in the field was not an impulse on a free-free system as was the case in the laboratory.

7.4 Application of SWAT Using Continuous Connections

The test object on which the forces were calculated was a pipe. This pipe was captured by a fixture that clamped down on the pipe creating two continuous connections. A photo of the pipe and the fixture that supports the test pipe can be seen in Fig. 7.4.

Because calculating forces using SWAT was an inverse problem involving the inverse of the mode shapes of the pipe, the number of mode shapes and the location and number of responses determined the condition number of the experimental mode

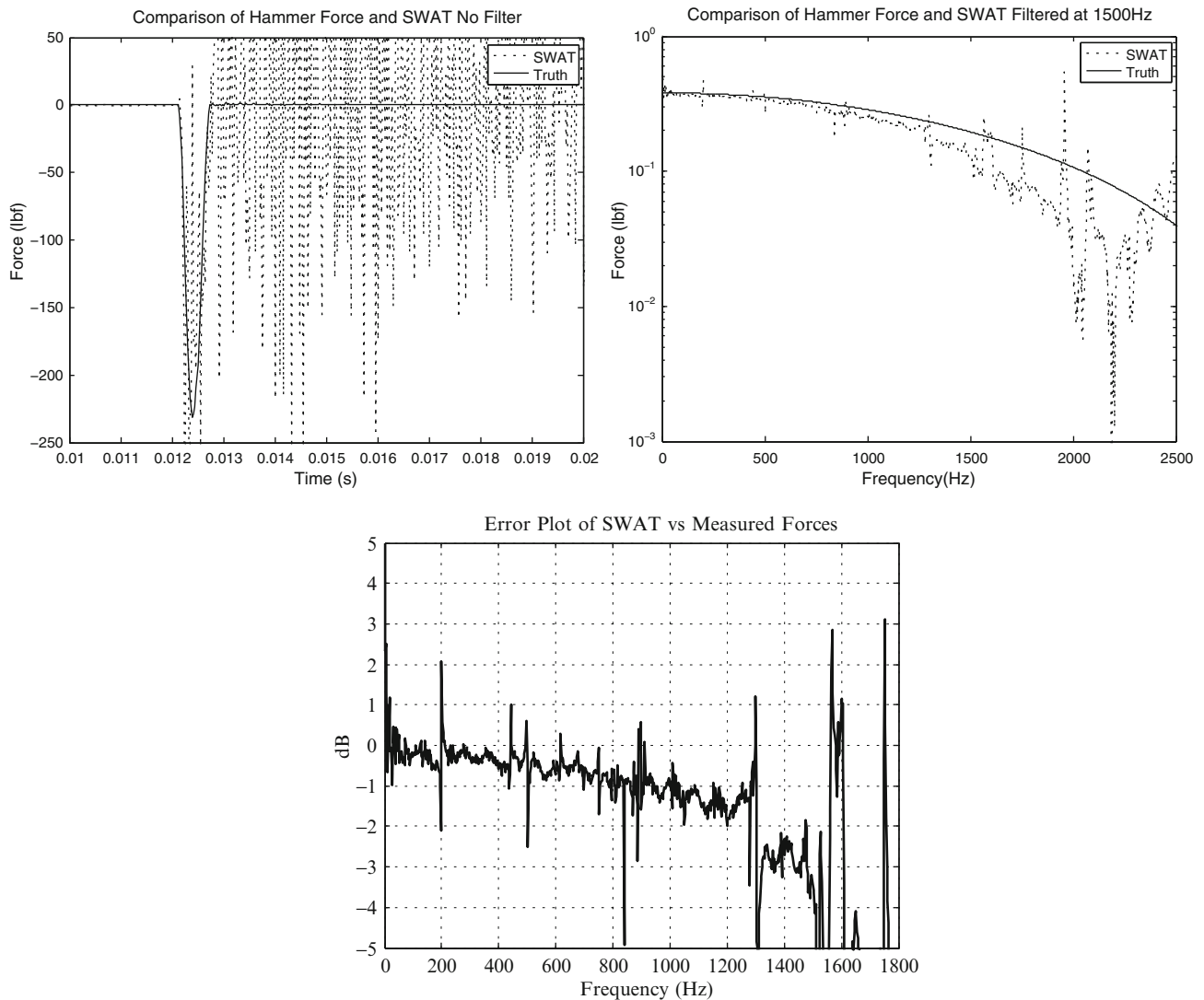


Fig. 7.1 SWAT force on hammer hit with no filter

shape matrix. If the condition number was too high, noise from either the lab or field measurements corrupted the results. Also, the forcing function was filtered to the highest frequency mode shape used in the analysis. Due to these constraints, the modal data taken from the lab was used to determine where the final subset of accelerometers should be placed during the environment to minimize the condition number of the matrix and to what frequency to perform the analysis.

The process for predicting the environment can be seen in Fig. 7.5. The accelerations measured during the test were filtered to a frequency of 1,500Hz because this was the frequency found in the lab where the ability of SWAT began to deteriorate. The SWAT forces were then resolved to the assumed locations that they actually imparted the pipe.

To check the validity of these calculated forces, they were used on a FEM of the pipe and the responses of the model were compared to the data obtained in the environment test. This process can also be seen in Fig. 7.5. These forces were then put on a FEM of the pipe and a modal transient analysis performed by Salinas.

SWAT calculated the sum of the forces and moments. Because there were three moments and three forces calculated, this was resolved to six assumed locations that the fixture was imparting forces on the pipe. These assumed locations were simplifications as the real connection was continuous around the pipe. These assumed locations and directions can be seen in a drawing in Fig. 7.6. These forces were chosen to be a best guess as to where the resultant of the force at each connection. Forces pointed in the Y and Z direction where the circular constraint was imposed was chosen to be at the bottom because that is around where the weight of the pipe was centered. Also, the lug on the top of the pipe was captured by the fixture which had a force preventing motion in the direction of its axis and about its axis.

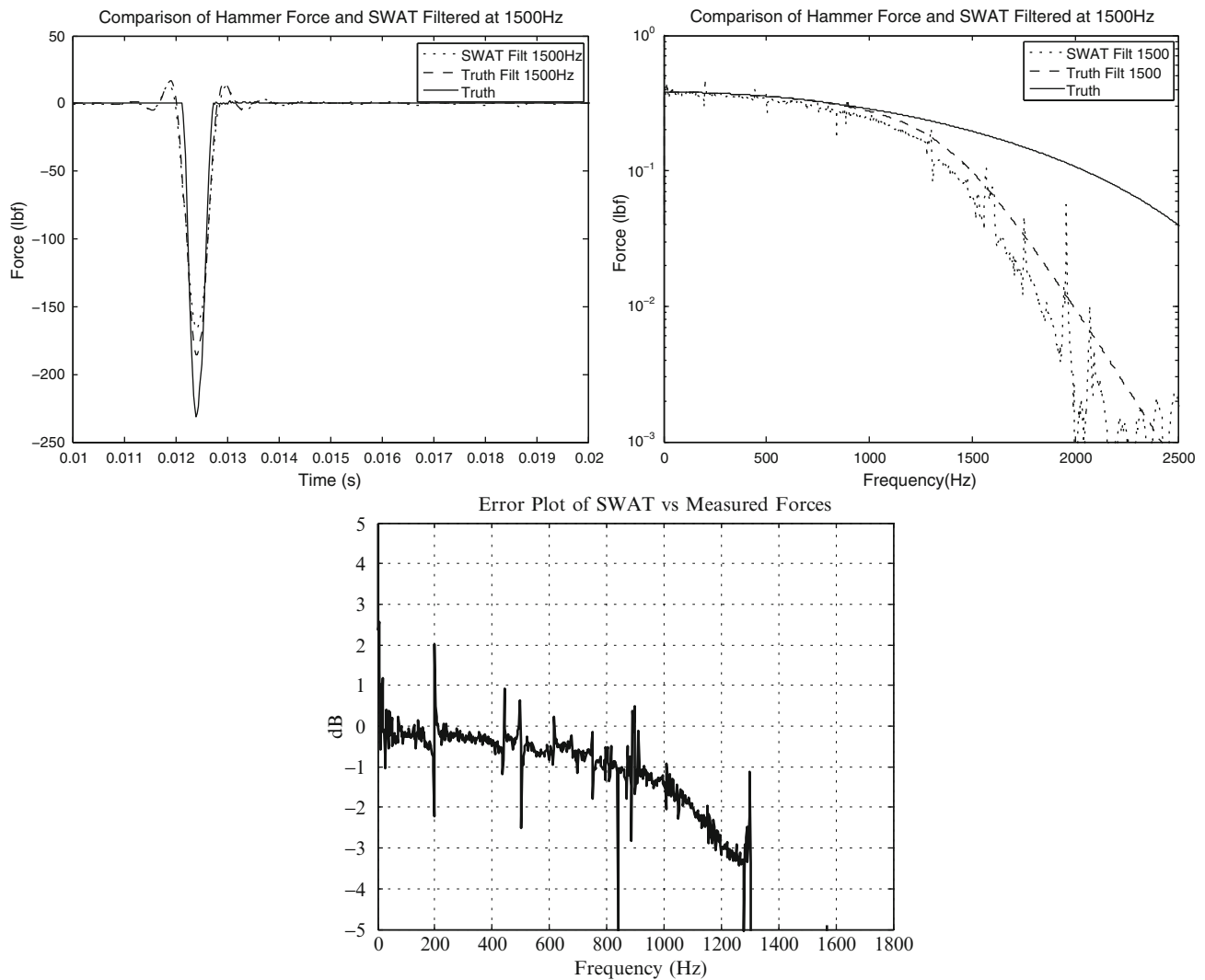


Fig. 7.2 SWAT force on hammer hit with 1,500 Hz filter

To verify the results, the forces that were calculated were given as inputs to the FEM of the pipe. This FEM was calibrated to match the modes that were calculated in the lab within 3% of the natural frequencies. The acceleration of a point that was measured during testing was the output of the analysis. The point used was node 92. A snapshot of the FEM can be seen in Fig. 7.7.

The comparison between the raw data and the SWAT force induced acceleration of the XYZ component of node 92 can be found in Figs. 7.8, 7.9, 7.10. The frequency domain of the accelerations can also be found in Figs. 7.11, 7.12, 7.13.

The results of comparing the acceleration predictions using the forces derived from SWAT and the experimental accelerations were made qualitatively by examining Figs. 7.8, 7.9, 7.10, 7.11, 7.12, 7.13. It was noted that the FEM predictions under 180 Hz were excellent and because most of the energy of the environment was in this frequency range, the time domain predictions were excellent.

Because there was confidence in the low frequency response and the rigid body response, there was reason to believe that the boundary conditions and force location assumptions were adequate. The boundary conditions included continuous surfaces that were assumed to be resolved down to six discrete locations.

However, there were some discrepancies at the higher frequencies. There were higher frequencies where the FEM over predicted the response or had the response at different frequencies. This was identified to be a mode of the system at an incorrect frequency or an undamped mode. It is possible that the reconstructed forces could have been applied differently to the FEM so that the results would have improved.

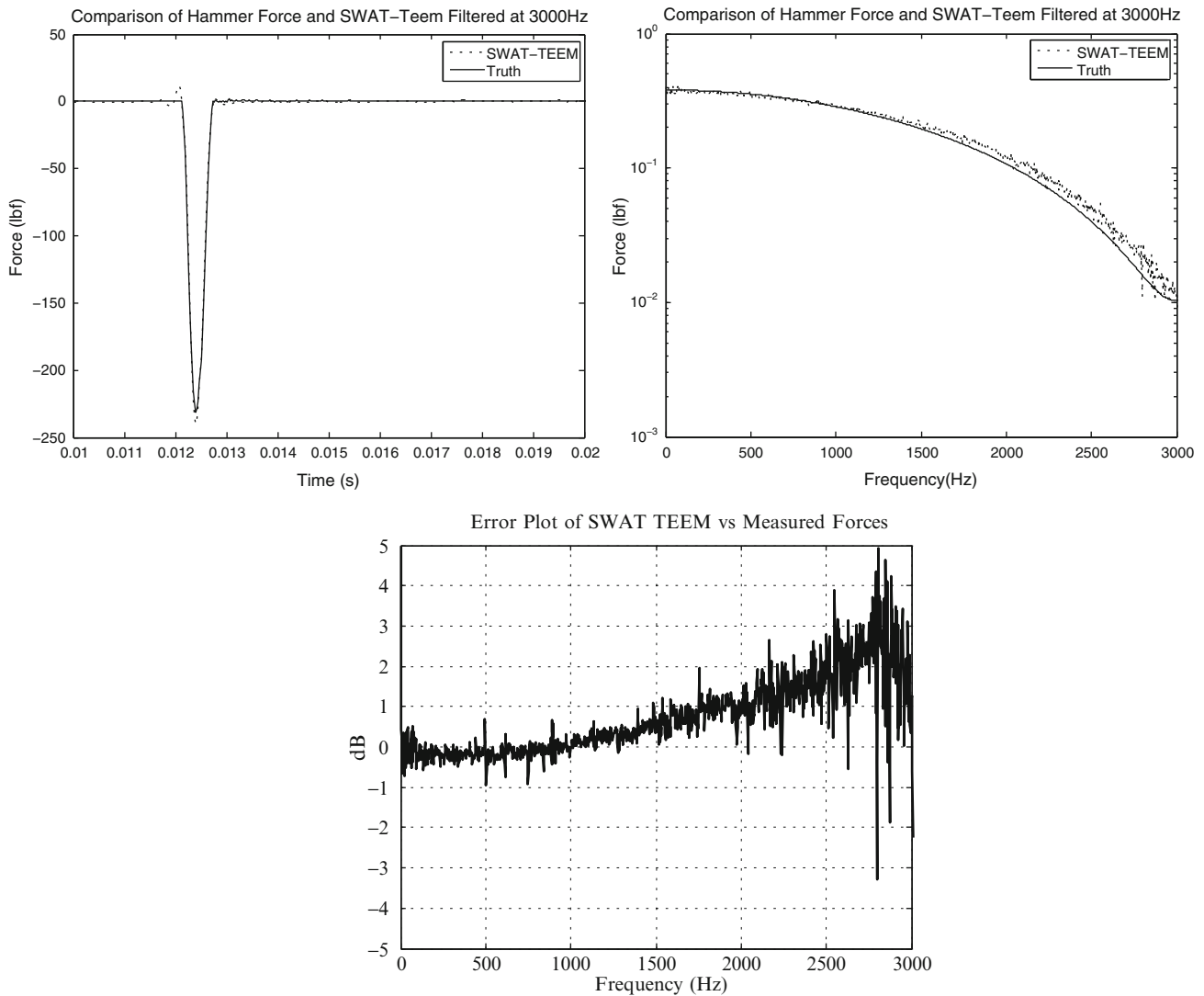


Fig. 7.3 SWAT-TEEM force on hammer hit with 3,000 Hz filter

7.5 Conclusions and Future Work

The SWAT algorithm was effective in predicting the forces on the pipe up to about 1,500Hz. This was shown through the laboratory testing by comparing the reconstructed force with a measured force. SWAT was also tested by comparing the experimental accelerations and the accelerations predicted by inputting the forces derived by SWAT into the FEM. The responses produced by the FEM when the environment forces were used as inputs showed excellent results under 200 Hz and fair results to 1,500 Hz. Because the environment had most of its energy at lower frequencies, the model provided an accurate prediction.

SWAT-TEEM was shown to work better on the laboratory data, but a method for extracting the weight vectors for the environment data would need to be explored. This is because the forces on the pipe were not an impact followed by the pipe being in a free-free condition. However, the SWAT-TEEM parameters used to filter out the dynamics of the pipe could be calculated by impacting the locations that the fixture was in contact with the pipe and then used during the environment.

Fig. 7.4 Photo of the boundary conditions of the test pipe



Fig. 7.5 Flowchart showing how SWAT was compared to field data

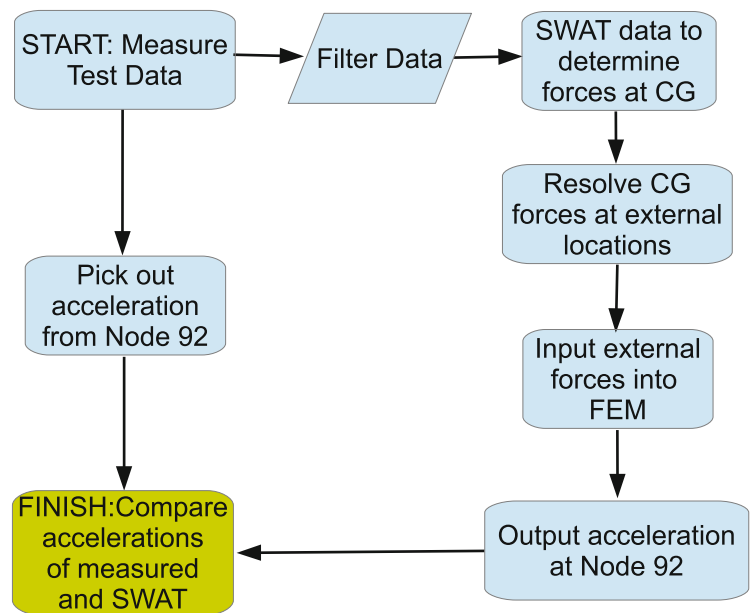


Fig. 7.6 Assumed location of the forces that the fixture imparted on the pipe

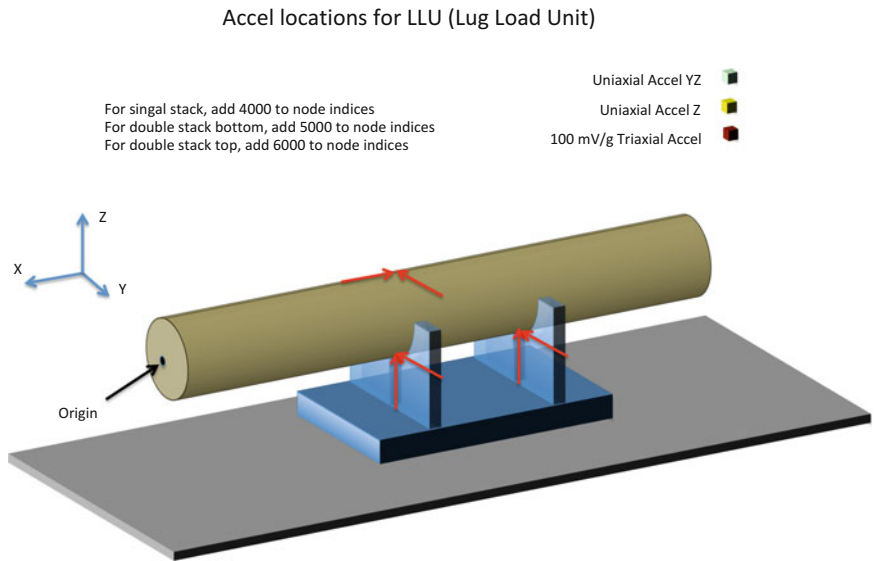


Fig. 7.7 Finite element model of the pipe and location of node 92

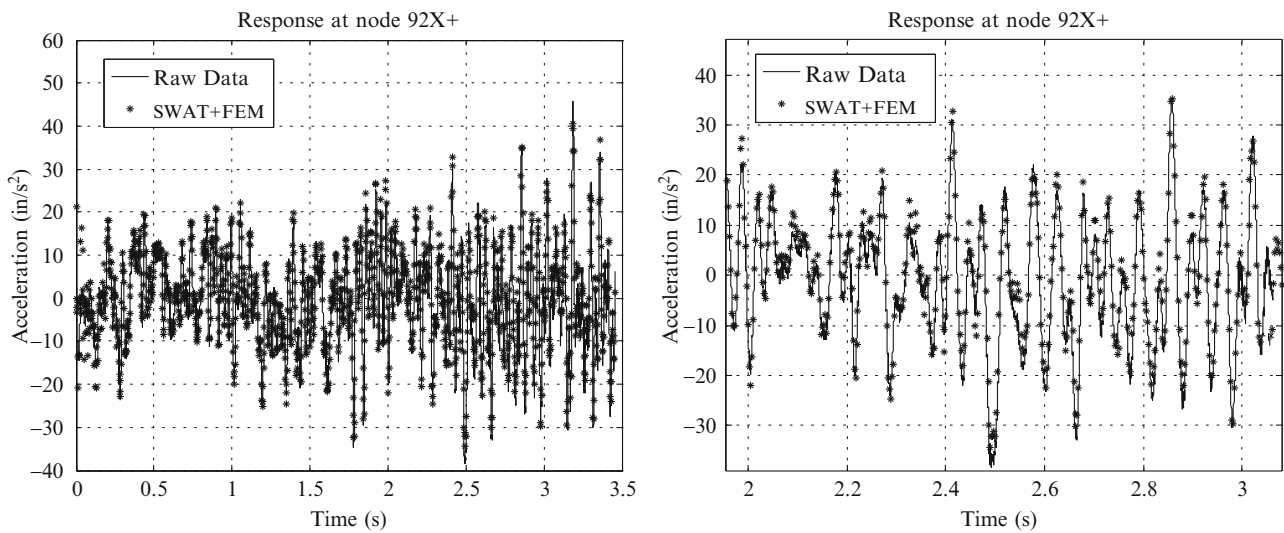
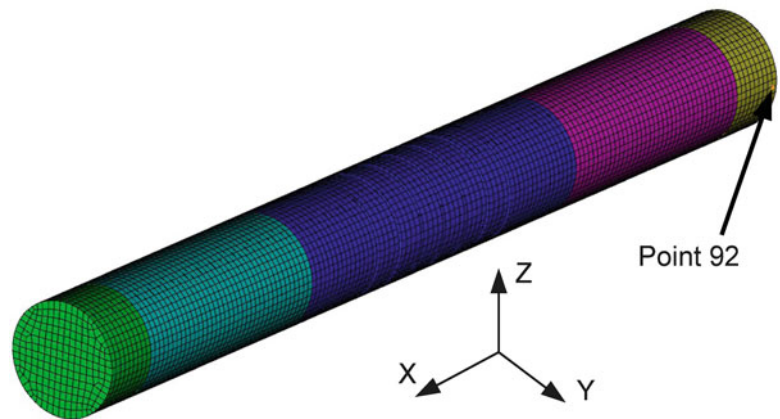


Fig. 7.8 Acceleration at node 92 in the +X dir during the environment: whole environment (*above*); expanded environment (*below*)

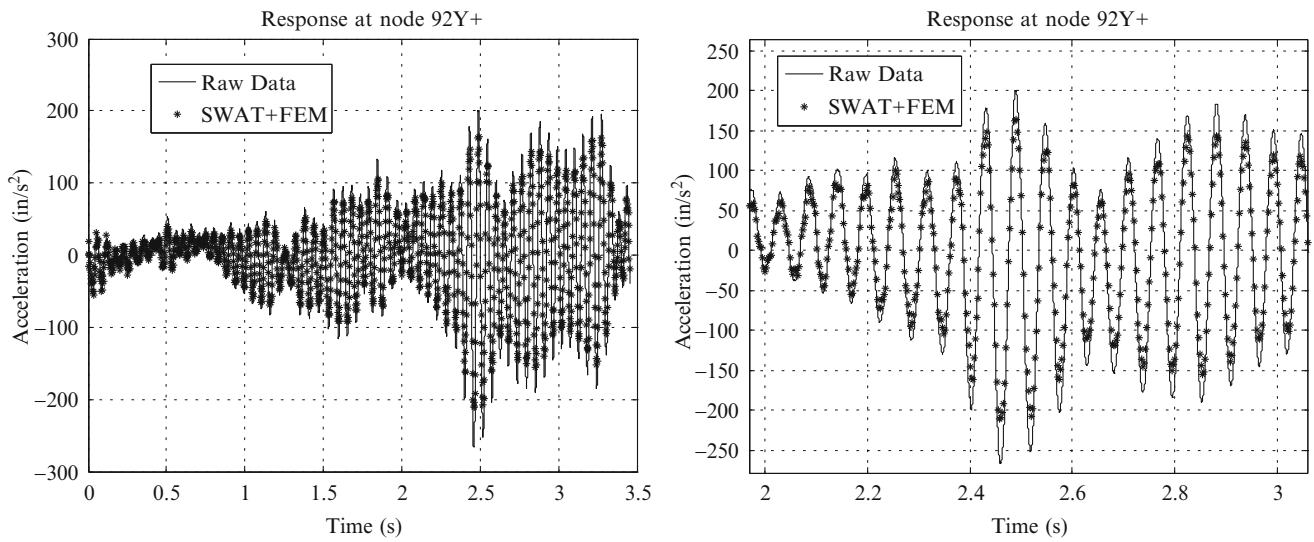


Fig. 7.9 Acceleration at node 92 in the +Y dir during the environment: whole environment (*above*); expanded environment (*below*)

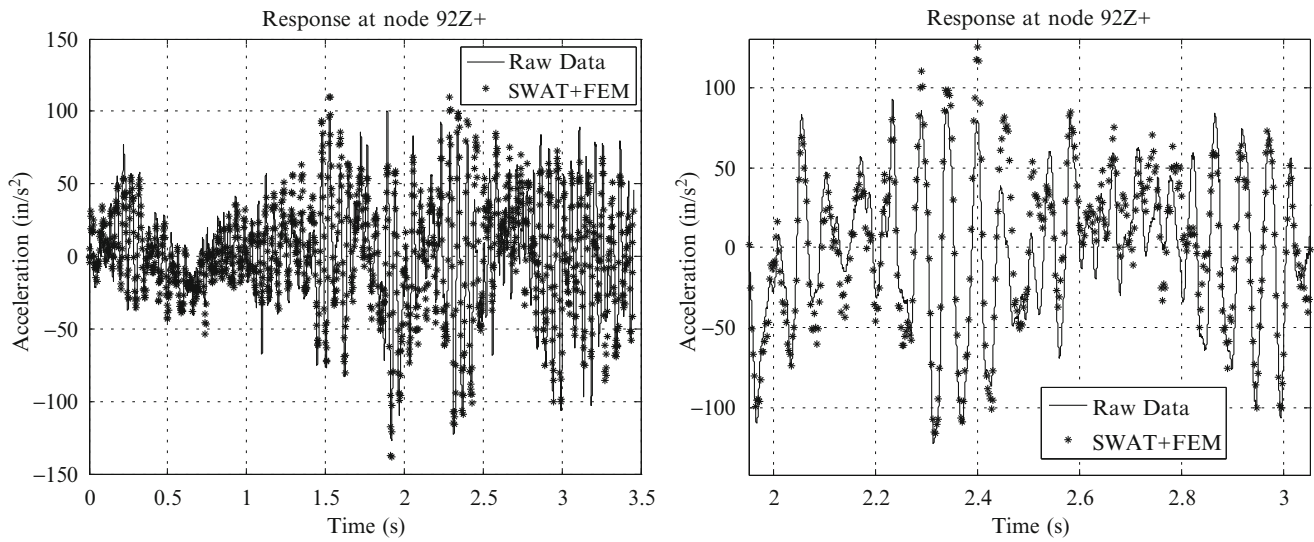


Fig. 7.10 Acceleration at node 92 in the +Z dir during the environment: whole environment (*above*); expanded environment (*below*)

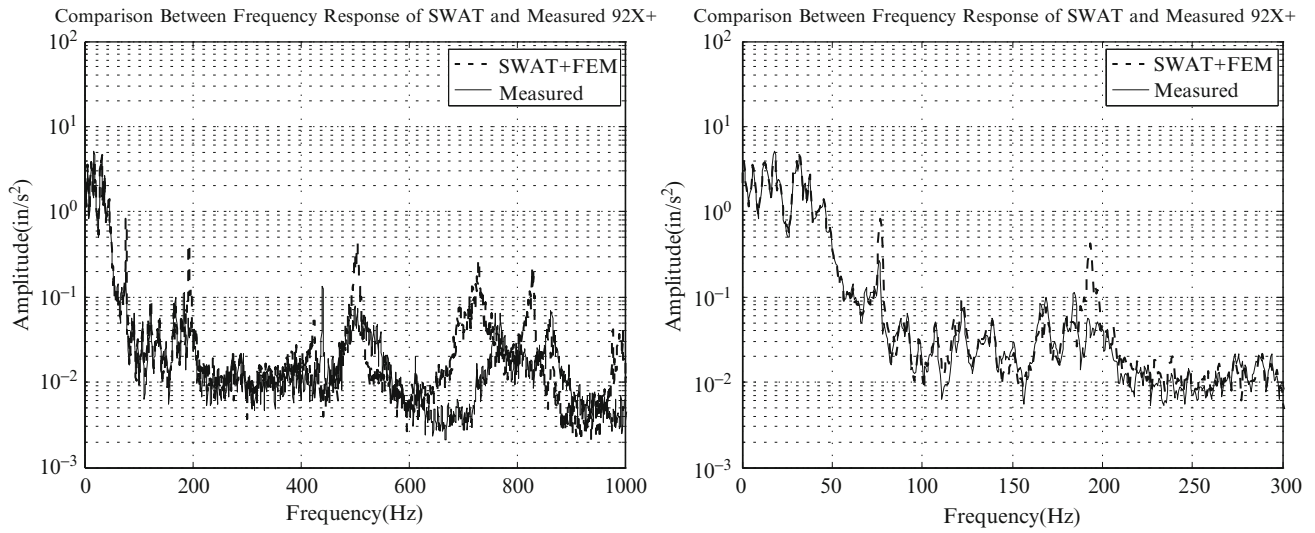


Fig. 7.11 FFT of Acceleration at node 92 in the +X dir during the environment

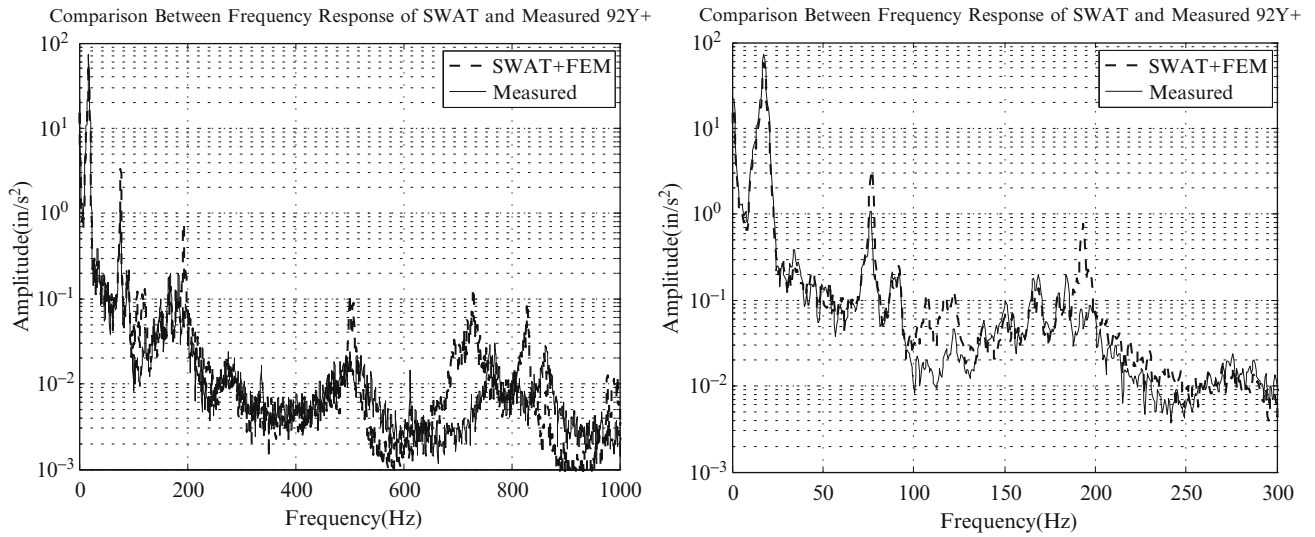


Fig. 7.12 FFT of Acceleration at node 92 in the +Y dir during the environment

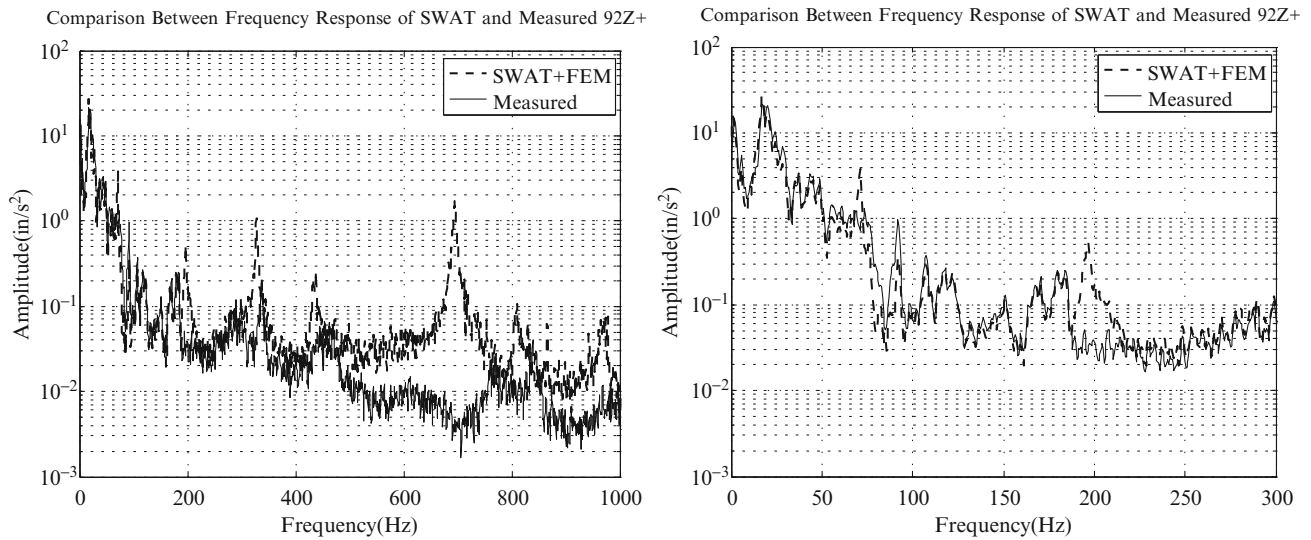


Fig. 7.13 FFT of Acceleration at node 92 in the +Z dir during the environment

References

1. Carne TG, Bateman VI, Dohrmann CR (1990) Force reconstruction using the inverse of the mode-shape matrix. Technical report SAND90-2737, Sandia National Laboratories, 1990
2. Gregory DL, Priddy TG, Smallwood DO (1986) Experimental determination of the dynamic forces acting on non-rigid bodies. SAE technical paper series, Paper no. 861791, Aerospace technology conference and Exposition, Long Beach, CA, October 1986
3. Mayes RL (1994) Measurement of lateral launch loads on re-entry vehicles using SWAT. In: Proceedings of the 12th international modal analysis conference, pp 1063–1068, February 1994

Chapter 8

Modal Analysis of Rotating Wind Turbine Using Multiblade Coordinate Transformation and Harmonic Power Spectrum

Shifei Yang, Dmitri Tcherniak, and Matthew S. Allen

Abstract Understanding and characterization of wind turbine dynamics, especially when operating, is an important though challenging task. The main problem is that an operating wind turbine cannot be truly modeled as a time invariant system, which limits the applicability of conventional well-established modal analysis methods. This paper compares two experimental techniques that characterize the dynamic behavior of an operating horizontal axis wind turbine (Vestas V27, 225 kW, rotor diameter 27 m, 12 accelerometers on each blade). The first method uses a multiblade coordinate transformation to convert the time periodic system into a time invariant one, assuming that the system is perfectly isotropic. Conventional operational modal analysis then can be applied to identify the modal parameters of the time invariant model. The second method processes the periodic response directly based on an extension of modal analysis to linear time periodic systems. It utilizes the harmonic power spectrum, which is analogous to the power spectrum for a time invariant system, to identify a periodic model for the turbine. This work demonstrates both of these methods on measurements from the operating turbine and discusses the challenges that are encountered. The procedure is demonstrated by using it to extract the time-periodic mode shapes of the first edge-wise modes, revealing that this turbine apparently has non-negligible blade-to-blade variations and hence the dynamics of these modes are considerably different than one would expect for an anisotropic turbine.

Keywords Linear time periodic • Output-only modal analysis • Wind turbine • Anisotropic • Dynamics

8.1 Introduction

The design of modern wind turbines heavily relies on accurate numerical models, which are used extensively to simulate the dynamic behavior of the wind turbines under different operating conditions. As a consequence, good experimental tools are necessary to validate the numerical models. However, it is quite challenging to experimentally characterize the dynamics of a wind turbine, especially when it is operating. One significant challenge is that many real turbines cannot be adequately modeled as a Linear Time Invariant (LTI) because of blade-to-blade variations, stratification in the flow field, and rotation of the rotor. If the angular speed of the rotor is constant then a wind turbine might be modeled as a Linear Time Periodic (LTP) system in order to characterize its behavior. This requires other methods, different from the conventional well-established modal analysis methods that are normally used for LTI systems.

This paper compares two experimental techniques for identifying wind turbines; the multiblade coordinate (MBC) transformation and the harmonic power spectrum. The MBC transformation, also known as the Coleman transformation, was first introduced in [1]. The idea behind the MBC transformation is to substitute the deflections of the blades measured in the blade coordinate system by some special variables, which combine the deflections of all three blades. MBC transformation results in elimination of the periodic terms in the equations of motion, thus making the system time invariant so that conventional modal analysis techniques can be applied. A fundamental requirement for the MBC transformation is that

S. Yang (✉) • M.S. Allen
Department of Engineering Physics, University of Wisconsin, Madison, WI, USA
e-mail: shifeiy@gmail.com; msallen@engr.wisc.edu

D. Tcherniak
Brüel & Kjær SVM, Nærum, Denmark
e-mail: dmitri.tcherniak@bksv.com

the rotor is isotropic [2], namely that all blades are identical and symmetrically mounted on the hub. When focusing on experimental techniques, it is also necessary that measurement system is symmetric, i.e. the sensors are mounted identically on all three blades [3]. In a prior work, Tcherniak et al. used the MBC transformation on simulated wind turbine data in order to obtain a wind turbine Campbell diagram, i.e. a graph presenting the dependency of the modal parameters on the rotor speed [4].

The second method, the harmonic transfer function for linear time periodic systems, was developed to process the response of the linear time periodic system directly [5]. It is known that when a single frequency input is applied to an LTI structure, the response will be at the same frequency but with a different phase and amplitude. In contrast, the response of an LTP system will contain a component at the excitation frequency as well as at an infinite number of its harmonics, separated by an integer multiple of rotation frequency. The harmonic transfer function is analogous to the transfer function of a time invariant system, but relates the exponentially modulated input (i.e., an input signal described by a central frequency and a series of equally spaced harmonics) to the exponentially modulated output at the same collection of frequencies. Allen et al. extended the harmonic transfer function to the case where the input cannot be directly measured by introducing the harmonic power spectrum [6], and the modal parameters of a 5 MW turbine were identified from simulated data. Later, the harmonic power spectrum was combined with continuous-scan laser Doppler vibrometry, measuring the first few mode shapes along a single blade of a parked 20 kW wind turbine under wind excitation [7].

In this work, both the MBC transformation and harmonic power spectrum were employed to process measurements from an operating turbine under wind excitation. First, the formulation of *modes* of an LTV system used in both methods is discussed and compared. Then, the methods are applied to a horizontal axis wind turbine (Vestas V27, 225 kW, rotor diameter 27 m), which was instrumented with accelerometers on three blades and in the nacelle [3]. The identified modal parameters from both methods are discussed and compared to evaluate their validity. The rest of this paper is organized as follows: Sect. 8.2 introduces the theoretical basis for the MBC transformation and the harmonic power spectrum; Sect. 8.3 introduces the wind turbine and sensor arrangement. Sections 8.4–8.6 demonstrate the analysis applied to the data; Sect. 8.7 summarizes the paper.

8.2 Theory

8.2.1 Multiblade Coordinate Transformation

A multiblade coordinate transformation (MBC) is typically used to convert degrees of freedom (DOFs) measured on the blades, i.e. in the rotating frame, to a non-rotating frame [8], making it possible to combine the blade DOFs with those on the tower and the nacelle. In the case of a three-bladed rotor, the sets of three coordinates $\{q_{1,k}, q_{2,k}, q_{3,k}\}^T$ measured at the position k on blades 1, 2, 3 will be converted to the sets of three multiblade coordinates $\{a_{0,k}, a_{1,k}, b_{1,k}\}^T$ given by

$$a_{0,k} = \frac{1}{3} \sum_{i=1}^3 q_{i,k}, \quad a_{1,k} = \frac{2}{3} \sum_{i=1}^3 q_{i,k} \cos \phi_i, \quad b_{1,k} = \frac{2}{3} \sum_{i=1}^3 q_{i,k} \sin \phi_i, \quad (8.1)$$

where ϕ_i is the instantaneous azimuth angle of the i th blade, and $k = 1 \dots M$ is a DOF number. The transformation assumes the blades are evenly distributed, i.e., $\phi_i = \phi_1 + 2\pi(i-1)/3$, $i = 1, 2, 3$. The backward transformation, from the multiblade coordinates to the blade coordinates is given by

$$q_{i,k} = a_{0,k} + a_{1,k} \cos \phi_i + b_{1,k} \sin \phi_i. \quad (8.2)$$

Typically the equation of motion (EoM) is written for a mixture of blade and tower/nacelle DOFs,

$$\mathbf{M}\ddot{\mathbf{x}} + \mathbf{C}\dot{\mathbf{x}} + \mathbf{K}\mathbf{x} = \mathbf{0}, \quad (8.3)$$

with

$$\mathbf{x} = \{q_{1,1} \dots q_{1,M}, \dots, q_{3,1} \dots q_{3,M}, s_1 \dots s_L\}^T, \quad \mathbf{x} \in R^{3M+L}, \quad (8.4)$$

where s_l , $l = 1 \dots L$ are DOF measured in the non-rotating frame. For an operating wind turbine, the mass matrix \mathbf{M} , gyroscopic/damping matrix \mathbf{C} and stiffness matrix \mathbf{K} are periodic in time: $\mathbf{M}(t) = \mathbf{M}(t + T)$, $\mathbf{C}(t) = \mathbf{C}(t + T)$,

$\mathbf{K}(t) = \mathbf{K}(t + T)$, where $T = 2\pi/\Omega$ is a period of the rotor rotation and Ω is its circular frequency. Thus Eq. (8.3) describes a linear time periodic (LTP) system, and application of the classical modal approach is impossible since the basic assumption of the modal decomposition, that the system under test is linear and time invariant, is violated here.

Using Eq. (8.2) to substitute the coordinates $q_{i,k}$ into Eq. (8.4), and leaving coordinates s_l unchanged, one arrives at EoM in multiblade coordinates:

$$\mathbf{M}_B \ddot{\mathbf{z}} + \mathbf{C}_B \dot{\mathbf{z}} + \mathbf{K}_B \mathbf{z} = \mathbf{0}, \quad (8.5)$$

where

$$\mathbf{z} = \{a_{0,1}, a_{1,1}, b_{1,1} \dots a_{0,M}, a_{1,M}, b_{1,M}, s_1 \dots s_L\}^T, \quad \mathbf{z} \in \mathbb{R}^{3M+L}. \quad (8.6)$$

Hansen et al. [2, 9] state that, if the rotor is isotropic, the matrices \mathbf{M}_B , \mathbf{C}_B and \mathbf{K}_B are constant, and thus MBC transformation converts the LTP system into an LTI system. Bir [8] generally disagrees with this statement but admits that, under the rotor isotropy assumption, the MBC transformation filters out all periodic terms from the EoM, except those that are integer multiples of 3Ω . In the same paper, Bir also clarifies some typical misconceptions regarding MBC, one of them is the necessity of the stationarity of the rotor speed ($\Omega = \text{const}$).

In any event, converting the LTP system in Eq. (8.3) into the LTI system in Eq. (8.5) allows the application of the classical modal approach to the new system, i.e., presenting the system dynamics as a superposition of modes, and finding the corresponding modal parameters: modal frequencies, damping and mode shapes. This paper concerns output-only modal analysis, i.e., the operating wind turbine is loaded by pure wind and unmeasured forces due to the rotation of the turbine. Then the obtained mode shapes are transferred back to the blade coordinates using Eq. (8.2). In [4], this method was applied to simulated wind turbine data; this paper extends the analysis to the measured data and compares it with the results from another method, outlined in the next section.

When considering a time variant mechanical system, the term ‘‘mode’’ becomes somehow vague. If an operating wind turbine with isotropic rotor is described in multiblade coordinates, the system becomes LTI where the ‘‘modes’’ are well defined. Let us consider a mode of system Eq. (8.5), and assume it has the following modal parameters: the eigenvalue

$$\lambda_r = -\zeta_r \omega_r + j\omega_r \sqrt{1 - \zeta_r^2}, \quad (8.7)$$

where ζ_r represents the modal damping and ω_r is the undamped natural frequency. The corresponding mode shape is

$$\boldsymbol{\psi}_r = \{a_{0,1}, a_{1,1}, b_{1,1} \dots a_{0,M}, a_{1,M}, b_{1,M}, s_1 \dots s_L\}^T, \quad \boldsymbol{\psi}_r \in \mathbb{C}^{3M+L}. \quad (8.8)$$

The elements of the mode shape vector are complex numbers.

Employing a backward MBC transformation, it is possible to map this mode into the natural blade coordinates. For rotor angular speed Ω , the motion at the k th DOF on the i th blade corresponding to this mode will be:

$$q_{i,k}(t) = \gamma_{i,k}(t) + \alpha_{i,k}(t) + \beta_{i,k}(t), \quad (8.9)$$

where

$$\begin{aligned} \gamma_{i,k}(t) &= e^{j\omega_r t - \zeta_r \omega_r t} a_{0,k}; \\ \alpha_{i,k}(t) &= \frac{1}{2} e^{j(\omega_r + \Omega)t - \zeta_r \omega_r t} (a_{1,k} - j b_{1,k}) e^{j\frac{2\pi}{3}(i-1)}; \\ \beta_{i,k}(t) &= \frac{1}{2} e^{j(\omega_r - \Omega)t - \zeta_r \omega_r t} (a_{1,k} + j b_{1,k}) e^{-j\frac{2\pi}{3}(i-1)}, \end{aligned} \quad (8.10)$$

As one can see, in the *blade coordinates* the modes of the LTI system in Eq. (8.5) occur in groups of three, with frequencies: $\omega_r - \Omega$, ω_r , and $\omega_r + \Omega$. In general each of these modes could have a different damping ratio, ζ_r , although in Eq. (8.10). The γ component does not depend on blade's number i , meaning that all three blades oscillate in phase; this is a so-called *collective mode*. The *backward whirling* (or *anti-symmetric*) mode α has a frequency $\omega_r + \Omega$; blade number $i + 1$ lags behind blade number i by -120° . The *forward whirling* mode β has frequency $\omega_r - \Omega$; blade number $i + 1$ lags behind blade number i by $+120^\circ$.

8.2.2 Harmonic Power Spectrum of LTP System

A single frequency input to an LTI system causes a response at the same frequency. In contrast, the same input to an LTP system, e.g., a wind turbine, causes a response that includes the excitation frequency and also an infinite number of its harmonics. An Exponentially Modulated Periodic (EMP) signal space [5] is defined to contain the frequency component at the single excitation frequency as well as its harmonics. Specifically, if the frequency of interest was ω then the EMP signal would consist of a collection of sinusoids at frequencies $\omega \pm n\Omega$, each having a different amplitude and phase. The harmonic transfer function is a matrix that relates an EMP input signal (expressed as a vector of harmonic amplitudes at $\omega \pm n\Omega$) to an EMP output signal. Details about how to derive the harmonic transfer function and then the harmonic power spectrum can be found in [10].

In practice, one would often like to express a measured signal as an EMP signal, for example in order to compute transfer functions. This is done by creating several frequency shifted copies of the signal. Specifically, suppose an output $y(t)$ is measured. An EMP output signal in the frequency domain would be expressed as,

$$\mathbf{Y}(\omega) = [\cdots Y_{-1}(\omega) Y_0(\omega) Y_1(\omega) \cdots]^T \quad (8.11)$$

where $Y_n(\omega)$ is the FFT of the n th modulated output signal $y_n(t)$,

$$y_n(t) = y(t)e^{-jn\Omega t} \quad (8.12)$$

This paper primarily focuses on how to interpret the harmonic power spectrum in order to identify the natural frequencies and time periodic mode shapes of an operating wind turbine, which is modeled as an LTP system.

Previous works have shown that the harmonic power spectrum of an LTP system can be expressed in a modal summation form as,

$$S_{YY}(\omega) = E(\mathbf{Y}(\omega)\mathbf{Y}(\omega)^H) = \sum_{r=1}^N \underbrace{\sum_{l=-\infty}^{\infty} \frac{\bar{\mathbf{C}}_{r,l} \mathbf{W}(\omega)_r \bar{\mathbf{C}}_{r,l}^H}{[j\omega - (\lambda_r - j\Omega)] [j\omega - (\lambda_r - j\Omega)]^H}}_{r^{\text{th}} \text{ mode}} \quad (8.13)$$

where $E()$ is the expectation and $()^H$ is the Hermitian. $\mathbf{Y}(\omega)$ is the exponentially modulated output signal defined in Eq. (8.11). Equation (8.13) has a similar mathematical form as the power spectrum of an LTI system,

$$S_{YY}(\omega) = E(Y(\omega)Y(\omega)^H) = \sum_{r=1}^N \frac{\psi_r S_{UU}(\omega) \psi_r^H}{[j\omega - \lambda_r] [j\omega - \lambda_r]^H} \quad (8.14)$$

where $Y(\omega)$ is the spectrum of measured output for the LTI system. The numerator in Eq. (8.13) contains $\mathbf{W}(\omega)_r$, which is the auto-spectrum of the net force exciting the r th mode of the time periodic system. This is similar to the input autospectrum, $S_{UU}(\omega)$ in Eq. (8.14), which reduces to an identity matrix when the structure is excited with uncorrelated white noise.

However, there are also two notable differences between the harmonic power spectrum in Eq. (8.13) and the conventional power spectrum in Eq. (8.14). First, the harmonic power spectrum not only contains a summation over the modes, whose eigenvalues are λ_r , but each mode also appears at several harmonics $\omega_r - l\Omega$. Hence, the harmonic power spectrum has peaks near each natural frequency ω_r , and also at the frequencies $\omega_r - l\Omega$ for any integer l . Second, the mode vector $\bar{\mathbf{C}}_{r,l}$ in the harmonic power spectrum is no longer a collection of vibration amplitudes at different measurement locations (note the definition of mode in Sect. 8.2.1), as ψ_r in Eq. (8.14). Instead, $\bar{\mathbf{C}}_{r,l}$ consists of the Fourier coefficients that describe the r th time periodic mode shape collected into a vector as,

$$\begin{aligned} \bar{\mathbf{C}}_{r,l} &= [\cdots C_{r,-1-l} \ C_{r,-l} \ C_{r,1-l} \ \cdots]^T \\ C(t)\psi_r(t) &= \sum_{l=-\infty}^{\infty} C_{r,l} e^{jl\Omega t} \end{aligned} \quad (8.15)$$

$C(t)$ is the output vector in the state space model of the equation of the motion [11], indicating which DOF is being measured. For the wind turbine measurement using accelerometers, $C(t)$ is simply a one at each sensor location. Theoretically, a periodic mode shape $\psi_r(t)$ should be described with a Fourier series of infinite order, yet one would expect that most systems can be well approximated with a finite, perhaps even small number.

The harmonic power spectrum is estimated in a conventional manner. Assuming $n = -p \dots p$ is used to modulate the acquired output, the modulated signal forms a matrix of $2p + 1$ copies of the signal at a certain number of frequency lines. The harmonic power spectrum then has a dimension of $(2p + 1) \times (2p + 1)$ by the number of frequency lines. Since each column (or row) in the harmonic power spectrum contains similar information about the LTP system, only the primary column (center column) is used in the identification. The procedure of identifying time periodic modes from the harmonic power spectrum can be summarized as,

1. Record the response $y(t)$ at any sensor on the wind turbine under random excitation.
2. Construct the exponentially modulated periodic output signals in the time domain using $y_n(t) = y(t)e^{-jn\Omega t}$, with $n = -p \dots p$
3. Split the modulated output signals into many sub-blocks with the desired level of overlap. Apply a Hanning window to each block and compute the spectra of modulated output signals, $Y_n(\omega)$
4. Compute the primary column of the harmonic power spectrum with $S_{\mathbf{Y}\mathbf{Y}}(\omega)_{n,0} = E(\mathbf{Y}(\omega)Y_0(\omega)^H)$ where the expectation operator denotes the average over all of the sub-blocks.
5. Use peak-picking or curve-fitting routines to identify the r th natural frequency ω_r and the mode vectors $\bar{\mathbf{C}}_{r,l}$ at different harmonics.
6. Align $\bar{\mathbf{C}}_{r,l}$ for various l to compare different estimates of the same mode vector using Eq. (8.15). Apply singular value decomposition to find the best estimate from all Fourier coefficient vectors [7].
7. Use Eq. (8.15) to reconstruct the time periodic mode shape $\psi_r(t)$.

8.3 Experimental Setup

This paper applies the two methods described in the previous section to operational measurements from a Vestas V27 wind turbine. The Vestas V27 is a 225 kW medium size upwind pitch regulated wind turbine (Fig. 8.1a). An extensive measurement campaign took place from October 2012 through May 2013. Each blade of the wind turbine was instrumented with 12 accelerometers (Bruel and Kjaer Type 4507 and 4508), including ten accelerometers in the flapwise direction (five on the leading edge and five on the trailing edge) and two accelerometers in the edgewise direction (Fig. 8.1b). Since the MBC-based method requires symmetry of the measurement system, special care was taken to mount the sensors on all three blades as similar to each other as possible, both location- and direction-wise. The nacelle was instrumented with three triaxial accelerometers (Fig. 8.1c). In order to estimate the instantaneous rotor position (azimuth) and rotor angular speed, two DC accelerometers, attached to the rotor's hub, were employed. To improve the estimate of the azimuth angle, a tachoprobe was also installed on the wind turbine's High-Speed Shaft (the HSS, connects the gearbox to the electrical generator). A pitch sensor was installed inside the hub; its readings were used for selecting recordings with no or relatively small pitch activity. In addition, two IRIG-B signals were used to synchronize the signals from the rotor and nacelle sensors. In total, 40 channels were recorded using B&K LAN-Xi data acquisition modules located in the hub and wirelessly transferred to the nacelle, where another 11 channels were measured. All channels were recorded synchronously at a sampling frequency of 4,096 Hz. Additional details regarding the measurement setup can be found in [3].

As described previously, the operating wind turbine is modeled as an LTP system. This modeling assumes constant rotor speed during the observation period. Unfortunately, the rotating speed is rarely constant in practice. Figure 8.2 shows a 5 min portion of the time history of the rotating speed computed from one of the DC accelerometers. The rotating frequency varies from 0.527 to 0.543 Hz over this time interval. Therefore, the first step was to select the datasets where the rotating speed is the steadiest. Furthermore, any pitch activity changes the in-plane and out-of-plane stiffness of the blade. Thus the second criterion was to select the datasets with minimum pitch activity. This was done using filtering and sorting options of the recording database. Eventually, the data taken at December 16, 2012 was selected (20 min long). The rotating speed, pitch angle and wind speed (30 m above the ground) for this data set are listed in Table 8.1.

The correct azimuth angle is a key parameter for both MBC and harmonic power spectra based methods. A lot of attention was paid to derive the azimuth angle from the readings of three redundant sensors: two DC accelerometers located in the hub and the tachoprobe measuring HSS angular speed (the exact gear ratio is around 23.3333). It was found that the tachoprobe provided the most accurate measurement of the rotating frequency. The average rotating frequency over this 20 min measurement was 0.5369 Hz with a standard deviation of 0.0007 Hz. This average rotating frequency was then used to compute the azimuth angle of each blade.

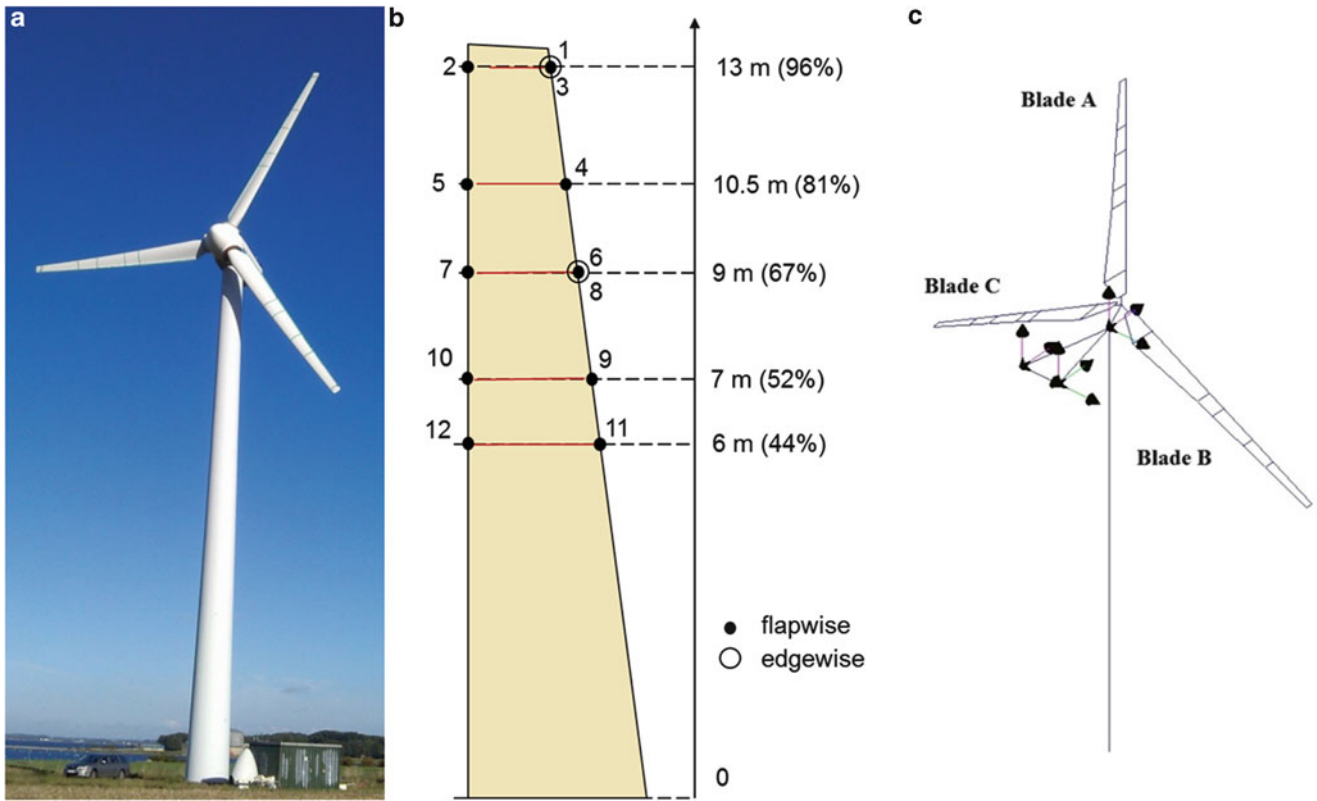


Fig. 8.1 (a) Vestas V27 with blades instrumented with accelerometers. (b) Location and orientation of the accelerometers on the blades. (c) Location of triaxial accelerometers in the nacelle

Fig. 8.2 Time history of rotating frequency

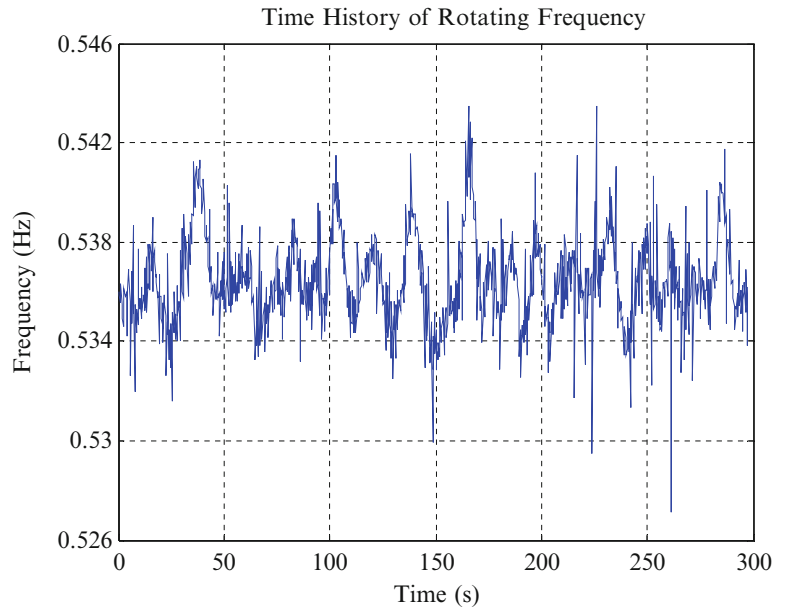


Table 8.1 Test conditions for the selected dataset

	DC1 (Hz)	DC2 (Hz)	Tacho (Hz)	Pitch angle (°)	Wind speed (m/s)
Mean	0.5370	0.5370	0.5369	-0.2150	4.7300
Maximum	0.5536	0.5548	0.5385	-0.0525	6.6850
Minimum	0.5228	0.5159	0.5352	-0.4925	2.6250
Standard deviation	0.0064	0.0074	0.0007	0.0850	0.6710

8.4 Preliminary Analysis

This section describes a preliminary analysis of the measured data, which can be conducted before stepping into the more complex modeling techniques. For the preliminary analysis, four sensors were selected, see Table 8.2. These sensors were located on the trailing edge at the tip, and at 9 m from the root of the blade.

First, the power density spectra (PSD) of the signals was calculated ($\Delta f = 1.125 \times 10^{-2}$ Hz; block size 89 s; 67 % overlap; Hanning window; 38 averages); the PSD of the tip acceleration signals averaged over 20 min of observation time, are shown in Fig. 8.3.

Analyzing Fig. 8.3, one can observe:

1. The level of the flapwise vibrations is higher than the level of edgewise vibrations;
2. At low frequencies, the response in both flapwise and edgewise directions is heavily dominated by harmonics. Two families of the harmonics can be identified: the first are the harmonics of the rotor (shown by the blue vertical lines in Fig. 8.3), the second family is due to the HSS fundamental frequency at 12.52 Hz modulated by the rotor frequency (the red vertical lines in Fig. 8.3);
3. The effect of the “fat tails” mentioned in [12] can be clearly seen on the lowest rotor harmonics. The higher harmonic peaks (starting from the fifth rotor harmonic) become narrower, and eventually have the appearance of typical harmonic peaks.
4. Flapwise vibrations are less contaminated by the rotor and gearbox harmonics at higher frequencies;
5. The readings of the accelerometers located in the same positions on different blades are not identical, which is either due to imprecise mounting or different dynamic characteristics of the blades (which is possible since one of the blade of this particular wind turbine was replaced some years ago). Since the MBC transformation assumes rotor isotropy and symmetry of the observation system, this could be a serious obstacle for the application of the MBC-based method. In contrast, the harmonic power spectrum method does not require these assumptions.
6. Note the double peak at approximately 3.5 Hz on the edgewise signal spectra (see the inset): one may expect a double peak (since the frequencies of the two anti-symmetric modes may slightly differ) but it is not normal that the higher frequency peak and the lower frequency peak dominate at different blades. If the rotor was isotropic, the shape of the spectra averaged over many rotor revolutions is expected to be the same for all three blades. Therefore this observation rather speaks for the rotor anisotropy than for the imperfection of the sensors mounting.

Table 8.2 Acceleration signals selected for analysis

Name (Fig. 8.1b)	Description
1f	Tip, trailing edge, flapwise direction
3e	Tip, trailing edge, edgewise direction
6f	9 m from the root, trailing edge, flapwise
8e	9 m from the root, trailing edge, edgewise direction

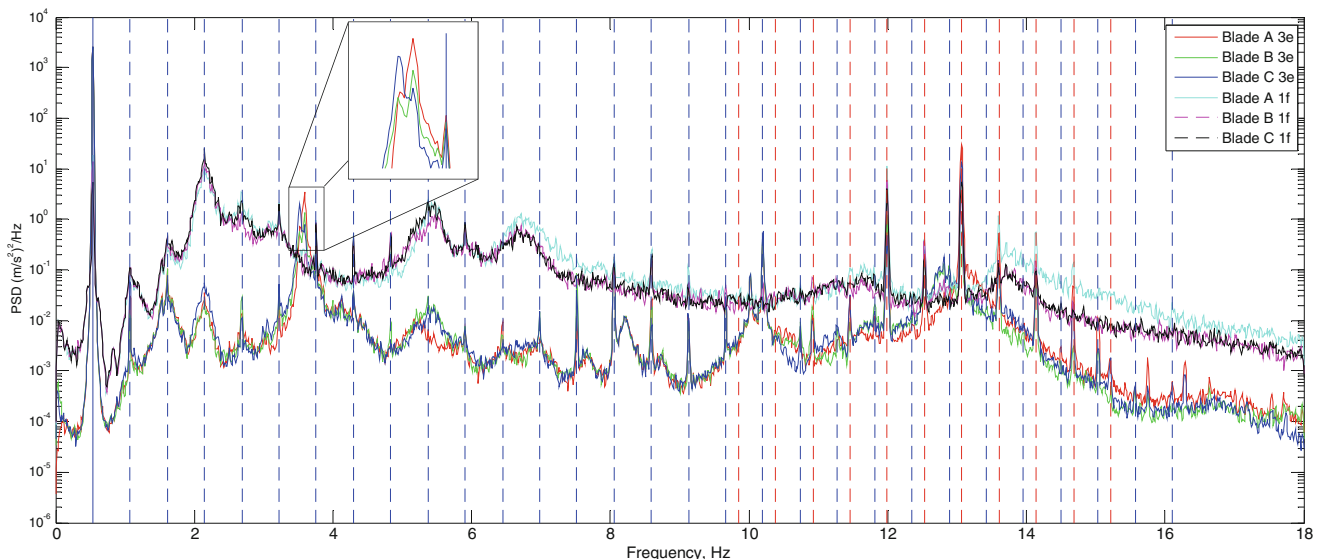


Fig. 8.3 PSD of the tip acceleration signals. *Blue dash line*—rotor fundamental, *blue dotted lines*—rotor harmonics, *red dashed line*—high speed shaft fundamental, *red dotted lines*—its sidebands

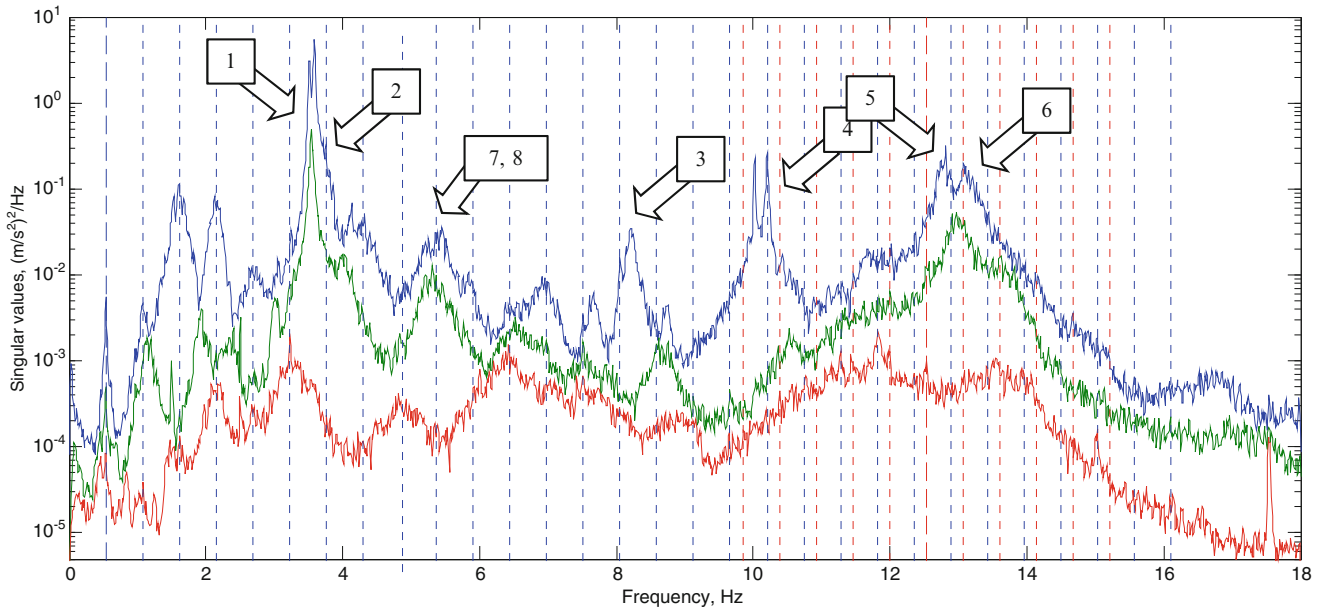


Fig. 8.4 Singular values of the cross-spectra matrices calculated for sensors 3e on all three blades

Since the harmonics are undesirable in further analysis, the time-synchronous averaging (TSA) algorithm was employed to remove the harmonics. TSA was applied in two runs, first removing the rotor harmonics, and second—the sidebands of the HSS fundamental frequency. The tachometer events are generated from the instantaneous rotor azimuth $\phi_1(t)$, which is estimated as explained in Sect. 8.3. The detailed explanation of the TSA method can be found in [13]. Due to the “fat tails” phenomena, TSA does not significantly affect the lowest rotor harmonics but effectively removes the higher harmonics and HSS sidebands.

Along with the PSD, the singular value decomposition (SVD) can shed some light on how many independent vectors should be used to describe system behavior at different frequencies. The SVD was performed on the 3×3 cross-spectra matrix computed between the sensors located at the same point on all three blades. Figure 8.4 shows the three singular values computed for the signal 3e after the harmonics were removed by TSA.

If focusing on the edgewise vibrations, SVD reveals some expected modal behavior, for example, arrows #1, 2 and #5, 6 in Fig. 8.4 denote the two edgewise anti-symmetric modes, #3, #4 are perhaps the edgewise collective modes, #7, 8 are the traces of the two flapwise anti-symmetric modes, which also have an edgewise component. However, at this point this is just a guess-work; the modal analysis shall reveal the true dynamics of the wind turbine.

The next step will be to apply the MBC transformation to the data according to Eq. (8.1). The instantaneous rotor azimuth $\phi_1(t)$, which participates in Eq. (8.1) is estimated as explained in Sect. 8.3. The geometrical interpretation of multiblade coordinates can be found in [14]. The spectra of the multiblade coordinates a_0 , a_1 and b_1 are shown in Fig. 8.5.

Analyzing Fig. 8.5, one can observe the following:

1. The peak at 1Ω (rotor fundamental) has almost disappeared, while the peak at 3Ω (3rd harmonic, the so-called *blade passing frequency*) has increased. This agrees with Bir’s statement that MBC transformation can be considered as a filter stopping all harmonics except those that are integer multiples of 3Ω [8].
2. The anti-symmetric coordinates a_1 and b_1 (green and blue curves respectively) follow each other closely, in contrast the symmetric (collective) coordinate a_0 (red curve) is quite distinct. Thus MBC effectively separated collective blade behavior from the anti-symmetric.
3. There are two types of behavior of the peaks identified in the blade spectra (Fig. 8.4): some peaks like peaks #1, 2 become two well separated peaks #A, B while the other peaks like #4 keep their location (peak #C). The first type of peaks is typical for anti-symmetric (or whirling) modes, while the second type—for collective modes. In blade coordinates, the whirling modes are often very close in frequencies (e.g. peak pair #1, 2 and pair #5, 6 in Fig. 8.4). In multi-blade coordinates, these peaks are typically separated: (peak pair #1, 2 becomes #A, B and pair #5, 6 becomes #D, E). The distance between the new peaks in the pairs is about 2Ω .

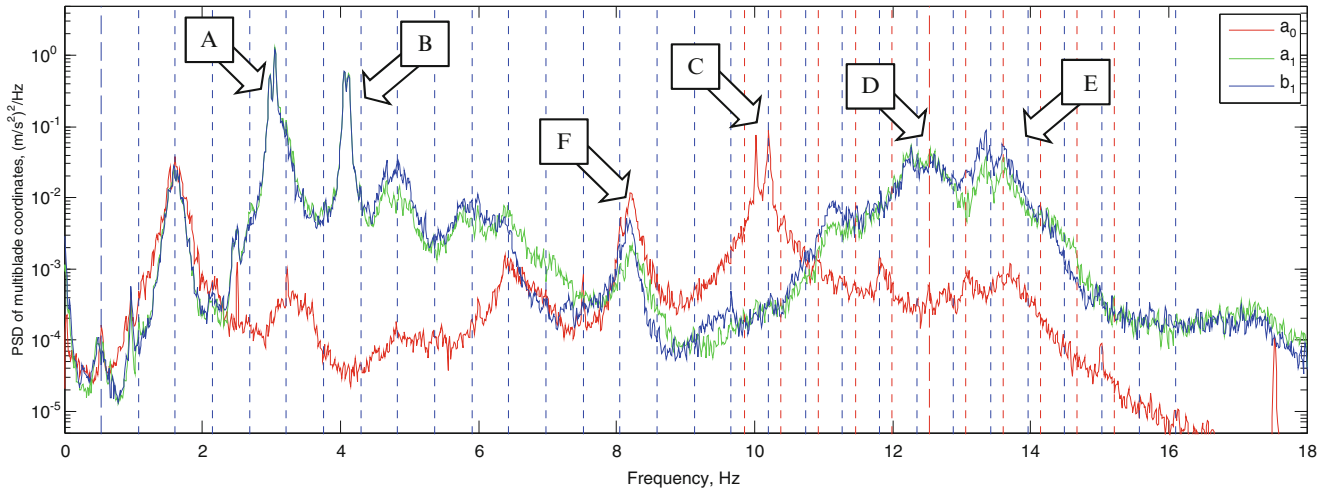


Fig. 8.5 PSD of multiblade coordinates for 3e sensor location

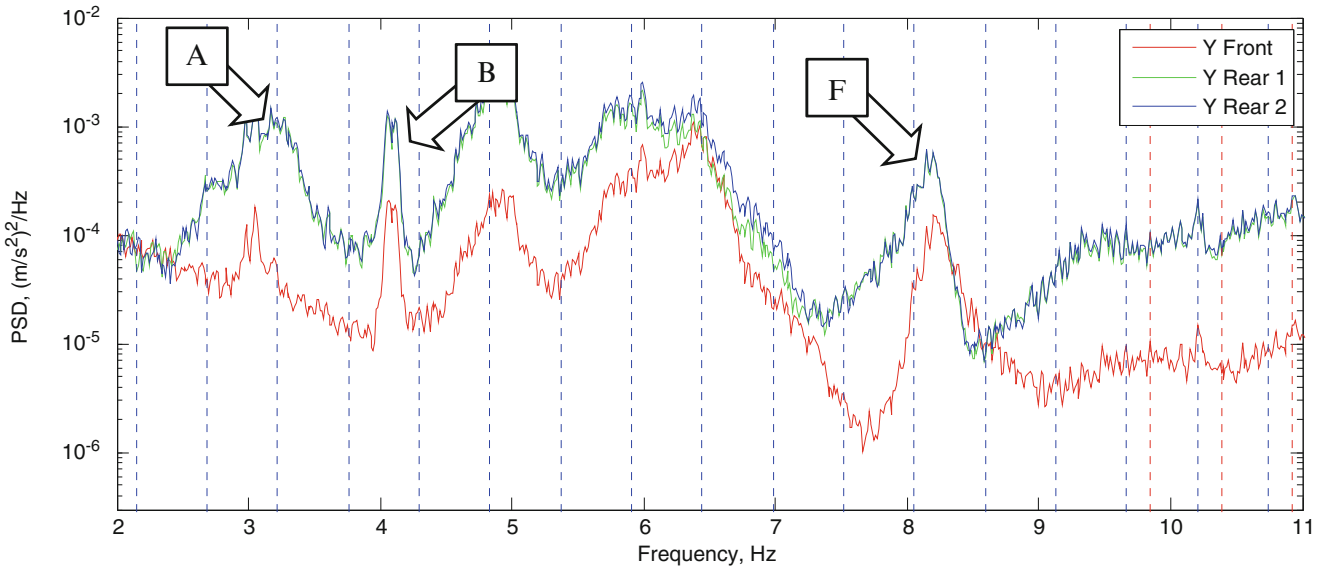


Fig. 8.6 PSD of the nacelle acceleration signals, side-to-side direction: *red*—front, *green*—rear right, *blue*—rear left. The *letters* denoting the peaks are the same as in Fig. 8.5

It is also important to note that the peaks seen on the MBC coordinates (Fig. 8.5) can also be traced in the nacelle acceleration spectra (Fig. 8.6). This makes it possible to identify many rotor modes using only tower and nacelle data, was reported in [15].

8.5 Modal Analysis of Operational Turbine using Multiblade Coordinate Transformation

The analysis performed so far is purely signal processing, with no modeling introduced and no assumptions made. In the following sections, we assume that the structure under test is LTP, and will model its dynamics via modal decomposition.

In this section we perform operational modal analysis (OMA) on the experimentally obtained data pre-processed by harmonic removal and multiblade coordinate transformation, as detailed in Sect. 8.4. The new time histories become the input to OMA. As will be explained later, the main focus is placed on the edgewise motion, since it has more interesting time-periodic behavior.

Fig. 8.7 Simple geometry indicating 6 multiblade coordinates

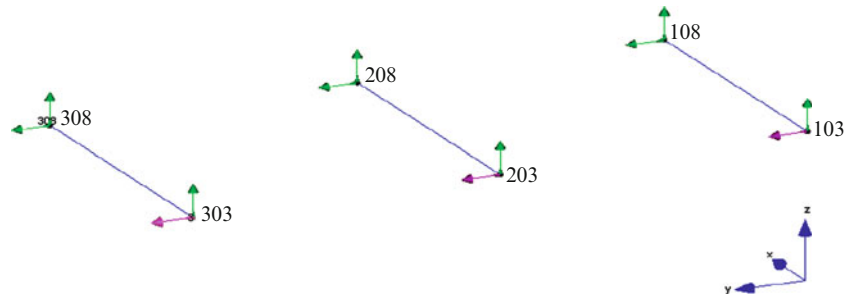


Fig. 8.8 Stabilization diagram around first in-plane modes

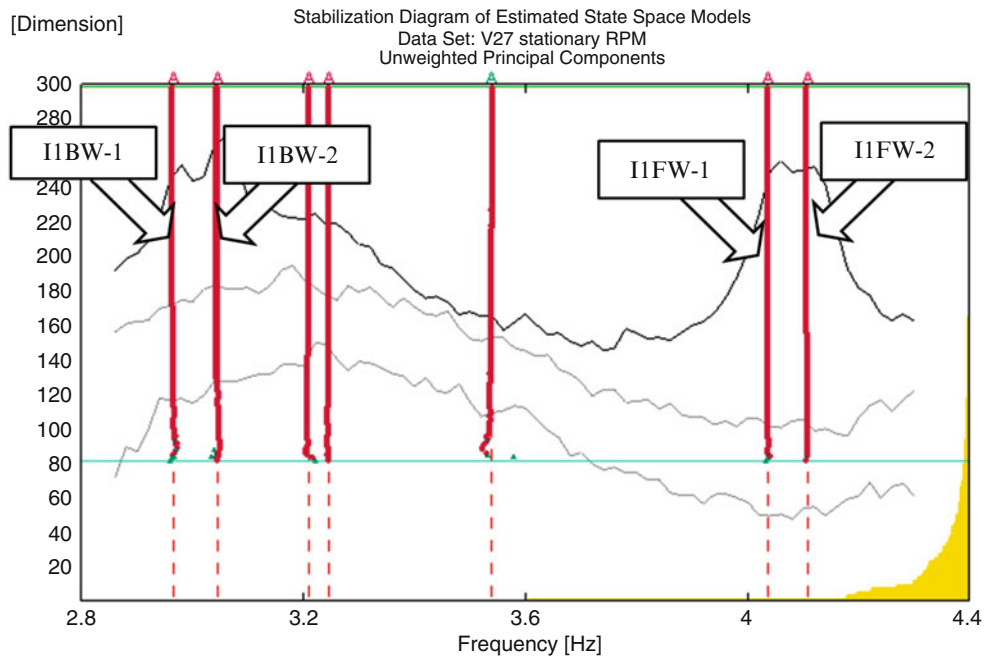


Table 8.3 Modal parameters of the mode shown in Fig. 8.8

Mode	Frequency (Hz)	Damping ratio (%)	Notes	(Average) phase difference between a_1 and b_1 (at the tip)
I1BW-1	2.97	2.8	$3.51 - \Omega$	-86.1°
I1BW-2	3.05	1.8	$3.58 - \Omega$	-87.4°
I1FW-1	4.04	1.1	$3.51 + \Omega$	85.2°
I1FW-2	4.11	0.8	$3.58 + \Omega$	90.2°

The OMA stochastic subspace identification (SSI) algorithm (Bruel and Kjaer Type 7760) was used for identification. Twelve channels [$3 \times (1f, 3e, 6f, 8e, \text{Fig. 8.1b})$] were selected for the analysis. The data were decimated ten times; thus the new sampling rate is 40.96 Hz.

Typically, modal analysis software uses test object geometry in order to visualize measured DOFs and to animate the modes. In the case of multiblade coordinates such visualization is not physical; however it is found very useful in order to give mode nomenclature. Figure 8.7 shows the simple geometry used for the visualization. DOFs 10^* denote multiblade coordinate a_0 , 20^* are a_1 and 30^* are b_1 . Points $*03$ correspond to the blade tip, and ones $*08$ —to the middle of the blade. Z-direction corresponds to flapwise DOFs, and Y—to edgewise direction. If, when animating the mode, a_0 dominates, this is a collective mode. Dominating a_1 and b_1 indicate anti-symmetric (whirling) modes. If the phase between a_1 and b_1 is -90° , this is a backward whirling mode; the phase of $+90^\circ$ indicates the forward whirling. If DOFs $*03$ and $*08$ move in-phase, this is a first bending mode, while anti-phase points to the second bending mode. Identification of higher modes is restricted by the low spatial resolution, especially in the edgewise direction.

Figure 8.8 shows the stabilization diagram in the range 2.8–4.4 Hz corresponding to peaks #A, B in Fig. 8.6; the corresponding mode table is shown below. SSI algorithm finds four edgewise modes, shown in the table (Table 8.3), the other modes are flapwise dominated or noise modes, which are not considered here. The modes I1BW-1 and I1FW-1 (abbreviations

Table 8.4 Multiblade coordinates dependence on phase ϕ

ϕ	a_0	a_1	b_1	Phase between a_1 and b_1	Mode name
0	$A \sin(\omega t)$	0	0	Not defined	Collective
$+120^\circ$	0	$A \sin((\omega + \Omega)t)$	$-A \cos((\omega + \Omega)t)$	$+90^\circ$	Forward whirling
-120°	0	$A \sin((\omega - \Omega)t)$	$A \cos((\omega - \Omega)t)$	-90°	Backward whirling

for in-plane 1st bending, back- or forward whirling respectively) are both originated from the peak at 3.51 Hz on the edgewise signals spectra; the frequencies of these modes are $3.51 \mp \Omega$ respectively. The modes I1BW-2 and I1FW-2 are originated from the peak at 3.58 Hz, and their frequencies are $3.58 \mp \Omega$. The presence of the four modes found by OMA-SSI in multiblade coordinate data is *an indication of rotor anisotropy*; these modes are not physical, this is an artifact due to the violation of the rotor isotropy assumption.

Indeed, if the rotor was isotropic, the (averaged) spectra of the accelerations measured on all three blades should have almost identical magnitude, and the phase between the signals measured on the neighboring blades should be equal and their sum should be $0 \pm 360^\circ$: $\phi_{AB} = \phi_{BC} = \phi_{CA} = \phi$ and $\phi_{AB} + \phi_{BC} + \phi_{CA} = 0 \pm 360^\circ$. This is only possible if the phase is either 0° (for collective behavior) or $\pm 120^\circ$ (“+” for forward whirling and “-” for backward whirling). Suppose the vibrations of the i th blade have a peak at a certain frequency ω : $q_i = A \sin(\omega t - \phi (i - 1))$. Depending on the phase ϕ , after the MBC transformation in Eq. (8.1), one obtains the multiblade coordinates according to Table 8.4.

This means that in the case of the isotropic rotor, a peak in the blade vibration spectra should become one peak in the multiblade coordinate spectra, not two, as we experienced here. Only one mode would then be found at that peak (in MBCs) but here two modes have erroneously been extracted. Here, we observe two closely spaced peaks in the blade spectra around 3.5 Hz (Fig. 8.3) which presumably correspond to backward and forward whirling modes; let’s denote the frequencies of the peaks by ω_{BW} and ω_{FW} respectively. If the rotor was isotropic, the spectral magnitudes of all three blades would be approximately the same, and the phase would be -120° at ω_{BW} and $+120^\circ$ at ω_{FW} . After MBC transformation, we would discover two peaks in the MBC spectra: the backward whirling mode at $\omega_{BW,MBC} = \omega_{BW} - \Omega$ and forward whirling at $\omega_{FW,MBC} = \omega_{FW} + \Omega$, and these modes would then correspond to the backward and forward whirling modes of the MBC system.

Unfortunately, in the case of the anisotropic rotor, this analysis does not bring such clear results. Applying MBC transformation here, we found four modes at $\omega_{BW} - \Omega$, $\omega_{BW} + \Omega$, $\omega_{FW} + \Omega$ and $\omega_{FW} - \Omega$, as it is seen in Fig. 8.8. Thus, one can conclude that use of the MBC transformation cannot be recommended in the case of anisotropic rotors. Instead, we will recommend the Harmonic Power Spectrum method demonstrated below.

8.6 Modal Analysis of Operational Turbine using the Harmonic Power Spectrum Method

The turbine rotated at an average speed of 0.5369 Hz. The measured response of the blades in the edgewise direction on all three blades (in-plane sensors 3e and 8e) as well as the response on the front of the nacelle in the lateral and vertical directions were collected into a response vector with eight outputs. This response was then exponentially modulated with $n = -4 \dots 4$ according to step 2 in Sect. 8.2.2, using the response at the tips of the three blades as references. Then, the modulated signals were split into 73 sub-blocks with a block size of 119 s (64 revolutions) and 88 % overlap. A Hanning window was applied to reduce the leakage. The resulting harmonic power spectrum matrix had 72 outputs (8 points and 9 harmonics for each) by 3 references. The complex mode indicator function (CMIF) of this HPSD matrix was then found and is shown in Fig. 8.9. Similar to that in preliminary analysis, the rotor harmonics and a cluster of sideband harmonics around 12.52 Hz due to the HSS dominate the response. Observing more closely, one can see another cluster of peaks centered around 3.59 Hz with several strong sideband harmonics, each separated with the rotating frequency. Those peaks are evidence of linear time periodic behavior and will be the focus of the following analysis.

Figure 8.10 shows an expanded view of the spectrum near 3.5 Hz, where the first edgewise modes of the blades are most active. The spectrum clearly shows two peaks near 3.5 Hz and the shape of the first (blue) and second (green) singular value curves strongly suggests that two modes are present at that peak. Several modulations of the peak are also seen near 3.0, 4.0 and 4.5 Hz. The full harmonic power spectrum matrix was curve fit using a variant of the AMI algorithm [16, 17], focusing only on the peaks near 3.5 Hz. Two modes were identified with natural frequencies 3.5184 and 3.5867 Hz and damping ratios 0.00569 and 0.00355. The mode vectors for each mode are vectors of Fourier coefficients which describe the motion of the mode at the natural frequency, plus motion at nine harmonics of the natural frequency for $n = -4 \dots 4$. This is summarized in Fig. 8.11, which shows the magnitude and phase of the response at several points on the turbine for each harmonic of each

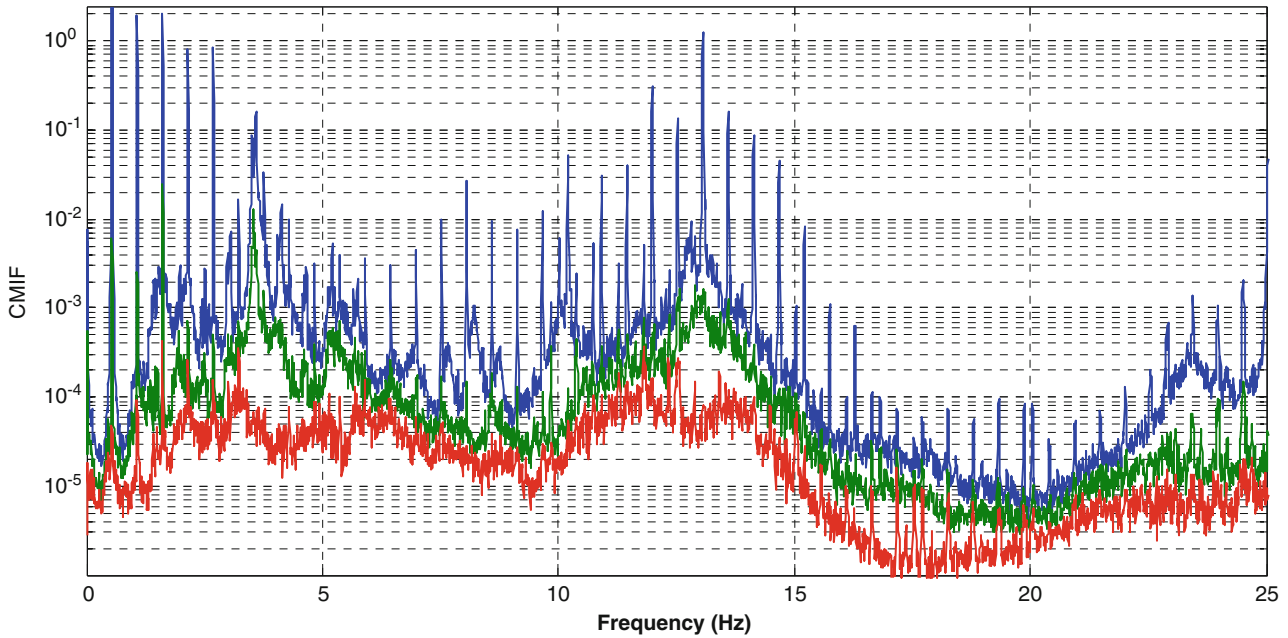


Fig. 8.9 Complex mode indicator function of the harmonic power spectrum matrix for the eight edgewise sensors using the edgewise response at the blade tips as references

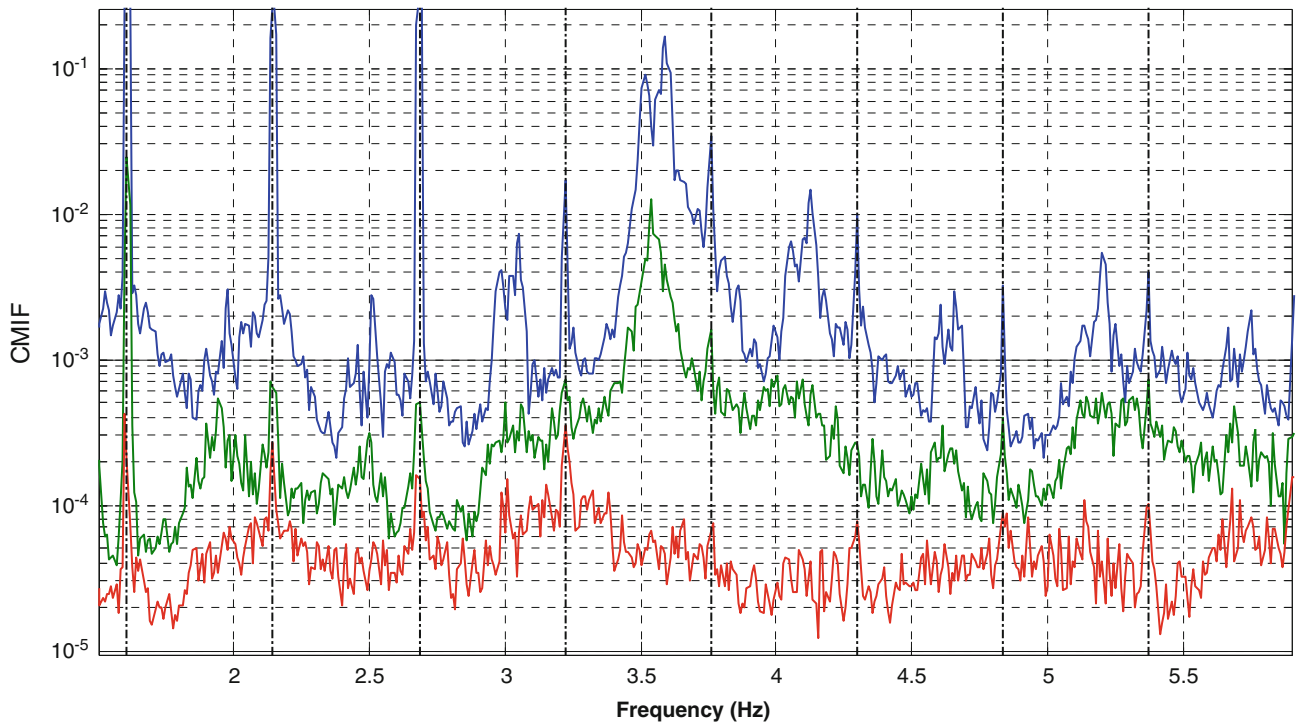
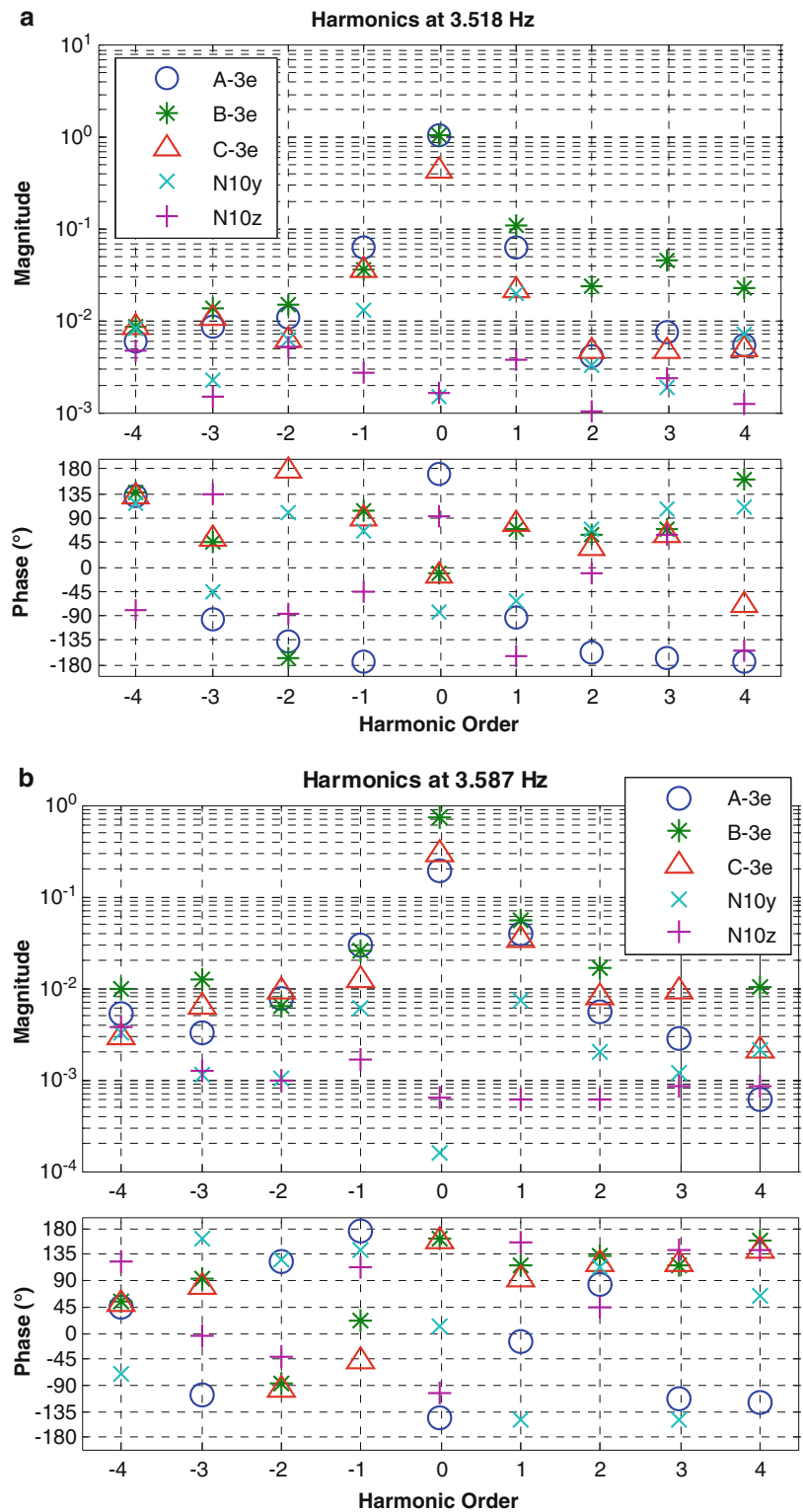


Fig. 8.10 Zoom in on harmonic power spectrum in Fig. 8.9

of these modes. As the motion is quite a bit more complicated than for an LTI system, some care will be taken to explain the meaning of this result.

First consider the mode at 3.518 Hz. The mode shape in Fig. 8.11 shows that the motion of the blades is dominated by motion at the 0th harmonic, or 3.518 Hz. Blade A moves about 180° out of phase with blades B and C. On the other hand, the tower motion is predominantly at the -1 and 1 harmonics, or 2.982 and 4.055 Hz. This was evident in Fig. 8.6 which showed the spectrum of the motion of the nacelle. The blades also exhibit some vibration at these frequencies, although at

Fig. 8.11 Identified Fourier coefficients on all the blades plotted against harmonic order.
 (a) Harmonic at 3.52 Hz,
 (b) harmonic at 3.59 Hz



4.055 Hz it is about an order of magnitude smaller than the dominant motion and at 2.982 Hz it is smaller still. The higher harmonics ($|n| > 1$) are quite small and so their validity is questionable.

The mode at 3.587 Hz behaves in a similar manner, with the dominant motion being at the 0th harmonic and with relatively weak higher harmonics. The motion of the tower is also considerably smaller in this mode. In this mode blade A is about 45° out of phase with the other two blades and blade B has significantly higher amplitude than the other blades. It is interesting to

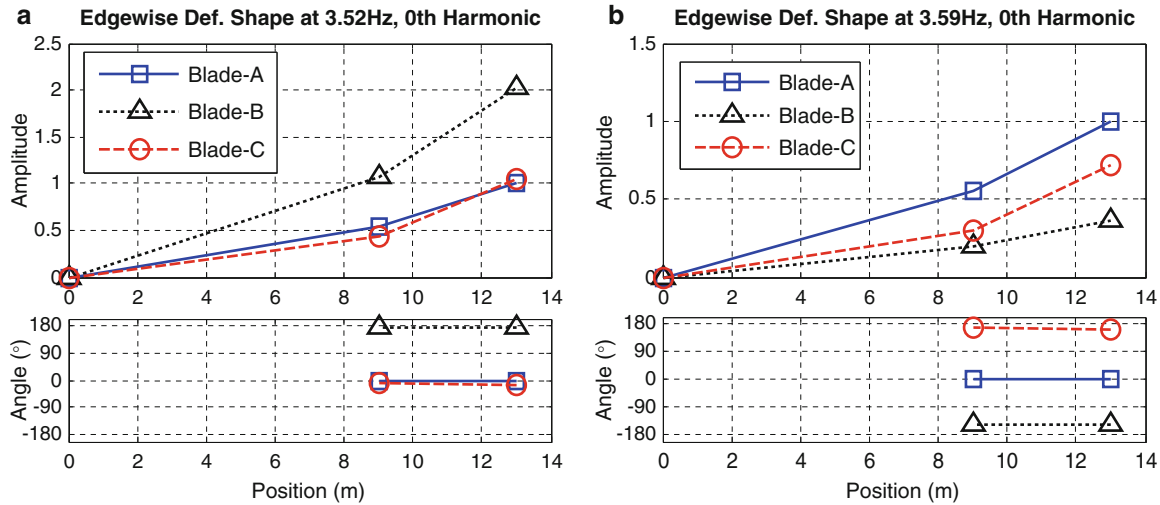


Fig. 8.12 Deformation shape identified by AMI in 0th harmonic (a) at 3.518 Hz, (b) at 3.587 Hz

note that these two modes do follow the expected trends for the edgewise modes of an isotropic wind turbine. As illustrated in [6, 9] and discussed in the previous section, a wind turbine typically exhibits backward and forward whirling modes, which in the tower reference frame (or in MBCs) occur at the tower vibration frequencies, or 2.982 and 4.055 Hz in this case. In the blade reference frame these modes would be closely spaced, and occur approximately equidistant between the two frequencies observed in the tower. While these modes are typically closely spaced (even repeated for an isotropic turbine, see e.g. [9]) they can be distinguished by the phase of the motion of the blades as discussed previously. The LTP modes identified for these two edgewise modes do not seem to follow the expected trends, but fortunately the motion observed is readily described by a linear time periodic model; the identified time-periodic shapes could be used to predict the motion of the structure or to validate a model that included the anisotropy of the turbine.

Figure 8.12 shows the deformation pattern that the structure would experience as a result of only the 0th harmonics at 3.518 and 3.587 Hz. Since the motion of the blades is dominated by the 0th harmonic, one can imagine the blades deforming into this shape and while simultaneously oscillating with perturbations about 10 % as large as these at the -1 and $+1$ harmonics. (These deformation shapes are also precisely what one would obtain if a conventional output-only modal analysis were performed.) The vibration amplitude at the hub (Position = 0 m) is shown as zero to aid in visualizing the blade motion. The blades clearly have different amplitudes in each mode, yet the two sensors on each blade move precisely at the same phase and the deformation shapes are as one might expect for a first bending mode of a cantilever beam. Figure 8.13 shows the motion of the blades in the 1st harmonic in a similar format. It is interesting that these harmonics also show about the same phase across the sensors on each blade, yet these shapes are different than those at the 0th harmonic. The net effect of these harmonics would be to cause the total deformation of the blades to change somewhat from blade to blade over each 3.52 or 3.59 Hz cycle.

8.7 Conclusion

An operating wind turbine has to be modeled as an LTP system to correctly characterize its time periodic behavior. In this work, two methods suitable for LTP systems, namely, the multiblade coordinate transformation and the harmonic power spectrum, were employed to identify the modes of an operating wind turbine. The vibration data were obtained from an operating Vestas V27 wind turbine instrumented with accelerometers on the blades and the nacelle.

From the accelerometer readings, it was observed that the wind turbine rotor is anisotropic; therefore the MBC transformation will fail to convert the LTP system into an LTI system. It was shown that application of the MBC transformation lead to erroneous results. In contrast, the harmonic power spectrum does not require the rotor to be isotropic. The method was successfully applied; for demonstration purposes, and two edgewise (in-plane) bending modes were identified and analyzed in detail. In this particular case, the experimental data revealed that the magnitude of the sideband harmonics in the blade reference frame was an order of magnitude lower than the central frequency component. If these sidebands were negligible then one could use straightforward operational modal analysis on the data. However, then one is

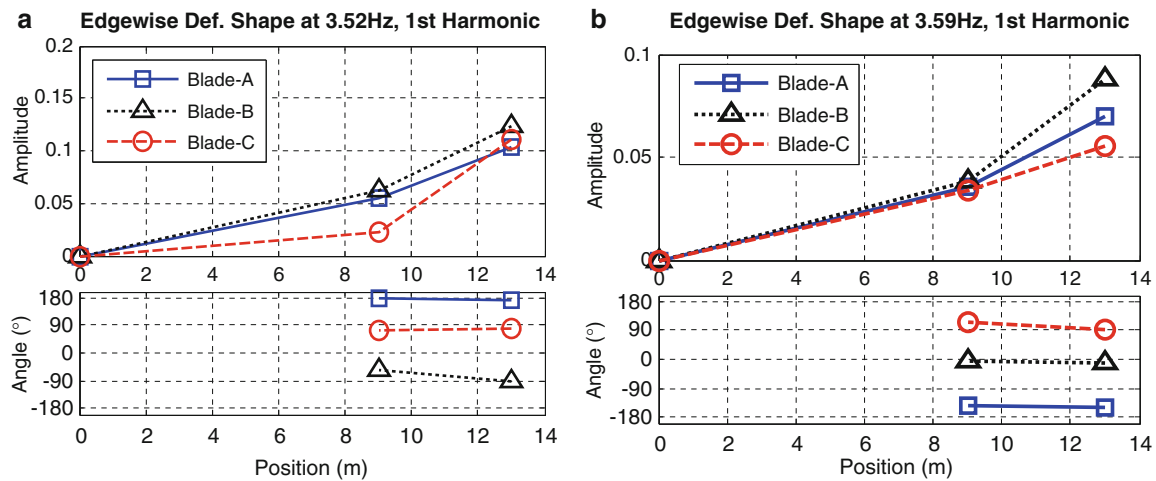


Fig. 8.13 Deformation shape identified by AMI in 1st harmonic for modes centered at (a) at 3.518 Hz, (b) at 3.587 Hz

faced with a dilemma because the same modes appear at different frequencies in the tower measurements. In any event, the harmonic spectrum method allows us to easily identify the harmonic content in each mode and to robustly determine the number of modes present in the data.

Comparing the two methods in application to experimental modal analysis of operating wind turbine, the harmonic power spectrum method is strongly recommended for most cases. Firstly, since the rotor isotropy is not initially known, using of MBC transformation may result in an erroneous modal identification. Secondly, the MBC method requires instrumentation of all three blades and, besides this, a precise symmetric mounting of accelerometers on the blades. If the sensors on one blade should fail then the method cannot be used. The harmonic power spectrum method does not require this, which makes it much more practical in a real life situation. The harmonic power spectrum directly identifies the natural frequencies, damping ratios and the periodically time-varying modes that describe the motion of the blades in the rotating frame and the motion of the tower in the fixed frame. These modal parameters can be compared with the analytically derived modes of the turbine, obtained through a Floquet analysis, to validate an anisotropic model for the turbine. The methods will be further compared and these ideas will be further developed in the next stage of the work.

References

1. Coleman RP (1943) Theory of self-excited mechanical oscillations of hinged rotor blades. Langley Research Center. <http://ntrs.nasa.gov/>
2. Hansen MH (2003) Improved modal dynamics of wind turbines to avoid stall-induced vibrations. *Wind Energy* 6:179–195
3. Tcherniak D, Larsen GC (2013) Applications of OMA to an operating wind turbine: now including vibration data from the blades. Presented at the 5th international operational modal analysis conference, Guimarães
4. Tcherniak D, Chauhan S, Rossetti M, Font I, Basurko J, Salgado O (2010) Output-only modal analysis on operating wind turbines: application to simulated data. Presented at the European wind energy conference, Warsaw
5. Wereley NM (1991) Analysis and control of linear periodically time varying systems. PhD, Department of Aeronautics and Astronautics, Massachusetts Institute of Technology, Cambridge
6. Allen MS, Sracic MW, Chauhan S, Hansen MH (2011) Output-only modal analysis of linear time periodic systems with application to wind turbine simulation data. *Mech Syst Signal Process* 25:1174–1191
7. Yang S, Allen MS (2012) Output-only modal analysis using continuous-scan laser Doppler vibrometry and application to a 20 kW wind turbine. *Mech Syst Signal Process* 31:2011
8. Bir G (2008) Multiblade coordinate transformation and its application to wind turbine analysis. Presented at the 2008 ASME wind energy symposium, Reno
9. Skjoldan PF, Hansen MH (2009) On the similarity of the Coleman and Lyapunov-Floquet transformations for modal analysis of bladed rotor structures. *J Sound Vib* 327:424–439
10. Yang S, Allen MS (2012) A lifting algorithm for output-only continuous scan laser Doppler vibrometry. Presented at the AIAA, Hawaii
11. Chen C-T (1999) Linear system theory and design, 3rd edn. Oxford University Press, New York
12. Tcherniak D, Chauhan S, Hansen MH (2010) Applicability limits of operational modal analysis to operational wind turbines. Presented at the 28th international modal analysis conference (IMAC XXVIII), Jacksonville
13. Jacob T, Tcherniak D, Castiglione R (2014) Harmonic removal as a pre-processing step for operational modal analysis: application to operating gearbox data. Presented at the VDI-Fachtagung Schwingungen von Windenergieanlagen
14. Hansen MH (2004) Aeroelastic stability analysis of wind turbines using an eigenvalue approach. *Wind Energy* 7:133–143

15. Tcherniak D, Basurko J, Salgado O, Urresti I, Chauhan S, Carcangui CE, Rossetti M (2011) Application of OMA to operational wind turbine. Presented at the international operational modal analysis conference, Istanbul
16. Allen MS (2005) Global and Multi-Input-Multi-Output (MIMO) extensions of the Algorithm of Mode Isolation (AMI). Doctorate, George W. Woodruff School of Mechanical Engineering, Georgia Institute of Technology, Atlanta
17. Allen MS, Ginsberg JH (2006) A global, Single-Input-Multi-Output (SIMO) implementation of the algorithm of mode isolation and applications to analytical and experimental data. *Mech Syst Signal Process* 20:1090–1111

Chapter 9

Lateral Vibrations in High Speed Over Critical Drive Train Systems

Sumit Singhal

Abstract A drive train system which has motor, gearbox and variable frequency drives operates on wide speed range. High vibration in rotating machinery drive train systems is undesirable as it reduces the reliability and life of system components. Lateral vibration and torsion analysis of system components along with complete drive train is powerful tool to design low vibration drive trains. This paper discusses the case study where the high speed drive system prototype experienced the vibration issue during a full system testing. Rotor dynamics calculations of coupled systems were performed to identify the cause of system vibration. During the experimental and theoretical investigation it was learned that the high speed gear box with oil film gear has large degree of nonlinearity in rotordynamics systems due to changing speeds, loading and inherent tooth contact forces.

Keywords Rotor dynamics • Gearbox • Fluid bearings • Drive train • High speed

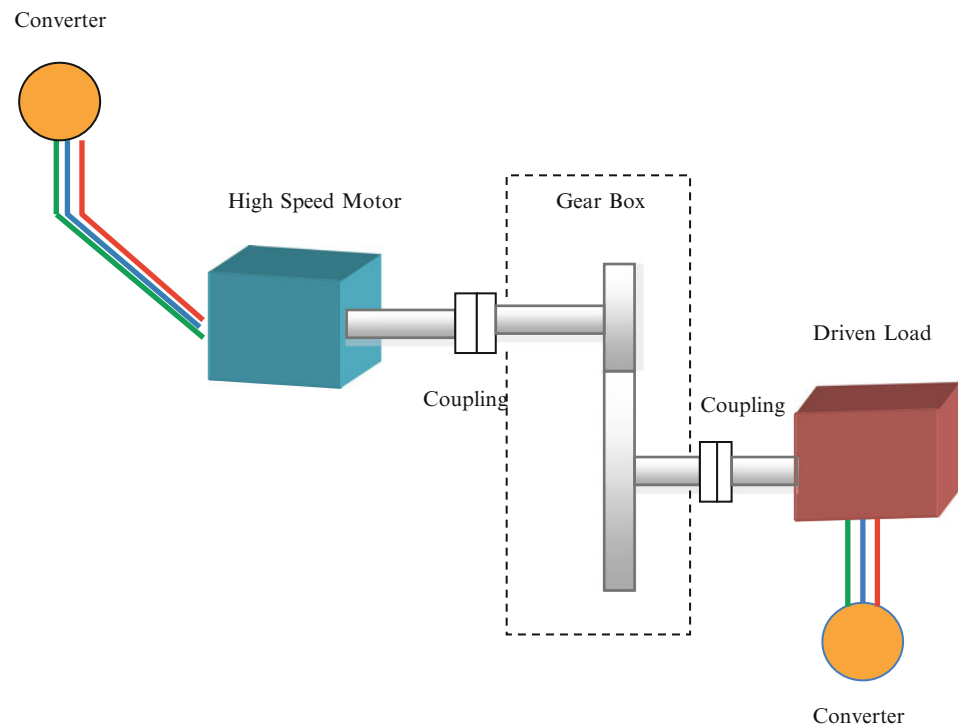
9.1 Introduction

Converter driven electric motors driving pumps and compressors with or without gear box are applied in various industrial applications for the production of oil, natural gas, cement and other products [1]. Converter driven electric motors driving pumps and compressors often has wide operating speed ranges in order to meet the process requirements and to increase the overall process efficiency by reducing electrical energy consumption. For the higher reliability and life of rotating mechanical equipments the overall vibration of individual components and entire drive train should be as low as possible for the entire speed range of operation. One common method of designing low vibration equipments is to have separation margin between the critical natural frequencies and operating speed range as required per API 541 [2]. Usually the individual rotating equipment in the drive train such as motors, gear box and driven equipments such as pumps, compressors and fans are manufactured by different OEM and applying different design specifications [2, 3]. The individual components are designed to specifications and meets the low vibration rotordynamics design criteria and requirements. But it may happen that system which consists of all the components which meets requirements may still have high vibration due to interactions of individual components. Usually the coupling between the various rotating equipments is an important mechanical component which can help to reduce the interaction and reduce vibration in the drive train systems. Proper choice of coupling type and optimized dimension is required to decouple the interactions of components and hence reduce the vibration of drive train systems. In order to choose and optimize coupling design, torsion and lateral rotor dynamics calculations of the entire drive train is required to understand the dynamics of rotor string and predict vibration on the field under various loading cases.

Recently a special system lateral vibration issue was observed during the prototype testing of high speed drive train. In the test field a drive train system consisting of high speed motor, high speed gear box and electric generator and electric converter was assembled. The electric motor, high speed gear box and generator rotor rides on oil film bearings. During the testing vibration was under acceptable limit for complete speed range under no load conditions. However when the load is applied to the gear box, the drive train shows vibrations beyond acceptable limits. Several measures such as better alignment, better balancing were applied with no success to reduce the vibration within acceptable limits. To simulate the measurement

S. Singhal (✉)
Siemens Industry Inc, Norwood, OH, USA
e-mail: Sumit.Singhal@siemens.com

Fig. 9.1 Setup of drive train system test



behaviour very detailed rotordynamic model of complete string was constructed to study the basic cause of vibration. Tested data was used for model updating but due to non linear bearings it was difficult to match the exact behaviour of drive train string measurement. However linear eigen analysis along with unbalance response calculation was performed to compare the measured shaft bending mode shape. It was found from the calculations that there is natural frequency of complete shaft string within the speed range when the alignment between motor–gear box, torque transmission in gear box, and non linear in the bearings is taken into rotor dynamics consideration. The coupling design between the motor and gear box was optimized to reduce the vibration.

9.2 System Test Setup

The prototype drive train system consists of high voltage 6 MW induction electric motor is designed to have an operating speed range of 3,800–5,000 rpm, which is driven through converter as shown in Fig. 9.1. The induction motor consists of two fluid film bearings. The induction motor is coupled to a high speed gear box with flexible coupling. The speed ration of gear box is 5:1. Due to high operating speed the gear box also consists of fluid film bearings. The driven side of gear box is connected to the load machine which is an electric generator and feeds power back to the electric grid.

9.3 Test Results

The vibration of a drive train under no load condition and especially motor is within specification as seen from Fig. 9.2. However when the drive train is coupled to load then entire drive train shows high vibration at 4,300 rpm which is within operating speed range of 3,800–5,000 rpm, which leads to emergency shutdown of the system to prevent any further damages. Vibration spectrum data shows that all the vibration occurs at one time rotational frequencies. Which strongly point towards the cause that the residual unbalances distribution in the drive train system may have caused the high vibration. In case of converter driven high speed electric motors there are several mechanical and electromagnetic forces which can lead to one time rotational frequencies. The first step to troubleshoot the vibration problem is to isolate the cause of vibration whether it is electrical or mechanical in nature [1].

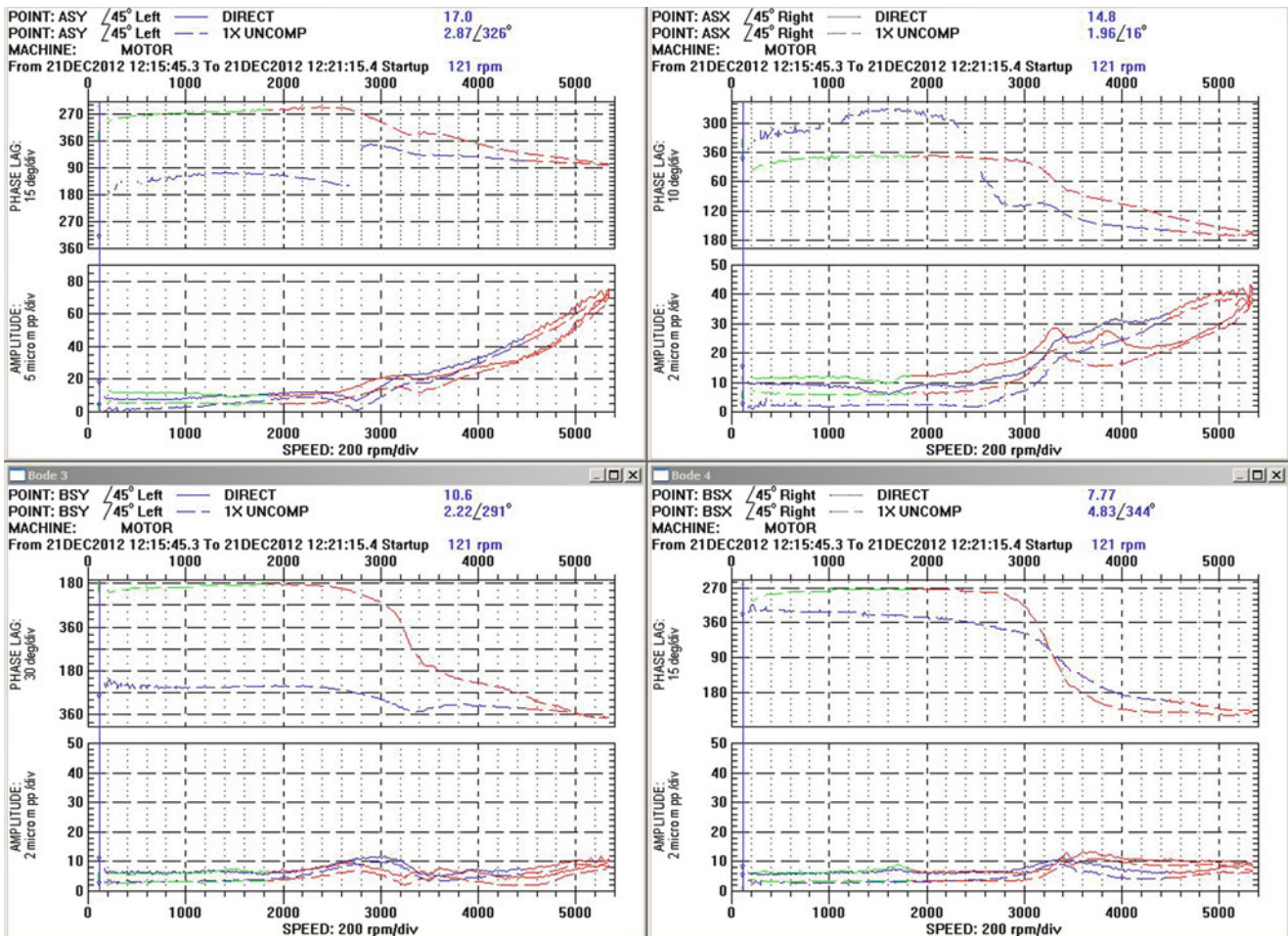


Fig. 9.2 Test measurements motor bearings under coupled unloaded conditions

In order to investigate the cause and reduction of train vibration further unbalance response test was performed where the known value and phase of unbalance was applied at specific position in the couplings. The collected unbalance vibration response data was for rotor dynamics calculations. Shaft vibration and phase values were used to update the rotor dynamics prediction model.

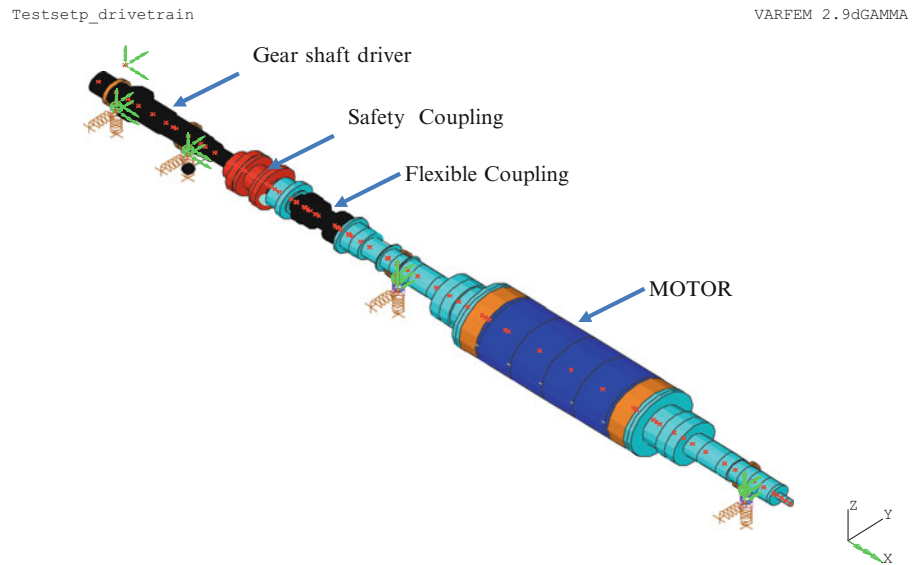
The unloaded couple test measurement data shows that vibration amplification in the gear box is at 3,800 rpm which is 500 rpm lower than what is observed from the vibration test data from loaded couple test measurement data. This big shift in vibration amplification speed indicates the presence of load dependent non linearity in the system. The two sources of non-linearity identified in the test drive system are due to non linear behavior of oil film or may be due to the non linear stiffness arising from the flexible coupling. From the unbalance response analysis of loaded and unloaded conditions shows that accurate modeling of fluid film bearings and coupling is required in the simulation model. Also the separate system simulation is required for loaded and unloaded conditions as the system is changing from one state to another.

9.4 Lateral System Calculation

During the design stage of the machine the lateral rotordynamics analysis of uncoupled electric motor was performed per API 541 standard. The natural frequencies and the vibration values meets the design requirement as per API standard. During the uncoupled test of electric motor the motor vibration meets the API criteria. But high vibration occurs when the load is applied to drive train.

In order to understand and simulate the cause of vibration as shown in Fig. 9.3; the rotordynamics model of electric motor rotor is extended to include complete drive train string. Rotor of gear, motor and flexible coupling is modeled using

Fig. 9.3 Rotor dynamics schematic of drive train



beam elements in rotordynamics program. The bearing housing, frame and foundation are modeled as mass and spring system based on stiffness derived from the modal analysis. The fluid film bearings on the motor and gears are modeled as speed varying load dependent stiffness and damping coefficients. Both direct and cross-coupled stiffness and damping of the rotor dynamic oil film is calculated using ALP3T program. Test field foundation stiffness for the rotor dynamic model is also considered which is derived from modal analysis data. The finite element rotor dynamic program employs the MADYN solver to calculate the natural frequency and unbalance vibration response of the drive train. Figure 9.4a–c shows the natural frequency and deflection shape of the drive train under unloaded condition. The predicted response is reconciled to measurement data by changing the stiffness and damping parameters at the gear box fluid film bearings. It can be seen that there is a natural frequency of the train within the operating speed range as shown in Fig. 9.4c. The damping of this mode is 17 % by calculation. The rotordynamics model is updated to simulate the loaded condition of gear by considering the transmitted torque by the gear teeth's leading to radial loads additional to rotor gravity loading at bearings locations. The direction of radial loads generated due to tooth forces can be opposite or in the direction of gravity loading. In the present case the net force due to tooth forces results in unloading of gear bearings connected to high speed motor side. Reduction of load on bearings leads to significant changes in the oil film stiffness and damping coefficients hence the drive train model was updated for loaded condition. Figure 9.4d shows the natural frequency and deflection shape of the drive train under loaded condition. The calculation shows that low damped train eigen frequency appears at 4,642 rpm. As seen from Fig. 9.5 the unbalance response shows that the motor vibration values on the drive end can be amplified at this eigen frequency. Rotordynamics calculations confirm the vibration behavior observed on the test field qualitatively. Quantitatively there is a deviation between the calculation and measurements which may be due to the non linear behavior of oil film due to light bearing loads caused by torque transmission mechanism in the gear box.

9.5 Problem Solution

From the rotor dynamic analysis it was found that there is a poorly damped drive train mode within the speed range which gets excited whenever the bearing damping changes due to load condition. The flexible coupling used to couple the motor and the gear box shaft is not soft enough to decouple the motion between the motor shaft and gear box. Soft coupling creates a drive train natural frequency leading to high vibration. In order to shift the drive train bending eigen frequency out of speed range various intermediate shafts designs are considered. The fastest design option for intermediate coupling shaft from the calculation was found to be rigid hollow bar with optimized diameter and length. Lateral rotordynamics calculations of drive trains shows that drive train eigen frequency shifted to 6,400 rpm which is outside of the maximum speed range and shaft vibration will be below acceptable limits as shown in Fig. 9.6. The measure data of shaft vibrations as shown in Fig. 9.7 shows that the peak of drive train shaft vibration is shifted to 5,300 rpm from 3,800 rpm with new design of intermediate coupling shaft. From the measurement data it can be seen that the measured critical speed is much lower than the predicted by the

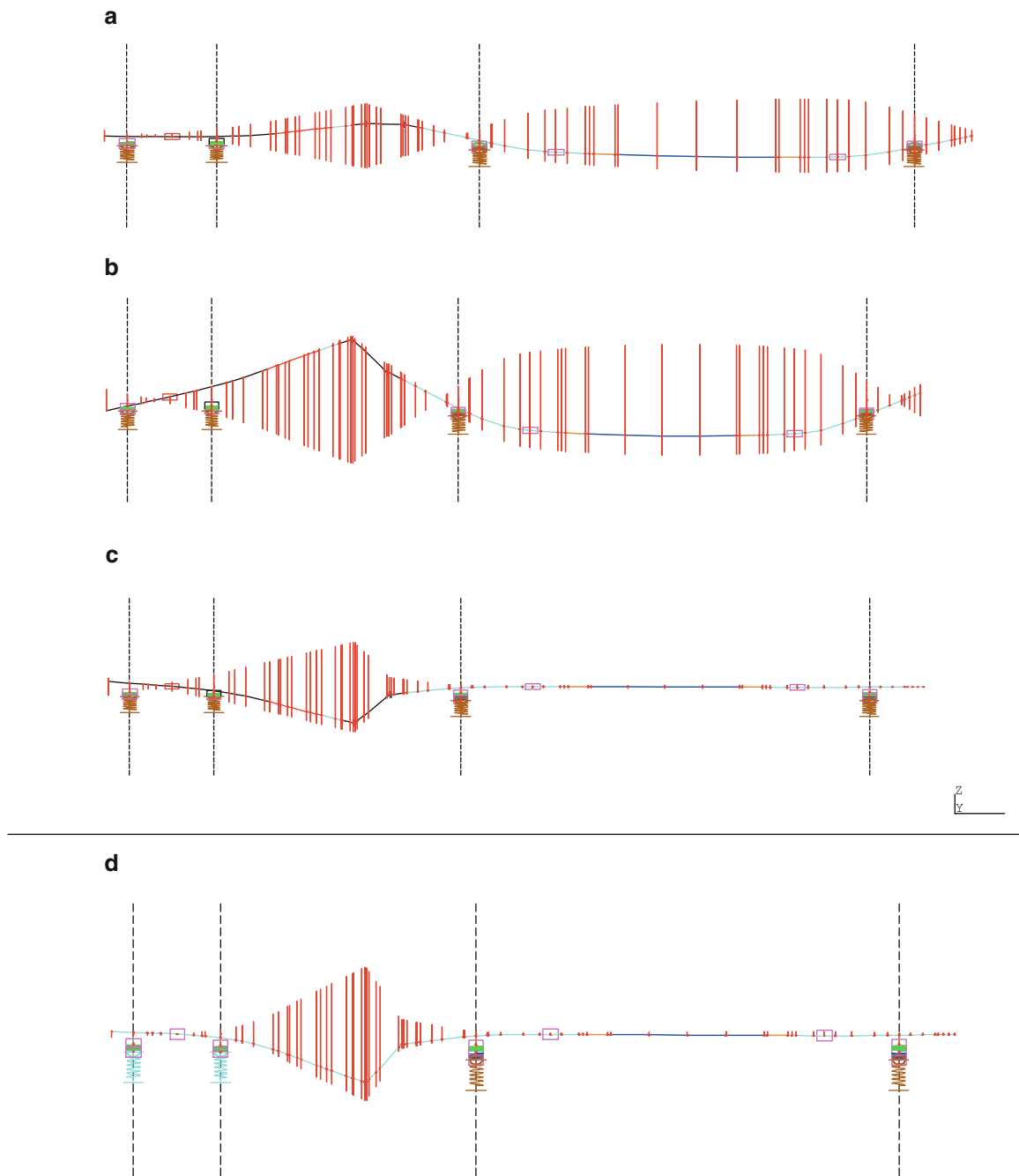


Fig. 9.4 Calculated mode shapes and natural frequencies of motor-coupling-gear box. (a) Frequency = 2,955 rpm, Damping = 2.5 % Motor Rotor Bending Unloaded condition. (b) Frequency = 3,236 rpm, Damping = 2.2 % Motor Rotor Bending Unloaded string. (c) Frequency = 3,991 rpm, Damping = 17.4 % Coupling Mode, Unloaded condition. (d) Frequency = 4,642 rpm, Damping = 1.3 % Coupling Mode: Loaded Condition

calculations, this is due to the non-linearity coming from the oil film bearings. Effects of the oil bearing in the rotordynamics calculations is considered by inclusion of stiffness and damping coefficients derived based on the static position of position of rotor inside bearings. The static position of rotor inside bearings changes with rotor speed and load on the bearings. In case of the system with high speed gear box which has oil film bearing the oil film bearing coefficients not only changes with speed but also with the amount of torque transmission between the gear mesh. Dynamic torque transmission in the gear mesh

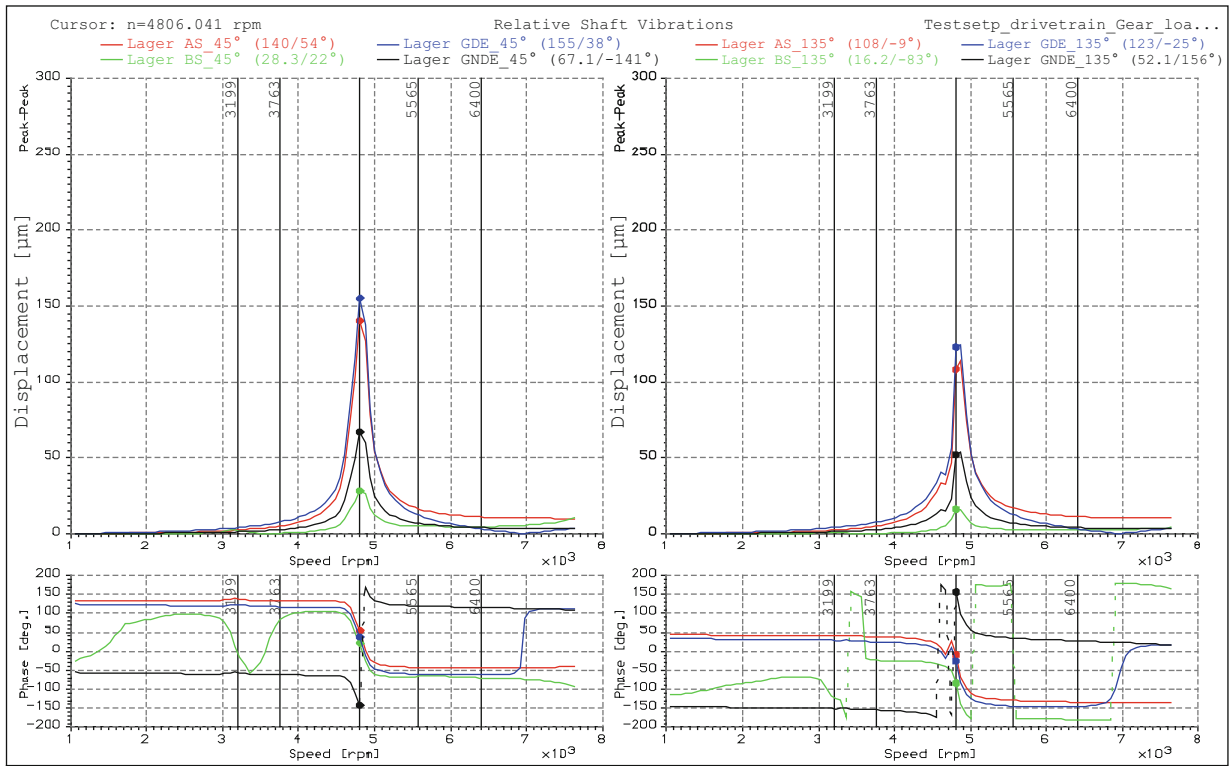


Fig. 9.5 Calculated unbalance response analysis of drive train under LOADED condition

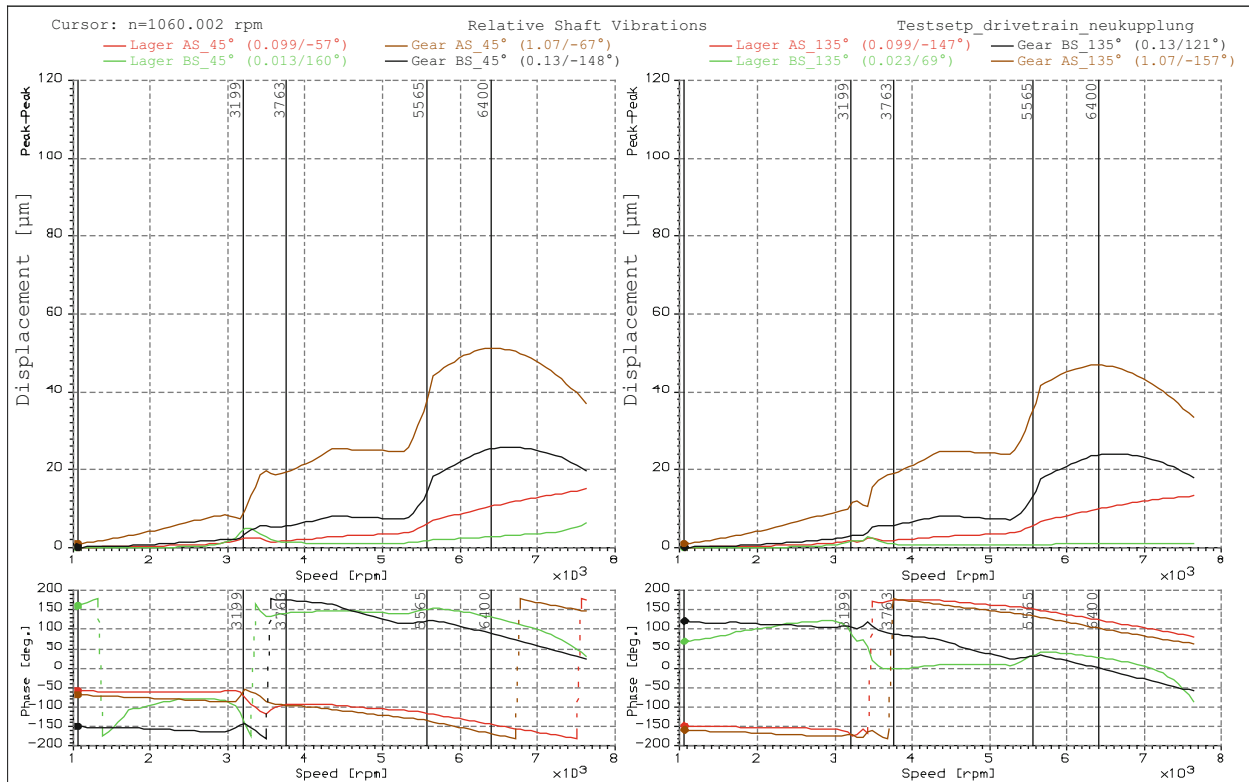


Fig. 9.6 Unbalance response analysis of drive train under loaded condition (new coupling design)

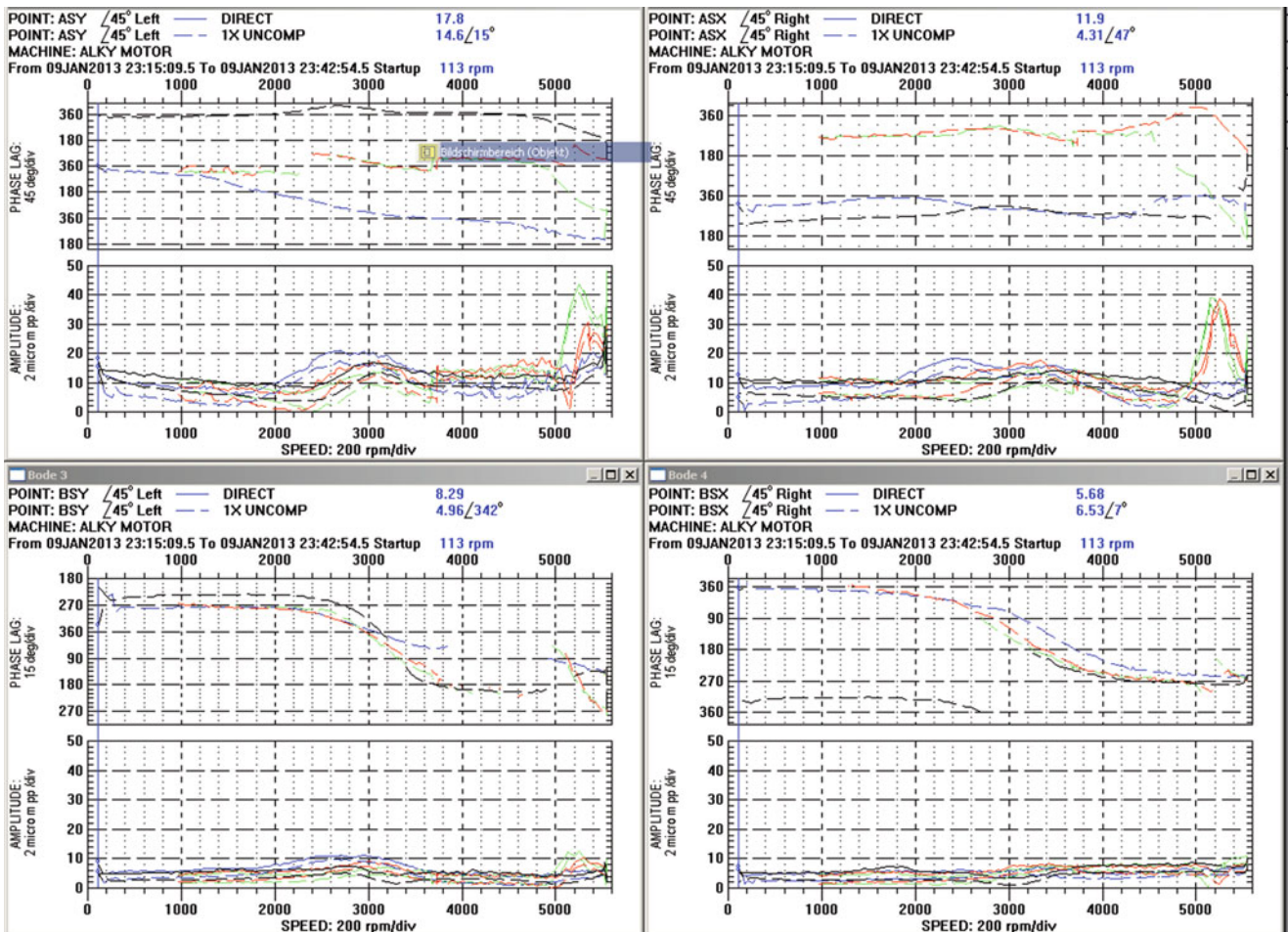


Fig. 9.7 Vibration data of a drive train under loaded condition (new coupling design)

leads to dynamic tooth forces which creates additional dynamic radial loading on bearing locations. Hence the drive train system consisting of high speed variable speed motor along with gear box with oil film bearings creates a highly non-linear rotor dynamics system. Hence it is very difficult to predict the exact vibration behavior of the drive train.

9.6 Conclusion

From the testing and from analysis it was concluded that

1. Gear Box does not have any natural frequency in the speed range
2. Motor does not have any natural frequencies in the speed range
3. Motor–Gear Box string coupled with flexible coupling has train natural frequency in the speed range
4. Natural frequency associated with Motor–Gear Box string depends on the loading of the gear.
5. Loading of the gear train by driven equipment changes the loading of gear box bearings hence changing the rotordynamic stiffness and damping coefficients of the gearbox bearings, thus changing the modal damping and frequency of train bending mode.
6. Gear Box Bearing Dynamics is highly non-linear under loading conditions.

In this drive train design the problem could be solved by changing the coupling design between the motor and gearbox.

References

1. Singhal (2012) Rotordynamics consideration for low vibration machines in oil and gas industry. In: IEEE PCIC
2. API 541 4th Edition-2003, Form-wound squirrel-cage induction motors – 500 horsepower and larger
3. API 617 – Centrifugal compressors for petroleum, chemical and gas service industry

Chapter 10

Vibration Energy Trending and Speed-Frequency Transformation in Run-Up/Coast-Down Tests

Nader Sawalhi and Suri Ganeriwala

Abstract Vibration data collected during a run-up and/or coast-down of machines gives useful indicators about their critical speeds and resonances. In this paper, a signal processing approach to interpret and utilize the start-up and coast-down data in an efficient and effective style is proposed. The vibration root mean squared values (RMS) for each shaft rotation is first trended by the aid of a tachometer signal. This RMS-speed trending provides a simple first examination of the transient data and proves very helpful if the system passes through a critical speed. A more detailed approach is used next, in which the power spectrum of each shaft rotation (speed) is extracted and plotted. This provides a speed-frequency transformation, analogous to the Short Time Fourier Transformation (STFT), in the sense that the frequency content is obtained for short time durations, but with the resolution that is very well comparable to the use of wavelets. The frequency content is taken on a shaft rotation basis, guided by the instances of the start of each shaft rotation. The window length is selected based on the lowest speed to maintain a uniform resolution, which means that the signal is zero padded at higher speeds where the actual shaft rotation length is shorter than the window length. The essence of this approach is illustrated and results in form of contour plots are compared to traditional STFT and Morlet wavelet analysis.

Keywords Start-up/coast-down • Transient • Speed-frequency transformation • Short time frequency transformation (STFT) and wavelet analysis

10.1 Introduction

Vibration signal processing under variable speed conditions (transient signals) requires in general a simultaneous treatment and processing of both the time and frequency content. Time-frequency presentations such as spectrograms [Short Time Frequency Transformation (STFT)] [1], Wigner-Ville distribution [1], wavelet analysis [2] etc. have been used extensively to analyze the content of these signals. For rotary machines during the Start-up (speed increase) or Coast-down (speed decrease), analysts monitor the vibrations of the machine as a function of time and/or speed. The measured signals are processed to extract information about the machine critical speeds and resonant frequencies. To perform the Start-up/Coast down measurements, a simultaneous acquisition of a vibration signal and a speed reference (Tachometer) is favored. The results are typically presented using spectrograms or waterfall plots (Multiple FFTs overlaid and offset). A spectrogram is a function of the window type and length and thus the signal presentation becomes a tradeoff between the resolution in the time domain and the frequency domain. Shorter window lengths result in poor resolution in the frequency domain. Waterfall provide a cascade plot of the frequency content at fixed speeds and thus requires order tracking to remove speed fluctuations.

In this paper two approaches to exploit a simultaneous presentation of vibration and tachometer data from a star up test are presented. In the first approach the Root Mean Squared (RMS) value for the vibration of each rotation is plotted against the shaft speed to give the analyst an overview about the change of the cyclic energy level in as a function of the speed.

N. Sawalhi (✉)
Prince Mohammad Bin Fahd University, Al Khober, 31952 Saudi Arabia
e-mail: nsawalhi@pmu.edu.sa

S. Ganeriwala
Spectra Quest Inc., Richmond, VA 23228, USA
e-mail: suri@spectraquest.com

In the second approach, the power spectrum for each shaft rotation is plotted as a function of the speed using contours to give a time-frequency representation that is similar to the spectrogram in the sense that the FFT is performed over a short time interval, but differs in the sense that the time length is determined by each shaft rotation length. The shaft rotation length is determined by the aid of the tachometer. The results of the signal processing are presented and discussed by utilizing a start-up data from a machine fault simulator test rig.

This paper is organized as follows. Section 10.2 describes the processing of the vibration signal by the aid of the tachometer signal to provide the cyclic energy tracking and the speed-frequency presentation (SFP). In Sect. 10.3, the experimental test rig setup is presented. Section 10.4 provides a summary and discussion of the results obtained using the proposed signal processing approaches of Sect. 10.2 and a comparison to traditional spectrograms and Morlet wavelets [3] are presented. Finally conclusions are provided in Sect. 10.5.

10.2 Vibration Transient (Start-Up or Coast-Down) Data Processing with Aid of a Tachometer

Figure 10.1 describes the general proposed processing algorithm for the tachometer signal and the vibration signal in a transient test. The steps are illustrated in Sects. 10.2.1–10.2.3.

10.2.1 Tachometer Processing

The tachometer signal is firstly processed to identify the instances (exact start) of each shaft rotation. To do so, the mean value of the tachometer signal is first subtracted. The zero crossings at the rise up edge are then identified by interpolating between the sample numbers below and above the zero crossing. Figure 10.2 shows a typical example of locating the zero crossing of a tachometer. Note that the instantaneous speed based on each rotation can be calculated and traced by dividing the sampling frequency by the difference between each two consecutive crossings. The speed profile obtained based on each shaft rotation estimate could be prone to fluctuations which may result from vibration levels instabilities and other errors. The speed profile should then be smoothed based on a number of shaft rotations. To do so, we propose using a median filter to capture around ten shaft rotations and provide a tracking of the speed based on a smoothed version.

Figure 10.3 compares the instantaneous shaft based speed estimate from one start up test with the smoothed ten shaft rotations obtained from the median filter. Note how the median filter works on correcting the apparent wrong speed estimate appearing as a jump after the 200 revolution.

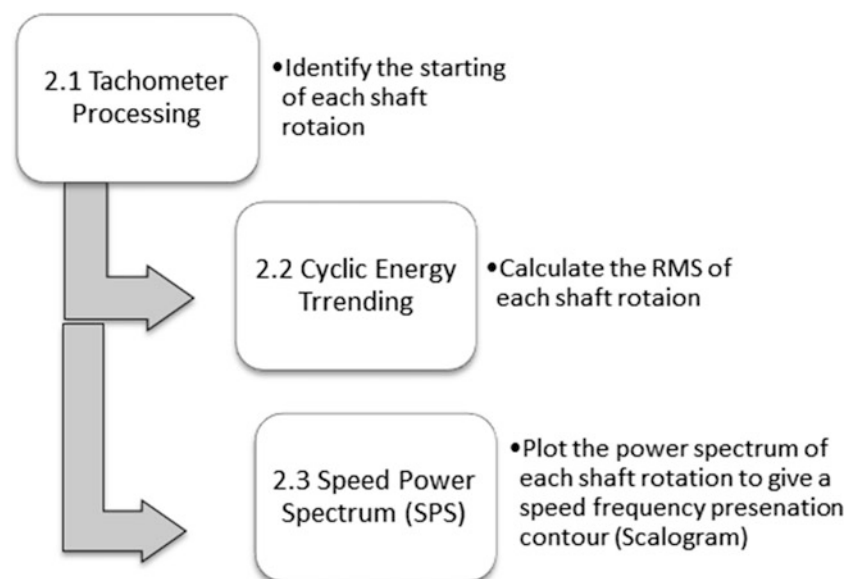


Fig. 10.1 Signal processing presentation

Fig. 10.2 Tachometer signal with zero crossing (*stars*) identified at the rise up of each period

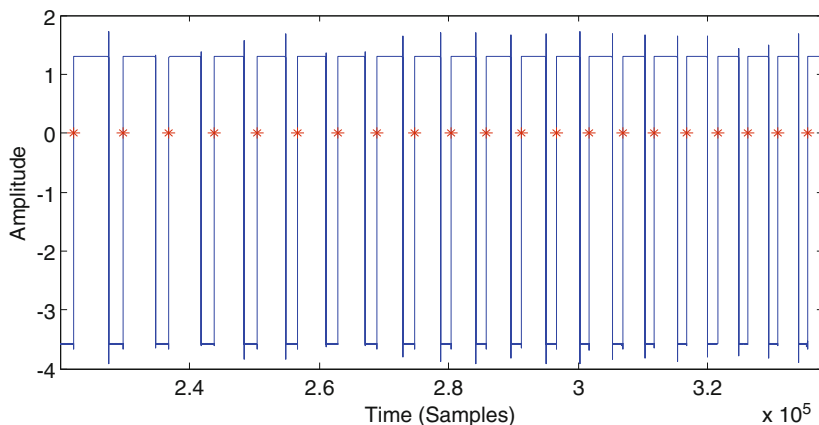
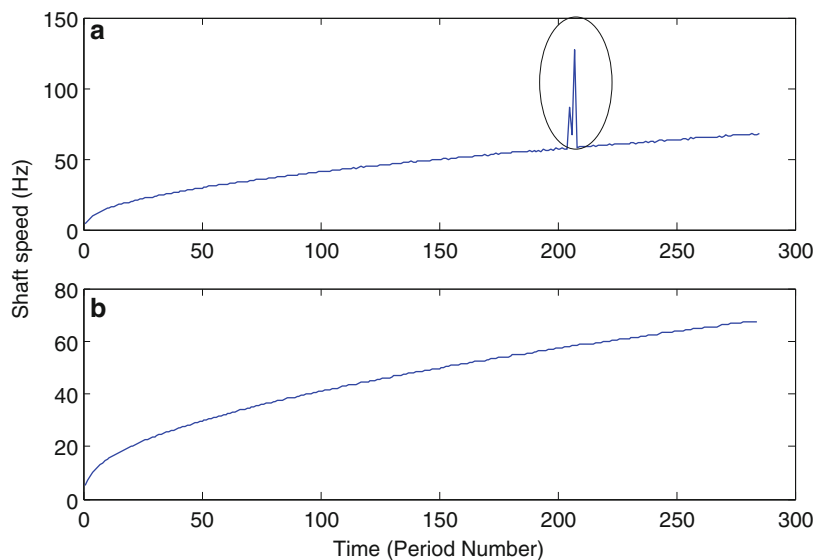


Fig. 10.3 (a) Speed profile obtained based on individual shaft rotations. (b) Smoothened estimate using a median filter with ten rotations



10.2.2 Cyclic Energy Tracking [Root Mean Squared (RMS) Value per Shaft Rotation]

The root mean squared value of each shaft rotation (shaft rotation bounded by the zero crossing indices located earlier using the zero crossing approach discussed in Sect. 10.2.1) is calculated using Eq. (10.1):

$$RMS = \sqrt{\frac{1}{N} \sum_{i=1}^N (x(i))^2} \quad (10.1)$$

where $x(i)$ is the digitized measured vibration signal and N is the number of samples.

The RMS value was selected to provide a measure for the effective energy content within the signal. The tracing of the RMS provides a simple means of observing the energy variation with the speed.

10.2.3 Contour Temporal Power Spectrum Content Variation with Speed [Speed-Power Spectrum (SPS)]

The power spectrum of each shaft rotation is estimated using FFT and the result is presented as a contour plot. The size of the FFT is selected as the next power of two of the lowest speed in the measurements. This means that zero padding (<http://www.bitweenie.com/listings/fft-zero-padding/>) is used in all the shaft rotations but with different extent. Zero padding means that

zeros are added to the end of the time domain signal to increase its length. Generally speaking, zero padding is often used to make the signal of power of two before the FFT. The purpose from using zero padding in this approach is not to resolve adjacent frequencies but rather to uniform the FFT window size for all shaft rotations to get a uniform apparent resolution for presenting the transformation at different speeds. The application of any window function should normally take place before the zero padding. In the current processing, no window function was applied (a default rectangle window is used) as window usage results in the attenuation of the beginning and end of the signal and this means that a number of averages are needed to obtain a good statistical representation of the spectrum. The results are presented using a contour plot to help identifying the transients of interest and are compared to results obtained using spectrograms and wavelet analysis.

10.3 Experimental Setup

The machine fault simulator of SpectraQuest[®] was used to acquire transient data during a startup test. Two configurations were used; a “shaft-only” configuration and a “resonance-set” configuration which is shown in Fig. 10.4. The resonance-set configuration included a steel rotor (black middle) and two aluminum rotors (gold colored) was used to observe the

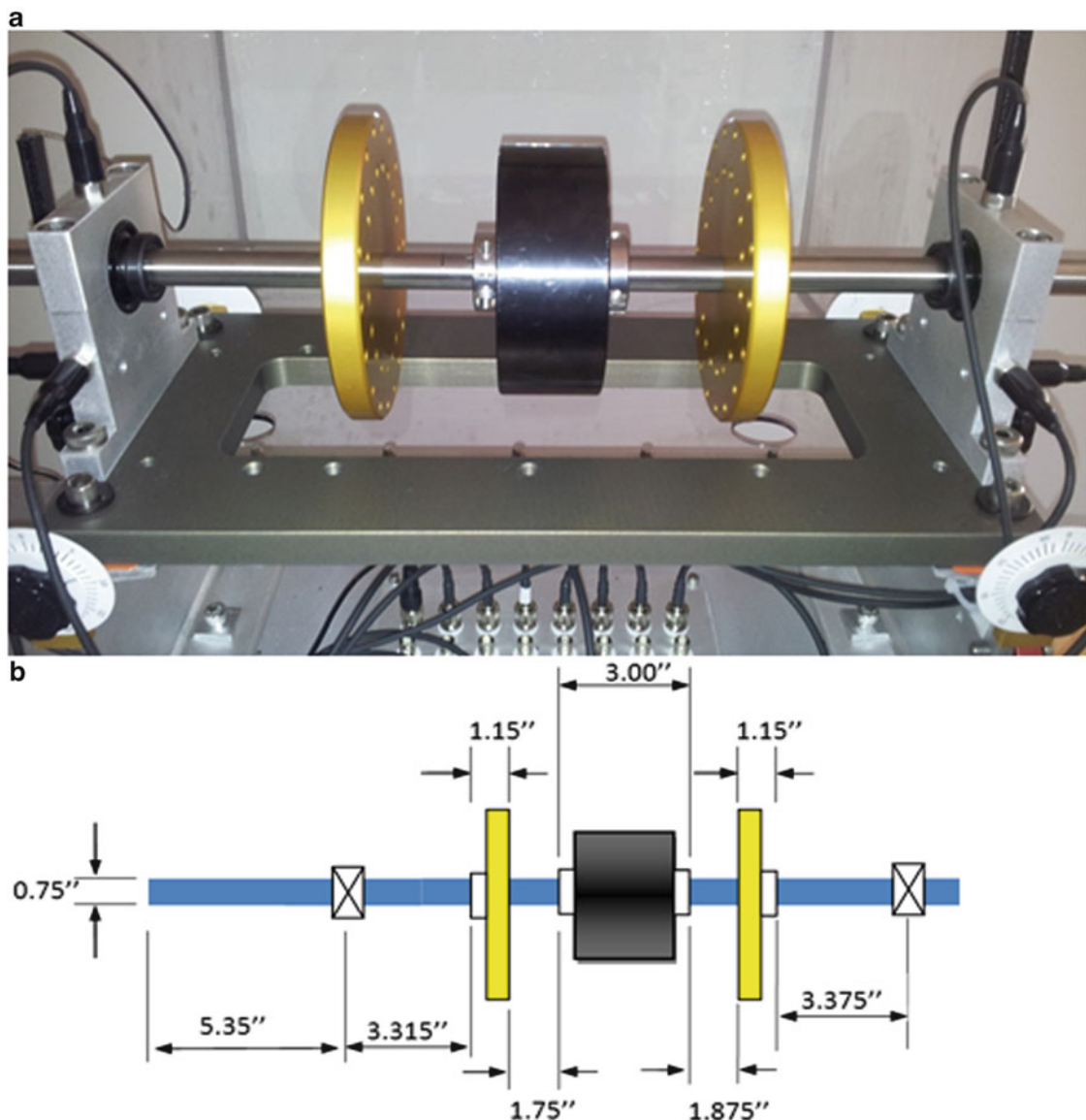


Fig. 10.4 Spectra Quest MFS with a loader (middle black disk) and two gold (aluminum) disks. (a) Image; (b) schematic presentation

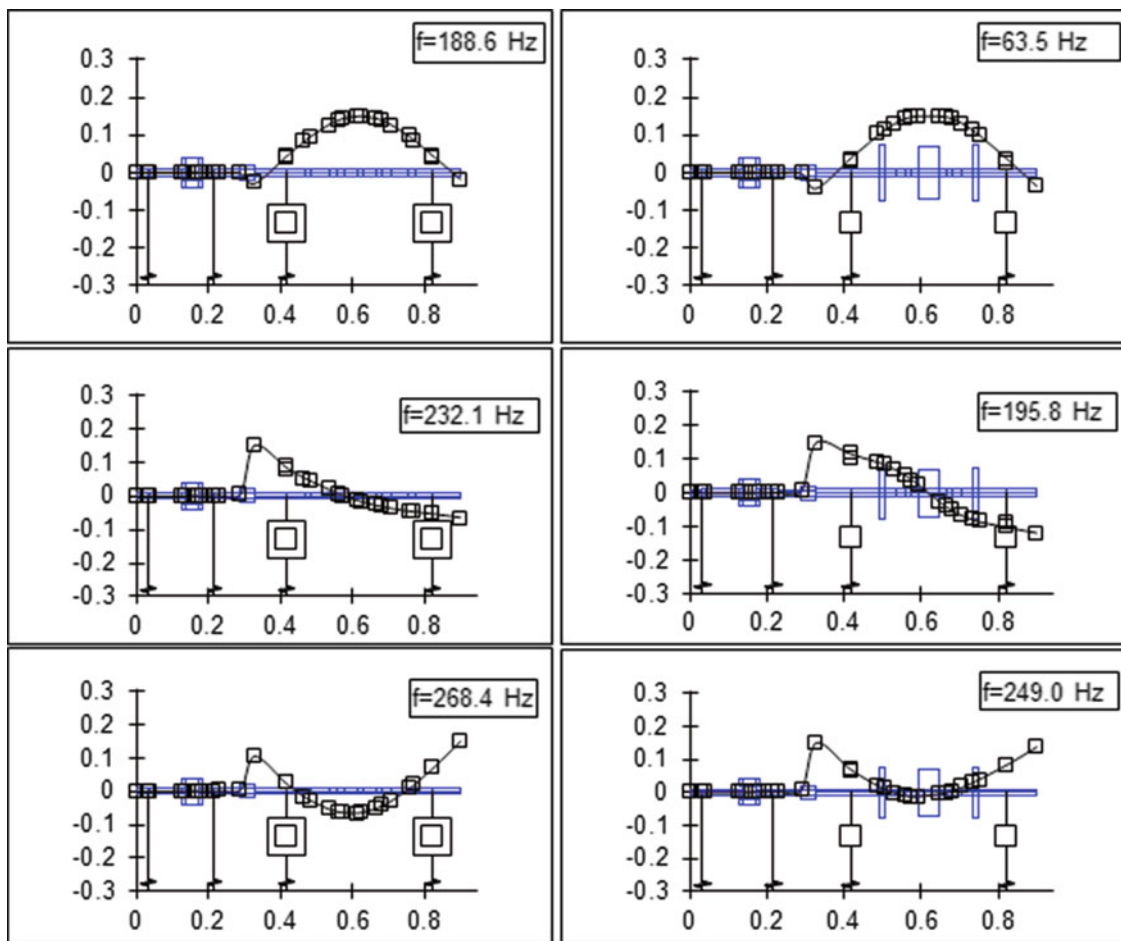


Fig. 10.5 Natural frequencies and mode shapes of the first three modes of two test configuration

1st critical speed within the speed range. Two vertical accelerometers and two horizontal ones were fitted at the bearing locations in addition to a vertical one on the motor inboard bearing. A 40 kHz frequency bandwidth (sampling frequency of 102,400 Hz) was used to capture 10 s of data during a startup test.

10.3.1 Critical Speeds of the Test Rig

To gain an understanding of the system critical frequencies an XL-Rotor[®] (<http://www.xlrotor.com/index.shtml>) model for the MFS was built. The details of the developed model are explained in [4]. Figure 10.5 shows the first three mode shapes and the corresponding natural frequencies of the two configurations.

10.4 Results and Discussion

10.4.1 Cyclic Energy Tracking

Figure 10.6 compares the RMS changes in the acceleration signals at the motor bearing and the inboard and outboard bearings in the vertical direction. The resonance-set configuration (Fig. 10.6b) shows an increase in the vibration levels starting from 60 Hz and peaking at around the 68 Hz before dropping back to lower levels. All bearings show the same behavior, with a

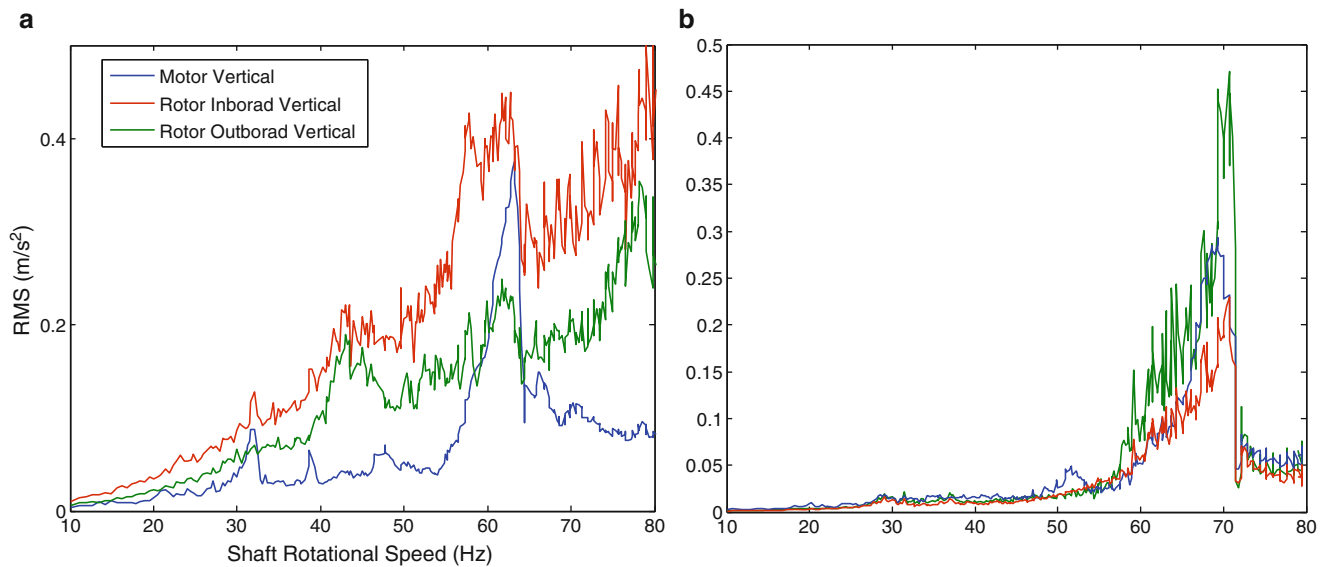


Fig. 10.6 RMS vs speed tracking. (a) Shaft only with no disks. (b) Shaft with resonance kit (one middle steel disk and two aluminum)

higher energy values recorded at the outboard bearing. The result of this case is consistent with the 1st critical speed of the resonance configuration, which expects the resonance to be around the 64 Hz mark.

For the case of the shaft-only configuration (Fig. 10.6a), the peaking appears to happen around the 60 Hz speed, but with other small peaks around 30 Hz and the 40–45 Hz. The most noticeable change happens in the vibrations of the motor bearing, while inboard bearing records the highest levels of vibrations. Although the system does not pass through its first critical (188 Hz), a number of speeds show increased levels of vibrations. The cyclic energy tracking is thus inconclusive in identifying critical speeds. It is however a useful tool to pinpoint problematic operating speeds for avoidance.

10.4.2 SPS Compared to Waterfall Plots, STFT and Wavelets

The result of the SPS transformation is compared to the spectrogram with a similar FFT size with 50 % overlapping and a wavelet representation based on Morlet wavelet. The comparisons are presented in Figs. 10.7 and 10.8 for the shaft-only configuration and the one with the resonance kit respectively. The first row of each figure present the contours obtained using the spectrogram, the second row shows the contours obtained using a Morlet wavelet while the third column shows the SPS contours.

For the shaft only configuration, the best bearings to show the critical speeds are the motor bearing and the inboard one. The motor bearing only shows the 1st critical speed, which is well defined and localized using the SPS and the Morlet wavelets in a much better way compared to the STFT. The inboard bearing shows two critical speeds and the SPS shows a very good performance that is well aligned with the wavelet presentation. It is very hard to locate the critical speed by relying on the outboard bearing for the shaft only configuration. Note that the speed location at which the critical speeds are identified is around the 62 Hz, which had previously showed the highest energy content in the cyclic energy tracking plot of Fig. 10.4.

The case of the resonance kit shows a similar behavior to the shaft-only test results except for the outboard bearing results, which have now a clear localization and identification of the shaft first critical. The best result comes from the motor bearing and is well comparable between the SPS and the Morlet wavelets. Morlet wavelet does however show better localized result in the case of the inboard bearing.

SPS in both cases was very useful in identifying the critical speeds within the frequency range of interest in a manner that is well comparable to the wavelet approach. The processing using SPS is however much faster and simpler to calculate. Presenting the results by the aid of contour plots gives an extra advantage of a better localization of the critical speed.

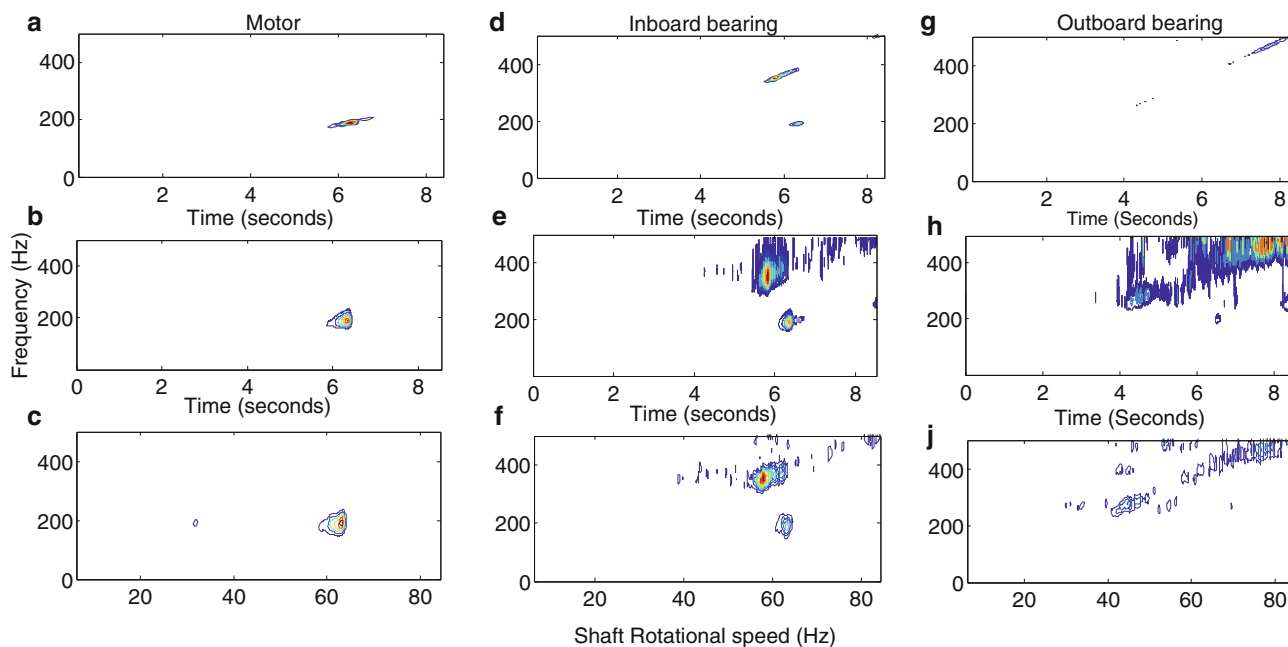


Fig. 10.7 Time frequency presentation for shaft only configuration: *first column (a–c) motor inboard bearing; second column (d–f) rotor inboard bearing; third column (g–j) rotor outboard bearing. First row: STFT; second row: wavelets; third row: SPS*

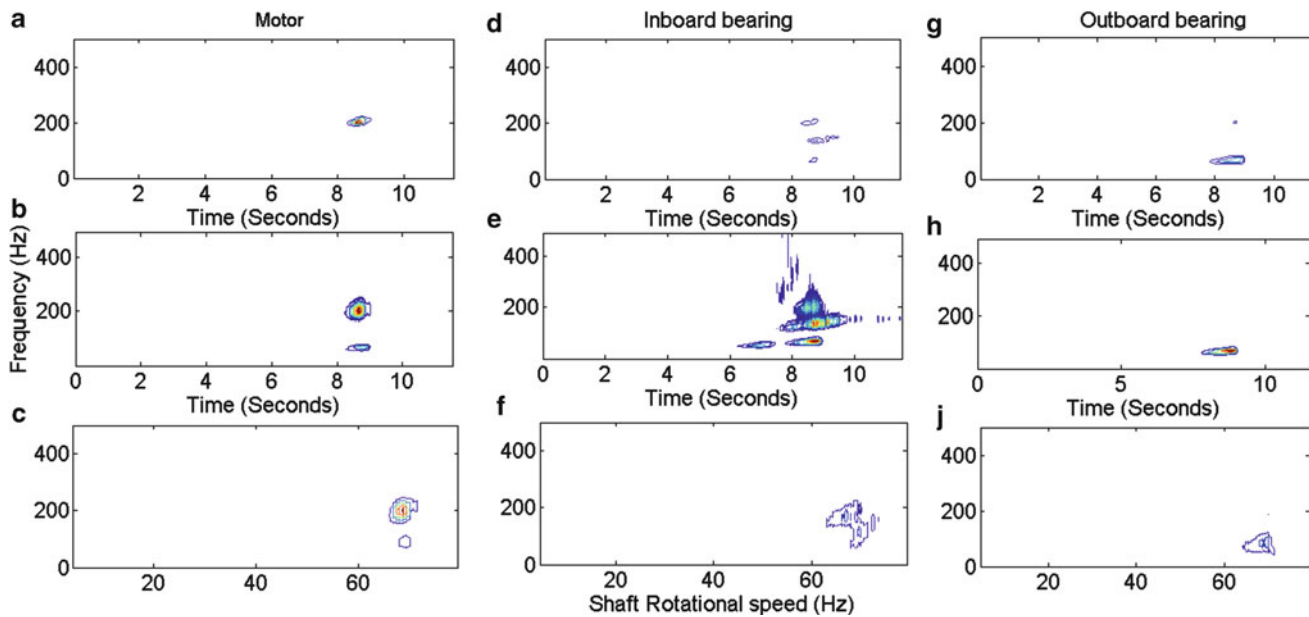


Fig. 10.8 Time frequency presentation for shaft only configuration: *first column (a–c) motor inboard bearing; second column (d–f) rotor inboard bearing; third column (g–j) rotor outboard bearing. First row: STFT; second row: wavelets; third row: SPS*

10.5 Conclusions

This paper has presented two simple and effective approaches to process simultaneously the speed and vibration signal in startup/Coast down analysis. The processing includes the tracking of the RMS of each shaft rotation and plotting the power spectrum of each revolution using a contour plot. The later included the use of zero padding to unify the resolution between the different rotation lengths. The tracking of the RMS gave conclusive results when the system passed through a critical speed, but was not of a great help in identifying the critical speeds of the rotor system when the system didn't pass through any of its critical speeds. The contour plots of the power spectrum gave a very good localization of the rotors' critical speeds

and was very well compared to the results obtained using Morlet wavelets and have outperformed the results obtained using STFT. The main advantage of the presented processing approach includes a very efficient computational algorithm which provides a first examination to the Startup and Coast down analysis to locate the critical speeds of the machine.

Acknowledgment The first Author is thankful for the all the support and help provided by SpectraQuest[®] to complete this work.

References

1. Cohen L (1995) Time-frequency analysis. Prentice-Hall, Englewood Cliffs
2. Mallat S (1998) A wavelet tour of signal processing. Academic, San Diego
3. Kronland-Martinet R, Morlet J, Grossmann A (1987) Analysis of sound patterns through wavelet transforms. *Int J Pattern Recogn Artif Intell* 1:273–301
4. Ganeriwala S, Sawalhi N (2014) Numerical and experimental dynamic system identification for the development of operational modal analysis in a physics-based diagnostic/prognostic model. In: De Clerck J (ed) *Topics in modal analysis I*, vol 7. Proceedings of the 32nd IMAC. A conference and exposition on structural dynamics, Orlando, 3–6 February 2014. Conference proceedings of the Society for Experimental Mechanics Series. doi:10.1007/978-3-319-04753-9_14 © The Society for Experimental Mechanics, Inc.

Chapter 11

Vibration Mitigation on Engine Test Stands Using Conventional Analysis Techniques

B. Swaminathan

Abstract A single cylinder optical engine run by an electric motor at a university engine research center was observed to have high levels of vibrations at specific speeds. This paper discusses the case where incorrect isolation of the engine test stand combined with driveline component vibrations caused high vibration levels to be transmitted into the building structure through the floor. Modal and operational tests were carried out on the entire engine—motor assembly to detect the magnitude and the frequency range of the vibrations. Order analysis was performed on the operating data and correlated with the modal data to identify system resonances excited by multiple orders in the operating ranges of the engines. Specific issues such as backlash in the coupling were also detected from the test data and suitable actions were recommended.

Keywords Engine test cells • Vibration isolation • Rotating machinery • Modal testing • Operational testing

Nomenclature

FRF	Frequency response function (FRF)
ODS FRF	Operating deflection shape frequency response function
EMA	Experimental modal analysis
PTD	Polyreference time domain
MAC	Modal assurance criterion
RFP	Rational fraction polynomial
CMIF	Complex mode indicator function

11.1 Introduction

Structural dynamics analysis of engine test cells [1, 2] have historically focused on development of the single most important piece of equipment within the confines of its four walls, the engine. While the internal combustion engine has hogged the limelight of the dynamics world with its complexities, a close second would be the dynamometer that puts the engine through its test routines in order to prepare it for the real world. When these two complex pieces of equipment, along with their required sub-components, come together to work as a single system, it opens up an entirely new set of dynamic challenges. This paper discusses a case where the behavior of the engine test cell was studied as a whole and various test and analysis methods [3] used to reduce high vibration levels.

The cell that was tested consisted of a single cylinder optical engine used for research in flow visualization techniques at a university lab. The engine is motored by an electric motor from speeds between 600 and 1,800 rpm. Test data collected from the cell was analyzed and solutions were proposed to mitigate the excessive levels of vibration. A follow-up test was performed at the cell to establish the vibration levels upon implementation of the recommended vibration isolation.

B. Swaminathan (✉)

Affiliated Construction Services (ACS), Madison, WI 53705, USA
e-mail: bswaminathan@acscm.com

11.2 Test Methodology, Instrumentation and Data Acquisition

The engine test cell discussed in this paper was subjected to two tests [4]:

1. An impact hammer modal test
2. An operating test

The two tests were done to understand the complete structural dynamics of the system. The impact test was used to obtain Frequency Response Functions (FRF) to extract modal parameters [5], while the operating test data was used to establish the vibration levels in various components of the system in real operating conditions. This data was further used for order analysis and order extraction [6].

The raw time histories were also processed to generate Operating Deflection Shape (ODS) FRFs [7]. ODS FRFs represent the true mode shape of vibration of the system in the actual running condition.

A 64 channel Bruel and Kjaer Pulse data acquisition system was used for the vibration testing. High sensitivity (1 V/g) tri-axial PCB accelerometers were used for the modal tests, while the operating measurements were made using high temperature resistant tri-axial PCB accelerometers with relatively lower sensitivity (10 mV/g).

X-Modal software from Structural Dynamics Research Lab (SDRL) at University of Cincinnati was used for modal parameter estimation using EMA based algorithms. The B&K Pulse Reflex software was used for order analysis of operating data. ME Scope from Vibrant Technologies was used to analyze the operating data to obtain Operation Deflection Shapes (ODS) and for computing ODS FRFs.

11.3 Test Setup

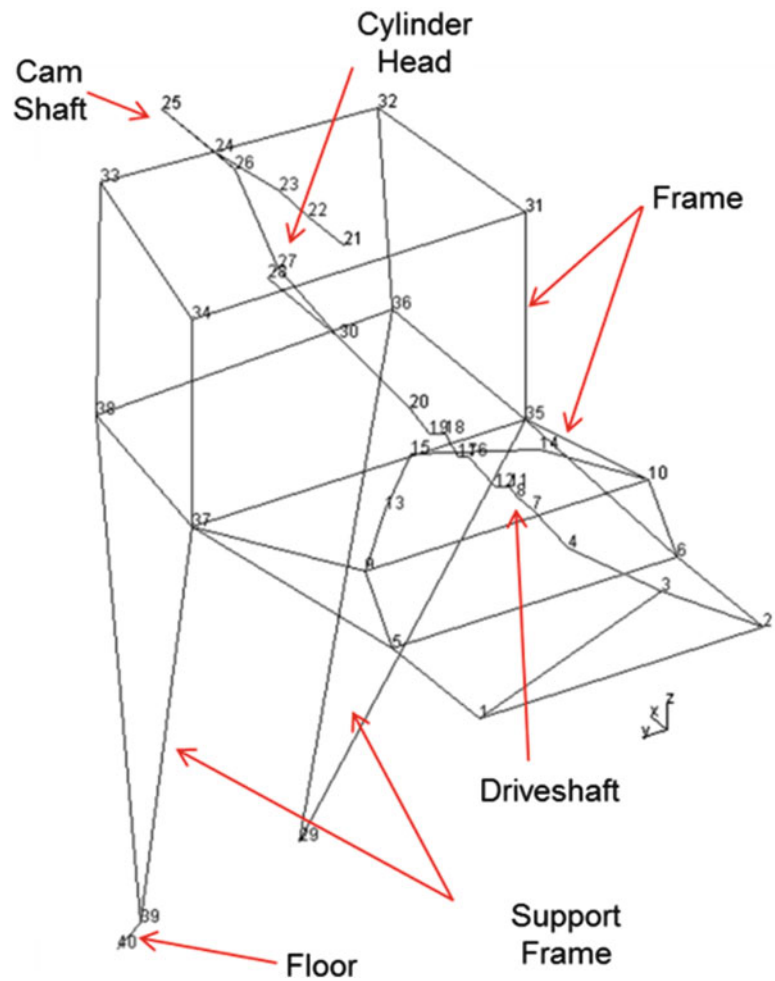
Figure 11.1 shows the engine test stand assembly consisting of the electric motor mounted on an aluminium frame. The single cylinder engine is mounted at the far end of the frame. A set of shafts connect the electric motor to the engine. A Lovejoy coupling is used at the electric motor end as part of the driveline. The engine is driven by the motor during normal operation. A series of belts and pulleys are used to transfer the torque from the motor to run a cam shaft. The entire test stand assembly is connected to the floor using rigid mounts.

The entire test stand assembly is represented by a wire frame model as shown in Fig. 11.2, with numbers indicating sensor locations. The driveshaft, pulleys, bearings, etc. along the driveline are represented by a line due to the small size of the components.



Fig. 11.1 Engine test stand assembly

Fig. 11.2 Wireframe model of engine test stand assembly



Forty response locations were picked for the impact hammer test, with eight reference locations. A set of 20 accelerometers were used in 2 sets to cover the 40 response locations. For the operational testing, a set of 20 accelerometers were used to record time histories at 20 locations.

11.4 Analysis and Recommendations

11.4.1 Baseline Test Results

Data from the impact hammer modal test was analyzed using the Complex Mode Indicator Function (CMIF) [8] algorithm. The first rigid body and driveline modes that lie close to the operating range of the engine were selected from the CMIF plot shown in Fig. 11.3.

The extracted modal parameters are listed in Table 11.1.

Modal Assurance Criteria (MAC) values [4] were computed in order to validate the modal vectors. An Auto-MAC plot of the modal vectors obtained using CMIF algorithm is shown in Fig. 11.4. Modal parameters were also extracted using other algorithms such as Polyreference Time domain (PTD) [4] and Rational Fraction Polynomial (RFP) [9]. These modal vectors were compared to the CMIF results using Cross-MAC calculations in order to identify real modes of the structure.

Figures 11.5 and 11.6 show the mode shapes obtained from the impact testing. These primarily represent the rigid body modes and the first bending mode of the driveline.

Time histories were recorded while motoring the engine through its normal operating speeds. Speed sweep data was taken from idle (600 rpm) to rated speed (1,800 rpm). Operating test data was processed using order analysis and order extraction

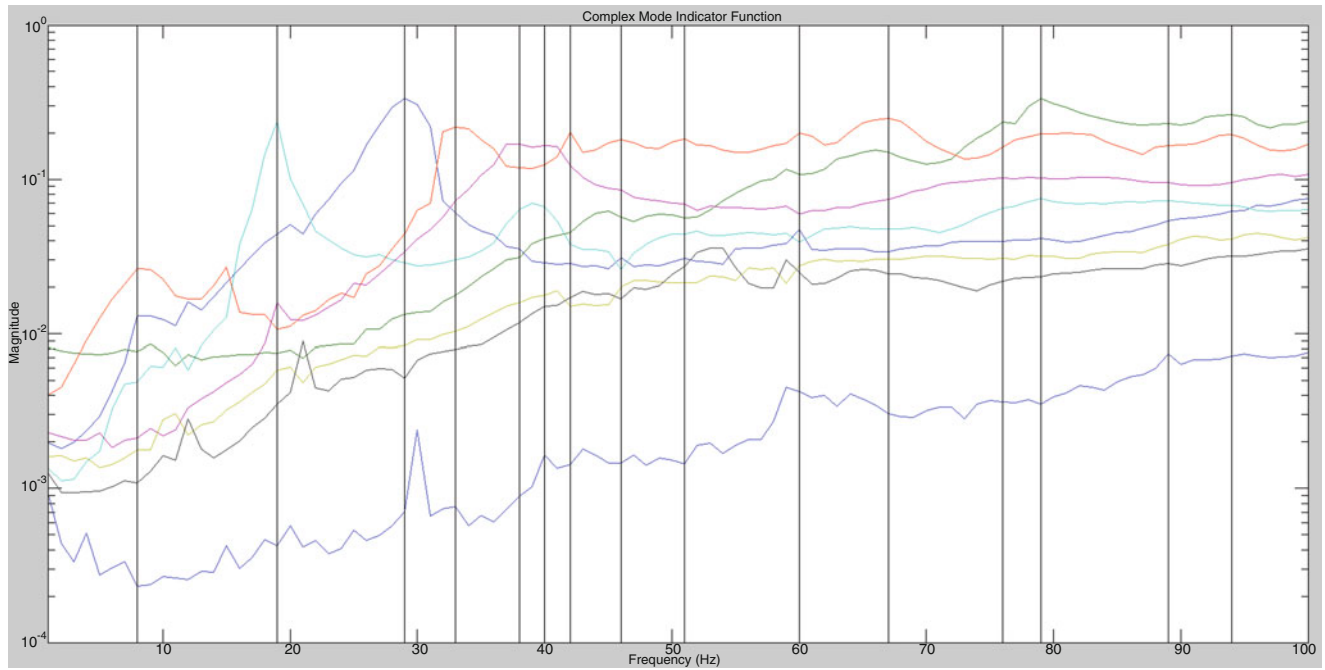


Fig. 11.3 CMIF plot from baseline modal test

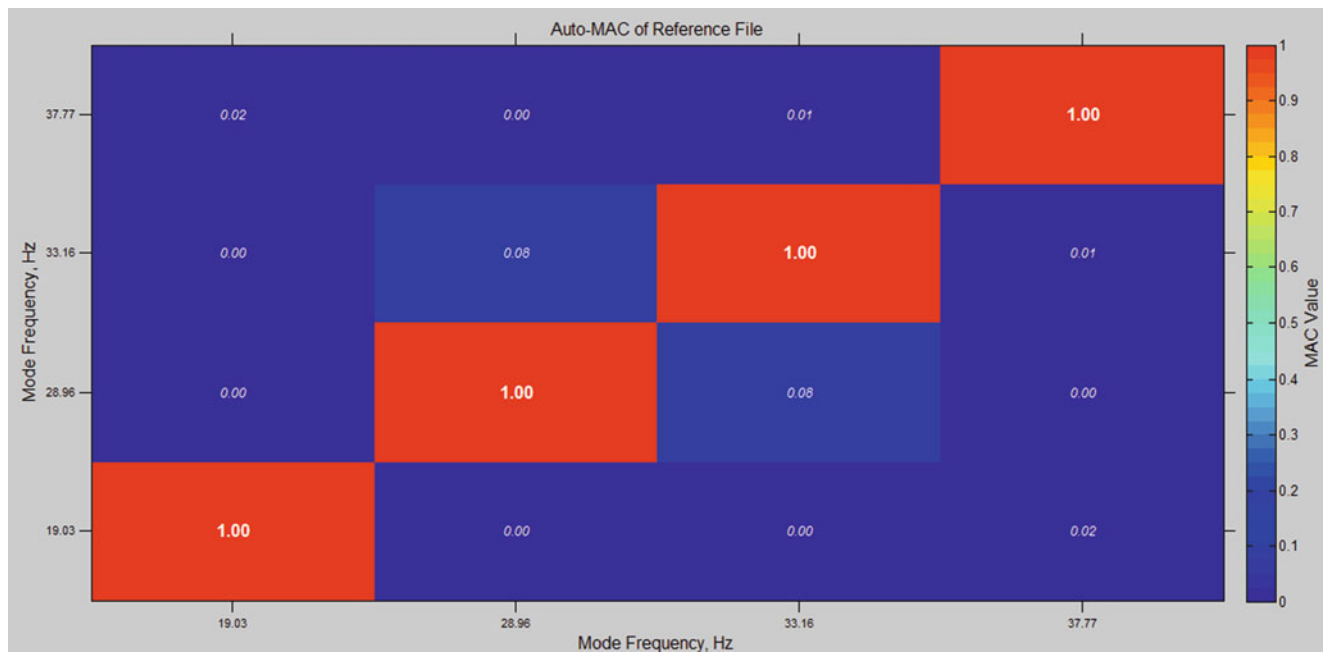


Fig. 11.4 Auto-MAC plot of modes from baseline test

Table 11.1 Modal parameters from baseline modal test

Frequency (Hz)	rpm	Mode shape
19	1,142	Lateral swaying mode
29	1,738	Pitching mode
33.7	2,020	Driveline bending mode
38.5	2,309	Yawing mode

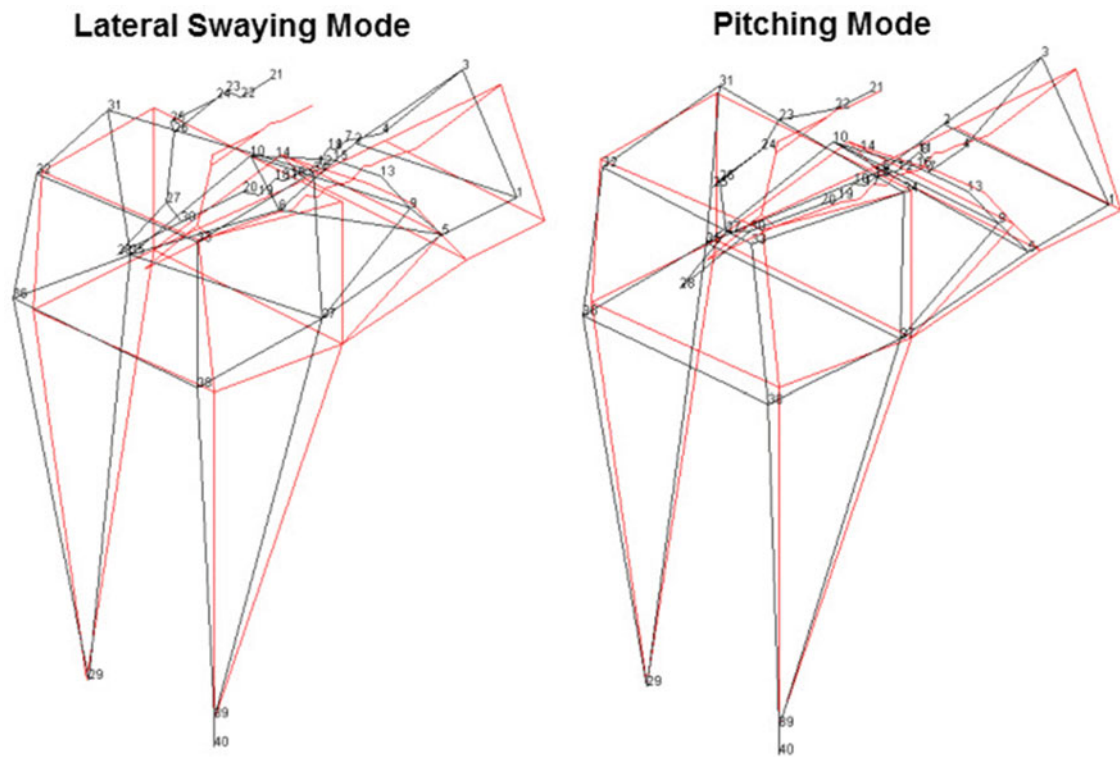


Fig. 11.5 Mode shapes from baseline modal test

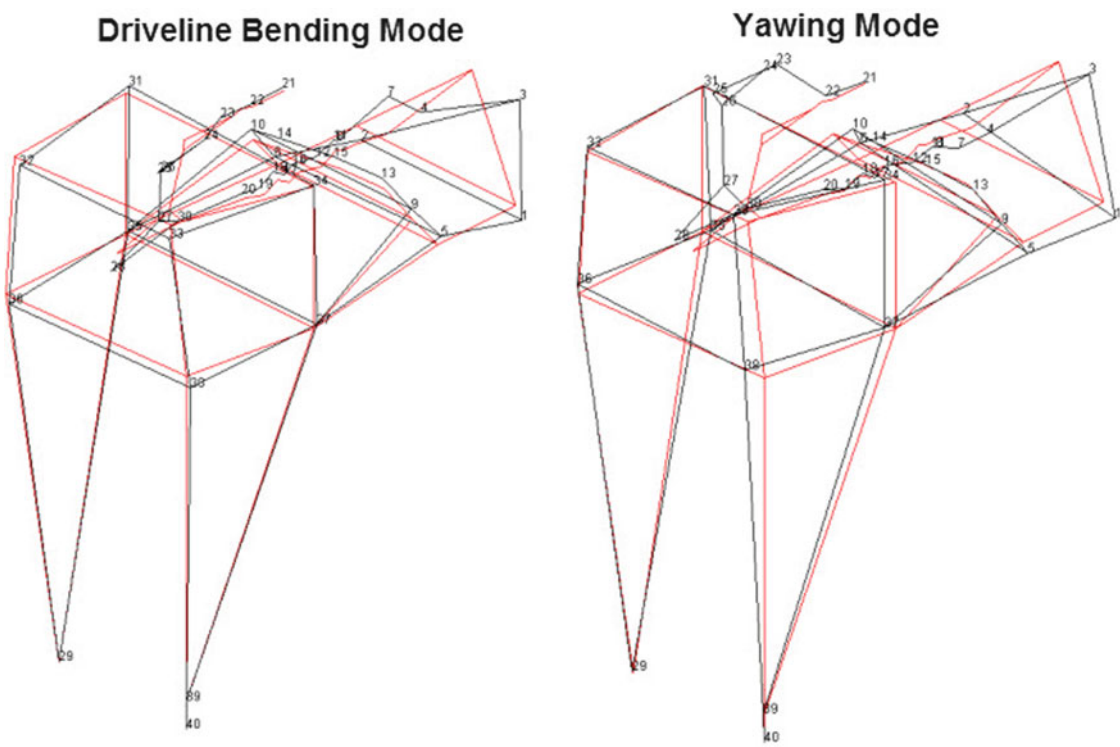


Fig. 11.6 Mode shapes from baseline modal test

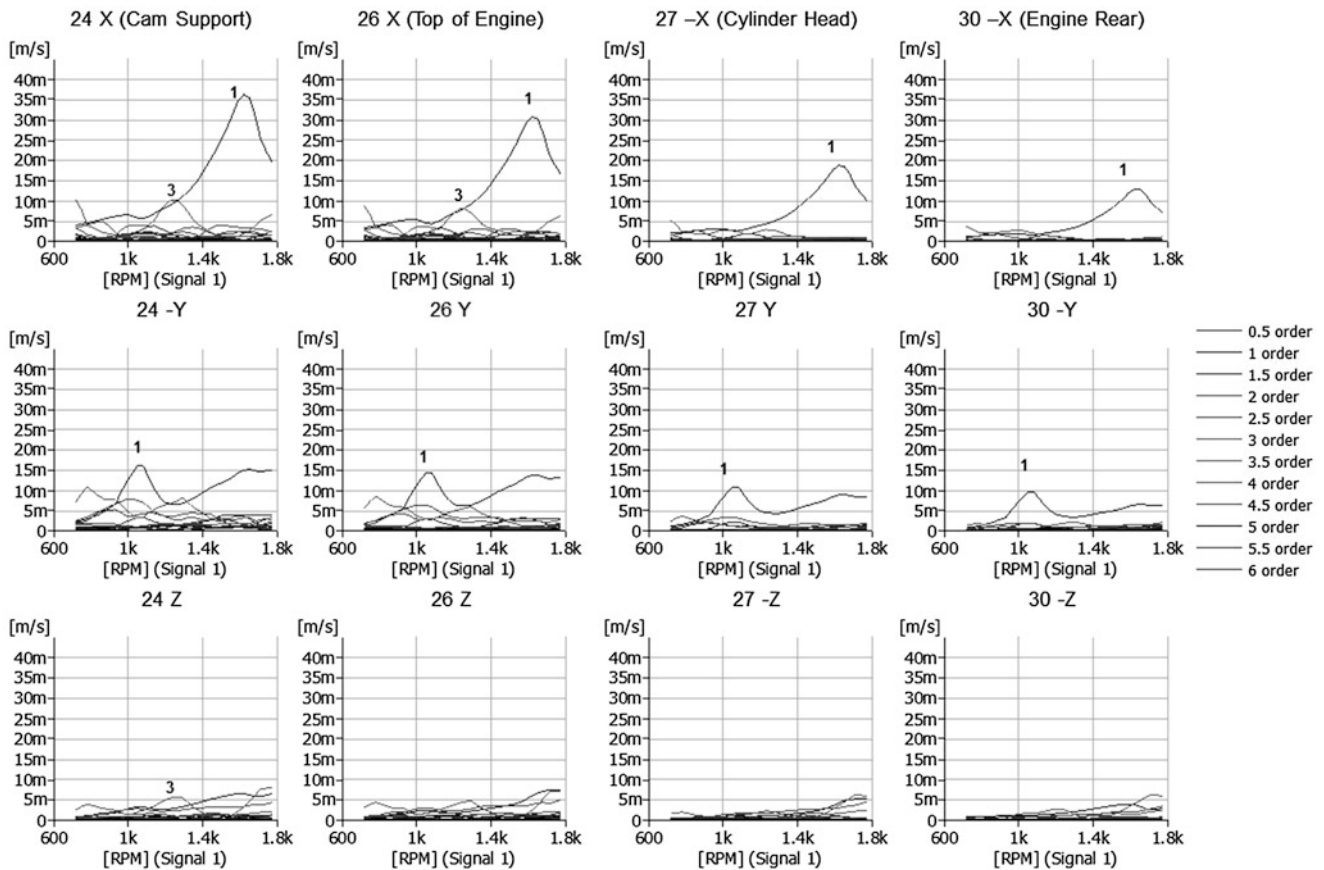


Fig. 11.7 Order extracted data from baseline operational testing—engine points

techniques. Figure 11.7 shows order extracted data from several points on the engine and its components from a 600 to 1,800 rpm speed sweep. FFT data was processed up to the tenth order and order extraction was done from half order up to the sixth order, in steps of half orders.

From the predominant first order peaks on the engine, it can be seen that the movement of the engine is primarily in the axial and lateral directions. Operating deflection shape (ODS) of the peak around 1,600 rpm reveals a yawing motion of the engine and a first order bending of the driveline. This indicates a strong influence of both the 29 and the 33.7 Hz modes during engine operation. ODS of the peak around 1,050 rpm indicates a lateral swaying motion, implying that it is exciting the 19 Hz mode obtained from the impact hammer test.

Operating data from points on the test frame and the electric motor are shown in Fig. 11.8. These graphs indicate similar peaks as the graphs from the engine. In addition to this, the electric motor also has a few third order peaks in the operating range. Due to the limited measurement points on the motor, this data is not correlated to impact test results. Being higher order vibrations with lower velocities, these peaks are not expected to cause high levels of displacement.

11.4.2 Recommendations

Based on the modal and operational results, the following recommendations were provided to mitigate the first order vibrations in the test system:

- Vibration isolators can be installed at the base of the test stand where it interfaces with the floor. The current setup consists of rigid mounts that do not offer any isolation. Properly sized isolators will reduce the vibrations transmitted to the floor.
- Resonances of the system are excited during engine operation. Some of these resonances are close to the steady state operating speeds of the engine. A finite element analysis of the entire test stand assembly can be used to make modifications to the frame and driveline such that the resonances are shifted away from these frequencies.

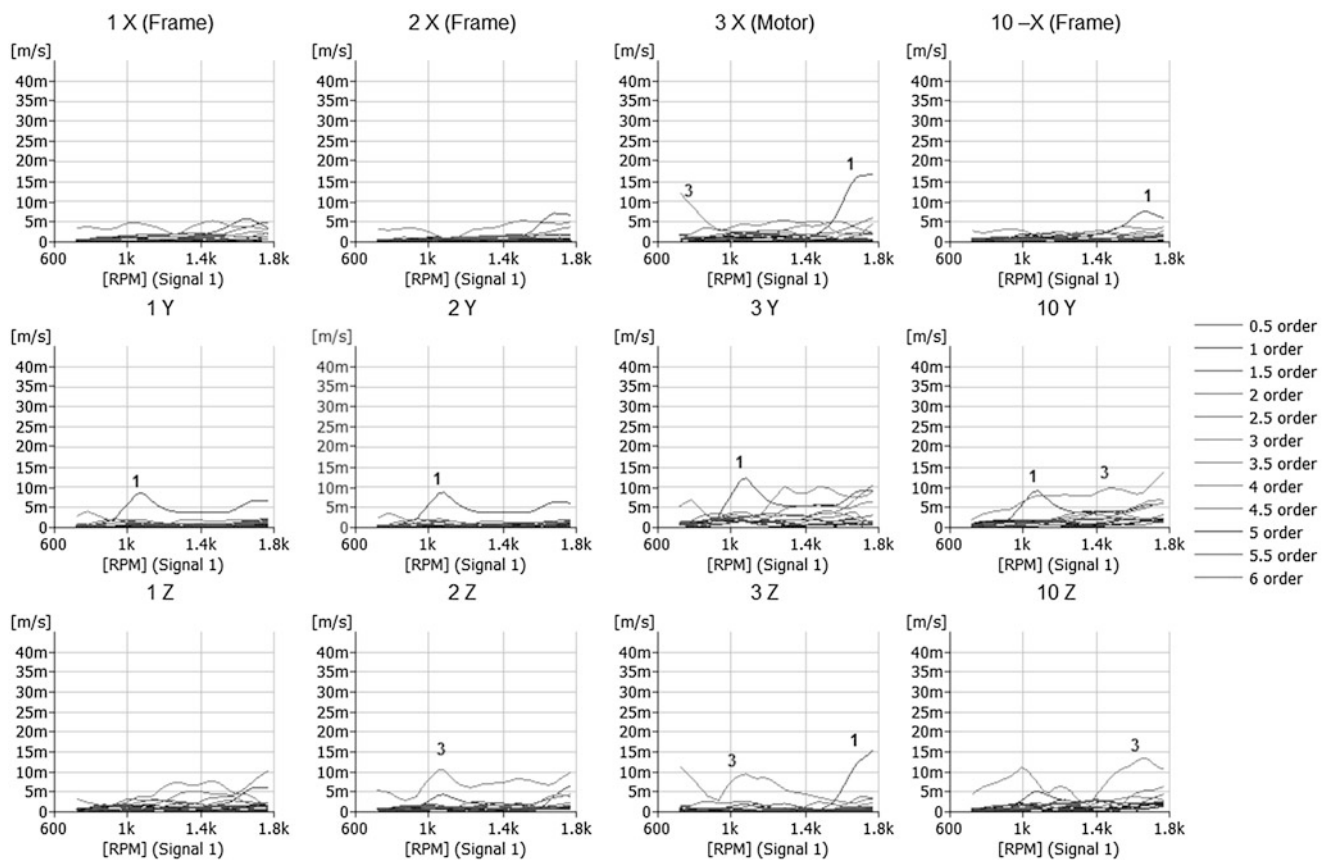


Fig. 11.8 Order extracted data from baseline operational testing—frame and motor

- The Lovejoy coupling used in the driveline has high relative displacement in the computed mode shapes. A new coupling with lower backlash would increase the stiffness of the joint and reduce vibration amplitude of the driveshaft.

The first recommendation was implemented on the test stand. Based on the modal test results, a low frequency Neoprene isolator with steel springs was chosen and installed. After installation, the modal impact and operational tests were repeated for validation purposes.

11.4.3 Validation Test Results

Figure 11.9 shows CMIF plot from the validation test performed after installing the vibration isolators. Rigid body modes and first driveline bending mode were chosen from the CMIF plot for comparison purposes.

Mode shapes and modal frequencies from the CMIF plot indicate that the rigid body modes have shifted lower in frequency when compared to the baseline results. This shift in modal frequencies is beneficial for this particular test cell as the engine is not capable of being motored below 500 rpm. The modal parameters from the validation test are listed in Table 11.2.

An Auto-MAC plot of the extracted modal vectors is shown in Fig. 11.10. It can be observed that a few modes have a high MAC value between them. Upon inspection of the mode shapes, they are found to be unique. The high MAC values could be attributed to the fact that some of the frame components might not have had enough measurement locations to define them completely.

Figures 11.11, 11.12 and 11.13 show the animated mode shapes extracted from the validation test. A few additional response locations were added near the base of the test stand to capture the effect of the vibration isolators.

Operating data was taken at the same points on the test stand assembly as earlier and processed to get order extracted plots. Figure 11.14 shows the extracted orders from points on the engine. Compared to the baseline tests, the first order vibration levels are observed to be lower. The peaks are shifted as expected, considering the fact that the rigid body modes have shifted to lower frequencies.

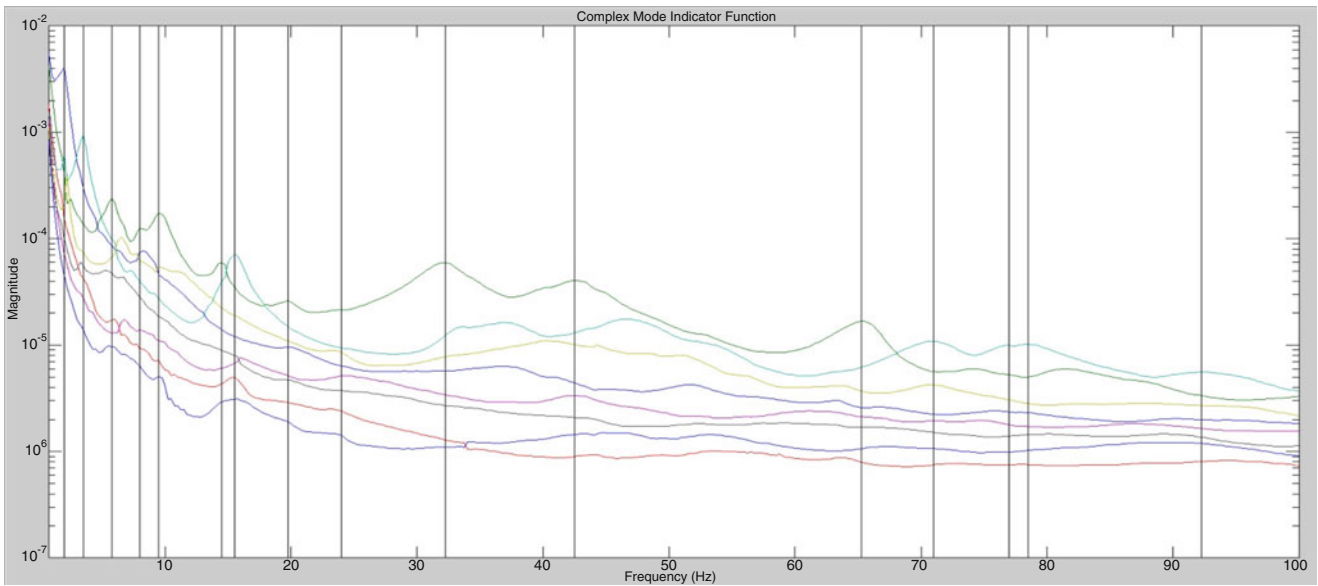


Fig. 11.9 CMIF plot from validation modal test

Table 11.2 Modal parameters from validation modal test

Mode no.	Frequency (Hz)	rpm	Mode shape
1	1.5	90	Lateral swaying mode
2	3.4	204	Axial mode
3	5.9	354	Yawing mode
4	6.9	414	Rolling mode
5	9.6	576	Vertical bouncing mode
6	13.9	834	Pitching mode
7	15.4	924	Second rolling mode
8	18.7	1,122	Frame bending mode
9	32.3	1,938	Driveline bending mode (cam shaft and motor out of phase)
10	41.9	2,514	Driveline bending mode (cam shaft and motor in phase)

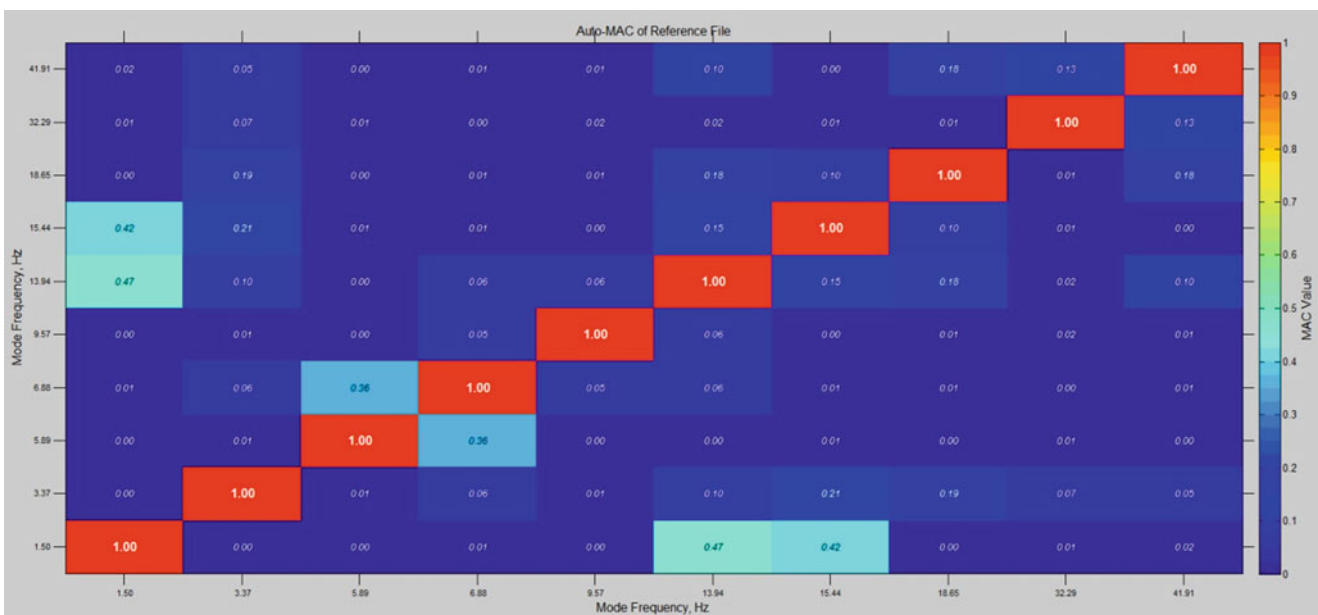


Fig. 11.10 Auto-MAC plot from validation testing

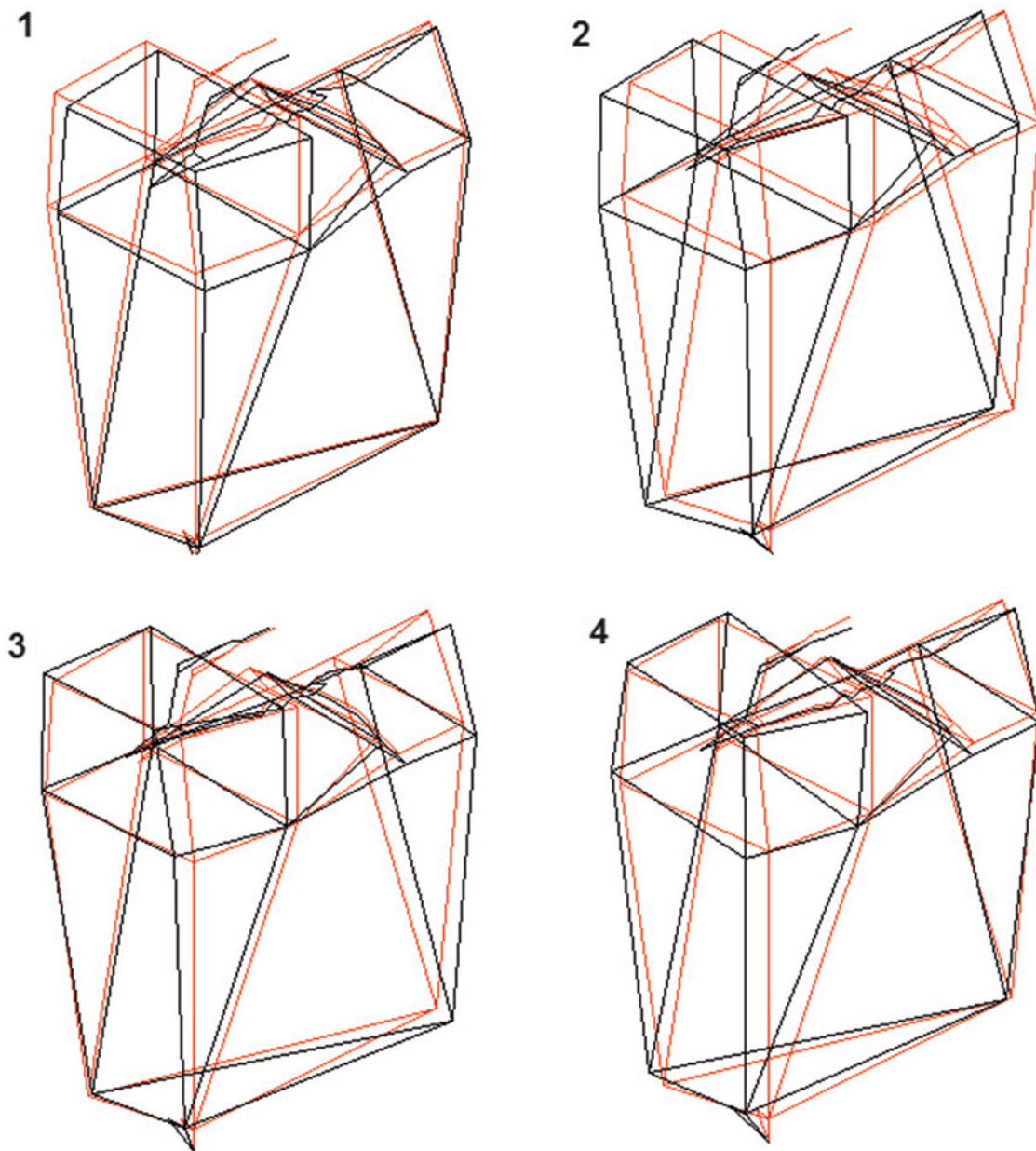


Fig. 11.11 Rigid body mode shapes from validation modal test

Figure 11.15 shows the order extracted data from the points on the frame. The vibration levels are again observed to be lower compared to the baseline levels. The third order peaks are still prominent in some of the components, although their magnitudes are comparable to the baseline test.

11.5 Summary and Scope for Future Work

Structural dynamic behavior of an optical engine test cell was studied as a whole using conventional EMA techniques. A baseline set of measurements were taken to identify the source of excessive vibrations in the test stand assembly. Based on the results of the baseline modal and operating tests, structural modifications were recommended to mitigate the vibration levels. Vibration isolators were installed as a corrective action and the tests were repeated to validate the effectiveness of

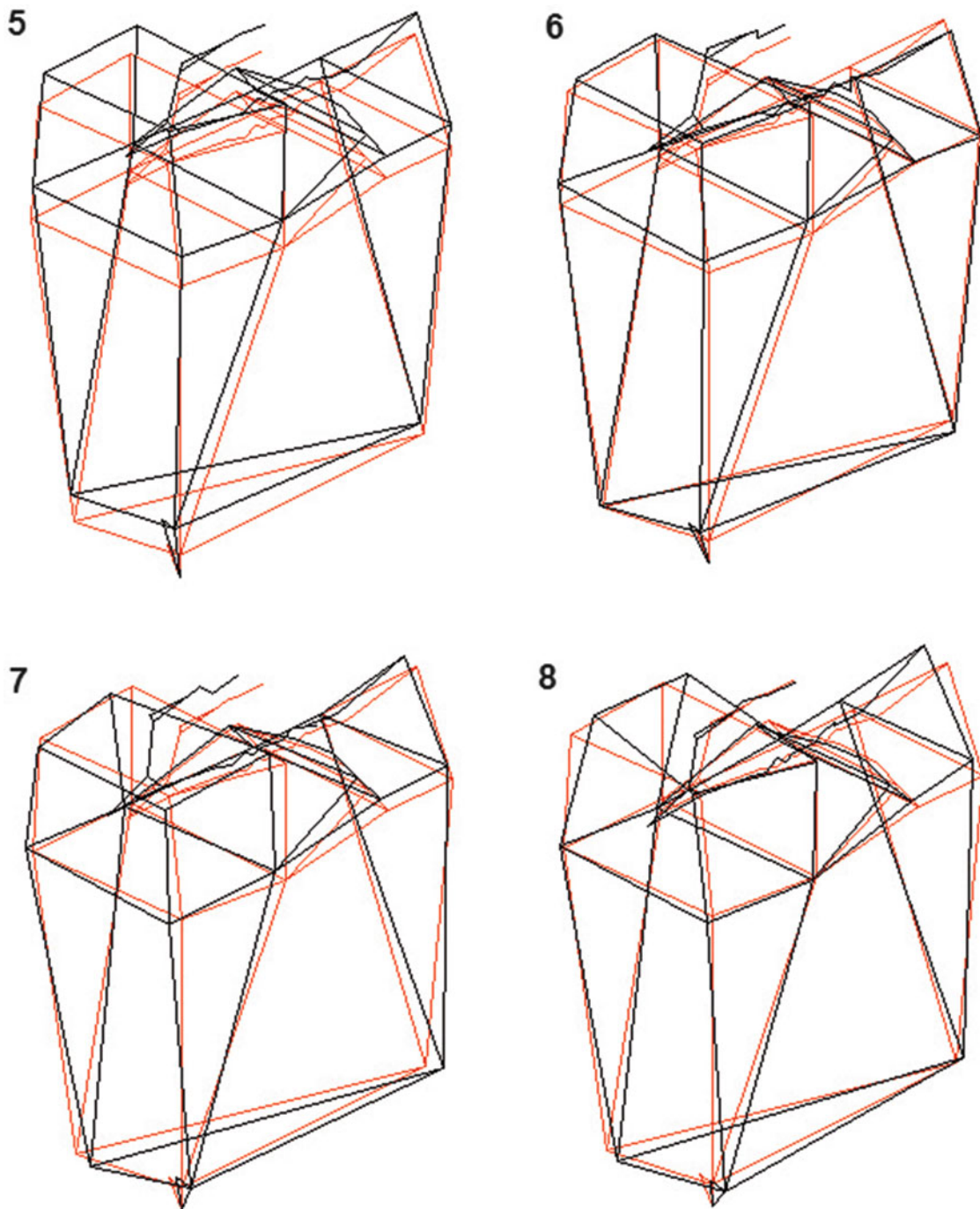


Fig. 11.12 Rigid body mode shapes from validation modal test

the isolators. Validation tests indicated that the installation of the isolators caused the rigid body modes to shift lower in frequency and out of the normal operating range of the engine. Vibration magnitude levels were also observed to be lower than earlier.

These tests and diagnosis indicate the benefits of studying an engine test cell as a whole in order to understand the effect of all the components interacting with each other. Vibration analysis of the complete test cell as a single system will lead to effective design that will reduce failures due to damaging levels of vibrations. This eventually means lower cost for replacing components and lesser downtime in the test cell.

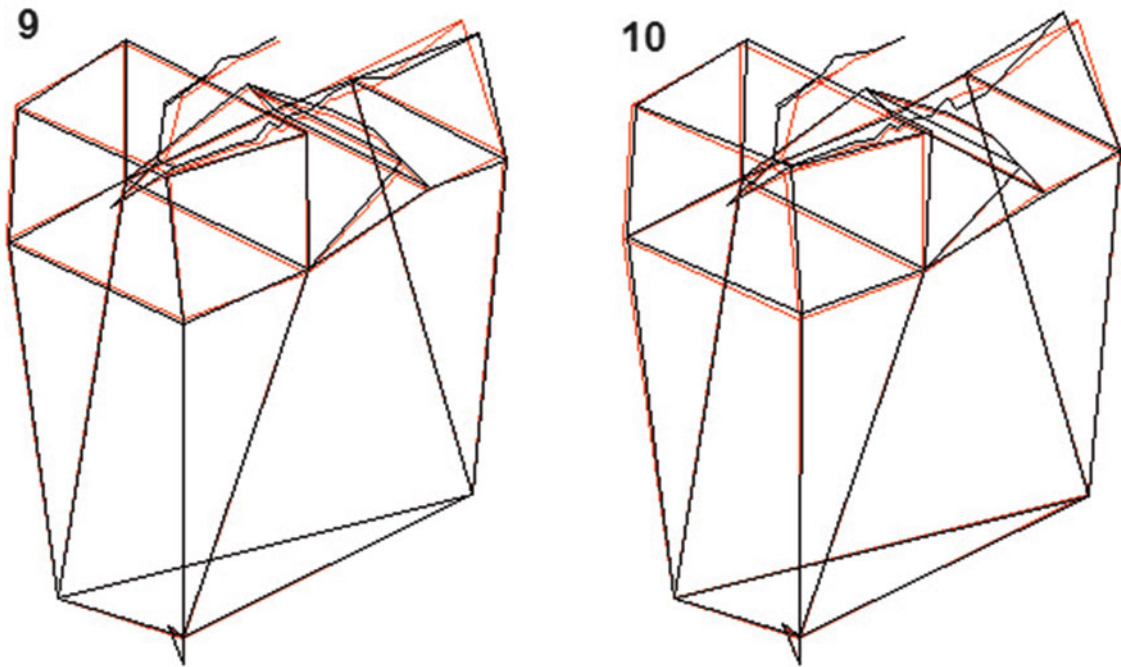


Fig. 11.13 Driveline modes from validation modal test

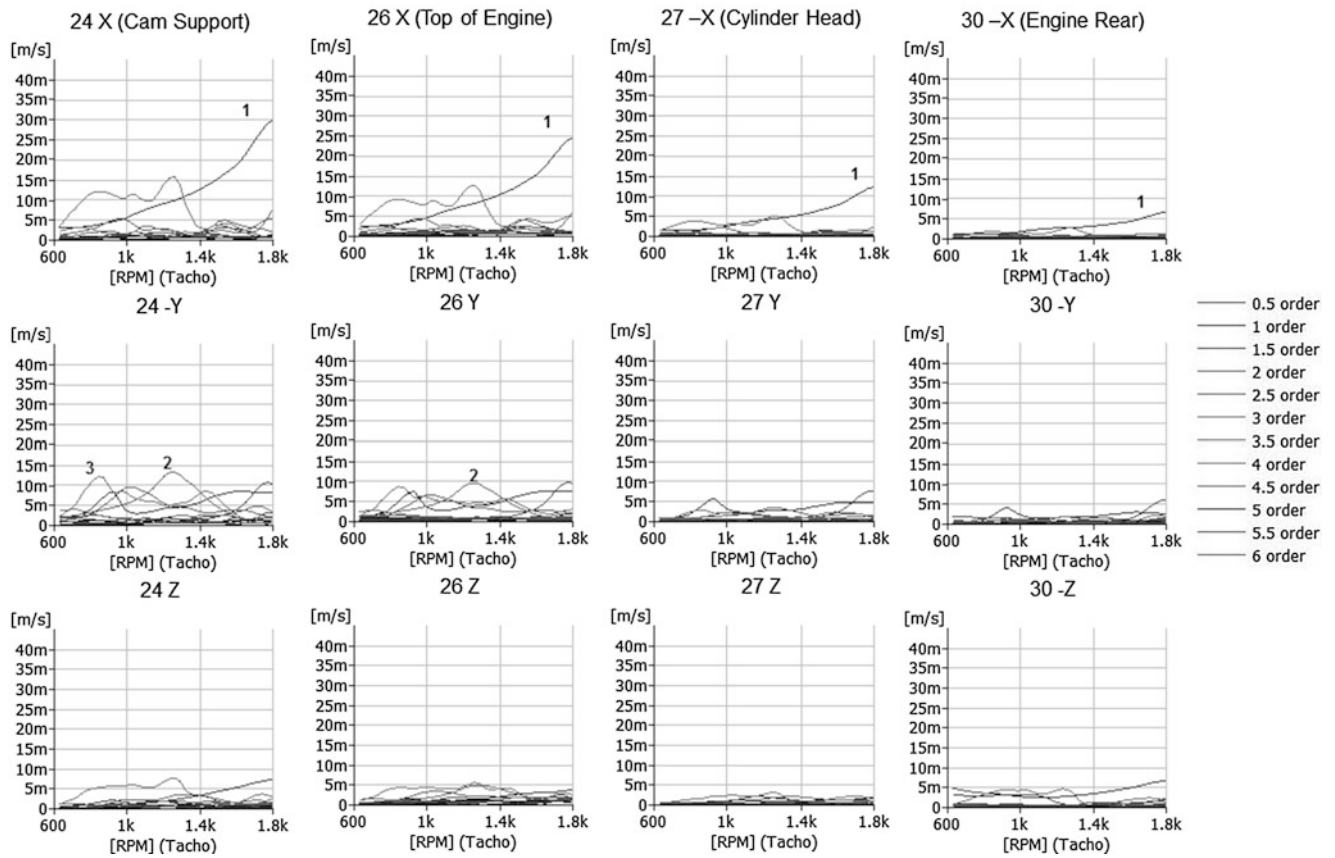


Fig. 11.14 Order extracted data from validation operational testing—engine points

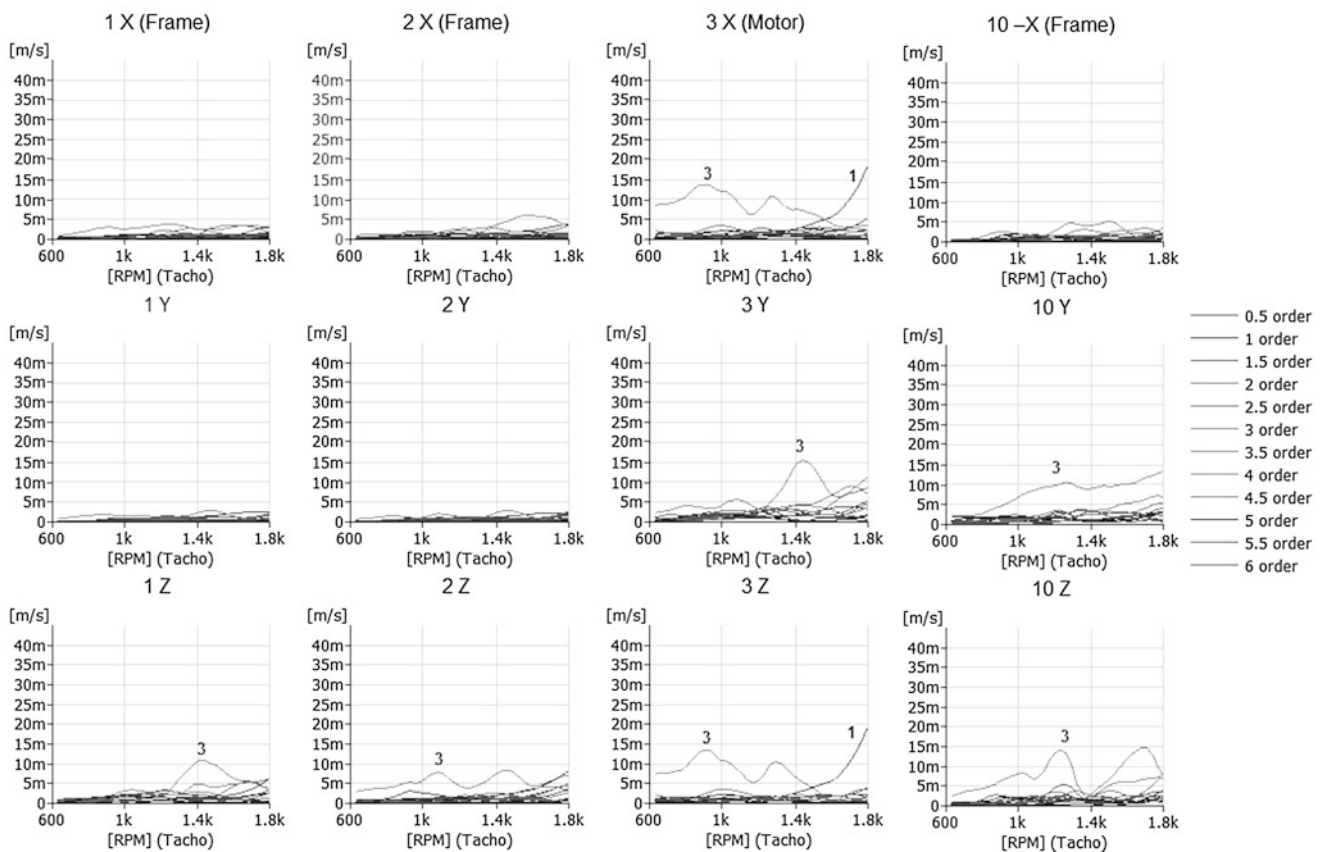


Fig. 11.15 Order extracted data from validation operational testing—frame points

Although the vibration isolators installed in the optical engine test cell are observed to be effective, there is scope for further reducing the overall vibration levels by implementing the recommendations discussed in Sect. 11.4.2

The test methodology used in this cell has been implemented in another test cell in the same facility that consists of a single cylinder diesel engine hooked to an A.C. Dynamometer. The engine is interfaced to the dynamometer through a driveline consisting of a shaft, dynamometer flywheel and adapter plates at both ends. This system is rated to operate from 600 to 2,100 rpm.

The test stand assembly is represented in the form of a wireframe diagram as shown in Fig. 11.16.

Diagnostic baseline testing was carried out to identify the source of excessive vibrations. Based on analysis of the data, suitable corrective actions were recommended and implemented. This test cell is awaiting validation testing to further verify the effectiveness of this approach to engine test cell design.

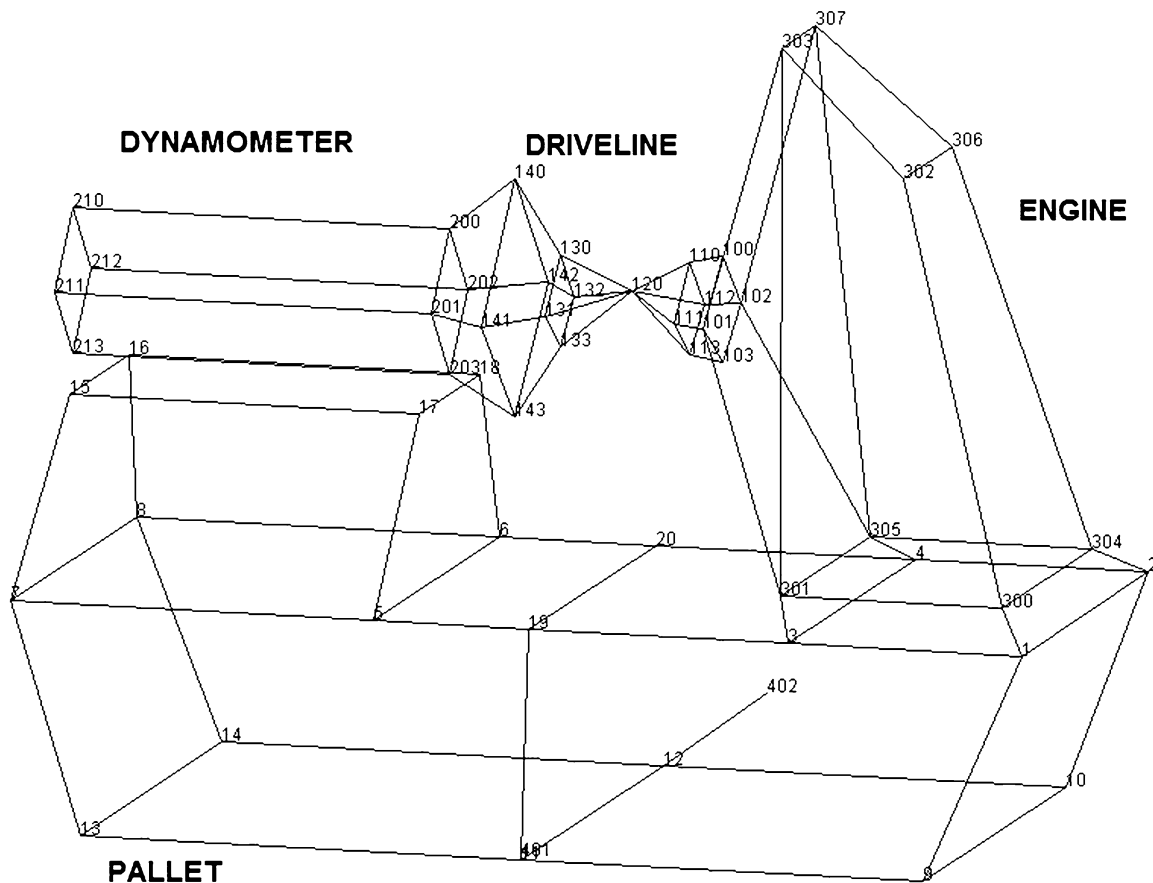


Fig. 11.16 Wireframe model of diesel engine test stand assembly

References

1. Armstrong RA (1996) Fault assessment of a diesel engine using vibration measurements and advanced signal processing. Master's Thesis, Naval Postgraduate School, Monterey
2. Gul KA, Bilal N, Adams DE (2009) Modeling and torsional vibration analysis of an engine cold-test cell for production fault diagnostics. In: ASME 22nd biennial conference on mechanical vibration & noise, San Diego
3. Bendat J, Piersol A (1986) Random data: analysis and measurement procedures, 2nd edn. Wiley, New York
4. Allemang RJ (1999) Vibrations: experimental modal analysis. UC-SDRL-CN-20-263-663/664. Structural Dynamics Research Laboratory, University of Cincinnati, Cincinnati
5. Allemang RJ, Phillips AW (2004) The unified matrix polynomial approach to understanding modal parameter estimation: an update. In: Proceedings of the ISMA international conference on noise and vibration engineering, Katholieke Universiteit Leuven
6. Bently DE, Hatch CT (2003) Fundamentals of rotating machinery diagnostics, 1st edn. ASME
7. Shwarz BJ, Richardson MH (1999) Introduction to operating deflection shapes. CSI Reliability Week, Orlando
8. Allemang RJ, Brown DL (2006) A complete review of the complex mode indicator function (CMIF) with applications. In: Proceedings of ISMA international conference on noise and vibration engineering, Katholieke Universiteit Leuven
9. Richardson M, Formenti D (1982) Parameter estimation from frequency response measurements using rational fraction polynomials. In: Proceedings of the 1st IMAC, Orlando

Chapter 12

Dynamic Modeling and Vibration Analysis of Oilwell Drillstring During Backreaming Operation

Cristiano Eduardo Agostini and Rodrigo Nicoletti

Abstract Oilwell drillstring vibrations have been thoroughly studied due to their high damaging effects in the drillstring elements. The high costs involved in the oilwell drillstring operations have led scientists and companies to seek optimized parameters in the wellbore project or during the real time operation. This work presents a non-linear mathematical model for representing drillstring vibrations during backreaming operations, i.e. during the operation of pulling out the drillstring with fluid pumping and string rotation simultaneously. The proposed model focuses on the effects of lateral vibrations on the lower portion of the drill string, commonly known as Bottom Hole Assembly (BHA). The modeling approach is based on analytical, nonlinear and lumped parameters, which considers the effects of drilling fluid damping, stabilizer and drill collar contact with the borehole wall. The results of numerical simulations show the occurrence of abnormal lateral vibrations during the drill string withdrawal (backreaming), which can cause several problems during wellbore construction, e.g. BHA electronic equipment failure, falling rocks into the well, drillstring blockage.

Keywords Rotor dynamics • Drillstring modeling • Backreaming operation • Vibration

12.1 Introduction

During the borehole drilling of oilwells, when the final depth is reached, there comes the task of pulling out the drillstring. There are two possible ways of pulling out the drillstring: dry operation (no rotation and no pumping of fluid) and backreaming operation (rotation and pumping of fluid). The dry operation represents a faster operation, but the friction between the drillstring and the borehole becomes so high that it usually jeopardizes the pulling-out operation. The backreaming operation is more commonly adopted, but their optimum conditions are still controversial in literature. In some applications, the backreaming operation represents a much better friction condition for pulling out the drillstring but, in other applications, the severe lateral vibration of the drillstring can cause serious damage to the Bottom Hole Assembly (BHA), and even borehole collapse with drillstring imprisonment [1].

The challenge of modeling the drillstring during backreaming operation is the correct representation of the coupling between the torsional and lateral movements of the drillstring and its longitudinal movement in contact with the borehole. The friction between the drillstring and the borehole during longitudinal movement, together with occasional impacts due to lateral vibration, lead the system to a strong nonlinear behavior.

In literature, one can find few studies on the subject, mainly focused on axial vibration. In [2, 3], axial vibration of the drillstring is studied to improve the dynamic behavior of the system during stick-slip phenomenon and to optimize the design of the stabilizers. Friction between the drillstring and the borehole is studied in [4], based on a low order mathematical model and experimental correlation to results shown in [5]. The results show that friction plays an important role in the dynamics of the system and in the impact level of the drillstring against the borehole walls. The control of the rotating speed of the drillstring has also been investigated to minimize lateral vibrations. In [6], the adopted mathematical model took

C.E. Agostini • R. Nicoletti (✉)

Department of Mechanical Engineering, University of São Paulo, School of Engineering of São Carlos, Trabalhador São Carlense 400, 13566-590 São Carlos, Brazil
e-mail: cr.agostini@gmail.com; rnicolet@sc.usp.br

into account the longitudinal movement of the drillstring and results showed that vibration is self-excited. Hence, in some cases, vibration was reduced by increasing the rotating speed of the drillstring. However, in other cases, the lateral vibration observed was severe.

Despite the advances in the study of lateral vibrations of drillstrings, there are no related studies on the backreaming operation, considering drillstring rotation and fluid pumping. In this work, one develops a mathematical model for the drillstring during backreaming. The modeling approach is based on analytical, nonlinear and lumped parameters, which considers the effects of drilling fluid damping, stabilizer and drill collar contact with the borehole wall. The results of numerical simulations show the occurrence of abnormal lateral vibrations during the drillstring withdrawal, but this effect decreases with higher friction coefficients, and for rotating speeds near the natural frequency of the system.

12.2 Mathematical Model

The following mathematical model was based on the two degree-of-freedom model presented by Jansen [7, 8], which takes into account the pumping fluid, contact of the stabilizers with the borehole walls, contact of the drillstring with the borehole walls, and excitation due to unbalance. The model is then complemented with additional degrees-of-freedom of torsion and longitudinal movement. The basic hypotheses of the model are:

- **Pumping Fluid:** drag in the annular gap between the drillstring and the borehole is proportional to the square of the rotating speed. There fluid also adds inertia to the system, as showed in [9];
- **Stabilizers:** the hydrodynamic effects in the gap between the stabilizers and the borehole walls are neglected;
- **Borehole:** the cross section of the borehole is circular, and contact between the drillstring and the borehole obey the Coulomb law;
- **Drillstring Vibration:** the adopted rotating speeds are close to the first natural frequency of the drillstring associated to the first bending mode. Hence, lateral vibration of the drillstring will be limited to that of the bending mode of a simply supported beam, which means that both stabilizers will be in contact at the same time;
- **Longitudinal Movement:** Coulomb friction is considered in the longitudinal direction of movement. The weight of the drillstring, and its effects, will not be considered in the model.

The mathematical model is composed of a cylindrical beam simply supported, represented by lumped parameters. The beam represents the BHA and the supports are the stabilizers (Fig. 12.1). Vibration is analyzed in the mid section of the beam (section A-A of Figs. 12.1 and 12.2). The model has two degrees-of-freedom to represent the lateral movements of the

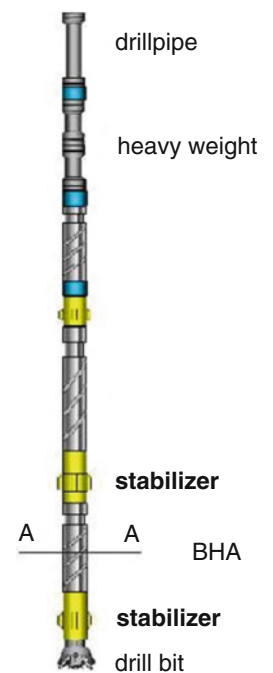
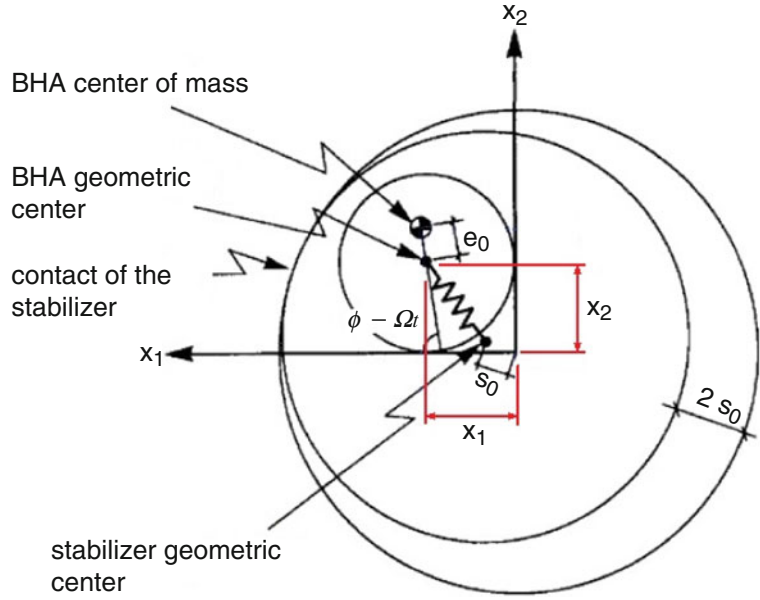


Fig. 12.1 Extremity of the drillstring and main components

Fig. 12.2 Section A-A with bending of the BHA and contact of the stabilizers with the borehole wall [8]



BHA in directions x_1 and x_2 , one degree-of-freedom to represent the torsion of the drillstring, and one degree-of-freedom to represent the longitudinal motion in x_3 direction. The origin of the coordinate system lies in the center of the borehole. The unbalance of the BHA is represented by an eccentricity, given by the difference between the center of mass of the BHA and its geometric center (Fig. 12.2).

The inertia forces due to acceleration of the BHA and of the fluid can be described by:

$$\begin{aligned} F_{m,x_1} &= -(m + m_f) \ddot{x}_1 + m \Omega^2 e_0 \cos(\phi - \Omega t) \\ F_{m,x_2} &= -(m + m_f) \ddot{x}_2 + m \Omega^2 e_0 \sin(\phi - \Omega t) \end{aligned} \quad (12.1)$$

where m is the equivalent mass of the BHA, m_f is the equivalent mass of the fluid in the gap between the BHA and the borehole, x_1 and x_2 are the coordinates of the geometric center of the BHA, Ω is the rotating speed of the drillstring, t is time, e_0 is the eccentricity of the center of mass, and ϕ is the angular position of the BHA.

The resultant damping force of the fluid is given by [8]:

$$\begin{aligned} F_{d,x_1} &= -c_f v^2 \frac{\dot{x}_1}{\sqrt{\dot{x}_1^2 + \dot{x}_2^2}} = -c_f \dot{x}_1 \sqrt{\dot{x}_1^2 + \dot{x}_2^2} \\ F_{d,x_2} &= -c_f v^2 \frac{\dot{x}_2}{\sqrt{\dot{x}_1^2 + \dot{x}_2^2}} = -c_f \dot{x}_2 \sqrt{\dot{x}_1^2 + \dot{x}_2^2} \end{aligned} \quad (12.2)$$

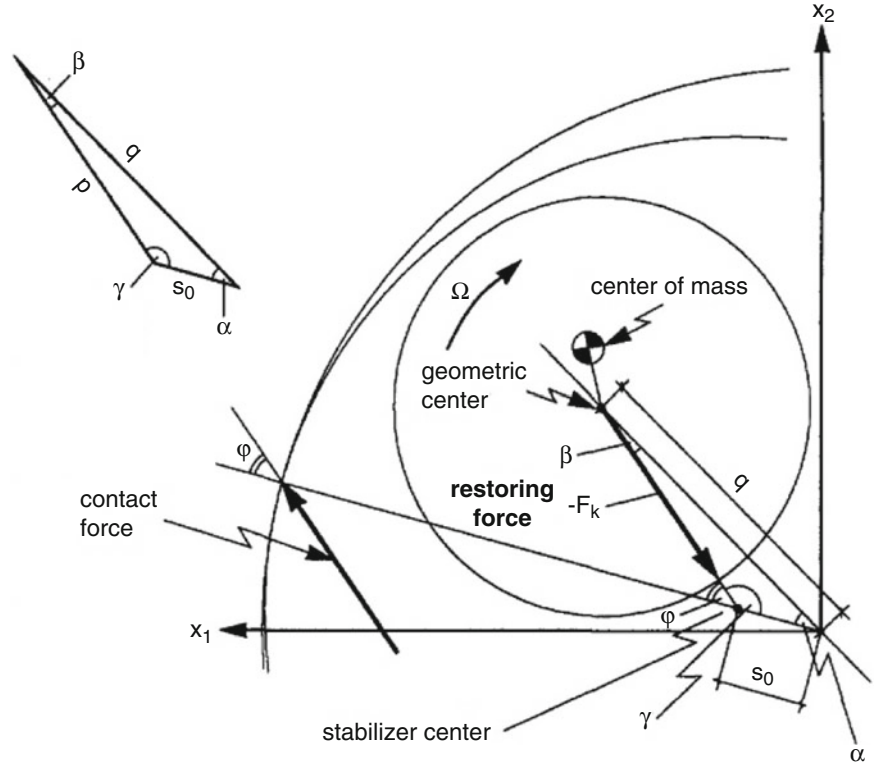
where c_f is the equivalent damping coefficient of the fluid, and $v = \sqrt{\dot{x}_1^2 + \dot{x}_2^2}$ is the amplitude of the lateral velocity of the BHA.

When the stabilizer hits the borehole wall ($q > S_0$ —Fig. 12.3), the restoring force can be decomposed into radial and tangential components, as follows:

$$\begin{aligned} F_{k,rad} &= -k p \cos \beta \\ F_{k,tan} &= -k p \sin \beta \end{aligned} \quad (12.3)$$

where q is the radial deflection of the BHA geometric center, $S_0 = \frac{1}{2}(D_h - D_s)$ is the gap between the stabilizer and the borehole (D_h is the borehole diameter, D_s is the stabilizer diameter), and $p = q \cos \beta + S_0 \cos \gamma = q \cos \beta - S_0 \cos \phi$ is the distance between the geometric center of the BHA and the geometric center of the stabilizer. It is important to note that, if $q < S_0$, there will be no restoring force in the system (no contact between the stabilizer and the borehole wall—Fig. 12.3).

Fig. 12.3 Contact force between the stabilizer and the borehole wall, and restoring force on the BHA [8]



The equations of the restoring force during contact can be simplified by the a first order Taylor series of the angular terms of the equations, as follows:

$$\begin{aligned} F_{k,rad} &= -k (q - S_0) \\ F_{k,tan} &= -k \varphi \left(S_0 - \frac{S_0^2}{q} \right) \end{aligned} \quad (12.4)$$

This is justified by the low friction values observed in practice during operation. Transforming to the Cartesian system of coordinates:

$$\begin{aligned} F_{k,1} &= -F_{k,rad} \frac{x_1}{q} + F_{k,tan} \frac{x_2}{q} \\ F_{k,2} &= -F_{k,rad} \frac{x_2}{q} - F_{k,tan} \frac{x_1}{q} \end{aligned} \quad (12.5)$$

where $q = \sqrt{x_1^2 + x_2^2}$.

The restoring force due to the contact of the BHA with the borehole wall is given by spring-damper model:

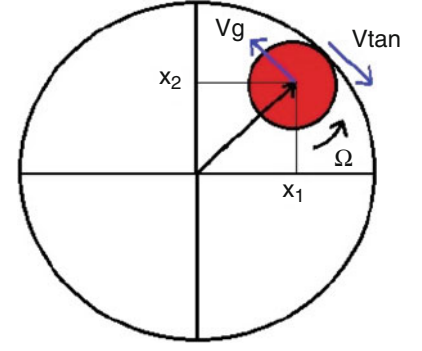
$$\begin{aligned} F_{w,rad} &= -k_w (q - c_0) - c_w \dot{q} \\ F_{w,tan} &= -S \mu_c F_{w,rad} \end{aligned} \quad (12.6)$$

where μ_c is the friction coefficient between the BHA and the borehole wall, k_w and c_w are the equivalent stiffness and damping coefficient of the borehole wall, respectively, and $S = \text{sign}(v_g - v_{tan})$ (Fig. 12.4). The BHA velocity and the tangential velocity in the contact point are given by:

$$v_g = \sqrt{\dot{x}_1^2 + \dot{x}_2^2} \quad (12.7)$$

$$v_{tan} = \frac{D_c}{2} \Omega \quad (12.8)$$

Fig. 12.4 Representation of the relative velocities in the BHA and in the borehole wall



During the longitudinal movement of the drillstring, the contact force against the borehole wall is given by [10]:

$$F_{c,axial} = \text{sign}(\dot{x}_3)(F_{k,rad} \mu_s + F_{w,rad} \mu_c) \tan \psi \quad (12.9)$$

where $\tan \psi = \dot{x}_3 / \Omega R_c$. Such contact force is only considered in the model when there is contact between the BHA and the borehole wall, or between the stabilizer and the borehole wall.

By adopting the following adimensional parameters:

$$\beta = \frac{m + m_f}{m} \quad \xi = \frac{c_f c_o}{m} \quad \zeta = \frac{S_o}{c_o} \quad \eta = \frac{\Omega}{\omega} \quad \rho = \frac{k_w}{k} \quad \tau = \omega t \quad \nu = \frac{c_w}{m \omega} \quad (12.10)$$

$$\omega = \sqrt{\frac{k}{m}} \quad c_o = \frac{1}{2}(D_h - D_c) \quad y_i = \frac{x_i}{c_o} \quad a = \sqrt{x_1^2 + x_2^2} \quad b = \sqrt{\dot{x}_1^2 + \dot{x}_2^2} \quad c = x_1^2 + x_2^2 \quad (12.11)$$

one can write the equations of motion of the drillstring for the backreaming operation, as follows:

$$\left\{ \begin{array}{l} \beta \ddot{y}_1 + \xi b \dot{y}_1 + \alpha F_{k,rad} y_1 - \alpha F_{k,tan} y_2 + \gamma F_{w,rad} y_1 - \gamma F_{w,tan} y_2 = \\ \epsilon \cos(\phi - \eta\tau) \frac{(\dot{\phi} - \Omega)^2}{\omega^2} - \frac{\epsilon}{\omega^2} \sin(\phi - \eta\tau) \ddot{\phi} = 0 \\ \beta \ddot{y}_2 + \xi b \dot{y}_2 + \alpha F_{k,rad} y_2 - \alpha F_{k,tan} y_1 + \gamma F_{w,rad} y_2 + \gamma F_{w,tan} y_1 = \\ - \epsilon \sin(\phi - \eta\tau) \frac{(\dot{\phi} - \Omega)^2}{\omega^2} - \frac{\epsilon}{\omega^2} \cos(\phi - \eta\tau) \ddot{\phi} = 0 \\ \ddot{\phi} + 2\xi_t \bar{w}_s \dot{\phi} + \bar{w}_s^2 \left(\phi - \eta\tau + \frac{T_o}{k_t} \right) + \bar{c}_h b \dot{y}_1 \sin(\phi - \eta\tau) - \bar{c}_h b \dot{y}_2 \cos(\phi - \eta\tau) = \\ \bar{F} (\alpha F_{k,tan} + \gamma F_{w,tan}) [\bar{R} - \epsilon \cos(\phi - \eta\tau)] - \bar{F} (\alpha F_{k,rad} + \gamma F_{w,rad}) \epsilon \sin(\phi - \eta\tau) \\ \frac{m_a}{KJ} \ddot{y}_3 + \frac{c_a}{KJ\omega} \dot{y}_3 + \frac{k_a}{KJ\omega^2} y_3 - F_{c,axial} = 0 \end{array} \right. \quad (12.12)$$

where:

$$F_{k,rad} = \left(1 - \frac{\zeta}{a} \right) \quad (12.13)$$

$$F_{k,tan} = \varphi \left(\frac{\zeta}{a} - \frac{\zeta^2}{c} \right) \quad (12.14)$$

$$F_{w,rad} = \rho (a - 1) + \nu b \quad (12.15)$$

$$F_{w,tan} = -S \mu_c F_{w,rad} \quad (12.16)$$

and:

$$\begin{cases} \alpha = 1 \text{ and } \gamma = 0, \text{ if } a > \zeta \text{ and } a \leq 1 & \text{(impact of stabilizer)} \\ \alpha = 1 \text{ and } \gamma = 1, \text{ if } a > 1 & \text{(impact of stabilizer and BHA)} \\ \alpha = 0 \text{ and } \gamma = 0, \text{ if } a \leq \zeta & \text{(no impact)} \end{cases} \quad (12.17)$$

12.3 Numerical Results

The equations of motion are integrated in time for different operating conditions of rotating speed of the drillstring, longitudinal velocity of the drillstring, and friction coefficient of the borehole wall. The adopted parameter values are those shown in Table 12.1. The eccentricity of 12.7 mm and the properties of the fluid are reference values that have been widely adopted in literature [6, 8, 11].

After integration of the equations of motion, one can calculate the adimensional impulse of the BHA against the borehole walls, as follows:

$$I_a = \int_0^\tau (F_{k,rad} + F_{w,rad}) dt \quad (12.18)$$

Figure 12.5 presents the obtained results for a friction coefficient of 0.1 and different longitudinal velocities and rotating speeds. In general, higher rotating speeds result in higher impulse of the BHA/stabilizers against the borehole wall. However, when the rotating speed is close to the natural frequency of the BHA (130 rpm), there is less impulse against the borehole walls and the results are very close to those obtained with a rotating speed of 90 rpm. In addition, in low longitudinal velocities (below 0.1 m/s), the impulse is even smaller, reaching values similar to those obtained with a rotating speed of 60 rpm. This is a result of the fact that, in these conditions, the BHA is oscillating chaotically in the borehole, barely touching the walls during the analyzed time (Fig. 12.6). In the other rotating speeds, there are no big variations in the impulse caused by a change in the longitudinal speed. However, for rotating speeds above the BHA natural frequency, the impulse increases significantly.

In the case of a friction coefficient of 0.2, the results in Fig. 12.7 show that the longitudinal velocity does not affect significantly the impulse against the borehole walls. However, there is a slight reduction of the impulse for longitudinal velocities above 0.10 m/s in the case of a rotating speed of 130 rpm (near the BHA natural frequency). In addition, there is a

Table 12.1 Geometric and operational data of the oilwell and drillstring

Drillstring	E	Modulus of elasticity	210.0	GPa
	G	Modulus of rigidity	80.0	GPa
	N	Axial drag	89.0	kN
	T	Initial torque	13.56	kN.m
	ρ_c	Material density	7850.0	kg/m ³
	D_c	BHA outer diameter	241.0	mm
	D_i	BHA inner diameter	76.2	mm
	d_c	Drill pipe outer diameter	127.0	mm
	d_i	Drill pipe inner diameter	95.0	mm
	D_s	Stabilizer diameter	382.0	mm
	l_2	BHA total length	230.0	m
	l_3	Drill pipe length	3.27	km
	e_o	BHA center of mass eccentricity	12.7	mm
	c_a	Axial damping coefficient	4.0	kN.s/m
	Borehole	D_h	Borehole diameter	422.0
σ		Gap ratio between the BHA and the borehole	1.33	
S_o		Gap between the stabilizer and the borehole	20.1	mm
c_o		Gap between the BHA and the borehole	90.5	mm
ρ		Relative stiffness ratio (borehole/BHA)	100	
κ		Elastic restitution coefficient of the wall	0.5	
Fluid		ρ_f	Fluid density	1500.0
	μ_f	Dynamic viscosity	0.2	N.s/m ²
	C_a	Drag coefficient in the fluid	1.7	
	C_d	Additional mass coefficient	1.0	

Fig. 12.5 Adimensional impulse as a function of the longitudinal velocity and rotating speed, for friction coefficient of 0.2

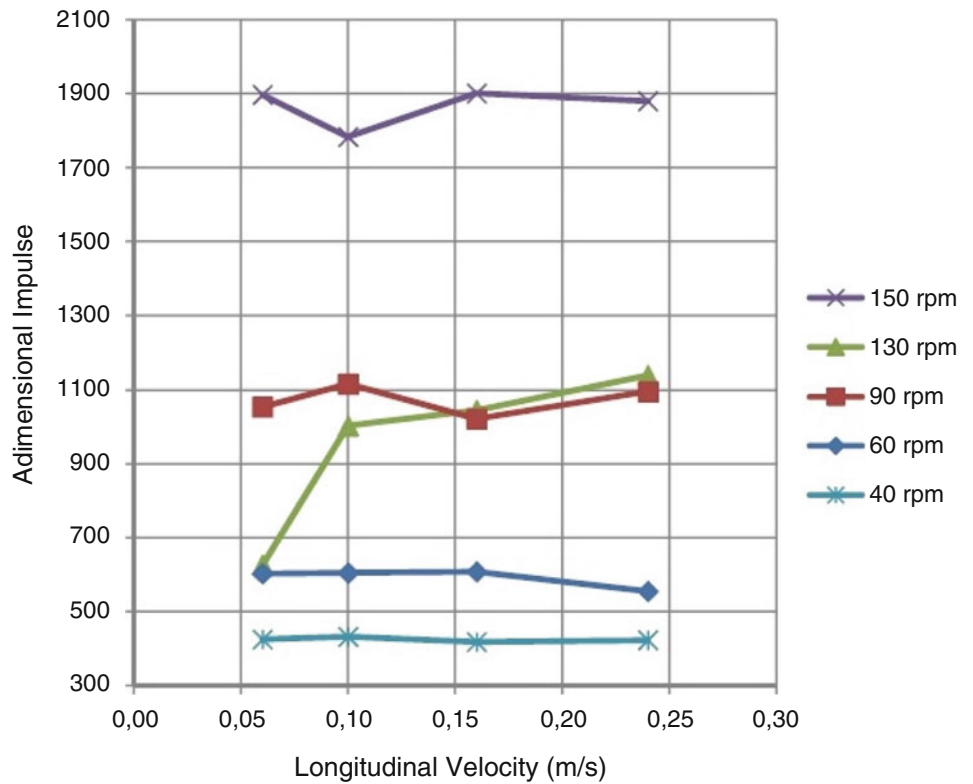
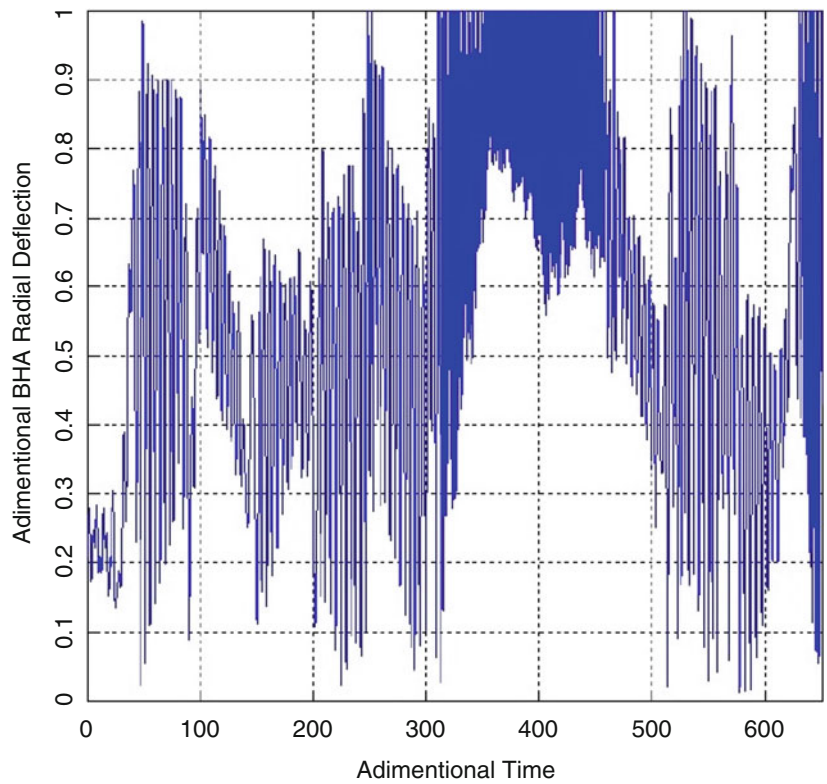


Fig. 12.6 BHA radial deflection at the rotating speed of 130 rpm, longitudinal velocity of 0.06 m/s, and friction coefficient of 0.1



significant rise of the impulse at the rotating speed of 150 rpm, when the longitudinal velocity is increased. In the case of a friction coefficient of 0.3, the results in Fig. 12.8 also show the significant rise of the impulse at the rotating speed of 150 rpm, when the longitudinal velocity is increased. But, at lower rotating speeds, there is no significant effect of the longitudinal velocity in the impulse against the borehole walls.

Fig. 12.7 Adimensional impulse as a function of the longitudinal velocity and rotating speed, for friction coefficient of 0.2

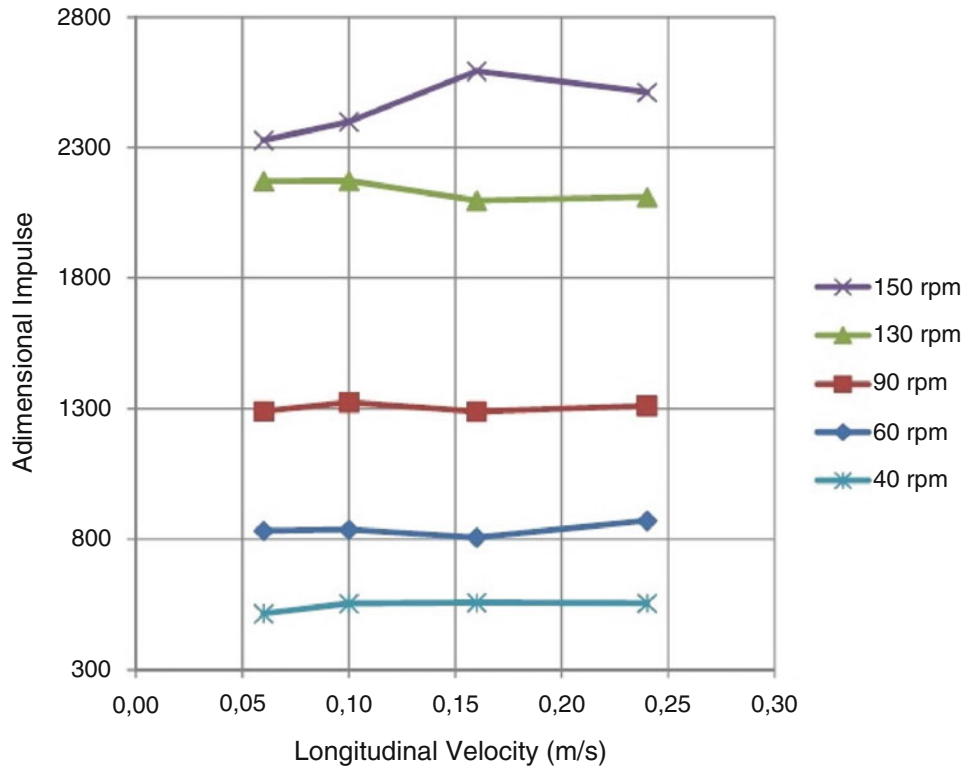
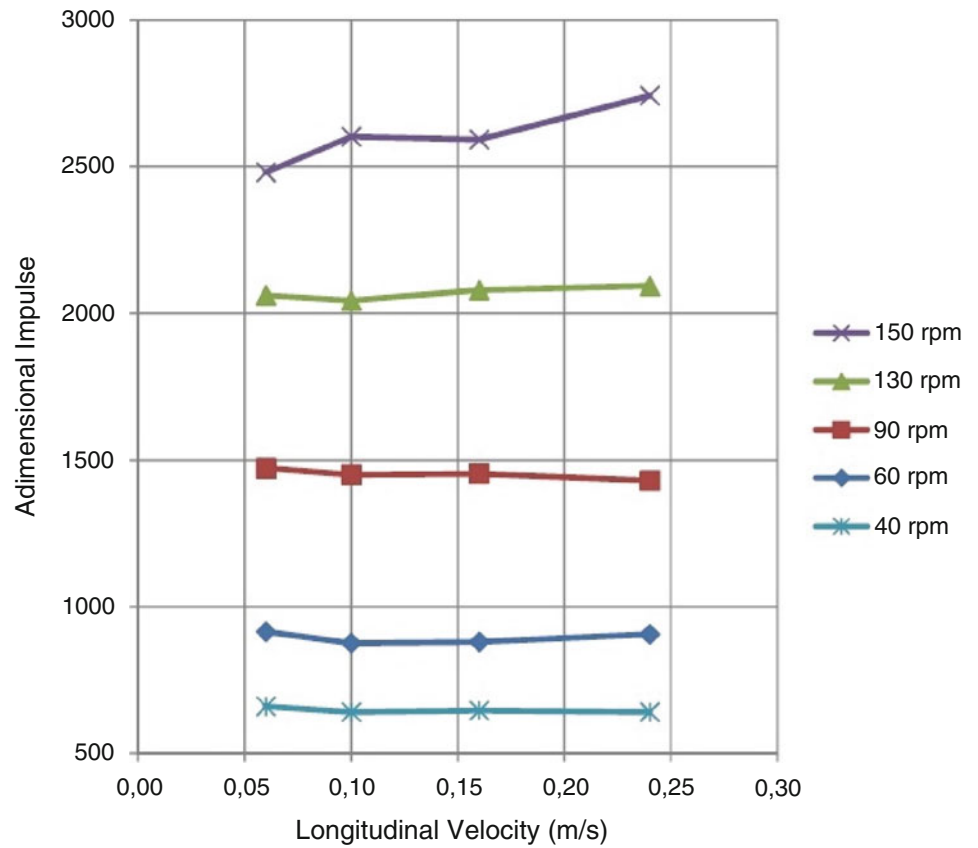


Fig. 12.8 Adimensional impulse as a function of the longitudinal velocity and rotating speed, for friction coefficient of 0.3



The results in Figs. 12.5, 12.7, 12.8 show that friction dominates the dynamic response of the BHA, and the longitudinal motion of the drillstring has some influence on the dynamics only at high rotating speeds (above the first bending natural frequency of the system). At low rotating speeds (40, 60, and 90 rpm), the axial motion of the drillstring does not affect the resultant impulse against the walls, being the friction against the walls the only mechanism responsible for impulse.

12.4 Conclusion

The Bottom Hole Assembly (BHA) of an oilwell drillstring has been modeled by lumped parameters, considering the effects of the pumping fluid, the impact of stabilizers and the BHA against the borehole walls, and the longitudinal movement of the drillstring and respective friction against the wall. Such conditions refer to a backreaming operation of the drillstring and numerical results show that:

- at low rotating speeds, the dynamics is dominated by friction against the walls, and no effect of the longitudinal motion is observed in the resultant impulse of the BHA/stabilizers against the walls;
- for a friction coefficient of 0.1, impulse is strongly reduced at the rotating speed close to the natural frequency of the BHA. This reduction is even bigger for low longitudinal velocities of the drillstring;
- at high rotating speeds (above the BHA natural frequency), impulse increases significantly.

Hence, it is clear that there are operating conditions that are favorable for backreaming operation. Such conditions result in much less impact of the BHA against the borehole walls during the withdrawal of the drillstring. In the case that, at a given rotating speed, the impulse level is acceptable, it is even possible to increase the longitudinal speed without significantly affecting the results (friction dominated conditions), thus representing a more efficient and profitable operation of the oilwell.

Acknowledgements This project was supported by the Brazilian research foundations FAPESP (Fundação de Amparo à Pesquisa do Estado de São Paulo) and CNPq (Conselho Nacional de Desenvolvimento Científico e Tecnológico).

References

1. Yarim G, Ritchie GM, May RB (2010) A guide to successful backreaming: real-time case histories. *J Soc Petrol Eng* 25(1):27–38
2. Forster I (2010) Asymmetric vibration damping tool: small scale rig testing and full scale field testing. In: Proc. SPE/IADC drilling conference, Louisiana, USA, n.128458
3. Forster I (2011) Axial excitation as a means stick-slip mitigation: small scale rig testing and full scale field testing. In: Proc. SPE/IADC drilling conference, Amsterdam, Netherlands, n.139830
4. Liao CM, Balachandran B, Karkoub M, Abdel-Magid YL (2011) Drill-string dynamics: reduced-order models and experimental studies. *J Vib Acoust* 133(4):041008
5. Melakhessou H, Berlioz A, Ferraris G (2003) A nonlinear well-drillstring interaction model. *J Vib Acoust* 125(1):46–52
6. Yigit AS, Christoforou AP (1998) Coupled torsional and bending vibrations of drillstrings subject to impact with friction. *J Sound Vib* 215(1):167–181
7. Jansen JD (1991) Non-linear rotor dynamics as applied to oilwell drillstring vibrations. *J Sound Vib* 147(1):115–135
8. Jansen JD (1993) Non linear dynamics of oilwell drillstrings. Master Dissertation, Delft University, Delft
9. Wambsgans MW, Chen SS, Jendrzeczyk JA (1974) Added mass and damping of vibrating rod in confined viscous fluid. Argonne National Laboratory, Argonne, ANL-CT-75-08
10. Aadnoy BS, Fazaelizadeh M, Hareland G (2010) A 3D analytical model for wellbore friction. *J Can Petrol Tech* 49(10):25–36
11. Christoforou AP, Yigit AS (2002) Fully coupled vibrations of actively controlled drillstrings. *J Sound Vib* 267:1029–1045

Chapter 13

Torsional Damping Identification in Rotating Machinery

Bram Vervisch, Kurt Stockman, and Mia Loccufier

Abstract The characterization of torsional vibrations in rotating machinery is of major importance to ensure reliability. Excessive torsional vibrations can cause wear and even breakdown. At a constant operating speed, risks are generally diminished by avoiding coincidence with torsional natural frequencies. This becomes virtually impossible when there are multiple exciting frequencies occurring in reciprocating engines, variable frequency driven motors or systems that exhibit harmonics. A viable prediction of the vibration amplitudes is the calculation of the forced response provided that there is an accurate knowledge of the system parameters. Modeling of torsional inertias and stiffnesses is generally straightforward, whereas vibration amplitudes or amplification factors highly depend on damping. However, damping is difficult to model especially when being nonlinear. In this research, a method based on the systems eigensolutions is used to reconstruct the physical damping matrix of an experimental setup exhibiting torsional vibration. This experimentally identified matrix provides information of both the spatial distribution of the damping and the reliability of the proposed damping model. The results are compared with a mathematical linear model. A correct interpretation of the results indicates where extra damping should be added.

Keywords Torsional vibrations • Damping matrix estimation • Spatial distribution • Frequency response functions • Experimental validation

13.1 Introduction

Torsional vibrations are inevitable in rotating machinery. Understanding the physical behavior and the root causes of these vibrations is important to improve performance. Mathematical models are often used to fulfill these expectations. A mathematical model allows to identify natural frequencies, mode shapes, actual displacements, stresses, etc. In the literature, a general overview of the analysis procedures is provided by [1, 2]. A variety of modeling procedures such as finite elements are widely known and used [3, 4]. Unfortunately, these methods rely on an approximation of the system parameters such as inertia, stiffness and damping. Also, the assumption of linearity is commonly made and the discretization of continuities is widespread. Whereas mass and stiffness can be modeled quite accurately, damping is rather difficult to model, especially when linearized. Hence, the physical damping phenomenon is usually replaced by a dissipation function leading to a damping matrix that can be diagonalized with the eigenvectors of the undamped system. This “type of damping” is introduced by Rayleigh [5] and is still popular due to its computational simplicity. In classic modal analysis this kind

B. Vervisch (✉)

Department of Industrial Systems and Product Design, Ghent University, Graaf Karel de Goedelaan 5, B-8500, Kortrijk, Belgium

Department of Electrical Engineering, Systems and Automation, Ghent University, Technologiepark 914, B-9000, Ghent, Belgium

e-mail: bramf.vervisch@ugent.be

K. Stockman

Department of Industrial Systems and Product Design, Ghent University, Graaf Karel de Goedelaan 5, B-8500, Kortrijk, Belgium

M. Loccufier

Department of Electrical Engineering, Systems and Automation, Ghent University, Technologiepark 914, B-9000, Ghent, Belgium

of damping leads to real mode shapes and damping factors per mode that can easily be understood and applied. However, this kind of damping rarely occurs and there is no physical evidence that damping behaves this way. An experimental identification of the physical damping matrix could help to gain insight in the matter.

Literature provides several identification techniques to estimate the damping matrix of linear structures [6, 7]. Matrix methods are directly based on the frequency response function (FRF) matrix and modal methods are based on the modal parameters deduced from the FRF's, for instance eigensolutions. One of these methods is proposed by Adhikari [8]. This method not only has a low computational cost but also promises a correct spatial distribution of the physical damping matrix. The latter is important to understand the damping mechanism. In this paper, Adhikari's method is used to extract the damping matrix of a torsional system. A test bench is used in combination with a mathematical model to validate the usefulness of the method. In Sect. 13.2, the test bench is described and the mathematical model is derived. In Sect. 13.3, two damping identification procedures are described. The first procedure allows an asymmetric matrix and the second procedure forces the damping matrix to be symmetric. In Sect. 13.4 a combination of theoretical results and experiments is used to identify the damping matrix. First, the damping matrix of the original system is identified, and secondly extra damping is added. The results are discussed for the resulting asymmetric and symmetric matrices.

13.2 The Torsional Vibration Setup

13.2.1 Theoretical Model

The system, as presented in Fig. 13.1 has four rotational degrees of freedom. A linear, time invariant model is used to describe its dynamic behavior.

$$\mathbf{M}\ddot{\boldsymbol{\theta}} + \mathbf{C}\dot{\boldsymbol{\theta}} + \mathbf{K}\boldsymbol{\theta} = \mathbf{T} \quad (13.1)$$

$\boldsymbol{\theta} = [\theta_1 \ \theta_2 \ \theta_3 \ \theta_4]^T$ is the vector of generalized coordinates each denoting the absolute rotation. The mass matrix, \mathbf{M} , contains the inertia of the disks increased with the remaining inertia added by the encoder and the transmission gears and the stiffness matrix, \mathbf{K} , contains the torsional stiffnesses of the steel shaft. \mathbf{T} is the external torque, generated by the electric motor.

The mass, damping and stiffness matrices \mathbf{M} , \mathbf{C} and \mathbf{K} are

$$\mathbf{M} = \begin{bmatrix} m_1 & 0 & 0 & 0 \\ 0 & m_2 & 0 & 0 \\ 0 & 0 & m_3 & 0 \\ 0 & 0 & 0 & m_4 \end{bmatrix}, \mathbf{C} = \begin{bmatrix} c_1 + c_{01} + c_{12} & -c_{12} & 0 & 0 \\ -c_{12} & c_2 + c_{12} + c_{23} & -c_{23} & 0 \\ 0 & -c_{23} & c_3 + c_{23} + c_{34} & -c_{34} \\ 0 & 0 & -c_{34} & c_4 + c_{34} \end{bmatrix},$$

$$\mathbf{K} = \begin{bmatrix} k_{01} + k_{12} & -k_{12} & 0 & 0 \\ -k_{12} & k_{12} + k_{23} & -k_{23} & 0 \\ 0 & -k_{23} & k_{23} + k_{34} & -k_{34} \\ 0 & 0 & -k_{34} & k_{34} \end{bmatrix} \quad (13.2)$$

Fig. 13.1 Theoretical and experimental model. (a) Schematic representation of the theoretical model. (b) CAD drawing of the experimental model. (c) Picture of the experimental model

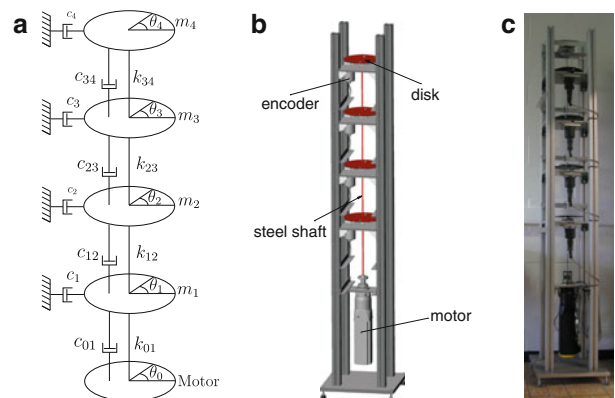


Table 13.1 Values used in experiments

Parameter	Value
m_{1-4}	$3.5 \times 10^{-3} \text{ kgm}^2$
k_{01}	35.57 N/m
k_{12}	35.09 N/m
k_{23}	35.45 N/m
k_{34}	34.80 N/m

Table 13.2 Calculated undamped natural frequencies

Natural frequency	Value [Hz]
f_1	5.56
f_2	15.99
f_3	24.43
f_4	30.03

The torsional stiffness of the spring steel shaft is given by

$$k_{ij} = \frac{\pi G}{32L_{ij}} D^4 \quad (13.3)$$

with G the shear modulus, D the diameter of the spring steel shaft and L_{ij} the length of the shaft in between disks i and j . The damping is arbitrary. In this research, the damping matrix is taken proportional to the stiffness matrix with a factor of 4×10^{-5} . The dampers c_1, c_2 and c_4 are and c_3 is adjusted from zero to 1.5×10^{-2} Ns/m. These damping parameters are the result of a trial and error procedure and are adjusted to fit the measurements. The used values of inertia and stiffness are depicted in Table 13.1 and the undamped natural frequencies in Table 13.2.

13.3 Damping Identification

13.3.1 General Method

In [8] Adhikari describes a method that is based on the eigensolutions to reconstruct the physical damping matrix of an experimental setup. By reconstructing the physical damping matrix, the spatial distribution of the damping is visualized. The procedure is described as follows

1. Measure a set of transfer functions $H_{ij}(\omega)$.
2. Choose the number m of modes to be retained in the study. Determine the complex natural frequencies $\hat{\lambda}_j$ and complex mode shapes $\hat{\mathbf{z}}_j$ from the transfer functions, for all $j = 1, \dots, m$. Obtain the complex mode shape matrix $\hat{\mathbf{Z}} = [\hat{\mathbf{z}}_1, \hat{\mathbf{z}}_2, \dots, \hat{\mathbf{z}}_m] \in \mathbb{C}^{N \times m}$.
3. Estimate the “undamped natural frequencies” as $\hat{\omega}_j = \Re(\hat{\lambda}_j)$.
4. Set $\mathbf{U} = \Re[\hat{\mathbf{Z}}]$ and $\hat{\mathbf{V}} = \Im[\hat{\mathbf{Z}}]$, and from these obtain $\mathbf{W} = \hat{\mathbf{U}}^T \hat{\mathbf{U}}$ and $\mathbf{S} = \hat{\mathbf{U}}^T \hat{\mathbf{V}}$. Now denote $\mathbf{B} = \mathbf{W}^{-1} \mathbf{S}$.
5. From the \mathbf{B} matrix get $C'_{kj} = (\hat{\omega}_j^2 - \hat{\omega}_k^2) B_{kj} / \hat{\omega}_j$ for $k \neq j$ and $C'_{jj} = 2\Im(\hat{\lambda}_j)$.
6. Finally, carry out the transformation $\mathbf{C} = \left[(\hat{\mathbf{U}}^T \hat{\mathbf{U}})^{-1} \hat{\mathbf{U}}^T \right]^T \mathbf{C}' \left[(\hat{\mathbf{U}}^T \hat{\mathbf{U}})^{-1} \hat{\mathbf{U}}^T \right]$ to get the damping matrix in physical coordinates.

In this method the symmetry of the damping matrix is never assumed so the outcome can be asymmetric. An asymmetric matrix indicates that the proposed damping model is incorrect. However, in some cases numerical study has shown that the identified damping matrix becomes asymmetric although a symmetric damping matrix was expected. Therefore, another method that forces the damping matrix to be symmetric can be used [9].

13.3.2 Symmetry Preserving Method

1. Measure a set of transfer functions $H_{ij}(\omega)$ at a set of N grid points. Fix the number of the modes to be retained in the study, say m . Determine the complex natural frequencies $\hat{\lambda}_j$ and the complex mode shapes $\hat{\mathbf{z}}_j$ from the transfer functions, for all $j = 1, \dots, m$. Denote by $\hat{\mathbf{Z}} = [\hat{\mathbf{z}}_1, \hat{\mathbf{z}}_2, \dots, \hat{\mathbf{z}}_m] \in \mathbb{C}^{N \times m}$ the complex mode shape matrix.
2. Set the “undamped natural frequencies” as $\hat{\omega}_j = \Re(\hat{\lambda}_j)$. Denote the diagonal matrix $\hat{\mathbf{\Omega}} = \text{diag}(\hat{\omega}_1, \hat{\omega}_2, \dots, \hat{\omega}_m) \in \mathbb{R}^{m \times m}$.
3. Separate the real and imaginary parts of $\hat{\mathbf{Z}}$ to obtain $\hat{\mathbf{U}} = \Re[\hat{\mathbf{Z}}]$ and $\hat{\mathbf{V}} = \Im[\hat{\mathbf{Z}}]$.
4. From the obtain the $m \times m$ matrices $\mathbf{W} = \hat{\mathbf{U}}^T \hat{\mathbf{U}}$, $\mathbf{D} = \hat{\mathbf{U}}^T \hat{\mathbf{V}}$, $\mathbf{Q} = \hat{\mathbf{\Omega}}^{-1} \hat{\mathbf{W}}$ and $\mathbf{P} = \hat{\mathbf{\Omega}}^{-1} \mathbf{D} \hat{\mathbf{\Omega}} - \mathbf{D}^T$.
5. Now denote $\mathbf{p} = \text{vec}(\mathbf{P}) \in \mathbb{R}^{m^2}$ and calculate $\mathbf{R} = (\mathbf{\Omega} \otimes \mathbf{Q}) + (\mathbf{Q} \otimes \hat{\mathbf{\Omega}}) \in \mathbb{R}^{m^2 \times m^2}$.
6. Evaluate $\text{vec}(\mathbf{B}) = [\mathbf{R}]^{-1} \mathbf{p}$ and obtain the matrix \mathbf{B} .
7. From the \mathbf{B} matrix obtain $\mathbf{C}' = \mathbf{B} \hat{\mathbf{\Omega}} - \hat{\mathbf{\Omega}} \mathbf{B} \hat{\mathbf{\Omega}}^{-1}$ and $C'_{jj} = 2\Im(\hat{\lambda}_j)$.
8. Finally, carry out the transformation $\mathbf{C} = \left[(\hat{\mathbf{U}}^T \hat{\mathbf{U}})^{-1} \hat{\mathbf{U}}^T \right]^T \mathbf{C}' \left[(\hat{\mathbf{U}}^T \hat{\mathbf{U}})^{-1} \hat{\mathbf{U}}^T \right]$ to get the damping matrix in physical coordinates.

The operation vec is defined as a transformation from a matrix to a vector by stacking the columns in a sequence one below another or $\text{vec} : \mathbb{R}^{m \times n} \rightarrow \mathbb{R}^{mn}$ and \otimes is the Kronecker product. This symmetry preserving method has the advantage that a resulting symmetric matrix is easy to interpret. Yet, by forcing the damping matrix to be symmetric, physical phenomena could be masked.

13.4 Theoretical and Experimental Results

The damping identification method is validated on the torsional setup. The mathematical model provides reference for the experimental results. In both theory and experiments one row of the frequency response function matrix is used, where the input is the angular displacement of the motor and the output are the four angular displacements of the disks. In the numerical model this FRF matrix is calculated directly from the equations of motion while in the experimental model a sine sweep is imposed to the motor and the displacements are measured with the encoders. A least squares complex exponential method [10] is used to extract the eigensolutions of both FRF matrices.

13.4.1 Without Extra Damping

In the case of no extra damping only material damping and friction in the bearings is present. The results are plotted in Fig. 13.2 for the mathematical model and in Fig. 13.3 for the experiments. The calculated and the measured FRF's are similar as was intended and therefore the synthesized FRF's and the calculated eigensolutions also agree quite well. For the mathematical model, Adhikari's procedure leads to a damping matrix represented in Fig. 13.4a. The values of the matrix are represented in a three dimensional graph to focus on the spatial distribution rather than on the amplitudes. In the graph, the x and y -axis are the rows and columns of the damping matrix and the z -axis is the actual value.

As expected, the results from the mathematical model allow to identify the damping matrix correctly. When, however, the damping matrix is identified with the general procedure used on the experiments, an asymmetric matrix occurs (Fig. 13.4b). Except for a peak on the fourth diagonal value, not many conclusions can be made. By using the symmetry preserving method, the damping matrix is forced to be symmetric and a more acceptable damping matrix is constructed. Comparing this matrix to the theoretical damping matrix, leads to some conclusions. Firstly, the damping of the setup is quite low, and there is an obvious peak on the fourth diagonal value. This means that the value of c_4 in Fig. 13.1a is higher than the others, and can be explained that there is a higher damping in the experiment than initially assumed in the model. By taking a look at the picture this can be clarified. For other purposes than this experiment, an extra component is fixed to the fourth disk leading to extra energy dissipation.

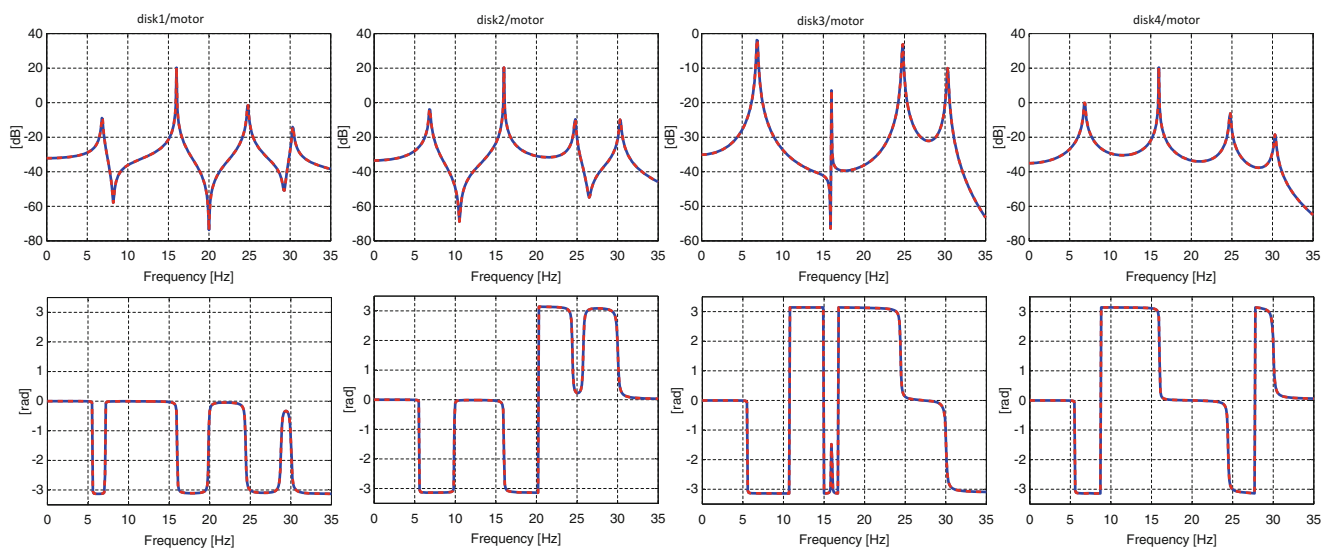


Fig. 13.2 Simulated FRF's (blue) and synthesized FRF's (red) after the identification procedure with no extra added damping

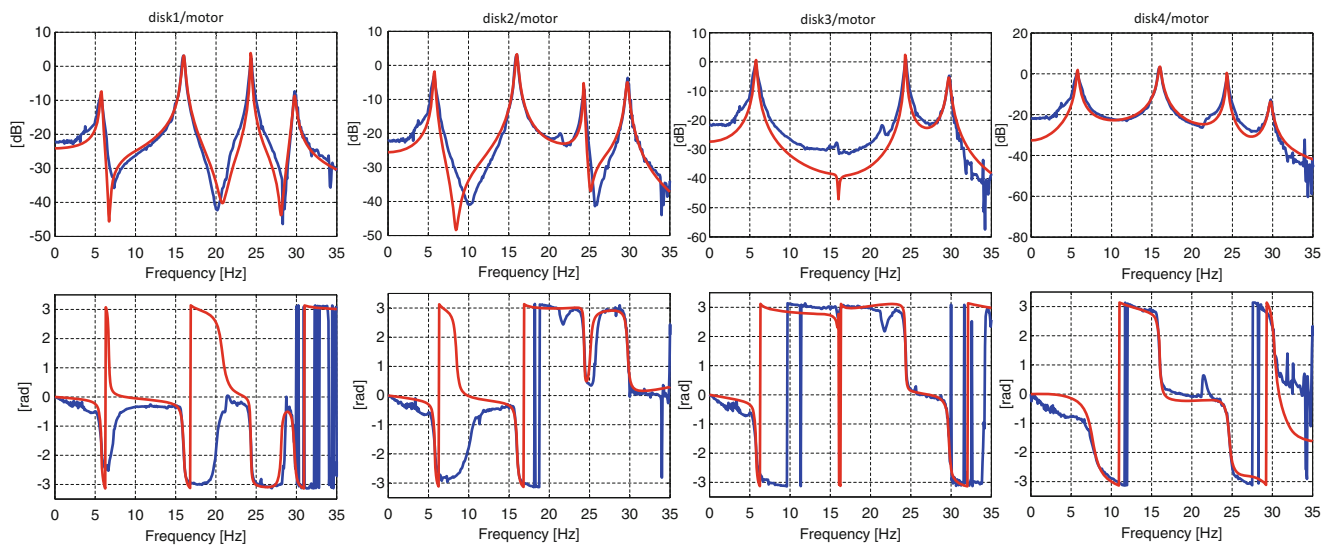


Fig. 13.3 Measured FRF's (blue) and synthesized FRF's (red) after the identification procedure with no extra added damping

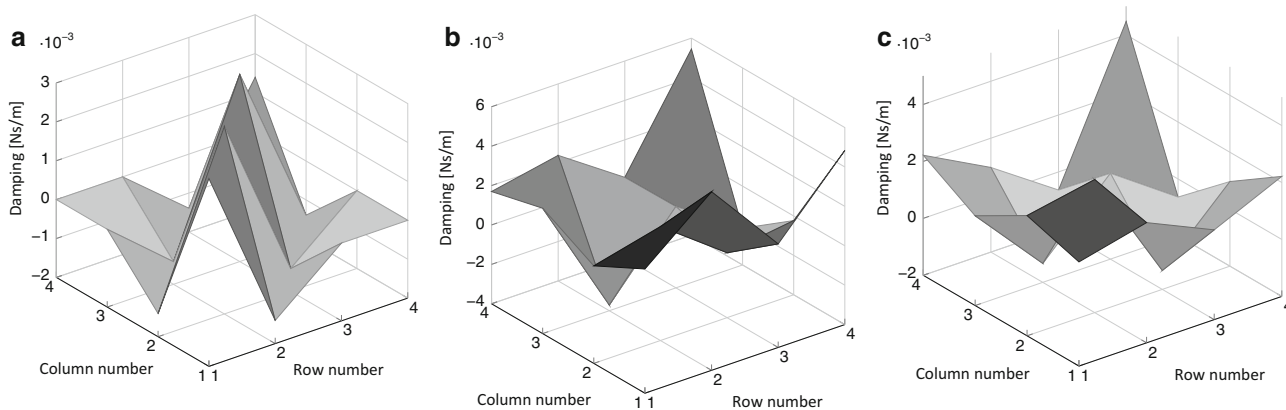


Fig. 13.4 Identified matrices from the theoretical and the experimental model. (a) Identified damping matrix from the theoretical model. (b) Identified matrix from the experiments. (c) Identified matrix from the experiments with the symmetry preserving method

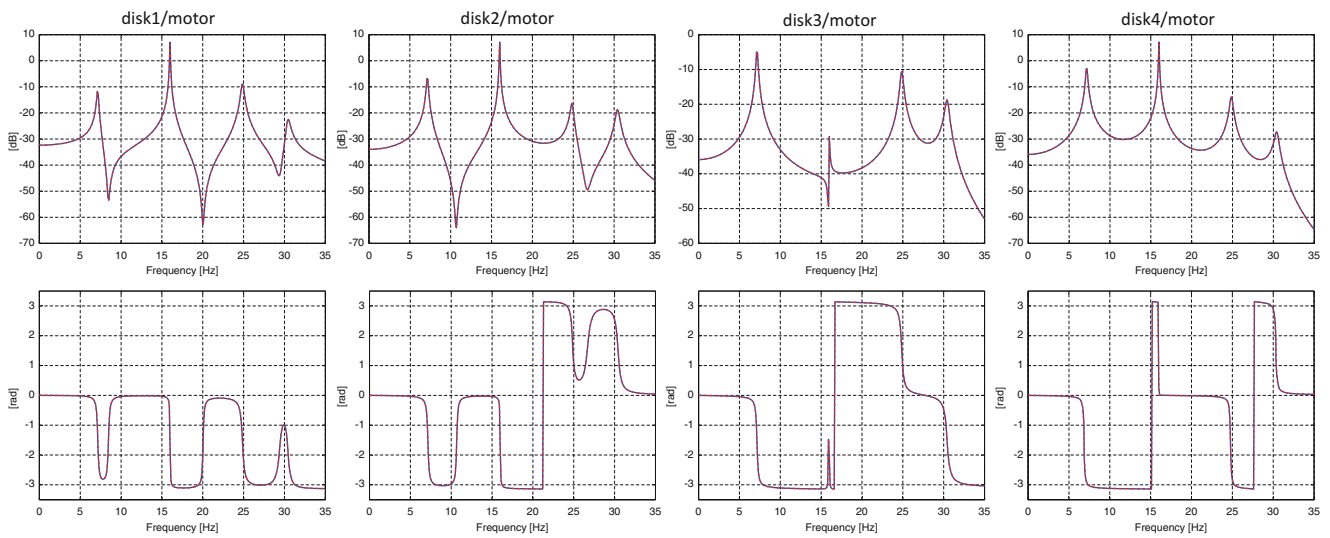


Fig. 13.5 Simulated FRF's (blue) and synthesized FRF's (red) after the identification procedure with extra added damping

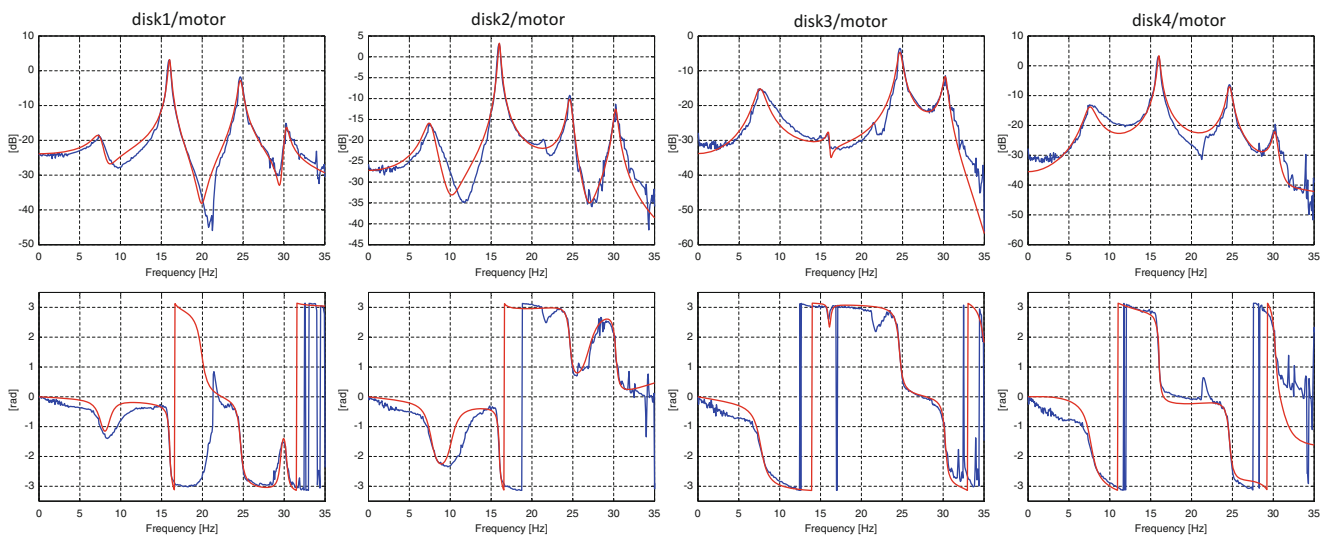


Fig. 13.6 Measured FRF's (blue) and synthesized FRF's (red) after the identification procedure with no extra added damping

13.4.2 With Extra Damping

Adding a realistic extra damping to this lightweight test stand is not straightforward. The damping should be low compared to the mass and stiffness. Therefore, a small damping is added by tying the disk to the chassis with a ribbon. This ribbon does add extra stiffness to the setup, but also adds small damping. In the model, the stiffness of the ribbon can also be accounted for. In this example, the extra damping is added to the third disk or c_3 on Fig. 13.1a. Both the theoretical and the measured FRF's are shown in Figs. 13.5 and 13.6. Again, the theoretical and the experimental FRF's agree quite well.

For the damping identification procedure, the theoretical damping matrix is plotted in Fig. 13.7a. This results in a combination of the proportional damping matrix and a peak on the third diagonal element as was intended. The peak on the third diagonal element is caused by the extra damping on the third disk. When the first procedure is implemented, again an asymmetric matrix is constructed (Fig. 13.7b). Other than being asymmetric, a peak also appears on the third diagonal element and it could be concluded that the damping is detected. When the symmetry preserving method is applied, this peak is emphasized even more and the resulting matrix resembles the theoretical expected matrix.

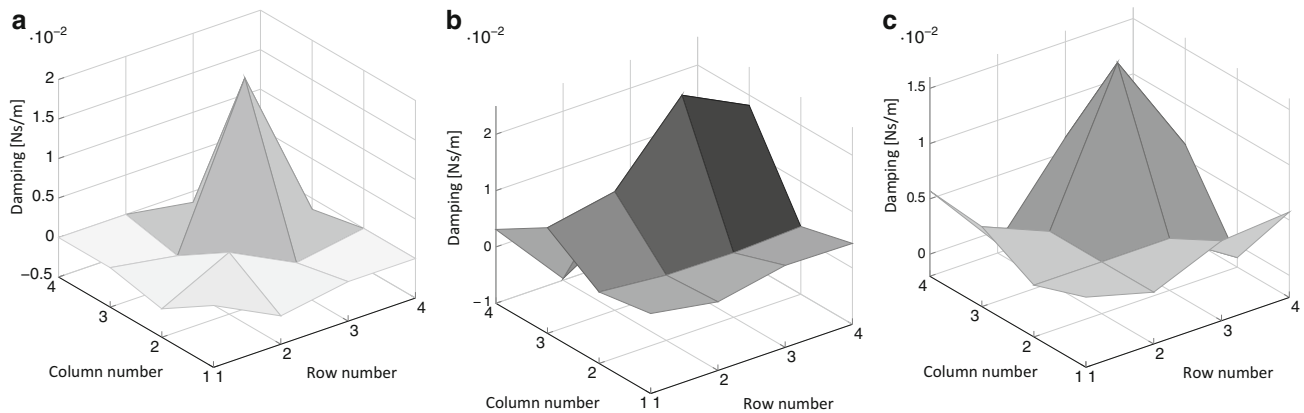


Fig. 13.7 Identified matrices from the theoretical and the experimental model with extra damping. (a) Identified damping matrix from the theoretical model. (b) Identified matrix from the experiments. (c) Identified matrix from the experiments with the symmetry preserving method

13.5 Conclusions

In this work, a method to identify the damping matrix from experimental results is validated on a torsional setup. The method depends on the eigensolutions of the system. The torsional setup is modeled and the mathematical model is used as a reference for the expected results. A method that allows the damping matrix to be asymmetric is compared to a method that forces a symmetric damping matrix. The latter leads to promising results. However, it should be taken into account that the apparent asymmetry in the result could be caused because the damping model can not be assumed to be viscous. This implies that, whenever the purpose is to fit a viscous damping model on measurements, that a symmetry preserving method works quite well. When the purpose is to gain insight into the physical behavior, caution is advised. Another important remark is that this torsional setup is constructed such that a mathematical can easily be obtained. In practice, such a correspondence rarely occurs. Future research will be carried out to validate this on more complex and realistic setups.

References

1. Eshleman RL (1977) Torsional vibration of machine systems. In: Proceedings of the sixth turbomachinery symposium, 1977
2. Wachel JC, Szenasi FR (1993) Analysis of torsional vibrations in rotating machinery. In: Proceedings of the twenty-second turbomachinery symposium, 1993
3. Adams ML (2009) Rotating machinery vibration: from analysis to troubleshooting. CRC Press/Taylor & Francis, Hoboken, NJ
4. Genta G (2005) Dynamics of rotating systems, vol 1. Springer, New York
5. Rayleigh JWS, Lindsay RB (1945) The theory of sound, vol 1: unabridged second revised edition. Dover Publications, New York, NY
6. Pilkey DF, Inman DJ (1998) A survey of damping matrix identification. In: IMAC XVI proceedings, pp 104–110, 1998
7. Srikantha Phani A, Woodhouse J (2007) Viscous damping identification in linear vibration. *J Sound Vib* 303(3–5):475–500
8. Adhikari S, Woodhouse J (2001) Identification of damping: Part 1, viscous damping. *J Sound Vib* 243(1):43–61
9. Adhikari S, Woodhouse J (2002) Identification of damping: Part 3, symmetry-preserving methods. *J Sound Vib* 251(3):477–490
10. Brandt A (2011) Noise and vibration analysis: signal analysis and experimental procedures. Wiley, Chichester

Chapter 14

Numerical and Experimental Dynamic System Identification for the Development of Operational Modal Analysis in a Physics-Based Diagnostic/Prognostic Model

Suri Ganeriwala and Nader Sawalhi

Abstract The work presented in this paper is a part of an ongoing research for developing a sound operational modal analysis for diagnostic and prognostic applications. The aim is to build a physics-based diagnostic/prognostic model, for condition monitoring purposes, with the ability to insert different types of faults. In this paper, a numerical model for a machinery fault simulator (MFS) is developed using rotor dynamic system analysis software XLRotor™. The use of the XLRotor™ software provides an ideal replacement for creating a traditional finite element model and is used as a base to build and assemble mass and stiffness matrices in Matlab® for a number of configurations of the test rig. The Matlab® code will form a valid base for developing a dynamic simulation model by the aid of Simulink®. A number of layouts of the MFS are tested and their corresponding models are created. Models include: the motor of the MFS, the coupling, the shaft, a number of inertia rotors at different locations, the rolling element bearings and the rotor pedestal (base). The results obtained from the model, in terms of the critical damped speeds and mode shapes are compared to those obtained experimentally for validation. Experimental validation includes simple bump. Numerical results obtained from this study were found to compare well with the experimental data.

Keywords Machinery fault simulator (MFS) • Critical speeds • Run-up/coast-down analysis • Rotor dynamics and physics based model

14.1 Introduction

Building a trustworthy dynamic simulation model for the rotor of a mechanical system provides an endless capability for studying the behavior and the response of the system under different types of excitation forces. The understanding of such behavior and response is very crucial for developing health monitoring systems that can be implemented and tested virtually without the hassle of undergoing timely and costly experiments. A number of approaches to build a dynamic system for rotors include using lumped mass models (LPM) [1, 2] finite element modeling, model sub-structuring and reductions [3, 4] and/or a combination of both, e.g. [5]. Developing a physical model involves building mass, stiffness and damping matrices and solving the corresponding equations of motion using a numerical integration approach such as Rung–Kuta. Lumped parameter models are easier to handle, but they have limited structural dynamic range. Finite element modeling and sub structuring provides a more accurate models but requires more computational resources and high technical capacity. Changing the model setup necessitates re-creating the model and modifying it to reflect on the update. In this paper a methodology of constructing a dynamic simulation model for a machinery fault simulator (MFS) which can be easily updated with a number of configurations is described. The focus of the current work is to validate the first few modes of the models against the experimental results to enable using the model later for building a physics-based diagnostic/prognostic model, for condition monitoring purposes, with the ability to insert different types of faults in the rotor and the bearings.

S. Ganeriwala
Spectra Quest Inc., Richmond, VA 23228, USA
e-mail: suri@spectraquest.com

N. Sawalhi (✉)
Prince Mohammad Bin Fahd University, Al Khober 31952, Saudi Arabia
e-mail: nsawalhi@pmu.edu.sa

The paper is organized as follows. Following this introductory section, a brief description for the machinery fault simulator under modeling is given in Sect. 14.2. In Sect. 14.3, the methodology of building the models and producing its mass and stiffness matrices is described. This includes building the rotor-bearing model and the inclusion of the pedestal (base) in the commercial software XLRotor™ (<http://www.xlrotor.com/index.shtml>) (see also [6]) and the assembly of mass and stiffness matrices in Matlab®. Results and discussions are presented in Sect. 14.4 and the conclusions are provided in Sect. 14.5.

14.2 The Machinery Fault Simulator (MFS)

The machinery fault simulator (MFS) of SpectrQuest® consists of a center-hung rotor which is driven by a two pole motor through a flexible coupling. MFS can be configured by adding a number of disks between the rotor bearing to enable changing the critical speeds of the system, loading of the system and studying faults such as unbalance, rotor cracks, etc. Bearing faults as well as a number of rotor faults can be inserted and the system response can be measured through accelerometers and other sensors. An image showing the test rig is shown in Fig. 14.1.

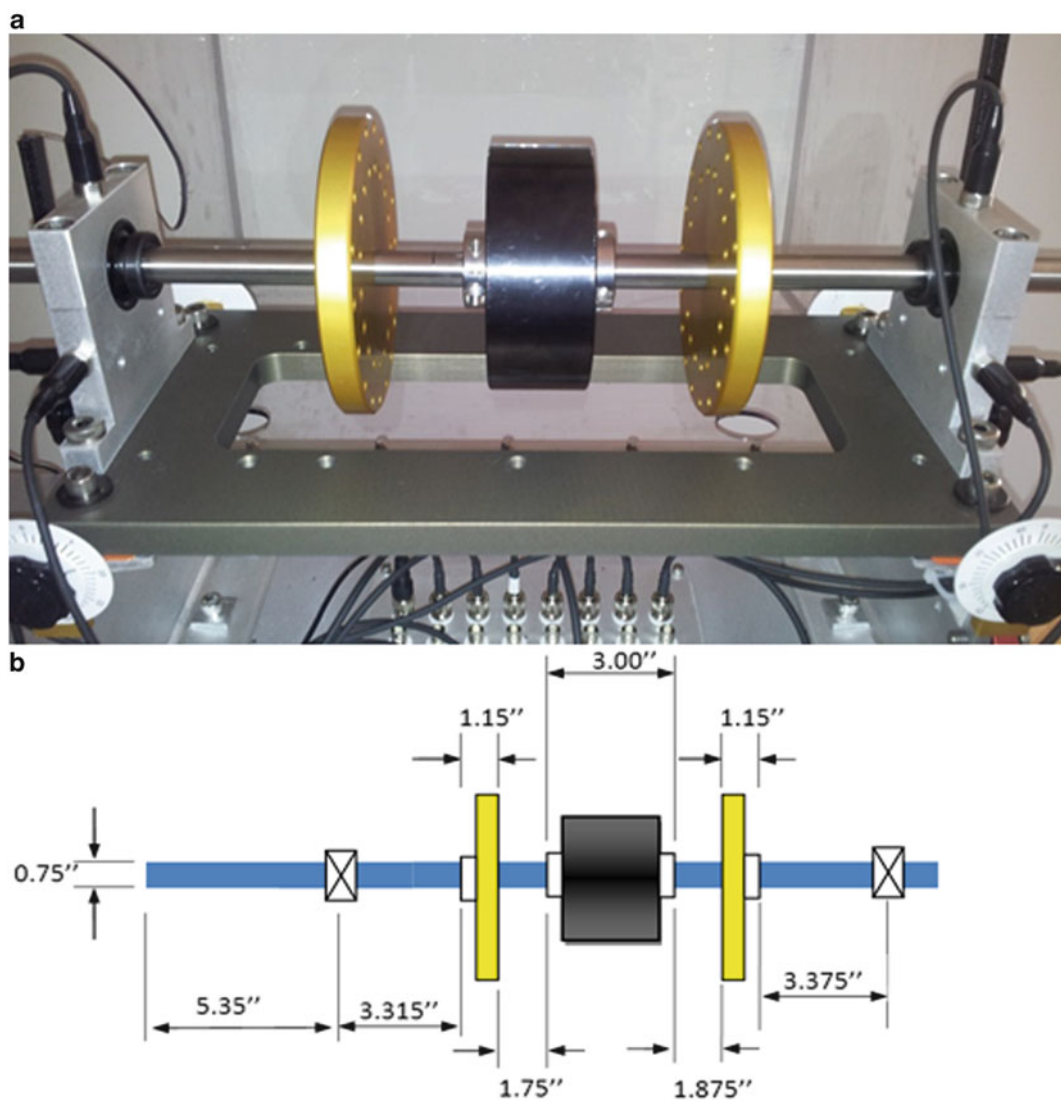


Fig. 14.1 Spectra Quest MFS with a loader (middle black disk) and two gold (aluminum) disks. (a) Image; (b) schematic presentation

14.3 Building the Model

The modeling approach included the development of a finite element model of the MFS (Motor-Coupling-rotor-bearings and pedestal) using XLRotor™ (<http://www.xlrotor.com/index.shtml>). In XLRotor™, the system is divided into a number of “stations”. The stations’ spreadsheet will then be used as an input into Matlab® to build the mass and stiffness matrices. The methodology for creating the model is described and illustrated in the subsections to follow. The utilization of XLRotor™ means that any changes in terms of adding disks and loaders to the system can be easily done and the updates are directly reflected in the spreadsheet input to Matlab® for building the mass and stiffness matrices.

14.3.1 Rotor-Bearing Modeling

To provide a flexibility of building the mass and stiffness matrices of the system with a number of configurations, XLRotor™ was used to generate a spreadsheet containing the basic building blocks of a consistent mass and stiffness matrices. In XLRotor™, the MFS is divided into a number of stations. Each station is configured from one or more beam elements. Each beam is identified by a length (l_i), inner diameter (d_i) and outer diameter (d_o) and material (material defines density (ρ_i), modulus of elasticity (E_i) and modulus of rigidity (G_i)).

The MFS rotor was divided into 26 stations as seen in Fig. 14.2. The divisions between the bearing locations were determined based on the different possibilities of disks and loader arrangements, and the total number of stations remained the same regardless of any change in the configuration. The number of stations should remain constant, but the addition of a disk means that the station will have an extra beam element and the physical characteristic of that station will change accordingly. Figure 14.2 shows two different configurations for the MFS. The second (Fig. 14.2b) has a disk (loader) added in the middle of the rotor. The number of stations for the rotor remains the same between the two configurations.

For each station, the mass (m), transverse moment of inertia (I_t), polar moment of inertia (I_p), flexure rigidity (EI) and the shear rigidity parameter (GA) are calculated as a summation of the corresponding beam values that form the station. For each beam, the corresponding mass, transverse moment of inertia and polar moment of inertia values are calculated as per Eqs. (14.1)–(14.3). The station spreadsheet which contains the summation of all beam properties at each station is used as an input to construct the mass and stiffness matrix of each station (consistent matrices based on Timoshenko’s beam theory). The transverse shear effect is considered in the model in the form of a parameter (\varnothing), which is defined in Eq. (14.4).

$$m_i = \rho_i \times \pi \times \left(\frac{d_o - d_i}{2} \right) \times l_i \quad (14.1)$$

$$I_p = \frac{1}{2} m_i \left(\frac{d_o - d_i}{2} \right)^2 \quad (14.2)$$

$$I_t = m_i \times \left[\left(\frac{l_i}{12} \right) + \left(\frac{(d_o - d_i)}{16} \right) \right] \quad (14.3)$$

$$\varnothing = \frac{12EI}{kGA l^2} \quad (14.4)$$

where:

E : Young’s modulus

G : shear modulus

I : area moment of inertia

A : cross-section area

K : is a shape factor [7] which is defined in terms of Poisson ratio (ν) and equals 0.886 for $\nu = 0.3$.

The bearing stiffness is derived in XLRotor™ from a load deflection curve in the contact zones between the rolling elements and the inner and outer races. In rotor dynamics rolling element bearings are often represented by an isotropic radial stiffness ($k = k_{xx} = k_{yy}$) and very small damping [6]. The damping factor estimated in [8] is in the range of 0.0004 and 0.004. The bearing stiffness and damping results obtained for the rotor bearing (ER 12 K) are shown in Fig. 14.3. The rotor bearing stiffness is in the range of 1.3E7 to 1.5E7 N/m and the damping is estimated at 525.3 N s/m. The Motor bearing gave a similar result and was in the range of 1.4E7 to 1.6E7 N/m.

Fig. 14.2 (a) Rotor only configuration. (b) Rotor with loader

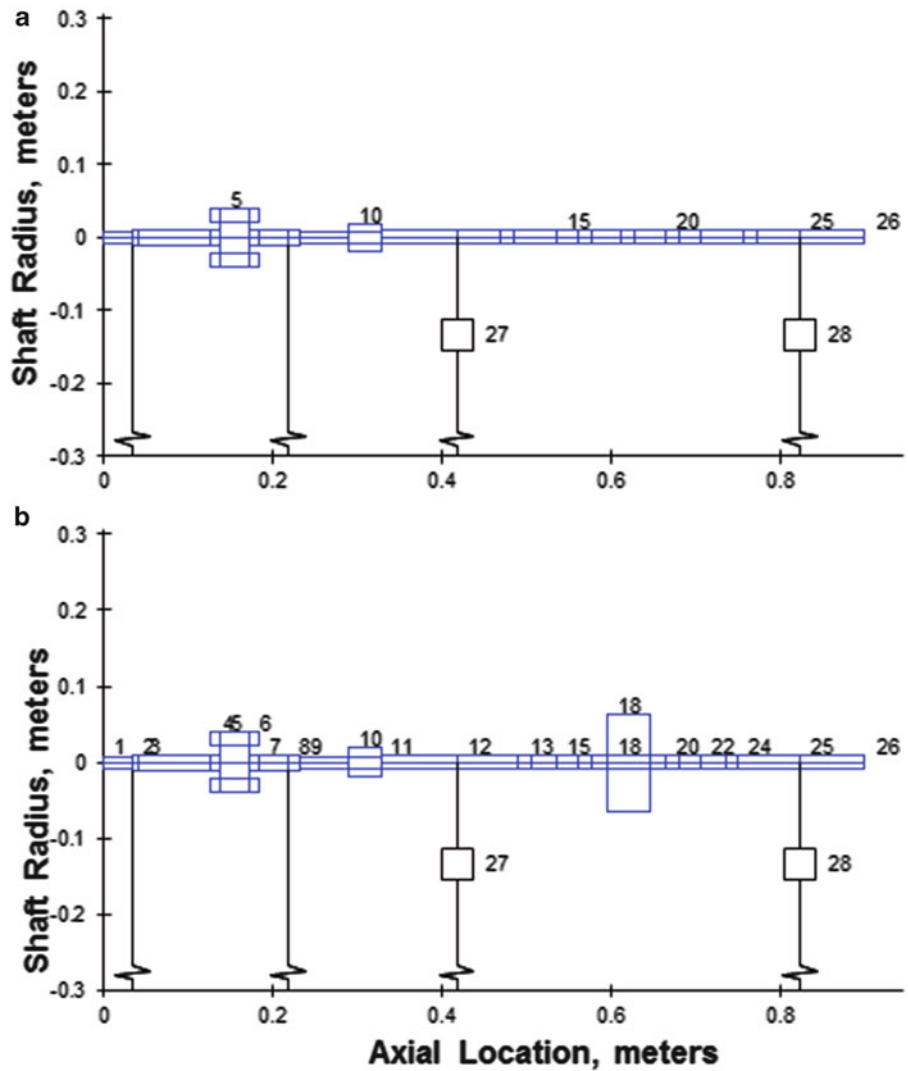
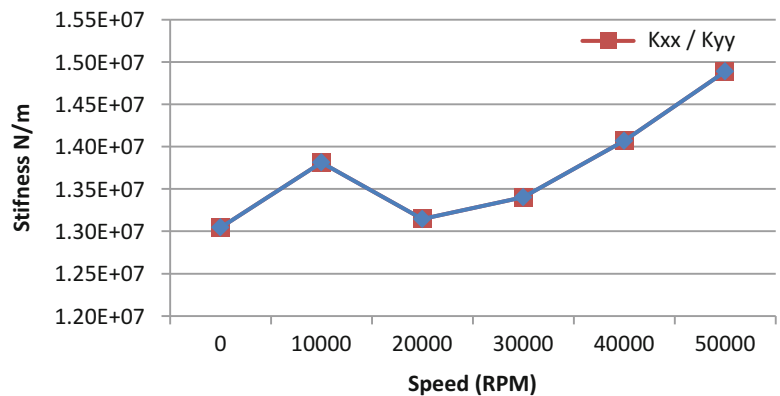


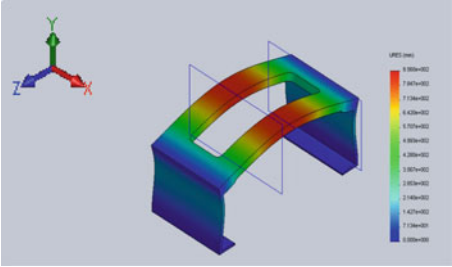
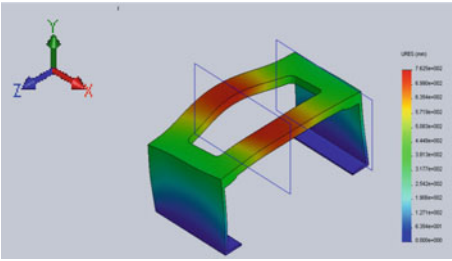
Fig. 14.3 Horizontal and vertical rotor bearing stiffness vs shaft speed in revolution per minute (RPM)



14.3.2 Pedestal Modeling

In order to include the effect of the rotor pedestal (base) into the model, a simple finite element model was created using Solidworks®. The stiffness of the base in the vertical direction (Y) and the Horizontal direction (X) was calculated using the corresponding natural frequency of the highest contribution in that direction. Table 14.1 shows the mass participation (normalized) for the first five modes of the base. The second mode (288.67 Hz) has the highest contribution to the Y direction,

Table 14.1 Mass participation (normalized)

Mode number	Frequency (Hz)	X direction	Y direction	Mode shapes
1	174.07	1.6326e−007	1.373e−005	
2	<u>288.67</u>	4.4983e−009	0.45377	
3	491.42	0.0035744	1.632e−007	
4	875.59	3.3391e−006	1.8202e−008	
5	<u>1134.8</u>	0.70228	3.1066e−006	

while the fifth mode (1134.8 Hz) contributes most to the X direction. The 174.07 Hz was the one that contributed the most to the axial direction (Z), but this was not incorporated in this model. The effective stiffness in the Y-direction and in the X-direction were calculated by using a normalized mass of 1 kg at the location of each bearing, thus the stiffness in the Y-Direction for the pedestal was estimated as: $k_{py} = (2 \times \pi \times 288.68)^2 \approx 3.29$ MPa, while that in the X-direction was estimated as $k_{px} = (2 \times \pi \times 1134.8)^2 \approx 50.8$ MPa.

14.3.3 Mass and Stiffness Matrices Formulation in Matlab[®]

A consistent mass and stiffness matrices were built for the model in Matlab[®]. As an input for building these matrices, the required information for each section of the model was sourced through the “stations sheet of the transverse XLRotor™”. The effect of the shear has been added to the mass and stiffness matrices through the transverse shear effect parameter given in Eq. (14.4). Torsional mass and stiffness matrices were embedded within the model, so that each node contains five degrees of freedom. The bearing stiffness and the pedestal stiffness were used and the rotor model was connected to the bearings and the pedestal to form a universal mass and stiffness matrices.

Eigenvalue analyses were performed on the assembled mass and stiffness matrices in Matlab[®] and were compared to the results obtained earlier for the XLRotor™ and the experiments to form a valid base for the model.

14.4 Results and Discussions

Sample results are discussed in this paper and another example is shown in [9]. The first three main vertical bending modes for the case of a loader are shown in Fig. 14.4. The first bending mode is seen at 71.8 Hz, while the second appears at 388.1 Hz. The third mode is seen at 665 Hz. Other modes were also observed as can be seen from Fig. 14.5 where main deflections are noticed in the motor (417.8 Hz) and for the rotor bearings (224.7 Hz). To check the validity of these modes, a simple bump test was carried out on the rotor by attaching three accelerometers and observing the FFT (Fast Fourier Transformation) of the measured impulse response after applying a proper exponential window and taking a number of averages. The experimental setup is shown in Fig. 14.6, while the FFT results are presented in Fig. 14.7.

Fig. 14.4 Main three bending modes for the rotor with loader. (a) First mode; (b) second bending; (c) third bending

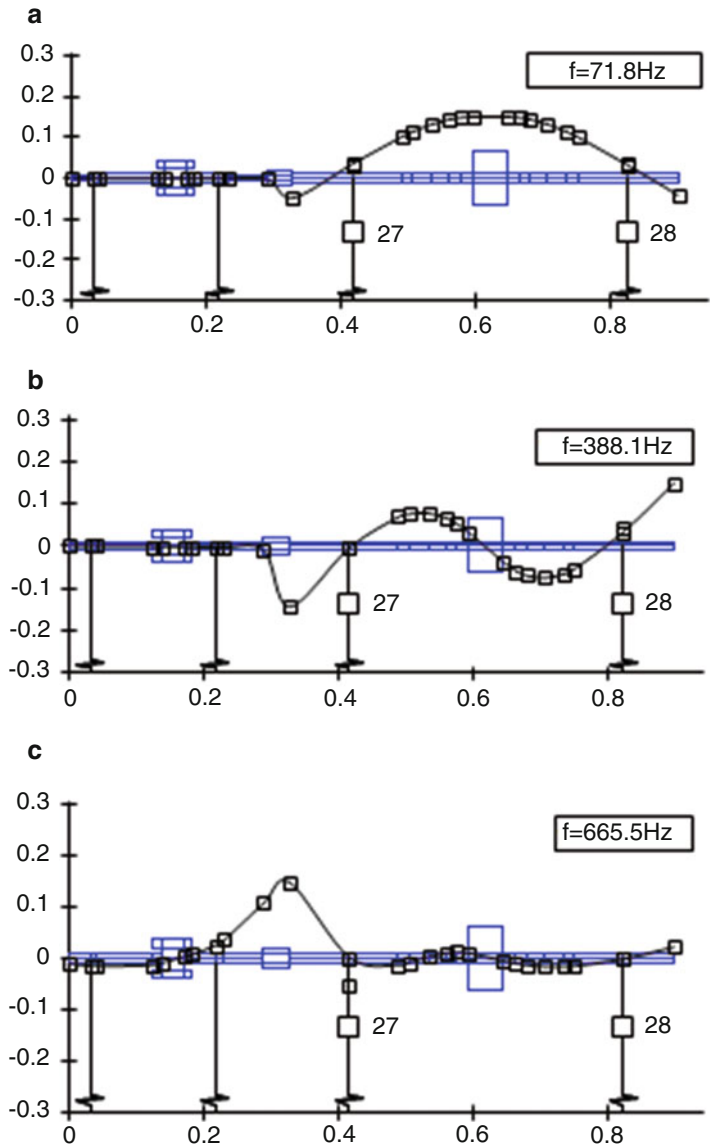
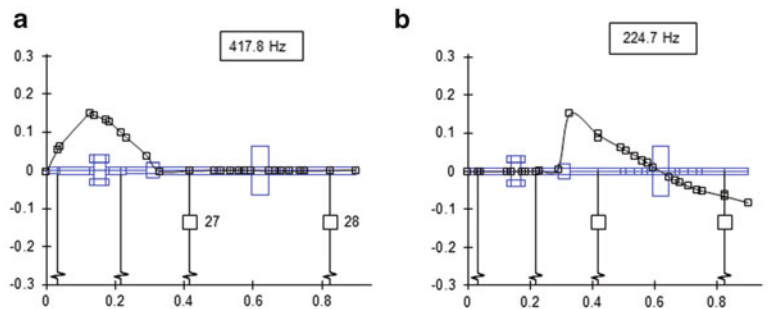


Fig. 14.5 Two additional observed modes. (a) Motor deflecting at 417.8 Hz. (b) Rotor bearing maximum deflection



In Fig. 14.7 it is noticed that the middle accelerometer shows clearly the first mode around 75 Hz, which agrees well with the numerical mode of 71.8 Hz. The second mode can be seen in the experimental results at around 370 Hz while the third mode is seen around the 634 Hz. A sole mode at 282 Hz can only be seen from the left accelerometer. It is noticed that the accuracy is not high enough due to the resolution of the FFT and a more comprehensive testing and validation will be sought.

Fig. 14.6 Positions of three accelerometers for the bump test (*L* left, *M* middle, *R* right)

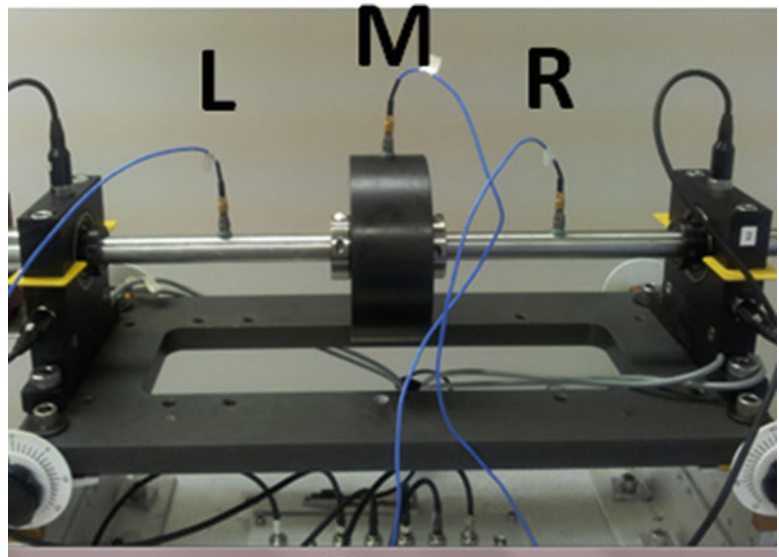
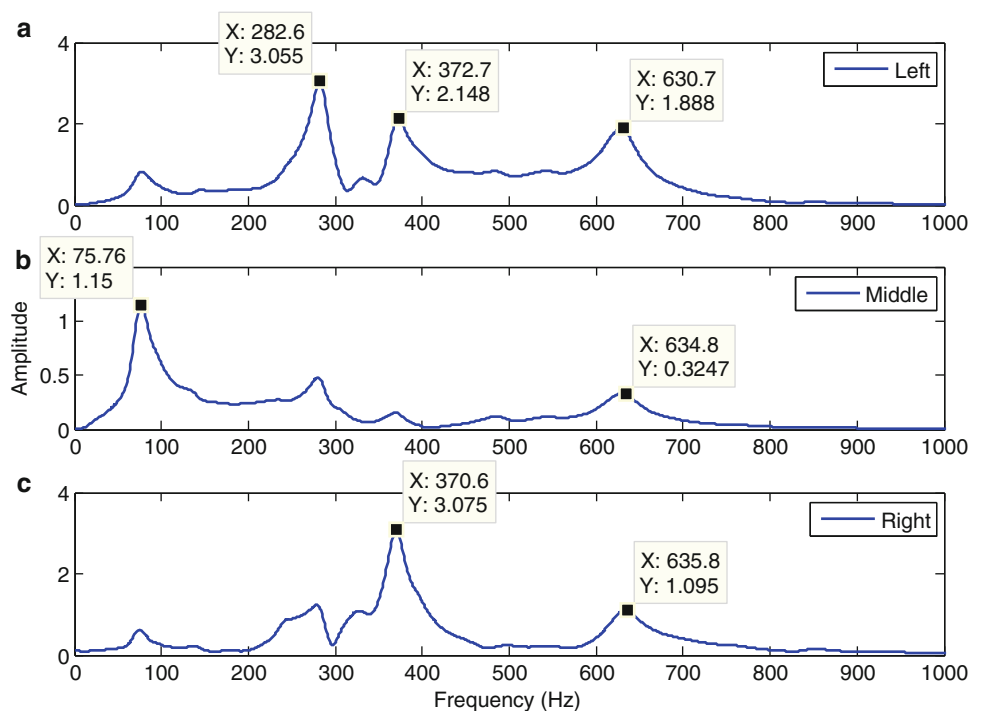


Fig. 14.7 FFT of the impulse response. (a) Left accelerometer. (b) Middle accelerometer. (c) Right accelerometer



14.5 Conclusions

In this paper, a numerical model of a machinery fault simulator (MFS) has been developed by utilizing XLRotor™. The built model include: the motor of the MFS, the coupling, the shaft, a number of inertia rotors (disks) at different locations, the rolling element bearings and the rotor's base. Two main layouts have been presented and tested. The results obtained from the model, in terms of first three natural frequencies have been compared to these obtained experimentally through a simple bump test. The experimental results are sound, but need more verification. A comprehensive accurate modal testing will be undertaken to further verify the model, fine tune it and update it to enable a robust study of the system response in the presence of faults.

Acknowledgements The second author is thankful to SpectraQuest® for their support during the course of this work.

References

1. Tiwari M, Gupta K, Prakash O (2000) Dynamic response of an unbalanced rotor supported on ball bearings. *J Sound Vib* 238:757–779
2. Sawalhi N, Randall RB (2008) Simulating gear and bearing interactions in the presence of faults: part II: simulation of the vibrations produced by extended bearing faults. *Mech Syst Signal Process* 22:1952–1966
3. Qu Z-Q (2004) Model order reduction techniques: with applications in finite element analysis. Springer, England
4. Craig R, Bampton M (1968) Coupling of substructures for dynamic analysis. *Am Inst Aero Astro J* 67:1313–1319
5. Deshpande L, Sawalhi N, Randall RB (2012) Gearbox bearing fault simulation using a finite element model reduction technique. In: 25th international congress on condition monitoring and diagnostic engineering. IOP Publishing. *Journal of Physics: Conference series* 364. <http://www.iopscience.iop.org/1742-6596/364/1/012082>
6. Chen WJ, Gunter EJ (2007) Introduction to dynamics of rotor-bearing system. Trafford, Victoria. ISBN 978-1-41205-190-3
7. Cowper GR (1966) The shear coefficient in Timoshenko's beam theory. *ASME J Appl Mech* 33(2):335–340
8. Kramer E (1993) Dynamics of rotors and foundations. Springer, Berlin
9. Sawalhi N, Ganeriwala S (2014) Vibration energy trending and speed-frequency transformation in run-up/coast-down tests. In: De Clerck J (ed) Topics in modal analysis I, vol 7. Proceedings of the 32nd IMAC. A conference and exposition on structural dynamics, Orlando, 3–6 February 2014. Conference proceedings of the Society for Experimental Mechanics Series. doi:10.1007/978-3-319-04753-9_10 © The Society for Experimental Mechanics, Inc.

Chapter 15

The Influence of Loading Conditions on the Static Coefficient of Friction: A Study on Brake Creep Groan

Sebastian Kruse, Bernhard Stingl, Jakob Hieke, Antonio Papangelo, Merten Tiedemann, Norbert Hoffmann, and Michele Ciavarella

Abstract This work focuses on the phenomenon of creep groan in brake systems as a problem leading to customer complaints (Kinkaid et al., *J Sound Vib* 267:105–166, 2003). It is potentially induced by a stick-slip phenomenon in the friction interface, but the dynamics are not well understood yet. This work tries to contribute to the understanding of the excitation mechanisms, the interaction of different length scales and possible measures to influence the phenomenon.

It presents a dual—based on simulation and experiment—approach to investigate the phenomenon employing works of Ben-David and Fineberg (*Phys Rev Lett* 106, 2011) and Bar Sinai et al. (*Geophys Res Lett* 39, 2011). On the one side using the approach of Bar Sinai et al. (*Geophys Res Lett* 39, 2011) a one-dimensional simulation model is built up based on the contact state evolution of a representative brake pad and disc couple. This model is used to describe the interface dynamics while taking into account the surrounding simplified loading geometry. Parallel to this approach an experimental setup with a simplified disc brake is built up. As the simulation model allows to predict the level of the average static friction coefficient for different load cases, the simple test setup allows a validation. The experimental results show that the static friction coefficient can be systematically changed by modification of the loading geometry while one still observes the perturbing influence of uncontrolled process parameters.

Keywords Friction • Vibration • Brake • Creep groan • Coefficient of friction

Nomenclature

G	Bulk shear modulus
ν	Poisson modulus
μ_0	Interfacial elastic modulus
η	Viscous friction coefficient
f	The steady-state friction coefficient
τ	Shear stress
τ_c	Asperity yielding shear stress
τ^{el}	Elastic shear stress

S. Kruse (✉)
Hamburg University of Technology, Dynamics Group, Hamburg 21073, Germany

Audi AG, Development Foundation Brake, Ingolstadt 85045, Germany
e-mail: sebastian.kruse@audi.de

B. Stingl • J. Hieke • M. Tiedemann
Hamburg University of Technology, Dynamics Group, Hamburg 21073, Germany

A. Papangelo • M. Ciavarella
Politecnico di Bari, Centre of Excellence for Computational Mechanics, Bari, Italy

N. Hoffmann
Hamburg University of Technology, Dynamics Group, Hamburg 21073, Germany

Imperial College London, Dynamics of Machines and Structures Group, London SW7 2AZ, UK

τ^{vis}	Shear stress related to the velocity of sliding v
ρ	Density of material
σ_H	Hardness of the material
φ	State variable
A	Ratio of real contact area
D	Typical size of contact asperities
h	Effective height of asperities
v^*	Reference velocity scale
$\vartheta(^*)$	Step function
u	Displacement in the x direction averaged along y
w	Average slip velocity
v_{BD}	Braking disk velocity
c	Damping constant

15.1 Introduction

15.1.1 Motivation

Friction induced vibration is a challenge in brake system design for decades already. Besides the mainly discussed issue of brake squeal [1] there are different types of brake noises that cause customer complaints. One of these types is low frequency creep groan situated in a frequency range between 100 and 500 Hz [2].

Creep groan occurs due to friction induced vibration based on stick slip cycles. The phenomenon stems from a difference in static and dynamic coefficient of friction for the frictional contact between brake disc and brake pad [1]. The occurring stick-slip oscillation leads to vibrations and noise in the vehicle. The phenomenon of creep groan typically occurs, when the driver slightly lifts of the brake pedal with an automatic gear box or at a downward slope in a neutral gear position. The phenomenon usually becomes most severe when the brake system is cold and there is a high level of humidity. These outer conditions lead to a maximum difference between static and dynamic coefficient of friction and hence to a high level of creep groan.

There is a vast amount of literature dealing with friction induced vibrations due to a reoccurring change of a friction interface's contact state from slipping to sticking. Stick-slip phenomena are well known and discussed in many textbooks as an example for friction induced oscillations [3]. Besides very general works there is some literature dealing with stick-slip oscillations leading to creep groan in brakes. There are basically three main groups of literature analyzing creep groan in brake systems. The first group deals with the detection and quantification of creep groan. Most works in this group discuss measurement and quantification methods for creep groan [4–10]. Most approaches attach accelerometers to single components of the brake and use their signals to describe and analyze the level of creep groan in detail. The second group of literature deals with the modeling of creep groan. These works deal rather with different small dynamical models and varying friction laws for a better understanding of underlying mechanisms [5, 11–13] or they describe an approach to simulate creep groan [10, 14, 15]. Eventually, a third group of literature deals with factors contributing to creep groan and with measures to influence the occurrence of this phenomenon in brake systems [6, 10, 16–18]. These works mainly discuss the influence of frictional material mixtures and contact conditions in the frictional interface on the level of creep groan. The literature generally states that a low level of static coefficient of friction and a friction level changing as little as possible with the speed in the friction interface leads to a lower level of creep groan due to stick-slip oscillations.

Hence, the level of creep groan depends on the level of static coefficient of friction. Recent research in the field of friction dynamics shows that the level of the static coefficient of friction can be influenced by the loading conditions of the frictional interface. Ben-David and Fineberg [19] show with an experimental setup consisting of two polymethyl-methacrylate blocks sliding on each other that an asymmetric loading of the frictional interface can considerably reduce the level of static coefficient of friction. This is due to the fact that the local onset of slip in a frictional interface depends on the local values of shear τ and normal stresses σ . Hence, a change of loading does also change the onset of slip and thus the static coefficient of friction μ_s . However, based on the literature on creep groan in brake systems, a change of static coefficient of friction should also change the level of creep groan.

A detailed investigation of the level of static coefficient of friction and its relation to the loading conditions on a brake setup has not been undertaken yet. Moreover, the necessary investigation on static loading conditions and the level of creep groan has not been analyzed, neither in simulation nor in experiment.

Hence, this work tries to close this gap in literature by modeling brake creep groan dynamics with the help of a rate and state dependent frictional model and explores the influence of loading conditions on the onset of slip. Key parameters to influence the static coefficient of friction are identified. Based on these parameters a simple experimental setup based on a commercial vehicle brake system is used in order to validate the simulation results.

15.1.2 Structure

This work starts out by describing the dynamics of the minimal model used for the simulation study. Key parameters influencing the loading conditions are varied and these parameters' influence on μ_S is presented. Subsequently the experimental setup is presented and the methods to determine μ_S from the experiment are discussed, including statistical methods due to a natural spread in the measurements of coefficient of friction. Based on the simulation results key variations of the loading conditions are experimentally investigated and their influence on the static coefficient of friction is analyzed. Eventually, conclusions and outlook discuss this work's impact on future measures to reduce the level of creep groan in brake systems.

15.2 Simulation Model and Results

This section introduces a simple simplified brake model and presents the most important results that show the influence of external loading conditions on the static coefficient of friction μ_S .

15.2.1 Model

The explored model is chosen to be as simple as possible while representing the main dynamics of a coupled brake pad and brake disc that can be used to influence the interface loading conditions. The one-dimensional model is shown in Fig. 15.1.

As it is known that the frictional behavior of a brake is dominated by the brake pad's characteristics, all other components are modeled as simplistic as possible. Hence, the model is based on a rigid brake disc with a finite driving velocity, that is used to control the speed in the frictional interface. The brake pad's backing plate is assumed to be rigid as well. The backing plate is in frictionless contact with a rigid support. As this support allows for positive and negative contact forces this model does not take the difference between a pushed and a pulled pad into account. The dynamics of the caliper and the suspension system are neglected as this work is focusing on the detachment process only. To study complete stick slip cycles the model can easily be extended to take simplified structural dynamics into account.

In contrast to the remaining components the brake pad is modeled using methods of continuum mechanics. The displacement field u_x and u_y of the friction material is given in the inertial (x,y) frame with the origin in the center of the pad disc interface.

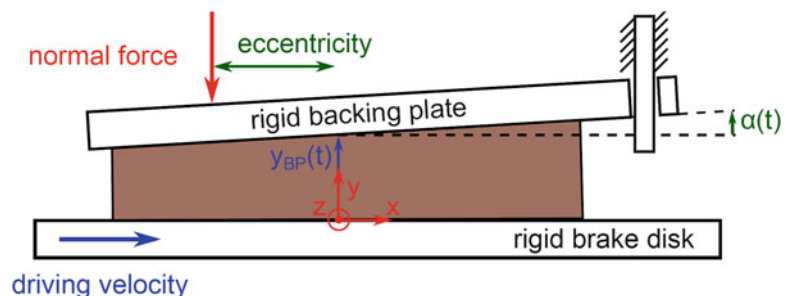


Fig. 15.1 Minimal model employed in simulation study

Assuming a linear isotropic pad material and plain strain conditions the equation of motion of the brake pads material becomes

$$\begin{aligned} \rho H \frac{\partial w(x,t)}{\partial t} &= \frac{2G}{1-\nu} H \frac{\partial^2 u(x,t)}{\partial x^2} \left(1 + \frac{\nu^2}{1-2\nu}\right) \\ &+ G\alpha(t) \left(1 + \frac{2\nu}{1-2\nu}\right) - \frac{2Gu(x,t)}{H} \\ &+ \tau_{fric}(x,t) - cw(x,t) \end{aligned}$$

by averaging the x -momentum balance over the pad height and neglecting the dynamics in the vertical direction. In this equation H describes the height of the brake pad, ρ describes its' density, G represents the bulk shear modulus and ν the pad's Poisson's ratio, while c describes the brake pad's damping constant. $\alpha(t)$ describes the angle of the pad with respect to the rigid brake disc. Eventually, $w(x,t)$ is the average slip velocity of the brake pad. $\tau_{fric}(x,t)$ is part of the description of the friction law as described in detail consequently.

In this work, we assume a rate-and-state dependent friction model, known as Bouchbinder friction model. This model is dedicated to model slow slip rupture phenomena in frictional interfaces. It takes the elastic asperity deformation and changes of the contact area into account. The velocity strengthening branch of the friction force originally included in the model is left out as there is no evidence for this effect in friction materials. This model is introduced and described in [20]. The utilized friction law in the reference system of the pad

$$w(x,t) = \frac{\partial u(x,t)}{\partial t}$$

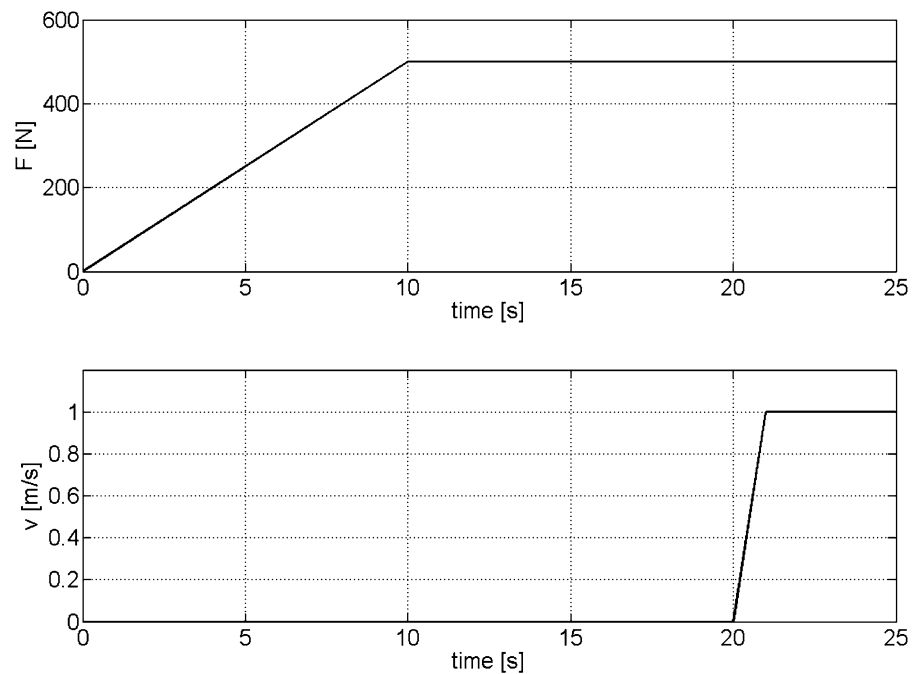
is described by the following equations.

$$\begin{aligned} \frac{\partial \tau_{fric}}{\partial t} &= \frac{\mu_0 A}{h} v_{rel} - \frac{\tau^{el} |v_{rel}|}{D} \vartheta \left(\frac{|\tau|}{A} - \tau_c \right) \\ \frac{\partial \varphi}{\partial t} &= 1 - \frac{\varphi |v_{rel}|}{D} \vartheta \left(\frac{|\tau|}{A} - \tau_c \right) \\ A(\sigma_{yy}, \varphi) &= A_0 \left[1 + b \ln \left(1 + \frac{\varphi}{\varphi_0} \right) \right] \\ A_0 &= \left. \frac{|\sigma_{yy}|}{\sigma_H} \right|_{x,0,t} \\ \sigma_{yy}|_{x,0,t} &= \frac{2G}{1-2\nu} \left[2\nu \frac{\partial u(x,t)}{\partial x} + (1-\nu) \frac{(y_{BP} - H + \alpha(t)x)}{H} \right] \\ v_{rel}(x,0,t) &= v_{BD} - \left. \frac{\partial u_x}{\partial t} \right|_{x,0,t} = v_{BD} - 2w(x,t) \end{aligned}$$

Following [20] in these governing equations τ_{fric} describes the frictional stress by elastic asperity deformation in the interface, μ_0 represents the interfacial elastic modulus, A describes the real contact area, h describes the effective height of the asperities, τ^{el} the elastic shear stress, D is the average size of the contact asperities, ϑ is a step function, whereas τ describes the shear stress and τ_c describes the yielding shear stress of the asperities. Moreover, φ describes a state variable, σ_H the hardness of the pad material and v_{BD} the brake disc velocity. The frictional model shall not be presented here in more detail. As stated, for a detailed presentation and motivation of the single parameters the reader is referred to [20].

The loading of the brake pad in normal direction is assumed to be represented by a force on the backing plate that acts in negative y -direction. This force can act at any point on the backing plate such that the loading takes place with a finite eccentricity e . Hence, the equilibrium of the backing plate depends on the force F , the shear and normal stress acting in the pad-backing plate interface, and the reaction force of the rigid support.

Fig. 15.2 Loading of the normal force and velocity of brake disc during simulation



To complete the model equations the vertical and the rotational momentum balance for the backing plate is derived. The brake pad PDE is reduced by spatial discretization using finite differences to a system of ODEs. Equating the friction model pointwise along the interface finally results in a system of ODEs which is integrated using the software package MATLAB with a solver for stiff systems.

This model is used to study the influence of loading conditions on the static coefficient of friction in the next section.

15.2.2 Simulation Results

The simulation results presented consequently are generated following a well defined simulation procedure. The external normal force rises within 10 s to its chosen maximum. After 10 s of resting the rigid disc is accelerated to its maximum velocity within 1 s as shown in Fig. 15.2. Based on the maximum of the frictional shear stress in the interface and the applied level of normal force the macroscopic coefficient of friction is determined. For the next simulation the eccentricity of the normal force is slightly changed and the same simulation is repeated. Hence, for a set of model parameters the influence of the eccentricity of the normal force on the macroscopic coefficient of friction is evaluated.

For the model two simplistic test cases are evaluated that can also be verified during later experiments. The first parameter which is evaluated is the height of the pad H , while the second one is the level of the normal force F .

15.2.2.1 Influence of the Eccentricity and the Height of the Pad on μ_s

In this set of numerical experiments three different pad heights are chosen: 7, 14 and 21 mm. Figure 15.3 shows that the static coefficient of friction increases nearly in a linear manner when the eccentricity increases. This implies that moving the force from the leading to the trailing edge the static friction coefficient becomes higher. This behavior can be explained looking at Fig. 15.1; in fact, the frictional shear stress provides an induced torque on the brake pad that entails such a wedging on the leading zone of the pad. For a positive eccentricity the friction induced torque is partially compensated and a more homogeneous pressure distribution in the interface can be expected. This observation is consistent with the experimental results in [19]. The friction induced torque can explain even why the slope of the curve is affected by the height of the pad. It is in fact proportional to the height and thus the wedging becomes more important for thicker pads.

Fig. 15.3 Simulation results for static coefficient of friction for varying eccentricities and different heights of the brake pad

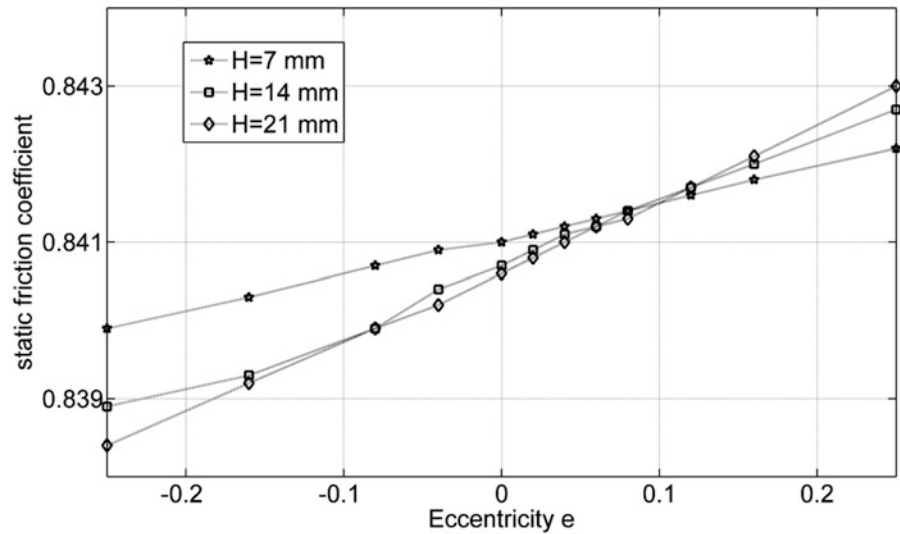
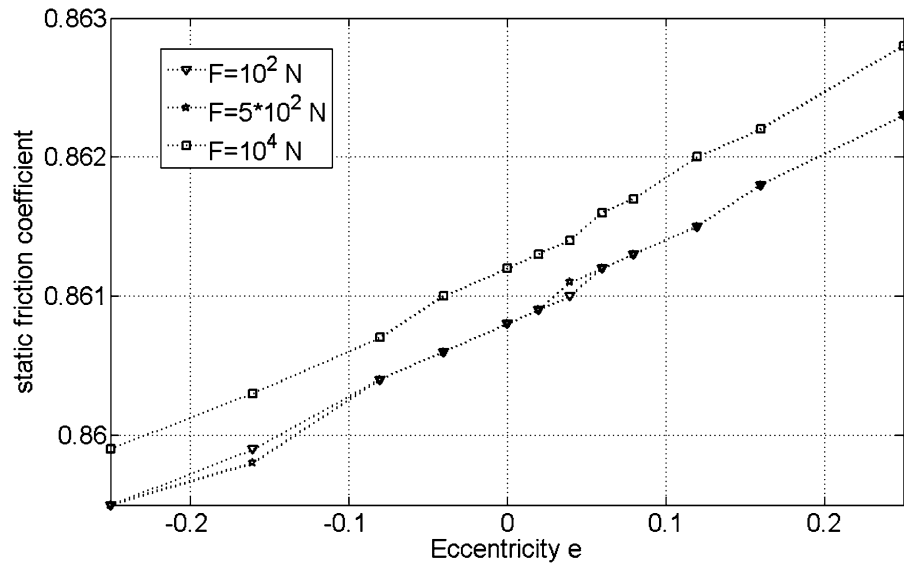


Fig. 15.4 Simulation results for static coefficient of friction for varying eccentricities and different levels of normal force



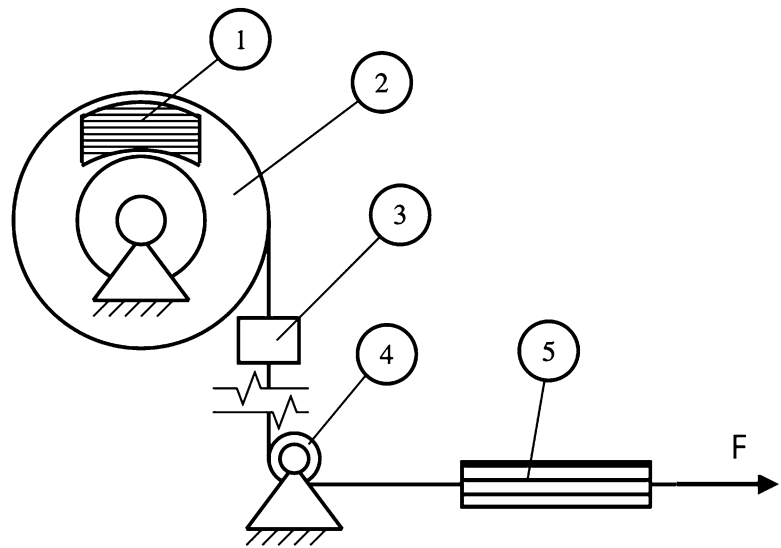
15.2.2.2 Influence of the Level of Normal Force on μ_s

Figure 15.4 presents the results for different levels of normal force. The normal force is varied between 100 and 10,000 N, which is the typical range of normal forces in the brake system. The results show only a small dependency of the normal force on coefficient of friction. This result is due to the strength limit of the asperities which is proportional to the real area of contact. The contact area itself is—neglecting the aging which only depends on time—proportional to the contact pressure and hence the normal force.

15.3 Experimental Setup and Results

In order to prove the validity of the simulation results an experimental setup based on an commercial brake system was built up. This section introduces the test rig and the experimental methods and provides the results.

Fig. 15.5 Schematic concept of test rig for the experimental determination of static coefficient of friction. 1 represents the brake pad, 2 the brake disc, 3 the force sensor, 4 the pulley for the steel wire, 5 an elastic spring



15.3.1 Setup

The used test setup consists of a knuckle including hub and bearing, a brake carrier, a brake disc and two brake pads. These parts stem from a passenger car brake produced for a serial vehicle. Instead of the brake caliper the normal force is applied via two bar clamps. These bar clamps are employed to adjust the overall force level as well as the eccentricity. The disc is equipped with a steel wire in order to easily apply torque by pulling the wire. Due to the concept of the brake system the pad is pulled in the brake carrier and not pushed.

Signals from accelerometers on the brake pad are used in order to detect the movement of the pads while force sensors are employed to measure the normal force applied via the bar clamps and the driving force applied to the disc. Moreover, pressure sensitive foil is employed to determine the pressure distribution based on the position and the force of the bar clamps. All experiments are executed with the minimal setup shown in Fig. 15.5.

15.3.2 Measurement Routine

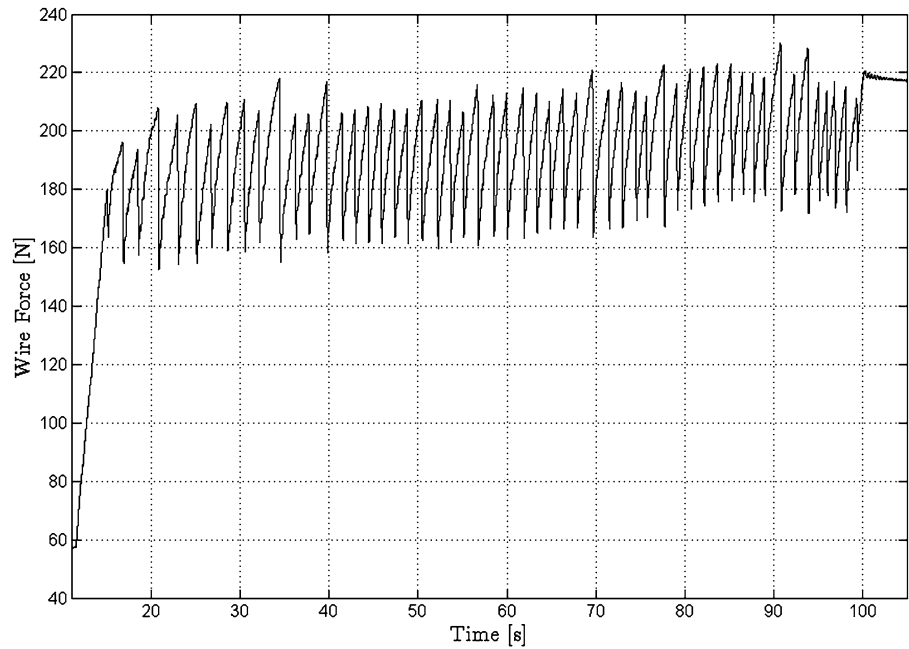
In order to detect the static coefficient of friction for a defined setup of the test rig, a series of measurements is executed. The bar clamps' loading force is set to a value for a fixed eccentricity and a defined level of overall normal force. With the fixed setup the torque in the brake system is raised by pulling on the steel wire until the disc starts rotating. When the disc starts rotating the friction interface dynamics change from a sticking to a sliding state. At the onset of sliding the force in the steel wire is stored. Once the disc starts rotating the system relaxes due to an elastic spring at the end of the steel wire. Hence, the system comes to a rest again and the friction interface changes to a sticking state again.

Each time the system changes from a sticking to a sliding state the force in the steel wire at the instant of the transition from sticking to sliding is stored. For one set of experiments the length of the steel wire allows about 50 transitions from a sticking to a sliding state that are analyzed. For statistical reasons this procedure is repeated several times.

Based on the force at the instant of a change from a sticking to a sliding state and the radius of the brake disc the torque in the system is calculated. With this torque the friction force is calculated using the dynamic friction radius (meaning the radius from the center of the brake disc to the center of pressure in the friction interface) of the system. From the ratio of friction force and normal force determined by the bar clamps the static coefficient of friction is approximated. Figure 15.6 shows an example for the development of the force in the steel wire during one set of experiments.

Based on this procedure the coefficient of friction is determined for different setups. The results are presented consequently.

Fig. 15.6 Development of the wire force during one set of experiments. Peaks in the plot are used to determine the static coefficient of friction



15.3.3 Results

15.3.3.1 Statistic Evaluation of Measurements

Obviously the static coefficient of friction is subject to variation. Hence, statistical methods are needed in order to evaluate the results. This work's goal is to confirm or refute the trends shown by the simplistic simulation model introduced above rather than detecting the exact evolution of the coefficient of friction. For the latter, the test conditions would need to be monitored and kept constant with a higher effort since it is known that influences like temperature in the friction interface or humidity of the surrounding air have a considerably large influence on the coefficient of friction.

Hence, statistical methods are chosen in order to show that differences in the average of the coefficient of friction based on a series of measurements are systematic and not random. In order to prove the trends in the developments of coefficient of friction, Pearson's correlation coefficients are employed which indicate the correlation of the loading conditions to the static coefficient of friction. Moreover, p-values based on the Student's *t*-test [21] are used in order to prove statistically that measured differences are statistically significant and not random. The p-values are employed to reject the Null Hypothesis that measured data is scattered randomly as they represent the probability that the null hypothesis is true.

15.3.3.2 Influence of the Eccentricity of the Pad on μ_s

To show the influence of the eccentricity on the coefficient of friction the above setup with an overall but constant force level of 400 N is employed. By changing the force ratio of the two bar clamps the eccentricity is changed in three steps. The used relative eccentricity is defined depending on the leading and trailing clamp forces, F_L and F_T , as

$$e = \frac{F_T - F_L}{F_T + F_L} \cdot \frac{d_c}{l_p}$$

with d_c describing the distance of the clamps and l_p being the overall length of the pad. The result are shown in Fig. 15.7.

The results indicate that the static coefficient of friction grows with a growing eccentricity. In the set of experiments the coefficient of friction can be changed about 5.8 % on average by a manipulation of the eccentricity. The low p-value proves results to be statistically significant.

Fig. 15.7 Experimental average values for static coefficient of friction for varying eccentricity at an overall force level of 400 N. *Error bars* indicate standard deviations. The data is based on 708 measurement points. The correlation of the static coefficient of friction and the eccentricity is characterized by a Pearson's coefficient of correlation of 0.34. The null hypothesis of randomly scattered data can be rejected based on a p-value of $2.9e-21$. This proves results to be statistically significant

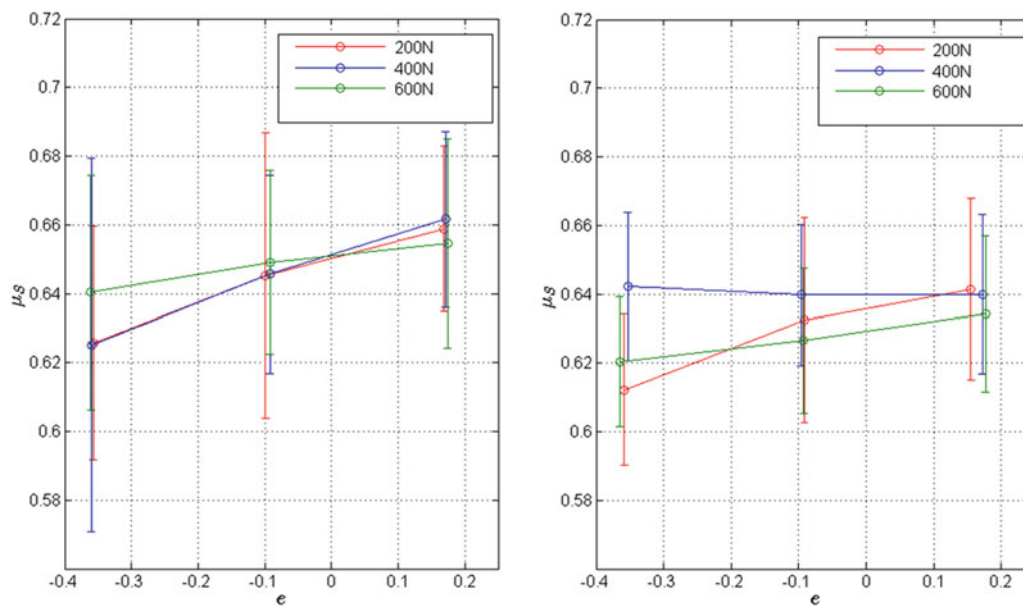
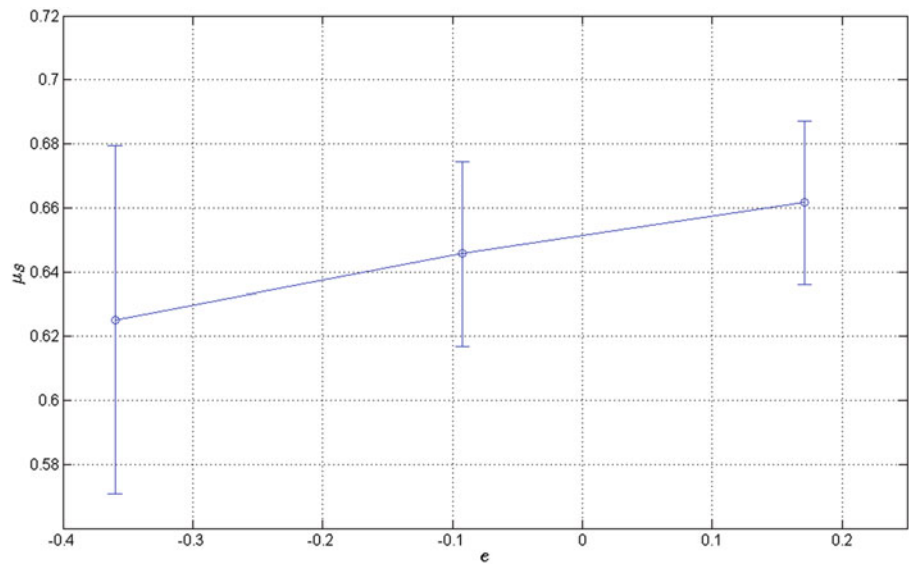


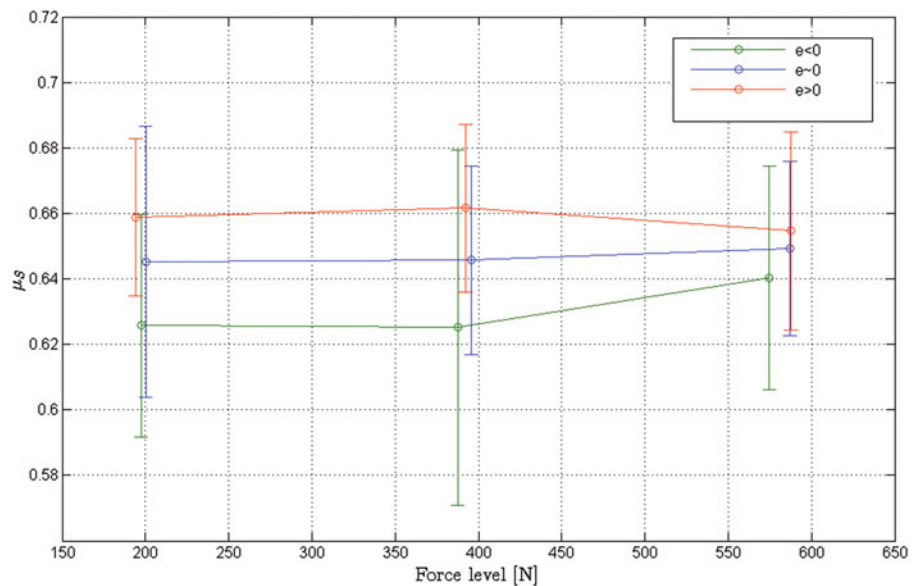
Fig. 15.8 Development of the static coefficient of friction for varying eccentricities for a low pad thickness on the left and a high pad thickness on the right. *Circles* represent average values and *error bars* indicate standard deviations. The data is based on 2,265 measurement points for the thin brake pad and 1,229 for a thick brake pad. Correlation of static coefficient of friction and eccentricity can be characterized by Pearson's coefficients of correlation between 0.19 and 0.36 for the different force level for the thin pad and Pearson's coefficients of correlation between -0.04 and 0.42 for the different force level for the high pad. p-values are between $1.4e-36$ and $6.9e-5$ for the thin brake pad and between $9.3e-31$ and 0.35 for the thin brake pad

15.3.3.3 Influence of the Eccentricity and the Height of the Pad on μ_s

In order to evaluate the influence of the pad height on the efficiency of an eccentricity changing the coefficient of friction the above introduced experiment is executed with the same pad but the point of support is raised by about 10 mm. Hence the same test series as performed above is executed with a thicker brake pad. Moreover, overall force levels form 200, 400 and 600 N are taken into account. Again, the eccentricity is manipulated by the distribution of the force on the two bar clamps. Figure 15.8 shows the results.

The results indicate that the influence of the eccentricity on the static coefficient of friction becomes weaker with a higher brake pad thickness (meaning a raise of the point of support of the frictional force). While results are very consistent for different force levels for a thin brake pads, the trend becomes much weaker for the thicker brake pad. Especially the

Fig. 15.9 Development of the static coefficient of friction for different levels of normal force and eccentricity. *Circles* represent average values while *error bars* indicate standard deviations. The data is based on 2,265 measurement points. The correlation of static coefficient of friction and normal force is characterized by Pearson's coefficient of correlation of 0.08 for a negative eccentricity, 0.02 for an eccentricity close to zero and -0.05 for a positive eccentricity. p-values are 0.01 for negative eccentricity, 0.44 for an eccentricity close to zero and 0.18 for a positive eccentricity. The Null hypothesis of randomly scattered data cannot be rejected with a high probability



consistency of different force levels becomes weaker. For the thinner pad the coefficient of friction can be changed about 4.3 % on average while it can only be changed about 1.6 % in average for the thicker brake pads. Especially for the force level of 400 N no growing static coefficient of friction can be observed when the eccentricity is growing. Hence, for the thick brake pads there is nearly no rise in the coefficient of friction remaining for a rising eccentricity.

15.3.3.4 Influence of the Level of Normal Force on μ_s

Eventually, the influence of the force level on the coefficient of friction is analyzed. Hence, the experiment for the thinner brake pads is plotted over the different overall force levels of 200, 400 and 600 N of normal force. The experimental data is the same as used for the experiments in the previous chapter. The results are shown in Fig. 15.9.

The result indicates no clear systematic difference regarding a change of the force level. For all three sets of the overall force level there is no clear trend for the development of the static coefficient of friction. This observation is supported by the low values for Pearson's coefficient of correlation as well as by the high p-values. Hence, the observed changes seem to be rather randomly induced due to non controlled parameters in the measurement setup.

15.4 Comparison of Test and Simulation

This section will provide a short comparison of results shown in the simulation and results from the experimental setup. However, the comparison has a qualitative manner due to the strong simplification of the simulation and the rather complex experimental setup. Moreover, simulation results are repeatable while experimental results are object to variation. Generally, it needs to be mentioned that there will be an influence of uncontrolled variables such as temperature or humidity in the experimental setup.

15.4.1 Influence of the Eccentricity of the Pad on μ_s

The comparison of simulation and experiment confirms results from literature motivating this research [19] and transfers them to a real world technical system. An eccentricity of the loading conditions influences the static coefficient of friction. A rising eccentricity—meaning a distribution of force showing a stronger loading of the leading edge of the pad—leads to a rising static coefficient of friction. However, the influence seems to be rather small. The simulation model shows change of only 0.6 % for the maximum pad height, whereas the experimental setup indicates a change between 4.3 and 1.6 % depending on the pad's thickness or the height of the support of the frictional force in the brake carrier.

15.4.2 Influence of the Eccentricity and the Height of the Pad on μ_s

Simulation results show that the height of the brake pad influences the efficiency of a manipulation of the static coefficient of friction by the eccentricity of loading. A lower height of the pad reduces the influence of the eccentricity on the static coefficient of friction. The influence of the pad height on the development of the static coefficient of friction is verified by the experiment. However, the influence of the brake pad's height shows opposed character comparing simulation and experiment. While a higher thickness of the pad maximizes the influence of the eccentricity on the static coefficient of friction, the influence of the eccentricity is reduced in the experimental setup with a growing pad thickness. Based on this observation it seems that the simplistic model is not able to correctly represent the experimental setup in the fashion of an analysis of the brake pad's height. There seem to be systematic differences that are not represented in simulation. These differences might be determined by the strong simplification of the pad continuum dynamics. The tangential degree of freedom is reduced to a 1D approximation and the vertical behavior is taken into account only statically. Therefore the model does not incorporate potential lift off at the trailing edge. Results indicate that lift off at the trailing edge—especially for negative eccentricities or larger pad heights—is crucial for the onset of the detachment process. This might explain why simulation and experiment compare better for lower pad heights.

15.4.3 Influence of the Level of Normal Force on μ_s

In the simulation setup the influence of the level of normal force seems to be negligible and does not influence the level of static coefficient of friction considerably. This seems to hold true for the experimental investigation as well.

15.5 Summary and Conclusions

This work analyses the influence of the loading conditions on the static coefficient of friction in a brake like system. The correlation of the static coefficient of friction and the loading conditions are examined by a small simulation model as well as an experimental setup based on a commercial brake of a passenger car.

Results indicate that the loading conditions influence the static coefficient of friction. Whereas the overall level of normal force seems not to have a considerable influence on the static coefficient of friction, the eccentricity of the loading can be used to manipulate the static coefficient of friction. Hence, the conditions for a change of a sticking state to a sliding state of a friction brake can be manipulated without a change of the employed components or the friction material.

To the authors' knowledge, this work is the first to provide a numerical confirmation of the frictional behavior observed in Fineberg's experiments [19]. However, experimental values indicate a much stronger variability of friction than the numerical results suggest, and this is in line with Fineberg's experiments [19]. The developed model shows the same general trends and the authors are unaware of any more sophisticated model which would provide a better agreement. Obviously, the employed model is just 1D, which will be extended in a next step.

The observed effect of loading conditions on the static coefficient of friction indicates that the eccentricity of loading can be used to manipulate the criticality of creep groan in an existing brake systems. Hence, results will be carried over to a full scale brake system in order to evaluate the influence of an external loading to the level of creep groan. This may lead to a new measure to reduce creep groan in passenger cars. Moreover, a more thorough understanding of the underlying effects needs to be gained by a deeper analysis of simulation results and the microscopic friction dynamics. Eventually, a test setup will be developed which is able to control more variables of the system and also to monitor these more efficiently in order to reduce variability of results and to be able to get more exact data from the experimental setup.

References

1. Kinkaid NM, Reilly OM, Papadopoulos P (2003) Automotive disc brake squeal. *J Sound Vib* 267(1):105–166
2. Breuer B, Bill KH (2006) *Bremsenhandbuch 3*. Vieweg Verlag, Wiesbaden
3. Magnus K, Popp K (2005) *Schwingungen: eine Einführung in physikalische Grundlagen und die theoretische Behandlung von Schwingungsproblemen*. Teubner, Stuttgart
4. Jung T, Chung S (2012) Research for brake creep groan noise with dynamometer. SAE Paper

5. Abdelhamid MK, Bray W (2009) Braking systems creep groan noise: detection and evaluation. SAE Paper
6. Okayama K, Fujikawa H, Kubota T, Kakihara K (2005) A study on rear disc brake groan noise immediately after stopping. SAE Paper
7. Crowther AR, Yoon J, Singh R (2007) An explanation for brake groan based on coupled brake-driveline system analysis. SAE Paper
8. Fuadi Z, Maegawa S, Nakano N, Adachi K (2010) Map of low-frequency stick-slip of a creep groan. SAE Paper
9. Bettella M, Harrison MF, Sharp RS (2002) Investigation of automotive creep groan noise with a distributed-source excitation technique. *J Sound Vib* 255(3):531–547. <http://www.sciencedirect.com/science/article/pii/S0022460X01941781>
10. Brecht J (2000) Untersuchungen zum Bremsenknarzen – Ein Beitrag zur Beschreibung von Schwingungen in Bremssystemen. Shaker Verlag, Aachen
11. Crowther AR, Singh R (2007) Analytical investigation of stick-slip motions in coupled brake-driveline systems. *Nonlinear Dyn* 50(3):463–481
12. Zeng J, Luo R (2011) Non-linear analysis of disc brake-induced vibrations for railway vehicles. *Proc Inst Mech Eng, Part F: J Rail Rapid Transit* 225(1):48–56
13. Hetzler H, Seemann W (2004) Brake vibrations at very low driving velocities. *PAMM* 4(1):87–88
14. Brecht, Schiffner (2001) Influence of friction law on brake creep-groan. SAE Paper
15. Vadari, Jackson (1999) An experimental investigation of disk brake creep-groan in vehicles and brake dynamometer correlation. SAE Paper
16. Kim JK, Lee CK, Kim SS (2004) Investigation on correlation between groan noise and coefficient of friction with friction material's difference. *SAE Trans* 113:462–471
17. Jang H, Lee JS, Fash JW (2001) Compositional effects of the brake friction material on creep groan phenomena. *Wear* 251(1):1477–1483
18. Fuadi Z, Adachi K, Ikeda H, Naito H, Kato K (2009) Experimental model for creep groan analysis. *Lubr Sci* 21(1):27–40
19. Ben-David O, Fineberg J (2011) Static friction coefficient is not a material constant. *Phys Rev Lett* 106
20. Bar Sinai Y, Brener E, Bouchbinder E (2011) Slow rupture of frictional interfaces. *Geophys Res Lett* 39
21. Sachs L (1974) *Angewandte Statistik*. Springer, Berlin

Chapter 16

Linear Superposition and Modal Participation

Brian J. Schwarz and Mark H. Richardson

Abstract Modes of vibration are defined as solutions to a set of linear differential equations which characterize the resonant dynamic behavior of structures. One of the properties of these linear equation solutions is *superposition*. That is, the overall structural response can be represented as a *summation* of contributions from all of the modes.

In this paper, it is shown how the superposition property of mode shapes can be used to;

- Decompose a set of Operating Deflection Shapes (ODS's) into a summation of mode shape contributions.
- Expand a set of shapes using another set of shapes with more DOFs in them.
- Decompose a set of frequency or time domain waveforms into a summation of resonance waveforms.
- Scale a set of operational mode shapes or ODS's so they can be used as a modal model for modeling & simulation studies.
- Derive the Modal Assurance Criterion (MAC) as a measure of the correlation between a pair of shapes.

All of these applications lend more meaning to the term *modal participation*, which is commonly used to characterize structural vibration as a summation of resonant contributions. This new definition of *modal participation* is illustrated with several examples.

Keywords Operating deflection shapes (ODS's) • Experimental modal analysis (EMA) mode shapes • Finite element analysis (FEA) mode shapes • Modal assurance criterion (MAC)

16.1 Introduction

When all excitation forces are removed from a structure, its resonant vibration response is characterized by a time domain *decaying sinusoidal waveform*, as shown in Fig. 16.1. This resonant response can be modeled as a *summation of contributions* due to each of the structure's resonances. Each resonant contribution is itself modeled with a *decaying sinusoidal* waveform. The frequency of each resonant response is invariant unless the physical properties or boundary conditions of the structure change. Each resonant frequency is therefore called a *natural frequency* of the structure.

The decay envelope of each resonant response is modeled with a decreasing exponential function, and the coefficient in the exponential term is called the *damping decay constant*.

A mode of vibration is a *compact mathematical description* of a structural resonance. Not only are modal parameters solutions to a set of differential equations, but they are also used to model the resonant vibration of a real structure, assuming that it behaves in a linear dynamic manner.

The natural frequency of each structural resonance is also called its *modal frequency*. Likewise, the damping decay constant of a resonance is also called its *modal damping coefficient*. This damping is also called the *half power point* or *3 dB point* damping [4].

B.J. Schwarz • M.H. Richardson (✉)
Vibrant Technology, Inc., Scotts Valley, CA, USA
e-mail: brian.schwarz@vibetech.com; mark.richardson@vibetech.com

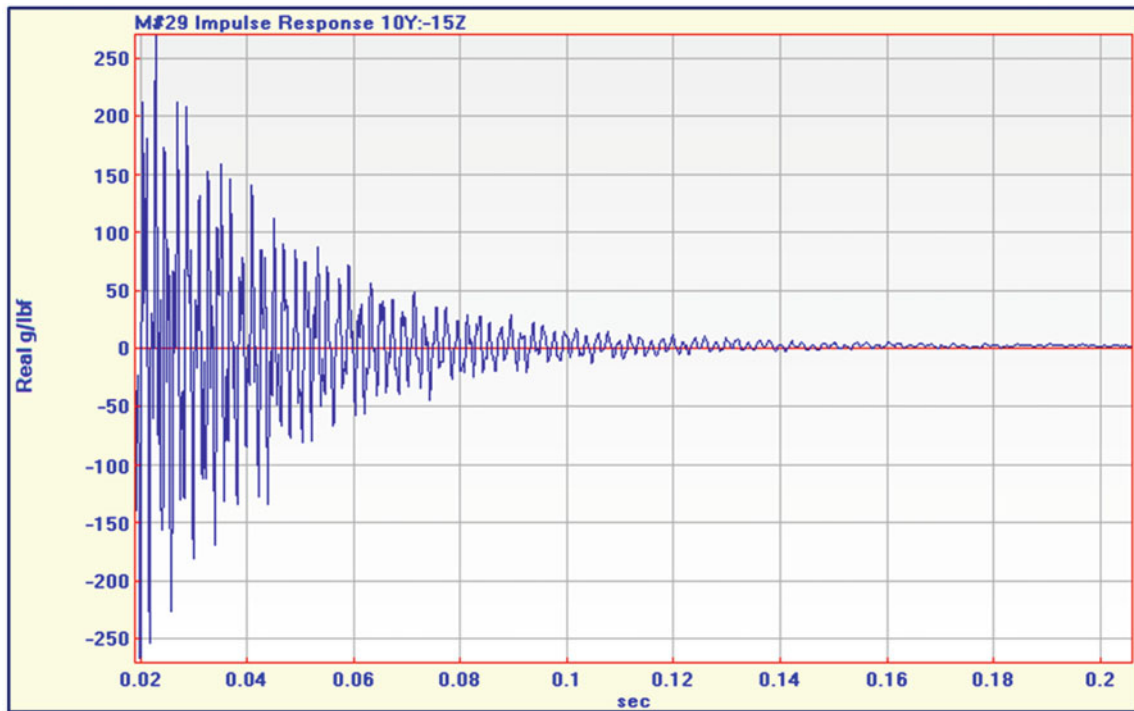


Fig. 16.1 Resonant response after forces removed

16.2 Background

In this paper two different kinds of shapes will be discussed; Operating Deflection Shapes (ODS's) and Mode Shapes.

ODS: The response at a frequency or time value, of *two or more* DOFs on a structure. A DOF is motion at a point in a direction. [5].

Therefore, the values at each frequency sample of a set of frequency domain functions (Auto & Cross spectra, Fourier spectra, FRFs, etc.) *is an ODS*.

Likewise, the values at each sample of a set of time domain functions (Auto & Cross Correlations, Impulse Response Functions, etc.) *is also an ODS*.

Mode Shape: A mode shape can either be an experimental (EMA) mode shape, derived by curve fitting a set of experimentally derived FRFs, or it can be an analytical (FEA) mode shape, an eigenvector calculated as part of an *eigensolution* to a set of linear homogeneous differential equations that model the dynamics of a structure [6].

16.2.1 Equating Two Sets of Shapes

Two sets of complex valued shapes can be assembled into two matrices ([**U**] & [**V**]), where *each column* of each matrix contains a shape. The shapes in matrix [**U**] can be thought of as *un-scaled* shapes, and the shapes in matrix [**V**] as *scaled* shapes. The two shape matrices can be equated to each other with the following matrix equation,

$$[U][W] = [V] \quad (16.1)$$

[**V**] = matrix of **scaled** complex shapes

[**U**] = matrix of **un-scaled** complex shapes

[**W**] = matrix of **complex scale factors**

Writing out the matrices in terms of their components,

$$\begin{bmatrix} u_{1,1} & \cdots & u_{1,n_u} \\ \vdots & \ddots & \vdots \\ u_{m,1} & \cdots & u_{m,n_u} \end{bmatrix} \begin{bmatrix} w_{1,1} & \cdots & w_{1,n_s} \\ \vdots & \ddots & \vdots \\ w_{n_u,1} & \cdots & w_{n_u,n_s} \end{bmatrix} = \begin{bmatrix} v_{1,1} & \cdots & v_{1,n_s} \\ \vdots & \ddots & \vdots \\ v_{m,1} & \cdots & v_{m,n_s} \end{bmatrix}$$

(m by n_u) (n_u by n_s) (m by n_s)

n_u = number of **un-scaled** shapes

n_s = number of **scaled** shapes

m = number of **matching shape DOFs** or shape components

16.2.2 Least-Squared-Error Solution

Equation (16.2) below is the least-squared-error solution of Eq. (16.1). In addition to requiring a matrix inverse, the other requirement for a solution is that the two matrices [U] & [V] have *at least some matching shape DOFs*, or shape components.

$$[W] = \left[[U]^h [U] \right]^{-1} [U]^h [V] \quad (16.2)$$

h denotes the *transposed conjugate* matrix

-1 denotes the *inverse* matrix

16.3 Modal Participation Factors

When [U] is a matrix of mode shapes, and [V] is a matrix of ODS's, then *each column* of the scale factor matrix [W] is a measure of how much each mode shape *contributes* to or *participates* in each ODS. If [W] is a diagonal matrix (with *non-zero diagonals* and zeros everywhere else), then each ODS is being *dominated* by a *single* mode shape.

16.3.1 Example #1: Mode Shapes Dominating ODS's

For this example, ODS's of the Jim Beam structure shown in Fig. 16.2 were obtained by *saving the cursor values* at each resonance peak in the *imaginary part* of a set of experimental FRFs.

Figure 16.3 shows the imaginary parts of the FRFs overlaid on one another.

The FRFs were acquired from an impact test of the Jim Beam structure. The beam was impacted at point 15 in the vertical (Z) direction, and a tri-axial accelerometer was roved to the 33 different (numbered) points on the beam. An FRF was calculated between the impact force applied at DOF (15Z) and each of the resulting acceleration responses (3 DOFs at each Point). The ODS's taken as the resonance peak values of the 99 FRFs are listed in Fig. 16.4.

An FEA model of the Jim Beam structure was also built and solved for its mode shapes, or *eigenvectors* [7]. The FEA mode shapes are listed in Fig. 16.5.

The Jim Beam model was meshed to provide more DOFs before solving for its modes. Hence, the FEA mode shapes had 630 (translational and rotational) DOFs in them, but only 99 matched with the DOFs of the ODS's.

Using these two shape matrices, the scale factor matrix [W] was calculated using Eq. (16.2). Its *magnitudes* are shown in Fig. 16.6.

This matrix is *nearly diagonal*, indicating that each experimentally derived ODS is being *dominated* by an FEA mode shape. In other words, each FEA mode shape is a *close representation* of the spatial amplitude distribution of each structural resonance.

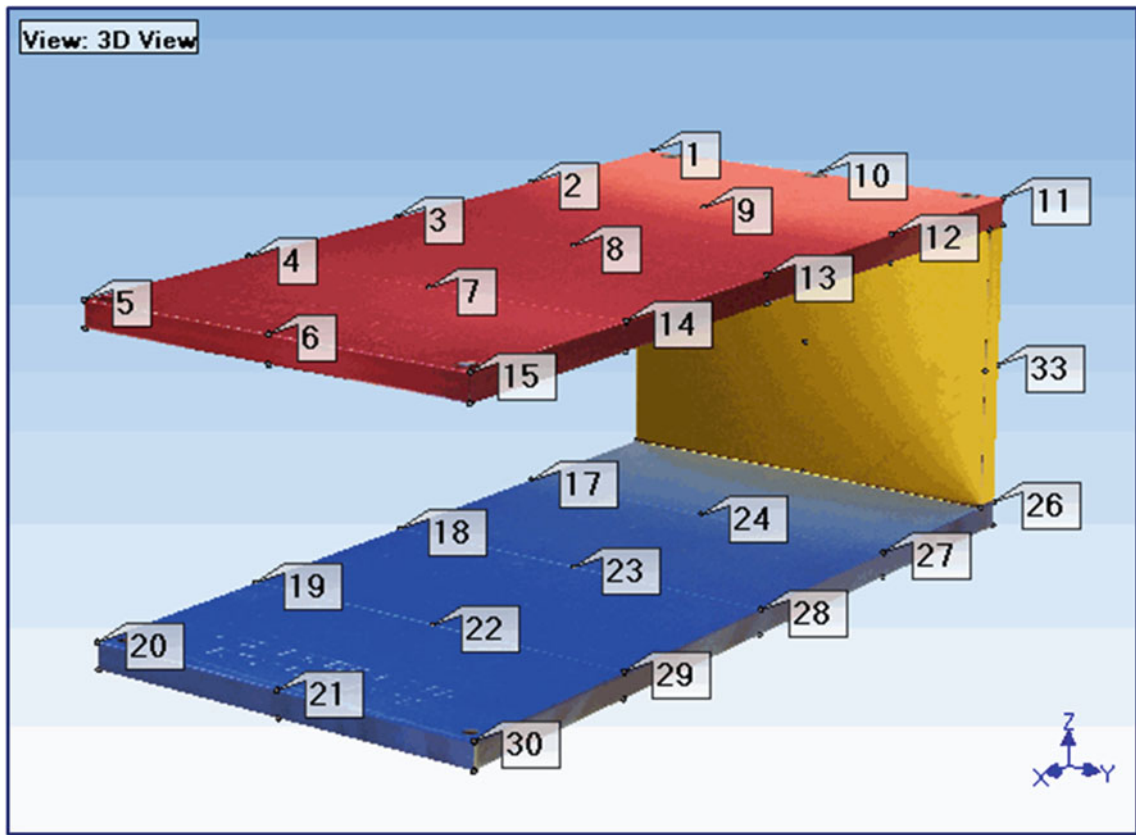


Fig. 16.2 Jim Beam structure

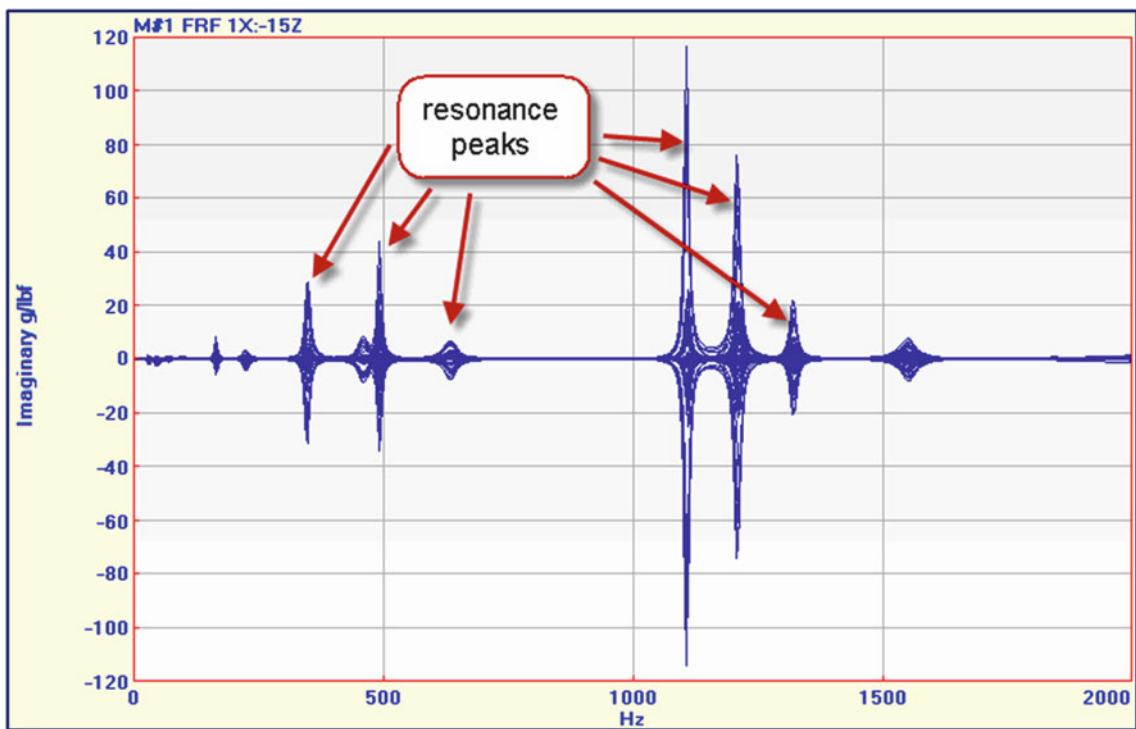
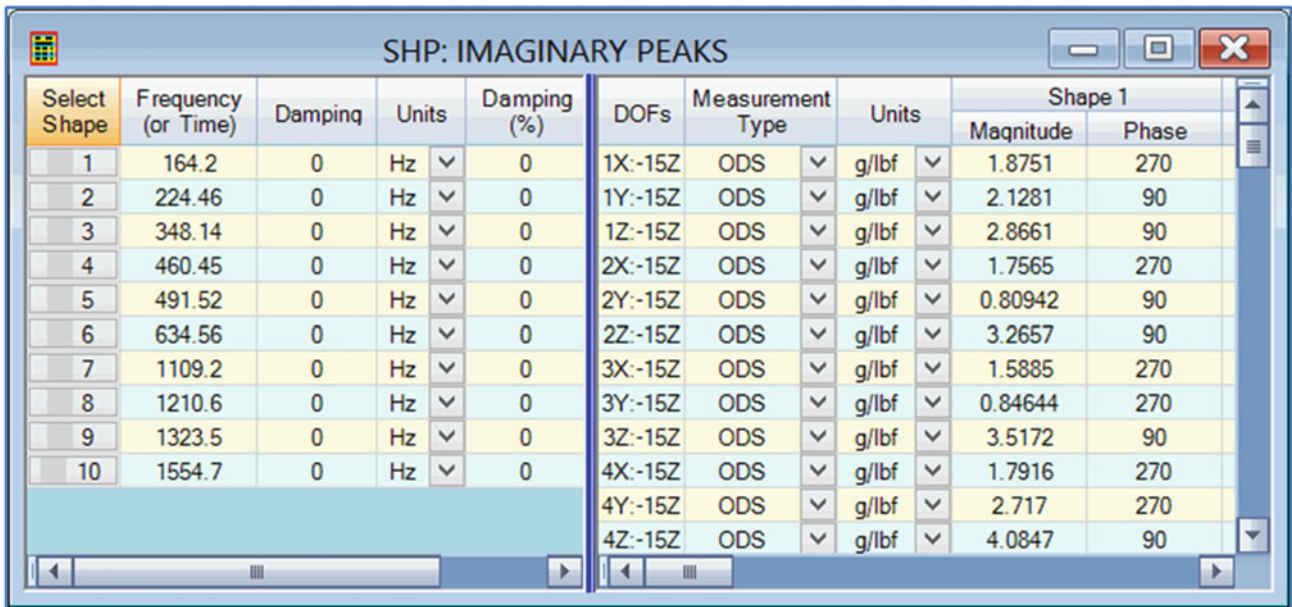
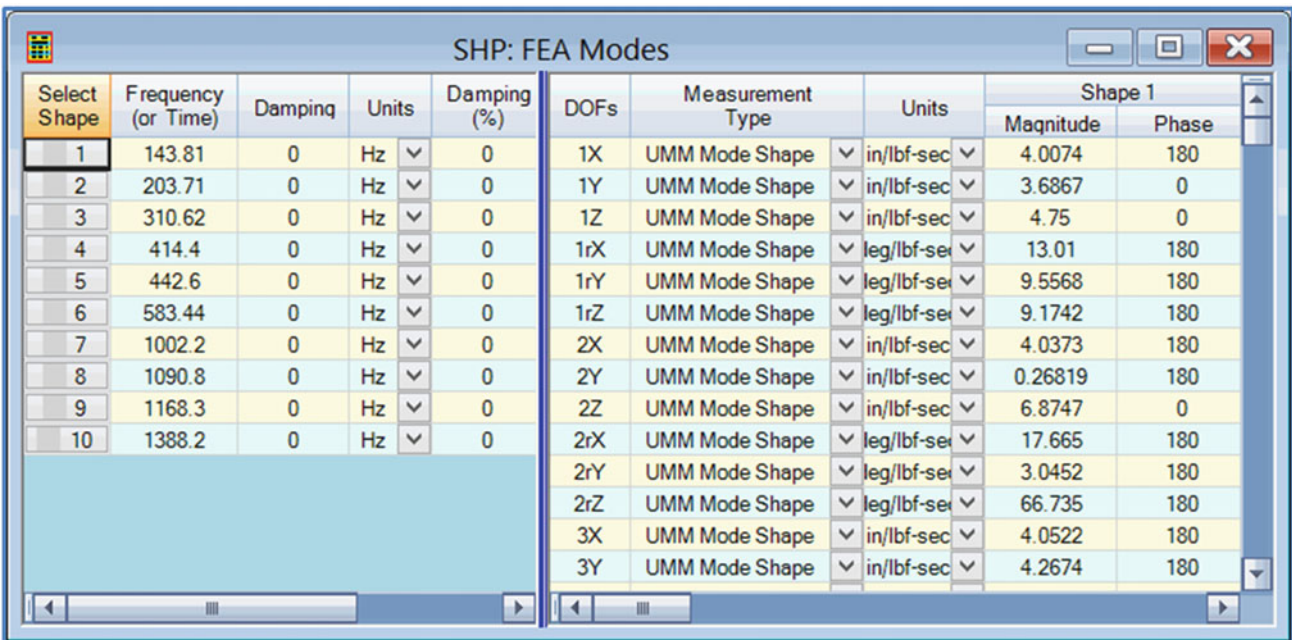


Fig. 16.3 Imaginary parts of FRFs overlaid



Select Shape	Frequency (or Time)	Damping	Units	Damping (%)	DOFs	Measurement Type	Units	Shape 1	
								Magnitude	Phase
1	164.2	0	Hz	0	1X:-15Z	ODS	g/lbf	1.8751	270
2	224.46	0	Hz	0	1Y:-15Z	ODS	g/lbf	2.1281	90
3	348.14	0	Hz	0	1Z:-15Z	ODS	g/lbf	2.8661	90
4	460.45	0	Hz	0	2X:-15Z	ODS	g/lbf	1.7565	270
5	491.52	0	Hz	0	2Y:-15Z	ODS	g/lbf	0.80942	90
6	634.56	0	Hz	0	2Z:-15Z	ODS	g/lbf	3.2657	90
7	1109.2	0	Hz	0	3X:-15Z	ODS	g/lbf	1.5885	270
8	1210.6	0	Hz	0	3Y:-15Z	ODS	g/lbf	0.84644	270
9	1323.5	0	Hz	0	3Z:-15Z	ODS	g/lbf	3.5172	90
10	1554.7	0	Hz	0	4X:-15Z	ODS	g/lbf	1.7916	270
					4Y:-15Z	ODS	g/lbf	2.717	270
					4Z:-15Z	ODS	g/lbf	4.0847	90

Fig. 16.4 Jim Beam ODS's



Select Shape	Frequency (or Time)	Damping	Units	Damping (%)	DOFs	Measurement Type	Units	Shape 1	
								Magnitude	Phase
1	143.81	0	Hz	0	1X	UMM Mode Shape	in/lbf-sec	4.0074	180
2	203.71	0	Hz	0	1Y	UMM Mode Shape	in/lbf-sec	3.6867	0
3	310.62	0	Hz	0	1Z	UMM Mode Shape	in/lbf-sec	4.75	0
4	414.4	0	Hz	0	1rX	UMM Mode Shape	leg/lbf-sec	13.01	180
5	442.6	0	Hz	0	1rY	UMM Mode Shape	leg/lbf-sec	9.5568	180
6	583.44	0	Hz	0	1rZ	UMM Mode Shape	leg/lbf-sec	9.1742	180
7	1002.2	0	Hz	0	2X	UMM Mode Shape	in/lbf-sec	4.0373	180
8	1090.8	0	Hz	0	2Y	UMM Mode Shape	in/lbf-sec	0.26819	180
9	1168.3	0	Hz	0	2Z	UMM Mode Shape	in/lbf-sec	6.8747	0
10	1388.2	0	Hz	0	2rX	UMM Mode Shape	leg/lbf-sec	17.665	180
					2rY	UMM Mode Shape	leg/lbf-sec	3.0452	180
					2rZ	UMM Mode Shape	leg/lbf-sec	66.735	180
					3X	UMM Mode Shape	in/lbf-sec	4.0522	180
					3Y	UMM Mode Shape	in/lbf-sec	4.2674	180

Fig. 16.5 Jim Beam FEA shapes

16.4 Shape Expansion

After a participation matrix [W] has been calculated between the matching DOFs of two shape matrices ([U] & [V]), an expanded set of shapes can be calculated with the following equation,

$$\begin{bmatrix} V_m \\ V_u \end{bmatrix} = \begin{bmatrix} U_m \\ U_u \end{bmatrix} [W] \tag{16.3}$$

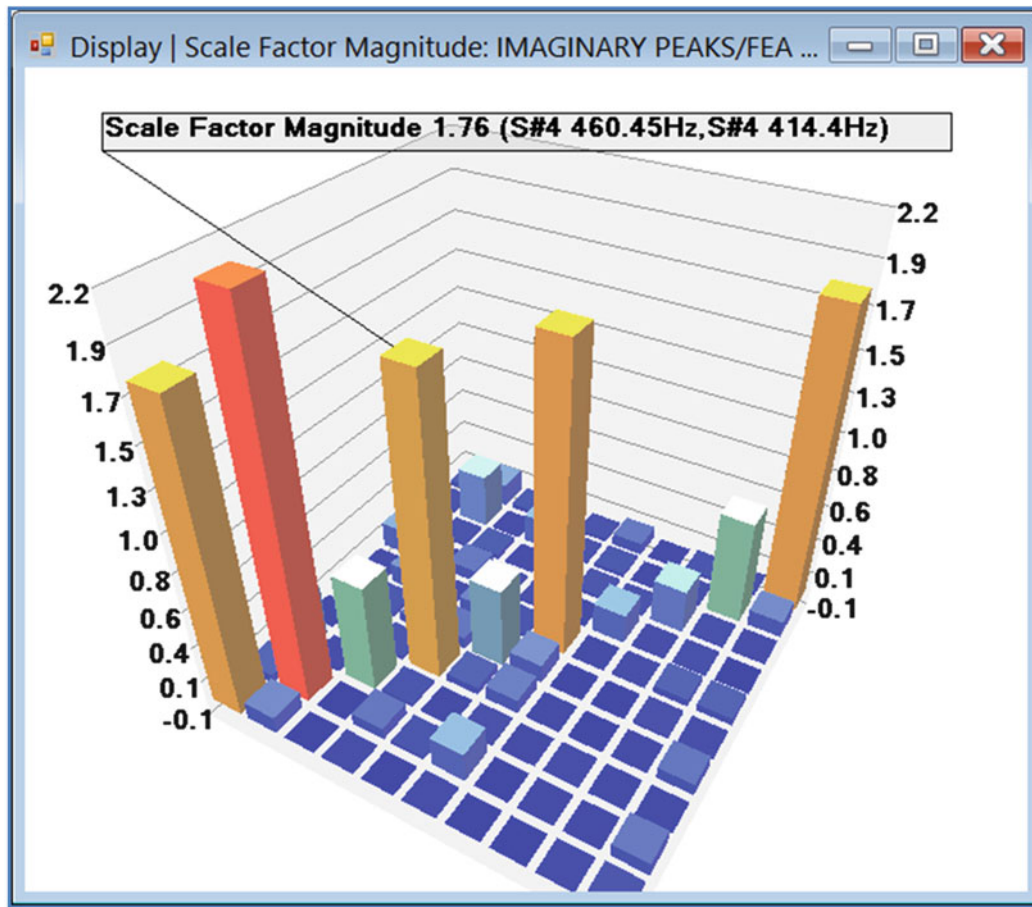


Fig. 16.6 Participation of FEA shapes in Jim Beam ODS's

$[U_m], [V_m]$ = sub-matrices of *matching* shape DOFs

$[U_u], [V_u]$ = sub-matrices of *un-matched* shape DOFs

Equation (16.3) is useful for;

1. Expanding an ODS with a few DOFs in it using a set of mode shapes with more DOFs in them.
2. Expanding a set of EMA mode shapes using a set of FEA mode shapes with more DOFs in them.

16.4.1 Example #2: Expanding EMA Mode Shapes

In some experimental situations, it may not be possible to measure the structural responses at all desired DOFs because some DOFs are inaccessible. However, if a set of FEA mode shapes *correlate well* with the EMA mode shapes at matching DOFs (meaning that the $[W]$ is a *nearly diagonal* matrix), then Eq. (16.3) can be used to expand the EMA mode shapes to include the *un-measured* DOFs.

Figure 16.7 shows the EMA mode shapes of the Jim Beam. These modal parameters were obtained by curve fitting the 99 experimental FRFs acquired during an impact test of the test article. Figure 16.8 is a bar chart of the scaling matrix $[W]$ between the EMA & FEA mode shapes. Because it is *nearly diagonal* it indicates that the FEA mode shapes *correlate one for one* with the EMA mode shapes at the 99 matching DOFs.

Equation (16.3) was then used to solve for the expanded EMA shapes, and the MAC values between the expanded EMA shapes and the FEA shapes are shown in Fig. 16.9. (MAC is discussed in a succeeding section of this paper [1–3].) The MAC values in Fig. 16.9 show that each expanded EMA shape also correlates well (is *co-linear* with) an FEA shape.

SHP: EMA Modes

Select Shape	Frequency (or Time)	Damping	Units	Damping (%)	DOFs	Measurement Type	Units	Shape 1	
								Magnitude	Phase
1	164.95	3.1125	Hz	1.8866	1X	UMM Mode Shape	in/lbf-sec	4.3398	101
2	224.57	6.5228	Hz	2.9033	1Y	UMM Mode Shape	in/lbf-sec	4.297	282.16
3	347.56	5.1556	Hz	1.4832	1Z	UMM Mode Shape	in/lbf-sec	5.8486	282.52
4	460.59	11.501	Hz	2.4963	2X	UMM Mode Shape	in/lbf-sec	4.0502	94.675
5	492.83	4.6426	Hz	0.94198	2Y	UMM Mode Shape	in/lbf-sec	1.6331	276.43
6	635.19	14.247	Hz	2.2425	2Z	UMM Mode Shape	in/lbf-sec	8.4653	281.6
7	1108.3	4.9645	Hz	0.44795	3X	UMM Mode Shape	in/lbf-sec	3.4371	92.988
8	1210.6	7.1298	Hz	0.58894	3Y	UMM Mode Shape	in/lbf-sec	1.9026	94.856
9	1322.7	7.2499	Hz	0.54812	3Z	UMM Mode Shape	in/lbf-sec	8.4476	279.43
10	1555.1	17.112	Hz	1.1003	4X	UMM Mode Shape	in/lbf-sec	3.9866	97.353
					4Y	UMM Mode Shape	in/lbf-sec	6.0798	95.502
					4Z	UMM Mode Shape	in/lbf-sec	8.5708	274.35
					5X	UMM Mode Shape	in/lbf-sec	3.9078	97.921
					5Y	UMM Mode Shape	in/lbf-sec	9.4375	96.119
					5Z	UMM Mode Shape	in/lbf-sec	9.4663	281.56

Fig. 16.7 EMA modes of the Jim Beam

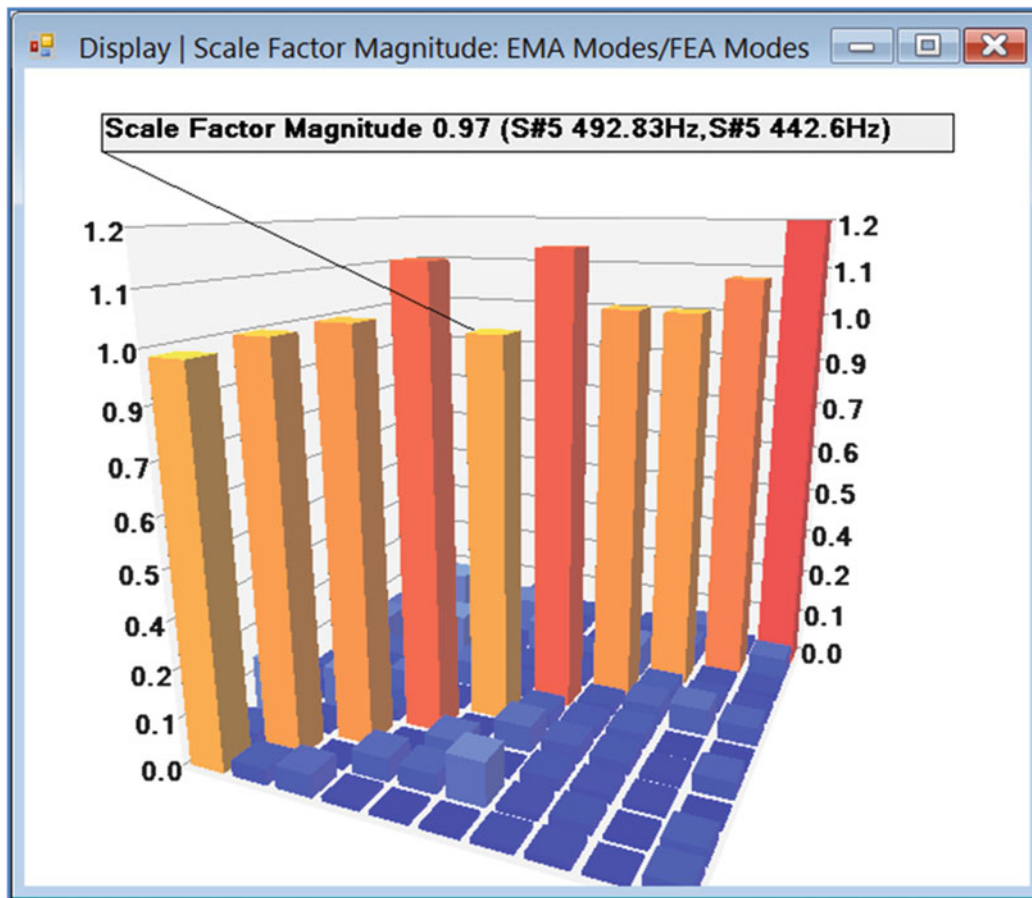


Fig. 16.8 Scaling matrix for EMA & FEA mode shapes

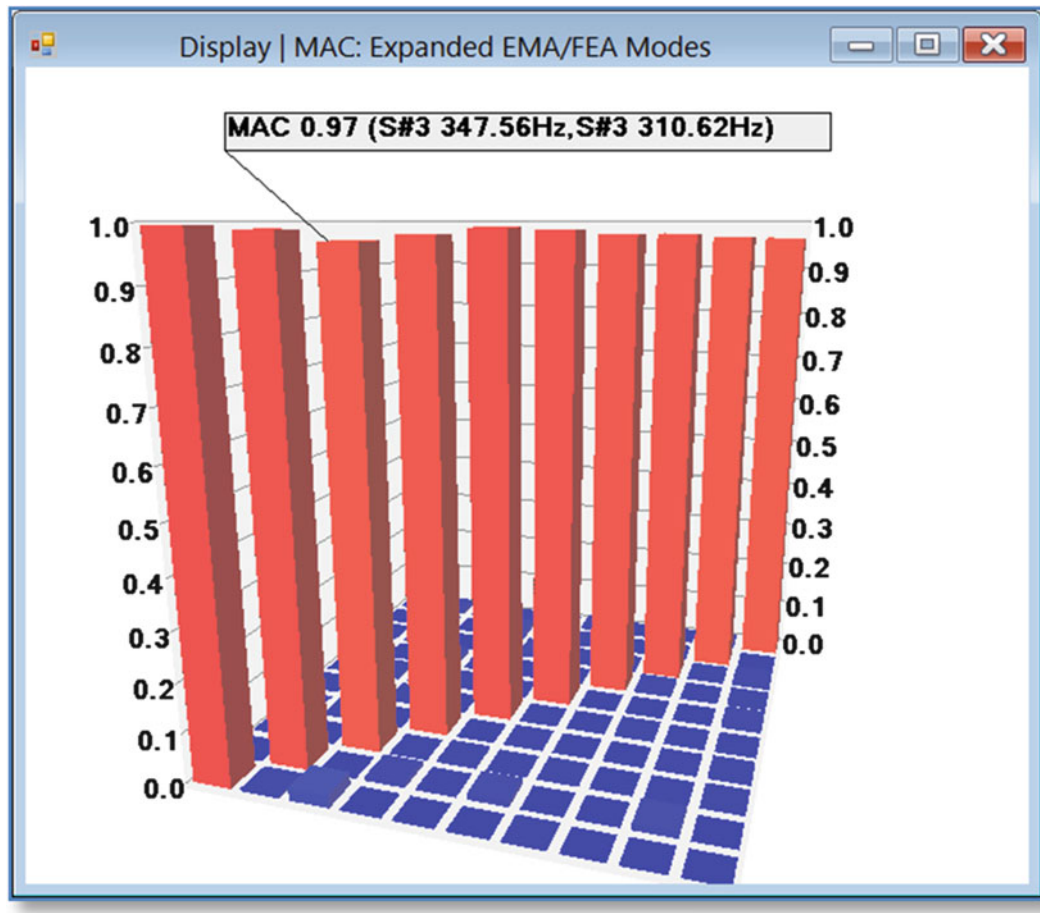


Fig. 16.9 MAC values between expanded EMA & FEA shapes

16.5 Modal Decomposition of Waveforms

A set of mode shapes with DOFs that match the DOFs in a set of time or frequency functions can be used to decompose those waveforms into contributions from each of the modes. The scale factor matrix $[W]$ in Eq. (16.1) will therefore contain a column of scale factors corresponding to each time or frequency sample. These columns result in a set of waveforms showing how each mode participates in the overall structural response at each time or frequency value.

16.5.1 Example #3: Modal Decomposition of FRFs

In this example the EMA mode shapes of the Jim Beam will be used to decompose the experimental FRFs into multiple resonance waveforms, one for each mode. Equation (16.2) was used to calculate the decomposition (scale factors) of the FRFs at each frequency.

An FRF is overlaid together with their ten modal resonance curves in Fig 16.10. Notice how each resonance curve *dominates* the overall FRF response by having a peak *at or near* each resonance peak in the FRF.

It is important to note that this decomposition *only requires the mode shapes*. Modal frequency & damping are not used. In fact, the resonance curves *can be curve fit* to obtain modal frequency & damping estimates.

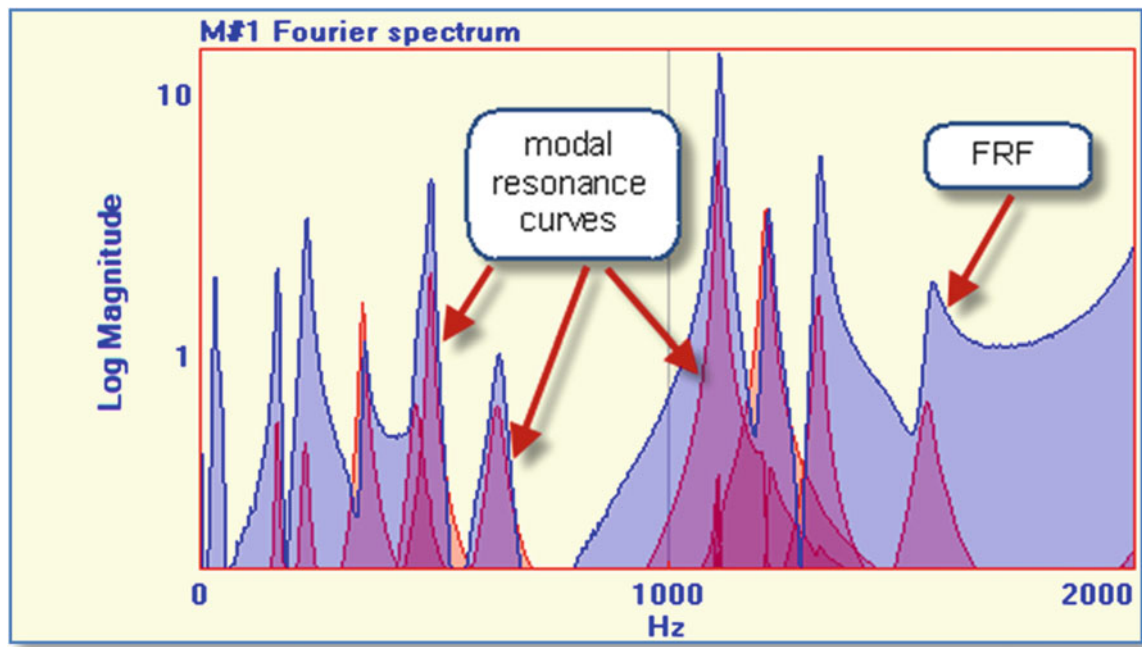


Fig. 16.10 FRFs decomposed using EMA mode shapes

16.6 Modal Model

Mode shapes are eigenvectors, and as such are only unique in “*shape*”, not in value. Therefore, mode shapes don’t normally have units associated with them.

However, if a set of mode shapes is scaled to properly account for the mass & stiffness properties of a structure, it is called a **modal model**. Modal models **do have units** associated with them. A modal model is useful for several modeling & simulation applications;

- **FRF Synthesis**

- FRFs can be created between **any two DOFs** of the mode shapes.
- Overlaid synthesized & experimental FRFs provide a graphical comparison.
- FRAC values between synthesized & experimental FRFs provide a numerical comparison.

- **MIMO Modeling**

- Time or frequency waveforms can be used.
- Multiple Outputs calculated from Multiple Inputs.
- Multiple Inputs calculated from Multiple Outputs.

- **Structural Dynamics Modification (SDM)**

- Provides rapid investigation of many “*what if?*” structural modifications.
- Modes of the **unmodified** structure plus **modification elements** attached to a geometric model are required.
- FEA elements are used by solution is **much faster** than FEA eigensolutions.

One of the popular ways to create a **modal model** is to scale the mode shapes to yield **Unit Modal Masses**. FEA mode shapes are commonly scaled using **Unit Modal Mass** scaling [7]. Scaled mode shapes have units associated with them which are [response units/(force units – seconds)].

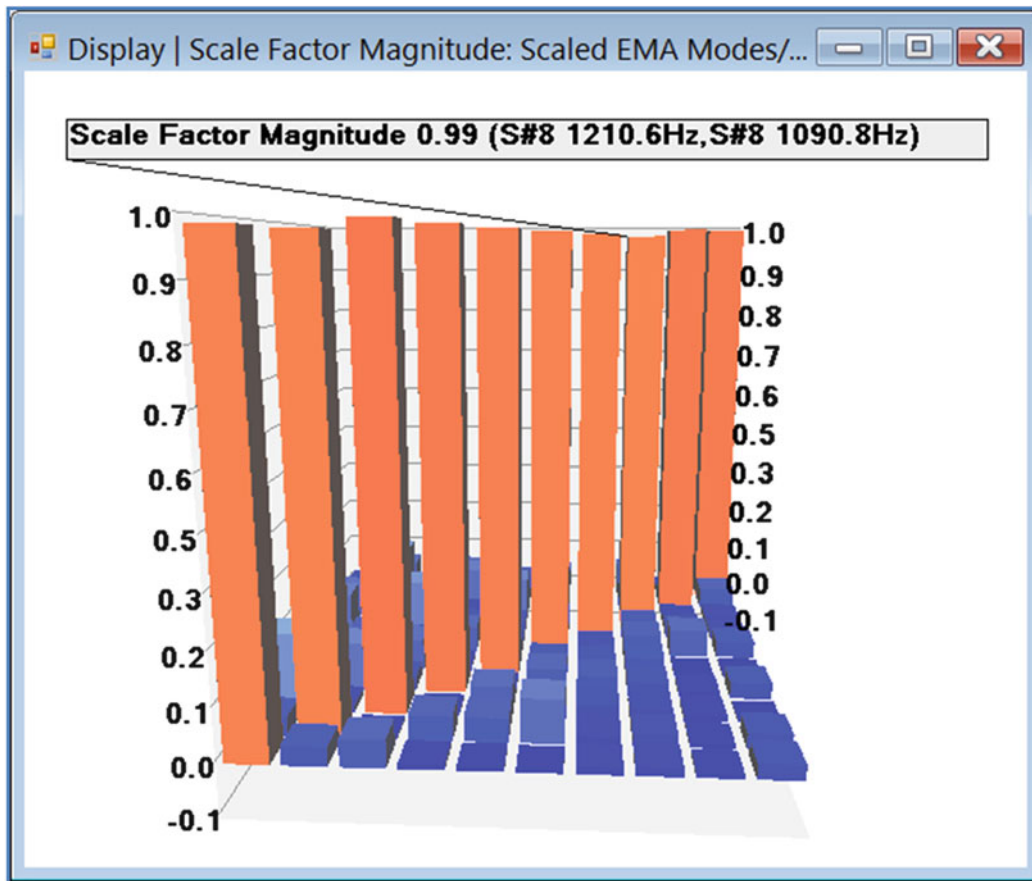


Fig. 16.11 Scale factors between UMM EMA & FEA shapes

16.6.1 Example #4: Scaling Mode Shapes to Unit Modal Masses

In this example, the EMA mode shapes of the Jim Beam will be scaled using its FEA mode shapes, which are already scaled to Unit Modal Masses. First, Eq. (16.2) is solved for the scale factors $[W]$, where $[U]$ = the un-scaled EMA mode shapes and $[V]$ = the FEA shapes. The magnitudes of the $[W]$ are shown in Fig. 16.8. Next, the scale factors $[W]$ and the un-scaled EMA mode shapes $[U]$ are used in Eq. (16.3) to scale the EMA mode shapes to **Unit Modal Masses**.

To confirm the scaling, the scaled EMA mode shapes and the FEA mode shapes are again used in Eq. (16.2) to calculate scale factors, which are shown in Fig. 16.11. The diagonal scale factors are *nearly all* “1”, indicated that the EMA mode shapes and FEA mode shapes are both scaled to Unit Modal Masses.

16.7 Modal Assurance Criterion (MAC)

For two shapes $\{u_i\}$ and $\{v_i\}$, Eq. (16.1) reduces to,

$$\begin{Bmatrix} u_{1,i} \\ \vdots \\ u_{m,i} \end{Bmatrix} [w_{i,j}] = \begin{Bmatrix} v_{1,j} \\ \vdots \\ v_{m,j} \end{Bmatrix} \quad (16.4)$$

m = number of **matching shape DOFs** or shape components

The single scale factor for equating the two shapes is,

$$w_{i,j} = \frac{\left\{ u_{1,i}^* \dots u_{m,i}^* \right\} \begin{Bmatrix} v_{1,j} \\ \vdots \\ v_{m,j} \end{Bmatrix}}{\left\{ u_{1,i}^* \dots u_{m,i}^* \right\} \begin{Bmatrix} u_{1,i} \\ \vdots \\ u_{m,i} \end{Bmatrix}} \quad (16.5)$$

* denotes the **complex conjugate**.

Now, if $\{u_i\}$ and $\{v_i\}$ are interchanged in Eq. (16.4), the scale factor that equates them is written,

$$z_{i,j} = \frac{\left\{ v_{1,i}^* \dots v_{m,i}^* \right\} \begin{Bmatrix} u_{1,j} \\ \vdots \\ u_{m,j} \end{Bmatrix}}{\left\{ v_{1,i}^* \dots v_{m,i}^* \right\} \begin{Bmatrix} v_{1,i} \\ \vdots \\ v_{m,i} \end{Bmatrix}} \quad (16.6)$$

The Modal Assurance Criterion is simply the product of the two scale factors,

$$MAC_{i,j} = w_{i,j} z_{i,j} = \frac{\left| \left\{ u_{1,i}^* \dots u_{m,i}^* \right\} \begin{Bmatrix} v_{1,j} \\ \vdots \\ v_{m,j} \end{Bmatrix} \right|^2}{\left\{ u_{1,i}^* \dots u_{m,i}^* \right\} \begin{Bmatrix} u_{1,i} \\ \vdots \\ u_{m,i} \end{Bmatrix} \left\{ v_{1,j}^* \dots v_{m,j}^* \right\} \begin{Bmatrix} v_{1,j} \\ \vdots \\ v_{m,j} \end{Bmatrix}}$$

MAC has values *between 0 and 1*. For $\{u_i\} = \{v_j\}$ **MAC = 1**. Otherwise, **MAC < 1** (Fig. 16.12).

16.8 Conclusions

Several applications of the linear relationship between two shape matrices were explored in this paper. Each shape matrix can consist of EMA mode shapes, FEA mode shapes, ODS's, or any matrix, the columns of which can be called "*shapes*". The linear relationship in Eq. (16.1) *only involves the shapes themselves*, not their frequencies (or damping in the case of EMA mode shapes), and is only valid for *matching DOFs* or shape components between the two matrices.

It was shown that this relationship can be used for scaling shapes, expanding shapes, and for time or frequency waveform decomposition. It was also shown how the Modal Assurance Criterion (MAC) is derived from this relationship [1, 3].

It was also pointed out that when the scaled matrix [V] contains ODS's and the un-scaled matrix [U] contains mode shapes, the columns of the scale factor matrix [W] are a measure of the *participation* of each mode in each ODS, more commonly known as *modal participation factors*. Moreover, when a set of time or frequency domain waveforms is decomposed using mode shapes, the decomposition at each time or frequency sample a measure of the modal participation at that (time or frequency) sample.

All of these examples verify that the linear superposition property of mode shapes is useful in a number of different ways for visualizing and understanding how the resonant vibration of a mechanical structure can be characterized in terms of its modes.

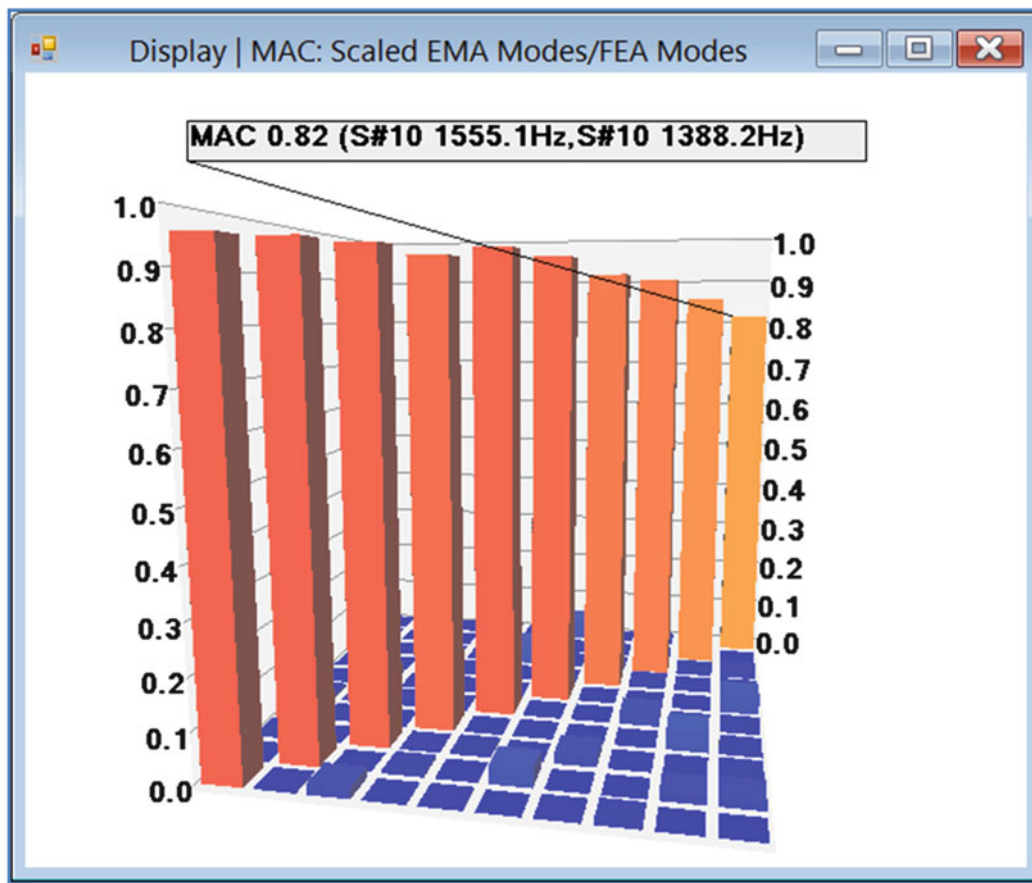


Fig. 16.12 MAC values between EMA & FEA mode shapes

References

1. Allemang RJ (1980) Investigation of some multiple input/output frequency response function experimental modal analysis techniques. Doctor of Philosophy Dissertation, Department of Mechanical Engineering, University of Cincinnati
2. Allemang RJ (2002) The modal assurance criterion (MAC): twenty years of use and abuse. In: Proceedings of the international modal analysis conference
3. Allemang RJ, Brown DL (1982) A correlation coefficient for modal vector analysis. In: Proceedings, international modal analysis conference, pp 110–116
4. Formenti D, Richardson M (1982) Parameter estimation from frequency response measurements using rational fraction polynomials. In: Proceedings of the 1st international modal analysis conference
5. Richardson M (1997) Is it a mode shape or an operating deflection shape? *Sound Vib Mag* (March)
6. Richardson M (2005) Modal analysis versus finite element analysis. *Sound Vib Mag* (September)
7. Richardson SC, Richardson MH (2008) Using photo modeling to obtain the modes of a structure. In: Proceedings of the international modal analysis conference
8. Schwarz B, Richardson M (2013) Proportional damping from experimental data. In: Proceedings of the 31st international modal analysis conference

Chapter 17

Un-weighted and Weighted Versions of the Modal Assurance Criterion (MAC) for Evaluation of Modal Vector Contamination

R.J. Allemang and A.W. Phillips

Abstract Modal vectors frequently have small amounts of contamination or distortion from random errors or bias errors, particularly when compared to results from modeling where normal modal vectors are the common result since damping is not included in the model. In order to understand, and possibly eliminate the contamination, tools are needed to evaluate the contamination. While the traditional modal assurance criterion (MAC) is useful, more sensitive methods are desirable. Several altered forms of MAC are reviewed for this purpose. These methods include evaluating the real part of a modal vector compared to the complex valued modal vector (rMAC), evaluating the imaginary part of the modal vector compared to the complex valued modal vector (iMAC) and evaluating the real part of a modal vector compared to the imaginary part of the modal vector (riMAC). Weighted versions of each of these evaluations are also utilized (rwMAC, iwMAC and riwMAC). These methods have shown to be very useful when evaluating modal vectors associated with close modal frequencies and suggest a need for improved processing (numerical estimation procedures for modal vectors) or “decontamination” (post processing procedures for modal vector sets) are required.

Keywords Modal assurance criterion • MAC • Modal vector correlation • Modal vector consistency • Modal parameter estimation

Nomenclature

N_i	Number of inputs
N_o	Number of outputs
N_S	Short dimension size
N_L	Long dimension size
λ_r	Complex modal frequency (rad/s)
λ_r	$\sigma_r + j\omega_r$
σ_r	Modal damping
ω_r	Damped natural frequency
$\{\psi_r\}$	Base vector (modal vector)
$\{\varphi_r\}$	Pole weighted base vector (state vector)
r	Mode number
MAC	Modal assurance criterion
rMAC	MAC (real part versus complex)
iMAC	MAC (imaginary part versus complex)
riMAC	MAC (real part versus imaginary part)
wMAC	Weighted modal assurance criterion
rwMAC	Weighted MAC (real part versus complex)

R.J. Allemang (✉) • A.W. Phillips
Structural Dynamics Research Laboratory, Department of Mechanical and Materials Engineering, College of Engineering and Applied Science, University of Cincinnati, Cincinnati, OH 45221-0072, USA
e-mail: Randall.Allemang@UC.EDU

iwMAC Weighted MAC (imaginary part versus complex)
 riwMAC Weighted MAC (real part versus imaginary part)

17.1 Introduction

The evolution of modal parameter estimation over the last 40 years or so has changed the way that modal vectors are estimated from experimental data. The progression from single measurement modal parameter estimation to autonomous (MIMO) modal parameter estimation has meant that the modal vector coefficients that once were estimated DOF by DOF and mode by mode can now be estimated vector by vector (including all DOFs) from clusters of estimates of each modal vector in MIMO procedures. This has resulted in statistically significant estimations of the individual modal vectors that reduce the impact of measurement noise as well as other random and bias errors. In the end, the modal vectors always have some small amount of contamination. When a structure is tested where normal modes are expected, the estimated modal vectors will always contain a small amount of contamination that will yield a slightly complex estimate of the modal vectors.

For this situation, the contamination can often be ignored or eliminated through a real normalization procedure. This can be justified, particularly when the contamination appears to be dominantly random. However, when the contamination is biased, this justification becomes complicated. Even with the most sophisticated modal parameter estimation algorithms and numerical procedures, the contamination will often be biased in the form of contamination that looks like a nearby mode. This indicates that the estimated modal vectors satisfy whatever algorithm and numerical procedure that are being utilized but the estimated modal vectors still contain characteristics that may be perceived as a non-physical result.

Recent use of autonomous modal parameter estimation methods indicate that these small amounts of contamination still persist even when statistically significant data is included in the estimation of the modal vectors and estimation of the modal vectors involve alternate numerical methods. The common form of this contamination is most notable when the modal frequencies are closely spaced, or repeated, in frequency. In these cases, when the modal vectors are expected to be real-valued, normal modes, the estimated modal vectors will often contain a small imaginary valued component that correlates with the dominant (real-valued) characteristic of a nearby modal vector.

17.2 Background: Modal Vectors from Autonomous Modal Parameter Estimation

Before continuing, some comments relative to how modal vectors are estimated when using autonomous modal parameter estimation methods are in order [1–3]. In the end, the modal vector contamination that is being studied is present in all modal parameter estimation approaches. However, the autonomous modal parameter estimation procedures often use a statistically based solution that involves a singular value decomposition of a cluster of modal vectors estimates. This yields an extremely good result where the modal vectors have much less contamination than that found historically. Even so, the modal vector contamination problem cannot be eliminated.

The following discussion is a brief summary of how the Common Statistical Subspace Autonomous Modal Identification (CSSAMI) method estimates the modal vectors. Essentially, any modal parameter estimation algorithm can be utilized to get a consistency diagram. This consistency diagram represents hundreds of solutions for the possible modal parameters (modal frequencies and modal vectors). The vectors in these solutions are combined with the modal frequencies to create state vectors. Now the hundreds of state vectors can be sorted into clusters where each cluster represents a single modal vector. This sorting procedure involves the modal assurance criterion between all of the state vectors. The final modal frequency and modal vector can now be determined from the singular value decomposition of each cluster. This is a slightly different procedure than historical methods that used least squares or weighted least squares methods to determine modal vectors via a partial fraction residue model.

Note that much of the background of the CSSAMI method is based upon the Unified Matrix Polynomial Algorithm (UMPA) [4, 5]. This means that this autonomous method can be applied to both low and high order modal parameter estimation methods with short or long dimension modal (base) vectors. These different methods can now be combined in one procedure. In these cases, it may be useful to solve for the complete, unscaled or scaled, modal vector of the large dimension N_L . This will extend the temporal-spatial information in the modal (base) vector so that the vector will be more sensitive to change. This characteristic is what gives the CSSAMI autonomous method a robust ability to distinguish between computational and structural modal parameters. The reader is directed to a series of previous papers in order to get an overview of the methodology and to view application results for several cases [6–8].

17.3 Modal Assurance Criterion

The traditional modal assurance criterion (MAC) computation [9–12], restated in Eq. (17.1), is widely used in modal parameter estimation and structural dynamics to sort the numerous possible solutions of modal vectors from either modeling or experiment.

$$MAC_{cd} = \frac{|\{\psi_c\}^H \{\psi_d\}|^2}{\{\psi_c\}^H \{\psi_c\} \{\psi_d\}^H \{\psi_d\}} = \frac{\{\psi_c\}^H \{\psi_d\} \{\psi_d\}^H \{\psi_c\}}{\{\psi_c\}^H \{\psi_c\} \{\psi_d\}^H \{\psi_d\}} \quad (17.1)$$

Once modal vectors are estimated in any modal parameter estimation procedure, the MAC computation is often utilized to evaluate the quality of the solutions. This begins with an evaluation of the MAC between all of the modal vectors in the final set to ascertain whether the modal set is an independent set of vectors. This often involves including the estimates of the modal vectors associated with the conjugate poles. Since the conjugate poles and vectors are estimated separately, if non-conjugate relationships exist between the associated modal vector estimates (between the modal vector for pole and the modal vector of the conjugate pole), the MAC between these two vectors will not be unity as expected. A number of users have noted that this often correlates with modal vectors that are exhibiting some unexpected characteristics.

Figure 17.1 is a graphical representation of this situation. While the MAC values are acceptable, the comparisons between modal vectors and the associated conjugate modal vectors do exhibit slightly lowered consistency or correlation.

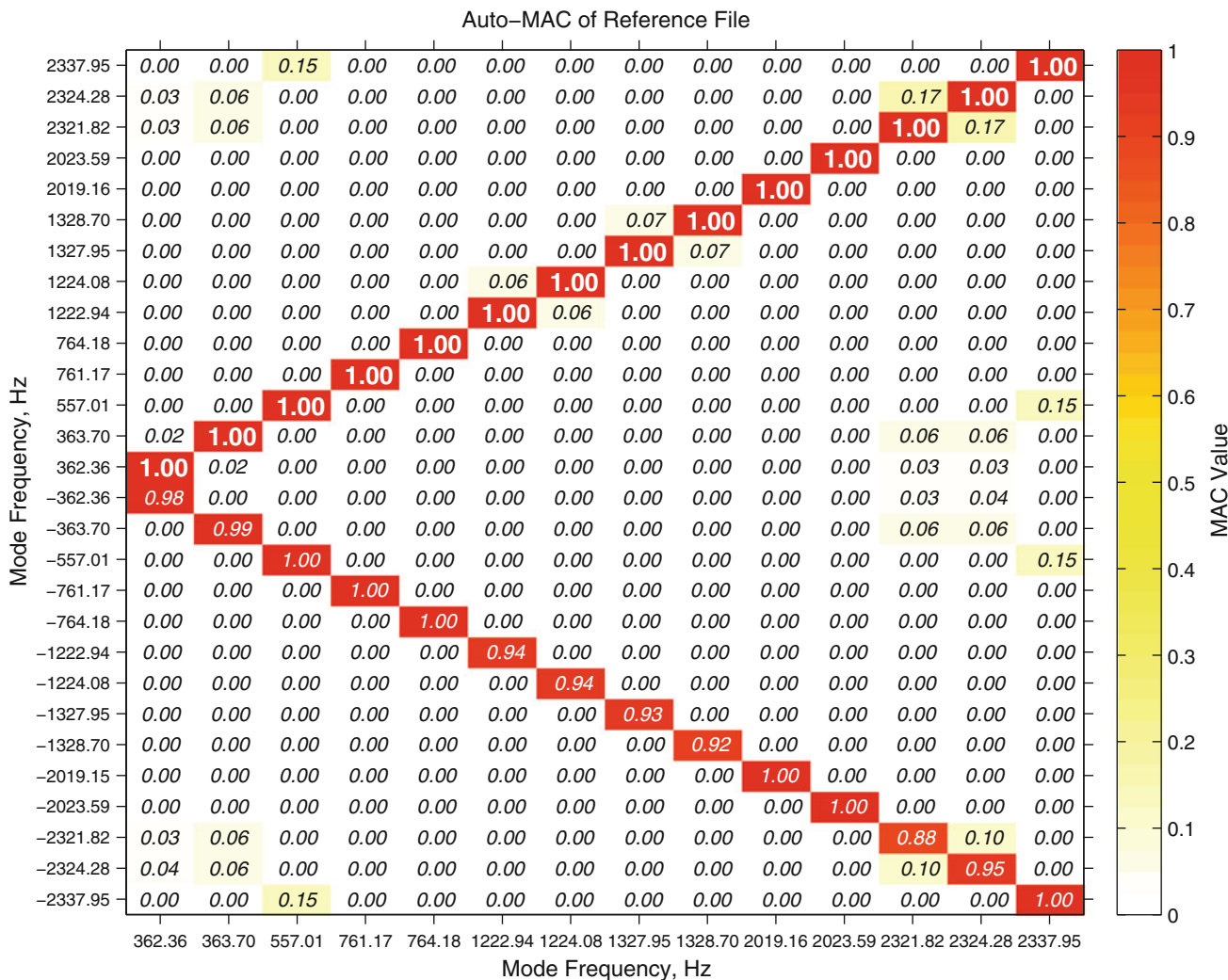


Fig. 17.1 MAC of modal vectors and conjugate modal vectors

Mode#23: 2,321.0217 Hz: 0.1607 %zeta
Pole Results

SDRL
Structural Dynamics Research Laboratory

Mode#25: 2,324.4193 Hz: 0.1402 %zeta
Pole Results

SDRL
Structural Dynamics Research Laboratory

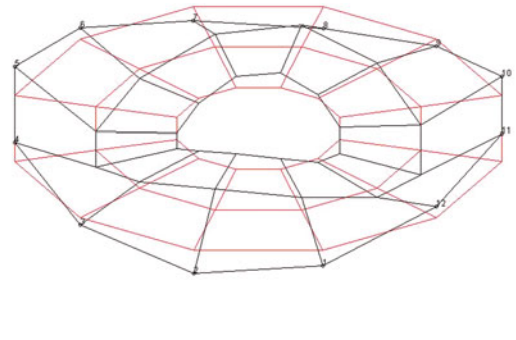
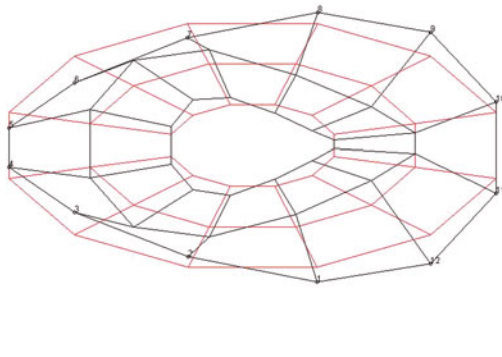
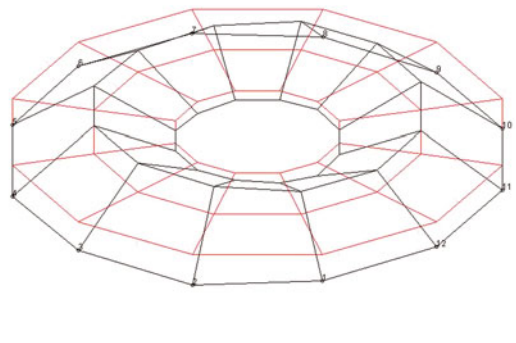


Fig. 17.2 C-Plate example: modal vectors—2,321.8 and 2,324.3 Hz

Fig. 17.3 C-plate example:
modal vector—2,337.9 Hz

Mode#27: 2,337.9464 Hz: 0.1794 %zeta
Pole Results

SDRL
Structural Dynamics Research Laboratory



When the last three modal vectors are visualized, as in Figs. 17.2 and 17.3, no particular problem can be noted until the modal vectors are animated. Then, the two modes in Fig. 17.2 clearly show a small complex mode characteristic. As these results are statistically consistent across many solutions, the limitations of the data, both in frequency and spatial resolution, are the root of the problem.

Unlike the historical approach to estimation of the modal vectors, many recent modal parameter estimation algorithms, including the autonomous procedures, are based upon numerical processing methods like singular value decomposition (SVD). The solutions that are identified, based upon the data associated with a cluster of estimates, have no physical or causal constraint. An example of a physical or causal constraint would be the expectation of real-valued, normal modes for systems where no expectation of non-proportional damping is likely. SVD methods will identify the most dominant unitary (orthogonal and unit length) vectors in a cluster, yielding a complex-valued vector in general. Experience has shown that when modes are very close in frequency with minimal spatial resolution, the complex-valued vectors will still show significant independence.

However, when these complex-valued vectors are examined closely, the non-dominant portion of the complex-valued vector often correlates very highly with one or more nearby modal vectors. This can be examined by several variants of the MAC calculation and the weighted MAC calculation. This is discussed in the next Section.

17.4 Weighted Modal Assurance Criterion

Identifying the potential contamination of modal vectors is helpful to the thorough understanding of modal parameter estimation algorithms and autonomous procedures as well as being instructive for potential removal of the contamination [13]. If some sort of real normalization is desirable (to match up well with an undamped analytical model, for example),

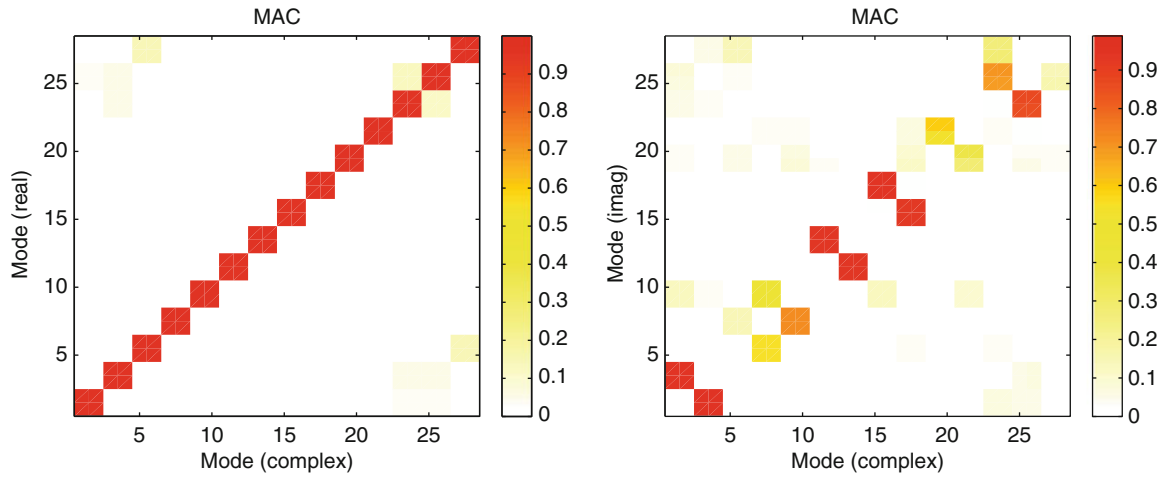


Fig. 17.4 Real and imaginary MAC evaluations

understanding of the contamination that is being removed is a prerequisite to any procedure. Random contamination may simply be ignored, smoothed or averaged out, but if the contamination is related to nearby modes, it may indicate that the modal parameter estimation may need further evaluation or that more data is required.

For this evaluation of the modal vector contamination, it will be easiest to first rotate each complex-valued modal vector to a real (or imaginary) dominant vector. This is done by using a least squares method to identify the rotation of the modal vector away from the real or imaginary axis and then using the associated complex phasor to rotate each original complex-valued modal vector to a new complex-valued modal vector that aligns with the real or imaginary axis [13]. For all following discussion, the original complex-valued modal vectors are rotated to be dominantly real-valued. It is convenient, for display reasons, to also normalize the new complex-valued modal vector to a unity maximum or unity vector length. Naturally, the rotation and rescaling must be considered in any final estimates of modal scaling (modal mass, modal A, residue, etc.)

To understand the nature of the possible modal vector contamination in a complex-valued modal vector, three conventional MAC calculations can be performed (1) between the real parts of the modal vectors and the complex-valued modal vectors (rMAC), (2) between the imaginary parts of the modal vectors and the complex-valued modal vectors (iMAC) and (3) between the real parts of the modal vectors and the imaginary parts of the modal vectors (riMAC). These three MAC calculations and the interpretation of these MAC values will be sensitive to the rotation and normalization of the complex-valued modal vector estimates. The following use and discussion assumes that the complex-valued modal vectors have been rotated so that the central axis of the complex-valued modal vector is centered on the real axis. These three MAC computations identify (1) that the real part of the modal vector is the dominant part of the complex-valued modal vector (rMAC), (2) that the imaginary part of the modal vector is the dominant part of the complex-valued modal vector (iMAC) and (3) that the real and imaginary parts of the modal vector are, or are not, related to one another. All MAC computations in this case are, as always, bounded from zero to one. If near normal modes are expected, (1) the rMAC should be close to one, (2) the iMAC should be close to zero and (3) the riMAC should also be close to zero. Note in the following definitions, complex-valued modal vectors c and d can again be any of the modal vectors that the user wishes to include in the evaluation.

$$\text{rMAC}_{cd} = \frac{(\text{Re}\{\psi_c\}^H) \{\psi_d\} \{\psi_d\}^H (\text{Re}\{\psi_c\})}{(\text{Re}\{\psi_c\}^H)(\text{Re}\{\psi_c\}) \{\psi_d\}^H \{\psi_d\}} \quad (17.2)$$

$$\text{iMAC}_{cd} = \frac{(\text{Im}\{\psi_c\}^H) \{\psi_d\} \{\psi_d\}^H (\text{Im}\{\psi_c\})}{(\text{Im}\{\psi_c\}^H)(\text{Im}\{\psi_c\}) \{\psi_d\}^H \{\psi_d\}} \quad (17.3)$$

$$\text{riMAC}_{cd} = \frac{(\text{Re}\{\psi_c\}^H)(\text{Im}\{\psi_d\}) \{\psi_d\}^H (\text{Re}\{\psi_c\})}{(\text{Re}\{\psi_c\}^H)(\text{Re}\{\psi_c\}) \{\psi_d\}^H (\text{Im}\{\psi_d\})} \quad (17.4)$$

Figures 17.4 and 17.5 are graphical representations of Eqs. (17.2)–(17.4). Each block or cluster in these diagrams contains the information from both the complex modal frequency and the associated conjugate modal frequency. The rMAC in

Fig. 17.5 Real versus imaginary
MAC evaluation

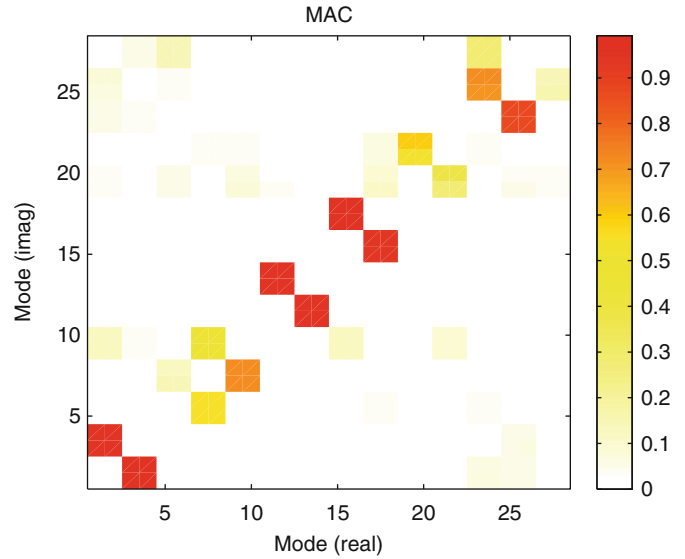


Fig. 17.4 shows that the modal vectors are real dominant and linearly independent. The iMAC in Fig. 17.4 and the riMAC in Fig. 17.5 both show that the imaginary portion of the vectors are linearly and strongly related to a nearby mode, which is frequently the pseudo-repeated root twin to the mode, in this case.

The above graphical representations indicate that the imaginary part (contamination) of a given mode is strongly related to the real part (dominant) part of the modal vector associated with its pseudo-repeated root companion. This is consistent with theory that explains the cause of a complex-valued modal vector when two real-valued modal vectors are close in frequency and misidentified as a single modal vector.

The above MAC evaluations identify whether, and how, the contamination of a complex-valued modal vector is related to another of the identified modal vectors. However, the MAC computation is normalized by vector length, vector by vector, for the vectors used in the calculation. A weighted MAC can be used to determine the degree or scale of the contamination. The following three definitions of the weighting for each of the above MAC calculations limits the associated MAC value to a fraction of the zero to one scale. If near normal modes are expected, (1) the weighting and rwMAC should be close to one, (2) the weighting and iwMAC should be close to zero and (3) the combined weighting and riwMAC should also be close to zero. Note in the following definitions, complex-valued modal vectors c and d can again be any of the modal vectors that the user wishes to include in the evaluation.

$$\text{riMAC}_{cd} = rW_c \times \text{rMAC}_{cd} \quad \text{where } rW_c = \frac{(\text{Re}\{\psi_c\}^H)(\text{Re}\{\psi_c\})}{\{\psi_c\}^H\{\psi_c\}} \quad (17.5)$$

$$\text{iwMAC}_{cd} = iW_c \times \text{iMAC}_{cd} \quad \text{where } iW_c = \frac{(\text{Im}\{\psi_c\}^H)(\text{Im}\{\psi_c\})}{\{\psi_c\}^H\{\psi_c\}} \quad (17.6)$$

$$\text{riwMAC}_{cd} = rW_c \times iW_d \times \text{riMAC}_{cd} \quad (17.7)$$

Figures 17.6 and 17.7 are graphical representations of Eqs. (17.5)–(17.7). These figures yield the same conclusions as Figs. 17.4 and 17.5. In addition, the iwMAC and riwMAC values show that the contamination is at a relatively low level.

At this point, now that the contamination of the complex-valued modal vectors can be confirmed to be from the dominant portion (real part) of the other complex-valued modal vectors and that the contamination is not significant, a strategy for determining the best set of real-valued modal vectors can be identified. One reasonable option would be to place the real parts and imaginary parts of each complex-valued modal vector into a matrix as separate real-valued vectors. A singular value decomposition of this real-valued matrix will yield real-valued singular vectors and the most significant singular vectors, equal to the original number of complex-valued modal vectors, associated with the largest singular values can be utilized as the final set of real-valued, normal modes. A simpler solution would be to eliminate the imaginary parts since the scale of the contamination is shown to be small.

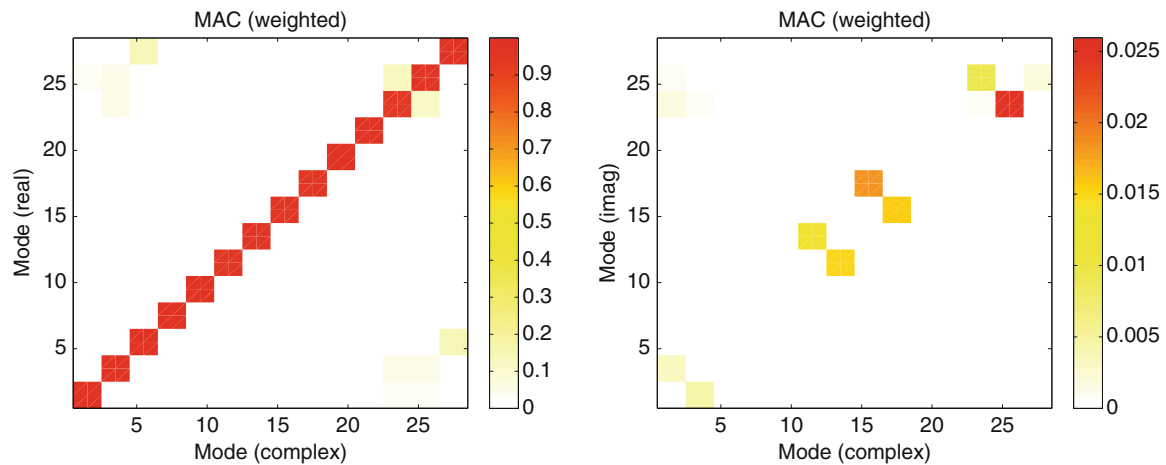
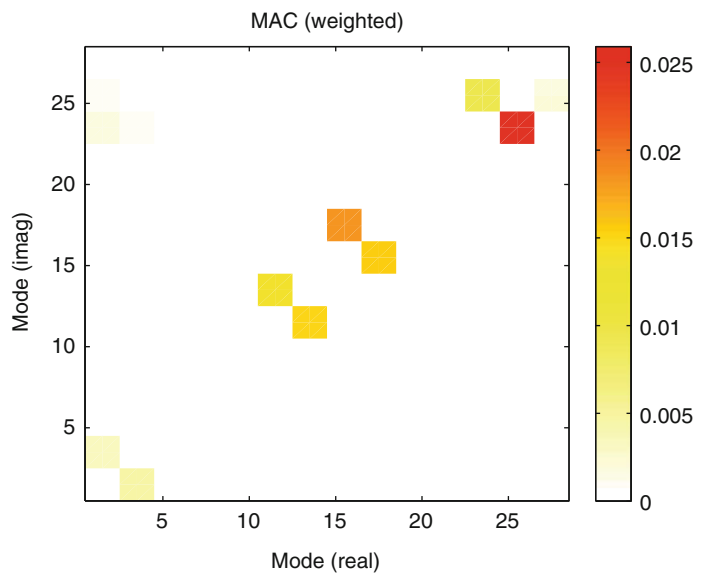


Fig. 17.6 Real and imaginary weighted MAC evaluations

Fig. 17.7 Real versus imaginary weighted MAC evaluation



17.5 Summary and Future Work

With the advent of more computationally powerful computers and sufficient memory, it has become practical to evaluate sets of solutions involving hundreds or thousands of modal parameter estimates and to extract the common information from those sets. In many cases, autonomous procedures give very acceptable results, in some cases superior results, in a fraction of the time required for an experienced user to get the same result. The modal assurance criterion, both unweighted and weighted, is instrumental in evaluating the quality of the modal vector results.

Future work will involve better numerical methods for combining algorithms into a single consistency diagram and autonomous methods for identifying the best causal solution are still needed. The modified application of MAC is helpful but numerical solution methods that identify both real-valued modal vectors (normal modes) and complex-valued modal vectors, when appropriate, would be truly autonomous.

Acknowledgements The authors would like to acknowledge the collaboration and assistance from the graduate students and faculty of the Structural Dynamics Research Lab at the University of Cincinnati. In particular, the discussions and collaborations with Dr. David L. Brown have been instrumental in the progress made to this point.

References

1. Hawkins FJ (1965) An automatic resonance testing technique for exciting normal modes of vibration of complex structures. In: Symposium IUTAM, "Progres Recents de la Mecanique des Vibrations Lineaires", pp 37–41
2. Hawkins FJ (1967) GRAMPA—an automatic technique for exciting the principal modes of vibration of complex structures. Royal Aircraft Establishment, RAE-TR-67-211
3. Taylor GA, Gaukroger DR, Skingle CW (1967) MAMA—a semi-automatic technique for exciting the principal modes of vibration of complex structures. Aeronautical Research Council, ARC-R/M-3590, 20 pp
4. Allemang RJ, Phillips AW (2004) The unified matrix polynomial approach to understanding modal parameter estimation: an update. In: Proceedings, international conference on noise and vibration engineering (ISMA)
5. Allemang RJ, Brown DL, Phillips AW (2010) Survey of modal techniques applicable to autonomous/semi-autonomous parameter identification. In: Proceedings, international conference on noise and vibration engineering (ISMA), Katholieke Universiteit Leuven, Leuven, p 42
6. Phillips AW, Allemang RJ, Brown DL (2011) Autonomous modal parameter estimation: methodology. In: Proceedings, international modal analysis conference (IMAC), p 22
7. Allemang RJ, Phillips AW, Brown DL (2011) Autonomous modal parameter estimation: statistical considerations. In: Proceedings, international modal analysis conference (IMAC), p 17
8. Brown DL, Allemang RJ, Phillips AW (2011) Autonomous modal parameter estimation: application examples. In: Proceedings, international modal analysis conference (IMAC), p 26
9. Allemang RJ, Brown DL (1982) A correlation coefficient for modal vector analysis. In: Proceedings, international modal analysis conference, pp 110–116
10. Heylen W (1990) Extensions of the modal assurance criterion. *J Vib Acoust* 112:468–472
11. Lallement G, Kozanek J (1999) Comparison of vectors and quantification of their complexity. In: Proceedings, international modal analysis conference, pp 785–790
12. Allemang RJ (2002) The modal assurance criterion (MAC): twenty years of use and abuse. In: Proceedings, international modal analysis conference, pp. 397–405. *Sound Vib Mag* 37(8):14–23 (2003)
13. Phillips AW, Allemang RJ (2014) Normalization of experimental modal vectors to remove modal vector contamination. In: Proceedings, international modal analysis conference (IMAC)

Chapter 18

Modal Properties of Rotating Shafts with Order-Tuned Absorbers

Steven W. Shaw, Mustafa Ali Acar, Brian F. Feeny, and Bruce K. Geist

Abstract We consider the properties of torsional vibration modes of rotating shafts fitted with centrifugally driven pendulum vibration absorbers. These systems feature interesting modal behavior that arises from the coupling of constant-stiffness elements, namely the shaft torsional modes, and engine-order-based elements, namely the absorbers. These models are relevant to automotive crankshafts fitted with pendulum absorbers, which are being considered for reducing vibrations in a number of advanced technology engines. The coupled system modes exhibit frequency veering as the rotor speed varies, and when the system is subjected to engine-order excitation the resonances depend in a non-trivial manner on the system parameters. The absorbers are typically tuned to suppress shaft torsional vibrations, and proper tuning of the absorbers requires a thorough understanding of this resonance behavior. In this paper we describe the manner in which natural frequencies depend on rotor speed and how this influences the overall frequency response of the rotor. We also discuss how to tune absorbers to achieve the desired vibration reduction, and we consider some examples that demonstrate the rich response behavior of these systems.

Keywords Order-tuned vibration absorbers • Flexible rotating systems • Eigenvalue veering • Speed dependent modal properties • Resonance suppression

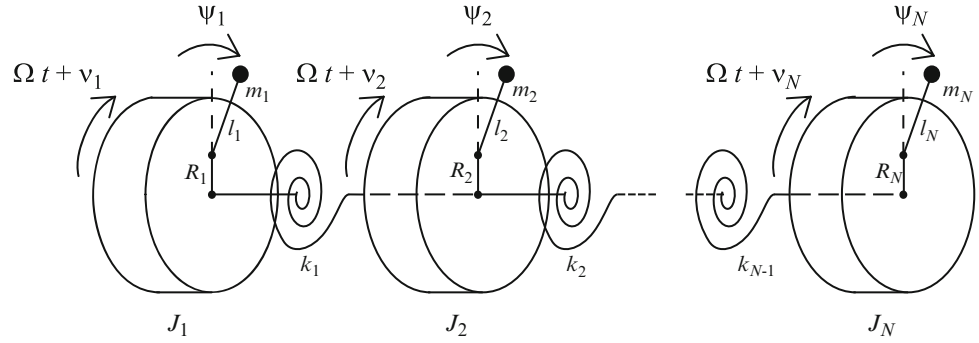
18.1 Introduction

Centrifugally driven pendulum vibration absorbers are used to reduce engine-order torsional vibrations in rotating systems [2, 3]. They are widely used in light aircraft piston engines and have recently been introduced for smoothing torsional vibrations in automotive powertrain applications [2, 4]. These absorbers make use of the centrifugal field due to rotation, rather than elastic elements, so that they are tuned to a particular engine order [1, 3]. The design of these absorbers often assumes a rigid rotor, that is, it ignores the flexibility of the rotor, and small amplitude vibrations of the absorbers, so that linear vibration analysis applies. However, when one accounts for rotor torsional flexibility [6] or nonlinearity [3, 5], the design process becomes significantly more complicated. In this paper we consider the linear frequency response characteristics of general systems with rotor torsional modes and pendulum absorbers. These individual components have natural frequencies that are constant as the rotor speed varies (rotor torsional frequencies) and that are proportional to the rotor speed (absorber frequencies). When these elements are coupled the system natural frequencies exhibit veering as the rotor speed varies, and when the system is subjected to engine-order excitation, the resonant rotor speeds depend in a non-trivial manner on the system parameters, including the absorber tuning. Proper tuning of the absorbers for vibration reduction requires a thorough understanding of this resonance behavior, which is considered in this work.

S.W. Shaw (✉) • M.A. Acar • B.F. Feeny
Department of Mechanical Engineering, Michigan State University, 428 S. Shaw Lane, East Lansing, MI 48824, USA
e-mail: shawsw@msu.edu; acarmust@msu.edu; feeny@egr.msu.edu

B.K. Geist
Chrysler Group LLC, Powertrain Virtual Engineering, Auburn Hills, MI, USA
e-mail: geist@chrysler.com

Fig. 18.1 Schematic of the system considered



18.1.1 Dynamical Model

In this work, we consider the general model shown in Fig. 18.1. The components of this model account for the flexibilities between relatively rigid crank-webs, and the inclusion of torsional frequency-tuned mass absorbers, such as dual-mass flywheels, along with order-tuned pendulums fitted to the rotor inertia elements.

The pendulums attached to the rotational inertias represent the absorbers. Although schematically, a pendulum is attached to each inertia in Fig. 18.1, it is not practical to do so, so one generally uses only a subset of the absorbers depicted. For a model with N rotors and M absorbers, the system will have $N + M$ degrees-of-freedom (DOF). The absolute angle of i^{th} inertia is taken as $\Omega t + \nu_i$ where Ω represents the mean speed of the entire system while ν_i is the rotational deflection of the i^{th} rotor from its nominal (rigid rotor) position. The angular deflection of the i^{th} absorber from its vertex is denoted by ψ_i . The mean speed Ω generates the restoring force on the pendulums. Hence, as can be seen in the linearized equations of motion, the system dynamics depend on parameters and also on Ω . Torsional vibration of the rotors is caused by fluctuating torques Q_j applied to the rotor inertia elements, which arise from reciprocating forces applied through connecting rods, stemming from gas pressure and the inertia of slider-crank components. In this work, this engine excitation order is denoted by n , and it is assumed that the excitation is only applied to the first rotor, J_1 , i.e., $Q_j = 0$ for $j \neq 1$. For this model the equations of motion take the form,

$$\begin{bmatrix} \mathbf{M}_1 & \mathbf{M}_2 \\ \mathbf{M}_3 & \mathbf{M}_4 \end{bmatrix} \begin{bmatrix} \ddot{\nu}_1 \\ \vdots \\ \ddot{\nu}_N \\ \ddot{\psi}_1 \\ \vdots \\ \ddot{\psi}_N \end{bmatrix} + \begin{bmatrix} \mathbf{K}_1 & \mathbf{K}_2 \\ \mathbf{K}_3 & \mathbf{K}_4 \end{bmatrix} \begin{bmatrix} \nu_1 \\ \vdots \\ \nu_N \\ \psi_1 \\ \vdots \\ \psi_N \end{bmatrix} = \begin{bmatrix} Q_1 \\ \vdots \\ \vdots \\ \vdots \\ \vdots \\ Q_{2N} \end{bmatrix}$$

Where \mathbf{M}_1 to \mathbf{M}_4 and \mathbf{K}_1 to \mathbf{K}_4 are $N \times N$ matrices, Q_1 is the order n torque applied to the first rotor. The forms of the sub-matrices are given by,

$$\mathbf{M}_1 = \begin{bmatrix} m_1(R_1 + l_1)^2 + J_1 & \cdots & 0 \\ \vdots & \ddots & \vdots \\ 0 & \cdots & m_N(R_N + l_N)^2 + J_N \end{bmatrix}$$

$$\mathbf{M}_2 = \begin{bmatrix} m_1 l_1 (R_1 + l_1) & \cdots & 0 \\ \vdots & \ddots & \vdots \\ 0 & \cdots & m_N l_N (R_N + l_N) \end{bmatrix}$$

$$\mathbf{M}_3 = \mathbf{M}_2$$

$$\mathbf{M}_4 = \begin{bmatrix} m_1 l_1^2 & \cdots & 0 \\ \vdots & \ddots & \vdots \\ 0 & \cdots & m_N l_N^2 \end{bmatrix}$$

$$\mathbf{K}_1 = \begin{bmatrix} k_1 & -k_1 & 0 & & & \\ -k_1 & k_1 + k_2 & -k_2 & \cdots & & 0 \\ 0 & -k_2 & k_2 + k_3 & \ddots & & \vdots \\ \vdots & & & & k_{N-3} + k_{N-2} & -k_{N-2} & 0 \\ 0 & \cdots & -k_{N-2} & k_{N-2} + k_{N-1} & -k_{N-1} & \\ & & 0 & -k_{N-1} & k_{N-1} \end{bmatrix}$$

$$\mathbf{K}_2 = \mathbf{K}_3 = \mathbf{0}$$

$$\mathbf{K}_4 = \begin{bmatrix} \Omega^2 m_1 l_1 R_1 & \cdots & 0 \\ \vdots & \ddots & \vdots \\ 0 & \cdots & \Omega^2 m_N l_N R_N \end{bmatrix}$$

Note that the block elements of this system reflect the different natures of the rotor and absorber elements. Of particular interest is the fact that the restoring stiffness of the absorbers is proportional to Ω^2 . In fact, the centrifugal pendulums, when the rotor runs at a constant speed, have a natural frequency, $\tilde{n}\Omega$, where the tuning order \tilde{n} is determined by hardware design ($\tilde{n}_i = \sqrt{\frac{R_i}{l_i}}$), and is generally chosen near n , or multiples of n or possibly multiples of n when dealing with higher order interactions [5, 6]. The tuning of a pendulum absorber does not depend on its moment of inertia. However, the ratio of pendulum moment of inertia to the rotor inertia ($\epsilon_i = \frac{m_i(R_i+l_i)^2}{J_i} \ll 1$) has significant influence on the behavior of the overall system and the performance of the pendulum absorber. In fact, this ratio will dictate the ability of the absorber to remain in the linear operating range for a given level of applied torque [3].

18.1.2 Analysis of Model

We consider a number of examples that demonstrate the salient features of these systems. We begin with a simple system with two rotor elements and then subsequently consider more complex models. For consideration of vibration reduction we examine the frequency response of the rotor that is subjected to the order n torque excitation and compare it for various cases; the baseline vibration level for comparison is that for which the pendulum absorbers are locked at their vertices, since this accounts for their added inertia. Vibrations away from this baseline, when the absorbers are free to move, are the result of absorber dynamics. Unless otherwise stated, the order of the excitation is taken as $n = 1.5$ during these simulations, corresponding to the dominant net torque loading for a three cylinder, four-stroke engine. Both the natural frequency and frequency response calculations are carried out by evaluating the analytical expressions at each rotational speed value throughout the range, namely 0–5,000 RPMs.

Our first investigation is for a system with two rotor inertias, i.e. $N = 2$. The number of absorbers, their placement, and tuning are varied. In Fig. 18.2, the frequency response of a system having two identical rotor inertias with a single absorber attached to the first rotor is plotted for different values of the absorber tuning (\tilde{n}). As one can see from these curves, when the absorber is undertuned ($\tilde{n} < n$), the frequency at which resonance occurs shifts to lower RPMs. Moreover, below a certain tuning value of the pendulum, the resonance disappears ($\tilde{n} = 1.479$). It should also be noted that, reducing the tuning value with the aim of eliminating the resonance results in an increase in the vibration amplitude of the first rotor compared to the reference model, except around and above the resonance. As can be seen from Fig. 18.2, there is a tuning value between ($\tilde{n} = 1.482$) and ($\tilde{n} = 1.496$) below which this vibration amplification occurs.

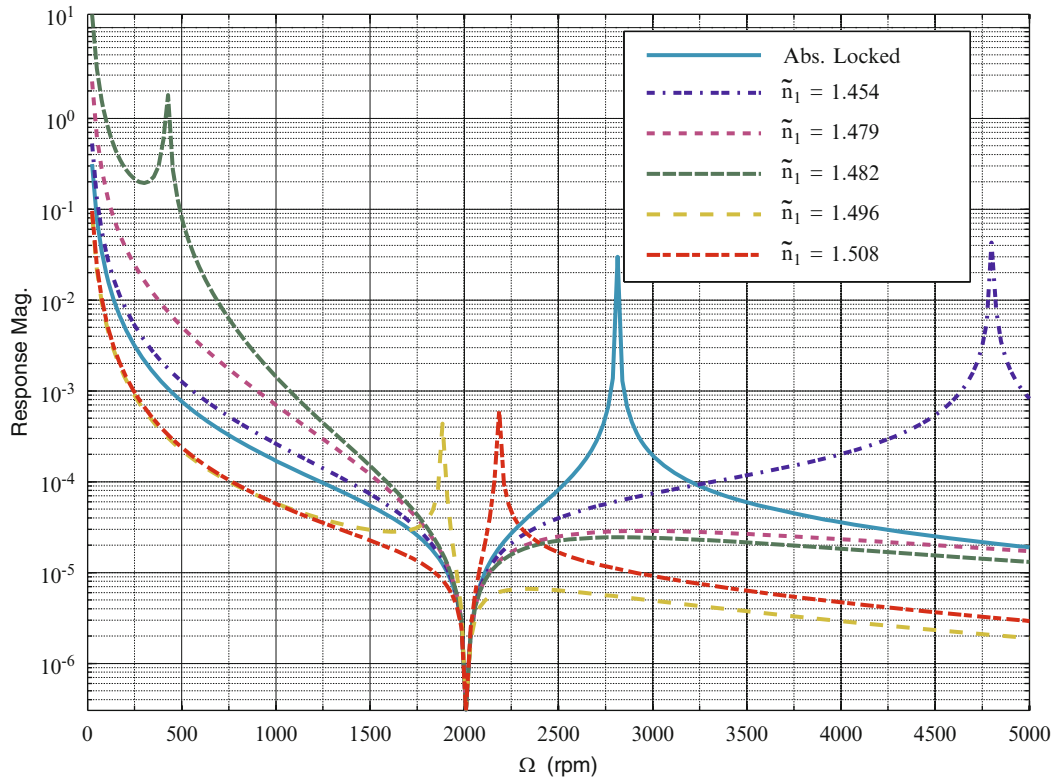


Fig. 18.2 Two-rotor system with absorber attached to the first rotor; frequency response of the first rotor as the rotor speed varies. $N = 2, M = 1, J_1 = J_2 = 0.1, \epsilon_1 = 0.05, \epsilon_2 = 0$

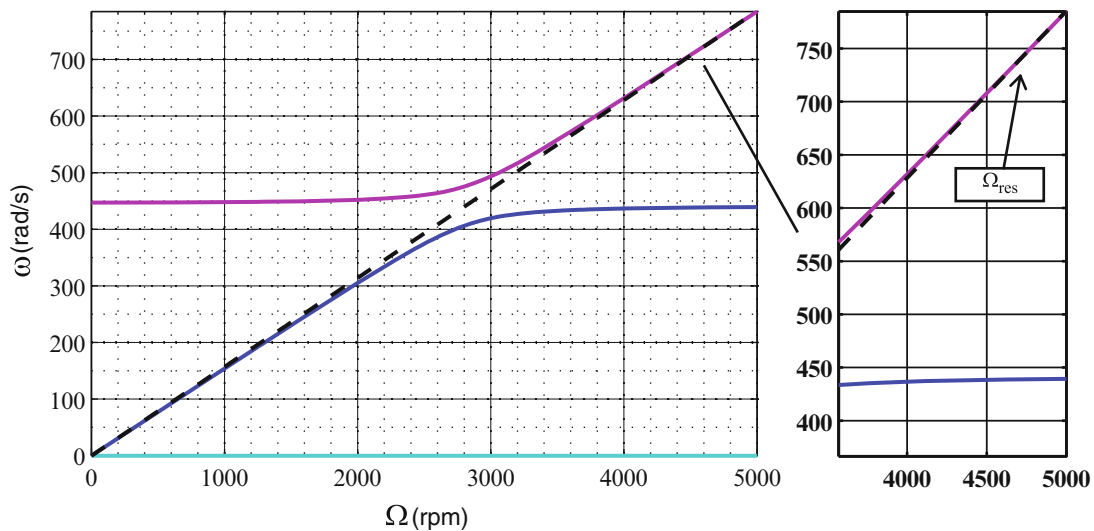


Fig. 18.3 Two-rotor system with absorber attached to the first rotor; natural frequencies vs. rotor speed Ω . $J_1 = J_2 = 0.1, \epsilon_1 = 0.05, \epsilon_2 = 0, \tilde{n}_1 = 1.454$. The *dashed line* is the frequency of order excitation, while the *solid lines* are system modal frequencies

Another observation that can be made from Fig. 18.2 is that the anti-resonance point, which is created by the second rotor acting as a frequency tuned torsional vibration absorber, is not affected by the addition or tuning of the pendulum vibration absorber. Also, over-tuning ($\tilde{n} > n$) the pendulum in this configuration does not eliminate the resonance of the reference system. However, both the overall vibration amplitude is attenuated, except at resonance, and the resonance speed is decreased.

In Figs. 18.3, 18.4, and 18.5, the system natural frequencies of the system are plotted versus the rotor speed for $\tilde{n}_1 = 1.454, \tilde{n}_1 = 1.496$ and $\tilde{n}_1 = 1.508$, respectively. Note that the DOF of the system is three ($N = 2, M = 1$) and there are three

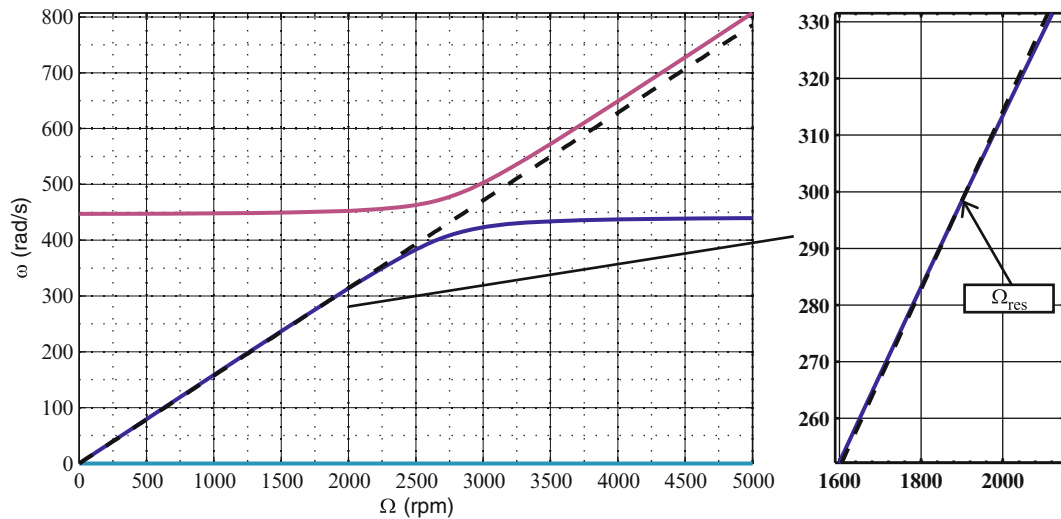


Fig. 18.4 Two-rotor system with absorber attached to the first rotor; natural frequencies vs. rotor speed Ω . $J_1 = J_2 = 0.1, \epsilon_1 = 0.05, \epsilon_2 = 0, \tilde{n}_1 = 1.496$. The dashed line is the frequency of order excitation, while the solid lines are system modal frequencies

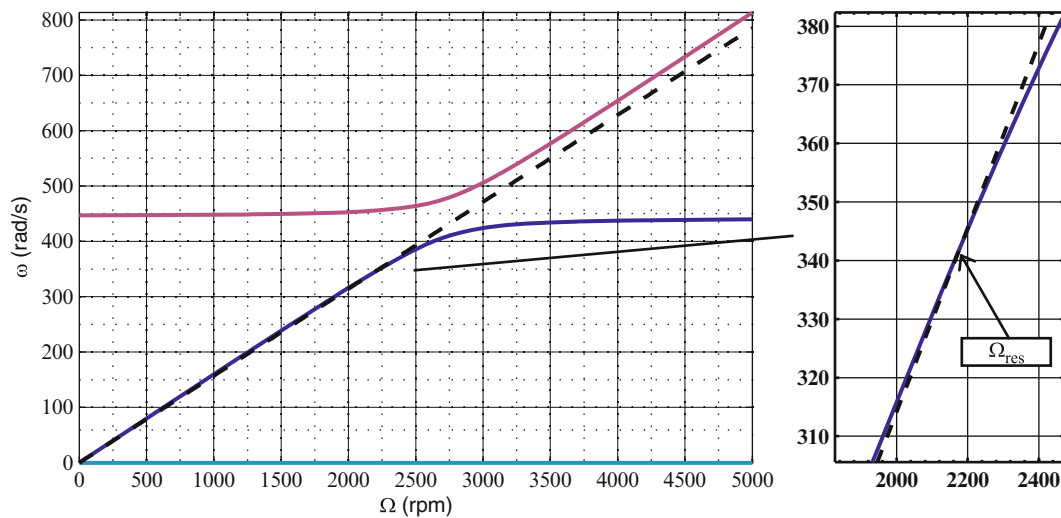


Fig. 18.5 Two-rotor system with absorber attached to the first rotor; natural frequencies vs. rotor speed Ω , $J_1 = J_2 = 0.1, \epsilon_1 = 0.05, \epsilon_2 = 0, \tilde{n}_1 = 1.508$. The dashed line is the frequency of order excitation, while the solid lines are system modal frequencies

natural frequencies. The first mode is the zero frequency rigid body mode. The other two depend on the mean rotation speed, Ω , and these arise from the interaction of a constant frequency (rotor torsional mode) and an order frequency (absorber). For zero absorber inertia, these are a flat curve and a line with slope n , and with finite absorber inertia these split and exhibit veering [1]. When the excitation frequency ($n\Omega$), depicted by the black dashed curve, intersects with one of these natural frequency curves, resonance occurs at the corresponding rotor speed. As the absorber tuning is decreased from overtuned (Fig. 18.5), the resonance point moves from the dark blue natural frequency curve down to zero rotor speed, and disappear for a small range of tuning values. Further undertuning has the resonance appear at larger rotor speeds, on the purple curve, and moving again to lower speeds along this curve. Note that for a small range of absorber tuning values the excitation curve lies between the two veering natural frequency curves, leading to elimination of the resonance, as in the purple frequency-response curve in Fig. 18.2. This also happens when absorbers are applied to flexible blades fixed to a rotor and subjected to engine order excitation [1]. Another interesting characteristic is that the resonances may occur at intersections of curves with very similar slopes, meaning that a small error due to manufacturing tolerances can lead to large changes in the resonant speeds.

In Fig. 18.6 the frequency response for a two rotor element system with the absorber attached to the second rotor is shown for various \tilde{n} values. In this case, again, under-tuning reduces the resonant speed and below a certain tuning the resonance

Fig. 18.6 Two-rotor system with absorber attached to the second rotor; frequency response of the first rotor as the rotor speed varies. $J_1 = J_2 = 0.1$, $\epsilon_1 = 0, \epsilon_2 = 0.05$

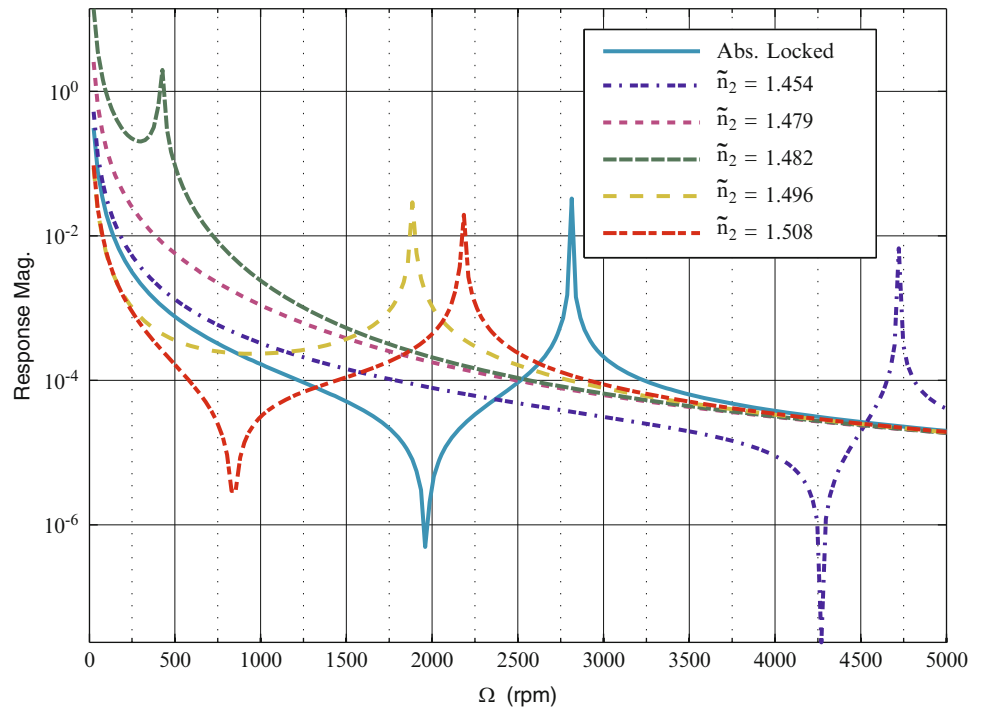
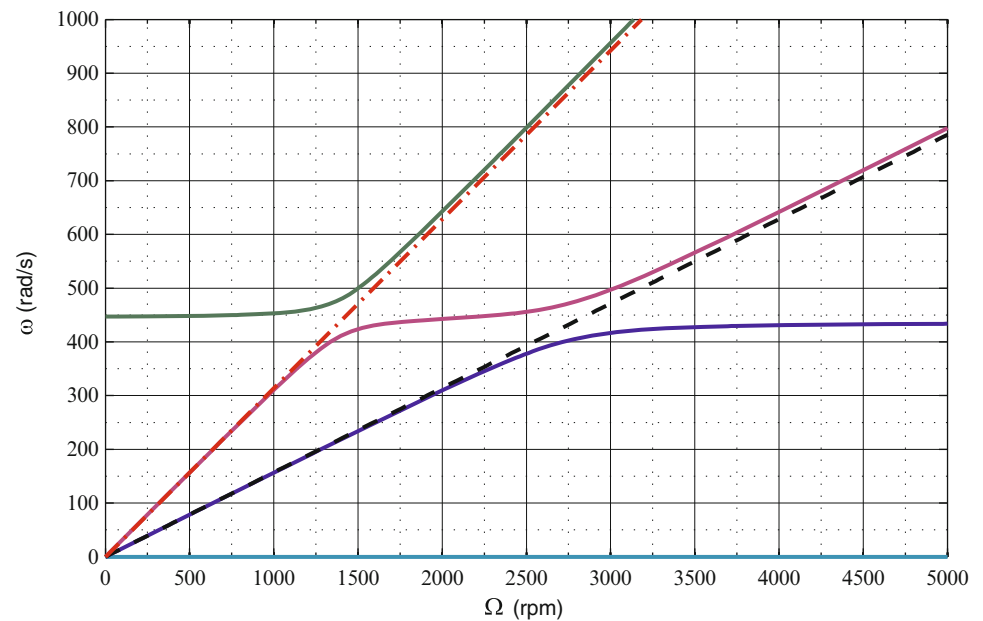


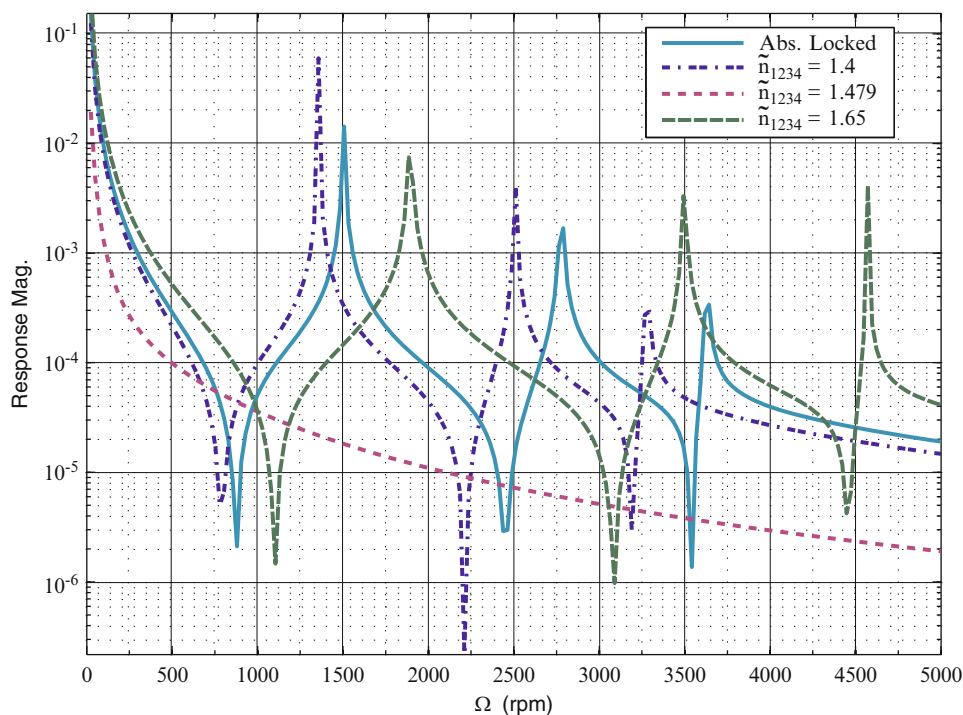
Fig. 18.7 Two-rotor system where one absorber is attached to first rotor and another to second rotor; natural frequencies vs. rotor speed Ω . $J_1 = J_2 = 0.1, \epsilon_1 = 0.05, \epsilon_2 = 0.05, \tilde{n}_1 = 1.479, \tilde{n}_2 = 2.961$



completely disappears. However, the anti-resonance region does not appear when the pendulum is under-tuned. The effective inertia of the second rotor that is equipped with an absorber in this configuration depends on the rotation speed [6]. Thus, unlike the case where only the first rotor is equipped with an absorber, the antiresonance point shifts or disappears as observed in the figure.

Pendulum absorbers of multiple orders are of practical interest, due to the fact that pendulums tuned at a given order can generate higher order harmonics due to nonlinear effects [5]. In these cases one can utilize multiple absorbers tuned at different orders [5]. With this in mind, we consider a two rotor system that is coupled with one absorber placed at first rotor, J_1 , tuned near order 1.5 and one absorber placed at the second rotor, J_2 tuned near order 3. In Fig. 18.7, the natural frequencies vs. Ω curves are plotted with two excitation curves, namely $n = 1.5$ (dashed line) and $n = 3.0$ (dashed-dotted line). Note that, since the DOF is $N + M = 4$, there are four natural frequency curves, including the rigid body motion mode. This figure shows that one can find no resonance regions in applications with multiple excitation orders.

Fig. 18.8 Four-rotor system where each rotor is equipped with an absorber; frequency response of the first rotor as the rotor speed varies. $J_1 = J_2 = J_3 = J_4 = 0.1$, $\epsilon_1 = \epsilon_2 = \epsilon_3 = \epsilon_4 = 0.05$



The last case investigated in this work has a configuration consisting of four identical rotors. Each rotor is equipped with a pendulum absorber. The inertial properties and the tuning of these absorbers are kept identical to each other. In Fig. 18.8, the frequency response curves of the first rotor of this configuration for various \tilde{n} values are plotted along with the reference case where the absorbers are locked. It is evident from these curves that even with high DOFs, with a correct set of parameters and tuning one can obtain a no-resonance zone. Moreover, we see that when the absorbers are tuned to $\tilde{n} = 1.479$, the response of the first rotor is lower than the reference case almost throughout the RPM range. The resonances emerged in these cases can easily be seen in Figs. 18.9, 18.10, and 18.11 at RPMs where the dashed excitation line crosses the natural frequency lines.

18.1.3 Conclusions and Future Work

This work is a first step towards developing analytical tools for the design of order-tuned absorbers for systems with torsional flexibility. Understanding the parameter dependence of the system resonances is essential to tuning these pendulum absorbers for good performance, and to avoid resonances at low rotor speeds. It is seen that avoiding resonance and reducing torsional vibration levels are sometimes competing goals, and absorber tuning will depend on the specific goals in a given application. Note that due to the fact that the resonance points correspond to intersections of lines with nearly equal slopes, the resonance points are highly sensitive to small changes in system parameters. Results from simple models like those considered here provide guidance for interpreting results obtained from more complete and complex finite-element models of powertrain systems. In addition, since these absorbers are typically designed to operate into their nonlinear range, the design tools developed for these linear models must be generalized to account for nonlinear dynamic behavior. While these models do not consider damping, the present analysis provides valuable information about the resonance properties of the system. Also, the damping in many applications is small, in which case these models can provide valuable quantitative response predictions away from the resonance conditions.

Acknowledgements This work is supported by the US National Science Foundation under grant CMMI-1100260. The authors are grateful to Brendan Vidmar and Abhisek Jain of MSU for helpful discussions.

Fig. 18.9 Four-rotor system where each rotor is equipped with an absorber; natural frequencies vs. rotor speed Ω .

$J_1 = J_2 = J_3 = J_4 = 0.1, \epsilon_1 = \epsilon_2 = \epsilon_3 = \epsilon_4 = 0.05, \tilde{n}_1 = \tilde{n}_2 = \tilde{n}_3 = \tilde{n}_4 = 1.4$

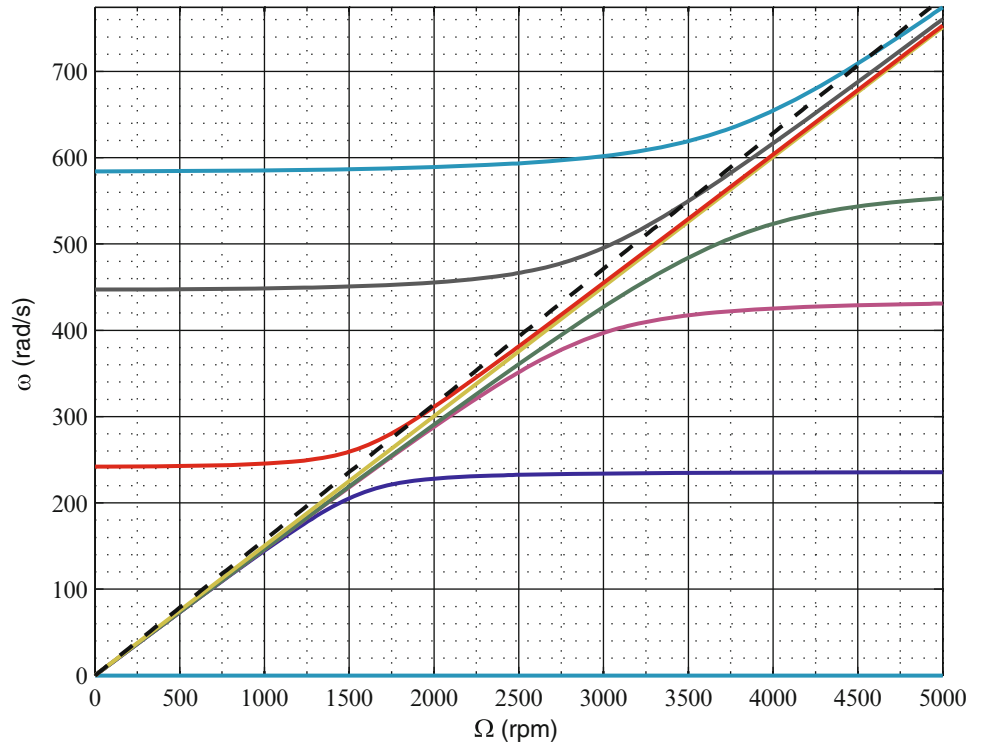


Fig. 18.10 Four-rotor system where each rotor is equipped with an absorber; natural frequencies vs. rotor speed Ω .

$J_1 = J_2 = J_3 = J_4 = 0.1, \epsilon_1 = \epsilon_2 = \epsilon_3 = \epsilon_4 = 0.05, \tilde{n}_1 = \tilde{n}_2 = \tilde{n}_3 = \tilde{n}_4 = 1.479$

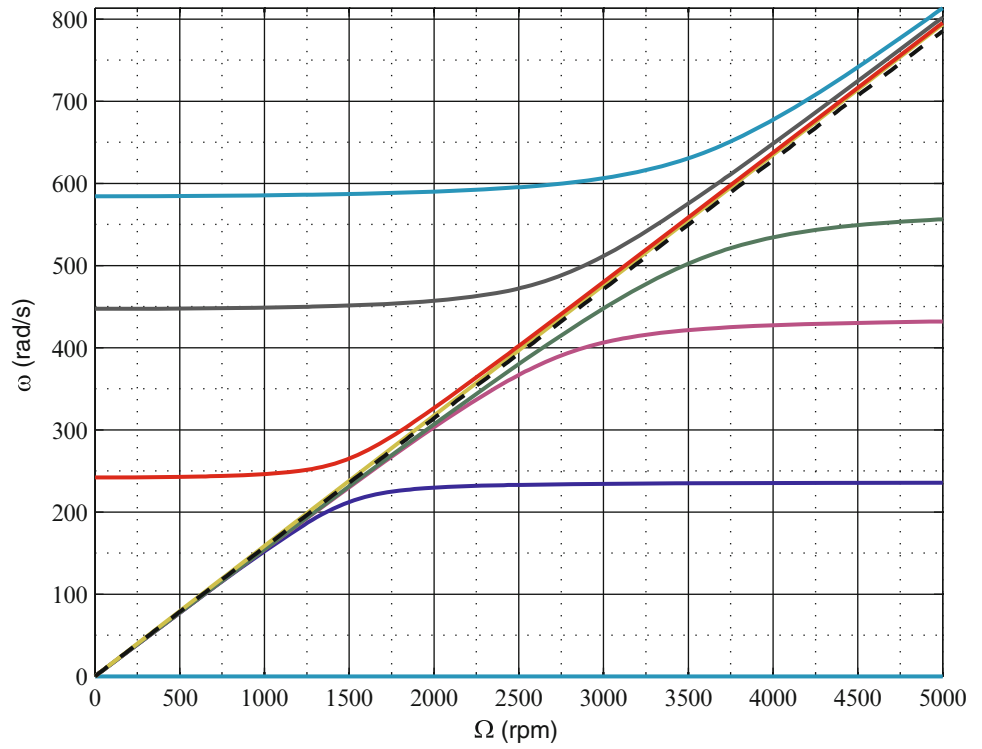
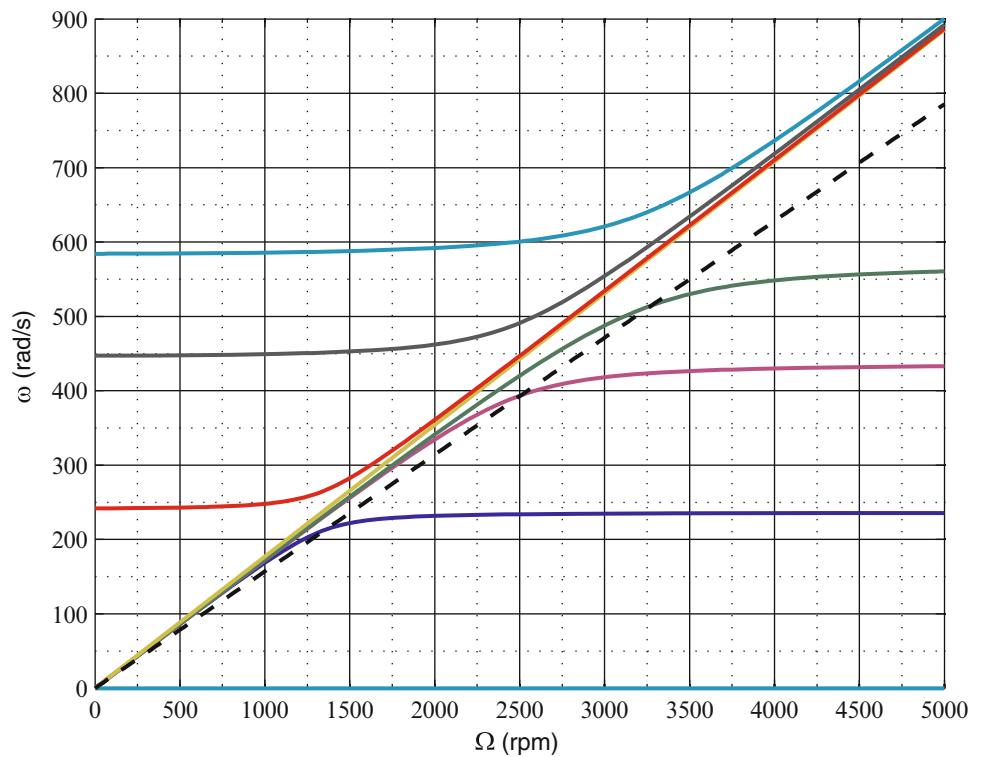


Fig. 18.11 Four-rotor system where each rotor is equipped with an absorber; natural frequencies vs. rotor speed Ω .

$$J_1 = J_2 = J_3 = J_4 = 0.1, \epsilon_1 = \epsilon_2 = \epsilon_3 = \epsilon_4 = 0.05, \tilde{n}_1 = \tilde{n}_2 = \tilde{n}_3 = \tilde{n}_4 = 1.65$$



References

1. Gozen S, Olson BJ, Shaw SW, Pierre C (2012) Resonance suppression in multi-degree-of-freedom rotating flexible structures using order-tuned absorbers. *J Vib Acoust* 134:061016
2. Nester TM, Haddow AG, Shaw SW, Brevick JE, Borowski VJ (2003) Vibration reduction in variable displacement engines using pendulum absorbers. In: Proceedings of the SAE noise and vibration conference and exhibition, Paper 2003-01-1484
3. Shaw SW, Geist BK (2010) Tuning for stability and performance in nearly-tautochronic torsional vibration absorbers. *J Vib Acoust* 132:041005
4. Swank M, Lindemann P (2011) Dynamic absorbers for modern powertrains. SAE Paper 2011-01-1554. SAE International
5. Vidmar BJ (2012) Analysis and design of multiple order centrifugal pendulum vibration absorbers. Ph.D. dissertation, Michigan State University, 164 pp; AAT 3548768
6. Wilson K (1968) Practical solutions of torsional vibration problems. Chapman and Hall Ltd, London (Chapter XXX)

Chapter 19

Structural Modal Identification Through High Speed Camera Video: Motion Magnification

Justin G. Chen, Neal Wadhwa, Young-Jin Cha, Frédo Durand, William T. Freeman, and Oral Buyukozturk

Abstract Video cameras offer the unique capability of collecting high density spatial data from a distant scene of interest. They could be employed as remote monitoring or inspection sensors because of their commonplace use, simplicity, and relatively low cost. The difficulty is in interpreting the video data into a usable format, such as displacement, that is familiar to engineers. A methodology called motion magnification, developed for visualizing exaggerated versions of small displacements, is extended to modal identification in structures. Experiments in a laboratory setting on a cantilever beam were performed to verify the method against accelerometer and laser vibrometer measurements. Motion magnification is used for modal analysis of cantilever beams to visualize mode shapes and calculate mode shape curvature as a basis for damage detection. Suggestions for applications of this methodology and challenges in real-world implementations are given.

Keywords Computer vision • Standoff condition assessment • Modal identification • Mode shape • High speed video

19.1 Introduction

Modal analysis of structures depends on the accurate and swift collection of data from a vibrating structure so the data can be later analyzed to determine the modal characteristics. The end goal for the development of a sensor system for modal analysis is to be able to robustly, precisely, quickly, and remotely collect data from a vibrating structure. Contact accelerometers are commonly used for modal analysis and are extremely accurate, however densely instrumenting a structure is difficult and tedious, and when the structure is small compared to the size of an accelerometer, the presence of added mass from accelerometers can affect the result. Non-contact methods of measurement avoid these drawbacks and are being researched intensely for the purposes of modal analysis.

Non-contact methods of vibration measurement generally depend on some sort of electromagnetic radiation to transmit the information. Microwave interferometry has been studied [1], and laser methods such as laser vibrometry have also been studied [2]. Cameras measuring visible light provide an interesting method for measuring movement. They can range from precise instruments for high-frequency and high-resolution video or inexpensive units such as those on cell phones. There are also cameras that already monitor infrastructure for traffic or security reasons.

Motion can be quantified in video using a number of image processing techniques. Less sophisticated methods use edge detection, target objects, or lights to more easily measure any structural motion [3–5]. More recent methods make use of computer vision techniques, such as measurements of optical flow to determine the displacements of structures which is related to the techniques to be presented in this paper [6].

Recently, new computer vision techniques, collectively called motion magnification, were introduced to magnify small motions in videos [7–9]. The most recent motion magnification techniques use a signal processing approach to analyze image

J.G. Chen • Y.-J. Cha • O. Buyukozturk (✉)
Department of Civil and Environmental Engineering, Massachusetts Institute of Technology, 77 Massachusetts Avenue,
Cambridge, MA 02139, USA
e-mail: obuyuk@mit.edu

N. Wadhwa • F. Durand • W.T. Freeman
Computer Science and Artificial Intelligence Laboratory, Massachusetts Institute of Technology, 77 Massachusetts Avenue,
Cambridge, MA 02139, USA

motions in a way analogous to an Eulerian framework for fluid flow analysis. They are ideal for computing and visualizing mode shapes because they are capable of detecting small subpixel motions that are present in the modal motions of vibrating structures and because they are able to separate the different modal motions through the use of temporal filtering.

The objective of this paper is to show how a camera can be used with computer vision techniques and motion magnification to identify the mode shapes of a cantilever column. We will first present the theory behind how videos can be analyzed for sensing of displacements or mode shapes. Then, results from a verification experiment comparing the derived displacements from a camera to a laser vibrometer and accelerometer measurement will be presented. Measurements identifying the mode shapes of a cantilever beam will be presented, and conclusions and suggestions for future studies will be given.

19.2 Derivation

Our processing consists of taking a video of a vibrating structure and computing the displacement signal everywhere on the structure in the image using a technique related to phase-based motion magnification [9]. Peaks in the Fourier transform of the displacement signal are used to compute the modal frequencies. For each modal frequency, the displacement signal at all points on the structure in the video is filtered with a narrow temporal bandpass filter centered at the modal frequency. The resulting spatially varying temporally filtered displacement signal can be used to estimate the corresponding mode shape.

The displacement signal is only well defined at edges in the video and then only in the direction perpendicular to the edges. This is because the motion of textureless, homogeneous regions is locally ambiguous. Determining the motion at places where it is ambiguous is an open problem in computer vision known as dense optical flow [10, 11]. However, this approach is often inaccurate and for the purposes of modal detection, it is sufficient to know the motion only at the edges of the structure. In the case of the cantilever beam, the entire beam is an edge and the displacement signal can be determined everywhere on it. We use a technique based on local phase and local amplitude in oriented complex spatial bandpass filters to simultaneously compute the displacement signal and edge strength [12, 13]. The edge strength can then be used to perform a spatially local weighted average of the displacement signal to improve SNR as in phase-based motion magnification [9].

The local phase and local amplitude are locally analogous quantities to the phase and amplitude of Fourier series coefficients. The phase controls the location of basis function while the amplitude controls its strength. In the case of the Fourier transform, the phase corresponds to global motion. Local phase gives a way to compute local motion. For a video, with image brightness specified by $I(x, y, t)$ at spatial location (x, y) and time t , the local phase and local amplitude in orientation θ at a frame at time t_0 is computed by spatially bandpassing the frame with a complex filter $G_2^\theta + iH_2^\theta$ to get

$$A_\theta(x, y, t_0)e^{i\phi_\theta(x, y, t_0)} = (G_2^\theta + iH_2^\theta) \otimes I(x, y, t_0) \quad (19.1)$$

where $A_\theta(x, y, t_0)$ is the local amplitude and $\phi_\theta(x, y, t_0)$ is the local phase. The filters G_2^θ and H_2^θ are specified in the appendix [14]. To increase SNR and change the scale on which the filters are operating, the video sequence is downsampled four times in each dimension spatially prior to application of the filters.

It has been demonstrated that constant contours of the local phase through time correspond to the displacement signal [12, 13]. Using the notation of Eq. (19.1), this can be expressed as

$$\phi_\theta(x, y, t) = c \quad (19.2)$$

for some constant c . Differentiating with respect to time yields

$$\left(\frac{\partial \phi_\theta(x, y, t)}{\partial x}, \frac{\partial \phi_\theta(x, y, t)}{\partial y}, \frac{\partial \phi_\theta(x, y, t)}{\partial t} \right) \cdot (u, v, 1) = 0 \quad (19.3)$$

where u and v are the velocity in the x and y directions respectively. It is approximately the case that $\frac{\partial \phi_\theta(x, y, t)}{\partial y} \approx 0$ and $\frac{\partial \phi_{\pi/2}(x, y, t)}{\partial x} \approx 0$. Thus, the velocity in units of pixel is

$$u = - \left(\frac{\partial \phi_\theta(x, y, t)}{\partial x} \right)^{-1} \frac{\partial \phi_\theta(x, y, t)}{\partial t} \quad \text{and} \quad v = - \left(\frac{\partial \phi_{\pi/2}(x, y, t)}{\partial y} \right)^{-1} \frac{\partial \phi_{\pi/2}(x, y, t)}{\partial t} \quad (19.4)$$

The velocity between the i th frame and the first frame for all i is computed to give a displacement signal in time. The SNR of this signal is increased by performing a spatially local weighted average of the displacement signal using the local amplitude as weights. The displacement signal is converted to units of millimeters by multiplying by the length of an object in the scene divided by the number of pixels it spans.

The result of the aforementioned processing is a displacement signal at all points in the image. Peaks in the Fourier transform of the resulting signal correspond to modal frequencies. Once the modal frequencies are determined, the spatially varying displacement signal can be temporally filtered around each modal frequency. The user can then specify points along the cantilever beam at which to compute the corresponding mode shape.

19.3 Experimental Setups

19.3.1 Verification Test

In order to validate the camera as a sensor for the measurement of displacements and mode shapes an experiment was formulated to compare the results to standard sensors. An accelerometer was mounted on a cantilever beam, and the motion of the accelerometer was simultaneously measured by a laser vibrometer, an accelerometer, and a high speed camera, as shown in Fig. 19.1a. A screenshot of the video from the camera is shown in Fig. 19.1b, and the resolution of the camera was 480×288 , and the frame rate was 5,000 frames per second. In the plane of the accelerometer, the video frame was 104 mm wide. The cantilever beam was excited with an impact hammer, and the subsequent vibration was measured for comparison. The velocity time series from the laser vibrometer was integrated to obtain displacement to verify against the displacements derived from camera measurements of the optical flow of the accelerometer movement. Time synchronization was not possible between the camera and laser vibrometer data set, so in the data the time series were aligned by hand. The data from the laser vibrometer, accelerometer, and camera derived displacement was fast Fourier transformed (FFT), and integrated to be displacement so that the frequency peaks and noise floors could be directly compared.

19.3.2 Cantilever Beam Test

To test the camera as a sensor for determining the mode shape of structures, an experiment measuring a cantilever beam was formulated. The cantilever beam was instrumented with nine accelerometers so that the extracted mode shapes from the accelerometers could be compared with those extracted from the camera data. As before, the beam was excited with an impact hammer and the subsequent vibration was measured by the camera and accelerometers. Figure 19.2a shows a side view of the instrumented cantilever beam, and Fig. 19.2b shows a screenshot from the camera video. Video was taken with the camera at 1,500 frames per second, and the resolution of the video was $1,056 \times 200$. In the plane of the column, the video frame was approximately 124 mm wide.

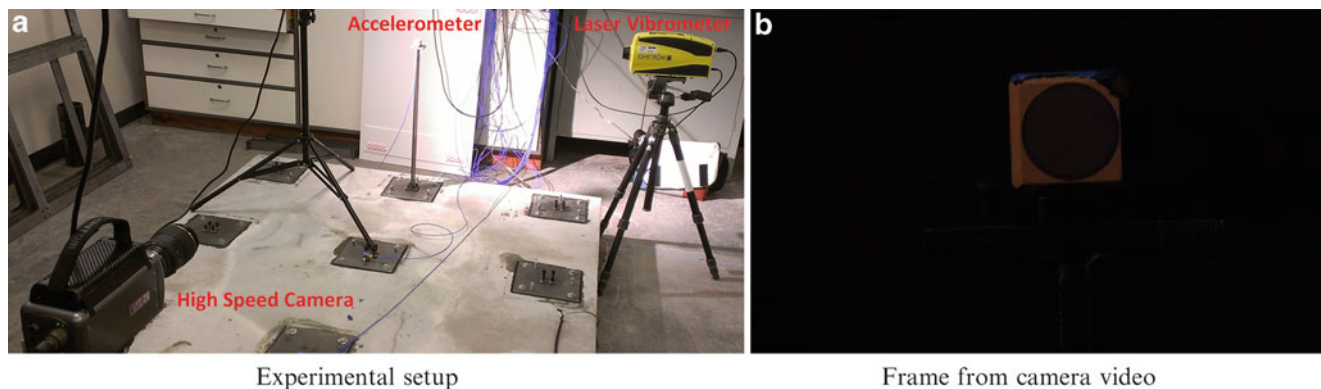
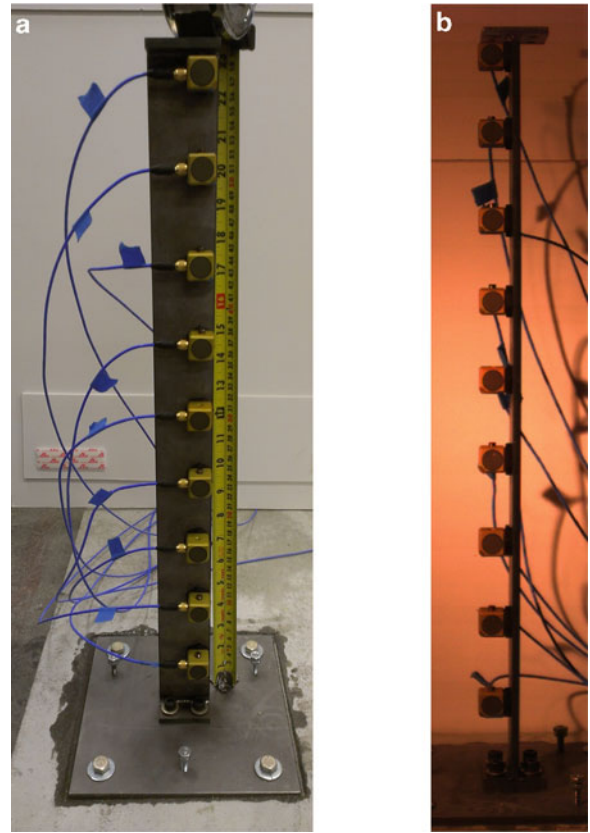


Fig. 19.1 Experimental setup for verification test (a) and frame from high speed camera video (b)

Fig. 19.2 Cantilever beam experimental setup: instrumented cantilever beam side view (a), screenshot from video camera (b)



19.4 Results

19.4.1 Verification Test

The results of the verification measurement were the various signals of the accelerometer movement as measured by a laser vibrometer, an accelerometer, and a high speed camera. The displacement from the camera was extracted using the local phase of the measured video (Sect. 19.2). The raw signals were the displacement time series from the camera, velocity time series from the laser vibrometer, and acceleration from the accelerometer. To directly compare the time series results, the laser vibrometer velocity time series was integrated numerically and results are shown in Fig. 19.3. The displacement derived from the camera closely matches the integrated laser vibrometer displacement for the whole 9 s of data. In general however, the camera signal shows less detail and is more noisy than the laser vibrometer.

To compare the noise floor of the displacement derived from the camera with the other measurement methods, the signals were fast Fourier transformed and integrated in the frequency domain to obtain the displacements. The plot comparing them is shown in Fig. 19.4. Both the accelerometer and laser vibrometer data show 8 resonant frequencies above the noise floor from 0 to 2,500 Hz, while the camera only shows the first 4 resonant frequencies of the cantilever beam. The noise floor of the camera for this 9 s measurement is approximately 40 nm, while the laser vibrometer has a noise floor of about 0.2 nm, and the accelerometer has a noise floor of about 0.02 nm. Given the conversion factor of 480 pixels for 104 mm, and accounting for the length of the measurement, this gives a noise floor of the camera of approximately 1×10^{-5} pixels per root Hertz. This verification measurement gives us reasonable confidence that the mode shapes of a column can be successfully measured by extracting displacement from video measured with a high speed camera.

19.4.2 Cantilever Beam Test

The method for extracting mode shapes of the cantilever beam is analogous to the method used to extract displacement from the high speed camera video in the verification test. The accelerometer instrumented cantilever beam was measured with the high speed camera and the video was cropped to a region containing only one of each of the nine accelerometers.

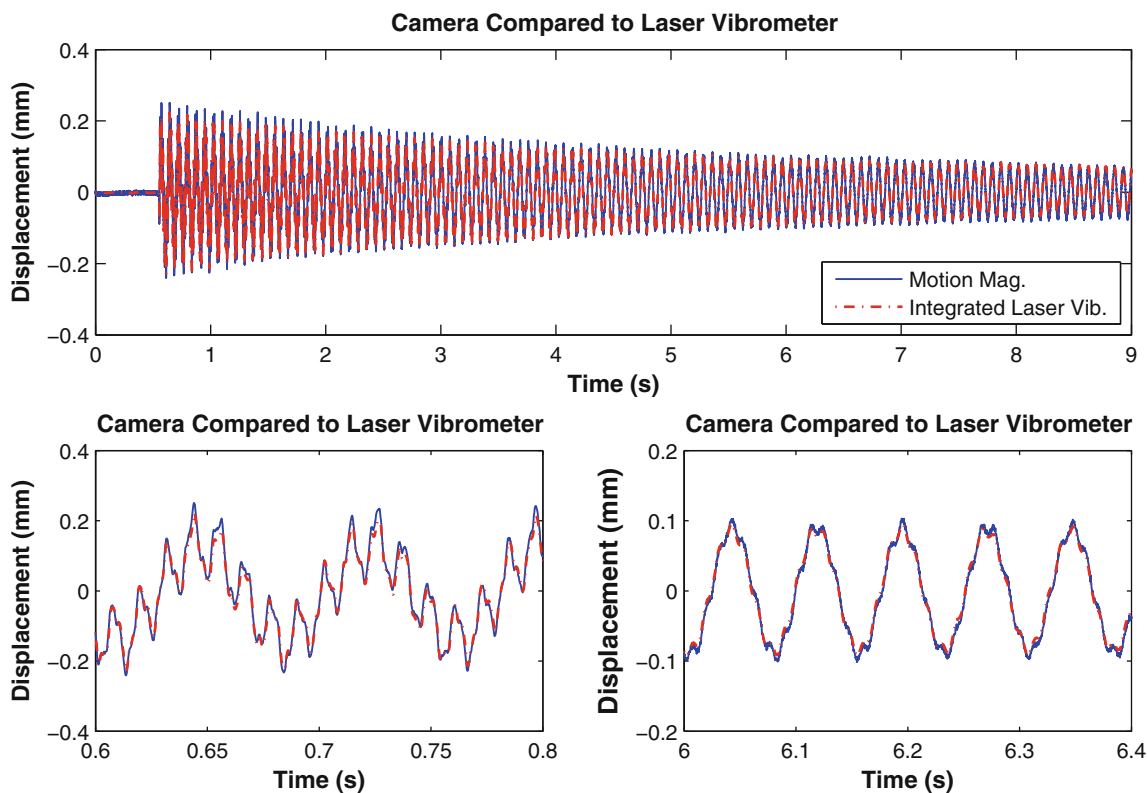
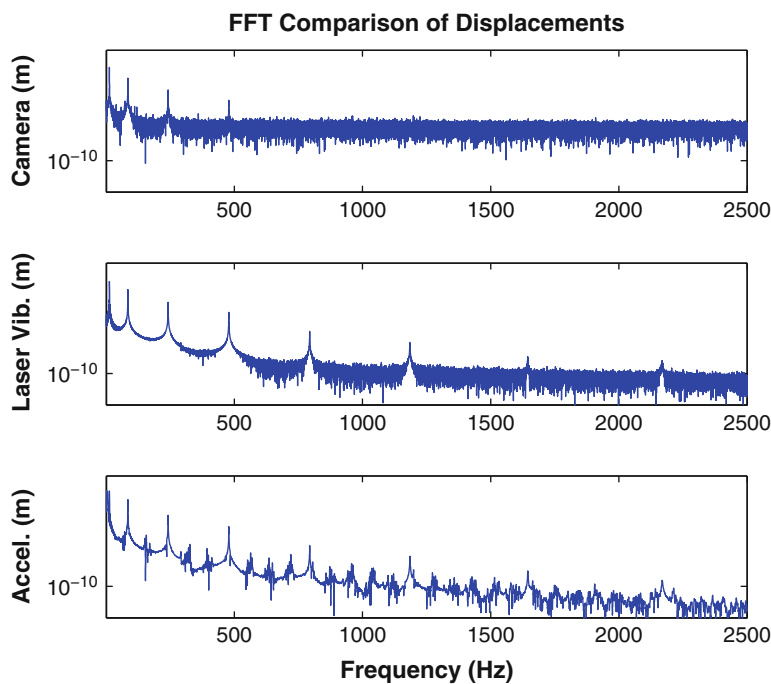


Fig. 19.3 Comparison between displacements derived from the camera and the laser vibrometer

Fig. 19.4 Frequency space comparison between displacements derived from the camera, laser vibrometer, and accelerometers



The motion magnification derived algorithm was used to extract the displacement of the accelerometers on the column, and then processed to determine the mode shape. The camera was capable of discerning the vibration of the first four resonant frequencies of the column at 12.5, 80, 226, and 444 Hz, and thus four mode shapes were extracted. The mode shapes extracted from the camera measurement are shown in Fig. 19.5a. The mode shapes are close to the expected theoretical shape for the mode shapes of a cantilever beam. Mode shape curvatures were also calculated from the mode shapes shown in Fig. 19.5b,

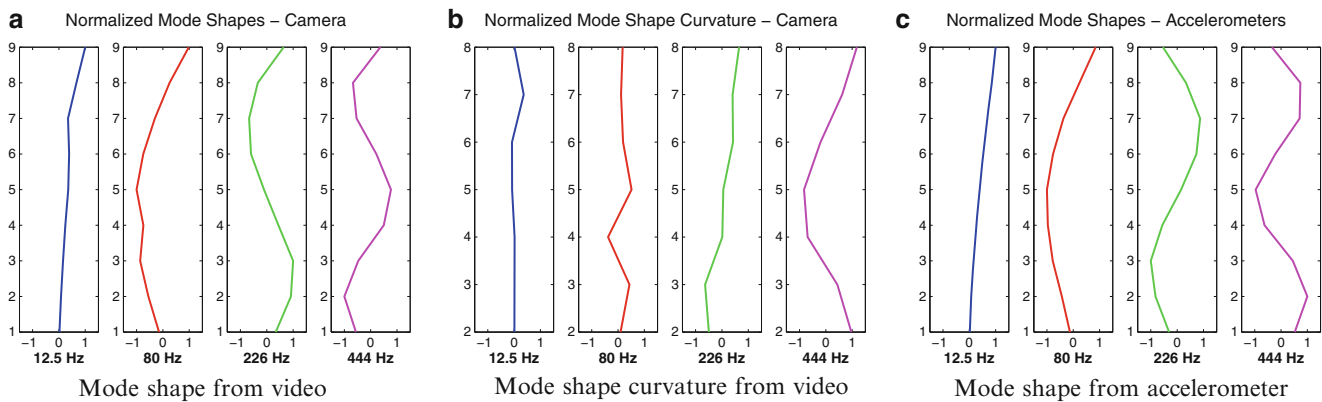


Fig. 19.5 Normalized mode shapes from displacements extracted from camera video (a), normalized mode shape curvature from camera video (b) and normalized mode shape from accelerometers (c)

demonstrating that the data extracted from the camera could be useful for eventual damage detection in structures. It is expected that the camera can be a much easier way of instrumenting a structure with a denser set of measurements which would be useful for more accurate determination of mode shape and mode shape curvature.

The cantilever beam was instrumented with accelerometers to provide mode shapes from a conventional method of measurement for comparison. The mode shapes from the accelerometer data are shown in Fig. 19.5c. The camera extracted mode shapes compare well to mode shapes derived from the accelerometer data.

19.5 Conclusion

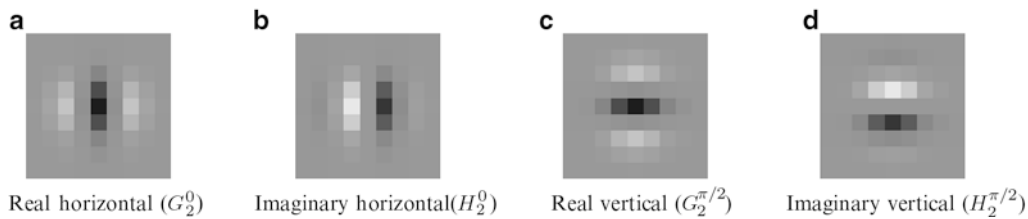
In this paper we have assessed motion magnification for extracting displacements from high speed video and demonstrated the algorithm's capability of extracting the mode shapes of a cantilever beam from a video measurement. Motion magnification represents a novel method for deriving mode shapes and displacements from videos of vibrating structures. Changes in local phase in the video are processed to determine the displacement signal at every point in the video. When the displacement signal of an accelerometer on a beam is computed, the displacements extracted closely match those extracted by a laser vibrometer, and the resulting noise floor of the camera is approximately 1×10^{-5} pixels per root Hertz. The first four mode shapes of an instrumented cantilever beam at 12.5, 80, 226, and 444 Hz were extracted and compared favorably to both the expected theoretical mode shapes and the accelerometer data derived mode shapes. Mode shape curvature was calculated from the video extracted mode shapes as a basis for the potential use of the technique for damage detection.

Several areas of this methodology can be improved with further research. Automation of the algorithms used such that moving objects in the frame of the video can have their mode shapes extracted would be immensely useful for modal analysis. For the measurement of outdoor structures, further challenges need to be overcome, specifically atmospheric aberration due to changes in the index of refraction of air with variations in temperature. This issue may be solved by further use of the methods derived from motion magnification. Further studies on using the camera derived displacements for damage detection in structures will also be conducted. The eventual goal is to be able to measure any structure, measure the displacement, characterize its modal behavior, and potentially detect any damage.

Acknowledgements The authors acknowledge the support provided by Royal Dutch Shell through the MIT Energy Initiative, and thank chief scientists Dr. Dirk Smit, Dr. Sergio Kapusta, project manager Dr. Yile Li, and Shell-MIT liaison Dr. Jonathan Kane for their oversight of this work. We also acknowledge Draper Laboratory for providing experimental equipment. At the time of this work, Neal Wadhwa was supported by the DoD through the NDSEG fellowship program. Special thanks are due to Reza Mohammadi for his help with experimental collection of the data, specifically as the hammer man.

Table 19.1 Filter coefficients to compute horizontal and vertical local phase and local amplitude

Tap #	G_{f1}	G_{f2}	H_{f1}	H_{f2}
-4	0.0094	0.0008	-0.0098	0.0008
-3	0.1148	0.0176	-0.0618	0.0176
-2	0.3964	0.1660	0.0998	0.1660
-1	-0.0601	0.6383	0.7551	0.6383
0	-0.9213	1.0000	0.0000	1.0000
1	-0.0601	0.6383	-0.7551	0.6383
2	0.3964	0.1660	-0.0998	0.1660
3	0.1148	0.0480	0.0618	0.0176
4	0.0094	0.0008	0.0098	0.0008
Filter	Filter in x	Filter in y		
Real horizontal (G_2^0)	G_{f1}	G_{f2}		
Imaginary horizontal (H_2^0)	H_{f1}	H_{f2}		
Real vertical ($G_2^{\pi/2}$)	G_{f2}	G_{f1}		
Imaginary vertical ($H_2^{\pi/2}$)	H_{f2}	H_{f1}		

**Fig. 19.6** Two dimensional representation of filters used to compute horizontal (a-b) and vertical (c-d) local phase and local amplitude

Appendix: Steerable Filter Taps

Freeman et al. [14] specify steerable filters that we use in this paper. For convenience, we reproduce their filters here in Table 19.1 and Fig. 19.6.

References

1. Farrar CR, Darling TW, Migliori A, Baker WE (1999) Microwave interferometers for non-contact vibration measurements on large structures. *Mech Syst Signal Process* 13(2):241–253
2. Stanbridge A, Ewins D, Khan A (2000) Modal testing using impact excitation and a scanning LDV. *Shock Vib* 7(2):91–100
3. Patsias S, Staszewskiy W (2002) Damage detection using optical measurements and wavelets. *Struct Health Monit* 1(1):5–22
4. Wahbeh AM, Caffrey JP, Masri SF (2003) A vision-based approach for the direct measurement of displacements in vibrating systems. *Smart Mater Struct* 12(5):785
5. Lee JJ, Shinozuka M (2006) A vision-based system for remote sensing of bridge displacement. *Ndt & E Int* 39(5):425–431
6. Caetano E, Silva S, Bateira J (2011) A vision system for vibration monitoring of civil engineering structures. *Exp Tech* 35(4):74–82
7. Liu C, Torralba A, Freeman WT, Durand F, Adelson EH (2005) Motion magnification. *ACM Trans Graph* 24:519–526
8. Wu H-Y, Rubinstein M, Shih E, Guttag J, Durand F, Freeman W (2012) Eulerian video magnification for revealing subtle changes in the world. *ACM Trans Graph (Proc SIGGRAPH 2012)* 31(4):65
9. Wadhwa N, Rubinstein M, Durand F, Freeman WT (2013) Phase-based video motion processing. *ACM Trans Graph (Proc SIGGRAPH 2013)* 32(4):80
10. Horn B, Schunck B (1981) Determining optical flow. *Artif Intell* 17(1–3):185–203
11. Lucas BD, Kanade T (1981) An iterative image registration technique with an application to stereo vision. In: *Proceedings of the 7th international joint conference on artificial intelligence (IJCAI '81)*, pp 674–679, Apr 1981
12. Fleet DJ, Jepson AD (1990) Computation of component image velocity from local phase information. *Int J Comput Vis* 5(1):77–104
13. Gautama T, Van Hulle M (2002) A phase-based approach to the estimation of the optical flow field using spatial filtering. *IEEE Trans Neural Network* 13(5):1127–1136
14. Freeman WT, Adelson EH (1991) The design and use of steerable filters. *IEEE Trans Pattern Anal Mach Intell* 13(9):891–906

Chapter 20

Operational Modal Analysis with Photo Images from Low Speed Digital Camera

Marcos Tan Endo, Arlindo Neto Montagnoli, and Rodrigo Nicoletti

Abstract Structural vibration is commonly measured with single point sensors, thus requiring a number of sensors equal to the number of points to be measured in the structure. Depending on the structure, the number of sensors needed is large resulting in significant costs in the measurement procedure. For this reason, full field measurement systems have been developed, where one sensor is responsible for measuring the entire structure. However, such systems require expensive devices (fast cameras, stereographic cameras, laser scanners). In this work, one presents a more affordable approach for full field measurement based on photographic images obtained with a low speed camera (maximum of 3 fps). The method is suitable for structures under periodic excitations and 2D motion. Images of the vibrating structure are taken and post processing is used to calculate the displacements of points of interest in the structure. Gathering the information of all images, a sub-sampling technique is used to reconstruct the vibration signal. Experimental results show the effectiveness of performing an Operational Modal Analysis and retrieving normal modes and natural frequencies up to 20 Hz with an acquisition period of 1.5 s.

Keywords Photogrammetry • Operational modal analysis • Sub-sampling • Image processing

20.1 Introduction

In literature, there are many methods dedicated to the measurement of vibration. They can be divided into contact and non-contact sensing devices. The contact sensors, like the accelerometers, strain gauges and LVDTs (Linear Variable Differential Transformers), must be coupled to the system to be measured, thus generating inconveniences as the addition of mass in the system and the difficulty of installation in hard-to-reach places. On the other hand, the non-contact sensors do not require any physical contact with the system to be measured. Examples of such devices are the ESPI (Electronic Speckle Pattern Interferometry), DSPI (Digital Speckle Pattern Interferometry), non-scanning LDV (Laser Doppler Vibrometry) and proximity sensors that have a relatively high cost compared to the traditional contact sensors. In the measuring methods listed above (contact and non-contact), the measurements are generally performed in a specific point (single point measurements). Hence, if there is interest in more points of measurement, it is necessary to use several sensors or increase the number of samples, significantly increasing the time and cost of the measurement process. An alternative for doing multipoint measurements of vibration, with no contact and low cost, is by using a digital camera.

Technological evolution contributed to the development of the method known as digital photogrammetry, which uses only digital cameras for vibration measurements. Photogrammetry has more than a century of history and development, and can be defined as a science-based technology that, through images, can perform measurements and interpretations of the shape and

M.T. Endo • R. Nicoletti (✉)

Department of Mechanical Engineering, University of São Paulo, School of Engineering of São Carlos,
Trabalhador São Carlense 400, 13566-590 São Carlos, Brazil
e-mail: marcos.tan.endo@gmail.com; micolet@sc.usp.br

A.N. Montagnoli

Department Electrical Engineering, Federal University of São Carlos, Center of Exact Sciences and Technology,
Rodovia Washington Luiz km235, 13565-905 São Carlos, Brazil
e-mail: arlindo@ufscar.br

location of an object from one or more photographs [1]. Initially, the measurements were implemented with compact digital cameras. Olaszek [2] was one of the first authors to use the photogrammetric technique to measure the dynamic behavior of bridges, using a single video camera. Other approaches studied vibration measurements in three dimensional space (3D), as in the case of [3] that used a single CCD camera, perfectly synchronized with the stroboscopic illumination, for measuring the vibrating modes of an airplane wing. In other example, Yoshida et al. [4] measured the three-dimensional dynamic behavior of membranes with three synchronized CCD cameras and a sampling rate of 30 fps. However, due to limitations of compact digital cameras, such as low resolution and sampling rate set at 30 fps (maximum), the vibration measurements do not exceed the frequencies of 5 Hz [5].

Aimed at increasing the range of measures frequencies, high speed cameras, which are equipment able to capture images with high sampling rates, began to be used in the vibration measurement. With such devices, Jeon et al. [6] performed measurements of structural vibrations. However, the lower resolution of the cameras restricted the distance of measurements. Due to the increasing utilization of high-speed cameras for vibration measurements, commercial softwares were developed for camera control and image processing. Helfrick et al. [7] used the commercial ARAMIS system together with high-speed cameras for measurements of mechanical and structural systems. Despite the cost of such systems, the high-speed cameras are the most widely used equipment in photogrammetric techniques today.

In this work, in order to measure the vibrations of a structure, the principles of photogrammetry are applied using a digital camera. In this case, the maximum sampling rate of the camera is 3 frames per second and a sub-sampling technique is used. The measurements were performed in a structure excited by a periodical signal via shaker. The specific points of each image are obtained by computational post processing, being later compared with laser vibrometer measurements. An Operational Modal Analysis is performed in the system and results obtained with the camera are compared to those obtained with the laser vibrometer.

20.2 The Operational Modal Analysis

The Operational Modal Analysis (OMA) is an experimental procedure that allows the determination of modal parameters of a structure from its operational response, i.e. from measurements of structure vibration without necessarily knowing the excitation [8,9]. Therefore, the OMA is an input-only identification procedure. Since its development in the beginning of the 1990s, the OMA has been increasingly established in the Engineering community as one of the tools available for dynamic identification of machines and structures. Among its advantages are:

- low cost of implementation, not needing any source of excitation;
- possibility of identifying dynamic characteristics of the whole system in its the most representative points;
- possibility to use the information from OMA in Structure Health Monitoring.

The main disadvantage of the OMA lies on the fact that, if there is no need to measure the input, there is also no guarantee that the input exciting the system actually causes response of all the desired system characteristics. Another disadvantage is that its predicted damping appears to be higher than it actually exists [10].

From the measured time response data of the structure, one can build the spectral density matrix \mathbf{A} :

$$\mathbf{A} = \begin{bmatrix} E_{11} & E_{12} & \cdots & E_{1N} \\ E_{21} & E_{22} & \cdots & E_{2N} \\ \vdots & \vdots & & \vdots \\ E_{N1} & E_{N2} & \cdots & E_{NN} \end{bmatrix} \quad (20.1)$$

where E_{ii} is the auto-spectral density function of the i -th signal, and E_{ij} is the cross-spectral density function between the i -th and the j -th signals.

By applying the Singular Value Decomposition to the spectral density matrix [11], one has:

$$\mathbf{A} = \mathbf{U}\mathbf{S}\mathbf{V}^H \quad (20.2)$$

where \mathbf{U} and \mathbf{V} are orthogonal matrices, and \mathbf{S} is the diagonal matrix with singular values of matrix \mathbf{A} . In this case, vector \mathbf{U} is composed of the eigenvectors of matrix $\mathbf{A}\mathbf{A}^H$ and vector \mathbf{V} is composed of the eigenvectors of matrix $\mathbf{A}^H\mathbf{A}$ [12].

The singular values in \mathbf{S} present peaks at frequencies that correspond to the natural frequencies of the structure/machine (natural frequencies excited by the operational source). The singular vectors in \mathbf{U} or \mathbf{V} , at these frequencies, correspond to the associated eigenvectors of the system.

20.3 Image Acquisition and Processing

In this work, one adopts the coherent sub-sampling technique for capturing the sequence of images of the vibrating system. Therefore, the signal is reconstructed from long acquisition periods. The reconstruction of a signal through the sub-sampling method depends on the assumption that vibration is periodic and its frequency is known. By knowing this, the next step is to perform image acquisition using a micro controller, which adds a small increment of time in each period sampled, or mathematically:

$$T_S = n(kT + \Delta t) \quad (20.3)$$

where T_S is the sampling period, n is an integer, k is the integer number of periods between consecutive samples, T is the period of the signal, and Δt is the time increment.

The position of interest in each image is obtained by computational post processing, which relates the 2D image coordinates (in pixels) with the 3D space coordinates (in millimeters). The relationship between the image coordinates and the space coordinates is given by [13]:

$$s\tilde{\mathbf{m}} = \mathbf{P}\tilde{\mathbf{w}} \quad (20.4)$$

where s is an arbitrary scale factor, $\tilde{\mathbf{m}}$ is the vector of image coordinates, $\tilde{\mathbf{w}}$ is the vector of space coordinates, and \mathbf{P} is the perspective projection matrix, given by:

$$\mathbf{P} = \mathbf{K}[\mathbf{R} \mathbf{t}] \quad (20.5)$$

where \mathbf{R} is the matrix of extrinsic parameters (rotation and translation), and \mathbf{K} is the matrix of intrinsic parameters of the camera (focal lengths and pixel skew).

After finding the matrices of extrinsic and intrinsic parameters, it is necessary to correct radial lens distortion, because the adopted digital camera is non-metric. According to [13], the coefficients k_1 and k_2 that represent the radial distortion of the camera can be calculated by the equation:

$$\begin{bmatrix} (u - u_0)(x^2 - y^2) & (u - u_0)(x^2 - y^2)^2 \\ (v - v_0)(x^2 - y^2) & (v - v_0)(x^2 - y^2)^2 \end{bmatrix} \begin{Bmatrix} k_1 \\ k_2 \end{Bmatrix} = \begin{Bmatrix} \tilde{u} - u \\ \tilde{v} - v \end{Bmatrix} \quad (20.6)$$

and, the coefficients k_1 and k_2 are estimated by the linear method of least squares [14], where \tilde{u} and \tilde{v} are points of the distorted image.

In this work, all parameters were calculated with the aid of a camera calibration toolbox for MATLAB developed by Jean-Yves Bouguet at Computer Vision Research Group of the Department of Electrical Engineering California Institute of Technology. The toolbox finds the camera parameters by processing a sequence of images in different positions of a planar pattern, as shown in Fig. 20.1, using the method of camera calibration proposed by [13].

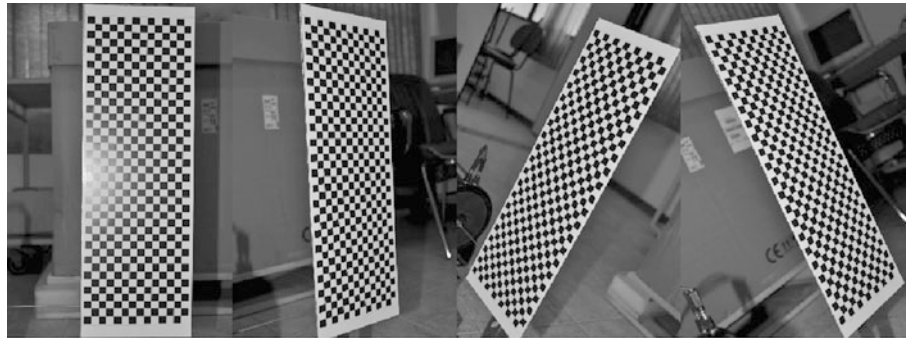


Fig. 20.1 Sequence of images used to calibrate the measurement system

After the definitions of intrinsic and extrinsic parameters of the camera, and of the radial distortion correction of the lenses, it is necessary to convert the points of interest (in pixels) of each sampled image for space coordinates (in millimeters). In the case of finite cameras, the expression that relates the coordinates in pixels to those in millimeters can be represented by:

$$\mathbf{w} = \mu \begin{bmatrix} (\mathbf{KR})^{-1} \mathbf{m} \\ 0 \end{bmatrix} + \begin{bmatrix} (\mathbf{KR})^{-1} p_4 \\ 1 \end{bmatrix} = \mu \begin{bmatrix} \tilde{\mathbf{x}} \\ 0 \end{bmatrix} + \begin{bmatrix} \tilde{\mathbf{c}} \\ 1 \end{bmatrix} \quad (20.7)$$

where p_4 is the last column of matrix \mathbf{P} , $\tilde{\mathbf{x}}$ is an inhomogeneous vector representing the coordinates of a point in the space coordinate frame, and $\tilde{\mathbf{c}}$ is the inhomogeneous representation of the camera center. The coefficient μ is given by:

$$\mu = -\frac{\tilde{c}_3}{\tilde{x}_3} \quad (20.8)$$

with \tilde{c}_3 and \tilde{x}_3 being the last elements of each vector $\tilde{\mathbf{c}}$ and $\tilde{\mathbf{x}}$, respectively.

20.4 Experimental Set-Up

The adopted camera is a Nikon D3100, configured with 18–55 mm lenses, shutter speed of 1/4000 s, and image resolution of 14.2 Mp. Due to the need of high illumination in the points of interest of the structure, five LED modules are used, with luminous flux of 170 lm and color temperature of 6,500 K.

The vibrating structure is composed of a cantilever steel beam, with dimensions 630×30×0.8 mm, and five image targets are mounted on the structure to help acquiring the displacement of the structure (Fig. 20.2a, b). The location of the camera and of the illumination system is shown in Fig. 20.3, where each LED module focuses on one target.

The structure is excited by a shaker coupled to the lower mass of the system. The adopted excitation signal is a Schroeder signal [15], composed of 30 harmonics with period 1.5 s and maximum frequency of 20 Hz, repeatedly sent to the shaker. A laser Doppler vibrometer is also used to measure the behavior of the structure. The results obtained with the camera and image processing are then compared to those obtained with the laser vibrometer, as a reference.

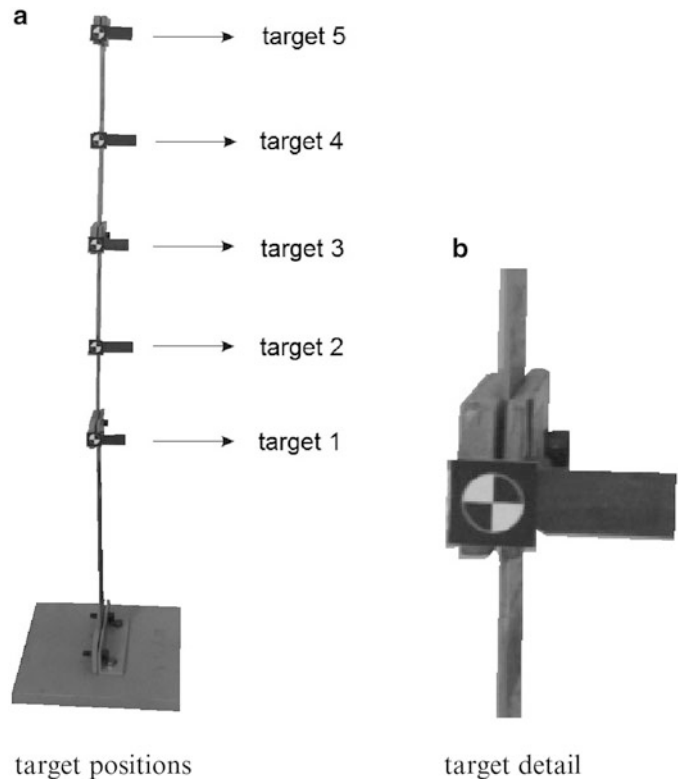
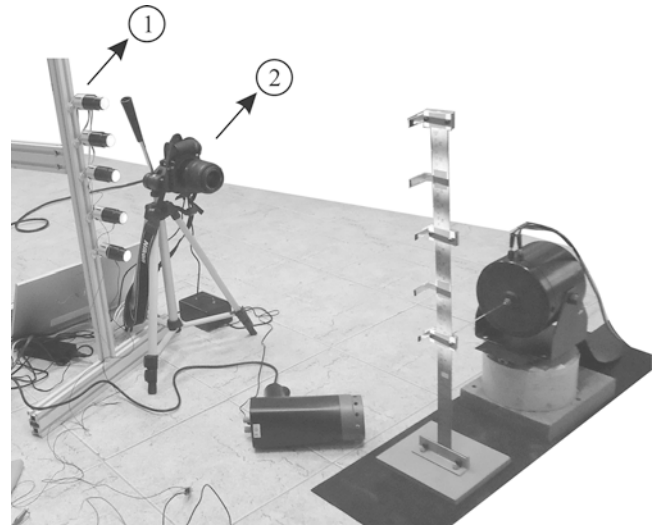


Fig. 20.2 Cantilever beam structure used in the experiments

Fig. 20.3 Experimental set-up:
(1) illumination system, (2)
camera



The calibration of the image acquisition system required 33 images with different orientations, as those shown in Fig. 20.1. The intrinsic and extrinsic parameters were obtained with help of the Camera Calibration Toolbox for MATLAB.

20.5 Experimental Results

Because of the complexity of the signal wave to be measured (response of the structure due to a Schroeder signal with 30 harmonics up to 20 Hz), 102 images were necessary to rebuild one single period of vibration. In this case, the adopted sampling period was 1.5147 s. The obtained results are shown in Fig. 20.4.

As one can see in Fig. 20.4, there are noticeable differences between the vibration measured with the camera system and the vibration measured with the laser vibrometer. When the OMA is performed with the measured data, the resultant values of natural frequencies and mode shapes are those shown in Tables 20.1 and 20.2.

As one can see, bigger error is observed in the first natural frequency and in the associated mode shape. This is caused by the fact that targets 1, 2, and 3 present low vibration amplitudes at the first mode shape, as illustrated in Fig. 20.5a. Due to the resolution of the image acquisition system, at the order of 0.1 mm/pixel, it is difficult to predict the real position of points presenting low vibration amplitudes with precision. For this reason, bigger discrepancies are observed in the first mode shape as well as in the natural frequency value. On the other hand, in the case of the second mode shape, the vibration amplitude of the targets in the structure is higher (Fig. 20.5b), and one has a better identification of the structure dynamics.

20.6 Conclusion

In this work, one performed an Operational Modal Analysis (OMA) from data obtained with a low speed photographic camera and adopting a sub-sampling technique. The experimental results show that:

- it is feasible to measure the vibration of structures with a digital camera with low acquisition rate provided that vibration is periodic with known fundamental frequency;
- image resolution is a critical and limiting factor in the measurement procedure, because it limits measurement precision of low vibrating points of the structure;
- the OMA performed with the measured data and the data obtained from laser vibrometer measurements presented results with fair agreement, with better results at modes with higher vibration amplitudes.

Acknowledgements This project was supported by the Brazilian research foundations CNPq (Conselho Nacional de Desenvolvimento Científico e Tecnológico).

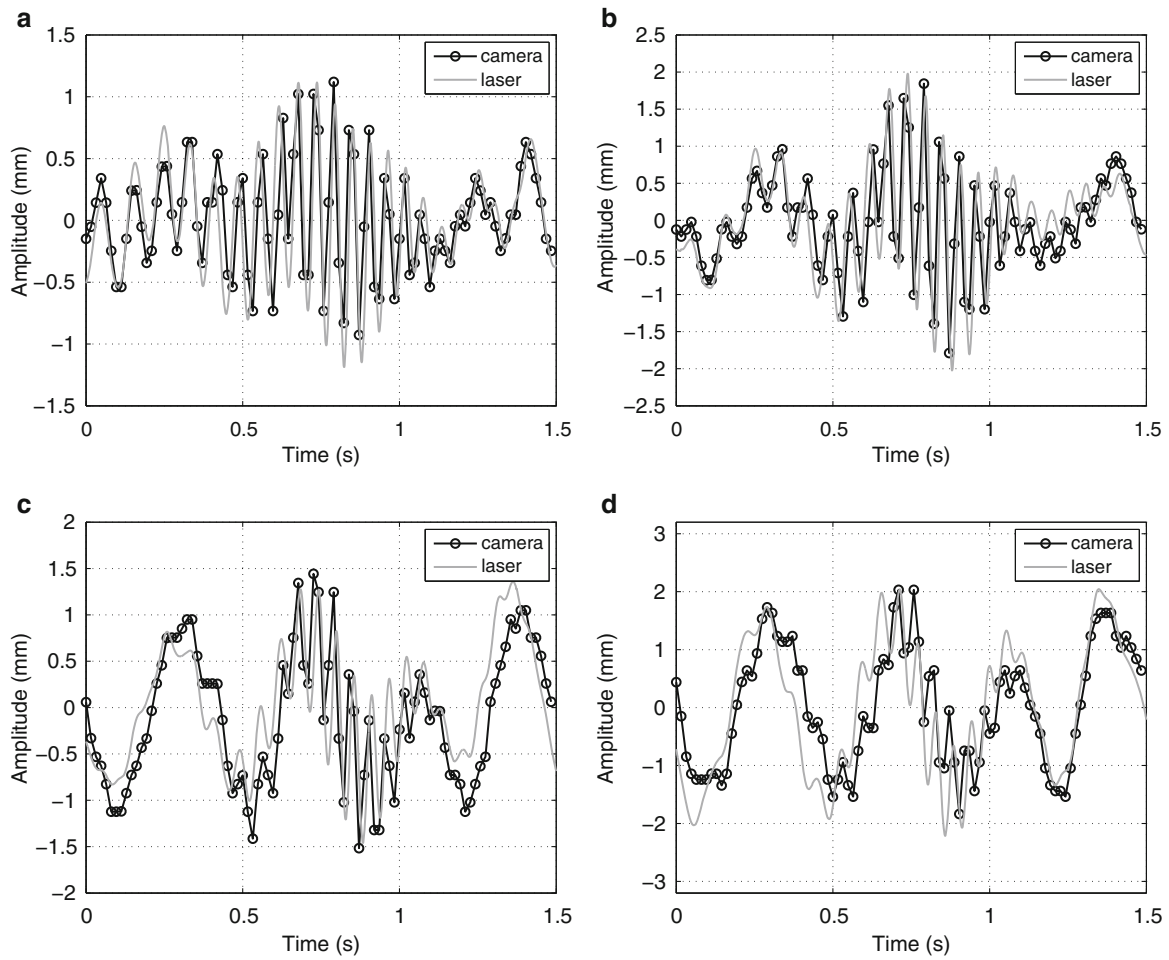


Fig. 20.4 One period of vibration of the structure at different points: comparison between camera measurements and laser vibrometer measurements. (a) target 2 (b) target 3 (c) target 4 (d) target 5

Table 20.1 First two natural frequencies of the system estimated by the OMA

Frequency	Camera	Laser	Error (%)
ω_1 (Hz)	2.00	2.67	25.1
ω_2 (Hz)	18.67	17.33	7.7

Table 20.2 First two mode shapes of the system estimated by the OMA

Mode	Target	Camera (mm)	Laser (mm)	Error (%)
First	1	0.101	0.021	380.9
	2	0.212	0.089	136.1
	3	0.449	0.348	28.9
	4	0.710	0.658	7.9
	5	1.000	1.000	–
Second	1	0.419	0.340	23.2
	2	0.699	0.681	2.6
	3	1.000	1.000	–
	4	0.545	0.543	0.4
	5	–0.548	–0.550	0.4

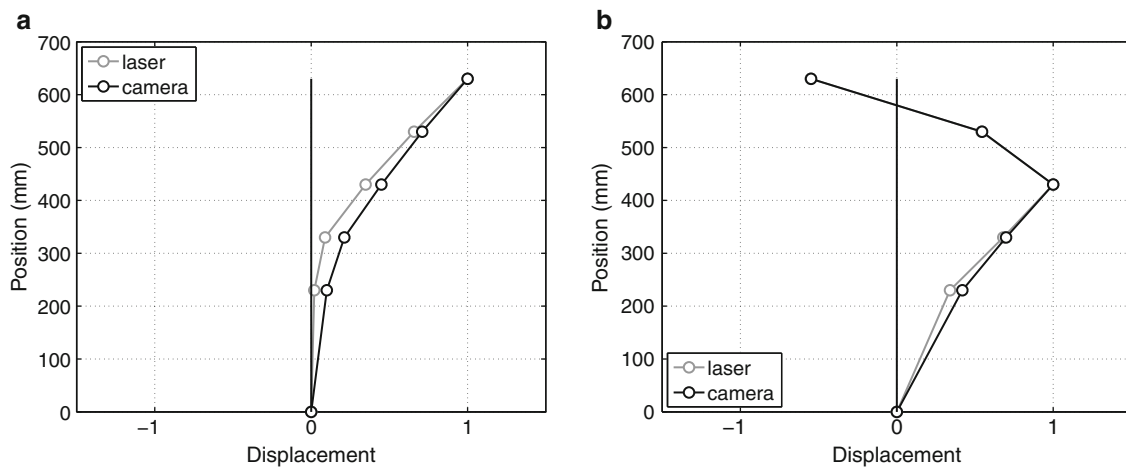


Fig. 20.5 Mode shapes of the structure obtained with the OMA. (a) first mode (b) second mode

References

- Linder W (2009) Digital photogrammetry: A practical course. Springer, Berlin
- Olaszek P (1999) Investigation of the dynamic characteristic of bridge structures using a computer vision method. *Measurement* 25(3):227–236
- Ryall TG, Fraser CS (2002) Determination of structural modes of vibration using digital photogrammetry. *J Aircraft* 39(1):114–119
- Yoshida J, Abe M, Kumano S, Fujino Y (2003) Construction of a measurement system for the dynamic behaviors of membrane by using image processing. In: *Proceedings of the first international conference on textile composites and inflatable structures*, Barcelona, Spain, pp 1–10, 2003
- Chang C, Ji Y (2007) Flexible videogrammetric technique for three-dimensional structural vibration measurement. *J Eng Mech* 133(6): 656–664
- Jeon HS, Choi YC, Park JH, Park JW (2010) Multi-point measurement of structural vibration using pattern recognition from camera image. *Nucl Eng Tech* 42(6):704–711
- Helfrick MN, Niezrecki C, Avitabile P, Schmidt T (2011) 3D digital image correlation methods for full-field vibration measurement. *Mech Syst Signal Process* 25(3):917–927
- Richardson M, Schwartz B (2003) Modal parameter estimation from operating data. *Sound Vib* 1–8
- Mohanty P, Dixen D (2004) A modified Ibrahim time domain algorithm for operational modal analysis including harmonic excitation. *J Sound Vib* 275:375–390
- Avitabile P (2006) MODAL SPACE: Someone told me that Operational Modal Analysis produces better results and damping is more realistic. *Exp Tech* 30(6):25–26
- Brincker R, Zhang L, Andersen P (2000) Modal identification from ambient responses using frequency domain decomposition. In: *Proc IMAC XVIII*, pp 625–630
- Maia NMM (1991) Fundamentals of singular value decomposition. In: *Proc IMAC IX*, pp 1515–1521
- Zhang Z (2000) A flexible new technique for camera calibration. *IEEE Trans Pattern Anal Mach Intell* 22:1330–1334
- Watson GA (1977) *Numerical analysis*. Springer, Berlin
- Schoroeder MR (1970) Synthesis of low-peak-factor signals and binary sequences of low auto-correlation. *IEEE Trans Inform Theory* 16: 85–89

Chapter 21

Recovery of Mode Shapes from Continuous Scanning Laser Doppler Vibration Data: A Mode Matching Frequency Domain Approach

P. Chiariotti, P. Castellini, and M. Martarelli

Abstract The paper illustrates a method for processing, in a blind way, data obtained by Continuous Scanning Laser Doppler Vibrometry (CSLDV). CSLDV makes it possible to measure the structure vibration joining together the spatial and time information. The vibration datum obtained from the laser, which continuously scans (over time and space) the structure under test, is in fact modulated by the Operational Deflection Shape (ODS) excited during the experiment. The idea that we propose in this paper is based on the fact that, if the mode shapes of the structure under test are known a priori, e.g. from a numerical model or from an analytical formulation, it is possible to settle a procedure that searches for similarities between those known mode shapes (the candidate mode shapes) and ODSs that actually modulate the signal. This procedure can be considered a pattern matching technique that makes it possible to identify the resonance frequency related to each ODS and the mode shapes that better match with ODSs excited. A detailed description of the algorithm is given in this paper.

Keywords Laser doppler vibrometry • Continuous scanning laser doppler vibrometry • Pattern matching • Vibration testing • Mode matching

21.1 Introduction

The Continuous Scanning Laser Doppler Vibrometry (CSLDV) method was introduced by Ewins et al. [1] as an alternative to conventional Scanning Laser Doppler Vibrometry. This characteristic rises from the possibility to recover Operational Deflection Shapes (ODSs) from a unique time history acquired by the Laser Doppler Vibrometer (LDV) while the laser beam scans, in a continuous way, all over the vibrating surface. With respect to Discrete Scanning Laser Doppler Vibrometry, CSLDV presents the following advantages:

- extremely high spatial resolution,
- compact data structure (e.g. a single time history contains both time and spatial information),
- limited duration of the experiment (e.g. acquisition time depends only on the required frequency resolution).

When a vibration measurement is performed by CSLDV, the time history appears as an amplitude modulated signal whose modulation is due by the Operational Deflection Shapes excited during the experiment.

At the beginning the CSLDV technique was applied only in single frequency excitation conditions, e.g. step sine testing. Such testing methodology, however, had the drawback of being extremely time-demanding. During the years several works have demonstrated its functionality even in case of broadband excitation, e.g. impact testing [2], broadband [3] and operational [4] excitation. The CSLDV technique presented by Ewins et al. grounds on the hypothesis that an ODS can be modelled by a polynomial. The polynomial's coefficients are directly related to the sidebands that characterise the vibration spectrum of the CSLDV signal. The sidebands around the resonance frequency of a specific ODS are spaced by the laser

P. Chiariotti • P. Castellini (✉)
Università Politecnica delle Marche, Via Brecce Bianche, 60131 Ancona, Italy
e-mail: p.castellini@univpm.it

M. Martarelli
Università degli Studi e-Campus, Via Isimbardi, Novedrate (CO), Italy
e-mail: m.martarelli@univpm.it

beam scanning frequency. The number of sidebands are directly related to the ODS complexity. This characteristic spectrum will be referred hereafter as the sideband spectrum related to the ODS. The recognition of resonance frequencies and the recovery of ODSs in the processing of CSLDV data are performed, conventionally, starting from the visual inspection of the CSLDV output spectrum. This process has obviously to be performed by an expert experimentalist who is used to treat CSLDV data.

This paper presents a new philosophy for processing CSLDV data. The proposed approach reverses the point of view of the experimentalist who analyses CSLDV data. The standard approach proposed by Ewins et al. starts from CSLDV spectrum and identifies the dynamic characteristics of the structure under test (the ODSs) from the information extracted from the sideband patterns located within the spectrum. The technique proposed in this paper, on the contrary, reverses this approach. In fact, if a specific ODS produces a unique sideband pattern, then the identification of that pattern within the CSLDV spectrum proves that the same ODS was excited during the test. This assumption constitutes the basis of this new approach. It is therefore possible to create a set of sideband patterns starting from a set of ODSs (e.g. obtained theoretically, numerically, etc.) and look for those patterns within the CSLDV spectrum. The patterns that are recovered within the spectrum correspond to the ODSs that were effectively excited during the test. Basically the procedures can be depicted as a pattern matching technique that makes it possible the blind recognition of the resonance frequencies and the related ODSs of the structure under tests. A similar approach, analysing CSLDV time domain data, was presented by Castellini et al. [5].

21.2 Mode Matching Procedure in Frequency Domain

The aim of the method proposed in this paper is to exploit the knowledge of mode shapes or ODSs, which can be known a priori from other approaches like numerical analysis, analytical models, previous experimental testing, etc., to create a set of sideband patterns to be looked for within the CSLDV spectrum. The patterns that best match with those effectively present in the CSLDV spectrum enhance the actual ODSs that best resemble the ideal mode shapes/ODSs that constituted the input of the procedure. In practice, this technique both emulates and reverse what an expert experimentalist does, with the added value of making the approach automatic and blind. As the experimentalist looks for a sideband pattern within the CSLDV spectrum and recovers the ODS from it, the algorithm assign a sideband pattern (the kernel) to each mode shape/ODS constituting the initial set of data and perform a pattern matching procedure within the CSLDV spectrum. In such a way the pattern that best matches within the CSLDV spectrum indicates that an ODS that is similar to the corresponding mode shape/ODS that produced that kernel was excited during the test. At this point a clarification is needed. The CSLDV technique, applied in the conventional way, i.e. with single or multi-sine excitation, allows to extract only ODSs from the acquired signal. The mode matching procedure makes it possible to identify the candidate shapes that better match with the ODSs that effectively modulate the CSLDV signal. The procedure, therefore, does not extract neither ODSs nor mode shapes, but indicates which ODSs, among those excited, best resemble those constituting the set of candidate shapes. In this sense it is not inappropriate to state that the candidate shapes can be both mode shapes (e.g. obtained analytically or numerically) and ODSs (e.g. obtained experimentally). The shapes used from now on in this paper are mode shapes calculated from analytical models, and therefore the authors will refer to them only as mode shapes. Since the procedure looks for specific sideband patterns within the CSLDV spectrum, its output consists in:

- the natural frequencies corresponding to the central frequencies of the sideband pattern better matching with the candidate ones,
- a set of mode shapes that best matches with the ODSs that effectively modulate the measured signal.

As already said this technique reverses, in a certain way, the point of view of the traditional approach: it starts from the mode shapes, creates the sideband pattern and identifies those modes shapes, among the set of candidates, that best match with the actual ODSs that were excited during the test. The number of unknowns with respect to the traditional approach is therefore reduced, as reported in 1, where n indicates the mode shapes and m the degrees of freedom of the structure. A detailed description of the mode matching procedure is reported hereafter, divided in its four main steps.

21.2.1 Step 1: CSLDV Data Collection

The full field vibration of a structure excited in a wide frequency range is measured by CSLDV. An 1D example will be treated in this paper but it can be easily generalised to 2D. The laser beam is made to scan sinusoidally along the whole length of the 1D structure, e.g. a beam, with a scanning frequency much lower than that of the first expected mode. The CSLDV output time history is amplitude modulated by the excited ODSs.

21.2.2 Step 2: Selection of a Set of Candidate Mode Shapes

The mode shapes are selected a priori starting from the knowledge of the structure geometry and constraints. Those mode shapes can be calculated analytically or via numerical models (e.g. FE models). If we consider a clamped-free beam, the mode shapes can be defined analytically using the formulation proposed in [6]:

$$X_i = \left[\cosh\left(\lambda_i \frac{x}{L}\right) - \cos\left(\lambda_i \frac{x}{L}\right) \right] - \sigma_i \left[\sinh\left(\lambda_i \frac{x}{L}\right) - \sin\left(\lambda_i \frac{x}{L}\right) \right] \quad (21.1)$$

where

x is the coordinate position along the beam length

L , λ_i and σ_i are the non-dimensional frequency amplitude parameters.

The constraint of a real structure, however, can be partially known or even unknown. For this reason it is plausible to insert, in the set of candidate mode shapes, modes that are obtained with different types of constraints (e.g. free-free, clamped-free, etc.).

21.2.3 Step 3: Sideband Spectrum Kernel Synthesis

The basic assumption of the procedure is that each candidate mode shape, obtained from Eq. (21.1), can be fitted by a polynomial of degree p and coefficients V_R :

$$M(x) = \sum_{n=0}^p V_R x^n \quad (21.2)$$

This polynomial, $M(x)$, would therefore modulate the amplitude of the time history obtained from a CSLDV measurement when the laser beam scans along the vibrating structure. The real and imaginary coefficients (A_R and A_I) of the sidebands that characterise the spectrum of the thus amplitude-modulated vibration signal, are related to the polynomial coefficients (V_R) by means of the Chebyshev matrix ($[T]^{-1}$) [7], in accordance to:

$$\{A_R\} = [T]^{-1} \{V_R\}, \quad \{A_I\} = [T]^{-1} \{V_I\} \quad (21.3)$$

The pattern of these sidebands (*kernel*) identifies a unique mode shape, and therefore it can be exploited as a template for a pattern matching procedure (the procedure is described in the following) that aims at identifying the presence of that mode in the spectrum of the CSLDV vibration signal. Each kernel is reconstructed from the sideband amplitude coefficients, obtained from A_R and A_I , according to:

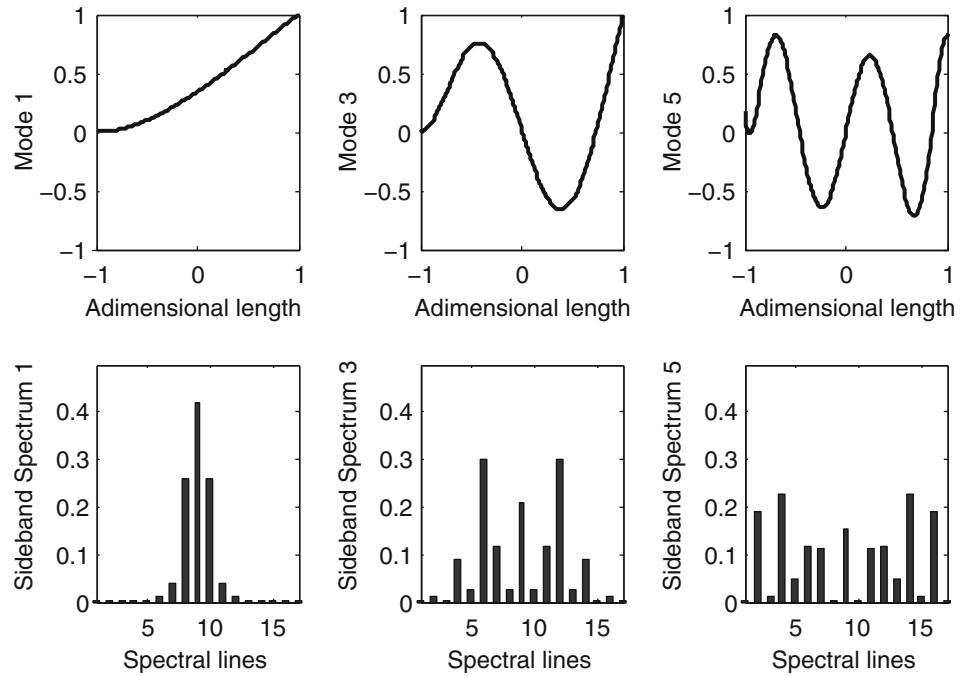
$$A = \sqrt{(A_R^2 + A_I^2)} \quad (21.4)$$

It is important, at this point, to enhance the fact that, even though the candidates mode shape can be amplitude normalised when they are obtained, for instance, from analytical equations as 1, the corresponding sideband spectrum is not. This happens because the energy of the mode shape is spread over several sidebands, see Fig. 21.1. It is thus clear that, increasing the complexity of the shape, which means considering mode shapes of higher spatial order, the number of sidebands increases and the amplitude of the kernel decreases accordingly.

21.2.4 Step 4: Sideband Spectra Matching

The kernels that identify the complete set of candidate mode shapes are then compared with the CSLDV experimental amplitude spectrum in order to find those ODSs that are effectively recognisable from the measured signal. The identification step follows a pattern matching procedure based on the minimisation of the Euclidean distance d_i between the template

Fig. 21.1 Mode shapes and related sidebands spectra



(each kernel) and the signal (the measured CSLDV amplitude spectrum). The method is based on the sliding window approach, that is a typical brute force method in Time-series Subsequence Matching [8, 9].

$$d_i = \left\| \frac{K}{\max(K)} - \frac{W_i}{\max(W_i)} \right\| \quad (21.5)$$

Where

$W_i = S_{(i: \Omega_{Laser}: i + N)}$ is the sliding window of the signal S

$\| \cdot \|$ represents the L^2 Euclidean distance

N is the number of spectral lines of the kernel K

M is the number of spectral lines of the signal spectrum S

$i = 1: M$ represents the position (frequency) of the sliding window

$\max(K)$ is the maximum value in the kernel K

$\max(W_i)$ is the maximum of amplitude spectrum S within the i th window of length N

Ω_s is the scan frequency adopted in the CSLDV measurement

d_f is the frequency resolution adopted in the CSLDV measurement

The portion of the amplitude spectrum of the CSLDV measured signal (the sliding window W_i) is extracted from the whole spectrum and compared with the template (*kernel*). The distance metric (Euclidean) is stored and the sliding window is shifted ahead by one spectral line. Only the amplitude values at the discrete spectral lines that are multiples of Ω_s are considered within the sliding window when calculating the distance to the kernel. Indeed, these are the only significant lines that contain the information related to the ODSs. Moreover, this approach both improves the computational effort and makes the procedure less sensitive to noise. Once the all amplitude spectrum is scanned, the sliding window showing the minimum distance for a certain kernel is identified and the central frequency of that window extracted accordingly.

The procedure is repeated for the whole set of candidate mode shapes, until the contribution of each mode shape is determined in terms of ODS and central frequency. The mode shapes that are not present with their equivalent ODSs within the CSLDV amplitude spectrum show high values of Euclidean Distance and central frequencies that are well far from the spectrum significant range.

Fig. 21.2 Kernel and virtual signals synthesised sidebands spectra

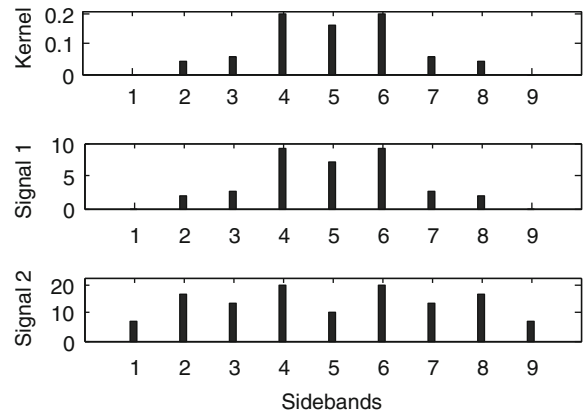
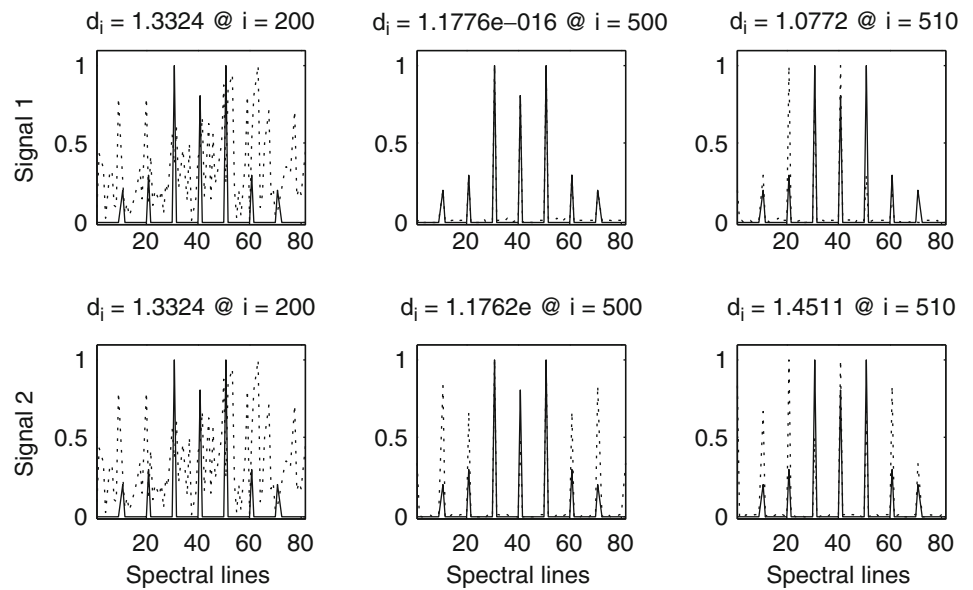


Fig. 21.3 Superimposition of the kernel (solid line) with the sliding signals (dashed line) at different spectral line position and their distance



21.3 Algorithm Testing on Simplified Data

The performances of the proposed approach were evaluated on a simple analytical model in order to deal with a well-controlled test-case. The algorithm was applied to two synthesised signals, Signal 1 and Signal 2 of Fig. 21.2, representing the sideband spectra obtained from two different mode shapes. Only one mode shape was assumed as the candidate mode shape. The kernel representing this mode shape is reported in the top plot of Fig. 21.2.

That kernel represents the template for the pattern matching procedure when analysing the two synthesised signals. The similarity between the kernel and Signal 1 is clear and therefore it would be expected the algorithm to converge to a distance close to zero when the kernel is compared to Signal 1. The same would not happen for Signal 2.

Figure 21.3 shows the process of sliding windowing of both Signal 1 (dashed line on top plot) and Signal 2 (dashed line on bottom plot) superimposed to the kernel (solid line). When the analysis window does not contain the sideband spectrum, for instance at the 200th spectral line, the signal is completely dissimilar to the kernel and the distance d_i is far from zero, see plots in the first column of Fig. 21.3. When the analysis window contains the characteristic sideband spectrum, for instance at the 500th spectral line, the comparison between the kernel and the portion of the signal within the analysis window is even more significant. With reference to the 500th spectral line, it can be seen that the kernel almost coincides with Signal 1 (distance 0.2) but not coincides with Signal 2 (distance 1.3). Since the relative distance between the kernel and Signal 1 assumes the minimum value the procedure thus recognise the candidate mode shape as present in Signal 1. Let's assume the analysis window is centred on a spectral line that does not coincide with the central frequency of the sideband pattern, but coincides with a sideband of the spectrum. This situation happens at the 510th spectral line. In this case, the distance is still low but higher than the value assumed when the analysis window is centred at the central frequency of the sideband spectrum.

Fig. 21.4 Euclidean distance trend for Signal 1 (*left*) and Signal 2 (*right*)

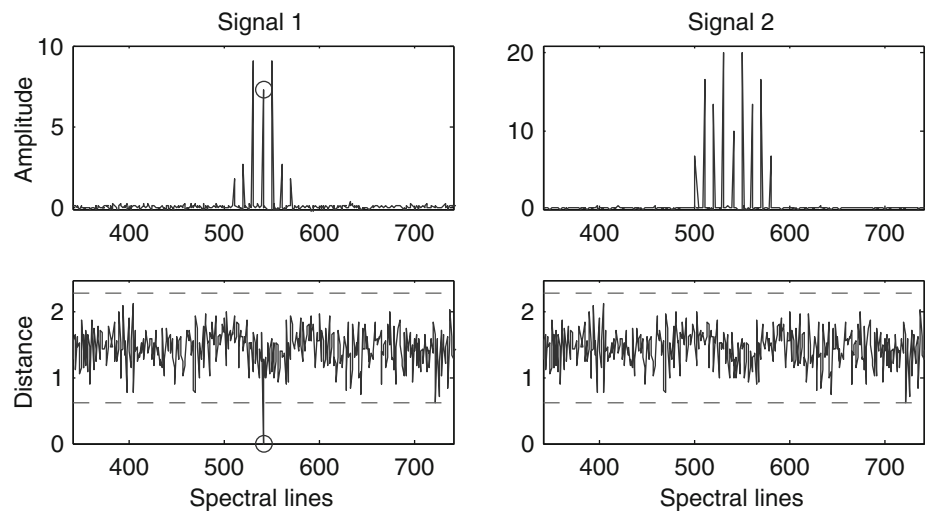


Figure 21.4 illustrates the trend of the L^2 distance with the spectral line sliding for both Signal 1 (left) and Signal 2 (right). The bottom left plot clearly shows a minimum of the Euclidean distance exactly at the spectral line coinciding with the central frequency of Signal 1, the 500th spectral line evidenced with a circle in figure. The bottom plots of Fig. 21.4 report, plotted in dashed lines, the standard deviation bands (coverage factor of 3) referred to the distribution of the Euclidean distance. It is clear that, when the kernel shape is matched at the 500th spectral line, the metric is well below the threshold represented by the standard deviation bands.

21.4 Conclusion

This paper presents an alternative method for the processing of experimental data measured by CSLDV aiming at overcoming the main drawback of such testing procedure. The standard approach indeed grounds on the experience and the knowledge of the experimentalist, who, starting from the visual inspection of the CSLDV spectrum, becomes able to extract the ODSs of the structure. The technique proposed is a sort of “blind” data processing and does not requires anymore that data be handled by a CSLDV expert experimentalist. The main assumption is based on the awareness that a mode shape produces a sideband pattern that is unique in nature. Therefore, it is possible to create a set of candidate sideband patterns, directly related to a set of candidate mode shapes/ODSs (this depending on the way these mode shapes/ODSs are obtained, if analytically, numerically or from previous experiments) and look for those patterns within the CSDLV spectrum exploiting a pattern matching approach. Those patterns that are found within the spectrum represent the mode shapes/ODSs the best match with the ODSs that were effectively excited during the vibration test.

The method has been applied on synthesised data and its effectiveness tested in recognising “true” and “fake” candidate mode shapes which are present or not in the synthesised signal.

References

1. Stanbridge A, Martarelli M, Ewins DJ (2000) Measuring area vibration mode shapes with a continuous-scan LDV, measurement. In: 4th international conference on vibration measurements by laser techniques: advances and applications, Ancona, June 2000
2. Stanbridge A, Martarelli M, Ewins DJ (1999) The scanning laser doppler vibrometer applied to impact modal testing. In: Proceedings of the XVII IMAC-SEM
3. Vanlanduit S, Guillaume P, Schoukens J (2002) Broadband vibration measurements using a continuously scanning laser vibrometer. *Meas Sci Technol* 13(10):1574
4. Martarelli M, Castellini P, Santolini C, Tomasini EP (2011) Laser doppler vibrometry on rotating structures in coast-down: resonance frequencies and operational deflection shape characterization. *Meas Sci Technol* 22(11):115106. doi:[10.1088/0957-0233/22/11/115106](https://doi.org/10.1088/0957-0233/22/11/115106)
5. Castellini P, Chiariotti P, Martarelli M (2014) Mode filtering of continuous scanning laser doppler vibration data. In: Topics in modal analysis, conference proceedings of the society for experimental mechanics series, vol 7. Springer, New York
6. Blevins RD (1979) Formulas for natural frequency and mode shape. Van Nostrand Reinhold Co, New York

7. Stanbridge A, Martarelli M, Ewins DJ (1999) Measuring area mode shapes with a scanning laser doppler vibrometer. In: Proceedings of the XVII IMAC-SEM
8. Vlachos M, Gunopoulos D, Kollios G (2002) Discovering similar multidimensional trajectories. In: Proceedings of the 18th international conference on data engineering, ICDE'02. IEEE Computer Society, Washington, DC
9. Goldin DQ, Millstein TD, Kutlu A (2004) Bounded similarity querying for time-series data. *Inf Comput* 194(2):203–241

Chapter 22

A Compact Device for Measuring Rigid-Body Properties Based on Five Unscaled Modes

Robert Kloepper, Masaaki Okuma, and Joerg Bienert

Abstract This article describes a new method and device for measuring the rigid-body properties of mechanical structures (the inertia tensor, the center of gravity coordinates, and optionally the mass). The setup consists of a platform constrained from underneath by soft coil springs and supported at its center by a 5-DOF air bearing mechanism. Following a random push by hand, laser distance sensors measure the platform's free vibrations. The rigid-body properties are then obtained by fitting a numerical model to the free vibration signals. The model's key components (a mass matrix, a stiffness matrix, and a kinematic transformation matrix) are obtained by calibration. Together with the unknown rigid-body properties, the three matrices define the natural frequencies and unscaled mode shapes, which are fitted to the sensor signals directly in time domain. A prototype of the device is presented and its accuracy is evaluated in an extensive series of tests. Advantages over previous methods include a faster and simpler procedure, higher accuracy, lower frequencies, and an unlimited work space.

Keywords Rigid-body properties • Mass properties • Moment of inertia • Center of gravity • Measurement

22.1 Introduction

The rigid-body behavior of a mechanical structure is defined by ten parameters: the mass, the three center of gravity coordinates (COG), and the inertia tensor (three moments of inertia and three products of inertia). These rigid-body properties are an essential component of structure dynamics models in fields such as power-train vibrations, chassis optimization, spacecraft control, and robotics. In the context of modal analysis, the rigid-body properties are important in defining the low-frequency response under free or elastic boundary conditions: the rigid-body properties can be translated into mass lines and, in combination with the boundary condition, determine the shapes and frequencies of the six rigid-body modes.

A lack of accurate CAD models of a structure's shape and density distributions often makes it necessary to determine the rigid-body properties experimentally, using either FRF-based methods or special-purpose measurement devices. Among the latter, pendulums are the simplest devices, but the measurements are difficult and time consuming, mainly because the test object must be rotated and repositioned multiple times; some reconfigurable pendulums exist that speed up the process [1,2], but at the expense of higher mechanical complexity. The least labor-intensive devices use strong actuators to move the test object in a defined way about multiple degrees of freedom (DOFs) and measure the resulting interface forces [3–5], but these automatic systems require the most complex hardware.

Compared with special-purpose devices, FRF-based methods have the advantage of using only standard modal testing equipment combined with a simple soft suspension. On the other hand, these methods require a significant amount of time

R. Kloepper (✉)
Resonic GmbH, Marie-Elisabeth-Lueders-Str. 1, 10557 Berlin, Germany
e-mail: robert.kloepper@resonic.de

M. Okuma
Department of Mechanical and Aerospace Engineering, Tokyo Institute of Technology, 2-12-1-I3-15, O-okayama,
Meguro-ku, 152-8552 Tokyo, Japan
e-mail: mokuma@mech.titech.ac.jp

J. Bienert
Faculty of Mechanical Engineering, University of Applied Sciences Ingolstadt, Esplanade 10, 85049 Ingolstadt, Germany
e-mail: joerg.bienert@thi.de

and skills. Moreover, unless the test object is very rigid, the low-frequency range influenced by the suspension overlaps with the higher frequency range influenced by the elastic modes, and as a result, modal analysis must be performed for either the rigid-body modes [6, 7] (problematic because accurate FRFs are difficult to measure at frequencies near 0 Hz) or of the first elastic modes [6, 8] (difficult in cases of high modal densities or nonlinear damping). Instead of modal analysis, two of the authors of this article used a model of the gravity-dependent suspension stiffness combined with a response measurement at a discrete frequency of about two times the highest rigid-body resonance [9–11]. However, in that frequency range, highly elastic structures such as automobiles or helicopters already show significant elastic behavior.

Another problem of FRF-based methods is the need to accurately align the excitation source with the test object, which is difficult to achieve with conventional impulse hammers or space-fixed shakers. Malekjafarian et al. proposed a method that eliminates the need for accurate excitations by using the mass change method in order to scale the rigid body modes [12, 13]. However, this method assumes that both the mode shapes and the suspension stiffness are unchanged by the additional masses. With moment of inertia errors of more than 10%, the method has achieved relatively low accuracy.

As a different way to eliminate the need for accurate excitations, the authors of this paper proposed a method that uses the gravity-dependent stiffness model [9–11] in order to derive the rigid-body properties from free vibrations of the rigid-body modes [14]. Implemented as a device consisting of a platform suspended in soft tension springs, this method achieves an almost automatic procedure with very simple hardware. The method was successfully applied to various objects, including race cars, motorcycles, combustion engines, washing machine drums and vehicle doors. The method's remaining limitation is the use of tension springs equipped with spherical joints at both ends: the tension springs limit the work space around the platform, and the joints cause a significant amount of dry friction.

The reason why the method [14] is limited to tension springs equipped with joints is that the stiffness of any soft suspension under the influence of gravity changes very significantly depending on the mass and COG location of the current test object: the load state and length of a spring changes the geometric stiffness, and the static platform position changes the spring orientation. For that reason, the stiffness model cannot be obtained through a one-time calibration measurement but must instead be derived from the current platform position and from the properties and attachment locations of the individual springs. Springs with clamped ends instead of joints would require elaborate finite element models that would not be accurate.

The new method proposed in this article uses a central bearing that keeps the static platform position constant and independent of the test object's COG or mass. As a result, it becomes possible to identify the stiffness model through calibration instead of building it up from the properties of the individual springs. Another benefit is that the springs can sit underneath the platform and can be connected to the platform without friction-inducing joints. Moreover, the spring stiffness can be reduced because the springs no longer need to carry the static load; the benefit is lower frequencies, i.e., the ability to measure more elastic objects.

22.2 Components of the Device

Figure 22.1 shows the main components of the measurement device, a prototype with a maximum load capacity of 350 kg. A platform frame is connected to a similarly-shaped support frame by a number of coil springs. Since the springs are mounted below the platform, the work space around the platform is unobstructed and objects much larger than the platform can be measured. Moreover, since there is no elevated support structure, the device is only half as wide as a device with the same platform size based on the older method [14]. The static load is not supported by the springs, but by a single low-friction bearing that sits underneath the platform center. This bearing, in combination with the springs, allows the platform to vibrate freely about five DOFs: all rigid-body DOFs except the vertical translation.

The bearing (Fig. 22.2) consists of a circular plate that floats on three conventional air bearing pads (rotation z , translation x and y). On top of the floating plate, a v-groove carries a thin cylinder made of hardened steel. A second cylinder is fixed to the bottom of the platform with an orientation perpendicular to the first cylinder. Between the two cylinders sits a hardened steel plate on whose surfaces the cylinders can perform a rolling motion (rotation about x and y). In order to minimize friction, the smallest possible cylinder diameter is chosen based on the allowable contact pressure. The mechanism can thus be categorized as a real-world knife-edge bearing. In order to prevent misalignment caused by the gradual slippage of the rolling cylinders, a reset mechanism actuated by three levers returns the floating plate and the hardened steel plate to a defined position before each series of measurements.

In order to guarantee rigid-body behavior for highly flexible test objects, it is important to minimize the spring stiffness. While the horizontal springs can be extremely soft, there is a limit for the stiffness of the vertical springs below which the system becomes unstable. This limit depends on the test object's mass and COG height. In order that the stiffness can be adapted to a given test object, the number of vertical springs is variable. By choosing a number of vertical springs for which

Fig. 22.1 Components of the device

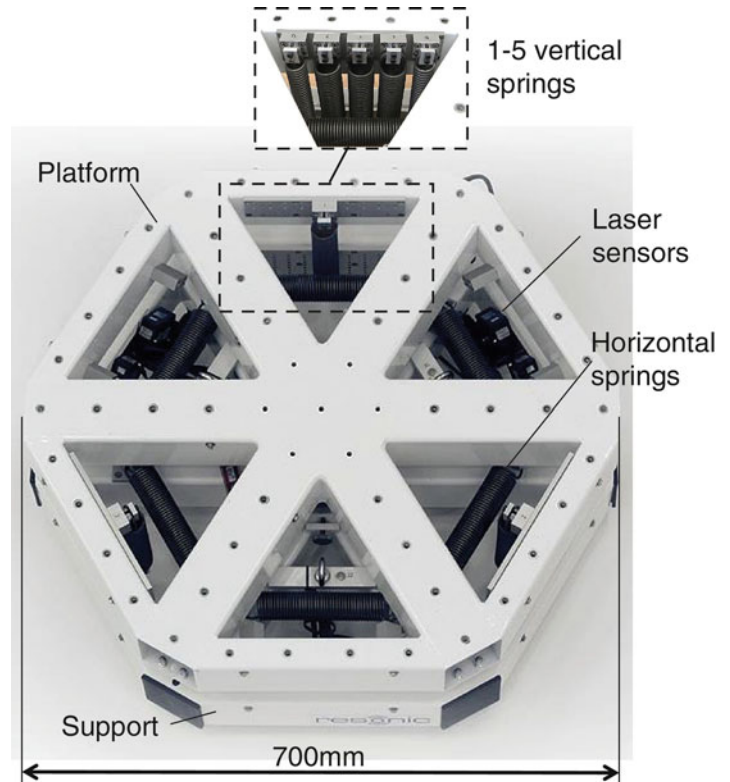
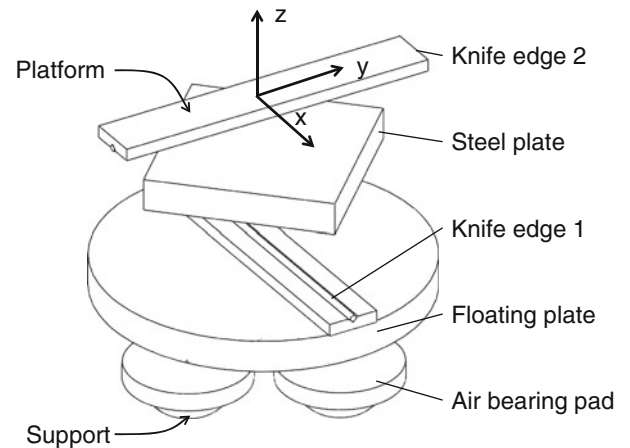


Fig. 22.2 Low-friction bearing with five DOFs



the system is just above the point of instability, the effective stiffness can be brought close to zero. At that point, the spring stiffness is matched to the negative stiffness term caused by the effect of gravity (mass multiplied by COG height and gravity constant).

The method requires no actuators and no force sensors. The only sensors are six conventional laser distance sensors that are fixed to the support frame and point onto small pads bolted to the platform. Besides measuring the dynamic platform motion, the laser sensors are also used for measuring the platform's static tilt angles.

22.3 Measurement Procedure

The test object is placed on the platform in such a way that its COG is near to the center. An easy way is to use crane equipped with a horizontal bar that carries one plumb line at a distance of half the platform diameter on each side of the hook (Fig. 22.3). The crane is moved to a position where the plumb lines point onto two opposite corners of the platform. In that

Fig. 22.3 Plumb-line mechanism used for positioning the object's COG near the platform center



position, the test object's COG is at the platform center. (Both the plumb lines and the imaginary line connecting the hook and the COG are always vertical; therefore, given that the hook is at the center between the upper ends of the plumb lines, the x and y position of the COG is always at the center between the lower ends of the plumb lines.)

Once the crane has reached its final position, the test object is lowered onto the platform. It is unnecessary to fix the test object to the platform because the accelerations during the measurement are very small. However, for odd-shaped objects such as engines, it is usually necessary to use elevated fixture components or struts to keep the object upright.

Next, the platform must be balanced in such a way that the tilt angles are zero. To this end, the user-interface software displays the tilt angles derived from the laser sensor signals in real time. Using this feedback, the operator balances the platform either by placing short steel cylinders upright on top of the platform or by inserting longer steel cylinders into slots inside the radial platform profiles. The goal of this balancing process is to bring the platform in exactly the same position for each measurement so that the spring stiffness is the same as during the calibration measurements (see next sections).

The positions and orientations of the balance masses are measured with a coordinate measurement arm. Based on this data, the software computes the combined rigid-body properties of the balance masses, which it later subtracts from the measured rigid-body properties. The measurement arm is also used to measure the test object's position and orientation relative to the platform, so that the results can later be transformed from platform coordinates into object coordinates.

After this preparation, the platform is given a random push by hand, resulting in free vibrations about all five DOFs. The free vibration signals are captured by the laser sensors over a period of about 20 s. The software then computes the rigid-body properties. The software also gives immediate feedback on the magnitude and shape of each mode, so that the operator can adjust his or her excitation technique. Usually, between four and ten of these individual measurements are taken in order to increase the accuracy through a sort of averaging process (see next section).

After the measurement, the test object is removed. If fixture components were used, the fixtures' combined rigid-body properties are determined in a second measurement and subtracted from the overall result. (The rigid-body properties of the respective balance masses are subtracted at the same time.)

22.4 Computation

The computation of the rigid-body properties starts with solving the following eigenvalue problem.

$$\left[-\omega_j^2 [\mathbf{M}_d + \mathbf{M}(m, \mathbf{c}, \Theta)] + \mathbf{K}_d + \mathbf{K}(m, \mathbf{c}) \right] \mathbf{X}_j = \mathbf{0}, \quad (22.1)$$

where \mathbf{K}_d is a stiffness matrix representing the constant device stiffness (spring stiffness and gravity effect on the platform), $\mathbf{K}(m, \mathbf{c})$ is a stiffness matrix representing the gravity effect on the test object, \mathbf{M}_d is a mass matrix representing the combined inertia of the platform and springs, and $\mathbf{M}(m, \mathbf{c}, \Theta)$ is a mass matrix representing the test object inertia. All matrices are symmetric and 5×5 .

Both $\mathbf{K}(m, \mathbf{c})$ and $\mathbf{M}(m, \mathbf{c}, \Theta)$ are functions of the unknown mass, m , and COG, \mathbf{c} , of the test object. In addition, $\mathbf{M}(m, \mathbf{c}, \Theta)$ is a function of the unknown inertia tensor,

$$\Theta = \begin{bmatrix} I_{xx} & \text{sym.} & \\ I_{xy} & I_{yy} & \\ I_{xz} & I_{yz} & I_{zz} \end{bmatrix}. \quad (22.2)$$

Besides the unknown rigid-body properties, the matrices $\mathbf{K}(m, \mathbf{c})$ and $\mathbf{M}(m, \mathbf{c}, \Theta)$ include only the known positions, orientations, and diameters of the two knife edges, and the orientation of the floating plate in the static equilibrium state. The composition of $\mathbf{K}(m, \mathbf{c})$ and $\mathbf{M}(m, \mathbf{c}, \Theta)$ can be derived in a straightforward way by using Lagrange's equations.

The mode shapes \mathbf{X}_j and natural frequencies ω_j ($j = 1, \dots, 5$) obtained from Eq. (22.1) define the free vibration signals at time t_k .

$$\mathbf{s}(t_k) = \mathbf{T} \sum_{j=1}^5 \mathbf{X}_j e^{-\zeta_j \omega_j t_k} (a_j \sin(\omega_j t_k) + b_j \cos(\omega_j t_k)), \quad (22.3)$$

where ζ_j is the modal damping ratio of mode j , the scaling factors a_j and b_j define the amplitude and phase of mode j and depend on initial excitation, and \mathbf{T} is a $N_l \times 5$ matrix that transforms the motion about the five platform DOFs into sensor signals. (The vector $\mathbf{s}(t_k)$ is composed of the signals of the N_l different sensors, $[s_1(t_k), \dots, s_{N_l}(t_k)]^T$.)

The rigid-body properties are identified by fitting the theoretical signals $\mathbf{s}(t_k)$ to the measured signals $\check{\mathbf{s}}(t_k)$ in a least-squares sense, i.e., by minimizing the following cost function.

$$F(m, \mathbf{c}, \Theta, \{\zeta_j\}) = \sum_{r=1}^{N_r} \sum_{k=1}^{N_k} \sum_{l=1}^{N_l} (s_l(t_k) - \check{s}_{lr}(t_k))^2, \quad (22.4)$$

where N_r is the number of repetitions. The nonlinear problem defined by Eq. (22.4) is solved by conventional Gauss-Newton optimization. The scaling factors, a_j and b_j , can be obtained by solving a linear least-squares problem at every iteration of the other unknown variables. In this way, the scaling factors can be removed from the nonlinear problem. The modal damping ratios (and implicitly also the scaling factors) are identified only as a by-product. However, the scaling factors have a practical use because they define the excitation levels which are used as feedback for helping the operator improve his or her excitation technique.

If the measurement is repeated N_r times, the overall result is not obtained by averaging over the results of the individual repetitions, but by solving Eq. (22.4) for all data sets at once. The damping ratios can be fixed to the values previously identified by solving Eq. (22.4) for the individual repetitions.

A modified version of the algorithm (which will prove to achieve higher accuracy in Sect. 22.6) requires a separate measurement of the mass with conventional scales. The mass is then turned into a known parameter. If the mass is known, it becomes possible to derive the x and y coordinates of the COG from the combined mass and COG of the balance masses (m_b , c_{xb} , and c_{yb}) and turn them into known parameters as well. Assuming that the z-axis runs vertically through the two knife edges, the test objects's COG coordinates are defined by

$$\begin{bmatrix} c_x \\ c_y \end{bmatrix} = -\frac{m_b}{m} \begin{bmatrix} c_{xb} \\ c_{yb} \end{bmatrix}. \quad (22.5)$$

22.5 Calibration

The matrices \mathbf{K}_d and \mathbf{M}_d and the kinematic transformation matrix \mathbf{T} are obtained in a single series of calibration measurements after the device has been manufactured.

The matrix \mathbf{T} is derived from static measurements: The platform is moved in n different static positions $\mathbf{x}_1, \dots, \mathbf{x}_n$ around the equilibrium state; each of these positions is measured with a 3d measurement arm and the static signals $\mathbf{s}_1, \dots, \mathbf{s}_n$ are captured at the same time. The matrix \mathbf{T} is then computed as the least-squares solution for

$$[\mathbf{s}_1, \dots, \mathbf{s}_k] \approx \mathbf{T} [\mathbf{x}_1, \dots, \mathbf{x}_k] \quad , \text{ i.e.} \quad (22.6)$$

$$\mathbf{T} \approx [\mathbf{s}_1, \dots, \mathbf{s}_n] [\mathbf{x}_1, \dots, \mathbf{x}_n]^T \left([\mathbf{x}_1, \dots, \mathbf{x}_n] [\mathbf{x}_1, \dots, \mathbf{x}_n]^T \right)^{-1} . \quad (22.7)$$

The matrices \mathbf{K}_d and \mathbf{M}_d are obtained by applying the measurement procedure (described in Sect. 22.3) to various objects with known rigid-body properties. The 15 independent elements of each matrix,

$$\mathbf{M}_d = \begin{bmatrix} M_1 & & & & & & \text{sym.} \\ M_2 & M_6 & & & & & \\ M_3 & M_7 & M_{10} & & & & \\ M_4 & M_8 & M_{11} & M_{13} & & & \\ M_5 & M_9 & M_{12} & M_{14} & M_{15} & & \end{bmatrix} \quad (22.8)$$

$$\mathbf{K}_d = \begin{bmatrix} K_1 & & & & & & \text{sym.} \\ K_2 & K_6 & & & & & \\ K_3 & K_7 & K_{10} & & & & \\ K_4 & K_8 & K_{11} & K_{13} & & & \\ K_5 & K_9 & K_{12} & K_{14} & K_{15} & & \end{bmatrix} , \quad (22.9)$$

are then computed based on a modified version of Eq. (22.4), where the rigid-body properties are known and the elements of \mathbf{K}_d and \mathbf{M}_d are identified.

$$F(\mathbf{M}_d, \mathbf{K}_d) = \sum_{c=1}^{N_c} \sum_{k=1}^{N_k} \sum_{l=1}^{N_l} (s_{cl}(t_k) - \check{s}_{cl}(t_k))^2 , \quad (22.10)$$

where N_c is the total number of calibration measurements. In order facilitate convergence, the damping factors should be determined through conventional modal analysis prior to this optimization.

22.6 Verification

After its kinematic transformation matrix \mathbf{T} had been obtained with the help of a 3d measurement arm, the prototype shown in Fig. 22.1 was calibrated for three different spring configurations: six horizontal springs plus (A) three, (B) nine, and (C) fifteen vertical springs. For each spring set, five calibration measurements with four repetitions were made with different configurations of various steel cylinders (Fig. 22.4). All signals measured with a given spring set, together with the known rigid-body properties of the cylinder sets, were then simultaneously fed into the optimization problem Eq. (22.10) in order to obtain the matrices \mathbf{K}_d and \mathbf{M}_d . (The “known” rigid-body properties were derived from the positions, orientations, weights, lengths, and diameters of the cylinders. The positions and orientations were measured with a 3d measurement arm with a specified accuracy of 0.04 mm.)

Next, the method’s accuracy was evaluated by measuring the rigid-body properties of a total of 18 different reference objects: six objects for each spring set (Fig. 22.4). Each of the 18 measurements included four repetitions, starting with a new excitation and followed by a signal acquisition time of 20 s. Like the calibration objects, the reference objects consisted of steel cylinders placed on the platform in various configurations. These configurations were different from those used for calibration, and care was taken to produce a wide range of different rigid-body properties.

Table 22.1 shows the “true” values of the rigid-body properties of the 18 reference objects. (Again, these reference values were derived from the positions, orientations, weights, lengths, and diameters of the cylinders.) The table also shows the absolute measurement errors produced by the device for the case where the object’s mass was known and the x and y coordinate of the COG were obtained by using the static method based on Eq. (22.5). Figure 22.5 (subplots 5–8) summarizes the same data in the form of statistical error distributions. With moment of inertia errors well below 1% and COG errors below 0.5 mm, accuracy was very high.

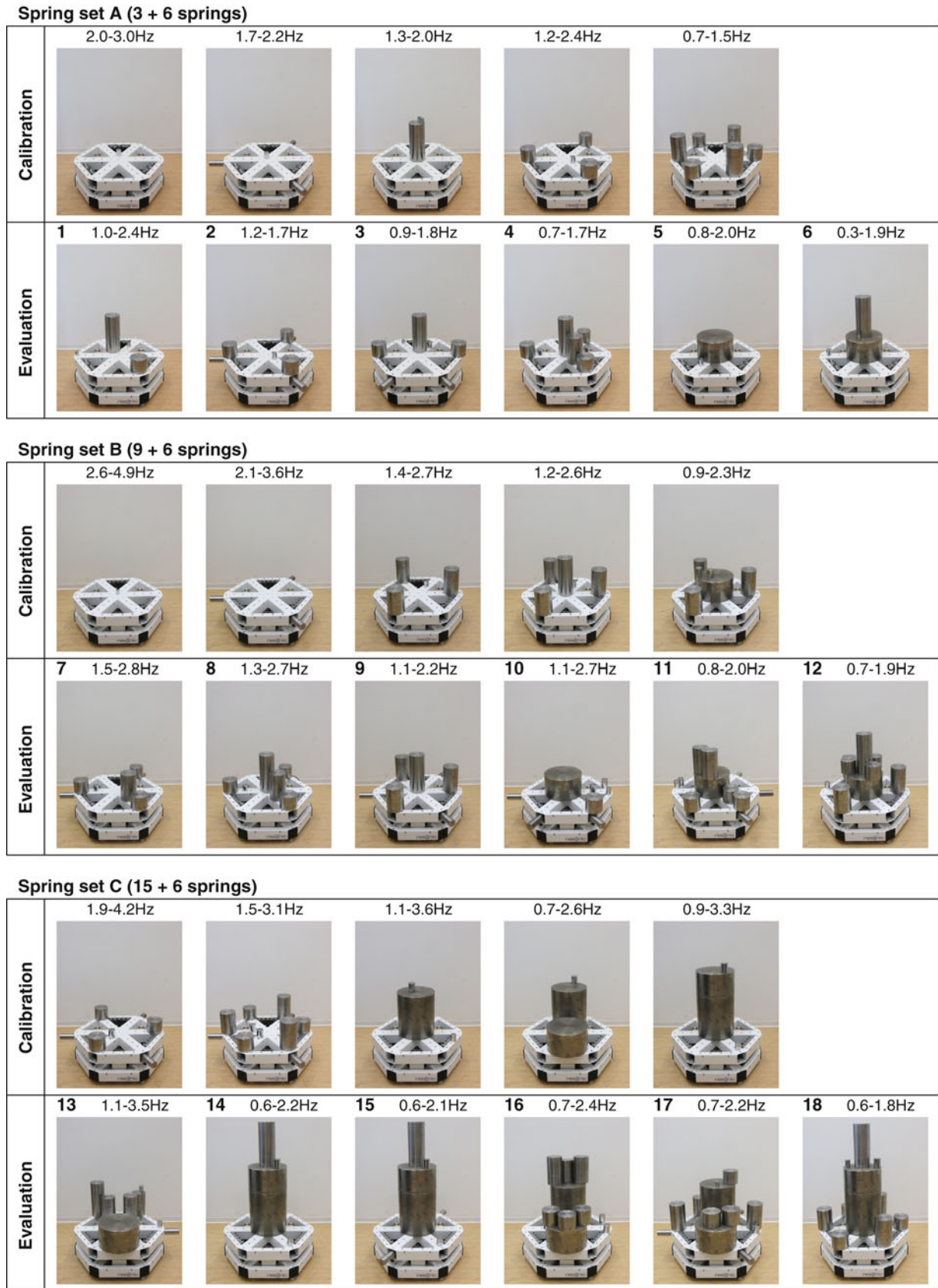


Fig. 22.4 Cylinder configurations used for calibration and accuracy evaluation

Table 22.1 True values and absolute errors for the 18 different test cases (mass known)

		m [kg]	I_{xx} [kgm ²]	I_{xy} [kgm ²]	I_{xz} [kgm ²]	I_{yy} [kgm ²]	I_{yz} [kgm ²]	I_{zz} [kgm ²]	c_x [mm]	c_y [mm]	c_z [mm]
1	True	34.44	0.524	0.394	0.206	0.966	-0.121	0.963	1.22	0.23	230.92
	Error	-	-0.003	0.000	-0.003	0.002	0.004	0.003	0.07	y 0.01	0.14
2	True	y40.37	2.080	-0.014	0.002	2.090	0.001	3.969	-1.24	0.43	122.76
	Error	-	-0.003	-0.000	y 0.001	-0.003	-0.004	-0.001	y 0.14	-0.02	0.01
3	True	52.74	1.752	-0.365	0.243	y 2.162	-0.427	2.930	0.65	-1.91	187.86
	Error	-	-0.000	-0.000	y 0.001	0.000	0.002	-0.001	0.10	y 0.00	y 0.05
4	True	y68.72	1.676	0.030	0.046	1.720	-0.026	2.594	-0.10	-0.28	206.14
	Error	-	-0.000	-0.001	-0.002	0.001	0.005	0.001	0.11	-0.00	-0.02
5	True	80.06	0.577	0.000	-0.000	0.577	-0.000	0.792	-0.05	1.16	188.50
	Error	-	0.000	0.000	0.001	0.000	0.002	0.000	0.10	0.02	-0.05
6	True	105.82	1.850	0.000	-0.020	1.850	0.005	0.837	1.01	0.90	245.22
	Error	-	0.004	-0.005	0.006	0.007	-0.000	-0.000	0.09	0.00	-0.22
7	True	52.78	2.000	-0.282	-0.195	1.684	0.116	3.267	-6.01	1.84	155.73
	Error	-	0.001	0.001	-0.005	-0.004	-0.007	-0.003	0.13	-0.03	-0.34
8	True	68.72	1.677	0.029	0.046	1.721	-0.026	2.596	-0.13	-0.31	206.16
	Error	-	-0.000	-0.001	0.002	0.000	-0.005	-0.002	0.11	-0.02	0.01
9	True	90.55	3.465	-0.055	-0.001	3.194	-0.078	5.248	-0.16	0.16	195.95
	Error	-	0.003	0.001	-0.014	0.000	0.000	-0.000	0.11	-0.00	0.06
10	True	103.26	1.750	0.473	0.106	2.239	-0.379	3.228	-5.33	-3.38	168.23
	Error	-	-0.003	0.000	-0.003	0.000	0.002	-0.005	0.09	-0.03	0.08
11	True	155.81	4.094	0.538	0.893	4.044	0.152	4.724	3.75	0.99	213.79
	Error	-	-0.003	-0.000	-0.011	0.004	0.000	0.005	0.10	-0.01	-0.04
12	True	181.50	4.455	-0.029	0.012	4.167	-0.072	4.917	0.93	0.21	244.52
	Error	-	0.021	0.004	-0.006	0.010	0.013	0.002	0.09	-0.04	-0.14
13	True	163.28	7.096	2.551	0.666	4.647	-0.369	10.262	-0.49	-1.26	201.72
	Error	-	-0.020	0.001	0.019	0.002	0.022	0.010	0.09	-0.05	-0.14
14	True	266.72	10.063	-0.000	0.008	10.063	0.017	2.428	-1.08	0.06	392.55
	Error	-	0.074	-0.015	-0.016	0.043	0.023	0.000	0.10	0.03	0.32
15	True	276.55	12.063	0.001	0.012	11.082	0.008	3.413	-1.04	-0.04	380.93
	Error	-	0.079	-0.017	-0.015	0.045	0.025	0.002	0.11	0.03	0.12
16	True	316.63	15.693	4.861	1.865	10.289	-2.873	14.498	-1.51	-0.90	296.28
	Error	-	-0.009	0.024	0.010	0.017	0.061	0.031	0.09	-0.00	0.38
17	True	331.37	13.414	3.260	0.420	10.987	-1.394	17.686	-0.94	-0.20	240.13
	Error	-	-0.011	0.009	0.028	-0.005	0.056	0.027	0.10	0.01	0.39
18	True	342.40	15.909	0.001	-0.018	16.069	-0.037	8.870	-0.28	0.06	347.22
	Error	-	0.137	-0.029	-0.015	0.077	0.032	0.019	0.11	0.02	0.18

Figure 22.5 (subplots 1–4) shows the error distributions for the case where the mass was unknown. While accuracy of the moments and products of inertia was almost unaffected, errors for the COG coordinates were more than two times larger than for the case where the mass was known. Moreover, with errors of up to 1.5 kg (or up to 0.5%), the accuracy for the dynamic mass measurement was relatively poor compared to the accuracy that can be achieved with conventional scales. For that reason, the authors recommend measuring the mass separately.

As an indicator for the method's suitability for highly elastic test objects, Fig. 22.4 includes the lowest and highest natural frequencies for each test case. In most cases, a softer spring set could have been used in order to lower the natural frequencies further, but testing each spring set with a wide range of different objects was considered to be more important for the purpose of this study. In essence, the experience showed that it is easy to keep the highest frequency below 2 Hz, whereas bringing the highest frequency close to 1 Hz requires careful fine tuning. For small objects, frequencies close to 1 Hz would also have required softer horizontal springs. (Note that the frequencies will be lower for larger versions of the device.)

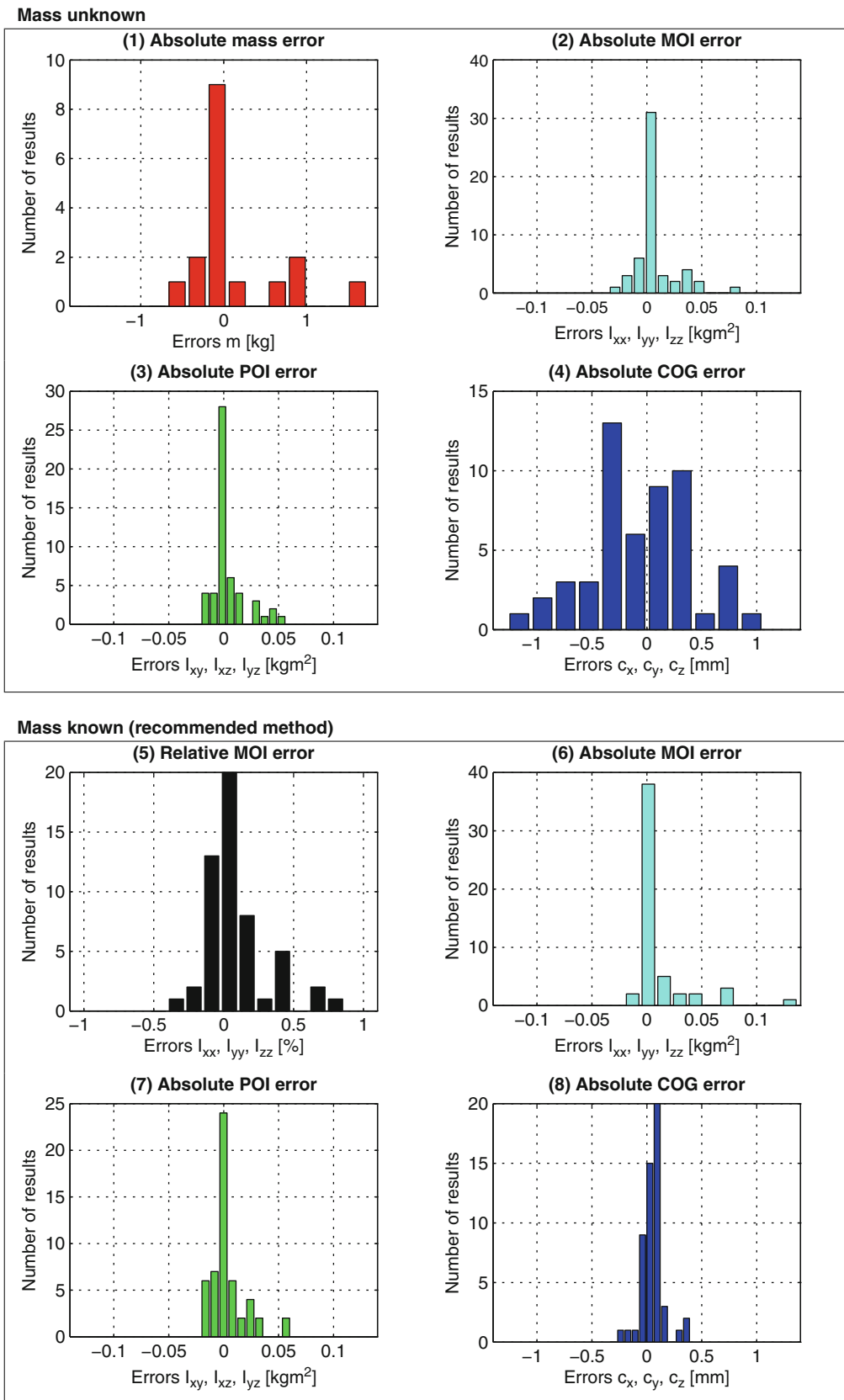


Fig. 22.5 Error distributions of 18 test cases

22.7 Conclusion

A new method and device have been presented for measuring the rigid-body properties of mechanical objects. The procedure is fast and simple, and the device is compact and portable. Moreover, the method uses free vibrations whose natural frequencies can be tuned to very low values in order to enable measurements of highly elastic objects. A prototype device with a maximum load capacity of 350 kg was tested with 18 reference objects and achieved high accuracy without exception.

Future research will focus on optimizing various parameters of the procedure, such as the measurement time, the spring and sensor positions, and the type and number of calibration objects. Moreover, future research should investigate whether the device can be calibrated for different measurement ranges in order to maximize accuracy. Future development efforts will also focus on implementing larger versions of the device that can accommodate objects such as automobiles and helicopters.

References

1. Heydinger G, Durisek N, Coovert D, Guenther D, Novak S (1995) The design of a vehicle inertia measurement facility. *SAE Trans* 104(6): 69–77
2. Lio MD, Doria A, Lot R (1999) A spatial mechanism for the measurement of the inertia tensor: theory and experimental results. *ASME J Dyn Syst Meas Contr* 121-1:111–116
3. Hahn H, Leimbach K, Piepenbrink A (1994) Inertia parameter identification of rigid bodies using a multi-axis test facility. In: *Proc. IEEE international conference on control and applications*, pp 1735–1737, 1994
4. Hahn H, Niebergall M (2001) Development of a measurement robot for identifying all inertia parameters of a rigid body in a single experiment. *IEEE Trans Contr Syst Tech* 9(2):416–423
5. Goertz H (2007) Identifikation von Fahrzeugträgheitsparametern in Fahrversuchen und auf Prüfständen. Ph.D. thesis, Institut für Kraftfahrwesen, RWTH Aachen
6. Bretl J, Conti P (1987) Rigid body mass properties from test data. In: *Proc. 5th international modal analysis conference (IMAC)*, pp 655–689
7. Conti P, Bretl J (1989) Mount stiffness and inertia properties from modal test data. *ASME J Vib Acoust Stress Reliab Des* 111:134–138
8. Wei Y, Reis J (1989) Experimental determination of rigid body inertia properties. In: *Proc. 7th international modal analysis conference (IMAC)*, pp 603–606, 1989
9. Kloepper R, Okuma M (2009) Elimination of bias errors due to suspension effects in frf-based rigid body property identification. *ASME J Dyn Syst Meas Contr* 131(4):041005
10. Kloepper R (2009) A measurement system for rigid body properties enabled by gravity-dependent suspension modeling. Ph.D. thesis, Tokyo Institute of Technology
11. Kloepper R, Akita H, Okuma M, Terada S (2010) An experimental identification method for rigid body properties enabled by gravity-dependent suspension modelling. In: *Proc. 1st joint international conference on multibody system dynamics*, 2010
12. Malekjafarian A, Ashory M, Khatibi M (2011) Estimation of rigid body properties from the results of operational modal analysis. *Struct Dynam* 3:1559–1567
13. Malekjafarian A, Ashory M, Khatibi M (2013) Identification of inertia properties from the results of output-only modal analysis. *Arch Appl Mech* 83(6):923–937
14. Kloepper R, Okuma M, Krueger J (2013) A new process for measuring complete inertia properties. *MTZ Worldwide* 74(3):40–44

Chapter 23

Three-Dimensional Modal Parameters of Tire

Jianfeng Qiao, Yongchang Du, and Peng Zhao

Abstract Modal test of a radial tire in radial, tangential and transverse directions is presented. The tire is under free suspension condition. Complete set of modal parameters, including modal frequencies, modal damping factors and modal shapes is given. The influences of inflation pressure and rim weight to modal parameters are analyzed and the differences between cavity mode and other elastic modes are distinguished from their characteristics.

Keywords Tire • Modal test • Three-dimensional modal parameters • Free suspension • Cavity mode

23.1 Introduction

The tire is the only component of the automobile which interacts with ground. So its mechanical characteristics significantly affect various behaviors of the automobile. The modeling of tire dynamics plays an important role in vehicle dynamics simulation. However, due to the complexity of tire structure and the non-linearity of its mechanical property, tire modeling has been a challenging assignment for researchers since 1950s.

For developing more physical and analytical tire model of larger frequency range, the ring, belt models and MPTM (modal parameter tire model) were proposed. The common feature of these tire models is that tire modal parameters are used to different extent. In particular, MPTM [1] considers modal parameter under free suspension representing tire native characteristics and independent of operating conditions. It uses modal parameter directing in modeling process.

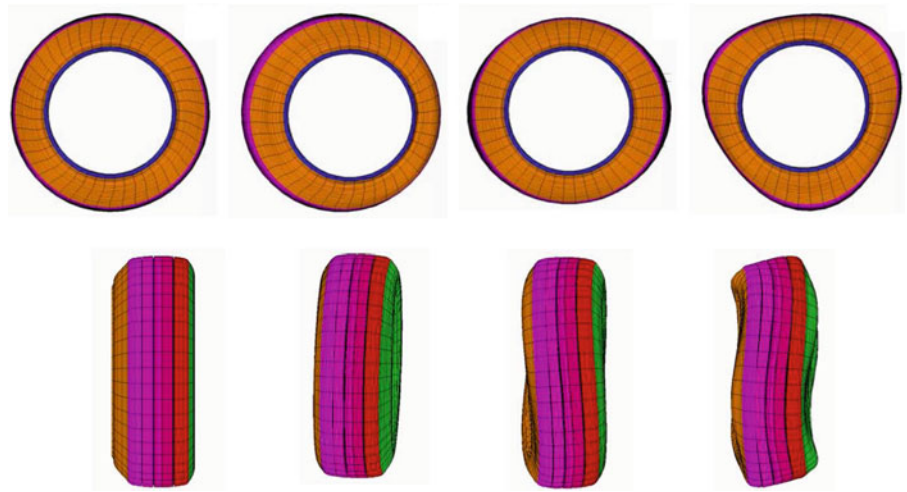
The research on tire modal test began in 1990s. Pacejka [2] and Gong [3] use lower tire modal parameters to calculate physical parameters of rubber tire in order to build a ring-model. Dihua and Jin, etc. [4–7] build MPTM, by applying modal parameters directly. So it is necessary to get accurate modal parameters of the pneumatic tire.

To get tire modal parameters, two test configurations, which are under free conditions and under constrained circumstances, are normally used. Modal parameters from the constrained method are inevitable to be influenced by constrained mechanisms. To decrease the bias, professional test equipment must be used. However, these kinds of devices are always expensive, heavy, poor repeatability and only available to lower frequency. Free constrained method has no constrained devices, so modal parameter show essential characters of the tire itself and can be used in various conditions. In this paper, modal parameter under free constrained conditions is presented and the influencing factors are discussed.

A vehicle tire is a rotation symmetry body. The modal shapes of a tire consist of three directions, including the radial direction, the tangential direction and the side direction. Previous researches have presented results in one or two directions, such as by Weidong [8], Baojiang [9] and Xianhai [10]. In consideration of the complex strained condition of a working tire, it is necessary to measure integrated three-dimensional modal parameters of a tire.

J. Qiao (✉) • Y. Du • P. Zhao
State Key Laboratory of Automotive Safety and Energy, Tsinghua University, Beijing, China
e-mail: qiaojianfeng0210@163.com

Fig. 23.1 Radial and tangential mode of a tire [11]



23.2 Modal Shapes and Representing Method

According to the report of Michelin [11], modal shapes of the first few tire modes are as shown in Fig. 23.1, which are trigonometric series of rising number. In this research “direction + number” is used to express different modal shapes. For instance, R1, R2, R3 etc. are representing different radial modal shapes; T0, T1, T2 etc. show diverse tangential modal shapes; S0, S1, S2 etc. indicate side modal shapes.

23.3 Modal Test Method

This study use free suspended circumstance, as shown in Fig. 23.2, to approximate the free constrained condition. The first elastic mode of a passenger vehicle tire, based on experience, is normally higher than 30 Hz, and the natural frequency of the rigid body modes of test system, according to actual measurement, is lower than 0.5 Hz. So, it is acceptable to assume that the system has very little influence on the tire’s elastic modes, and the tire can be considers in free constrained condition.

A 205/55R16 radial tire is used in the test. The temperature of the laboratory is 25 °C and the inflation pressure is set to its rated pressure as 250 kPa.

As a tire is symmetry, it is reasonable and convenient to arrange measure points on the half circle, as diagrammed in Fig. 23.3. Point 1 is the excitation point. Force-hammer is applied to excite in different direction, including radial, tangential and side. In order to pick up vibration responses, acceleration sensors are stuck to point 1 to point 11. Acceleration sensors are also arranged on point 21 and point 22 to monitor the vibration of tire rim. To minimize the influence of the sensors’ weight to modal shapes, balance blocks are stuck to the other half circle.

23.4 Modal Test Results

Modal test results are processed by commercial modal analysis software. All the modal parameters are as shown in Table 23.1.

Trigonometric curves are used to fit modal shapes, which are extended to the whole circle. Both original data and fitting data are shown in Figs. 23.3, 23.4, and 23.5. The tangential displacements, for clear indication, are shown in radial direction in Fig. 23.5.

Fig. 23.2 The suspension and excitation directions

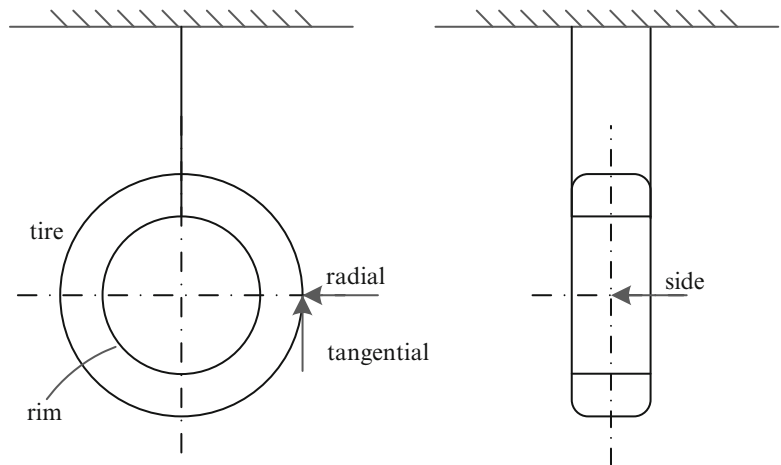


Fig. 23.3 Exciting and measuring points

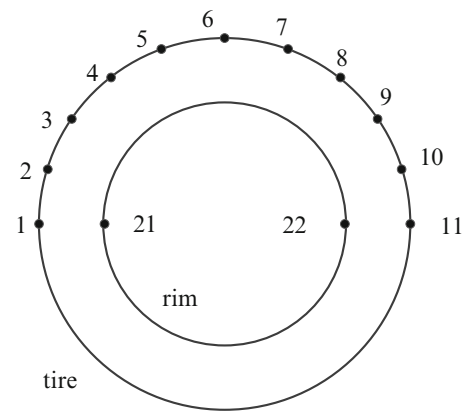


Table 23.1 Modal parameters from the test

Radial modes			Tangential modes			Side modes		
Modes	f (Hz)	d (%)	Modes	f (Hz)	d (%)	Modes	f (Hz)	d (%)
R2	105.329	3.13	T2	105.332	3.29	S0	50.222	2.28
R1	107.209	3.98	T1	108.114	3.81	S1	82.322	3.02
R3	131.036	2.65	T0	122.274	6.78	S2	99.098	3.24
R4	159.622	2.30	T3	131.467	2.66	S3	152.697	3.70
R5	188.974	2.73	T4	159.649	2.42	S4	192.885	3.81
R6	219.218	2.66	T5	188.689	2.89	S5	222.320	4.46
R7	250.880	2.86	T6	218.687	2.76	S6	250.425	3.94
R8	284.653	3.17	T7	250.154	3.02	S7	281.717	3.89
R9	319.313	3.65	T8	284.079	3.31	-	-	-
Cavity	229.270	0.23	T9	318.644	4.33	-	-	-

23.5 Influence of Rim Weight

It is obvious that the rim involves in the vibration in R1, T0, T1, S0, and S1 according to Figs. 23.4, 23.5 and 23.6. So these modes are affected by the rim’s weight and moments of inertia. To research these influences, different additional weights on the rim are applied during the tests, and the test results are indicated in Table 23.2 and Fig. 23.7. Based on these test results, the frequency of the five modes are lower when the rim’s weight and moments of inertia are higher, meanwhile other modes do not change.

Fig. 23.4 The lower eight mode shapes from radial excitation and radial response

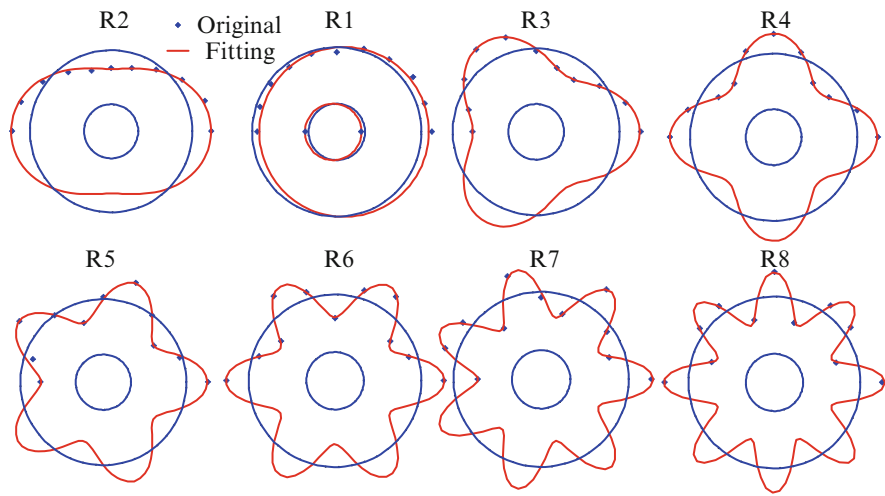


Fig. 23.5 The lower eight mode shapes from tangential excitation and tangential response

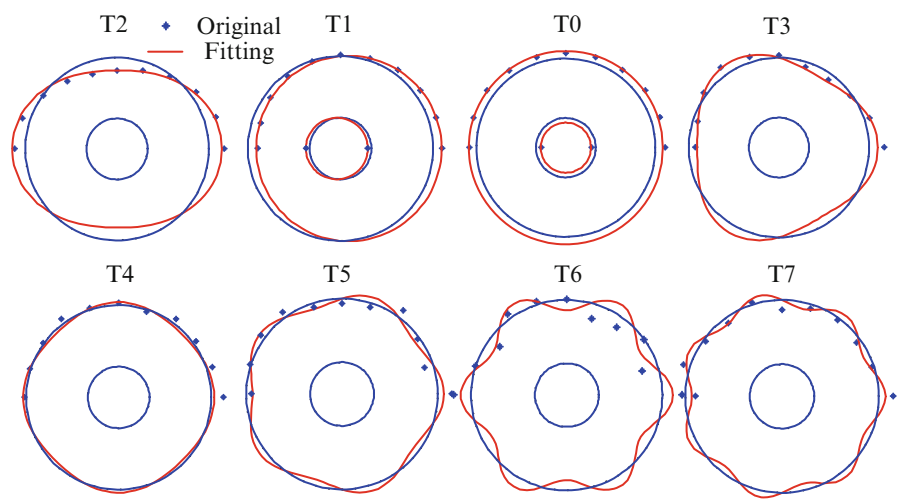
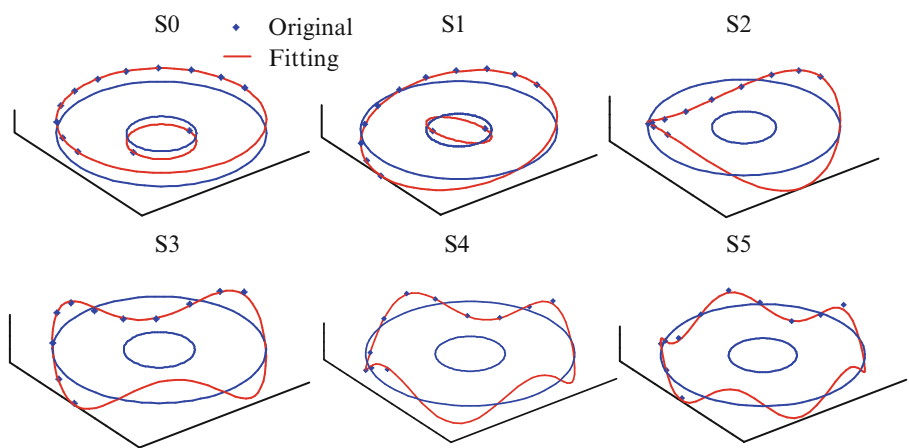


Fig. 23.6 The lower eight mode shapes from side excitation and side response



23.6 Cavity Mode

According to Table 23.1, a special mode exists in radial direction. In order to study this mode, we change the inflation pressure and do a set of tests. The results are as shown in Table 23.3 and Fig. 23.8. It can be seen that this mode is obviously different from other modes in two aspects:

1. The damping of this mode is clearly lower than other modes;

Table 23.2 Mode frequencies from different rim weights

Weight (kg)	9.99	20.23	34.39
R1 (Hz)	107.209	95.266	93.127
R2 (Hz)	105.329	105.232	105.137
T0 (Hz)	122.278	119.63	116.539
T1 (Hz)	108.241	95.826	93.922
T2 (Hz)	105.221	105.12	106.08
S0 (Hz)	50.222	45.629	43.565
S1 (Hz)	82.322	77.986	60.006
S2 (Hz)	99.098	99.319	99.137

Fig. 23.7 Mode frequencies from different rim weights

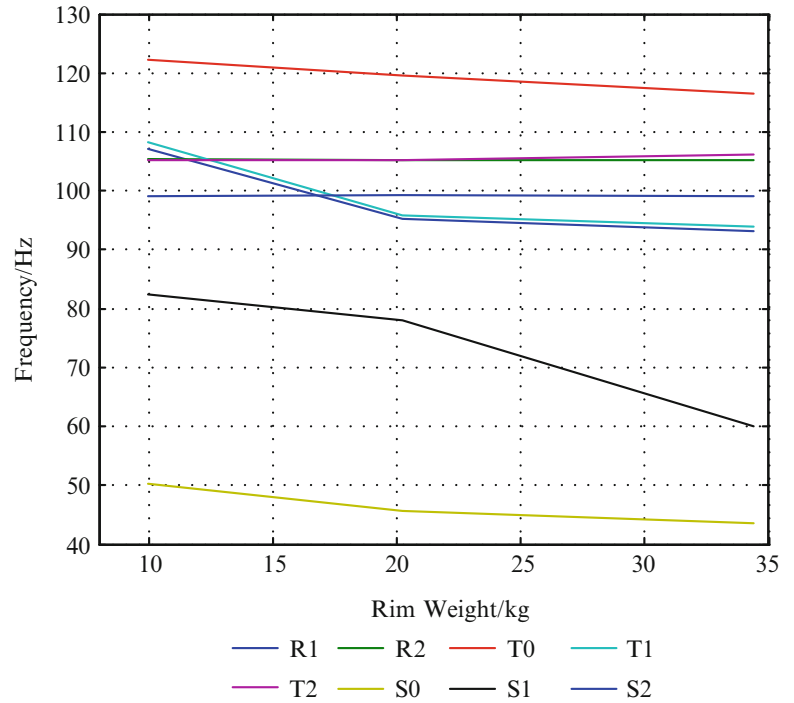


Table 23.3 Modal parameters from different inflation pressures

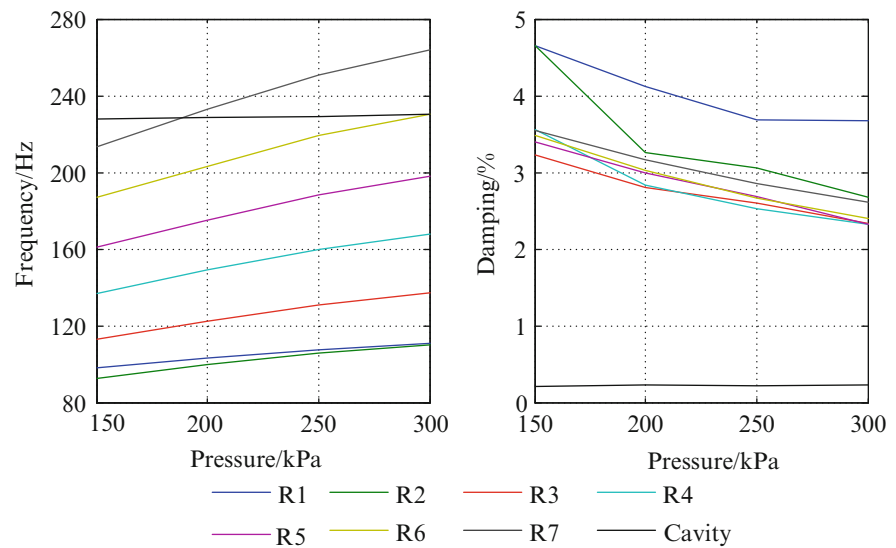
Modes	150 kPa		200 kPa		250 kPa		300 kPa	
	f (Hz)	d (%)						
R1	98.265	4.65	103.015	4.12	107.361	3.69	111.001	3.68
R2	92.637	4.65	99.700	3.26	105.538	3.06	109.840	2.68
R3	113.074	3.23	122.336	2.80	131.020	2.60	137.221	2.34
R4	136.798	3.56	148.980	2.83	159.888	2.53	167.671	2.32
R5	161.105	3.40	175.084	3.00	188.453	2.69	198.258	2.32
R6	187.171	3.48	203.328	3.03	219.265	2.66	230.570	2.40
R7	213.262	3.55	232.834	3.17	250.889	2.86	264.159	2.61
Cavity	227.704	0.21	228.571	0.23	229.280	0.22	230.311	0.23

2. The frequency does not vary when inflation pressure changes.

These results agree with the research of Yam [12, 13].

The preliminary conclusion is this mode is cavity mode of the tire. With the increase of pressure, frequencies of other tire modes raise and damping of other modes decrease, but the differences of frequency and damping of cavity mode is negligible. It is because cavity mode mainly depends on the shape of tire cavity, which nearly remains the same when the pressure varies.

Fig. 23.8 Modal parameters from different inflation pressures



23.7 Conclusions

- Three-dimensional modal parameters of a 205/55R16 tire are obtained by means of three direction modal tests.
- The influence of rim's weight and moment of inertia is studied through test method. Five modal frequencies, including R1, T0, T1, S0, S1, is decreased with the increase of weight and moment, but other modal parameters remain unchanged.
- The modal parameter of cavity mode is not affected by inflation pressure in the discussing range and its damping is notably small comparing to other elastic modes.
- All the elastic frequencies of tire modes, except cavity mode, become higher when increasing inflation pressure. But the damping factors become lower.

All the modal parameters of a tire are acquired under free constrained condition, which help us eliminate the influence of constrained mechanics, in this research. Substantive characters of rubber tire are reflected by these parameters. Researchers can also transform these numbers to other different constrained conditions for different objectives by using modal synthesis method [14, 15].

References

1. Dihua G, Zhaolong D, Chenjian F (2007) Tire model by using modal parameters directly (MPTM). SAE Technical Paper, 2007-01-1512
2. Pacejka HB (2006) Tyre and vehicle dynamics, 2nd edn. Butterworth-Heinemann, Oxford, pp 412–473
3. Gong SA (1993) Study of in-plane dynamics of tires. Faculty of Mechanical Engineering and Marine Technology, Delft University of Technology, Delft
4. Dihua G, Weidong W, Aiqian Z (1998) Tire modeling for vertical properties by using experimental modal parameters. SAE Technical Paper, 980252
5. Jin S (1999) Study on tire cornering properties by using experimental model parameters. Ph.D. dissertation of Tsinghua University, Beijing
6. Jin S, Dihua G, Yan LH (2000) Modeling of non-steady state tire cornering properties by experimental modal parameters. *Automot Eng* 22(3):145–149
7. Jin S, Dihua G (2001) Time domain simulation for tire cornering properties using experimental modal parameters. *J Tsinghua Univ* 41(4/5):81–84
8. Weidong W (1996) Tire experimental modal analysis and building tire model by using experimental modal parameters. Ph.D. Dissertation of Tsinghua University, Beijing
9. Baojiang L (2011) Research on several problems of modal parameter tyre model. Ph.D. Dissertation of Tsinghua University, Beijing
10. Xianhai X (2004) The study on some issues about tire modeling using experimental modal parameters. Department of Automotive Engineering, Tsinghua University, Beijing
11. MICHELIN-Technology Centre Ladoux (2003) Tire modal procedure test MICHELIN data description. MICHELIN-Technology Centre Ladoux, Clermont-Ferrand Cedex
12. Guan DH, Yam LH, Mignolet MP, Li YY (2000) Experimental modal analysis of tires. *Exp Tech* 24(6):39–45
13. Yam LH, Guan DH, Zhang AQ (2000) Three-dimensional shapes of a tire using experimental modal analysis. *Exp Mech* 40(4):369–375
14. Dihua G, Yongling S (2001) The use of modal synthesis techniques for determining modal parameters of tire. *Automot Eng* 23(3):148–151
15. Dihua G, Peilei D, Chenjian F (2003) Modal experiment and analysis of free and fixed suspended tires. *Automot Eng* 25(4):353–359

Chapter 24

Hybrid EMA/OMA Data Collection/Reduction for Improved Modal Characterization

Sergio E. Obando and Peter Avitabile

Abstract Experimental modal analysis (EMA) has a long tradition of use but requires measurement of an applied force. Operational modal analysis (OMA) on the other hand, requires no force measurement, but relies on all the system modes to be excited from the unmeasured excitation which can never be verified. Experience has shown that many times critical modes of the system cannot be obtained from the OMA; EMA will generally find all the modes when proper test techniques are utilized. Both techniques have their advantages and disadvantages to say the least and both offer unique opportunities to extract modal characteristics.

This work utilizes a hybrid testing approach to merge together the best of both of the EMA and OMA techniques to acquire a hybrid set of data. These data sets are used in a combined EMA/OMA extraction approach to find all the modes of the system. Test cases are shown to illustrate how OMA may miss certain modes but that the hybrid testing approach offers unique opportunity to find modes that may be missed. Various combinations of test cases are studied to show the pitfall of OMA and the advantages of the hybrid approach.

Keywords Experimental modal analysis • Operating modal analysis

24.1 Introduction

For years, traditional Experimental Modal Analysis [1] has been performed to identify the modal characteristics of a structure. Provided proper test techniques are employed and the selection of the reference point is carefully done, the traditional approach will provide very good system characteristics. However, there are many times that the traditional modal approach may be difficult for a variety of different reasons. This could be due to inability to adequately excite the structure, especially in the case of very large structures such as buildings and bridges, where it is not a simple task to provide adequate excitation for the structure. Furthermore, in many cases, the structure's modal characteristics may be different in operation when compared to the "in-laboratory" test configuration. Suffice it to say that there can be cases where the traditional modal test may be difficult to implement.

In recent years, the Operational Modal Analysis methodology (or output only systems) [2] has gained popularity because the structure can be tested both in place and in operation. The excitation of the structure comes from its natural environment whether it be operating condition with internally generated forces or in an operating condition where the natural excitation comes from ground motion or wind excitation in its natural working condition. This is a very good approach for determining the modes of the system due to its natural environment.

However, there is a very important concern that the natural excitation must be able to adequately excite all the modes of interest or else critical modes may be missed or improperly determined. The excitation for the system must be broadband in frequency content and must be spatially rich so that all the modes of the system are adequately excited. If this is not the case then some of the basic modal characteristics may not be adequately excited or defined from the extraction process.

S.E. Obando (✉) • P. Avitabile
Structural Dynamics and Acoustic Systems Laboratory, University of Massachusetts Lowell,
One University Avenue, Lowell, MA 01854, USA
e-mail: sergio.e.obando@gmail.com

In addition, many researchers have found that some of the operating modes may have significantly different characteristics describing the system depending on which set of data is used on a day to day basis. When this occurs, then there is a very serious concern that the extracted modes are not necessarily the primary modes of the system and may be highly dependent on the specific excitation that possibly changes as time progresses. In these cases, the extracted modes are then very highly suspect and may not be proper representations of the system modes.

A recent paper [3] showed that at times the OMA approach may not extract all the modes that would be obtained from a traditional EMA. Due to these difficulties observed and reported by many researchers using OMA, an alternate approach to the problem has been considered to blend together both the EMA and OMA approach in a hybrid form that merges together the best of EMA and OMA to identify modes of a system.

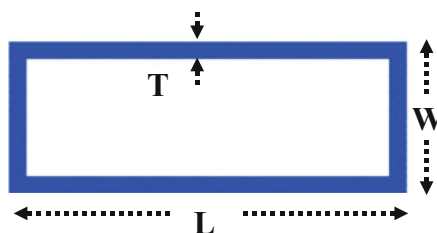
In essence, this hybrid approach utilizes the excitation from the environment but then augments the measured data by conducting a traditional EMA while measuring and collecting the data from the natural excitation of the structure. This hybrid set of collected data is then processed numerous ways using both OMA and EMA to extract the modes of the system. A simple test structure is used to illustrate the data collected and the post-processing to obtain modal characteristics.

24.2 Structure Description

The test structure consisted of rectangular Aluminum frame of dimensions as shown in Fig. 24.1. The structure was freely hung from above near the four corners of the frame.

24.3 Testing Methodology and Cases Studied

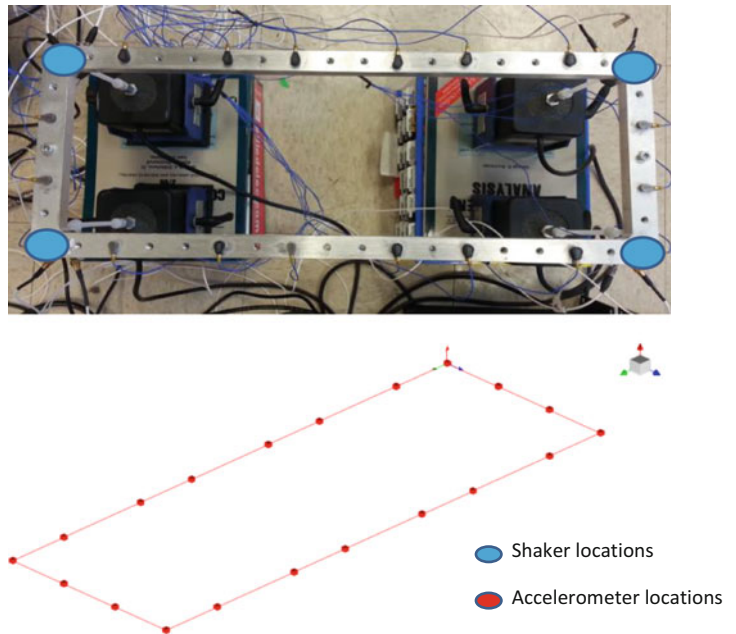
The structure was set up for a free-free test configuration using four shakers to excite the system for a traditional Multiple Input Multiple Output (MIMO) modal test. The shakers were attached to impedance heads mounted at the four corners of the frame. Two additional sources of excitation were applied to the structure to simulate operating data. One of those excitations consisted of random impacts to the structure but only at two locations which were expected to be node points for one of the first modes of the system; the other excitation consisted of random impacts that were spatially distributed around the entire structure. Data was collected from 20 accelerometers measuring the out of plane response of the frame as shown in Fig. 24.2.



Aluminum Frame Dimensions	
L – Length	17.75 in
W – Width	6.75 in
T – Thickness	0.75 in
H – Height	0.5 in

Fig. 24.1 Dimensions and characteristics of tested structure

Fig. 24.2 Experimental setup of studied aluminum frame



Various combinations of the MIMO shaker excitation and the two randomly impact excitation were combined to create several data sets. These are identified below and were used to create the entire set of data for the structure.

- Test 1—Traditional MIMO data collected with all four shakers used for excitation (reference data set)
- Test 2—Random impact excitations spatially distributed around the structure
- Test 3—Random impact excitation at two locations expected to be the node of the torsion mode
- Test 4—MIMO data collection with all four shakers (Test #1) AND random impact excitation at two locations (Test #3)

Each of these tests were performed using LMS Test [4]. Lab to acquire and stream data that was then processed using LMS Polymax (for the MIMO data) and LMS Operational PolyMAX (for OMA data) software packages. Each of the four different tests are described next and then the different sets of data are compared to each other.

24.3.1 Test Case #1

A traditional MIMO test was performed using a burst random excitation from the four shakers. The system response measured from the accelerometers and impedance heads was used to extract frequencies, mode shapes and damping from the FRF MIMO data. These mode shapes served as a reference solution and for comparison to the OMA and hybrid data. Figure 24.3 shows typical drive point FRF measurements from the MIMO tests conducted.

The FRF measurements from the 20 accelerometers were curvefitted using Polymax and the first five characteristic mode shapes are shown in Fig. 24.4.

24.3.2 Test Case #2

The frame was setup in the same configuration of Test Case #1, free-free with four shakers attached to the frame by impedance heads. However, in this case the input excitation to the frame originated from spatially distributed random impacts to the frame while the four shakers were left attached but not in use. Time data from the test was streamed to disk and used to calculate auto and cross spectra from selected reference accelerometers. Curvefitting was done using Operational Polymax and the characteristic mode shapes of the frame can be seen in Fig. 24.5.

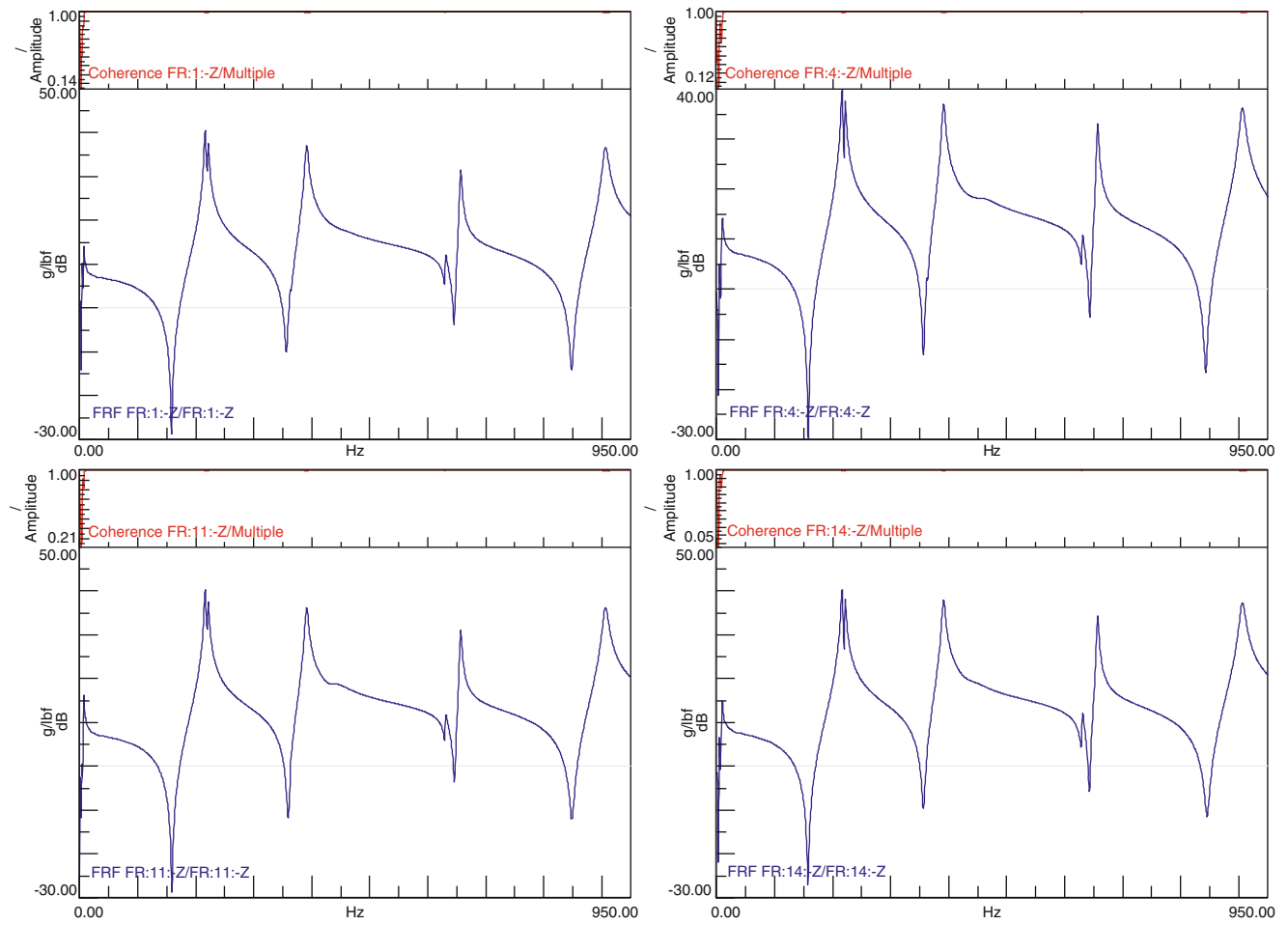


Fig. 24.3 Drive point FRF measurements of frame from traditional four shaker modal tests (MIMO)

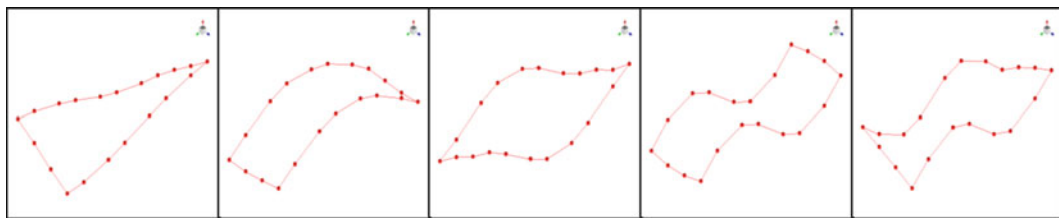


Fig. 24.4 Typical first five mode shapes from four shaker MIMO tests of frame

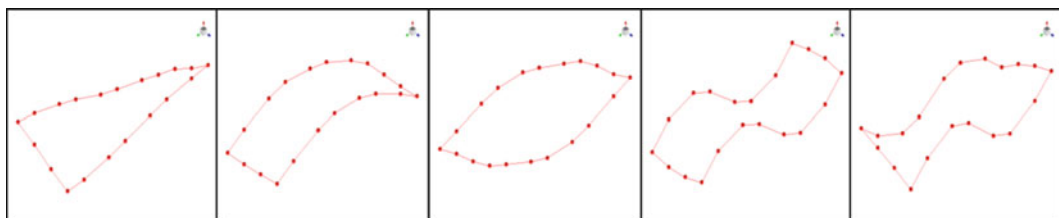


Fig. 24.5 Typical first five mode shapes extracted from OMA test of frame using spatially distributed random impacts

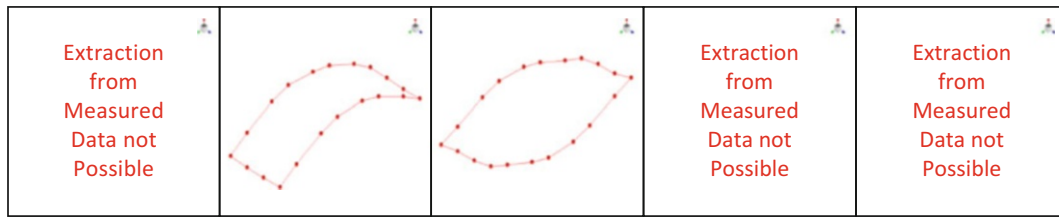


Fig. 24.6 Characteristic mode shapes of frame found through OMA test using random impact excitation restricted to the nodes of the first torsion mode

24.3.3 Test Case #3

Random impact excitations were performed at two locations on the frame using the same configuration of Test Case #2. The locations were chosen to be nodes of the first torsion mode of the system. The impacts were done randomly at the two locations and the throughput time data streamed directly to disk. The processing of auto and cross spectra as well as the curvefitting were completed using the same OMA methodology of Test Case #2. The mode shapes that were found can be seen in Fig. 24.6.

24.3.4 Test Case #4

The frame was configured as in Case #1 but using a random input excitation from the four shakers in conjunction with random impact excitations at the two locations used in Case #3 (nodes of the first mode). The FRF measurements obtained through the EMA portion of this case were only used to corroborate the OMA test mode shapes. Typical drive point FRF measurements can be seen in Fig. 24.7.

The throughput streamed time data was processed and used to calculate auto and cross spectra as in the two previous OMA tests. Operational Polymax was used to extract the frequencies and mode shapes and these can be seen in Fig. 24.8.

24.4 Comparison of Cases Studied

The mode shapes obtained in Case #1 were used as a reference solution and also verified with an available finite element model of the frame.

24.4.1 Comparison A

The traditional MIMO modal test results (Test Case #1) were compared to the spatially broad excitation from the operating modal test (Test Case#2) and it was clear that the operating modal data is very similar to the traditional modal test. Obviously, the unmeasured excitation for the operating test was sufficient to excite the modes of interest of the structure. This is an ideal situation in which use of either type of test methodology does not bring any significant loss in the quality of the characterization of the structure. However, in typical experimental settings there is no a priori guarantee that the unmeasured OMA excitation will yield the same results as the measured traditional input from EMA. Table 24.1 shows a MAC comparison of Test Cases #1 and #2. There is high correlation for all modes with some slight differences on the third mode of the frame (second torsion mode).

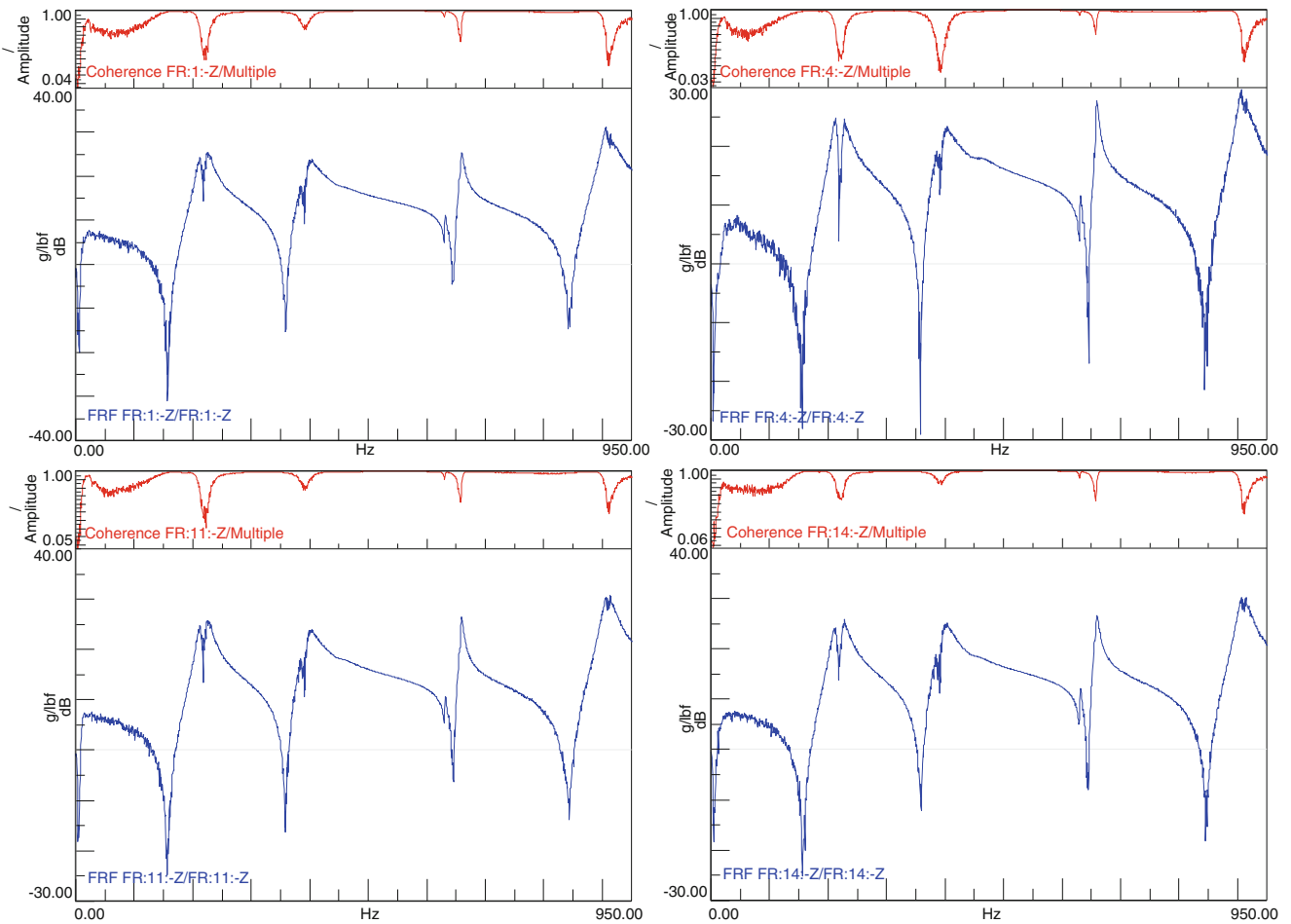


Fig. 24.7 Typical drive point FRF measurements of frame from EMA portion of hybrid test. Note the drop in coherence on the measurements due to the uncorrelated input excitation from the random impacts at the node of the first torsion mode

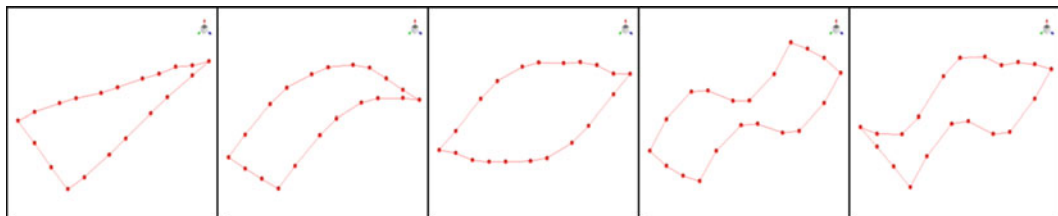


Fig. 24.8 Characteristic mode shapes of frame found through hybrid EMA and OMA test using four shaker random input excitation and restricted impact excitation at the nodes of the first torsion mode

Table 24.1 MAC of MIMO modal test (Test Case #1) and operational modal test (Test Case #2)

		Operational modal test (shakers off)				
		Mode 1	Mode 2	Mode 3	Mode 4	Mode 5
MIMO test	Mode 1	98.99	1.23	0.07	0.02	0.50
	Mode 2	0.48	93.84	5.40	0.00	0.15
	Mode 3	0.02	0.10	73.65	0.07	0.08
	Mode 4	0.01	0.00	0.00	99.50	1.44
	Mode 5	0.03	0.06	0.00	0.12	98.16

Table 24.2 MAC of MIMO modal test (Test Case #1) and operational modal test (Test Case #3)

		Operational modal test (node line-shakers off)				
		Mode 1	Mode 2	Mode 3	Mode 4	Mode 5
MIMO test	Mode 1	–	1.45	0.08	0.00	0.05
	Mode 2	–	94.61	0.61	0.04	0.58
	Mode 3	–	0.08	50.07	0.19	0.15
	Mode 4	–	0.01	0.01	0.46	0.02
	Mode 5	–	0.06	0.01	0.01	1.01

Table 24.3 MAC of MIMO modal test (Test Case #1) and operational modal test (Test Case #4)

		Hybrid modal test (node line-shakers on)				
		Mode 1	Mode 2	Mode 3	Mode 4	Mode 5
MIMO test	Mode 1	98.53	1.28	0.02	0.06	0.90
	Mode 2	0.39	91.16	0.01	0.02	0.13
	Mode 3	0.05	0.21	81.69	0.07	0.20
	Mode 4	0.01	0.05	0.01	99.54	0.72
	Mode 5	0.14	0.12	0.00	0.03	98.47

24.4.2 Comparison B

The traditional MIMO modal test results (Test Case #1) were compared to the spatially restrictive excitation from the operating modal test (Test Case#3) and as it can be observed, the operating modal data did not adequately excite all the lower order modes of the system when compared to the reference set of modes. Table 24.2 shows the MAC comparison of these test cases. Clearly if the excitation does not contain spatially rich excitation then the operating modal test cannot extract the necessary information as expected. However, because the input excitation may never be known, there is no way to assure that the modes of the system will be obtained from the operational test.

24.4.3 Comparison C

The traditional MIMO modal test results (Test Case #1) were compared to the spatially restrictive excitation from the operating modal test augmented with the hybrid testing approach (Test Case#4) which uses a random input excitation from the four shakers similar to a traditional MIMO test. Table 24.3 shows the MAC comparing Test Cases #1 and #4 and it is very clear that the operating modal data is dramatically improved and all the modes that were not previously found on Test Case #3 are better represented with the alternate testing approach proposed. Given sufficient broadband excitation, the hybrid mode of data collection can be expected to complement and improve the operational data collected and serve as a safeguard that no important modes of the system are missed.

24.5 Observations

This paper presents some of the findings of the testing that was performed; many other tests were performed to verify the findings but are not all presented here due to space restrictions. One very important observation was that the hybrid approach provided the additional excitation needed to assure that all the modes of the system were adequately excited and observed in the measured response. This provides a tremendous boost to the success of the OMA approach.

As far as implementation, the operating test can be augmented with either a shaker excitation set up or by applying arbitrary, randomly, spatially distributed impact excitations to the structure while the operating data is collected. This way the structure is exposed to a broad band, spatially rich excitation to augment whatever the actual operating condition may provide. Clearly from the results shown, the extracted shapes are improved and modes were not missed.

While more work is needed to explore this in more depth, these initial studies show great promise.

24.6 Conclusion

A hybrid method of data collection and reduction that blends traditional EMA and OMA testing was presented through a series of test cases. Operational modal tests were shown to depend highly on broadband frequency and spatially broad input excitation. Since these cannot always be guaranteed, important modes of the system may be missed even in simple structures. The hybrid approach improves the OMA test by setting a measurable broadband force input to the system that ensures all modes of interest receive sufficient excitation. For those modes that were found on the OMA test, the hybrid approach showed the same or better correlation to the reference set of modes obtained.

References

1. Avitabile P (1994) Overview of experimental modal analysis using the frequency response method. Modal seminar lecture notes, March 1994
2. Peeters B, Vecchio A, Van der Auweraer H (2004) PolyMAX modal parameter estimation from operational data. In: Proceedings of the ISMA 2004 international conference on noise and vibration engineering, Leuven, September 2004
3. Thibault L, Marinone T, Avitabile P, Van Karsen C (2012) Comparison of modal parameters estimated from operational and experimental modal analysis approaches. In: Proceedings of the thirtieth international modal analysis conference, Jacksonville, February 2012
4. LMS Test.Lab – Leuven Measurement Systems, Leuven, Belgium

Chapter 25

Numerical and Experimental Determination of Nonlinear Normal Modes of a Circular Perforated Plate

David A. Ehrhardt, Ryan B. Harris, and Matthew S. Allen

Abstract It is commonly known that nonlinearities in structures can lead to large amplitude responses that are not predicted by traditional theories. Thus a linear design could lead to premature failure if the structure actually behaves nonlinearly, or, conversely, nonlinearities could potentially be exploited to reduce stresses relative to the best possible design with a purely linear structure. When examining structures that operate in environments where a nonlinear response is possible, one can gain insight into the free and forced responses of a nonlinear system by determining the structure's nonlinear normal modes (NNMs). NNMs extend knowledge gained from established linear normal modes (LNMs) into the nonlinear response range by quantifying how the unforced vibration frequency depends on the input energy. Recent works have shown that periodic excitations can be used to isolate a single NNM, providing a means for measuring NNMs in the laboratory. An extension of the modal indicator function can be used to ensure that the measured response is on the desired NNM. The experimentally measured NNMs can then be compared to numerically calculated NNMs for model validation. In this investigation, a circular perforated plate containing a distributed geometric nonlinearity is considered. This plate has demonstrated nonlinear responses when the displacements become comparable to the plate thickness. However, the system is challenging to model because the nonlinear response is potentially sensitive to small geometric features, residual stresses within the structure, and the boundary conditions.

Keywords Nonlinear normal modes • Circular plate

25.1 Introduction

Structures have been shown to exhibit nonlinear responses when large deformations occur due to extreme mechanical and environmental loading conditions, or in other cases at seemingly small amplitudes if the structure contains materials with nonlinear constitutive properties or when thin shell geometries experience vibration levels approaching the shell thickness. Over the past several decades a suite of testing and modeling approaches has been developed for linear systems. The term linear is important here since characterization of systems using modal analysis is based on quantifying the system in terms of invariants such as resonant frequencies, damping ratios, mode shapes, and frequency-response functions. Once these system invariants are quantified, a system model, typically a finite element model, is updated to reflect the measured properties. These techniques cannot be directly applied to nonlinear systems since the linear system invariants become functions of input energy, so new methods are sought to address nonlinear behavior while preserving as much as possible the simplicity of the traditional design and test paradigms.

This work proposes to use the nonlinear normal mode (NNM) concept as a basis for testing and model updating of nonlinear structures. A structure's nonlinear modes provide significant insight into the structure's free and forced response and they allow its behavior to be expressed in terms of a few compact plots [1]. For example, in a companion paper the

D.A. Ehrhardt • R.B. Harris • M.S. Allen (✉)
Department of Engineering Physics, University of Wisconsin-Madison, 535 Engineering Research Building,
1500 Engineering Drive, Madison, WI 53706, USA
e-mail: dehrhardt@wisc.edu; msallen@engr.wisc.edu

authors explore how nonlinear modes can be used to evaluate the fidelity of a reduced order model [2], illustrating that when a structure's NNMs are correctly modeled the model will be accurate for a range of different types of inputs, excitation levels, etc.

Several advances in recent years have begun to make nonlinear modeling and testing for model updating a reality for realistic structures. First, new methods have been developed to calculate the nonlinear normal modes of a structure. Peeters et al. [3] recently presented a technique based on numerical integration and continuation which has proven effective for computing the NNMs of a structure with hundreds of degrees of freedom so long as the nonlinearities are localized. Allen et al. [4, 5] recently extended that approach to structures with geometric nonlinearities that are modeled within commercial finite element software, making high fidelity model updating a possibility. On the testing front various approaches have been explored and one of the more promising seems to be a variant on stepped sine testing in which a structure can be made to vibrate in only one nonlinear mode [6]. The excitation can then be removed and the response would then presumably decay along that NNM. Peeters et al. [7] applied this technique to a beam with a local nonlinearity at one end with good results. Kuether and Allen proposed a variant on this technique that was used to compute NNMs [8] but also could be extended to compute an NNM by progressively adjusting the excitation frequency and amplitude while observing an extension of the modal indicator function (MIF).

This work proceeds along similar lines, using stepped-sine testing to estimate the nonlinear frequency response of a structure over a range of excitation amplitudes and the NNMs are then estimated from the backbones of these nonlinear frequency responses. The methods developed in [4, 5] are then used to compute the NNMs of the geometrically nonlinear structure using a detailed finite element model, and then the experimentally estimated nonlinear modes are compared with those computed from the model to determine how the model should be updated.

A simplified analytical model of the plate was also used in the initial troubleshooting, based on the work of Leissa [9], which details the analysis of the vibration of plates with various boundary conditions, thicknesses, and geometries using continuum vibrations. In reference to circular plates, Leissa uses Kirchhoff-Love plate theory to derive the various mode shapes and natural frequencies based on the geometry and boundary conditions. Additionally, we exploit the work of Jung and Jo [10], who showed how one can precisely model a perforated plate by simply adjusting the elastic modulus and density based on the perforation geometry and pattern.

This initial investigation focuses on the first two symmetric modes of the plate. The following section provides some background information regarding nonlinear normal modes while Sect. 25.2 discusses the testing that was performed. Section 25.3 describes the comparisons that were used to update the computational model and the results.

25.2 Analysis and Experimental Setup

25.2.1 Test Specimen

The article under investigation is a circular perforated plate with rolled ends which is shown in Fig. 25.1. A mechanical punch was used to create the circular perforations in a flat 16 gauge (1.52 mm thick) 409 stainless steel plate in an array of equilateral triangles with 10.16 mm long edges. Once this process was completed, the plate was formed around a 317.5 mm diameter mold with the excess trimmed so a lip of 317.5 mm remained. The plate was then welded to a 89 mm high cylinder made from a 14 gauge (1.9 mm thick) 409 stainless steel plate that was cold rolled to the 317.5 mm diameter as shown in Fig. 25.1b. The welded plate assembly was then bolted to a 317.5 mm diameter by 19 mm thick aluminum fixture with twelve 6.4 mm evenly spaced holes. A 444 N modal shaker was then attached to the center of the fixture via a stinger to excite the structure. It is important to note that all stated dimensions are nominal and subject to variation. Additionally, the processes the plate is subjected to can induce residual stresses in the structure which also might modify the dynamics of the plate in its final configuration. While this system is relatively simple compared to the engine to which it is designed to be attached, work will show how important it is to have a test to validate any computational models that are created; there are a variety of subtle details that might easily be neglected initially, and yet they could change the response considerably.

25.2.2 Finite Element Model

Circular plates exhibit complex behavior which can be difficult to model, even in a linear range. In this investigation, a finite element model (FEM) was built based on the previously stated nominal geometries of the perforated plate before it was

Fig. 25.1 Perforated plate. (a) Perforated plate before welding into test configuration, (b) perforated plate welded into the supporting cylinder, (c) based plate to which the system was attached for testing

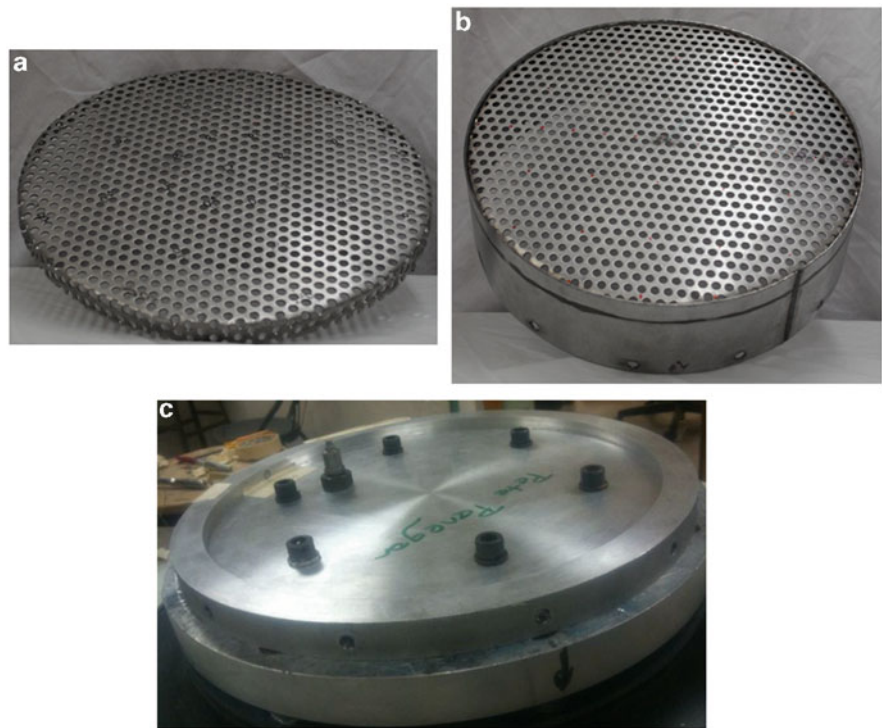
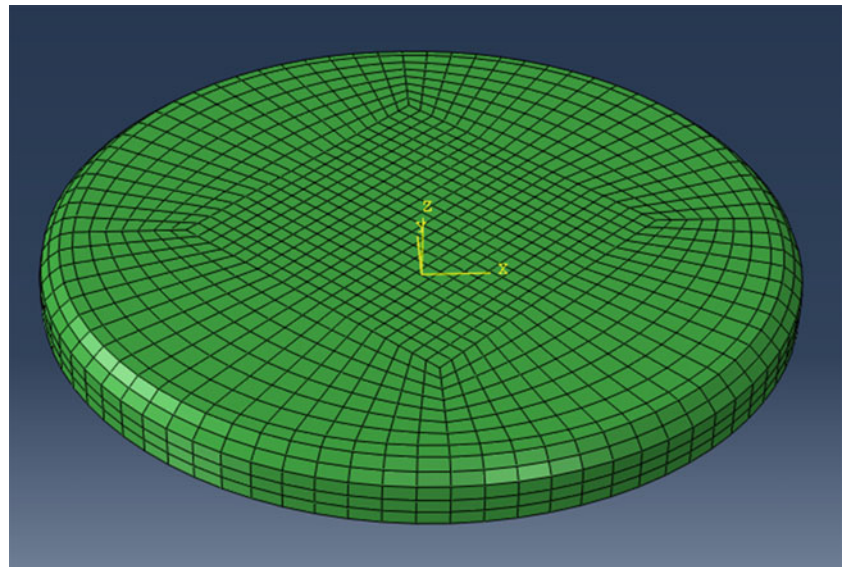
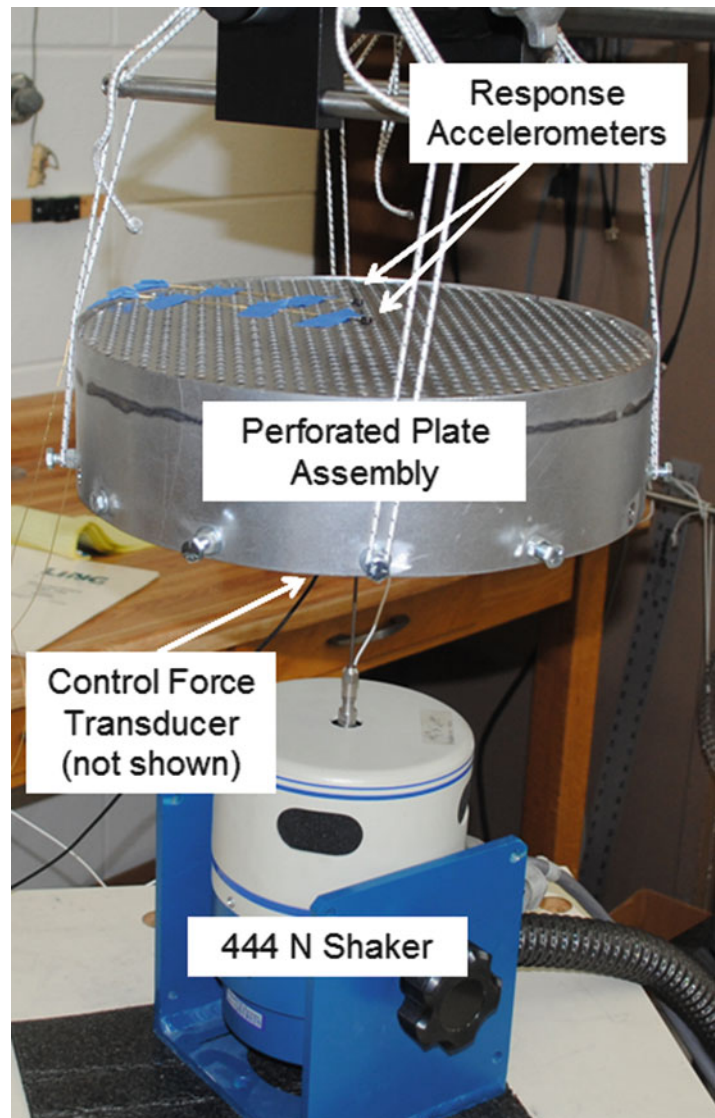


Fig. 25.2 Meshed perforated plate model



welded to the steel cylinder. Therefore, it is assumed that the welded boundary between the plate and steel cylinder provide fixed boundary conditions in the model. The plate curves from the weld and is flat over the entire central region, and hence will be referred to as a model with “No Initial Curvature (NIC)” in all of the following. A very fine mesh would have been required in order to model each of the perforations. However, Jhung and Jo [10] found that a perforated plate behaves identically to a non-perforated plate of the same dimensions, as long as the elastic properties are adjusted appropriately. Hence, the reduced elastic modulus and density were calculated based on the perforation geometry as detailed by Jhung and Jo [10], which for the triangular perforation pattern of this plate yields a new elastic modulus of 1.68 GPa and density of 5,120 kg/m³. The resulting meshed Abaqus model is shown in Fig. 25.2, and has 1,440 S4R shell elements. The elastic modulus was later updated based upon comparison with experiments. The reduced density was not updated because it can be computed from the geometric properties of the perforations (e.g. size of hole and count) and hence it was thought to be quite accurate. On the other hand, the effective modulus is dependent on any residual stresses from the addition of perforations, or imperfections of the perforation location geometry.

Fig. 25.3 Experimental setup

The nonlinear normal modes of the plate were computed from this model using the procedure discussed in [4, 5]. Specifically, a reduced order model was created for each mode of the plate (separately) using the Implicit Condensation method [11–13]. Then the ROM was integrated in the NNMCont Matlab routine provided by Peeters et al. [6] to compute the nonlinear modes. In [4, 5] this approach was found to provide an excellent approximation for the backbone of each NNM of a geometrically nonlinear beam while neglecting any internal resonances which would increase the computational cost.

25.2.3 Experimental Setup

The experimental setup is shown in Fig. 25.3. The 12.5 in circular perforated plate assembly previously described was attached to a Ling Dynamics LMT-100 electrodynamic shaker via a 5 mm diameter stinger. In some of the tests the shaker was controlled using closed loop feedback based on the input force measured by a Piezotronics PCB208C04 force transducer, with a sensitivity of 22 mV/N, mounted between the base plate and the stinger. The response of the plate is measured using two ISOTRON 25B accelerometers with a nominal sensitivity of 5 mV/g. The accelerometers were placed at two key points on the plate to ensure the dynamic response could be measured at the modes of interest. The first accelerometer, with a sensitivity of 4.627 mV/g; was placed in the center of the plate to identify modes that contain nodal diameters (e.g. Mode 1, Mode 4, etc.). The second accelerometer, with a sensitivity of 5.230 mV/g; was placed exactly one third of the radius

from the center of the plate to identify modes that have nodal lines. Since forces and frequencies were relatively low, all accelerometers were secured using wax. The setup was then suspended from four points by small bungee cords as seen in Fig. 25.3. A Data Physics[®], ABACUS data acquisition system was used to drive the shaker and to acquire measurements and the SignalCalc Mobilyzer software produced by Data Physics was used to compute the steady state response frequency and amplitude at each frequency.

Initially, quite a bit of effort was spent seeking to use the closed loop feature of the Data Physics software, together with a swept sine excitation to acquire the nonlinear frequency response. Unfortunately, the control software must adjust the input very quickly near resonance to avoid perturbing the system off of resonance and onto a co-existing low amplitude branch, so it proved challenging to obtain reasonable estimates of the nonlinear resonances using swept sine measurements. Furthermore, the swept sine measurements had to be post processed to estimate the amplitude and phase at each frequency and so it seemed that a stepped-sine test would be more reliable.

In the end the Stepped Sine capability of the Data Physics controller was used. In this mode the shaker is driven in open loop, but after each step the force amplitude is monitored and the shaker voltage adjusted until the force returns to the target value. For this study 100 steps were taken in a small band around each NNM that was only 10 Hz in width resulting in frequency steps of 0.1 Hz. The frequency was stepped up and then back down at each force amplitude. Considerable effort was required in order to assure that the software would wait long enough for steady state, and to adjust the number of iterations that the algorithm would attempt at each frequency line to drive the force amplitude towards the target value, but with some experience it proved fairly easy to acquire measurements at a range of forcing amplitudes.

25.3 Results

25.3.1 Linear Comparison

Although this system will be shown to be nonlinear, it is first helpful to test the structure and update the FEM for the low-amplitude, linear dynamic response. The first several modes of the FEM were extracted using the built in Lanczos Eigen solver in Abaqus. The experimental natural frequencies and mode shapes were determined using a roving hammer test while measuring the responses at the accelerometer locations previously discussed. The system exhibited nonlinearity for relatively small excitations, so a very small modal hammer (a PCB 086E80 modal hammer, Fig. 25.4) was used to keep the excitation force very small. A 50 mm grid of impact locations was selected on the surface of the perforated plate resulting in 37 evenly spaced nodes. The mode shapes determined from the FEM were interpolated at these locations for comparison.

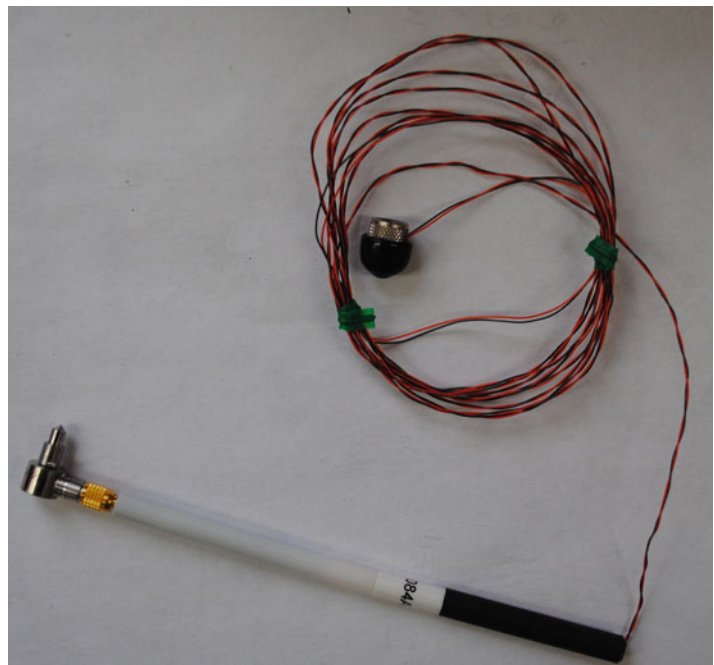


Fig. 25.4 Miniature modal hammer (PCB 086E80)

Table 25.1 Linear natural frequencies of the FEMs after updating the elastic modulus

	f_n , test	FEM 2-NIC mode #	f_n , FEM 2-NIC	% error	FEM 2-NIC MAC	FEM 2-IC mode #	f_n , FEM 2-IC	% error	FEM1-IC-MAC
1	205.36	1	204.80	0.27	0.980	1	205.26	0.05	0.773
2	327.86	2	424.88	-22.83	0.686 ^a	2	283.51	15.64	0.870 ^a
3	348.65	3	424.88	-17.94	0.707 ^a	3	283.51	22.98	0.835 ^a
4	489.17	4	701.64	-30.28	0.903 ^a	4	300.95	62.54	0.884 ^a
5	510.22	5	702.93	-27.42	0.945 ^a	5	303.02	68.38	0.925 ^a
6	572.61	6	803.68	-28.75	0.945	10	578.79	-1.07	0.657
7	699.94	7	1033.70	-32.29	0.651	7	349.70	100.16	0.544
8	814.12	9	1226.10	-33.60	0.930	13	618.63	31.60	0.736
9	827.68	10	1226.10	-32.50	0.906	14	618.63	33.79	0.750
10	916.77	11	1421.70	-35.51	0.933	8	465.22	97.06	0.934
13	938.96	12	1424.00	-34.82	0.941	9	466.01	101.49	0.941
14	1096.27	13	1713.70	-45.21	0.956	15	688.16	59.30	0.938
15	1178.72	15	1817.40	-35.14	0.444				
16	1191.36	16	1872.10	-36.36	0.401	12	615.51	50.79	0.488
17	1200.57	17	1872.10	-35.87	0.431	11	615.51	48.96	0.623

^aNo rotation applied to mode shape comparison

Five averages were taken at each impact location. The coherence and transfer function were monitored after each impact to ensure the response stayed in a linear region and the impact hammer adequately excited the modes of interest. Natural frequencies and mode shapes were extracted using the algorithm for mode isolation (AMI) [14].

The natural frequencies of the initial FEM were compared with those from the linear modal test revealing revealed that, while the mode shapes of the FEM agreed quite well with those from the test, the reduced modulus computed from [10] seems to be off by a factor of four or more so the natural frequencies are all far lower than those measured experimentally. In an effort to obtain better correlation, the modulus in the FEM was increased until the first natural frequency from the test matched that in the FEM very closely. The results are shown in Table 25.1. The natural frequencies extracted from the test are shown in the first column while those from the FEM frequencies are in the column labeled “ f_n , FEM NIC.” The other columns, denoted “FEM-IC” will be explained subsequently. For further comparison, Fig. 25.5 shows the measured mode shaped overlaid the mode shapes obtained from both FEM models. Figure 25.5a, c, e, g, i, and k are for NIC model. Figure 25.5b, d, f, h, j, and l are for the IC model. A reasonable comparison is shown in first six modes, as confirmed in Table 25.1. It is interesting to note that the model captures the higher modes of the system more accurately than the lower modes. The higher modes of a structure are typically affected more weakly by the boundary conditions, so perhaps this signifies that the weld where the perforated plate joints the can is not truly rigid.

The FEM with an updated elastic modulus matches the experiment much more closely, however, all of the natural frequencies except for the first are overestimated by 20–40 % or more. It is also interesting to note that the frequencies are uniformly too high, suggesting that the modulus is now too high. However, if the modulus were reduced slightly the model would still exhibit between 10 and 20 % error in each natural frequency and the first mode would be far less accurate. As the testing and analysis was being performed, some other contradictions were noted which shed additional light onto the situation, so rather than pursue further improvements to the linear FEA model we shall next consider how well the model captures the nonlinear response.

25.3.2 Nonlinear Comparison

A series of stepped sine measurements was acquired near each of the first few resonances of the structure and the amplitude of response was recorded (at steady state) at a series of frequencies around each resonance. A quasi-closed loop algorithm in the shaker control software assured that the force remained within 10 % of the desired amplitude. Figure 25.6 shows the amplitude of the response of the center of the plate for the first mode as the control frequency was stepped from 200 to 210 Hz. Because of the shaker/stinger setup that was used, the force was limited to a range of 0.44–13.44 N in these tests. Above this force level the plate would oscillate from side to side, apparently due to bending in the stinger, and the system would not reach steady state. From this figure, it is clear that the first mode has a softening nonlinearity, resulting in a frequency shift of 5.3 Hz over this range of forces. The peak displacement observed was about 1 mm (0.042 in.), or about

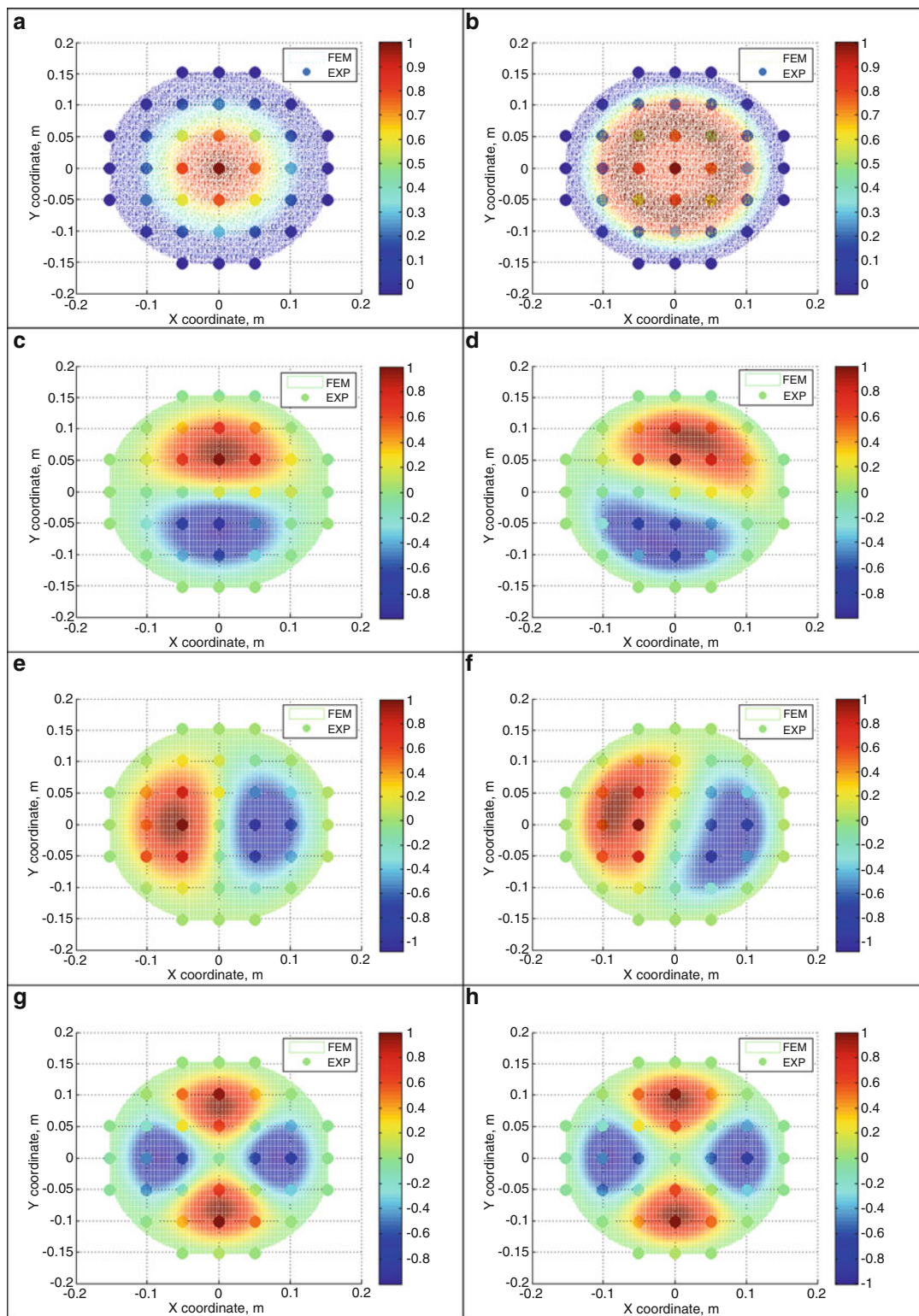


Fig. 25.5 First six mode shapes for the NIC and IC models. Sub plots (a), (c), (e), (g), (i), and (k) are for NIC model. Sub plots (b), (d), (f), (h), (j), and (l) are modes for IC model

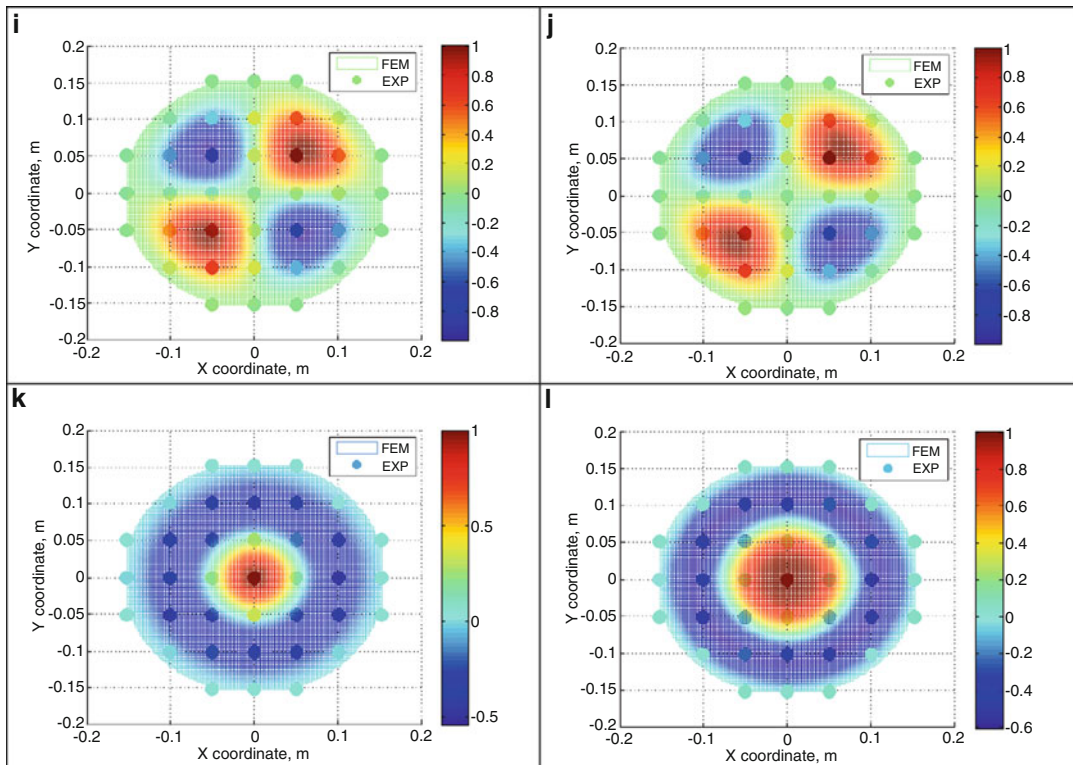


Fig. 25.5 (continued)

Fig. 25.6 (a) Transfer function of first mode stepping up in frequency, (b) transfer function of first mode stepping down in frequency, (c) FFT of first mode stepping up in frequency, (d) FFT of first mode stepping down in frequency

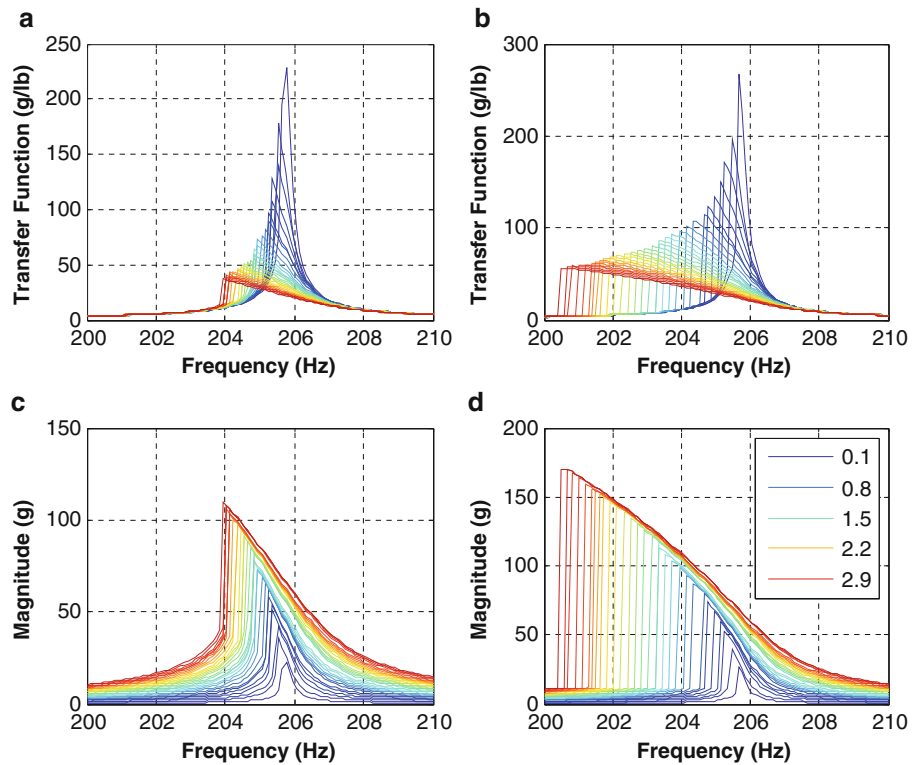


Fig. 25.7 Phase lag of the acceleration with respect to frequency of the first mode. The *dark circles* show the points at which the phase was closest to 90°, and from which the NNM was extracted

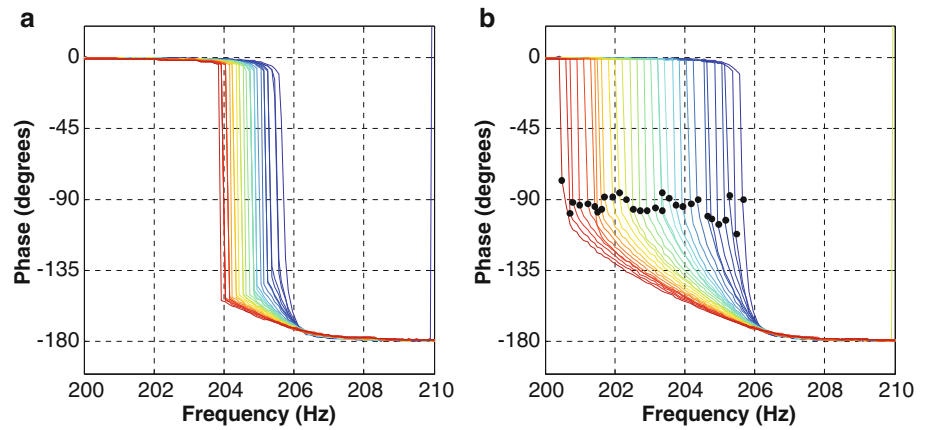
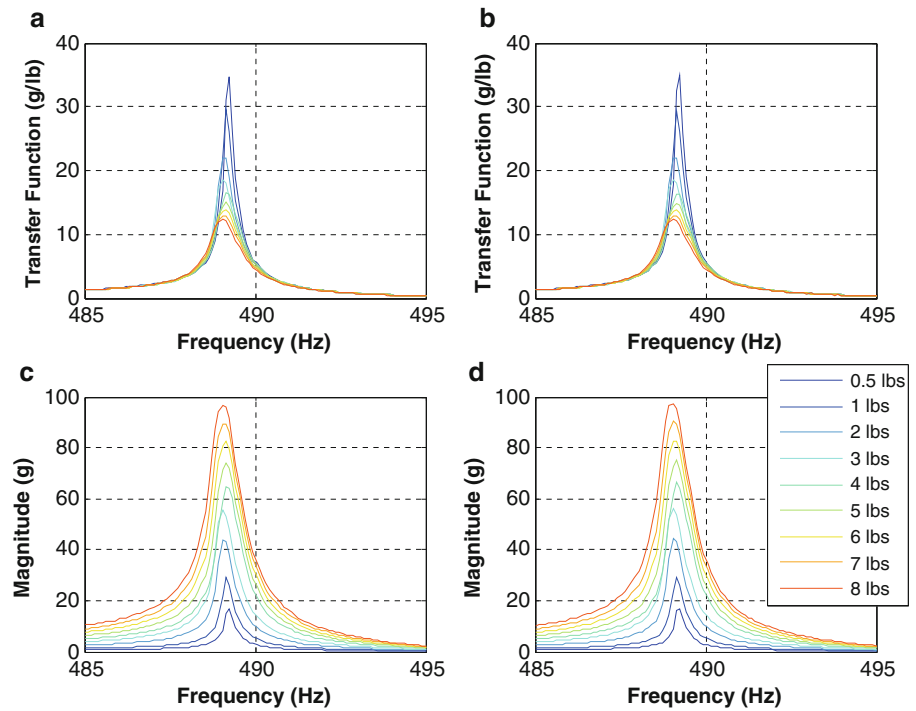


Fig. 25.8 (a) Transfer function of fourth mode stepping up in frequency, and (b) down in frequency. (c) FFT of fourth mode stepping up in frequency and (d) down in frequency



70 % of the thickness of the plate. In order to extract the NNM backbone, the phase between the force and response was plotted, revealing that the response is quite close to 90° at the point at which the response jumps down in amplitude in the downward sweeps. This is illustrated in Fig. 25.7, where the phase of the transfer functions is plotted with markers added corresponding to the peak the response curves. These points are all quite close to 90° as desired. As shown by Peeters et al. [6], a NNM has been isolated when all of the harmonics of the response are 90° out of phase with the force. The Data Physics software did not have any convenient feature for checking the phase of higher harmonics nor for saving the time history at each frequency, so this condition was not checked for the higher harmonics.

This same procedure was repeated for modes 4–6 (modes 2 and 3 were poorly excited anti-symmetric modes and hence were skipped). For these modes the maximum frequency shift that was observed was 0.3, 0.4, and 0.3 Hz respectively, for forces ranging from 0.1 to 8.0, 8.0 and 1.0 lbs respectively, revealing that these modes behave quite linearly at this range of force levels. Once again, the maximum force achieved was that at which the setup began to oscillate with excessive lateral motion. As an example, the nonlinear response of mode 4 is shown in Fig. 25.8; modes 5 and 6 showed a similar level of nonlinearity. While it is subtle, it appears that mode 4 is initially softening (only very slightly) after which the response appears to become slightly hardening. The nonlinearity is not strong enough to observe a jump, so the upward and downward sweeps were almost identical.

Once the backbone curves, or estimated NNM, had been extracted from each mode, they were compared with the NNM calculated from the finite element model, as shown in Fig. 25.9 by the green curve marked “NIC 2” (see Table 25.1).

Fig. 25.9 Backbone comparison

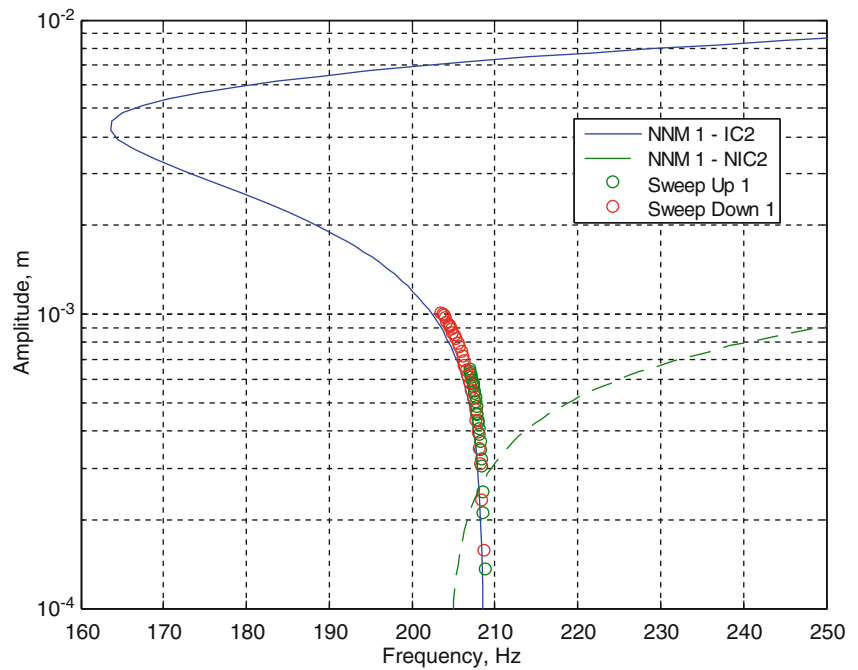
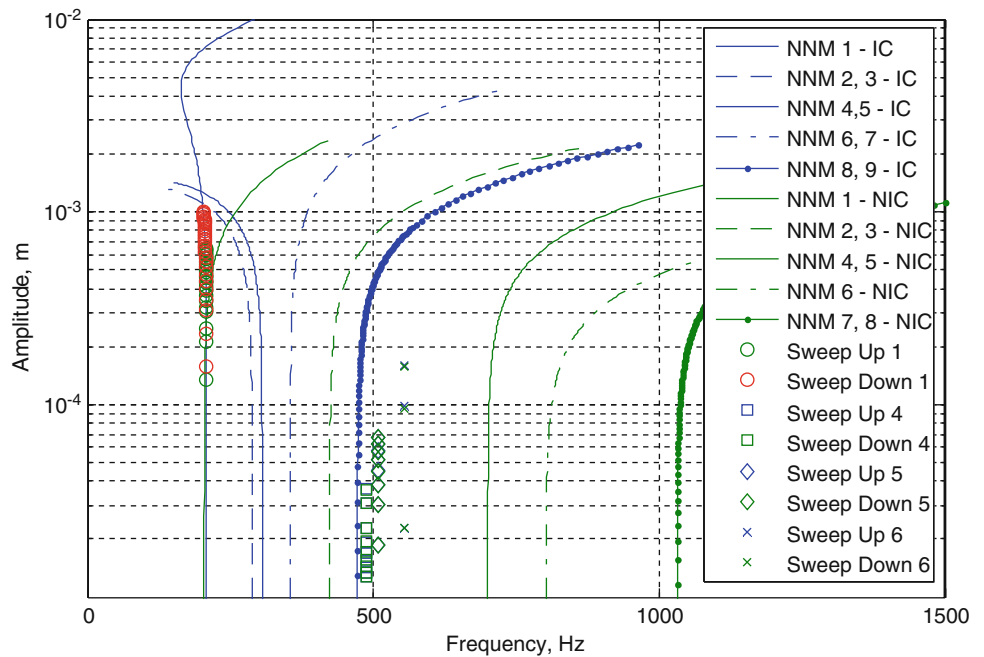


Fig. 25.10 Complete back bone curve comparison



As previously mentioned, the modal shaker is limited in the amount of force that can be used to excite the system, but the numerical simulation did not have this same constraint, so, the NNMs were numerically computed to a much larger maximum displacements than were tested. This comparison reveals that the finite element model and the actual nonlinear system exhibit completely different nonlinear behavior! The FEM predicts a hardening nonlinearity while the actual structure is softening. This unexpected behavior suggests that some important physics were missing from the model, as the sign of the nonlinearity is completely erroneous. Furthermore, the NIC 2 model also overestimates the degree of nonlinearity at a given displacement amplitude.

The measured and computed NNMs of modes 4–6 were also compared to further assess the NIC 2 model and the comparison is shown in Fig. 25.10. As was shown previously, there are clearly large errors in the linear natural frequencies, but it is also interesting to compare the degree of stiffening/softening that each mode exhibited in the model with what was observed experimentally. The results in Fig. 25.10 show that the NIC 2 model predicts that the plate will be significantly

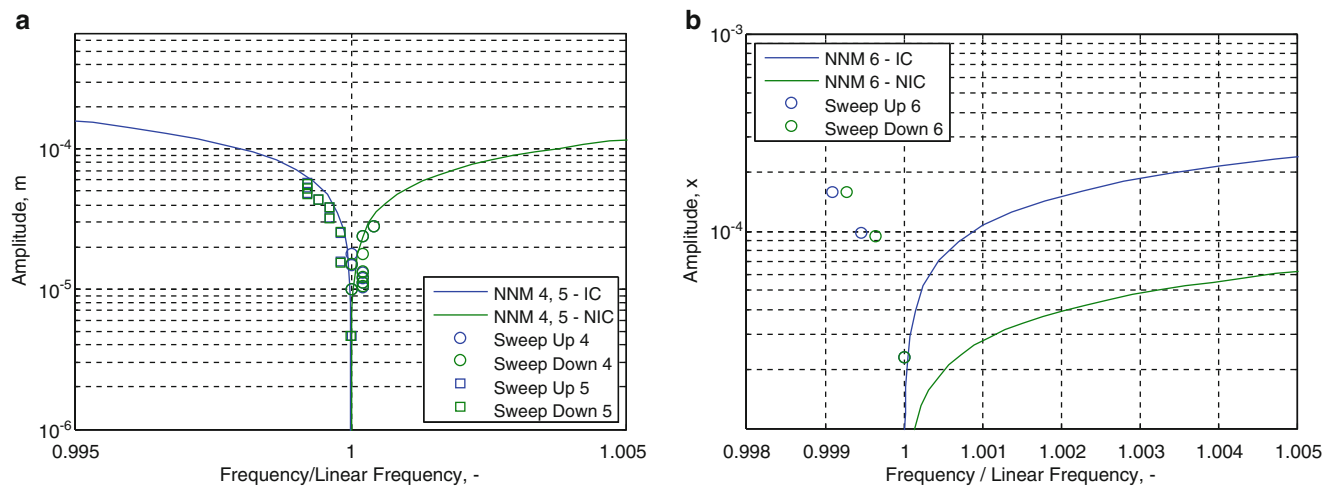


Fig. 25.11 Magnified view of experimentally measured backbones with included linear frequency shift. **(a)** NNMs 4 and 5, and **(b)** NNM 6

hardening over the amplitude range of interest for modes 4–6, while in fact the actual measured NNMs show only very slight softening/hardening. Furthermore, the measurements show that modes 4 and 5 have slightly different frequencies whereas the model suggests that these frequencies should be equal and also have identical nonlinearity.

25.3.3 Finite Element Model with Initial Curvature

Softening nonlinearities are characteristics of curved plates, plates with initial compressive stress, or other structures that might buckle. After this discrepancy was noted the plate was examined and it was discovered that the central region of the plate, which was supposed to have been flat, actually curved upwards slightly, with the center being about 4 mm higher than the edges of the plate. A detailed measurement of the topography was not available, so the surface was approximated as being deformed from the initial geometry in the shape of the first linear elastic mode with a peak central displacement of 4 mm. In all of the following this model will be referred to as the IC model or the model where the center of the plate has a nonzero initial curvature.

The results in Figs. 25.9 and 25.10 show that the first mode of the IC model shows an initial spring softening, which eventually becomes hardening at large displacement amplitudes; over the range of amplitudes tested the response is always softening and in excellent agreement with the measurements for NNM 1. The IC model predicts softening behavior for modes 4 and 5, and hardening behavior for mode 6, as shown in Fig. 25.10. A closer look at modes 4–6 is shown in Fig. 25.11. As a reminder, modes 4 and 5 are repeated roots in the FEM, but show up as separated modes in the test. In Fig. 25.11a a mode 4 from the test shows a spring hardening effect, while mode 5 shows a spring softening. When comparing these results to both FEM models, IC FEM shows spring softening, while the NIC FEM shows spring hardening, again leading to the conclusion that the test specimen operates between both models. Mode 6 is predicted as spring hardening in both FEMs; however, the test shows a clear softening effect. While it is clear that the system's nonlinear dynamics have not been captured, it is important to note that the NNMs computed by the IC model do not begin to show significant frequency shifts until a center displacement of 0.2–0.3 mm, which is beyond the range tested for all modes. To fully exercise the nonlinearities, larger amplitude excitations are needed.

It is also informative to consider whether adding initial curvature has improved the correlation between the linear natural frequencies at all. Returning to Table 25.1, the left hand columns compare the experimentally measured linear modes with those from the IC model before and after updating the elastic modulus, respectively. The results reveal that, while the updated IC model does more accurately predict a few of the natural frequencies, on average it is less accurate than the IC model. The MAC values reveal that the mode shapes were also generally more accurate with the NIC model; the MAC for mode 1 has dropped considerably although the MAC values for a few modes have increased. The IC model also predicts a very different order for the modes, and a few modes which did not appear in the test results.

It is also interesting to note that while the IC model consistently over predicts the natural frequencies, the NIC model consistently under predicted the natural frequencies. Perhaps the degree of curvature applied in the IC model was more than was warranted, or the shape of the curvature over the surface is not well approximated by the first mode shape as was

assumed. It was noted that the curvature was difficult to measure because the perforated plate did not sit completely flat inside the cylinder. The height of the center of the plate was compared with four measurement points taken around the plate resulting in measurements of 3.31, 3.7, 5.01, 5.03 mm when moving clockwise from the top point shown. So along different diameters the height of the center relative to the edges varied between 3 and 5 mm showing a rotation of the fixed plate in its welded position. Additionally, the procedure in [10] that was used to arrive at an effective modulus treats the perforated plate as isotropic, when in fact the hole pattern might make this plate somewhat orthotropic. Both of the FEMs have pairs of modes with repeated roots, while the test shows a slight separation in the natural frequencies of these pairs of modes, suggesting that the actual plate is not perfectly axisymmetric.

25.4 Conclusions

In this investigation, the nonlinear dynamic response of a circular perforated plate was measured using stepped sine excitation at various force levels in order to extract the first few nonlinear modes of the structure. The linearized natural frequencies and mode shapes were also measured in a low level modal hammer test. These results were then used to assess the ability of two finite element models to accurately predict the modal dynamics of the plate. The comparisons revealed that the linear and nonlinear tests provide complimentary information which is critical when seeking to update a nonlinear model. For example, when the measurements were compared with an initial finite element model with zero initial curvature over the center of the plate (the NIC model), the mode shapes compared well but the frequencies were in error by 30 % on average and there was no pattern in the comparison to suggest how the FEM might need to be updated to better predict the linear modes of the structure. In contrast, when the first nonlinear mode was compared with that of the FEM the two were found to exhibit completely different physics and this led the authors to notice a slight difference in curvature over the center of the plate which seems to be an important source of discrepancy between the models.

Unfortunately, the publication deadline for this article does not allow further iteration on these results, so one can only speculate as to the final outcome of this model updating exercise. In future works the authors will mount the test piece to a much larger shaker so that the nonlinear modes can be characterized out to much higher displacement levels, to provide a richer database for model updating. The initial geometry of the plate will also be measured more thoroughly and used to create a higher fidelity model of the system. There are also other physics which have not yet been considered, such as the residual stresses caused by the formation of the plate and the added perforations and perhaps in the end these factors will need to be considered to fully characterize the nonlinear behavior of this system. The NNMs of the structure might also be quite sensitive to the ambient temperature, as that will change the distribution of initial stresses in the plate, so that should also be considered.

Acknowledgements The authors gratefully acknowledge the support of the Air Force Office of Scientific Research under grant number FA9550-11-1-0035, administered by the Dr. David Stargel of the Multi-Scale Structural Mechanics and Prognosis Program. They also wish to thank Peter Penegor and David Nickel for providing the perforated plate samples.

References

1. Kerschen G, Peeters M, Golinval JC, Vakakis AF (2009) Nonlinear normal modes. Part I. A useful framework for the structural dynamicist. *Mech Syst Signal Process* 23:170–194
2. Kuether RJ, Brake MR, Allen MS (2014) Evaluating convergence of reduced order models using nonlinear normal modes. Presented at the 32nd international modal analysis conference (IMAC XXXII), Orlando
3. Peeters M, Viguie R, Serandour G, Kerschen G, Golinval JC (2009) Nonlinear normal modes, part II: toward a practical computation using numerical continuation techniques. *Mech Syst Signal Process* 23:195–216
4. Allen MS, Kuether RJ, Deane B, Sracic MW (2012) A numerical continuation method to compute nonlinear normal modes using modal reduction. Presented at the 53rd AIAA structures, structural dynamics, and materials conference, Honolulu
5. Kuether RJ, Allen MS (2014) A numerical approach to directly compute nonlinear normal modes of geometrically nonlinear finite element models. *Mech Syst Signal Process* 46(1):1–15
6. Peeters M, Kerschen G, Golinval JC (2011) Dynamic testing of nonlinear vibrating structures using nonlinear normal modes. *J Sound Vib* 330:486–509
7. Peeters M, Kerschen G, Golinval JC (2011) Modal testing of nonlinear vibrating structures based on nonlinear normal modes: experimental demonstration. *Mech Syst Signal Process* 25:1227–1247
8. Kuether RJ, Allen MS (2012) Computing nonlinear normal modes using numerical continuation and force appropriation. Presented at the ASME 2012 international design engineering technical conferences IDETC/CIE 2012, Chicago

9. Leissa AW (1969) *Vibration of plates*. NASA. U.S. Government Printing Office, Washington, DC
10. Jhung MJ, Jo JC (2006) Equivalent material properties of perforated plate with triangular or square penetration pattern for dynamic analysis. *Nucl Eng Tech* 38:689–696
11. Gordon RW, Hollkamp JJ (2011) Reduced-order models for acoustic response prediction. Air Force Research Laboratory, Dayton
12. Hollkamp JJ, Gordon RW (2008) Reduced-order models for nonlinear response prediction: implicit condensation and expansion. *J Sound Vib* 318:1139–1153
13. Hollkamp JJ, Gordon RW, Spottswood SM (2005) Nonlinear modal models for sonic fatigue response prediction: a comparison of methods. *J Sound Vib* 284:1145–1163
14. Allen MS (2005) Global and Multi-Input-Multi-Output (MIMO) extensions of the algorithm of mode isolation (AMI). Ph.D., George W. Woodruff School of Mechanical Engineering, Georgia Institute of Technology, Atlanta

Chapter 26

Experimental Identification of a System Containing Geometric Nonlinearities

Julian M. Londono and Jonathan E. Cooper

Abstract In this paper we discuss a technique for the experimental identification of structures exhibiting geometric nonlinearities, in particular aircraft with highly flexible wings. A half joined wing sensorcraft model is used to demonstrate the approach, which involves performing vibration tests whilst simultaneously applying static loads to the structure. A series of static and dynamic tests are undertaken and demonstrate that parts of the structure undergo both Hardening and softening behaviour, and then the Resonant Decay Method is used to identify the nonlinear parts of the structure.

Keywords Geometric nonlinearity • Experimental identification • Resonance decay method • Joined wing • Nonlinear identification

26.1 Introduction

There is a renewed interest in the development of aircraft with high aspect ratio wing designs either for HALE (high altitude long endurance) or novel civil airliner applications. Whereas this design leads to aerodynamically superior aircraft it is likely that large displacements will occur, leading to the tendency for nonlinear geometrical behaviour. There has been a body of work investigating how to model the aeroelastic characteristics of such designs, but little devoted towards the experimental measurement of the nonlinear stiffness behaviour.

Traditionally, aeroelastic analysis of aircraft for flutter and gust/manoeuvre loads prediction have been performed using a linear structural FE model and linear panel method aerodynamics (DLL) [1]. A Ground Vibration Test (GVT) is performed to validate the predicted natural frequencies and mode shapes, as well as providing measurements of the damping. However, for a highly flexible structure such an approach does not provide information about the structural behaviour in-flight where the wings deflect significantly upwards unlike the test situation of the wings drooping downwards slightly. A range of different methods exist to identify nonlinear structural systems [2]; however most of the methods are not compatible with the traditional linear GVT. One possible approach as an add-on to identify the nonlinear model is the Resonant Decay Method [3], whereby nonlinear structural components are identified in modal space from the decay response following a tuned excitation.

In this paper, an approach is described that can be used to identify geometric nonlinearities comparable to those obtained in-flight. Tests are performed on a half joined wing structural model. The nonlinear behaviour is identified using static and dynamic tests successfully.

26.2 Test Setup of a Joined Wing

A joined wing aircraft is one that connects the front wing to an aft wing. For the complete aircraft the front and aft wings are joined to form a diamond shaped planform from the front and top views. In this work, we used a half scaled joined wing sensorcraft model (2×2 m planform) as a test case (see Fig. 26.1). Note that the front and aft wings lie in planes tilted from

J.M. Londono (✉) • J.E. Cooper
Faculty of Engineering, University of Bristol, Queens Building, University Walk, Bristol, BS8 1TR, UK
e-mail: Julian.Londono@bristol.ac.uk

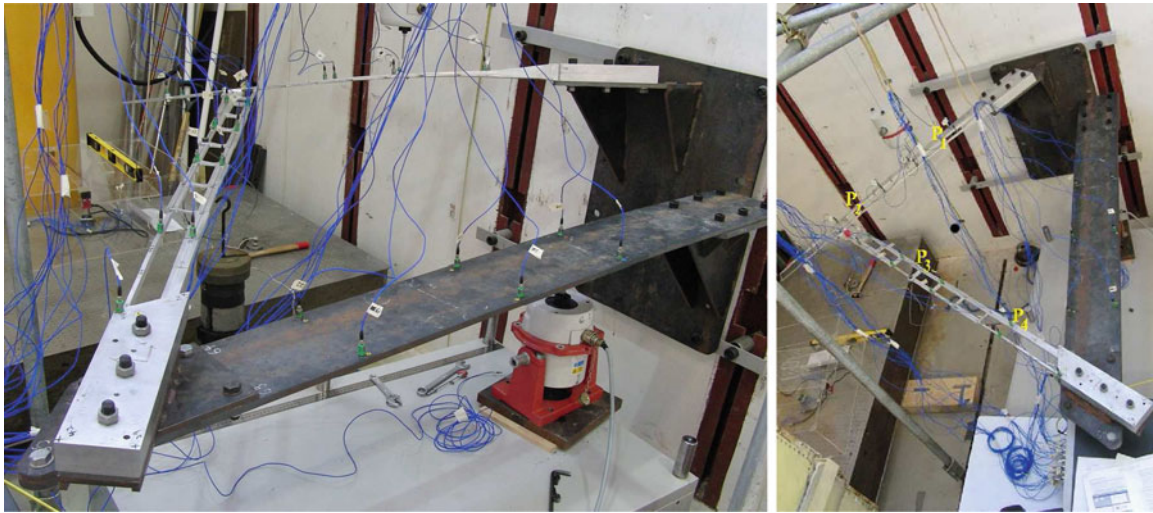


Fig. 26.1 Lateral and top view of the half scaled joined wing model used in this work. Note the deflected shape produced for the mass of 30 kg attached at the front and rear wings junction (*left*)

horizontal and that the aft wing is connected to a steel plate that was sized to recreate the fuselage behaviour. This scaled experimental rig was designed to maximize its flexibility so as to exhibit nonlinear deflections without over-stressing the material and to replicate the susceptibility to buckling due to the geometric bend-twist coupling expected of a joined wing configuration.

The joined wing model has been placed in the laboratory with upside down in order to facilitate the reproduction of the characteristic in-flight deflected shape by applying a number of additional static loads. This rig has previously been used for static aeroelastic scaling studies in [4]; however, here the testing was simplified by only applying weights to the structure vertically rather than attempting to apply follower forces. The model has been excited by two electro-dynamic shakers (LDS V406) and instrumented with 26 piezoelectric accelerometers (PCB 33M07) and two force sensors (PCB 208C03) to measure the shakers' driving force. Besides, the vibration tests were controlled and recorded by using the data acquisition systems LMS SCADAS Lab.

26.3 Nonlinearity Check

A number of experimental tests have been performed in order to get an insight into the overall structural behaviour of the wing model and to define the frequency ranges and modes that could be significantly affected by nonlinear features.

26.3.1 Static Tests

Weights were applied to the joined wing model in order to recreate its expected in-flight deflected shape. Figure 26.2 shows some sample deflection results for a range of static loads applied to the test model at the point where the front and rear wing are joined together. Points P_1 and P_2 are located on the forward wing whilst points P_3 and P_4 sit on the rear wing. It can be seen that there exists a clear nonlinear stiffening trend all over the structure when the static load applied exceeds the range of about 20kg. It is worth noting that this nonlinearity consists of both hardening and softening behaviour. This behaviour is to be expected due to the dihedral and anhedral inherent in the structure for the front and rear wings respectively; the rear wing is typically put under compression in flight resulting in a geometric softening on the structure.

Fig. 26.2 Deflection at four points when the joined wing is loaded and unloaded statically. Hardening and softening stiffness effects can be recognised in different parts of the structure

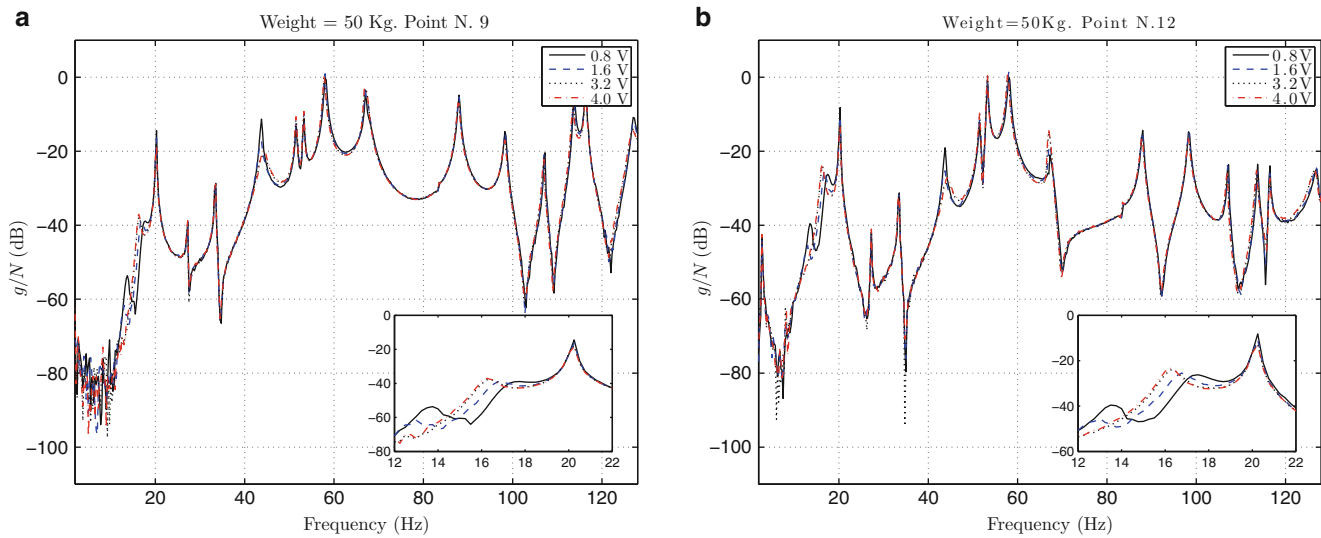
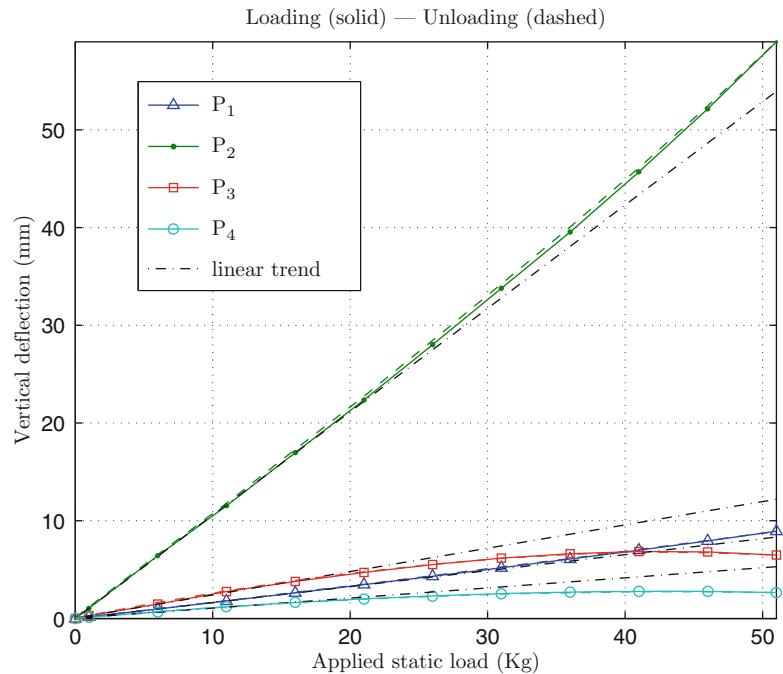


Fig. 26.3 Comparison among point FRFs for different levels excitation (burst random) and an applied weight of 50 kg; (a) For point N.9 located on the front wing and (b) for point N.12 located on the rear wing

26.3.2 Dynamic Tests

Several dynamic tests have also been conducted considering different applied vibration levels at a range of different static loading conditions. The idea behind these exploratory tests is to track the variations of frequencies and mode shapes with respect to different static load cases (i.e. deflected shapes) and vibration levels. Figure 26.3 shows typical Frequency Response Functions (FRFs) for the 50 kg static load case with different levels of excitation. The responses at one point on the front wing and one point on the rear wing are presented. The driving force employed to vibrate the model was a burst random signal with a bandwidth between 1 and 256 Hz. In addition, 25 averages were considered in the estimation of the FRFs. It can be seen that the FRFs do not overlay each other for all modes, indicating the presence of nonlinearity. The zoomed plots within the figures show that there is softening of the modes located between 12 and 18 Hz. In a similar manner, Fig. 26.4 presents the FRFs for the entire range of static loads from 10 to 50 kg and at the same level of excitation. Whereas most of the modes reduce in frequency as would be expected for the added mass, this is not always the case. The zoomed plots in Fig. 26.4a, b show this feature for modes located between 50 and 60 Hz.

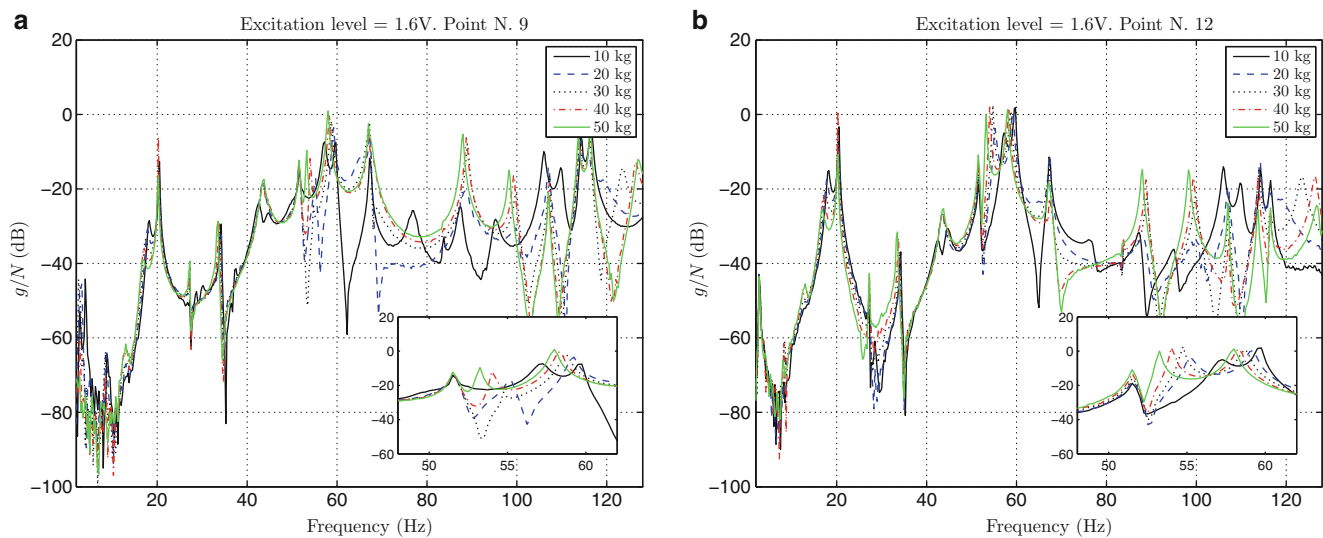


Fig. 26.4 Comparison among point FRFs for the same level of excitation and different applied weights; (a) For point N.9 located on the front wing and (b) for point N.12 located on the rear wing

Additionally, Table 26.1 presents the resulting natural frequencies and damping ratios for the entire range of static loads and excitation levels. Frequencies and damping ratios have been estimated using the Least Square Complex Exponential (LSCE) method [5]. This method uses the time-domain system response data, in the form of Impulse Response Functions (IRFs), to curve-fit the theoretical expression of the IRFs and find the coefficients that most closely match the measured data. Finally, the mode shapes found for two different static load cases are compared by means of the modal assurance criterion (MAC) coefficients map in Fig. 26.5 (left). This criterion is an statistical tool that provides a measure of the least-square deviation from a straight line correlation between two mode shapes. This yields to a indicator of the degree of consistency between the examined shapes. In the referred figure, *Processing A* denotes the 10 kg static load case and *Processing B* the 50 kg static load case. Both group of mode shapes were estimated for the same level of excitation at 1.6 V. The right-hand-side of the same figure shows a direct comparison among the first three modes with higher MAC values.

We note that most of the modes involve motion of the rear wing, which is most susceptible to compression from the fuselage and forward wing, thus explaining where the nonlinear behaviour that is observed due to the deflections occurring from both static loads and excitation levels.

26.4 Nonlinear Identification

The system identification will be carried out using the Resonance Decay Method (RDM) [6]. In this technique, individual modes of the system can be excited independently by applying an appropriated force pattern previously estimated. Such force pattern is determined by using the normal-force mode appropriation method, that enables for physically extracting the undamped natural frequency and normal-modes shapes of a structure [7]. Once the appropriated force pattern is computed, this is applied at the relevant frequency to the test model. When the structure is responding at resonance condition in the desired mode, the input is removed and the model undergoes free vibration from the steady state response reached. The resulting response can be curve-fitted to identify active nonlinear elements.

In this paper only one mode from those exhibiting nonlinear behaviour has been considered. The mode existing around a 17 Hz has been selected as a good candidate to evaluate the nonlinear characteristic behaviour of the test structure. We consider the static load case 40 kg applied at the forward-rear wing junction. The force pattern identified for appropriating the mode around 17 Hz (See Table 26.1) has been used to impose a constant sinusoid excitation to the structure by using only one shaker. After achieving the steady state condition, the input was ceased. The resonance decay response was then recorded for the 26 accelerometer placed throughout the structure. Figure 26.6a presents a couple of typical signals recorded during the decay stage along with a graphical representation of the frequency content variation of the structural response along time by way of the spectrograms. Once again one point on the front wing and one on the rear wing are shown.

Table 26.1 Natural frequencies and damping for the range of static loads and excitation levels

Excitation level		0.8 V		1.6 V		3.2 V	
Weight	Mode	f (Hz)	ζ (%)	f (Hz)	ζ (%)	f (Hz)	ζ (%)
10 kg	Mode 1	2.756	7.45	2.774	5.61	2.781	3.53
	Mode 2	13.674	4.05	4.039	0.37	4.016	0.54
	Mode 3	18.339	1.75	18.077	1.55	17.917	1.50
	Mode 4	20.487	0.26	20.450	0.28	20.434	0.26
	Mode 5	34.234	0.24	34.186	0.22	34.150	0.28
	Mode 6	42.917	0.81	42.395	1.67	41.448	3.34
	Mode 7	45.237	1.08	44.598	1.28	44.095	2.10
	Mode 8	51.713	0.55	51.620	0.37	51.582	0.36
20 kg	Mode 1	2.671	14.06	2.862	3.24	2.899	2.17
	Mode 2	13.643	4.21	12.939	8.87		
	Mode 3	17.984	2.10	17.753	1.74	17.508	1.58
	Mode 4	20.413	0.22	20.390	0.20	20.371	0.21
	Mode 5	27.333	0.12	27.321	0.15	27.318	0.14
	Mode 6	34.154	0.19	34.128	0.22	34.105	0.24
	Mode 7	43.601	0.70	43.370	1.27	43.657	3.03
	Mode 8	51.505	0.37	51.599	0.47	51.570	0.35
30 kg	Mode 1	2.724	5.07	2.779	3.99	2.777	2.77
	Mode 2	13.787	3.32	12.855	6.76		
	Mode 3	17.670	2.14	17.313	1.90	17.046	1.71
	Mode 4	20.349	0.16	20.322	0.14	20.303	0.14
	Mode 5	27.306	0.11	27.295	0.14	27.279	0.17
	Mode 6	33.981	0.21	33.963	0.20	33.927	0.23
	Mode 7	43.721	0.66	43.478	1.31	44.176	3.09
	Mode 8	51.509	0.41	51.589	0.50	51.547	0.35
40 kg	Mode 1	2.710	5.49	2.740	2.49	2.770	2.17
	Mode 2	13.679	3.12				
	Mode 3	17.428	2.38	16.945	2.23	16.611	1.86
	Mode 4	20.269	0.14	20.238	0.13	20.219	0.13
	Mode 5	27.277	0.09	27.261	0.14	27.252	0.12
	Mode 6	33.736	0.22	33.719	0.21	33.690	0.21
	Mode 7	43.831	0.53	43.373	1.19	43.746	2.72
	Mode 8	51.516	0.41	51.562	0.42	51.529	0.31
50 kg	Mode 1	2.692	6.47			2.605	8.94
	Mode 2	17.329	3.38	16.618	2.75	16.223	2.18
	Mode 3	20.184	0.13	20.169	0.13	20.153	0.12
	Mode 4	27.236	0.12	27.219	0.12	27.219	0.13
	Mode 5	33.435	0.21	33.414	0.21	33.402	0.20
	Mode 6	43.671	0.62	43.520	1.23	44.009	2.33
	Mode 7	51.536	0.42	51.579	0.35	51.513	0.29
	Mode 8	53.222	0.24	53.217	0.19	53.175	0.16

To verify the execution accuracy of the mode appropriation procedure, the structural response was then decomposed into the modal coordinates using Eq. (26.1); where $\{\ddot{\xi}\}$ represents a matrix containing the responses in modal space; $[\Phi]$ is the matrix of mode shapes identified for the underlying linear system; and $\{\ddot{X}\}$ is a matrix containing the measured response from all channels.

$$\{\ddot{\xi}\} = [\Phi^T \Phi]^{-1} \Phi^T \{\ddot{X}\} \quad (26.1)$$

Figure 26.6b shows the modal decomposition of the structural responses. Only the first six modes and their respective frequencies are plotted. It can be seen that the mode $\ddot{\xi}_2$ is predominant in the structural response what implies that the mode was correctly appropriated.

Looking at the identification of both the vibration frequency and damping ratio and their changes as the amplitude decreases, the decay response from the resonance condition was curve-fitted. A moving window of 30 s was considered travelling across the signal with overlaps of 50%. For each stepped window, a linear dynamic model was curve-fitted and the respective frequency and damping ratio estimated. The results are presented in Fig. 26.7. The variation of frequency and

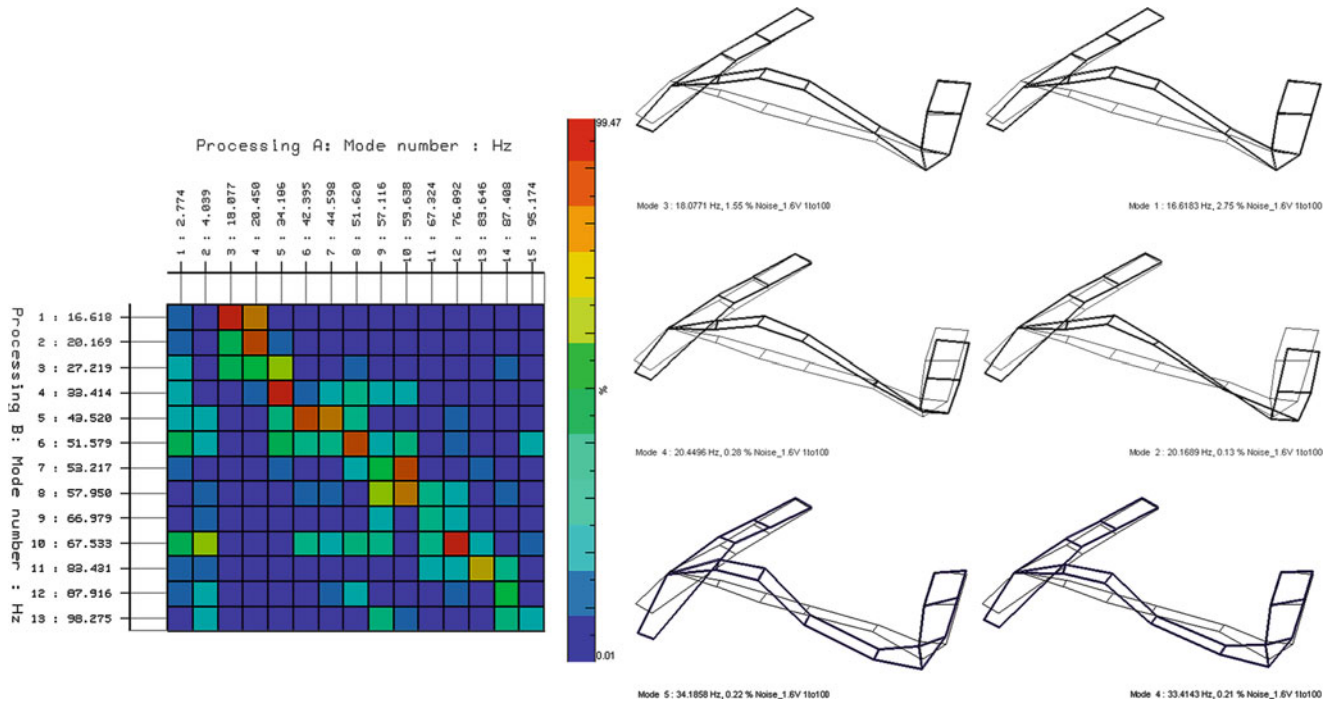


Fig. 26.5 (Left) Correlation of mode shapes for different weights based on the MAC coefficients: *Processing A* denotes the case of 10 kg and *Processing B* denotes the case of 50 kg. Both cases for the same level of excitation 1.6 V. (Right) Comparison among the first three modes with higher MAC values: the left-hand-side column is the case of 10 kg and the right-hand-side is the case of 50 kg

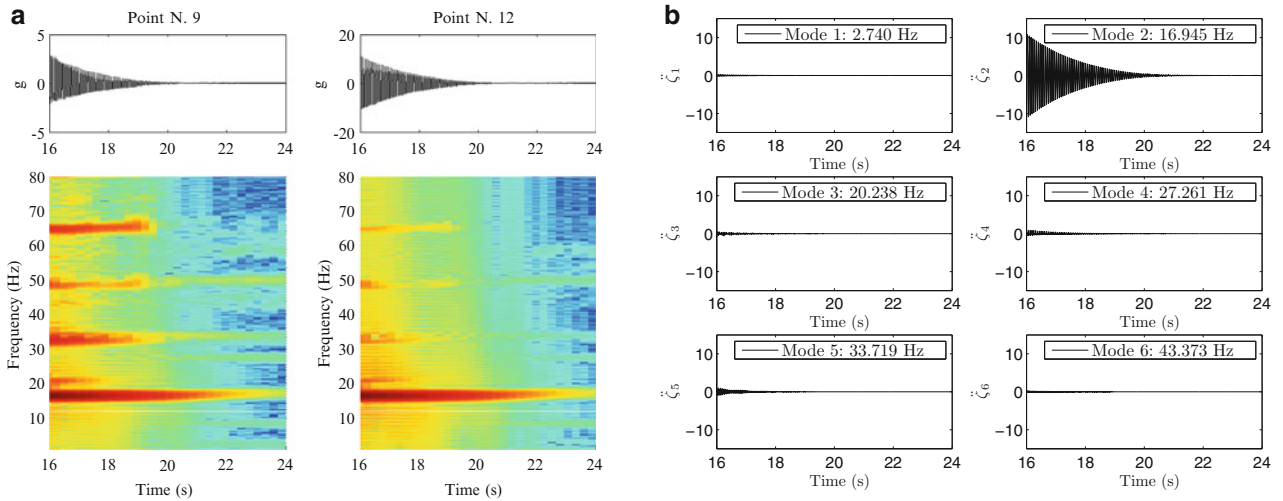


Fig. 26.6 (a) Typical system decaying response and their spectrograms. (b) Modal decomposition of the structural response when decaying from the appropriated mode

damping ratios along the decay time is shown in Fig. 26.7a. The envelope of the modal coordinate $\ddot{\zeta}_2$ was calculated and plotted against frequency and damping ratio changes in Fig. 26.7b.

The equation of the mode in study at a particular instant time along the decay can be expressed in modal space as in Eq. (26.2). Therein the contribution of cubic stiffness and quadratic damping were assumed here for illustrative purposes only.

$$\ddot{\zeta}_2(t) + C\dot{\zeta}_2(t) + K\zeta_2(t) + K^*\zeta_2(t)^3 + C^*\zeta_2(t)|\dot{\zeta}_2(t)| = 0 \tag{26.2}$$

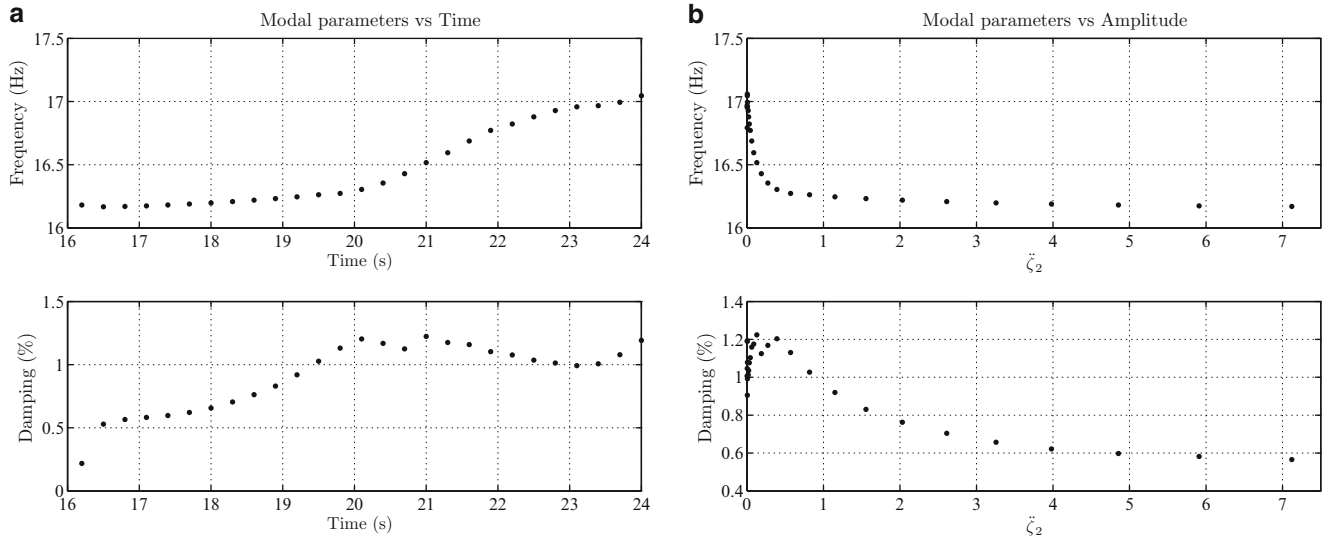


Fig. 17.67 Variation of frequency and damping ratio: (a) along time during the decaying response; (b) against the modal amplitude

This equation can be rewritten in terms of the unknowns coefficients and expanded to include a number n of time points over the decay response as:

$$\begin{bmatrix} \dot{\zeta}_{2_1} & \zeta_{2_1} & \zeta_{2_1}^3 & \dot{\zeta}_{2_1} & |\dot{\zeta}_{2_1}| \\ \dot{\zeta}_{2_2} & \zeta_{2_2} & \zeta_{2_2}^3 & \dot{\zeta}_{2_2} & |\dot{\zeta}_{2_2}| \\ \vdots & \vdots & \vdots & \vdots & \vdots \\ \dot{\zeta}_{2_n} & \zeta_{2_n} & \zeta_{2_n}^3 & \dot{\zeta}_{2_n} & |\dot{\zeta}_{2_n}| \end{bmatrix} \begin{bmatrix} C \\ K \\ K^* \\ C^* \end{bmatrix} = - \begin{bmatrix} \ddot{\zeta}_{2_1} \\ \ddot{\zeta}_{2_2} \\ \vdots \\ \ddot{\zeta}_{2_n} \end{bmatrix} \tag{26.3}$$

The physical acceleration data $\ddot{\zeta}_2$ were integrated numerically to obtain the physical velocity and displacement. Once the above matrix is populated with a number of time points, Eq. (26.3) can be solved in a least square sense for the vector of unknown parameter C , K , K^* and C^* . If couplings to other modes are present, the process may be extended by adding further terms to Eq. (26.2). For the example, the parameters found when solving Eq. (26.3) were (28.54, 1.09×10^4 , -6.49×10^7 , 4.75) respectively.

26.5 Conclusion

A procedure has been outlined for the vibration testing of structures that are susceptible to suffer from geometric nonlinearities. Vibration tests were performed on a joined wing structure for a range of static load cases at different vibration levels. Results showed that some modes are more sensitive and can be appreciably affected by the geometric nonlinearities. It has been shown how those interesting modes can be identified and excited independently by using the Resonance Decay Method. As illustration, only one mode exhibiting nonlinear behaviour was studied. Preliminary results indicate no coupling of the mode analysed to other modes, however more tests are required to determine in which extend this observation is correct.

A discussion is provided on how the nonlinearity can be identified in modal space from the decay response following a tuned excitation. A strategy for selecting a cluster of candidate models to be curve-fitted that fairly represent the structural nonlinearities still remains unclear. This procedure can be seen as an add-on tool able to extend traditional modal testing procedures to nonlinear applications.

Acknowledgements This work is supported as part of the EPSRC funded Programme Grant on Engineering Nonlinearity, grant EP/K003836/1.

References

1. Wright JR, Cooper JE (2007) Introduction to aircraft aeroelasticity and loads. Wiley, West Sussex
2. Worden K, Tomlinson GR (2001) Nonlinearity in structural dynamics. IoP Publishing, London
3. Platten MF, Wright JR, Dimitriadis G, Cooper JE (2009) Identification of multi-degree of freedom non-linear systems using an extended modal model. *Mech Syst Signal Process* 23:8–29
4. Bond VL, Canfield RA, Cooper JE, Blair M (2012) Experimental nonlinear static deflections of a subscale joined wing. *AIAA J Aircraft* 49:329–333
5. Ewins DJ (2000) Modal testing: theory, practice and application, 2nd edn. Research Studies Press, Hertfordshire
6. Naylor S, Platten MF, Wright JR, Cooper JE (2004) Identification of multi-degree of freedom systems with nonproportional damping using the resonant decay method. *J Vib Acoust* 126(2):298–306
7. Wright JR, Cooper JE, Desforges MJ (1999) Normal-mode force appropriation theory and application. *Mech Syst Signal Process* 13(2):217–240

Chapter 27

Experiment of Vibration Isolation Characteristics of a Periodic Curved Beam

Xiuzhong Xu, Zhiyi Zhang, Xiong Hu, Congxiao Zhou, and Long Liu

Abstract The periodic curved beam structure is designed based on the periodic structure band gap and waveform conversion mechanism. In order to analysis the vibration isolation performance, the periodic curved beam model is to be built in ANSYS and harmonious response analysis has been done. The simulation results show that the curved beam structure has good isolation properties in high frequency band. The vibration transmission characteristics of the periodic curved beam absorber system are verified by vibration generator experiment. The experimental results show that the periodic curved beam absorber system has better characteristics of vibration isolation than that of traditional absorber and it reflects in lower and wider frequency band.

Keywords Periodic curved beam • Waveform conversion • Vibration isolation performance • Simulation • Experiment

27.1 Introduction

The periodic curved beam structure have been used in the field of defense, aerospace and shipbuilding. Scholars from various countries have launched a large number of theoretical and experimental studies for the vibration characteristics of period structure. Current research focuses on periodic structures widely used in practical engineering, including periodic support beams, period curved beams with plates and shells periodic structure and the periodic structure. The others are curved beam detuning issues and active vibration isolation technology combine to achieve a periodic structure semi-active, active vibration band gaps. After the 1960s, the vibration characteristics of periodic structures widely used in engineering have been researched deeply. D.J. Mead of University of Southampton have studied the vibration characteristics of the periodic support beam with the wave equation [1], and then extended one-dimensional periodic support beam algorithm to two-dimensional periodic support plate to get approximation algorithm of structure [2]. The coupled vibration characteristics of compression waves, torsional waves and bending waves of Timoshenko beam have been studied by Heckl [3]. C. Mei proposed the method in which the support constraint condition and the damping have been changed to achieve a small range of adjustment of band gap frequency [4]. V. Mangaraju and others embedded the cyclical damping into periodic support beams, the impact of vibration attenuation within the band gap have been studied with damping material [5].

Main research areas about periodic structure with reinforced beams, plates, shells are: D.J. Mead studied bending vibration and longitudinal vibration coupling characteristics of periodic reinforced beam from the wave equation [6], and to proposed a new algorithm for calculating vibration characteristics of periodic stiffened panels [7], vibration characteristic of annular

X. Xu (✉)

Mechanical Engineering Department, Shanghai Maritime University, Shanghai 201306, People's Republic of China

State Key Laboratory of Mechanical System and Vibration, Shanghai Jiao Tong University, Shanghai 200240, People's Republic of China

e-mail: xuxz_sj@sina.com

X. Hu • C. Zhou • L. Liu

Mechanical Engineering Department, Shanghai Maritime University, Shanghai 201306, People's Republic of China

Z. Zhang

State Key Laboratory of Mechanical System and Vibration, Shanghai Jiao Tong University, Shanghai 200240, People's Republic of China

cylindrical shell reinforced radial have been studied [8, 9]. R.S. Langley used statistical energy analysis method to calculate vibration damping characteristics of the infinite cycle stiffened plate and limited transmission coefficient and absorption coefficient has been gotten [10].

About vibration characteristics of the periodic structure there has been a lot of research domestic. Shanghai Jiao Tong University, Huang XC [11], etc. taken the wave finite element method systematically to study the free wave propagation characteristics of the periodic structure, band gap structure, natural frequencies and forced response problems, and vibration transfer characteristics of periodic structure isolation system. And Liu JH, and other researcher have studied bending wave propagation characteristics of cycle stiffened plate. The vibration frequency and flexural wave propagation constants of the incident have been analyzed [12]. Vibration characteristics of periodic beam were analyzed according to vibration power flow by Zhang XM of Hua Zhong Science and Technology University. He proposed that the band gap frequency vibration source is not within the scope of the power flow to the input beam, which can control the structural vibration and noise radiation [13].

In this paper, the periodic damper isolation system has been built with curved beam structure based on the vibration isolation principle of periodic structure. Periodic curved beam vibration transmission characteristics and performance of periodic curved beam vibration isolation system have been analyzed by using the finite element modeling and dynamic response analysis method, and compared with the traditional absorber structure. The curved beam damper system isolation features have been verified by experiment and simulation results.

27.2 Periodic Curved Structure Optimization and Isolation Performance Simulation

Periodic curved beam can simultaneously transmit bending waves and longitudinal waves, and have special conversion function for the two waves. Waveform conversion is designed to provide new ideas for the efficient damping device when curved beam is coupling with other structure. But in order to achieve good isolation effect parameter optimization calculations and experimental verification must be repeated.

27.2.1 Modeling of Periodic Curved Beam and Transmission Characteristic Simulation

The finite element model of periodic curved beam structure constituted with curved beams and plates shown in Fig. 27.1, plate size is $0.15\text{ m} \times 0.15\text{ m} \times 0.01\text{ m}$, the thickness of the curved beam structure is 0.003 mm , outer diameter is 0.025 m and

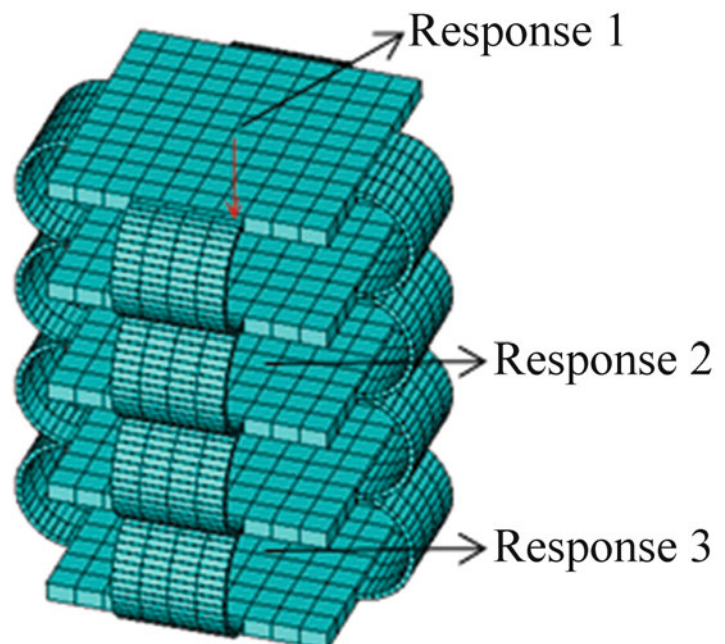


Fig. 27.1 The curved beam structure model

Fig. 27.2 The FRFs transmission characteristics of periodic curved beam structure

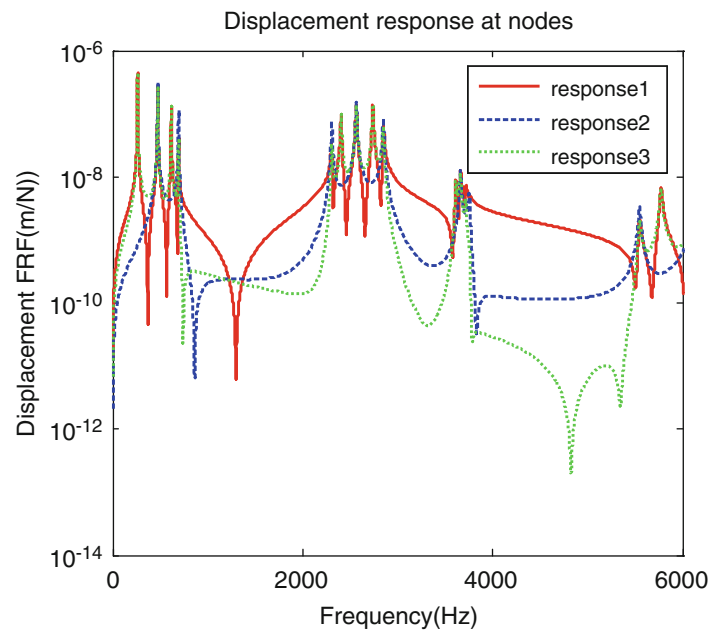
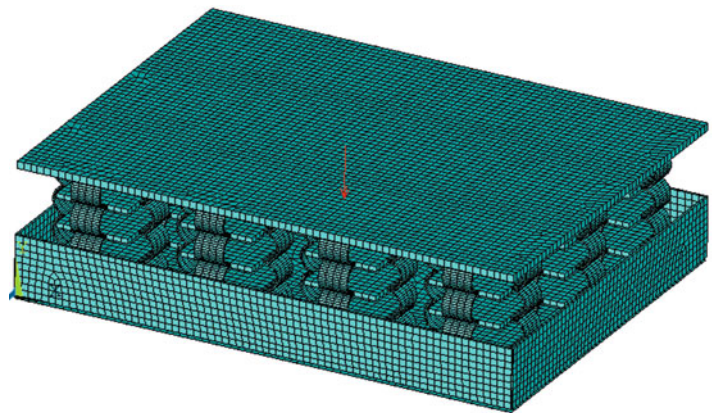


Fig. 27.3 Geometry model of periodic curved beam absorber



inner diameter is 0.023 m. Four sides of each unit are coupling with four curved beam. The total height of model is 0.25 m. Take the material is steel, the top panel in the vertical direction is applied to a unit harmonic force F , ANSYS calculated using the top-down first, third, fifth block panel nodal at the center displacements frequency response, draw periodic curved beam structural vibration transmission characteristics.

Dynamic analysis has been done to curved beam finite element model shown in Fig. 27.1. The displacement response of response of points 1–3 has been observed, and the results shown in Fig. 27.2.

The results shown that: vibration transmission attenuation is very clear in most frequency band (750–2,300, 2,500–3,500, 3,800–5,500 Hz) of this periodic curved beam structure. And this periodic curved beam structure has excellent isolation characteristics, it is the ideal basic unit of periodic curved beam absorber structure.

27.2.2 Analysis of Absorber Vibration Isolation Characteristics

The structure of periodic curved beam absorber shown in Fig. 27.3

Curved beam damper mainly composed of ten basic periodic curved beam structural unit, up plate, down plate and rib. The basic structural unit of periodic curved beam used models previously are analyzed, the overall size of absorber is 1,040 mm × 780 mm × 280 mm, material of steel, the overall quality of 350.97 kg. In addition to periodic structural unit itself have periodicity, the arrangement of curved beam in the X and Y directions are also periodic, respectively spacing 260 mm.

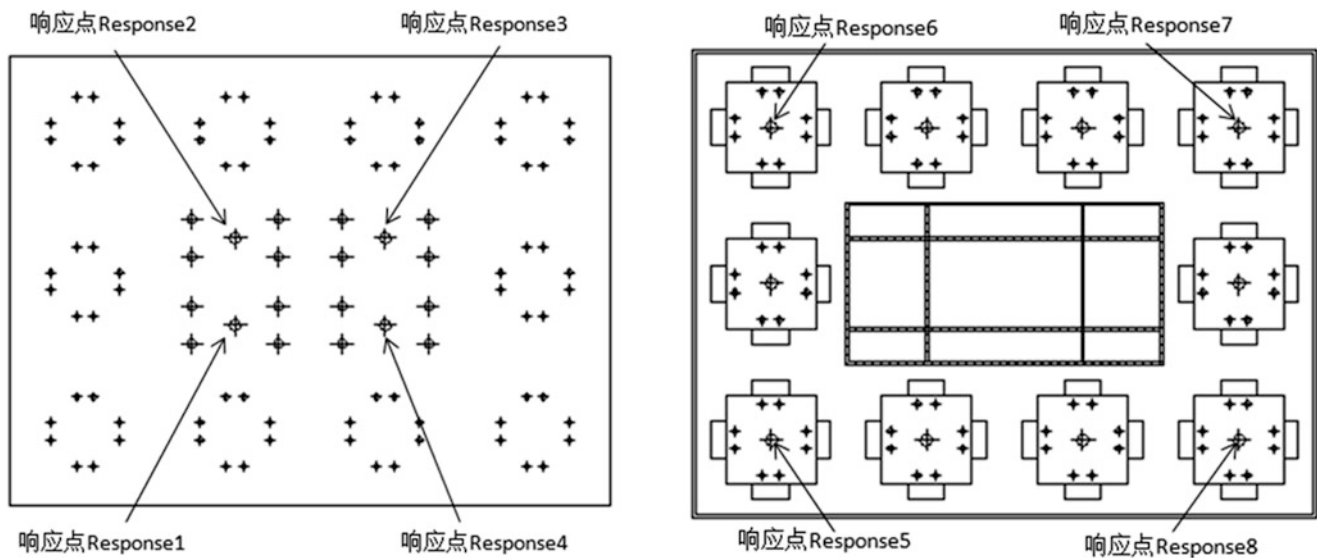


Fig. 27.4 The placement of response point in periodic curved beam absorber

The entire structure maximum used the function of waveform converting and frequency gap characteristics of periodic structure. In the bottom of the upper panel and outer sides of down plate the ribs have been set, the size of ribs is thickness of 5 mm, height of 125 mm.

By FRF synthesis method [14] for harmonic response analysis, applied vertical harmonic force at the center of the upper plate of the unit, observed displacement response on the lower shock absorber mounting isolator at the corresponding position in response to the position of point shown in Fig. 27.4.

Frequency response of placement correspondence measurement points shown in Fig. 27.5

Simulation results shown: without significant attenuation characteristic in the low frequency (0–200 Hz), but in frequencies band above 200 Hz, vibration attenuation is large, compared to the results of conventional vibration absorber, showing better vibration attenuation characteristics than conventional.

27.3 The Experiment Research of Vibration Isolation of Periodic Curved Beam Structure

A new shock absorber with periodic curved beam structure has been designed based waveform transmission and conversion function in the paper. The dynamics simulation studies show that isolation properties in the mid and high frequency band of curved beam damping are better than traditional shock absorber. In order to verify the theoretical analysis and numerical results, the following experimental methods have been used to verify above results.

Through experimental program and experimental systems, the vibration response of the structure has been tested. The transfer characteristics of designed curved beam damper have been studied. The tested results were compared with traditional test results.

27.3.1 Experiment System Setup

Experiment system shown in Figs. 27.6 and 27.7

Experimental system mainly consists of electromagnetic exciter, power amplifier, force sensors, acceleration sensors, charge amplifier, dynamic signal acquisition and vibration analyzers and damper system. A rectangular iron mass of 230 kg is used to be simulated machine group, four rubber shock absorbers typed WH150 are connected with upper part of shock absorber system. Conventional damper weight 375 kg, curved beam damper weight 350 kg, foundation using cast iron platform mass 3,500 kg, and shock absorber is connected with foundation through six with the same type of shock rubber absorber. Basis is connected with foundation through four ZTA1050 spring damping isolator which can be simulated analog

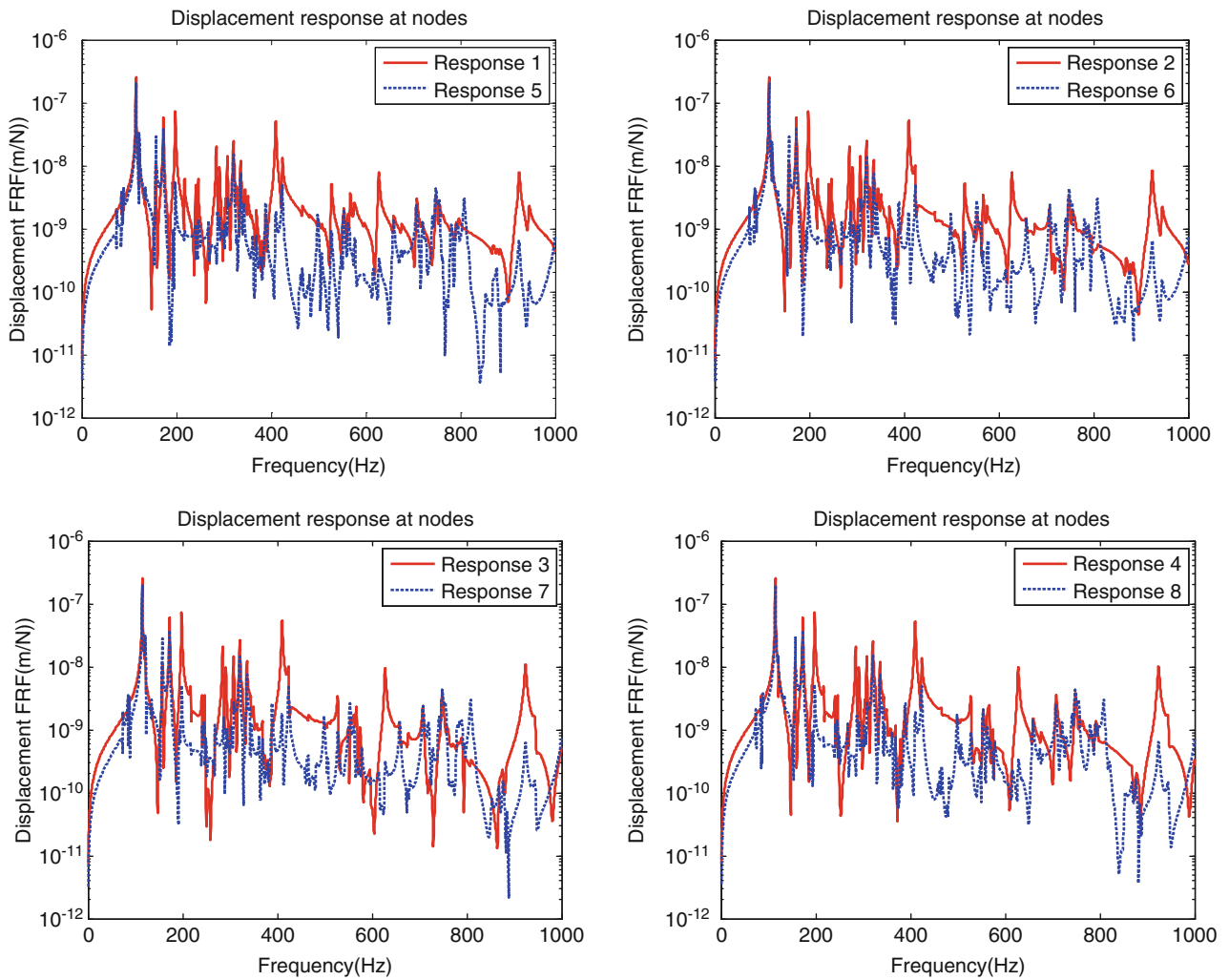


Fig. 27.5 Vibration transmission characteristics of periodic curved beam absorber

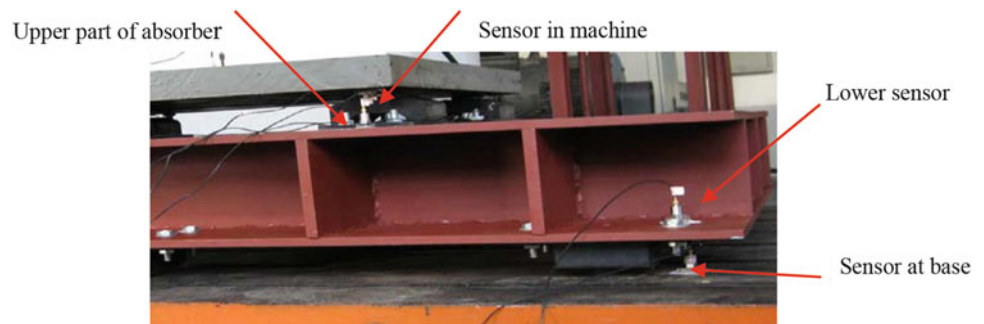
Fig. 27.6 Measurement of the curved beam absorber system



Fig. 27.7 Measurement of the traditional absorber system



Fig. 27.8 Placement of acceleration transducers on the absorber system



low-frequency vibration suspension structure and shielded from external interference. The exciter is hanging with elastic rope in the experiments which can also play the role of outside interference. Two kinds of damper isolation system used the same experimental equipment to ensure the reliability of experimental comparison.

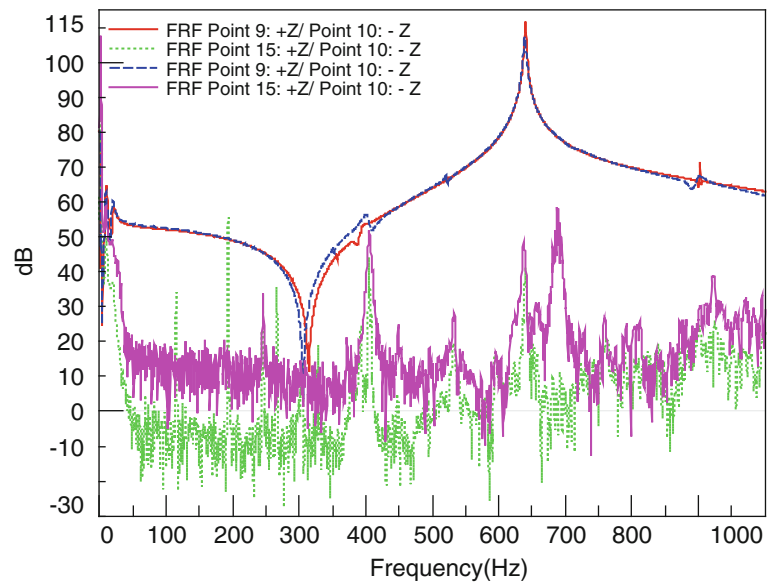
27.3.2 Analysis of Experimental Results

The acceleration responses have been measured in different positions which include the position at lower unit near the isolator, upper and lower parts of isolator and positions at base near isolator. Figure 27.8 is the setup of conventional damper system sensor location in experiments, periodic structure absorber experiments sensor position and the same.

The acceleration frequency responses of machine and base are shown below. Figure 27.9, pink for traditional shock absorber system and green for the periodic structure absorber system, and the red and blue curves respectively for periodic curved beams shock absorber systems and machine at traditional shock absorber system.

These experimental results shown that vibration energy has been significantly attenuated from vibration resource to base in wider frequency band, especially in low frequency band after combination periodic structure absorber, machine and base isolation system. The curved beam absorber has excellent isolation characteristics advance from 200 to 50 Hz. The acceleration response attenuation from the machine to base averaged about 40 dB in traditional damper system, while the periodic curved beam structural system in the range of 50–750 Hz bands can reached about 52 and 55 dB. In high-frequency range of 800–1,000 Hz, acceleration response attenuation of periodic curved beam structural system is only higher than conventional damper system just about 5 dB. The excellent isolation characteristics of periodic curved beam structure are more fully reflected.

Fig. 27.9 The acceleration FRFs comparison in base and power unit of traditional absorber and curved beam absorber



27.4 Conclusion

In this paper, based on energy transfer characteristics and waveform conversion function, the periodic curved beam structure has been designed, building a new curved beam damper isolation system. The vibration transfer characteristic of periodic structural unit and periodic curved beam vibration damper is analyzed through FE model. Vibration transmissibility of periodic curved beams and traditional damper have been verified by experiment. Simulation and experimental results show periodic curved beam absorber have better vibration damping characteristics than conventional shock absorber. Periodic curved beam damper isolation system can play better vibration isolation effect in a wider frequency band.

Acknowledgement This work was supported by Shanghai Natural Science Foundation (No. 11ZR1414900) and National High Technology Research and Development Program (863 Program) (2013AA04110).

References

1. Mead DJ (1970) Free wave propagation in periodically-supported, infinite beams. *J Sound Vib* 11:181–197
2. Mead DJ, Parthan S (1979) Free wave propagation in two-dimensional periodic plates. *J Sound Vib* 64(3):325–346
3. Heckl MA (2002) Coupled waves on a periodically supported Timoshenko beam. *J Sound Vib* 252(5):849–882
4. Mei C (2005) Vibration suppression through tunable periodic structures. In: Twelfth international congress on sound and vibration, 2005
5. Mangaraju V, Sonti VR (2004) Wave attenuation in periodic three-layered beams: analytical and FEM study. *J Sound Vib* 276:541–570
6. Mead DJ, Markus S (1983) Coupled flexural-longitudinal wave motion in a periodic beam. *J Sound Vib* 90(1):1–24
7. Mead DJ (1986) A new method of analyzing wave propagation in periodic structures; applications to periodic Timoshenko beams and stiffened plates. *J Sound Vib* 104(1):9–27
8. Mead DJ, Bardell NS (1986) Free vibration of a thin cylindrical shell with discrete axial stiffeners. *J Sound Vib* 111(2):229–250
9. Mead DJ, Bardell NS (1987) Free vibration of a thin cylindrical shell with periodic circumferential stiffeners. *J Sound Vib* 111(2):499–520
10. Langley RS, Smith JRD (1997) Statistical energy analysis of periodically stiffened damped plate structures. *J Sound Vib* 208(3):407–526
11. Huang XC, Feng GP, Zhang ZY, Hua HX (2010) Periodic structure mechanical filter to effect damper characteristics of isolation system. *Noise Vib Control* (2):9–12
12. Liu JH, Jin XD (2003) Bending wave propagation of periodic stiffened plate. *Noise Vib Control* (5):22–26
13. Zhang XM, Zhang WH (1990) Vibration power flow of Periodic Simply supported beam. *Vib Shock* 35:28–34
14. Wu ZD (2007) Analysis method of damper isolation system based on FRF synthesis [D]. Shanghai Jiaotong University, Shanghai

Chapter 28

Investigation on Damping of a Host Structure Induced by Attached Cables

Jiduck Choi and Daniel J. Inman

Abstract The development of a lightweight spacecraft structures has been a major issue in aerospace applications to reduce launch costs. While the structural weight has been decreased, spacecraft cabling has increased. Thus cabling represents an increased percentage of the mass of a lightweight structure. The attached cable harness also changes the mass distribution of the combined system. Eventually, the dynamic characteristics such as natural frequencies and damping are affected and altered. Damping has an important role in structural design because it reduces the dynamic response avoiding excessive deflection or stress, fatigue loads, and settling times. Experimental results with some specimens indicate a clear change of damping on the main structure with the inclusion of cable dynamics. In this paper, we investigate the modification of the damping of the total structure with various experiments. The identification of damping is conducted by using measured results. The effect of flexibility of cable harness on damping is observed through the experiments with various types of cables. The effect of the number of connections on damping is also investigated by changing the number of connections.

Keywords Damping identification • Dynamic Stiffness Matrix • Double beam system • Cable-harnessed structure

28.1 Introduction

The identification of damping in a real physical system is very important task in modeling the dynamics system. But it still remains an unsolved problem. In most methods of modeling damping, the damping matrix is expressed by using a simple model such as the viscous, structural, or proportional. But the actual physical system such as boundary condition and spatial distribution of the damping in the system are ignored. To present the proper damping matrix dealing with both the physical mechanism and spatial distribution of damping, various approaches have been proposed. Many of these approaches use experimentally identified modal parameters, frequencies, damping ratios and mode shape vectors, to find the damping matrix [1–5]. These approaches require modal parameter estimation of measurement data. Some papers present a way to obtain the damping matrix directly from the measurement data without the effort to find the modal parameters. Chen et al. [6] tried to obtain the damping matrix separately from mass and stiffness matrix. Lee and Kim [7, 8] proposed the direct identification of damping matrix by using the *Dynamic Stiffness Matrix* (DSM), the inverse of the measured *Frequency Response Function* (FRF). Ozgen and Kim [9] presented an experimental method to reduce the noise effect on DSM.

Choi and Inman [10] examined damping identification of a cable-harnessed structure. The results gave the interesting phenomenon of damping caused by the flexibility of the attached cable. In this previous result, the increase of flexibility of attached cable magnifies the damping of host structure. In this paper, the simulation of the flexibility of attachment is conducted. Based on the simulation, the experiments were performed with several different attached cables including a real satellite cable to verify the effect of flexibility of attached cables. Moreover the effect of the number of interconnections was also investigated.

J. Choi (✉)

Department of Mechanical Engineering, Virginia Tech, 100S Randolph Hall, Blacksburg, VA 24061, USA
e-mail: jdchoi@vt.edu

D.J. Inman

Department of Aerospace Engineering, University of Michigan, FXB Building, 1320 Beal Avenue, Ann Arbor, MI 48109, USA

28.2 The Damping Ratio Investigation with Two DOF Models

The change of damping ratio was investigated to verify the effect of the cable attachment. In Fig. 28.1, the left and right represent the simplified models of a host structure and a cable-harness structure. The mass and stiffness are fixed as 10 kg and 10 N/m. For each case, the damping coefficient of the host structure is fixed and that of attachment is changed. The change of natural frequencies and damping ratio are obtained with the state-space model [11].

28.2.1 Simulation 1: $c_1 = 1, c_2 = 10, 1, 0.1, 0.01, 0.001, 0.0001$

In the first simulation, the damping coefficient c_1 was fixed as 10 and the damping coefficient c_2 was changed from 10 to 0.0001. Figure 28.2 shows the simulated FRF of two DOF system.

The natural frequency of the host structure is 1 (rad/s). The damping ratio ($c/2m\omega_n$) is 0.05. In case 1 of Table 28.1, the damping coefficient c_2 of attached system is higher than damping coefficient c_1 of a host structure. Then the damping ratio of two DOF system is bigger than of host structure. In case 2, one of damping ratio is bigger than 0.05. But other one is

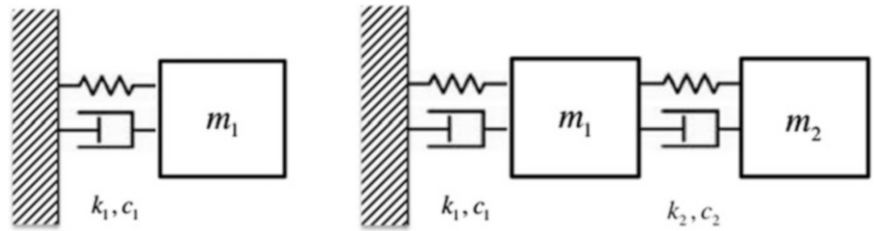


Fig. 28.1 One DOF and two DOF system ($m_1 = m_2 = 10$ kg, $k_1 = k_2 = 10$ N/m)

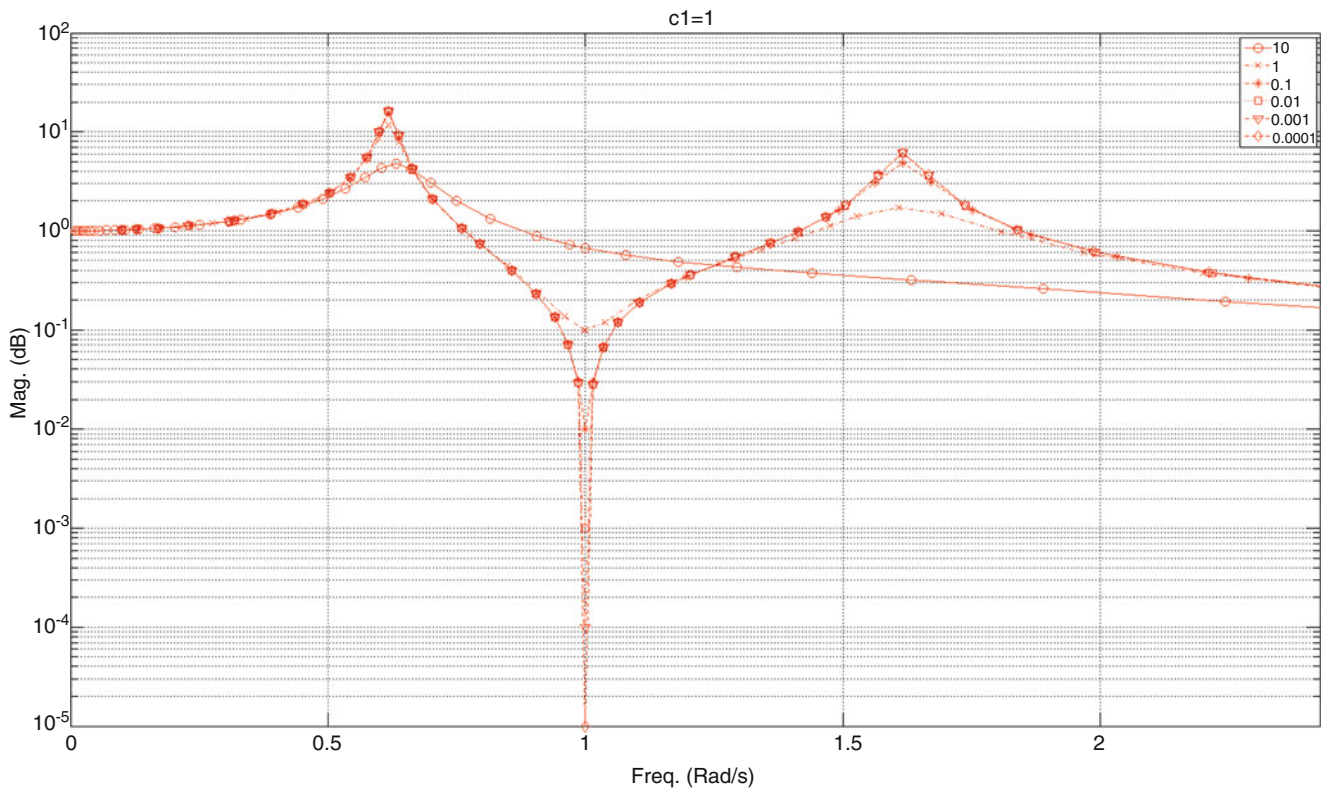


Fig. 28.2 Damping coefficient with $c_1 = 1, c_2 = 10, 1, 0.1, 0.01, 0.001, 0.0001$

Table 28.1 Natural frequencies and damping ratio of two DOF system

Case	c_1	c_2	ω_1	ω_2	ζ_1	ζ_2
1	1	10	0.6380	1.5671	0.0936	0.6318
2		1	0.6180	1.6180	0.0309	0.0608
3		0.1	0.6182	1.6174	0.0232	0.0282
4		0.01	0.6183	1.6173	0.02245	0.0229
5		0.001	0.6183	1.6173	0.02237	0.0224
6		0.0001	0.6183	1.6173	0.02236	0.0223

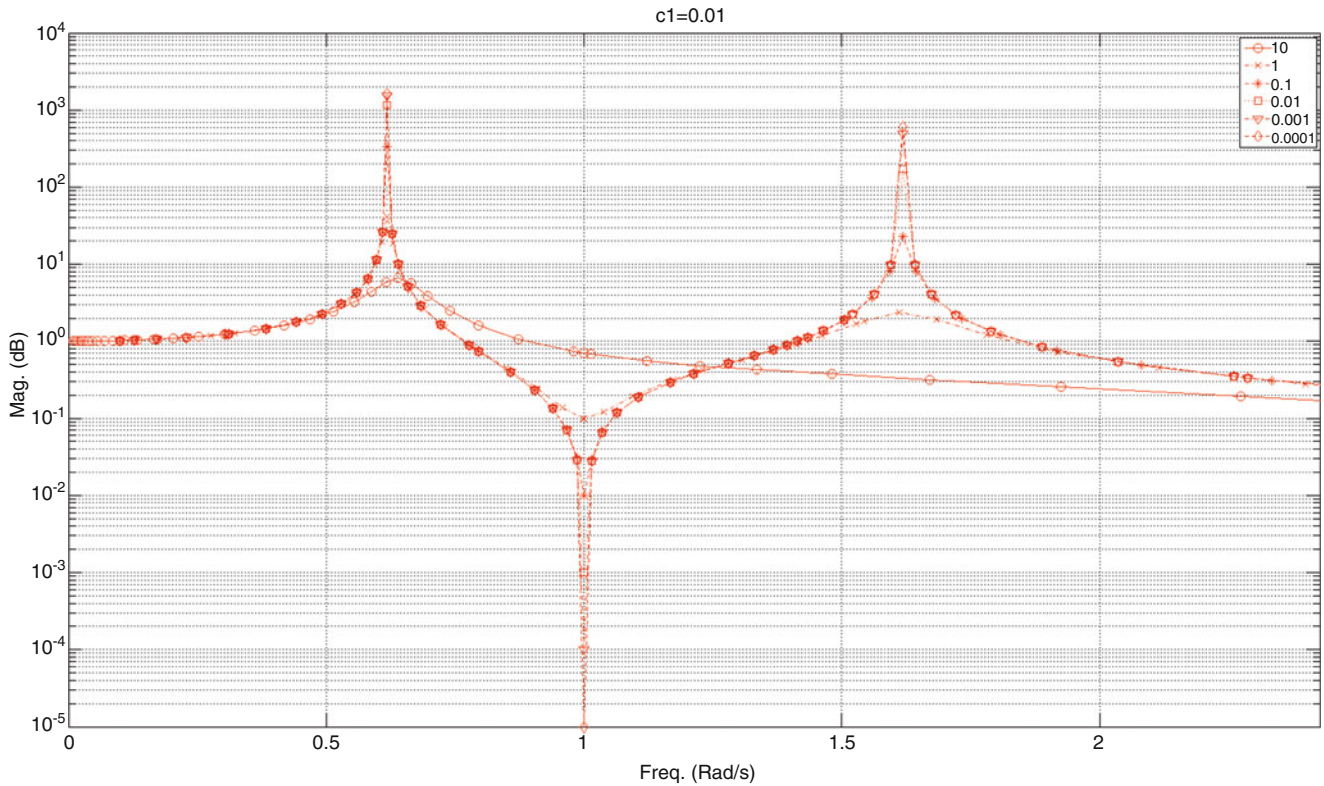


Fig. 28.3 Damping coefficient $c_1 = 0.01$, $c_2 = 10, 1, 0.1, 0.01, 0.001, 0.0001$

smaller than 0.05. In case 3–6, the damping ratio decreased for the smaller damping coefficient of the attachment. So, we can conclude that the damping increases with an attached structure with larger damping and decreases with the attached structure of smaller damping.

28.2.2 Simulation 2: $c_1 = 0.01, c_2 = 10, 1, 0.1, 0.01, 0.001, 0.0001$

In the first simulation, the damping coefficient c_1 was fixed as 0.01 and the damping coefficient c_2 was changed from 10 to 0.0001. Figure 28.3 shows the simulated FRF of two DOF system.

The natural frequency of the host structure is 1 (rad/s). The damping ratio is 0.0005. In case 1–3 of Table 28.2, the damping coefficients of the attached system are higher than that of host structure. Then the damping ratios are bigger than of host structure. In case 4, one of damping ratio is bigger than 0.0005. But the other one is smaller than 0.0005. After that, the damping ratio decreased for the smaller damping coefficient of the attachment. So, we can conclude with the same result as in simulation 1.

Table 28.2 Natural frequencies and damping ratio of two DOF system

Case	c_1	c_2	ω_1	ω_2	ζ_1	ζ_2
1	0.01	10	0.6426	1.5561	0.0676	0.6149
2		1	0.6183	1.6173	0.0087	0.0587
3		0.1	0.6180	1.6180	0.0010	0.0060
4		0.01	0.6180	1.6180	0.0003	0.0008
5		0.001	0.6180	1.6180	0.0002	0.0002
6		0.0001	0.6180	1.6180	0.0002	0.0002

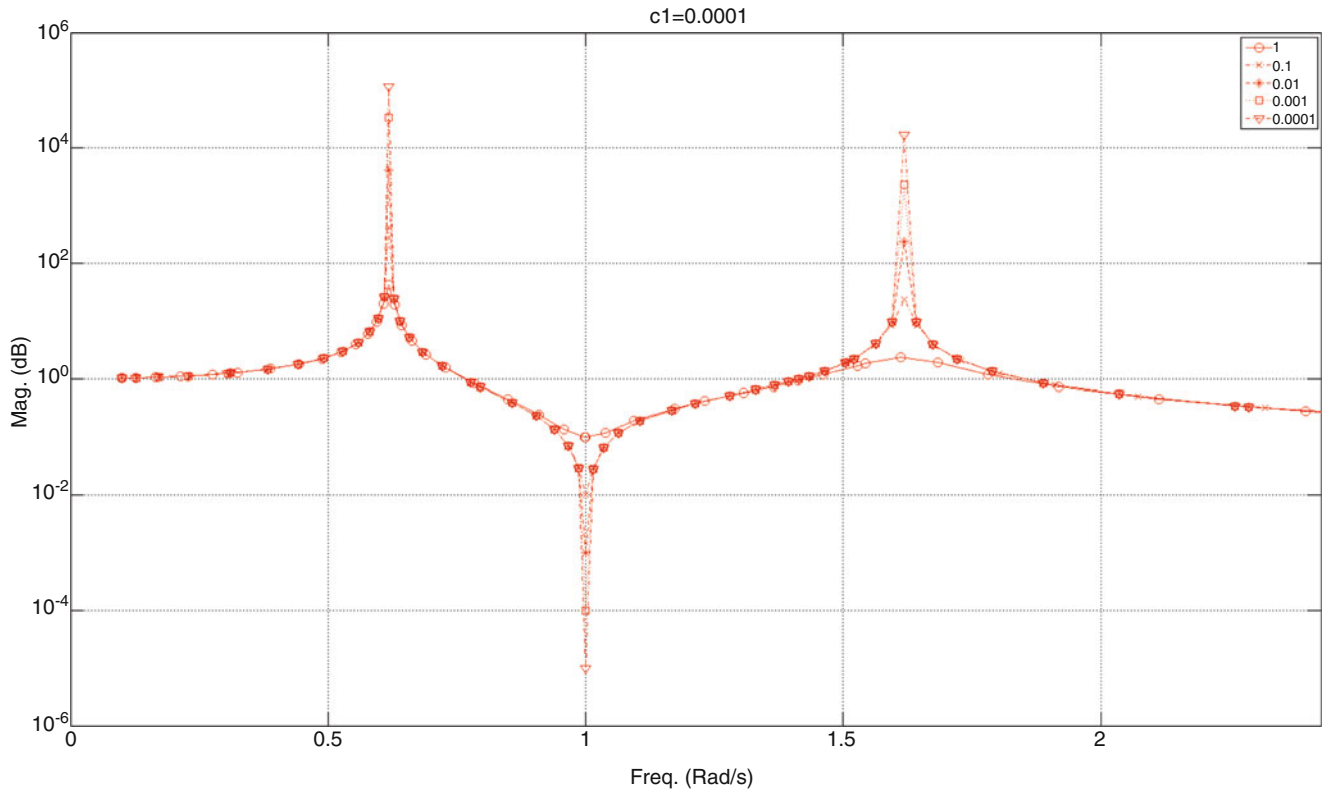


Fig. 28.4 Damping coefficient $c_1 = 0.0001$, $c_2 = 1, 0.1, 0.01, 0.001, 0.0001$

Table 28.3 Natural frequencies and damping ratio of two DOF system

Case	c_1	c_2	ω_1	ω_2	ζ_1	ζ_2
1	0.0001	1	0.61831	1.6173	0.0085	0.0585
2		0.1	0.6180	1.6180	0.0008	0.0058
3		0.01	0.6180	1.6180	8.7646e-05	0.0005
4		0.001	0.6180	1.6180	1.0777e-05	6.0777e-05
5		0.0001	0.6180	1.6180	3.0901e-06	8.0901e-06

28.2.3 Simulation 3: $c_1 = 0.0001$, $c_2 = 1, 0.1, 0.01, 0.001, 0.0001$

In the first simulation, the damping coefficient c_1 was fixed as 0.01 and the damping coefficient c_2 was changed from 10 to 0.0001. Figure 28.4 shows the simulated FRF of two DOF system.

The natural frequency of the host structure is 1 (rad/s). The damping ratio is 0.000005. In case 1–4 of Table 28.3, the damping coefficients of attached system c_2 are higher than that of host structure, c_1 . Then the damping ratios are larger than of the host structure. In case 5, one of damping ratio is bigger than 0.000005. But other one is smaller than 0.000005. So, we can conclude that the damping increases with the attachment of larger damping and decrease with the attachment of smaller damping.

In three simulations, the results show the tendency that the damping decreases in case that an attached structure has smaller damping than that of its host structure and increases when an attachment has larger damping than the host. Therefore, we can

conclude that the damping of a host structure can be affected by the damping of the attachments. To verify this conclusion, the experiments with several types of attached cables were conducted in Sect. 28.4.

28.3 Damping Matrix Identification from FRF Measurement

Lee and Kim [7, 8] presented a way to calculate the damping matrices from measured FRF. The procedure to obtain the damping matrices can be summarized as followings. The equation of motion of a dynamic system with damping is:

$$M \ddot{x}(t) + C \dot{x}(t) + (K + jD) x(t) = f(t) \quad (28.1)$$

where M , K , C and D are the mass, stiffness, viscous damping and structural damping matrices. $x(t)$ and $f(t)$ are the displacement vector and the applied forces vector. For a harmonic excitation, $x(t)$ and $f(t)$ are shown:

$$x(t) = X(\omega) e^{j\omega t}, \quad f(t) = F(\omega) e^{j\omega t} \quad (28.2)$$

Substituting Eq. (28.3) into (28.2) yields

$$[(K - \omega^2 M) + j(\omega C + D)] X(\omega) = F(\omega) \quad (28.3)$$

The dynamic stiffness matrix (DSM) is expressed as

$$[H(\omega)^c]^{-1} = (K - \omega^2 M) + j(\omega C + D) \quad (28.4)$$

where $H(\omega)^c$ is the frequency response matrix (FRM) in the form of

$$H(\omega)^c = [H_{ij}^c] = [X_i/F_j], i, j = 1, 2, 3, \dots \quad (28.5)$$

H_{ij}^c is the complex frequency response function (FRF) measured between the nodes i and j . The DSM is expressed as an inverse of measured complex FRM. FRM is much easier to measure than DSM. After obtaining the DSM by inverting the FRM, Eq. (28.4) can be express as

$$\text{imag}[H(\omega)^c]^{-1} = \omega C + D, \quad \text{real}[H(\omega)^c]^{-1} = K - \omega^2 M \quad (28.6)$$

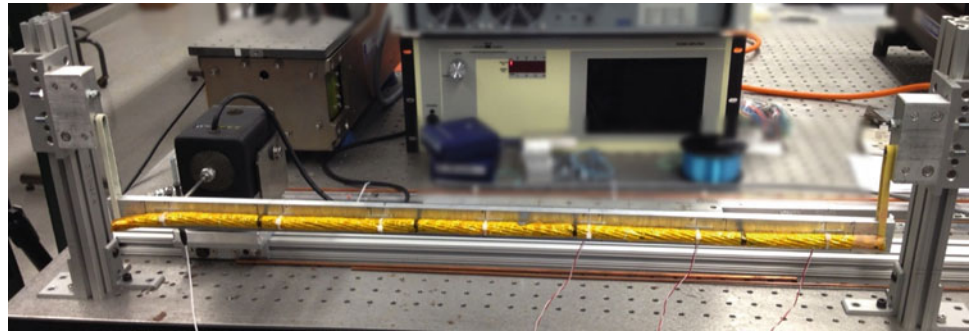
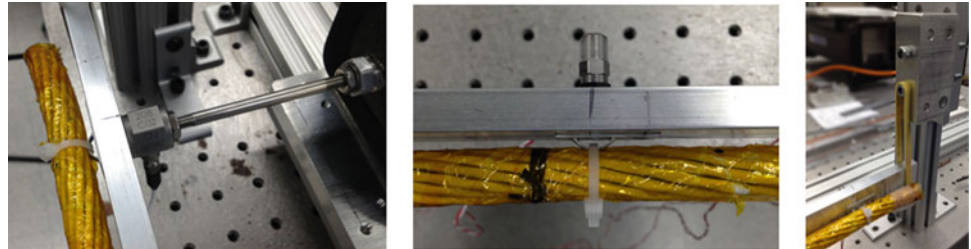
where *imag* and *real* represent the imaginary and real part. The imaginary part of Eq. (28.6) can be shown as

$$[I \ \omega] \begin{bmatrix} D \\ C \end{bmatrix} = \text{imag}[H(\omega)^c]^{-1} \quad (28.7)$$

Finally, the damping matrices C and D can be obtained by pseudo-inverse of Eq. (28.7)

$$\begin{bmatrix} D \\ C \end{bmatrix}_{2n \times n} = \begin{bmatrix} I & \omega_1 I \\ I & \omega_2 I \\ \vdots & \vdots \\ \vdots & \vdots \\ I & \omega_k I \end{bmatrix}_{kn \times 2n}^+ \begin{bmatrix} \text{imag}[H(\omega_1)^c]^{-1} \\ \text{imag}[H(\omega_2)^c]^{-1} \\ \vdots \\ \text{imag}[H(\omega_k)^c]^{-1} \end{bmatrix}_{kn \times n} \quad (28.8)$$

where “+” means the pseudo-inverse of the matrix.

Fig. 28.5 Experimental setup**Fig. 28.6** Shaker + force sensor, accelerometer, and boundary condition

28.4 Experimental Setup

The experimental setup is shown in Fig. 28.5. Aluminum beam with the dimension of 30 in. length, 1¼ in. width and 3/8 in. thickness was applied. The mini shaker (Labworks, ET-132), force sensor (PCB 208C02) and accelerometers (PCB 352C67) were used in measurements. The attachments are shown in Fig. 28.6. To prevent the measurement of torsional vibration, the shaker, force sensor and accelerometer were attached at the centroid of Aluminum beam. Vibrant Laser USB shaker controller and RT pro software were also used. The test specimen was hung by rubber band at the both ends as shown the right side of Fig. 28.6. The boundary condition was considered as free–free condition. During the experiments, the pseudo random noise was applied as an input force at seven points. Thus, 7×7 Full FRF matrix was measured for each test.

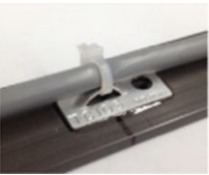
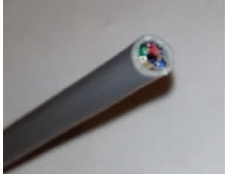
28.5 The Effect of the Type of Attached Cables

To look into the effect of the attached cables, modal tests were conducted with the single beam with three different attached cables. The cables were attached with three connections. The type of cables and connection structure are summarized in Table 28.4.

Figure 28.7 shows the driving point FRFs that were measured at the third point. The FRFs with an actual cable and an electric cable shows smoother shape and shift to right at the resonance peaks. Thus this shows the increase in damping induced by the attached cables. But the FRF with Cu beam shows the different tendency. The measured FRF of the case with the Cu beam shows a clear peak and additional peaks compared with single beam case. To investigate the details, the damping matrix identification in Sect. 28.3 was utilized to obtain the damping matrices.

The damping matrices were obtained by using Eq. (28.8). The calculated viscous damping and structural damping matrices are shown in Figs. 28.8 and 28.9. In Fig. 28.8, the plot (c) and (d) shows the increase of viscous damping compared with plot (a). But the plot (b) shows the similar or smaller damping matrix compared with the plot (a). Figure 28.9 also shows the similar tendency of structural damping with the viscous damping.

Table 28.4 Connection structure and three attached cables

Connection structure	Cu beam	Actual satellite cable	Electric cable
			
<ul style="list-style-type: none"> - T&B TC105 tie-down - Zip tie 	<ul style="list-style-type: none"> - Copper tube - Diameter 0.1265 in. × thickness 0.04 in. 	<ul style="list-style-type: none"> - 18 inner cables - Length 29.5 in. × diameter 0.5 in. 	<ul style="list-style-type: none"> - Commercial cable - Length 29.5 in. × diameter 0.2 in.

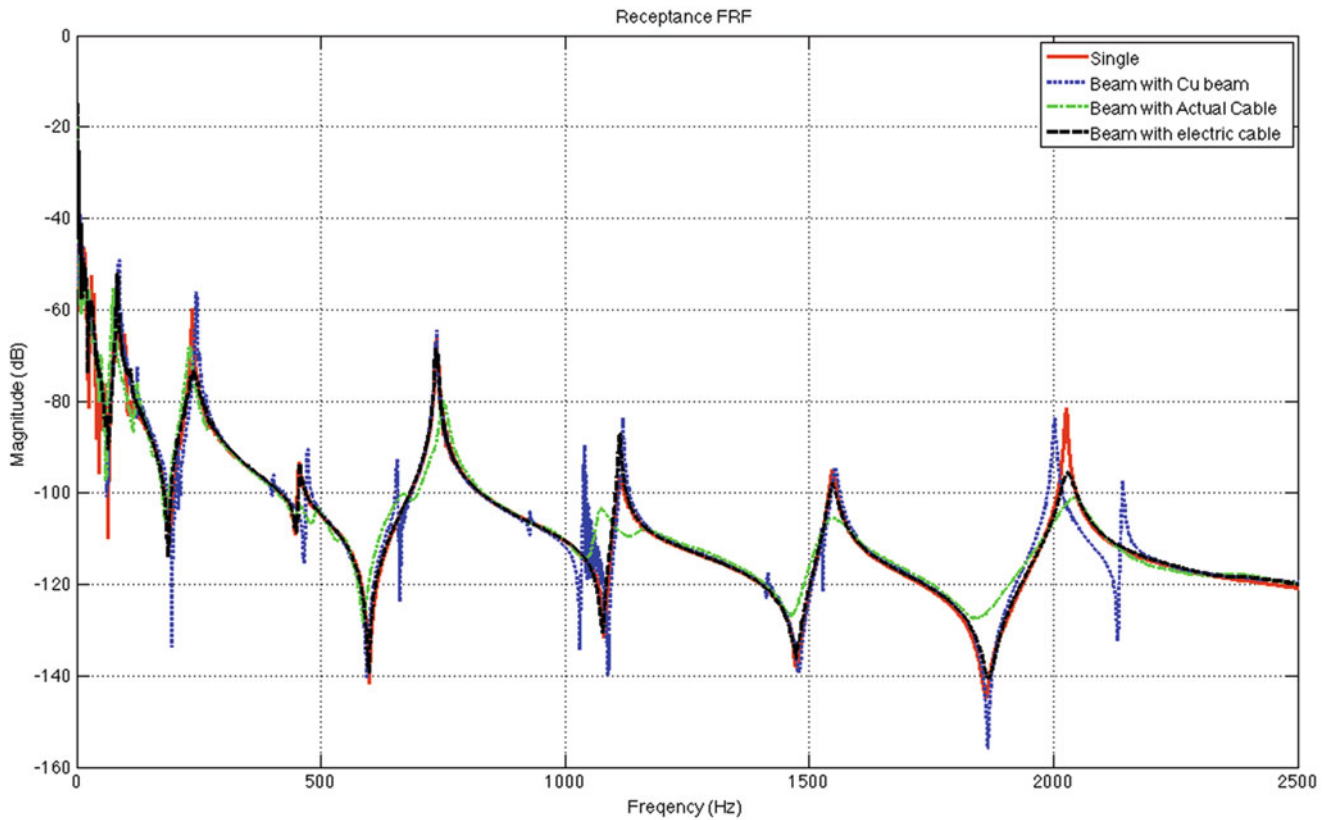


Fig. 28.7 Driving point FRFs, measured at third point

28.6 The Effect of Number of Interconnections on Damping

The effect of the number of interconnections is also investigated with four different connection cases (0, 3, 5 and 7 connections). Figure 28.11 shows the specimen with seven interconnections. The same Aluminum beam of Sect. 28.5 and actual cable were used in the tests. The measured FRFs are shown in Fig. 28.12. And the damping matrices are calculated as shown in Figs. 28.13 and 28.14. Figures 28.13 and 28.14 shows the increase of both damping matrices with more number of connections.

In Fig. 28.15, the matrix norm of the viscous damping and structural damping is compared. The beam with actual cable shows the increase in both damping matrices shown in Sect. 28.5. We also found that the damping would be increased when connected with more number of interconnections.

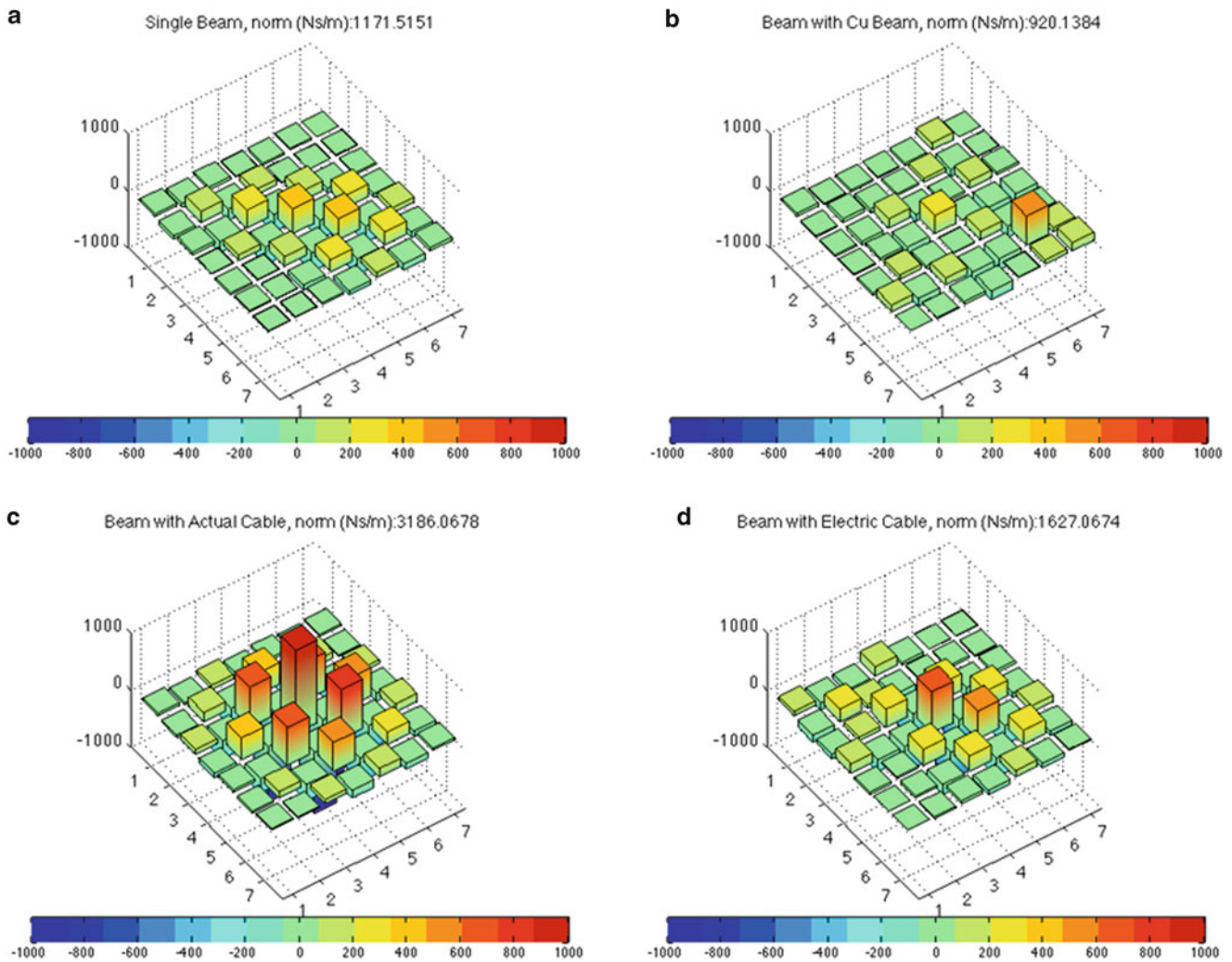


Fig. 28.8 The matrix norm comparison of Viscous Damping Matrices. (a) Single beam, (b) beam with attached Cu beam, (c) beam with attached actual cable, (d) beam with attached electric cable

In Fig. 28.10, the matrix norm of the viscous damping and structural damping is compared. The beam with the actual cable shows the increase in both damping matrices. The beam with an electric cable shows the biggest increase in the structural damping. But it shows less damping increase in the viscous damping than the case of the actual cable. The damping is decreased when attached with the Cu beam. From these results, we can conclude that the type of cables can affect the damping differently. Moreover, an increase in flexibility of the attached cable causes an increase of damping.

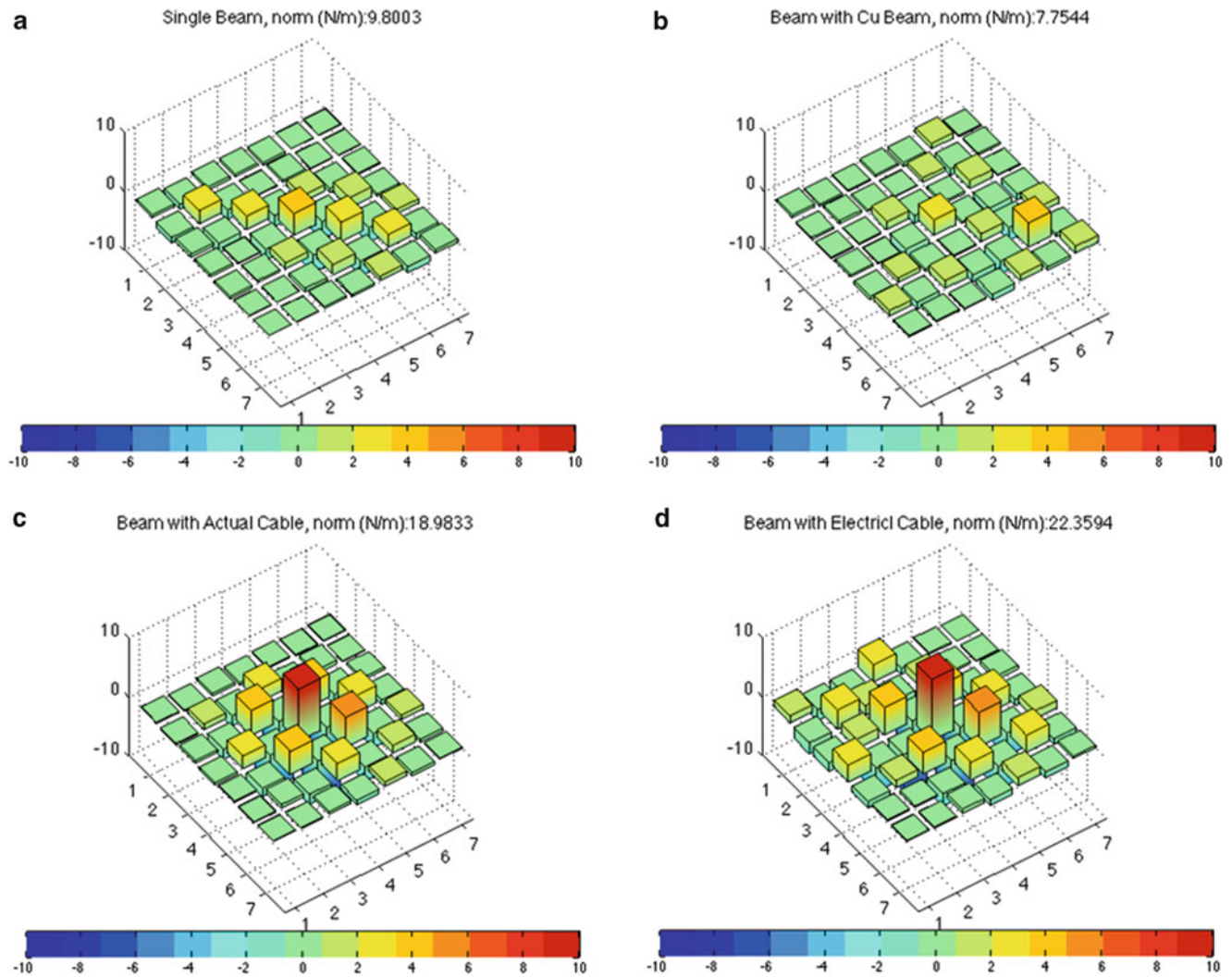


Fig. 28.9 The matrix norm comparison of Structural Damping Matrices. (a) Single beam, (b) beam with attached Cu beam, (c) beam with attached actual cable, (d) beam with attached electric cable

28.7 Conclusion

The modification of damping of the host structure induced by the attach cables are investigated. By using the measured full FRF matrix, the identification of the damping matrix was conducted. The results show that the damping increased with a flexible attached cable. But the damping decreased when connected with stiff cable. This implies that an increase in flexibility of the attached cable causes an increase in the damping. The effect of number of connections was also examined. The damping matrices tend to increase with more connections.

Fig. 28.10 The matrix norm comparison of Damping Matrices with four different attachments

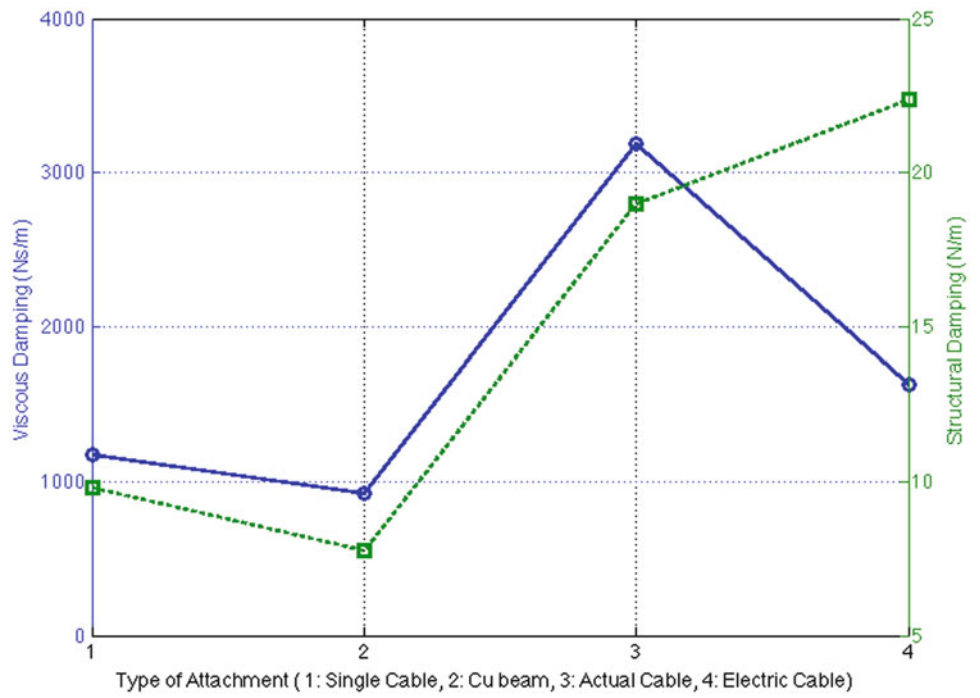


Fig. 28.11 Test specimen (seven connections)

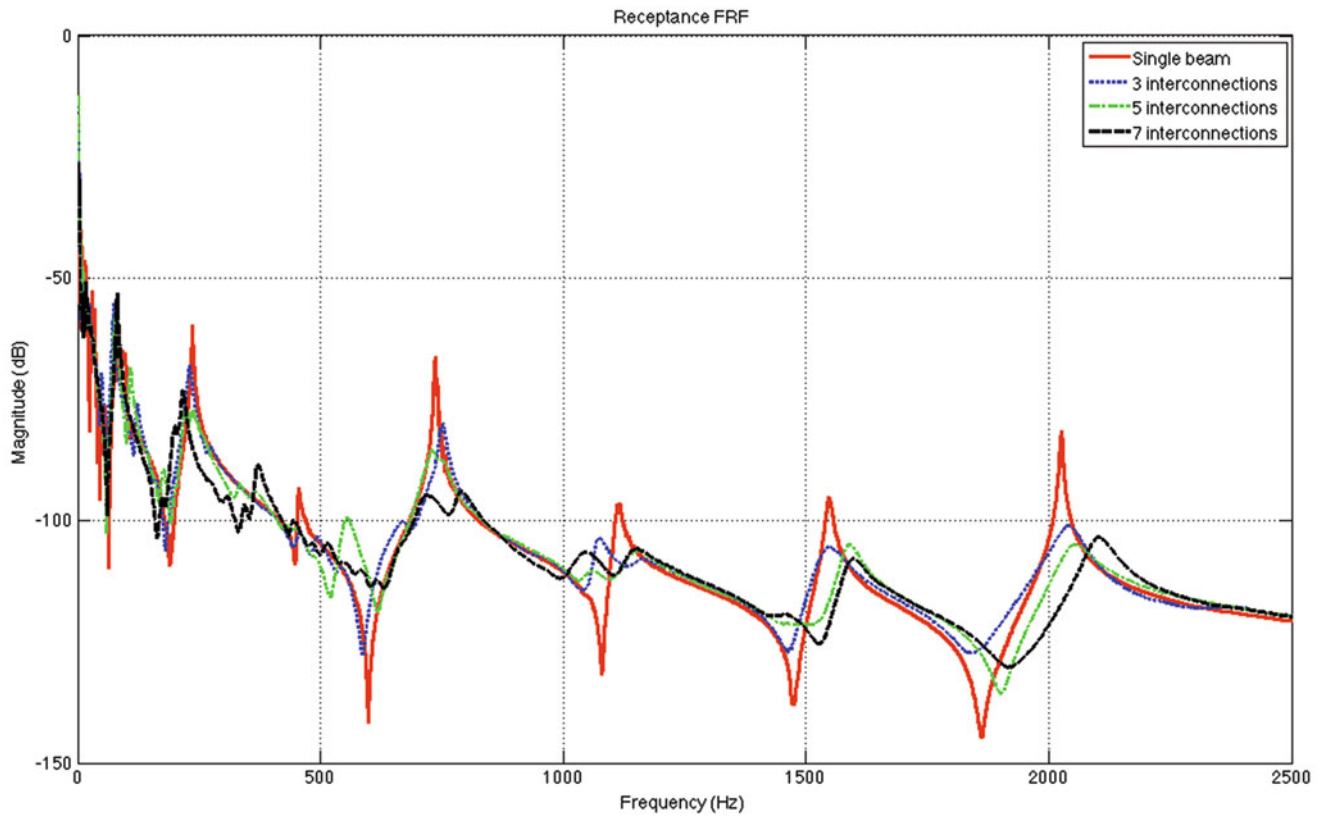


Fig. 28.12 Driving point FRFs, measured at third point

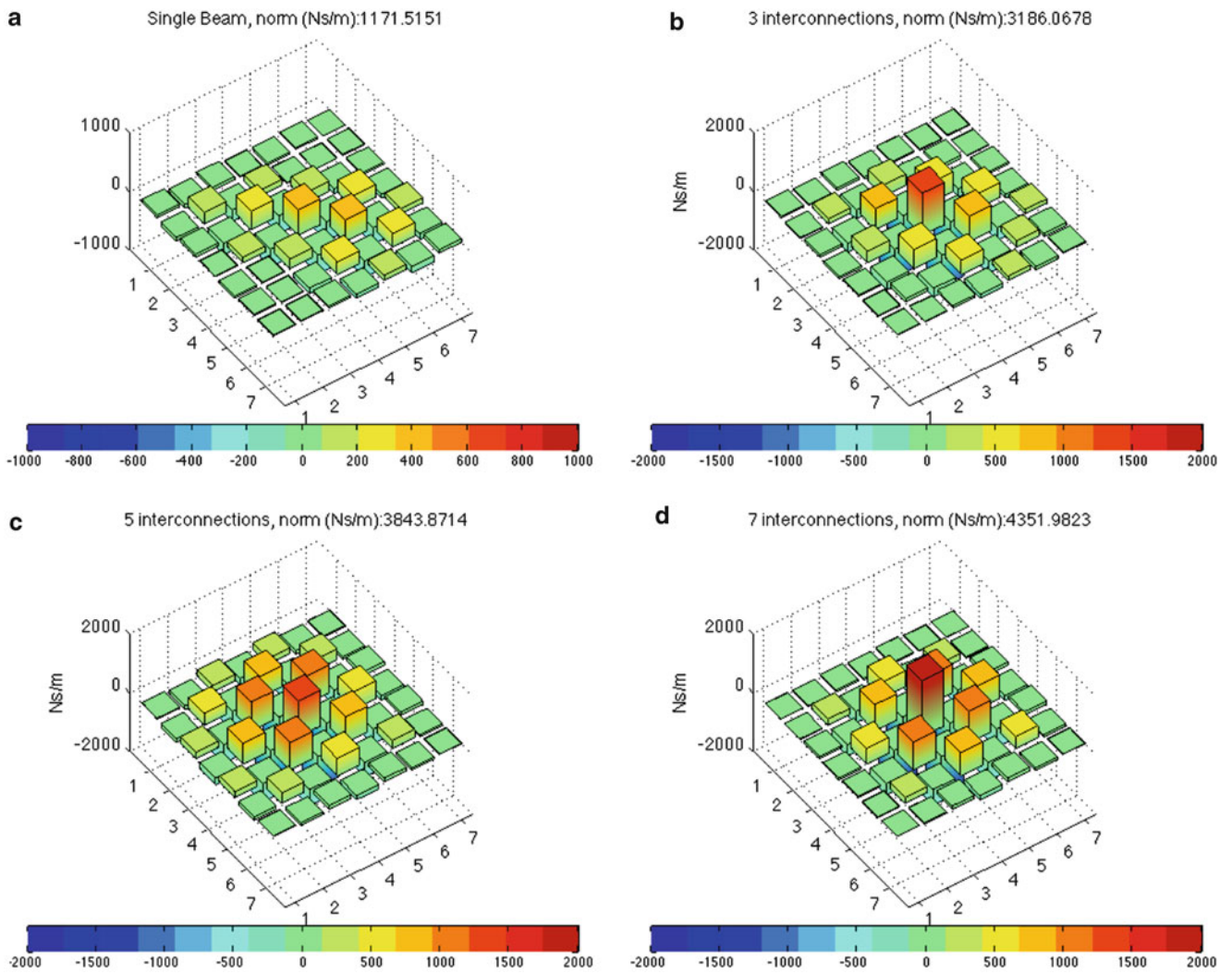


Fig. 28.13 The matrix norm comparison of Viscous Damping Matrices. (a) Single beam, (b) three interconnections, (c) five interconnections, (d) seven interconnections

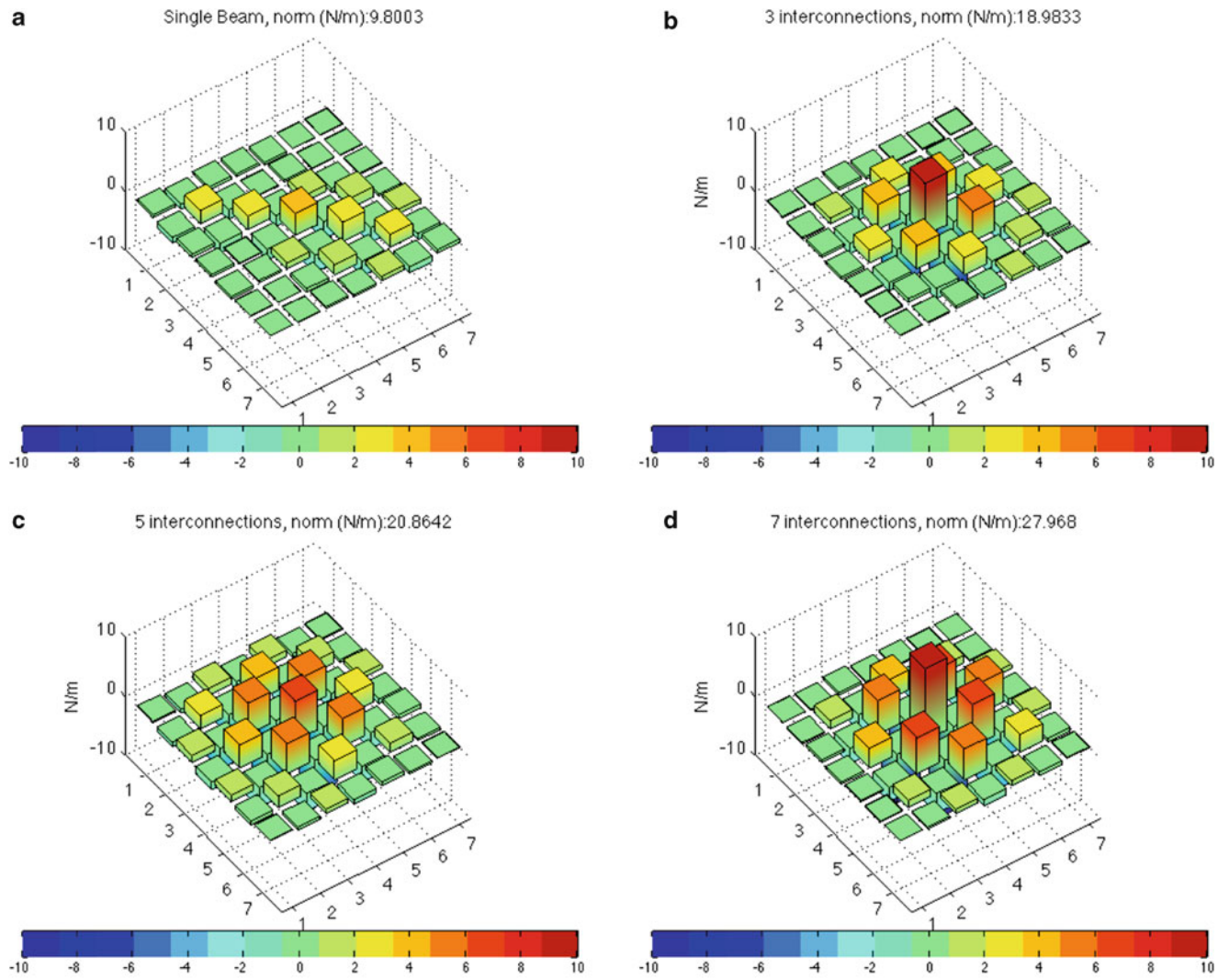
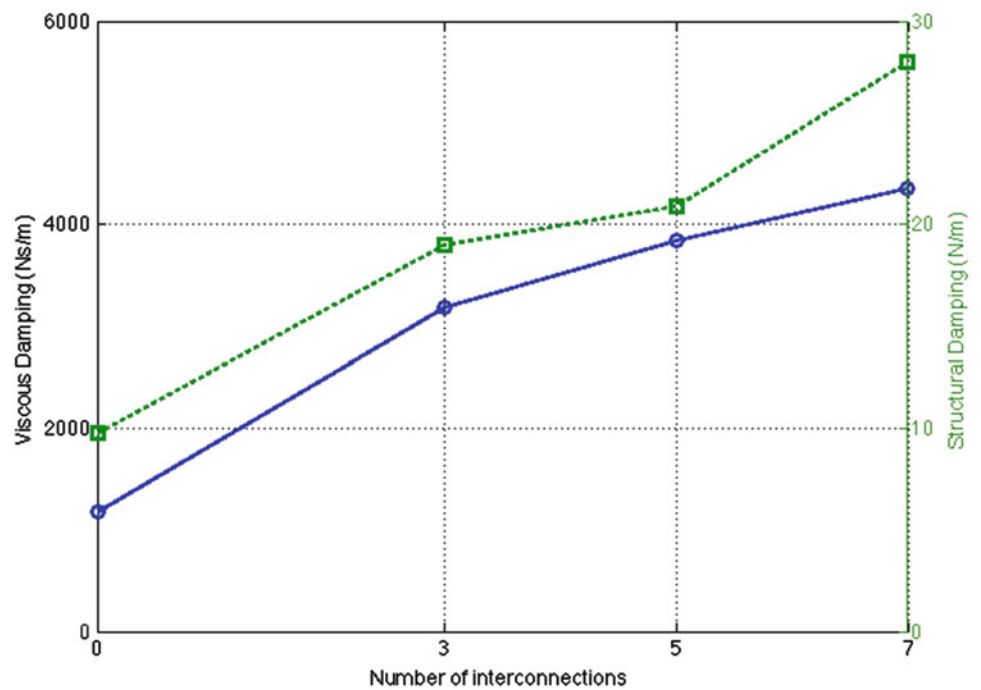


Fig. 28.14 The matrix norm comparison of Structural Damping Matrices. (a) Single beam, (b) three interconnections, (c) five interconnections, (d) seven interconnections

Fig. 28.15 Comparison of the norm of damping matrices with four different connection numbers



References

1. Fritzen CP (1986) Identification of mass, damping, and stiffness matrices of mechanical systems. *J Vib Acoust Stress Reliab Des* 108:9
2. Minas C, Inman DJ (1991) Identification of a non-proportional damping matrix from incomplete modal information. *J Vib Acoust* 113(2): 219–224
3. Pilkey DF, Park G, Inman DJ (1999) Damping matrix identification and experimental verification. In: 1999 symposium on smart structures and materials, International Society for Optics and Photonics, pp 350–357
4. Woodhouse J (1998) Linear damping models for structural vibration. *J Sound Vib* 215(3):547–569
5. Adhikari S, Woodhouse J (2000) Towards identification of a general model of damping. In: Proceedings of 18th international modal analysis conference (IMAC), pp 377–383
6. Chen S, Ju M, Tsuei Y (1996) Independent identification of damping matrix from contaminated frequency response functions. In: SPIE, pp 363–369
7. Lee JH, Kim J (2001) Identification of damping matrices from measured frequency response functions. *J Sound Vib* 240(3):545–565
8. Lee JH, Kim J (2001) Development and validation of a new experimental method to identify damping matrices of a dynamic system. *J Sound Vib* 246(3):505–524
9. Ozgen GO, Kim JH (2007) Direct identification and expansion of damping matrix for experimental–analytical hybrid modeling. *J Sound Vib* 308(1):348–372
10. Choi J, Inman DJ (2013) Development of modeling for Cable Harnessed Structures. In: 54th SDM 2013, Boston
11. Inman DJ (2013) *Engineering vibration*, 4th edn. Pearson Prentice Hall, Upper Saddle River

Chapter 29

Effect of Structural Damping on Vibrations Transmitted to Road Cyclists

Jean-Philippe Pelland-Leblanc, Julien Lépine, Yvan Champoux, and Jean-Marc Drouet

Abstract Improving ride quality is a paramount concern for road cyclists who are subjected to road induced vibrations during long rides. It has been hypothesized that adding structural damping to the bicycle can decrease the vibration levels transmitted to the cyclist. The human body is most sensitive to vibrations in the frequency range of 0–60 Hz, and the amount of damping added by the cyclist when riding the bicycle is very large. This could potentially reduce the net benefit of small improvements provided by structural damping. This paper reveals the effects of structural damping modifications on the modal parameters of a bicycle frame and on the amount of vibrations transmitted to the cyclist due to road surface excitation. A bicycle frame originally designed with damping gel inserts was tested in three different configurations: (1) with its damping gel inserts, (2) with its damping gel inserts and additional damping material wrapped around the frame's tubing and (3) without its damping gel inserts. Three different metrics were used to assess the damping material effect on vibrations transmitted to the cyclist at the hands and buttocks: acceleration, transmitted force and power absorbed by the cyclist. This paper shows that in all configurations and measurements, added damping did not reduce the vibrations transmitted to the cyclist.

Keywords Bicycle comfort • Ride quality • Damping • Vibration transmission • Absorbed power • Comfort metrics

29.1 Introduction

Road cyclists, who tend to ride for extended periods of time, are increasingly seeking enhanced comfort in the bicycles they choose. In addition to trials with new materials [1, 2] and novel shapes, adding structural damping to a road bike frame is a current attempt at reducing vibration transmitted to the cyclist and improving the frame's intrinsic comfort. Although adding structural damping is widely used in the bicycle industry to market comfort, the effectiveness of added damping has not yet been proven. When testing a bicycle, the added mass and damping of the cyclist completely alters the dynamic behavior of the system [3]. In the frequency range of 0–60 Hz, where the human body is most sensitive to vibration, the amount of damping added by the presence of the cyclist on the bicycle is already very large, and may even reduce the net benefit of adding damping material to the bicycle. This paper discusses the effects of structural damping modifications on the modal parameters of a bicycle frame alone and on the amount of vibrations transmitted to the cyclist from road excitation. A bicycle frame originally designed with damping gel inserts (polymer gel inserts pressed into holes on the fork, seat post and seat stays as lumped structural damping elements) was tested in three different configurations: (1) with its damping gel inserts, (2) with its damping gel inserts and additional damping material wrapped around the frame's tubing and (3) without its damping gel inserts. Three different metrics were used to assess the damping material effect on vibrations transmitted to the cyclist at the hands and buttocks: acceleration, transmitted force and the power absorbed by the cyclist.

J.-P. Pelland-Leblanc (✉) • J. Lépine • Y. Champoux • J.-M. Drouet
Engineering Faculty, Université de Sherbrooke, 2500 Blvd. Université, Sherbrooke, QC J1K 2R1, Canada
e-mail: jean-philippe.pelland-leblanc@usherbrooke.ca

29.2 Methods

This section describes the experimental setups (the modal analysis setup and the vibration transmission assessment setup) the transducers, experimental protocols, signal acquisition material and the data analysis method used to obtain the results.

29.2.1 Modal Analysis—Setup

To conduct the modal analysis, the bike was suspended in order to have a free–free boundary condition, as shown in Fig. 29.1. A road bicycle consisting of a frame, a seat post, a fork, headset bearings and a stem was used in this experiment. The cables, shifters, pedals, wheels and chain were removed from the bicycle. Wheel-equivalent masses were attached to the front and rear wheel axle. A cyclist-equivalent mass was also added to the seat post (25 kg), the stem (15 kg) and the bottom bracket (4 kg). The amount of mass to be added was determined by measuring the dynamic mass FRF using an impedance head at each point of contact between the cyclist and the bicycle. The peak values of the dynamic mass response curves were selected in a specific frequency subset (10–60 Hz) of the frequency range of interest (0–60 Hz) to obtain the previously discussed masses. The weighted frame is attached by the stem and the seat post to a concrete ceiling with bungee cables. The number of cables was chosen to obtain the rigid modes of the system under 1 Hz.

Modal analysis was conducted using a roving hammer technique. A tri-axial accelerometer (PCB model 356A32) was attached to the top tube at the driving point represented by an “x” in Fig. 29.1. On the same figure, every dot represents an excitation point and is impacted in at least two directions. For each direction on each excitation point, five impacts were made with an instrumented hammer (PCB model 086C01).

29.2.2 Modal Analysis—Protocol

Three different bicycle configurations were tested using the modal analysis setup:

- Configuration #1: a commercial road bike with its damping gel inserts (polymer gel inserts pressed into holes in the fork, seat post and seat stays as lumped structural damping elements)
- Configuration #2: same as configuration 1 with aeronautic constrained damping material bounded around frame tubes and fork
- Configuration #3: same as configuration 1 with the damping gel inserts removed

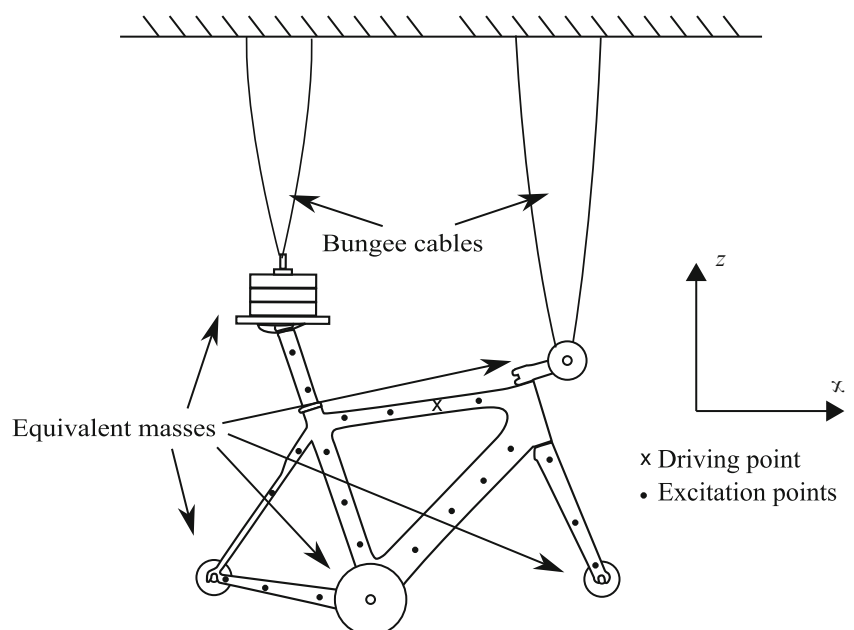


Fig. 29.1 Modal analysis setup

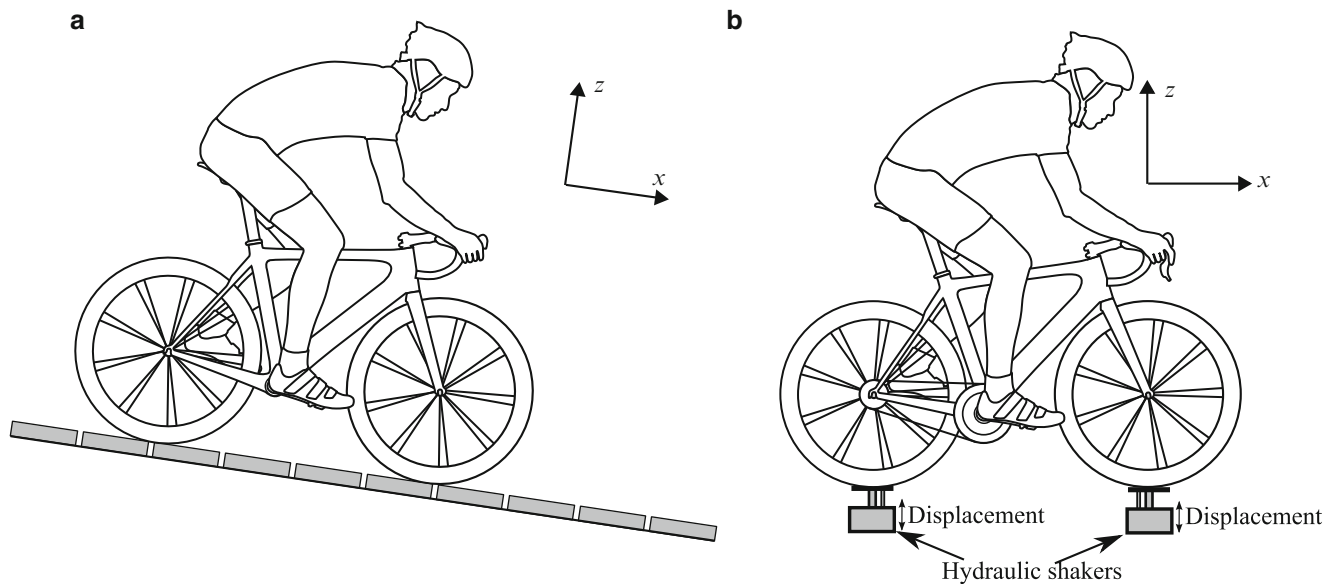


Fig. 29.2 Excitation types used under the tires. (a) Outside excitation setup. (b) Laboratory excitation setup

The accelerometer and hammer force data were acquired using an LMS Scadas acquisition system (model SCR01-08B) at a frequency of 8,192 Hz. LMS Test.Lab software was used for data processing. Modes were computed using the “Structure Acquisition – Impact testing” software package. The dominant modes in the 1–60 Hz frequency band were extracted and used for the modal synthesis (sum of the accelerance FRF).

29.2.3 Vibration Transmission Measurement—Laboratory and Outside Setups

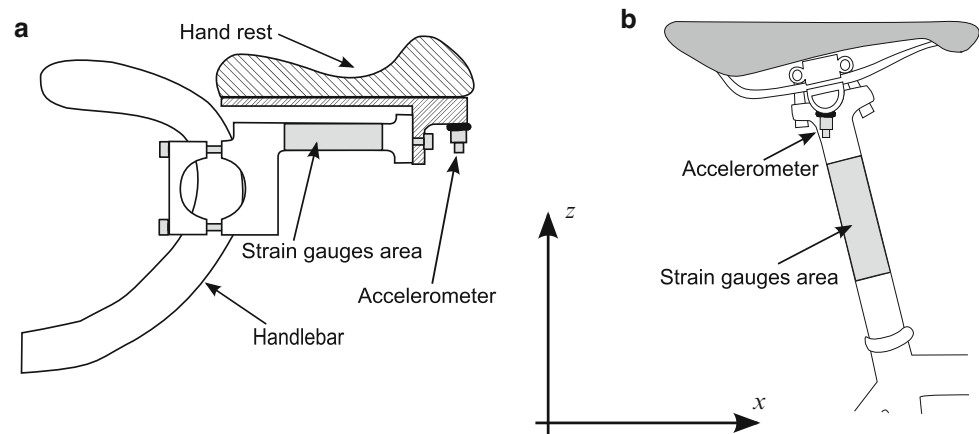
Two road excitation types were used to compare the level of vibration transmitted to the cyclist, in the different configurations: (1) outdoors on a cobblestone road and (2) in the lab on a road excitation simulator. In both setups, the cables, shifters and dangling chains that could potentially hinder the measurement procedures were removed. For outdoor measurements, since there is no way for the cyclist to propel the bicycle without a chain, a sloped cobblestone road was selected (see Fig. 29.2a). The bicycle was thus propelled by the force of gravity, allowing the rider to maintain a stable position thus providing repeatable measurements. To allow time for the cyclist to adopt a stable position, acquisition was initiated 5 s after the cyclist began riding from a stationary position. The data acquisition period was set at 30 s.

To reproduce road excitation in the more controlled environment of the laboratory, 2 Xcite hydraulic shakers (model 1107-4-T/C) were used to impose displacement on the wheels (see Fig. 29.2b). The excitation signals were purely vertical (z axis) and were selected to represent the vertical excitation that a bike undergoes when rolling on a harsh granular road. For this purpose, the signals played by the shakers were previously recorded by an accelerometer attached to the rear wheel axle of the bike, rolling at a constant speed of 26 km/h on a flat granular road outside. During the recording process, a cyclist was riding on the bike towed by a vehicle—as described by Lépine et al. [4]. Two different parts of this recorded signal were taken at the front and rear hydraulic shaker, as preliminary tests have shown that uncorrelated signals are more representative of real life excitation [5]. The bicycle was kept in a vertical position with bungee cables wrapped around the seat tube and attached to a fixed structure on each side of the bicycle. The bungee ropes were selected to be compliant enough not to affect the vibration measurement, but stiff enough hold the cyclist and bicycle in a vertical position.

The cyclist makes contact with the bicycle at three locations (feet, hands and buttocks) where vibration energy is absorbed. Since the level of vibration felt at the feet is four times lower than that perceived at the buttocks (ISO 2631), the force is measured only at the brake hood and the seat post. Therefore, only the level of vibration transmitted to the hands and buttocks is considered in this paper. Furthermore, only the vertical axis (z) component of the forces, accelerations and power is shown in this paper since most of the measured vibration is in that direction (as preliminary measurements have indicated).

To measure acceleration at the contact points, three accelerometers were used: two uniaxial (PCB model 352C65) under the brake hoods and one multi-axial (PCB model 356A32) on the seat post. To measure forces at the cyclist’s points of

Fig. 29.3 Custom made force transducers



contact, two different types of custom-made strain gauge transducers were used: an instrumented brake hood (Fig. 29.3a) and an instrumented seat post (Fig. 29.3b). The brake hood transducer was built to replicate the stiffness of the bicycle part it replaces and the seat post transducer was built around a commercial aluminum seat post. Those instrumented components thus provide similar dynamic forces that would be obtained with their non-instrumented counterpart [6].

For the vibration transmission measurements, we used the transducers to measure the accelerations and force signals using an LMS SCADAS acquisition system (model SCR01-08B) at a frequency of 8,192 Hz. LMS Test.Lab software was used for data processing. Accelerations and forces transmitted to the cyclist's hands and measured at the brake hoods were processed with a filter corresponding to human hand sensitivity (ISO5349 hand-arm vibration standard). Accelerations and forces transmitted to the cyclist's buttocks and measured at the seat post were treated with a corresponding filter (ISO2631-1 whole body vibration standard).

The average absorbed power P was computed using the force F and velocity V (integrated from the acceleration signal) measured at the same measurement point. This was computed in the frequency domain (where f represents the frequency) using the integration over the frequency range of interest (0–200 Hz) of the real part of the cross-spectrum G_{FV} between the force and velocity as shown in Eq. (29.1)

$$P = \int_0^{200} \text{Re} [G_{FV}(f)] df \quad (29.1)$$

29.2.4 Vibration Transmission Measurement—Protocol

The same bike and cyclist were used for two pairwise comparison tests. The bike model we used is reputed to be comfortable and is equipped with gel inserts pressed into holes in the fork, seat post and seat stays. Each of the tests compares two bike configurations in order to assess the effects of the two damping materials: the added aeronautic damping material and the damping gel inserts.

- Comparison test #1—Assessment of added aeronautic damping material
 - Configuration #1: the road bike with its damping gel inserts
 - Configuration #2: the same road bike (with its damping gel inserts) and added aeronautic damping material bonded around the tubing
- Comparison test #2—Assessment of damping gel inserts
 - Configuration #1: the road bike with the damping gel inserts
 - Configuration #3: the same road bike without the damping gel inserts

In comparison test #1, the two configurations were tested outdoors on the sloped cobblestone path and in the laboratory using the road simulator. In comparison test #2, the two configurations were tested indoors only. In both tests, eight 30 s excitation runs were conducted per configuration. The root mean square (RMS) value was measured at each run's acceleration and force signals. The average absorbed power was also computed at each run. These values are used in an analysis of

variance (ANOVA) to evaluate while comparing two damping configurations, if there is a statistically significant difference in the vibration transmitted to the cyclist. The ANOVA is done with a 0.05 level of significance, meaning that, for a particular criterion, if the p -value is below 0.05, then the compared damping situations are significantly different. It should be noted that since the tests were not done in a random order, the test order was included as a covariant in the ANOVA model.

29.3 Results

The results are divided in two sections. Section 29.3.1 shows the influence of added aeronautic damping material on the frame and the fork. Section 29.3.2 assesses the influence of the damping gel inserts. In each section, the result of the modal analysis is presented in the form of a sum of FRFs graph. The results of the vibration transmissibility tests are presented in a bar graph for each metric (acceleration, force and absorbed power) and each excitation method (in the lab: laboratory road simulator; outdoors: sloped cobblestone road).

29.3.1 Section 1: Added Aeronautic Damping Material Assessment (Configuration #1 vs. Configuration #2)

The sums of the acceleration FRFs for each modal analysis with and without the added aeronautic vibration damping material (configurations #1 and #2) are presented in Fig. 29.4. In the comparison of the dashed gray line on the solid line, certain modes are damped as shown by the lower amplitude peak. At a higher frequency range (3,060 Hz), the modal frequencies are slightly shifted down.

Figures 29.5, 29.6, and 29.7 represent the vibration transmission assessment presented for the three metrics used in this study (acceleration, force, absorbed power). The bars show the mean of the eight repeated run values (mean of RMS

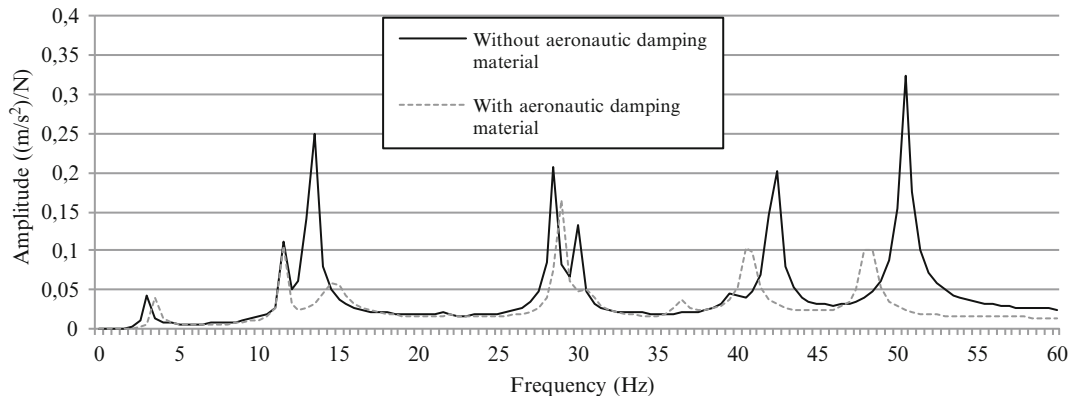


Fig. 29.4 Sum of FRFs for bicycle with and without aeronautic damping material (configurations #1 and #2)

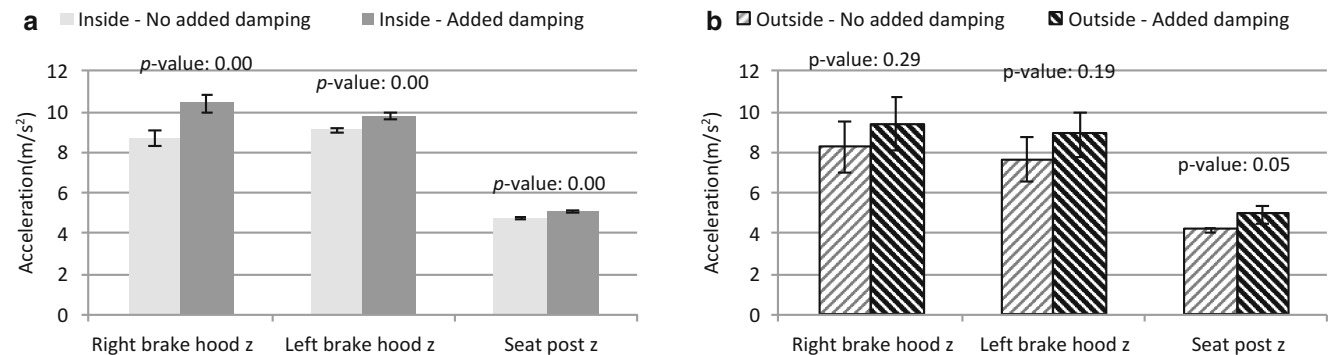


Fig. 29.5 Acceleration metric used for aeronautic damping material assessment. (a) Laboratory excitation setup. (b) Outside excitation setup

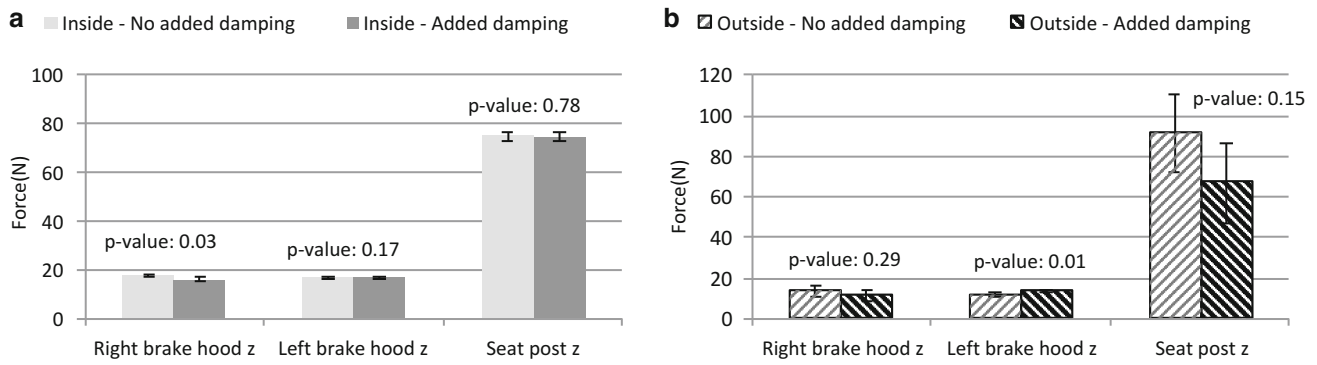


Fig. 29.6 Force metric used for aeronautic damping material assessment. (a) Laboratory excitation setup. (b) Outside excitation setup

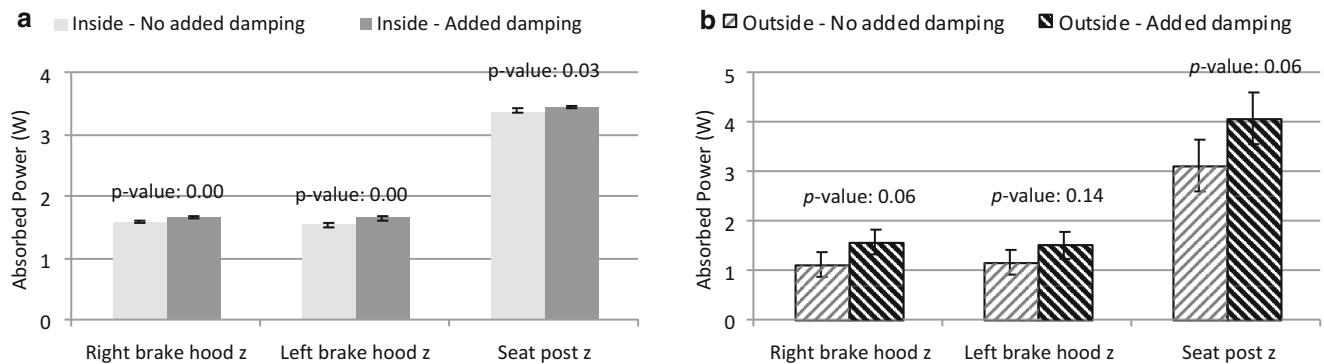


Fig. 29.7 Power metric used for aeronautic damping material assessment. (a) Laboratory excitation setup. (b) Outside excitation setup

acceleration values, mean of RMS force values and mean of averaged absorbed power values). In Figs. 29.5, 29.6, and 29.7, the vertical axis is the amplitude of the vibration measured in acceleration (Fig. 29.5), force (Fig. 29.6) and averaged absorbed power (Fig. 29.7). The horizontal axis indicates the position of the measurement on the bike. The error bars represent the 95 % confidence interval. The bars are shown in pairs to illustrate the difference between the two situations (with and without added vibration damping material). The p -value is indicated for each condition pair. Figure 29.5 suggests that the bike with no added vibration damping material (configuration #1) transmits less vibration measured with the acceleration metric. The outdoor excitation test could not show a significant difference as the p -values are above 0.05. In Fig. 29.6, the force metric does not show any clear tendency favoring configuration on vibration transmission. Figure 29.7a shows a clear tendency favoring the bike without added aeronautic damping material as the one transmitting less vibration power to the cyclist. Though the differences between the two bike configurations (#1 and #2) shown in Fig. 29.7b could not be considered significant, the tendency indicating that the bike without added aeronautic damping material (configuration #1) transmits less vibration remains valid.

29.3.2 Section 2: Vibration Damping Gel Inserts Assessment (Configuration #1 vs. Configuration #3)

The results of the modal analysis done on the bike with and without its damping gel inserts are shown in Fig. 29.8. The sum of FRF perfectly matches at lower frequencies (0–35 Hz), but there is a small shift at higher frequencies (35–60 Hz).

The results of the vibration transmission tests for the bicycle with and without its vibration damping gel inserts (configurations #1 and #3) are shown in Figs. 29.9 and 29.10. When using the acceleration metric (Fig. 29.9a) the test seems to favor the bike with no damping gel inserts as being the one that transmits less vibration. However, the difference cannot be considered significant. When using the force metric (Fig. 29.9b) the test seems to indicate that the bike with the damping gel inserts transmits less vibration, but again, the differences cannot be considered significant (except for the left brake hood). When using the absorbed power metric (Fig. 29.10), the test does not show any clear results regarding the power absorbed by the cyclist on both bike configurations.

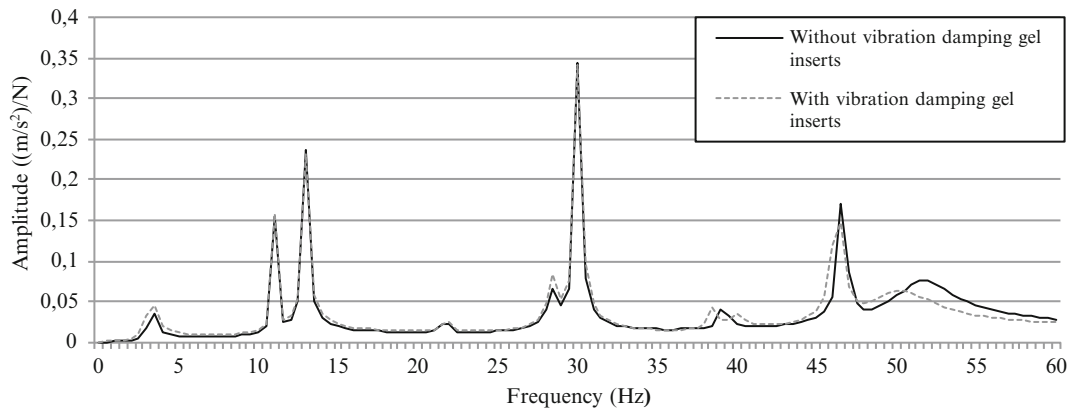


Fig. 29.8 Sum of FRFs for the bicycle with and without vibration damping gel inserts (configurations #1 and #3)

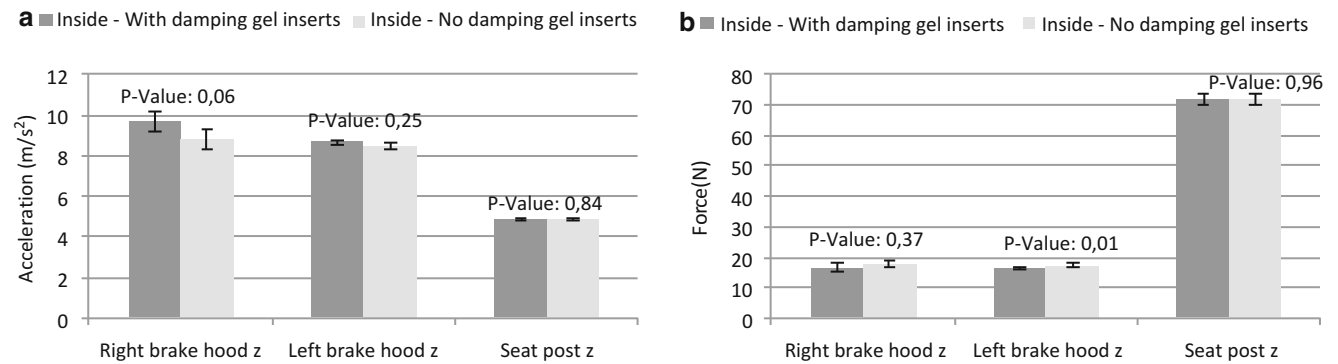
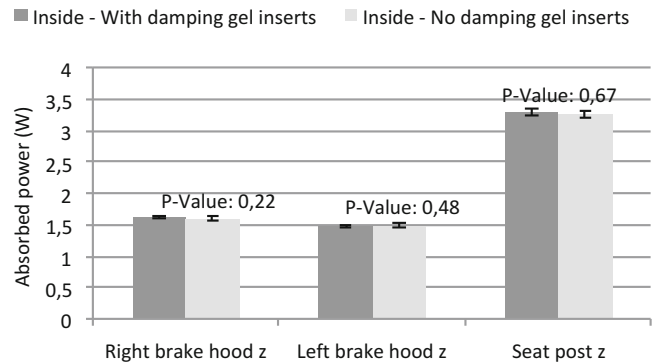


Fig. 29.9 (a) Acceleration and (b) force metric used for vibration damping gel inserts assessment

Fig. 29.10 Power metric used for vibration damping gel inserts assessment



29.4 Discussion

The aeronautic damping material added to the bicycle adds damping to the frame but does not reduce the vibration transmitted to the cyclist. In fact, vibration transmission even increases, as measured by the acceleration and power metrics. This result serves to reinforce the importance of having a cyclist sitting on the bike when testing vibration transmissibility to assess comfort. It is hypothesized that the increase in vibration shown when adding the aeronautic damping material could be caused by the added mass on the bicycle (880 g) associated with a greater transfer of energy. The added vibration damping gel inserts do not have any effect on either the modes damping or on the vibration transmitted to the cyclist. The mass added by these devices is also smaller (45 g) than that of the aeronautic damping material.

These studies reveal experimental evidence to indicate that added damping has no significant effect on three comfort-related metrics and does not significantly reduce the vibration transmitted to the cyclist.

Acknowledgments The authors gratefully acknowledge financial support from the National Science and Engineering Council of Canada (NSERC) and the participation of Cervélo and Vroomen-White Design.

References

1. Thite AN, Gerguri S, Coleman F, Doody M, Fisher N (2013) Development of an experimental methodology to evaluate the influence of a bamboo frame on the bicycle ride comfort. *Veh Syst Dyn* 51(9):1287–1304
2. Vanwalleghem J (2010) Damping and vibration behaviour of flax-carbon composite bicycle racing frames. In: UGent-FirW Doctoraatssymposium, 11e, p 89
3. Champoux Y, Richard S, Drouet J-M (2007) Bicycle structural dynamics. *Sound Vib* 41(7):16–25
4. Lépine J, Champoux Y, Drouet J-M (2012) Technique to measure the dynamic behavior of road bike wheels. In: Allemang R, Clerck JD, Niezrecki C, Blough JR (eds) *Topics in modal analysis II*, vol 6. Springer, New York, pp 465–470
5. Lépine J, Champoux Y, Drouet J-M (2013) A laboratory excitation technique to test road bike vibration transmission. *Exp Tech*. doi:10.1111/ext.12058
6. Caya A, Champoux Y, Drouet J-M (2012) Dynamic behaviour and measurement accuracy of a bicycle brake hood force transducer. *Procedia Eng* 34:526–531

Chapter 30

Statistical Approach for Active Buckling Control with Uncertainty

Georg C. Enss and Roland Platz

Abstract Buckling of load-carrying column structures is an important failure scenario in light-weight structures as it may result in the collapse of the entire structure. If the actual loading is unknown, stability becomes uncertain. To investigate uncertainty, a critically loaded beam-column, subject to buckling, clamped at the base and pinned at the upper end is considered, since it is highly sensitive to small changes in loading. To control the uncertainty of failure due to buckling, active forces are applied with two piezoelectric stack actuators arranged in opposing directions near the beam-column's base to prevent it from buckling. In this paper, active buckling control is investigated experimentally. A mathematical model of the beam-column is built and a model based Linear Quadratic Regulator (LQR) is designed to stabilize the system. The controller is implemented on the experimental test setup and a statistically relevant number of experiments is conducted to prove the effect of active stabilization. It is found that the load bearing capacity of the beam-column could be increased by more than 40% for the experimental test setup using different controller parameters for three ranges of axial loading.

Keywords Buckling • Active stabilization • Control • Experimental validation • Uncertainty

30.1 Introduction

Technical load-carrying structures are designed e.g. to withstand mechanical stress. Axially loaded structures, however, may fail due to instability. When exceeding the critical compressive buckling load, a column may buckle suddenly and may lead to the collapse of the entire structure. Buckling itself as well as any measure to control buckling actively are subject to uncertainty. According to a hypothesis by the German Collaborative Research Centre SFB 805 and where this work was performed, uncertainty occurs when process properties of a system can not or only partially be determined [8]. Furthermore, uncertainty may be categorized in (a) stochastic uncertainty when probability distributions and their parameters like expected value, standard deviation etc. as well as the effects of the uncertainty are known, (b) estimated uncertainty when only limits of values as well as the effects are known and (c) unknown uncertainty when no range of values and no effects are known [4].

One of the goals of this paper is to show a consistent description of uncertainty that is present in buckling and buckling control according to the hypothesis mentioned above. To investigate uncertainty in buckling control, the authors have chosen a critically loaded beam-column that is sensitive to buckling and therefore sensitive to small changes in axial loading and disturbances e.g. when a minimal deflection out of the straight axial line occurs. This minimal deflection leading to sudden buckling may occur due to lateral disturbance forces, beam-column predeflection or material inhomogeneity etc. [11]. Modifications in geometry or material of the beam-column may improve stability but will also increase weight and the use of resources in many cases [5]. Safety relevant structures are often designed with a safety factor of up to ten against buckling [9]. However, if geometry or material may not be changed due to constraints, active stabilization may be applied

G.C. Enss (✉)

Technische Universität Darmstadt, System Reliability and Machine Acoustics SzM, Magdalenenstraße 4, 64289 Darmstadt, Germany
e-mail: enss@szm.tu-darmstadt.de

R. Platz

Fraunhofer Institute for Structural Durability and System Reliability LBF, Bartningstraße 47, 64289 Darmstadt, Germany

to prevent a failure. In this case, structures may be equipped with sensors and actuators linked by control and, hence, may feature augmented functionality like compensation of imperfections or disturbances.

In literature, several works on active buckling control are present. In most cases, moments are applied along the beam-column axis to compensate the deflection induced by beginning buckling. Beam-columns with buckling length l_{eff} , cross section area A and moment of inertia I and different slenderness ratio $s = l_{\text{eff}} \sqrt{A/I}$ are considered [11]. In [3], a predeflected beam-column of fibre reinforced composite with slenderness ratio $s = 300$ is stabilized by embedded shape memory alloy wires and an increase of the buckling load of 11% is achieved. Further works are based on applying moments along the beam-column's length with piezoelectric patch actuators bonded to its surface [1, 2] and [13]. In [1], a flat steel beam-column with $s = 4,000$ with piezoelectric stack actuators attached to its entire surface is controlled and may carry a load up to 5.6 times above the buckling load compared to the uncontrolled beam-column experimentally. Numerical studies predict an increase of the buckling load by a factor of 8.8 by controlling the first two buckling modes for a steel beam-column with slenderness ratio $s = 870$ [13]. These works are focused on the increase of the buckling load but do neither deal with imperfections or disturbances nor with uncertainty within the stabilizing technology [14]. In the publications mentioned above, actuators are attached to the entire beam-column surface which may be inconvenient when used in environment.

In this work, the actuation is limited to an area close to the beam-column's boundaries to leave most of the surface free from actuators. The authors present an approach to actively stabilize a flat beam-column with slenderness ratio $s = 725$, clamped at the base and pinned at the upper end. The active stabilization is achieved by controlling its first buckling mode with actively controlled forces applied by two piezoelectric stack actuators located close to the beam-column's clamped base in opposing direction [7]. This position justifies the usage of piezoelectric stack actuators that can apply large forces and have relatively small strain [5]. However, by implementing a real active system for buckling control, more uncertainty arises within the stabilization technology. In this paper, uncertainty due to axial loading and predeflection is controlled by active stabilization on an experimental test setup.

30.2 Stabilization Concept and System Description

The considered active system, which has been already presented in earlier works by the authors [5, 6] and [7] is a flat slender beam-column with a rectangular cross section $A = bh$, pinned at the upper end $x = l$ and clamped at the base $x = 0$, Fig. 30.1. Its properties are: length l , bending stiffness EI and density ρ . The beam-column is loaded by the time-constant axial load

$$P \approx P_{\text{cr},1} = \frac{\pi^2 EI}{(0.7l)^2}, \tag{30.1}$$

[11]. Figure 30.2 shows photographs of the real beam-column system. Due to its rectangular cross section, the beam-column buckles preferably in x - z -plane. A time-dependent and reproducible lateral impact disturbance force $F_d(t)$ may be applied at x_d , e.g. by a pendulum by hand, Fig. 30.2a. However, in this paper, it is set to zero and not regarded any further. Simultaneously, three strain gauge sensors measure the strain $\epsilon(t)$ at positions $x_{s,1}$, $x_{s,2}$ and $x_{s,3}$. Using the measured strain signals of the three sensors, a controlled lateral active force $F_a(t)$ is applied close to the beam-column's base $x_a = l/30$ if it needs to be stabilized due to axial overloads. The reason for choosing position x_a for the active force is to keep most of the surface of the beam-column free from additional actuators even if higher active forces are needed, Fig. 30.2c. At x_a ,

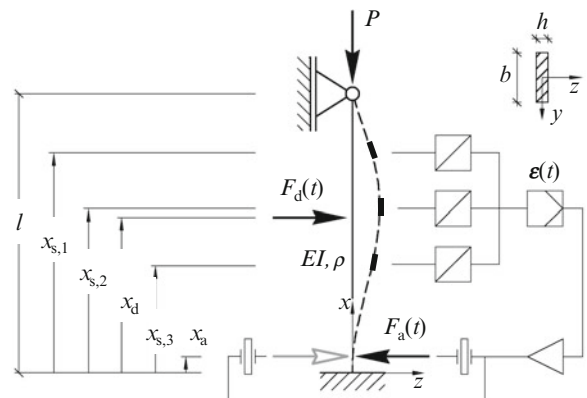


Fig. 30.1 Mechanical sketch of active beam-column system

Fig. 30.2 Real active beam-column system: (a) overview, (b) detail of pinned support and limit stop device and (c) detail of piezoelectric stack actuators near the base

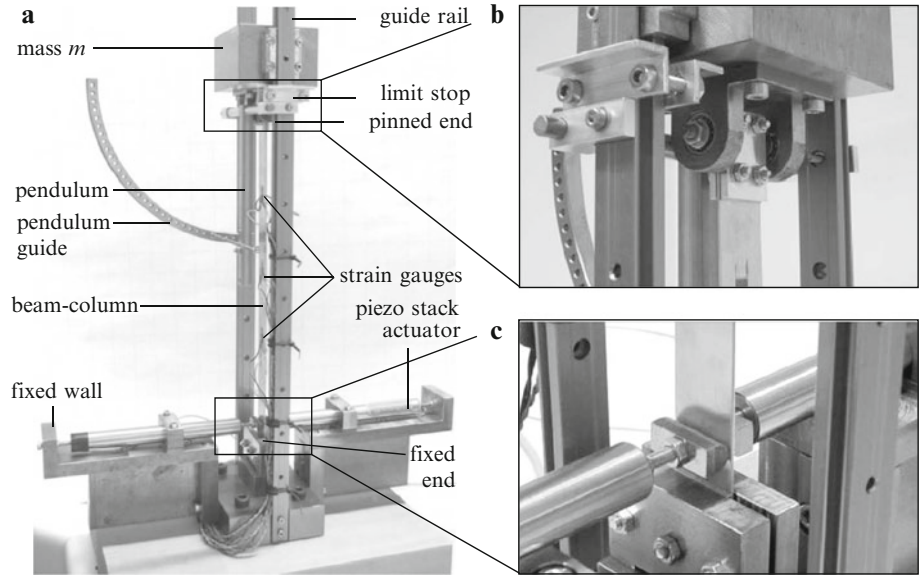


Table 30.1 Properties of the active beam-column system

Geometrical properties	Material properties (AlMg ³)	Boundary conditions/mechanical properties
$l = 305 \text{ mm}$	$E = 70 \text{ kN/mm}^2$	Pinned end at $x = l$
$b = 20 \text{ mm}$	$\rho = 2,660 \text{ kg/m}^3$	Clamped base at $x = 0$
$h = 1.04 \text{ mm}$	–	P constant in x -direction at $x = l$
$x_a = 10 \text{ mm}$	–	$F_a(t)$ controlled force in z -direction at x_a
$x_d = 150 \text{ mm}$	–	$F_d(t)$ pulse force in z -direction at x_d
$x_{s,1} = 232 \text{ mm}$	–	Strain at sensor positions $x_{s,1}$, $x_{s,2}$ and $x_{s,3}$
$x_{s,2} = 168 \text{ mm}$	–	–
$x_{s,3} = 100 \text{ mm}$	–	–

deflections are small and active control forces become relatively high, favouring the use of piezoelectric stack actuators for active stabilization. This location is reasonable for the chosen restrictions and boundary conditions. The pinned end of the beam-column is featured with a limit stop device to prevent it from buckling entirely and deforming its material plastically, Fig. 30.2b. The properties of the beam-column system presented in Figs. 30.1 and 30.2 are summarized in Table 30.1. For the given properties, Eq. (30.1) yields the individual buckling load $\tilde{P}_{cr,1} = 28.42 \text{ N}$, for the shortened buckling length $l-x_a$ due to prestressed actuators, it becomes $P_{cr,1} = 30.37 \text{ N}$.

In former investigations by the authors, a signal based control approach and a model based robust control approach for a mathematical model of the beam-column system with constant axial loading have been implemented [5]. Though, the beam-column's properties like stiffness and angular eigenfrequencies change considerably with varying axial loading. In this work, a mathematical model of the postcritically loaded system depending on the varying axial load is used for controller design. A state feedback controller is implemented to stabilize the postcritically loaded beam-column. Different controller parameters and, hence, deflection and velocity proportional feedback gains are shown for the experimental investigations to find the specific limit load the real actively stabilized beam-column system can carry and to find the boundaries of the controller parameters in which stabilization is achieved.

30.3 Mathematical Modelling

The slender beam-column presented in the previous section is modeled with the EULER-BERNOULLI beam equation extended by a term for axial loading P with constant mass distribution ρA , constant bending stiffness EI , deflection in z -direction $w(x, t)$ and external distributed load $f(x, t)$, [12],

$$\rho A \ddot{w}(x, t) + EI w^{IV}(x, t) + P w''(x, t) = f(x, t). \quad (30.2)$$

Solving (30.2) and considering the clamped/pinned boundary conditions leads to the characteristic equation

$$\tan \lambda_n l = \lambda_n l \quad (30.3)$$

that yields eigenvalues $\lambda_n, n = 1, 2, \dots, N$. The critical buckling loads of this beam-column can be expressed in dependence of its eigenvalues as

$$P_{cr,n} = \lambda_n^2 EI. \quad (30.4)$$

Each eigenvalue λ_n corresponds to one lateral eigenvector or mode shape $\phi_n(x)$ in z -direction along x [12]. Thus, the beam-column loaded with its first critical buckling load $P_{cr,1}$ will buckle in its first mode shape $\phi_1(x)$, etc. [11]. Naturally, the angular eigenfrequencies $\omega_n(P)$ depend on the axial load P acting on the beam-column and become

$$\omega_n(P) = \omega_{n,0} \cdot \sqrt{1 - \frac{P}{P_{cr,n}}}. \quad (30.5)$$

30.3.1 Continuous-Time Linear State Space Model of the Active Beam-Column System

For $P = P_{cr,1}$, the first angular eigenfrequency ω_1 vanishes and the beam-column may not vibrate in its first bending mode any more but may buckle instead. To describe the system's postcritical dynamic behaviour, also modal damping θ_n needs to be taken into account that was determined experimentally for the considered real system in [6]. For control purposes, a continuous-time linear state space representation of the previously described active beam-column system is built, considering $N = 3$ modes, [12],

$$\dot{\mathbf{q}}(t) = \mathbf{A}(P)\mathbf{q}(t) + \mathbf{b}u(t), \quad (30.6)$$

$$\mathbf{y}(t) = \mathbf{C}\mathbf{q}(t), \quad (30.7)$$

with $[6 \times 1]$ modal state vector $\mathbf{q}(t) = [\dot{q}_1(t), q_1(t), \dot{q}_2(t), q_2(t), \dot{q}_3(t), q_3(t)]^T$ with velocity and displacement of the first three modes, $[1 \times 1]$ input lateral force $u(t) = F_a(t)$ and $[3 \times 1]$ output strain vector $\mathbf{y}(t) = \boldsymbol{\varepsilon}(t) = [\varepsilon(x_{s,1}, t), \varepsilon(x_{s,2}, t), \varepsilon(x_{s,3}, t)]^T$ at the sensor positions $x_{s,1}$, $x_{s,2}$ and $x_{s,3}$. The $[6 \times 6]$ state matrix $\mathbf{A}(P)$ depends on axial load P and can be written as

$$\mathbf{A}(P) = \begin{bmatrix} -2\theta_1\omega_1(P) & -\omega_1^2(P) & 0 & 0 & 0 & 0 \\ 1 & 0 & 0 & 0 & 0 & 0 \\ 0 & 0 & -2\theta_2\omega_2(P) & -\omega_2^2(P) & 0 & 0 \\ 0 & 0 & 1 & 0 & 0 & 0 \\ 0 & 0 & 0 & 0 & -2\theta_3\omega_3(P) & -\omega_3^2(P) \\ 0 & 0 & 0 & 0 & 1 & 0 \end{bmatrix}. \quad (30.8)$$

The $[6 \times 1]$ input matrix \mathbf{b} is composed of the mode shapes $\phi_n(x_a)$ at the position of the active force x_a and the $[3 \times 6]$ output matrix \mathbf{C} can be expressed with second derivative of the mode shapes $\phi_n''(x_{s,n})$ at the three sensor positions $x_{s,1}$, $x_{s,2}$ and $x_{s,3}$ that represent strain on the surface of the beam-column at distance $h/2$ from its neutral axis. They can be written as

$$\mathbf{b} = \frac{1}{\rho A \ell} \begin{bmatrix} \phi_1(x_a) \\ 0 \\ \phi_2(x_a) \\ 0 \\ \phi_3(x_a) \\ 0 \end{bmatrix} \quad \text{and} \quad \mathbf{C} = \frac{h}{2} \begin{bmatrix} 0 & \phi_1''(x_{s,1}) & 0 & \phi_2''(x_{s,1}) & 0 & \phi_3''(x_{s,1}) \\ 0 & \phi_1''(x_{s,2}) & 0 & \phi_2''(x_{s,2}) & 0 & \phi_3''(x_{s,2}) \\ 0 & \phi_1''(x_{s,3}) & 0 & \phi_2''(x_{s,3}) & 0 & \phi_3''(x_{s,3}) \end{bmatrix}. \quad (30.9)$$

Table 30.2 Controller parameters used for active stabilization against buckling

	Controller parameter	Stabilization range	
	α	P_{\min}	P_{\max}
Controller 1	$300 \cdot 10^9$	23.5 N	34.5 N
Controller 2	$2500 \cdot 10^9$	34.5 N	38.5 N
Controller 3	$3000 \cdot 10^9$	38.5 N	40.5 N

30.3.2 Modal State Feedback Control with Linear Quadratic Regulator

To close the control loop, a modal state feedback control is implemented with

$$u(t) = F_a(t) = -\mathbf{K}_{\text{LQR}} \mathbf{q}(t), \quad (30.10)$$

such that the velocity and deflection of the first $N = 3$ modes are controlled. To determine the $[1 \times 6]$ feedback gain \mathbf{K}_{LQR} , a Linear Quadratic Regulator (LQR) is designed minimizing the quadratic cost function

$$J = \int_0^{\infty} \mathbf{q}(t)^T \mathbf{Q} \mathbf{q}(t) + u(t)^T R u(t) dt \quad \text{with} \quad \mathbf{Q} = \alpha \mathbf{C}^T \mathbf{C} \quad \text{and} \quad R = 1, \quad (30.11)$$

[10]. Herein, the ratio between \mathbf{Q} and R may be adjusted by the controller parameter α . The larger α , the more emphasis is placed by the controller on returning $\mathbf{q}(t)$ to zero. The smaller α , the less control effort $u(t)$ is allowed which leads to increasing $\mathbf{q}(t)$. \mathbf{K}_{LQR} is given by

$$\mathbf{K}_{\text{LQR}} = \mathbf{R}^{-1} \mathbf{b}^T \mathbf{P}, \quad (30.12)$$

[10], finding the auxiliary matrix \mathbf{P} from the solution of the algebraic Riccati equation

$$\mathbf{A}(P)^T \mathbf{P} + \mathbf{P} \mathbf{A}(P) - \mathbf{P} \mathbf{b} \mathbf{R}^{-1} \mathbf{b}^T \mathbf{P} = -\mathbf{Q}, \quad (30.13)$$

with $\mathbf{A}(P)$ and \mathbf{b} from Eq. (30.7) and \mathbf{Q} and R from Eq. (30.11) [10] and [13]. Due to the axial load P , the system matrix $\mathbf{A}(P)$ changes significantly, thus, different controller feedback gains \mathbf{K}_{LQR} are designed for three ranges of axial loads to guarantee stability of the postcritically loaded actively controlled beam-column system, Table 30.2.

30.4 Experimental Results

Experimental simulations are carried out as follows. First, both mechanically prestressed actuators are additionally electrically prestressed with $U = 75$ V that is half of the actuator's maximum voltage $U_{\max} = 150$ V. Thus, they can be operated from 0 to 150 V and each actuator can expand and contract from the original prestressed position such that it does not work against its counterpart. Once the prestress is established, the strain gauge sensors are calibrated to show zero signal for the straight beam-column. Therefore, the beam-column is pulled manually to be straightened and a zero point adjustment is carried out. At each sensor position, two strain gauge sensors are applied and connected as a Wheatstone bridge circuit with two resistors. With this measurement configuration, only strain due to bending is measured but strain due to tension or compression is compensated.

After these preparations are finished, each experiment is carried out at a certain axial load proportional to mass m on top of the beam-column, Fig. 30.2a. The initial load of $P = 23.5$ N is increased in steps of 1 N by laying extra weight on top. Each measurement of the modal deflection has a duration of $t_m = 5$ s and its mean value is calculated to suppress the effect of measurement noise. For each axial load P , the experiment is repeated 31 times to guarantee repeatability of the measurements. Figure 30.3a shows the modal deflection q_1 of the beam-column's first - critical - buckling mode for 31 experiments for each axial load P for the uncontrolled and actively stabilized system. First, all experiments are carried out with the control switched off, shown in Fig. 30.3a as crosses (\times). However, electrical prestress is also activated in the uncontrolled system to be able to compare the results to the experiments with control. Then, all experiments are carried out with a suitable controller, shown in Fig. 30.3a as squares (\square). Furthermore, the mean value μ_{q_1} and standard deviation σ_{q_1} of each set of 31 experiments are shown, Fig. 30.3b. For comparison, the analytical buckling load $P_{\text{cr},1}$ is also plotted.

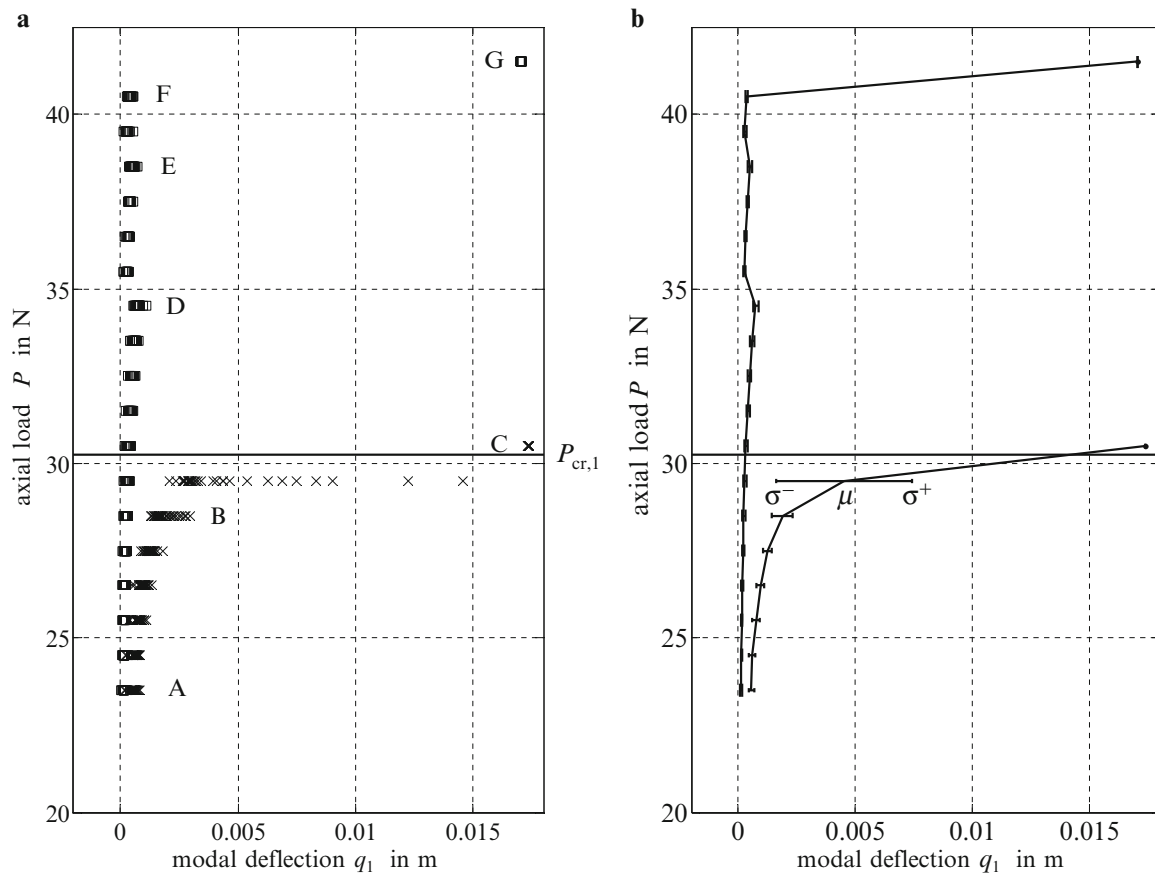


Fig. 30.3 Axial load P over modal deflection q_1 (a) for each of the 31 experiments on the uncontrolled system (\times) and actively stabilized system (\square) and (b) mean value μ_{q_1} with standard deviation σ_{q_1}

As described before, the beam-column is loaded initially with $P = 23.5$ N by mass m shown in Fig. 30.2a. Thus, the experimental data in the force deflection diagram in Fig. 30.3a starts at point A at $P = 23.5$ N. The axial load P is then increased in steps of 1 N by putting additional weight on top of mass m , Fig. 30.2. For the uncontrolled system, but with prestressed actuators, the modal deflection q_1 is finite and increases while increasing the axial load P . At $P = 28.5$ N, the uncontrolled system deflects significantly, point B. Increasing P by 1 N more, the beam-column buckles and the mass hits against a limit stop device to prevent the beam-column's plastic deformation for $P = 30.5$ N, Fig. 30.2c. For this reason, Fig. 30.3 shows no deflections larger than $q_1 = 0.017$ m and only small deviation between the 31 experiments, point C.

The controller is designed to be stable in a certain range of axial loads. By changing the controller parameters, this range may be adapted. In this experiment, a controller with three sets of parameters was designed, named controller 1, controller 2 and controller 3, Table 30.2. Using controller 1, the beam-column may be stabilized for axial loads ranging from $P = 23.5$ to 34.5 N. When reaching $P = 34.5$ N, controller 1 is switched to controller 2 that is stable in the range from $P = 34.5$ to 38.5 N, point D, Fig. 30.3a. This procedure is repeated, switching to controller 3 at $P = 38.5$ N, point E. At point F, the system is still stabilized. If the axial load is then increased to $P = 41.5$ N, the beam-column buckles immediately and stops when the mass hits the limit stop device for a deflection of $q_1 = 0.017$ m, point G.

Figure 30.3b shows that uncertainty in the beam-column's modal deflection between the 31 experiments may also be reduced by active control. The mean value of modal deflection μ_{q_1} is 4.3-16.1 times larger for different load steps for the uncontrolled system compared to the actively stabilized system. This factor increases the closer the axial load gets to the critical buckling load, i.e. the uncontrolled critical system obviously tends to have much larger deflections than the stabilized system. Furthermore, the standard deviation σ_{q_1} of the modal deflection is 3.8-48.3 times larger for the uncontrolled compared to the stabilized system. Here, σ_{q_1} also increases with increasing axial load P . When control is switched between controller 1 and controller 2 and from controller 2 to controller 3, μ_{q_1} and σ_{q_1} become smaller for a few load steps of P due to higher feedback gains and, thus, the system stays stable for postcritical axial loads. For both, the uncontrolled and the stabilized

system, only small standard deviations σ_{q1} occur, when the mass hits the limit stop device. Uncertainty may be quantified for active stabilization and described as stochastic uncertainty, Sect. 30.1.

30.5 Conclusion

In this paper, active buckling control is investigated experimentally. A Linear Quadratic Regulator (LQR) is designed and implemented on the experimental test setup and a statistically relevant number of experiments is carried out to prove the effect of active stabilization. It is found that the load bearing capacity of the beam-column could be increased by more than 40% for the experimental test setup using different controller parameters for three ranges of axial loading.

Furthermore, initial deflection of the passive beam-column for the initial axial load $P = 23.5\text{N}$ may be reduced significantly by active control. However, even with active control enabled the beam-column does not reach zero deflection. Thus, it buckles in positive x -direction when the limit load of the stabilized active beam-column system is reached. Uncertainty was reduced by the active control such that both the mean value and the standard deviation of the modal displacement of the beam-column could be reduced significantly in the experiments. The experimental data can be described as stochastic uncertainty.

These results were achieved knowing the actual axial load, i.e. the number of additional weights put on top of the beam-column. The controllers were switched manually by the operator. In future experiments, the axial load will be measured individually and, hence, the system may switch automatically between the designed controllers.

Acknowledgements The authors like to thank the German Research Foundation (DFG) for funding this research within the Collaborative Research Centre (SFB) 805. The authors also like to thank Alexander Gröninger for carrying out many of the experiments shown.

References

- Berlin AA (1994) Towards intelligent structures: active control of buckling. Ph.D. Thesis, Dept. of Electrical Eng. and Computer Science, Massachusetts Institute of Technology
- Chase JG, Yim M (1999) Optimal stabilization of column buckling. *J Eng Mech* 125(9):987–993
- Choi S, Lee JJ, Seo DC, Choi SW (1999) The active buckling control of laminated composite beams with embedded shape memory alloy wires. *Compos Struct* 47:679–86
- Engelhardt RA, Koenen JF, Enss GC, Sichau A, Platz R, Kloberdanz H, Birkhofer H, Hanselka H (2010) A model to categorise uncertainty in load-carrying systems. In: *Proc. MMEP modelling and management of engineering processes*, Cambridge, UK, pp 53–64, 2010
- Enss GC, Platz R, Hanselka H (2010) An approach to control the stability in an active load-carrying beam-column by one single piezoelectric stack actuator. In: *Proc. ISMA 2010*, Leuven, Belgium, pp 535–546, 2010
- Enss GC, Platz R, Hanselka H (2012) Mathematical modelling of postbuckling in a slender beam column for active stabilisation control with respect to uncertainty. In: *Proc. SPIE*, San Diego, CA, vol 8341, pp 834119-1–11, 2012
- Enss GC, Platz R, Hanselka H (2012) Uncertainty in loading and control of an active column critical to buckling. *Shock Vib* 19:929–937
- Hanselka H, Platz R (2010) Ansätze und Maßnahmen zur Beherrschung von Unsicherheit in lasttragenden Systemen des Maschinenbaus - Controlling uncertainty in load-carrying systems. *Konstruktion* 11/12:55–62
- ISO/TS 13725 (2001) Hydraulic fluid power cylinders - method for determining buckling load, 2001
- Skogestad S, Postlethwaite I (2005) *Multivariable feedback control: analysis and design*. Wiley, New York
- Timoshenko SP, Gere JM (1961) *Theory of elastic stability*. McGraw-Hill, New York
- Virgin LN (2007) *Vibration of axially loaded structures*. Cambridge University Press, New York
- Wang QS (2010) Active buckling control of beams using piezoelectric actuators and strain gauge sensors. *Smart Mater Struct* 19:065022
- Wang Q, Wu N (2012) A review on structural enhancement and repair using piezoelectric materials and shape memory alloys. *Smart Mater Struct* 21:013001

Chapter 31

An Overview of the Technology, History, and Application of Vibro-Acoustic Coupling

Kurt G. Schneider

Abstract Vibro-acoustically coupled systems represent a wide ranging field that extends from very simple systems to the very complex. A number of tools and techniques have been used over the years to investigate and understand vibro-acoustic phenomena. Presented here will be a brief overview of what constitutes the field of vibro-acoustics, as well as the mathematics that are commonly used to solve these problems with the latest computational methods. In particular, a basic look at the coupling of structures and fluids will be presented. Next, an overview of various engineering applications will be reviewed showing the depth and breadth of the application of these tools and techniques. Finally, an overview of the current technical challenges with the tools will be given.

Keywords Structure-acoustic • Structure-borne noise • Acoustic coupling • FEA • Boom noise

31.1 Definition of Vibro-Acoustic Coupling

A precise definition of vibro-acoustic coupling may be quite difficult to achieve. This is because in nearly all practical cases, the waves traveling through a fluid (acoustic) have a source in the motion of a solid object (vibration). As such, solids and fluids are constantly interacting. The key to the term may not be the vibro-acoustic part, but rather the coupling part.

Coupling is an engineering term that also lacks strict definition. Often it is described as being when two systems are joined together, and the dynamics of each individual system affect the dynamics of the systems they are joined to. This is a familiar phenomenon to those that have studied vibrations in complex systems. This is often described in the context of a mobility mismatch between components. Such a mobility mismatch can be seen in Fig. 31.1. In this example, the learned practitioner of noise and vibration engineering will clearly expect a resonance of the assembled blue and purple systems to appear at about 200 Hz but no interactions would occur between blue and green until about 300 Hz. This same interaction of systems can happen between fluids and structures. When this occurs, the dynamics of the fluid and the dynamics of the structure are changed by the presence of the other.

31.2 Applications

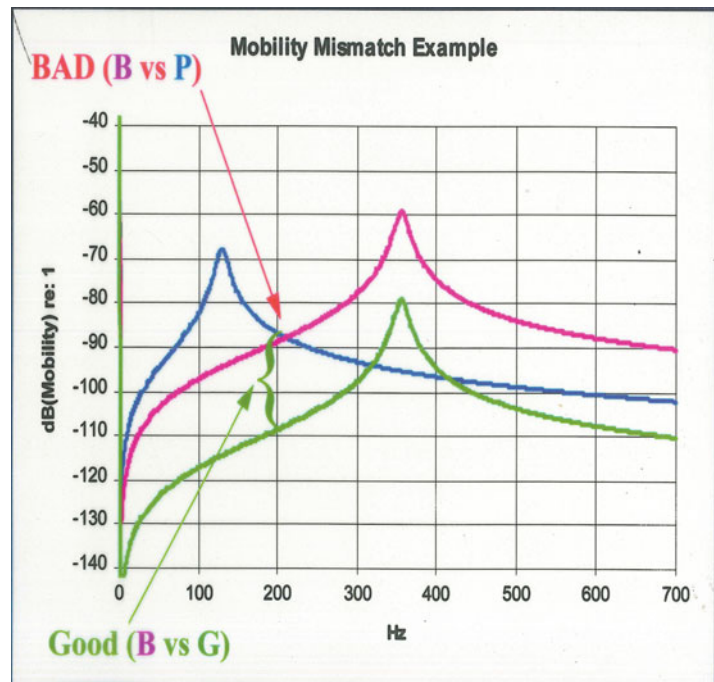
The application of structure-acoustic coupling ranges many functions. These include naval, aerospace, automotive, and petrochemical, as well as many others. However, in this paper, the focus will be on the automotive industry, its usages, and history, and the particular challenges present in those application.

For nearly all automotive applications of these tools, there are fundamentally only two basic phenomena being addressed. Either the source of the energy input is from the powertrain and related components, or from the road. In all cases, the basic phenomena are the same. Energy is introduced into the structure of the system. The energy travels through the structure.

K.G. Schneider (✉)

Engineering Group, General Motors, 30001, Van Dyke Avenue, Warren, MI 48090-9020, USA
e-mail: kurt.schneider@gm.com

Fig. 31.1 Example of a coupled system



There are isolating elements introduced along those paths of energy flow, and eventually, the energy finds its way to the body. Once at the body structure, the energy is radiated in the form of acoustic energy. This acoustic energy is attenuated with various noise control treatments in the form of soft trim or air leaks.

There are many points along this path where classic coupled dynamics may be occurring. The most basic ones are anywhere there are bolted joints. So, for example, at the interface of the cradle to the body structure, there is typically a bolted joint that may have a rubber isolator. Depending on frequency range, the dynamics of the cradle and the body may be highly coupled.

These types of structural coupling situations have been studied quite extensively in other papers and forums. The coupling of interest here is the structure-acoustic coupling. This typically happens between the body panels and the interior acoustic cavity. There are some well documented cases of the closures of the vehicle (e.g. doors) interacting with the acoustic cavity, as well as some cases of noise being radiated off components on the exterior of the vehicle which couple with the vehicle body structure through the air gap between the two.

31.3 History

The true history of structure-acoustic coupling may be quite old. It is referenced in some aspects as long ago as Rayleigh's *The Theory of Sound* (1877). However, with a much more automotive view of the problem, discussion and application of issues dates back at least to at least the mid 1970s, and quite likely much earlier than that.

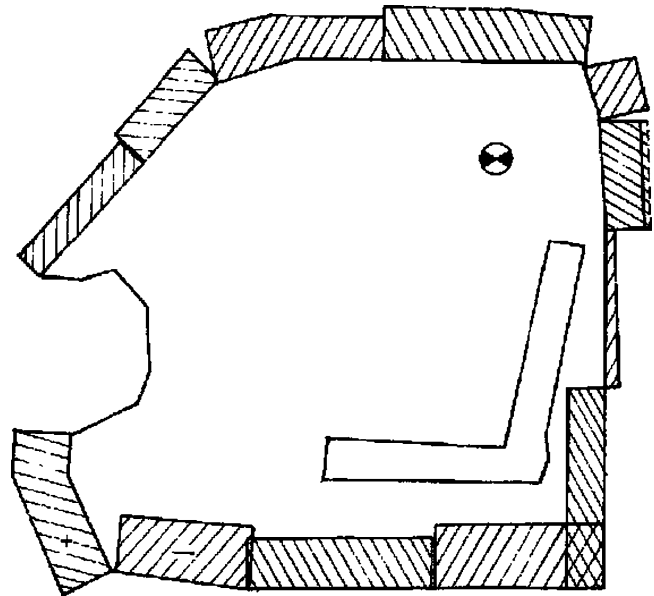
In an internal General Motors report, Smith [1], investigates the boom noise of a station wagon style vehicle. Among the conclusions of this work are these.

1. Using a simple tube model of the interior cavity of the vehicle, the first and second resonances of the vehicle cavity could be predicted accurately as compared to tests conducted on the vehicle
2. By introducing a small opening in the rear closure, the resonance of the cavity could be shifted quite substantially

The second conclusion appears at first glance to be simply a change in acoustic boundary condition, however, subsequent studies of similar phenomena have suggested a stronger coupling effect between the structure and the fluid.

In another internal GM paper dating from 1981, Sung [2] investigates the acoustic behavior of a truck cab. In this paper, she notes:

Fig. 31.2 Acoustic contribution plot from Sung [2]. *Thickness* indicates relative contribution at a given frequency



Depending on which part of the back panel is moving, the sound pressures show a phase change. Therefore, if the back panel vibrates with a particular mode shape which couples efficiently with the acoustic mode, the corresponding noise level at the driver's ear position would be significantly increased [2].

That observation demonstrates the degree to which the dynamics of the structure, and the dynamics of the acoustic cavity can interact.

In this paper, Sung also implements an early form of panel participation. She divides the truck cab into multiple panels. Then she individually excites the cavity with pistons of the same size and location at each panel. She then plots the individual responses due to normalized inputs to show how sensitive the response in the cavity is to the excitation at each panel. The plot from Sung, recreated in Fig. 31.2, shows how she related the relative contribution of each panel to the interior noise based on the piston input to the cavity.

In 1984, Sung and Nefske published a paper that outlined in great detail the mainstream method used for structural-acoustic finite element analysis [3]. This paper included what in the present paper will be referred to as the weakly coupled structural acoustic method (from Everstine [4]), along with the basic calculations for panel participation that accounted for panel flexibility. This method has been in use by many mainstream FEA solvers for many years. In Everstine's method, mathematical manipulations of the matrices are introduced to produce a symmetric set of mass, stiffness, and damping matrices. In this case, the coupling terms between structure and fluid are moved from the asymmetric mass and stiffness terms to a symmetric damping term. The process facilitates solving the problem in a weakly coupled fashion.

1. Solve the eigenvalue problem for the structure
2. Solve for eigenvalue problem of the fluid
3. Use the combined structure and fluid mode shapes to project the fully coupled damping matrix (including structure-acoustic coupling terms) into the same space as the structure and fluid modes.
4. Execute a forced response on this smaller, but coupled problem in the modal domain
5. Project the modal responses back to the physical domain

This process allowed for the calculation of the response of the fluid due to higher order motion of the structure, as well as motion of the structure due to motion of the fluid. Further, the data could be post processed in a way such that the engineer could understand what panels in the vehicle were the major constructive or destructive contributors to the noise. This, coupled with basic mode participation, offered a great opportunity to the engineer to understand the physics of the noise heard in the vehicle.

It should be noted that Ohayon [5] developed a strongly coupled version of the equations that allowed for solving for the structure and fluid as one system rather than two separate systems. (His paper roughly outlines the process with a bit more detailed presented in the Abaqus Theory Manual.)

In 2006, two papers were written formulating a model reduction technique to be applied to structural acoustic problems. The first, by Schneider et al. [6], made an extension to the classic Craig-Bampton method of model reduction. In this method, the structure and acoustic formulation from the weakly coupled formulation by Everstine is used. The same concepts of

Table 31.1 Comparison of run times for a Craig–Bampton reduced structure acoustic model (500 k DOFs) from Schneider et al.

Run type	Number of structure modes	Number of acoustic modes	Model reduction wall clock time (min)	Results run wall clock time (min)
Super element (direct solution)	N/A	N/A	96.53	1.17
Super element (modal solution)	417 (200 Hz + residuals)	63 (400 Hz + residuals)	96.53	1.28
Full shot (direct solution)	N/A	N/A	N/A	1,471.35
Full shot (modal solution)	423 (200 Hz + residuals)	61 (400 Hz)	N/A	102.45

constrained modes and constraint shapes used for structural formulations are applied independently to the fluid and the structure in order to reduce the model size. As can be seen from the table in their paper (Table 31.1), significant reductions in solution time could be realized for relatively large scale models.

In a similar way, Maess and Gaul [7] presented an alternate way to achieve a similar result. In this case, the asymmetric problem is addressed rather than Everstine’s symmetric formulation. The asymmetric formulation is reduced in a methods similar to the classic Craig and Bampton methods, but it is applied to fluid filled pipes. They present two formulations: One uses the same reduction vectors on both sides of the problem; the other uses different reduction vectors on the left and on the right. Their one-sided method, using the same reduction vectors on the left and the right, is similar to Schneider’s method, however it is applied to the fully asymmetric problem rather than the symmetric formulation of Everstine. Their two-sided method using different left and right eigenvectors, allows them to use model truncation vectors and pseudo eigenvectors to augment the problem. They demonstrated improved correlation with fewer modes than with the one-sided formulation.

31.4 Solution Methods

Already, several solution techniques have been mentioned which allow for the analysis of a design. All of those mentioned so far have been based in finite element analysis. There are several other techniques that could be used.

Boundary Element Analysis (BEM) has been used in some cases, but until the recent implementation of Fast Multi-Pole techniques, run times were not competitive for a large frequency range. Further, these techniques have not offered the ease of design diagnostics, such as the calculation of natural frequencies. Therefore, for interior acoustic problems, they have not been favored.

Extensions to the finite element method, such as infinite elements and perfectly matched layer (PML) techniques have been implemented, however, these are more suited to the exterior acoustics problem. Certainly there are plenty of exterior coupled structure-acoustic problems in engineering. However, within the automotive industry, they have not been studied or published as much as the interior problems.

Finally, higher frequency techniques such as energy finite element analysis [8], structural SEA, and coupled FEA/SEA [9] formulations have been implemented. These techniques are focused largely on the so-called mid-frequency domain. In this domain, the dynamics of the system are in transition between low modal density where discrete natural frequencies and mode shapes dominate, and the high frequency region where the problem is inherently statistical. Noises in this mid-frequency range are certainly part of a coupled structure-acoustic problem, but are outside of the scope of this paper.

31.5 Survey of Example’s

Although, as noted, coupled structure-acoustic problems exist in other engineering fields (naval [10] or petro-chemical for example [11]), this section will give a brief overview of some examples of structure-acoustic coupling in the automotive industry that have previously been published.

System coupling is an issue that dominates in the automotive industry. The common automobile has many subsystems that must interact with each other. As they interact, they can, and often do, cause coupled structure-acoustic problems. Bijwe et al. [12] investigated one such problem. In their paper, an in-cabin “boom” issue was to be diagnosed. (Boom, in the automotive industry, references a relatively pure tone noise below about 100 Hz. These noises, being at such low frequencies, can be very disturbing to the passengers and are often felt as a vibration as much as heard.) In this particular paper, the fully trimmed body exhibited a mode which coupled with the driveline. Along with these driveline modes and structure modes, there was also a sympathetic acoustic cavity mode. These three things, all aligning properly, led to a high amplitude acoustic response

at about 43 Hz. By studying the entire, coupled, structure-acoustic system, they were able to mitigate the noise concern by changing bushing stiffnesses. As a result, the coupling between the driveline and body was changed, and hence the noise was changed.

Tonge and Agrawal [13], investigated a classic, and contemporary issue in automotive design. They highlight an inherent conflict in automotive body structure development. Their focus was on the open plenum design which is becoming more common in automobiles. This open section design is used to enable the safety of pedestrians in pedestrian-vehicle collisions. However, this weakening of the structure which is good for pedestrian protection, is often not good for the boom noise of the vehicle. In this paper, a panel contribution analysis (per Sung and Nefske [3]) indicated that the windshield was the major contributor to the noise issues. In this paper, structural changes are implemented which increase the stiffness of the support structure of the windshield in an effort to change the coupling between the acoustics and the structure.

It is interesting to note that Tonge and Agrawal point out that the cavity modes predicted from a finite element analysis using the weakly coupled formulation will not match test because of the difference in boundary conditions. This comment lends itself to a suggestion that Ohayon's strongly coupled formulation may be more useful to the engineer in that the fully coupled modes are generated. These fully coupled modes are more easily compared to test.

31.6 Current and Future Trends

Due to the increased pressure on the mass of automobiles, and increasing challenges to meet customer requirements, the use of tools such as active noise control are becoming more common in the industry. With tools like active noise control, low frequency noise issues can be mitigated without structural changes. This can allow for lower mass solutions that can be fine-tuned late in the development cycle with minimal, if any, tooling costs. Active noise cancellation does introduce its own set of complications. In particular, there are frequency range issues, and controller development and calibration issues.

In 1993, Elliott and Nelson [14], give a thorough review of the history and state of the art for active noise cancellation. The principles outlined in their paper have not changed significantly since the publication of their work. In their work, they demonstrate a clear application of active noise cancellation to automobiles. They demonstrate a reduction of up to 20 dB (and in some small bands more) in the engine firing order related noise in the interior of the vehicle. Similarly architected systems were in production at least as early as the 2005 Acura RL, and are currently in production in such vehicles as the Chevrolet Equinox. There have been a number of efforts to adapt and adjust the process of implementing these technologies (i.e. [15, 16]). However, many of the fundamental limitations outlined by Elliott and Nelson (such as maximum frequency) still exist, and have not yet been conquered.

Finally, as computational capability continues to scale with Moore's law, the ability to introduce more and more complexity increases. As can be seen from the discussion above, original simulation techniques looked at the cavity as a single entity, which was excited by pistons. Then a weakly coupled FEA technique was introduced. Later, a strongly coupled FEA technique was introduced that allowed for the computation of the coupled structure acoustic modes. In all of these techniques, the soft trim is either ignored, or modeled in a simplistic way as mass and damping. However, it is now becoming practical to introduce poro-elastic models of the soft trim. With these models, the specific mass, stiffness, and damping of the soft acoustics can be modeled in the boundary between the structure and the acoustics further refining the exact coupling that is present.

Bertolini et al. [17] demonstrate some early attempts at modeling the soft trim in detail. Although this paper demonstrates only the structural response of part of the system, it shows the potential for these analysis tools to be used in the future for large scale simulations. As noted by Bertolini, being able to model these trim effects are essential to developing an ability to model coupled structure-acoustic problems to higher frequencies. Duval et al. [18] demonstrate clearly how these techniques can be extended to more complex systems by applying them to the dash and floor trim of a vehicle. The idea of a full vehicle coupled structure-acoustic model, with full poro-elastic representation of the soft trim is within reach.

31.7 Conclusions

Over many decades the knowledge and tool sets for understanding and addressing coupled structure acoustic phenomena have been evolving and growing. From the early stages of simple tube models to the present day inclusion of strongly coupled acoustics and structure, it can be seen how far the technology has advanced. When looking to the future, it is clear

that much more is needed to continue to advance the state of the art. Current trends toward inclusion of poro-elastics, along with the use of advanced active noise cancellation offer a view of the near future, as well as where the technical challenges reside.

A.1 Appendix

A.1.1 Weakly Coupled Structure Acoustic Method

The process (based on Everstine) for the weakly coupled structure-acoustic method starts with the basic matrix equation.

$$\begin{bmatrix} m_s & 0 \\ -A^T & m_f \end{bmatrix} \begin{Bmatrix} \ddot{x} \\ \ddot{p} \end{Bmatrix} + \begin{bmatrix} b_s & 0 \\ 0 & b_f \end{bmatrix} \begin{Bmatrix} \dot{x} \\ \dot{p} \end{Bmatrix} + \begin{bmatrix} k_s & A \\ 0 & k_f \end{bmatrix} \begin{Bmatrix} x \\ p \end{Bmatrix} = \begin{Bmatrix} F \\ -\dot{Q} \end{Bmatrix} \quad (31.1)$$

Equation (31.1) shows the mass (m), damping (b), and stiffness (k) for the structure (subscript s) and fluid (subscript f). Along with this are the structural forces (F) the acoustic input (Q), and the structure-acoustic coupling term (A). As can be seen quite quickly, this is an asymmetric problem, and therefore does not lend itself to quick and easy analysis. However, by making a simple coordinate change, the problem can be made symmetric.

$$p = j\omega\phi \quad (31.2)$$

$$\begin{bmatrix} m_s & 0 \\ A^T & m_f \end{bmatrix} \begin{Bmatrix} \ddot{x} \\ j\omega\ddot{\phi} \end{Bmatrix} + \begin{bmatrix} b_s & 0 \\ 0 & b_f \end{bmatrix} \begin{Bmatrix} \dot{x} \\ j\omega\dot{\phi} \end{Bmatrix} + \begin{bmatrix} k_s & A \\ 0 & k_f \end{bmatrix} \begin{Bmatrix} x \\ j\omega\phi \end{Bmatrix} = \begin{Bmatrix} F \\ -\dot{Q} \end{Bmatrix} \quad (31.3)$$

$$\begin{bmatrix} m_s & 0 \\ A^T & j\omega m_f \end{bmatrix} \begin{Bmatrix} \ddot{x} \\ \ddot{\phi} \end{Bmatrix} + \begin{bmatrix} b_s & 0 \\ 0 & j\omega b_f \end{bmatrix} \begin{Bmatrix} \dot{x} \\ \dot{\phi} \end{Bmatrix} + \begin{bmatrix} k_s & j\omega A \\ 0 & j\omega k_f \end{bmatrix} \begin{Bmatrix} x \\ \phi \end{Bmatrix} = \begin{Bmatrix} F \\ -\dot{Q} \end{Bmatrix} \quad (31.4)$$

$$\begin{bmatrix} m_s & 0 \\ \frac{1}{j\omega} A^T & m_f \end{bmatrix} \begin{Bmatrix} \ddot{x} \\ \ddot{\phi} \end{Bmatrix} + \begin{bmatrix} b_s & 0 \\ 0 & b_f \end{bmatrix} \begin{Bmatrix} \dot{x} \\ \dot{\phi} \end{Bmatrix} + \begin{bmatrix} k_s & j\omega A \\ 0 & k_f \end{bmatrix} \begin{Bmatrix} x \\ \phi \end{Bmatrix} = \begin{Bmatrix} F \\ -\frac{1}{j\omega} \dot{Q} \end{Bmatrix} \quad (31.5)$$

$$\begin{bmatrix} m_s & 0 \\ 0 & m_f \end{bmatrix} \begin{Bmatrix} \ddot{x} \\ \ddot{\phi} \end{Bmatrix} + \begin{bmatrix} b_s & A \\ A^T & b_f \end{bmatrix} \begin{Bmatrix} \dot{x} \\ \dot{\phi} \end{Bmatrix} + \begin{bmatrix} k_s & 0 \\ 0 & k_f \end{bmatrix} \begin{Bmatrix} x \\ \phi \end{Bmatrix} = \begin{Bmatrix} F \\ Q \end{Bmatrix} \quad (31.6)$$

Now, with Eq. (31.6), the problem is symmetric. Further, the acoustics and the structure are uncoupled in mass and stiffness. This leads to two separate eigenvalue problems.

$$[k_s][u_s] = [m_s][u_s][\lambda_s] \quad (31.7)$$

$$[k_f][u_f] = [m_f][u_f][\lambda_f] \quad (31.8)$$

These two eigenvalue problems are solved, and then used to reduce Eq. (31.6).

$$\begin{bmatrix} u_s & 0 \\ 0 & u_f \end{bmatrix}^T \begin{bmatrix} m_s & 0 \\ 0 & m_f \end{bmatrix} \begin{bmatrix} u_s & 0 \\ 0 & u_f \end{bmatrix} = \begin{bmatrix} I & 0 \\ 0 & I \end{bmatrix} = [\tilde{M}] \quad (31.9)$$

$$\begin{bmatrix} u_s & 0 \\ 0 & u_f \end{bmatrix}^T \begin{bmatrix} k_s & 0 \\ 0 & k_f \end{bmatrix} \begin{bmatrix} u_s & 0 \\ 0 & u_f \end{bmatrix} = \begin{bmatrix} \lambda_s & 0 \\ 0 & \lambda_f \end{bmatrix} = [\tilde{K}] \quad (31.10)$$

$$\begin{bmatrix} u_s & 0 \\ 0 & u_f \end{bmatrix}^T \begin{bmatrix} b_s & A \\ A^T & b_f \end{bmatrix} \begin{bmatrix} u_s & 0 \\ 0 & u_f \end{bmatrix} = [\tilde{B}] \quad (31.11)$$

$$\begin{Bmatrix} x \\ \phi \end{Bmatrix} = \begin{bmatrix} u_s & 0 \\ 0 & u_f \end{bmatrix} \{q\} \quad (31.12)$$

$$[\tilde{M}] \{\ddot{q}\} + [\tilde{B}] \{\dot{q}\} + [\tilde{K}] \{q\} = \begin{bmatrix} u_s & 0 \\ 0 & u_f \end{bmatrix}^T \begin{Bmatrix} F \\ Q \end{Bmatrix} \quad (31.13)$$

After these reductions are executed, a simple forced response can be conducted to calculate the response of the system.

A.1.2 Strongly Coupled Solution

The process, based on Ohayon (from the Abaqus Theory Manual), again starts with Eq. (31.1) above.

Now a coordinate transform is introduced.

$$\psi = \frac{p}{\omega^2} \quad (31.14)$$

With this transform, the second equation in the matrices of Eq. (31.1) can be manipulated. First, the damping terms are ignored; then the coordinate transform is applied.

$$\begin{bmatrix} m_s & 0 \\ -A^T & m_f \end{bmatrix} \begin{Bmatrix} \ddot{x} \\ \ddot{p} \end{Bmatrix} + \begin{bmatrix} b_s & 0 \\ 0 & b_f \end{bmatrix} \begin{Bmatrix} \dot{x} \\ \dot{p} \end{Bmatrix} + \begin{bmatrix} k_s & A \\ 0 & k_f \end{bmatrix} \begin{Bmatrix} x \\ p \end{Bmatrix} = \begin{Bmatrix} F \\ -\dot{Q} \end{Bmatrix}$$

$$\omega^2 A^T x - \omega^2 m_f p + k_f p = -j\omega Q \quad (31.15)$$

$$A^T x - m_f p + k_f \frac{p}{\omega^2} = \frac{Q}{j\omega} \quad (31.16)$$

$$A^T x - m_f p + k_f \psi = \frac{Q}{j\omega} \quad (31.17)$$

Once the coordinate transform is introduced the matrices from Eq. (31.1) are rewritten, again without damping.

$$\begin{bmatrix} m_s & 0 & 0 \\ 0 & 0 & 0 \\ 0 & 0 & k_f^T \end{bmatrix} \begin{Bmatrix} \ddot{x} \\ \ddot{p} \\ \ddot{\psi} \end{Bmatrix} + \begin{bmatrix} k_s & A & 0 \\ A^T & -m_f & k_f \\ 0 & k_f^T & 0 \end{bmatrix} \begin{Bmatrix} x \\ p \\ \psi \end{Bmatrix} = \begin{Bmatrix} F \\ \frac{Q}{j\omega} \\ 0 \end{Bmatrix} \quad (31.18)$$

This set of matrices are now symmetric. The matrices are increased in order, but they will generate real eigenvectors and eigenvalues. By removing the right hand side of the equation, this will form a classic eigenvalue problem.

$$\begin{bmatrix} k_s & A & 0 \\ A^T & -m_f & k_f \\ 0 & k_f^T & 0 \end{bmatrix} [U] = \begin{bmatrix} m_s & 0 & 0 \\ 0 & 0 & 0 \\ 0 & 0 & k_f^T \end{bmatrix} [U] [\lambda] \quad (31.19)$$

References

1. Smith DL (1975) Acoustic cavity resonance in an automobile passenger compartment. Internal General Motors Publication #FD-81, July 1975
2. Sung SH (1981) Acoustic analysis of a GMC truck cab. Internal General Motors Publication #EM-523, October 1981
3. Sung SH, Nefske DJ (1984) A coupled structural-acoustic finite element model for vehicle interior noise analysis. *J Vib Acoust Stress Reliab* 106(2):314–318
4. Everstine G (1981) A symmetric potential formulation for fluid–structure interaction. *J Sound Vib* 79:157–160
5. Ohayon R (1987) Fluid–structure modal analysis. New symmetric continuum-based formulations. Finite element applications. In: Pande GN, Middleton J (eds) *Proceedings of the international conference on advances in numerical methods in engineering: theory and applications*. MartinusNijhoff, Dordrecht
6. Schneider K, Murthy P, Bella D (2006) Extension of model reduction methods to coupled structure-acoustic problems. In: IMAC XXIV
7. Maess M, Gaul L (2006) Component mode synthesis for efficient structure-acoustic simulation of piping systems. In: IMAC XXIV
8. Zhang W, Wang A, Vlahopoulos N, Wu K (2003) High-frequency vibration analysis of thin elastic plates under heavy fluid loading by an energy finite element formulation. *J Sound Vib* 263:21–46
9. Shorter P, Zhang Q, Parrett A (2007) Using the hybrid FE-SEA method to predict and diagnose component transmission loss. SAE Technical Paper 2007-01-2172
10. Vlahopoulos N (2011) Structural-acoustic simulations of naval vehicles using an energy finite element method. In: *Proceedings of the ASME design engineering technical conference*, vol 1 (parts A and B), pp 509–516
11. Bruce RD, Bommer AS, LePage TE (2013) Solving acoustic-induced vibration problems in the design stage. *Sound Vib* 8–11
12. Bijwe V, Raut M, Suryawanshi S, Naidu S et al (2011) NVH refinement of passenger vehicle for in-cab boom noise using experimental operational deflection shape and full vehicle acoustic sensitivity simulations. SAE Technical Paper 2011-26-0063
13. Tonge G, Agrawal S (2013) Analysis of open plenum structure for reduction of booming noise. SAE Technical Paper 2013-01-0636
14. Elliot SJ, Nelson PA (1993) Active noise control. *IEEE Signal Process Mag* 10(4):12–35
15. Lee Y, Nasiri A (2007) Real time active noise control of engine booming in passenger vehicles. SAE Technical Paper 2007-01-0411
16. Kashani R (2003) Active boom noise damping of a large sport utility vehicle. SAE Technical Paper 2003-01-1694
17. Bertolini C, Gaudino C, Caprioli D, Misaji K et al (2007) FE analysis of a partially trimmed vehicle using poroelastic finite elements based on Biot’s theory. SAE Technical Paper 2007-01-2330
18. Duval A, Dejaeger L, Bischoff L, Morgenstern C (2012) Trim FEM simulation of a headliner cut out module with structureborne and airborne excitations. SAE Technical Paper 2012-01-1524

Chapter 32

EMA-BEM-NAH-SEA Path to a Dynamic Filter Model for Violin Radiativity

George Bissinger

Abstract By subsuming experimental modal and radiation analysis results on many violins, boundary element method computations for a violin undergoing soundpost removal, nearfield acoustical holography for port (f -holes) radiation, and statistical energy analysis into a generalized structural acoustics framework it is possible to construct a dynamic filter model for the averaged-over-sphere radiativity of the traditional, properly setup violin over the frequency range from 0.2 to 6 kHz. This model treats the low frequency “deterministic” region below 660 Hz—where all violins show two cavity and three body modes—three always radiating strongly through the f -holes, two with strong surface radiation, one hardly radiating, and one requiring induced surface motion to radiate—as a simplified *dual*-Helmholtz resonator where two low-lying bending modes “pump” the lowest Helmholtz-resonator-like cavity mode. The mid-high frequency region uses a band-averaged, “statistical” structural acoustics approach built on a distributed-excitation statistical mobility function (SEA) to incorporate bridge filter and critical frequency effects. Both regions were rejoined at 630 Hz where all violin quality classes had a common value. This dynamic filter model is capable of simulating the effects on violin radiativity of top-back plate and bridge tuning, holding the violin or soundpost removal, singly or in combination.

Keywords Vibro-acoustic • Ported shell • Violin • Radiativity model • Damping

32.1 Introduction

The violin, seemingly simple in shape, materials, and construction, has eluded all scientific efforts over the last two centuries to provide an analytic representation of its radiation. A short list of the difficulties encountered by any analytic approach includes: (a) bowed string energy being transported through a small, tuned, stress-loaded-by-string-tension bridge substructure into a nominally orthotropic spruce wood substructure at two places on the top surface (with obvious implications for mode excitation), (b) this substructure being doubly- and variably-arched as is the other main (maple) wood substructure, (c) glue joints between porous top and back main substructures and a thin (~ 1 mm) maple ribbing lined top and bottom with additional liner strips to ensure adequate adhesion, (d) two additional substructures hidden from the eye but crucial to good violin sound, viz., a bass bar running along the top substructure that falls under one foot of the bridge and more particularly the soundpost, an ~ 6 mm diameter, ~ 50 mm long rod of spruce, mainly stress-loaded-by-string-tension, propped post-assembly between top and back substructures under the other foot of the bridge, (e) mathematically intractable shapes, (f) “surface” varnish penetrating into the wood and changing orthotropic properties, (g) quite irreproducible materials, (h) impossible-to-analytically-specify-boundaries/discontinuities where bending \leftrightarrow longitudinal wave conversion occurs, (i) a somewhat flexible-walled ported cavity with significant radiation through the ports, (j) cavity air modes that back-couple to drive wall motion and subsequent radiation. Add the inevitable effects associated with aging, playing, exposure to wide temperature-humidity swings, all together these difficulties form a formidable challenge to any analytic analysis of body motions. Compound the mechanical difficulties outlined here with four known radiation mechanisms for converting vibrations into sound waves and any analytic solution seems forever out of reach.

G. Bissinger (✉)

Department of Physics (professor emeritus), East Carolina University, Greenville, NC 27858, USA
e-mail: bissingerg@ecu.edu

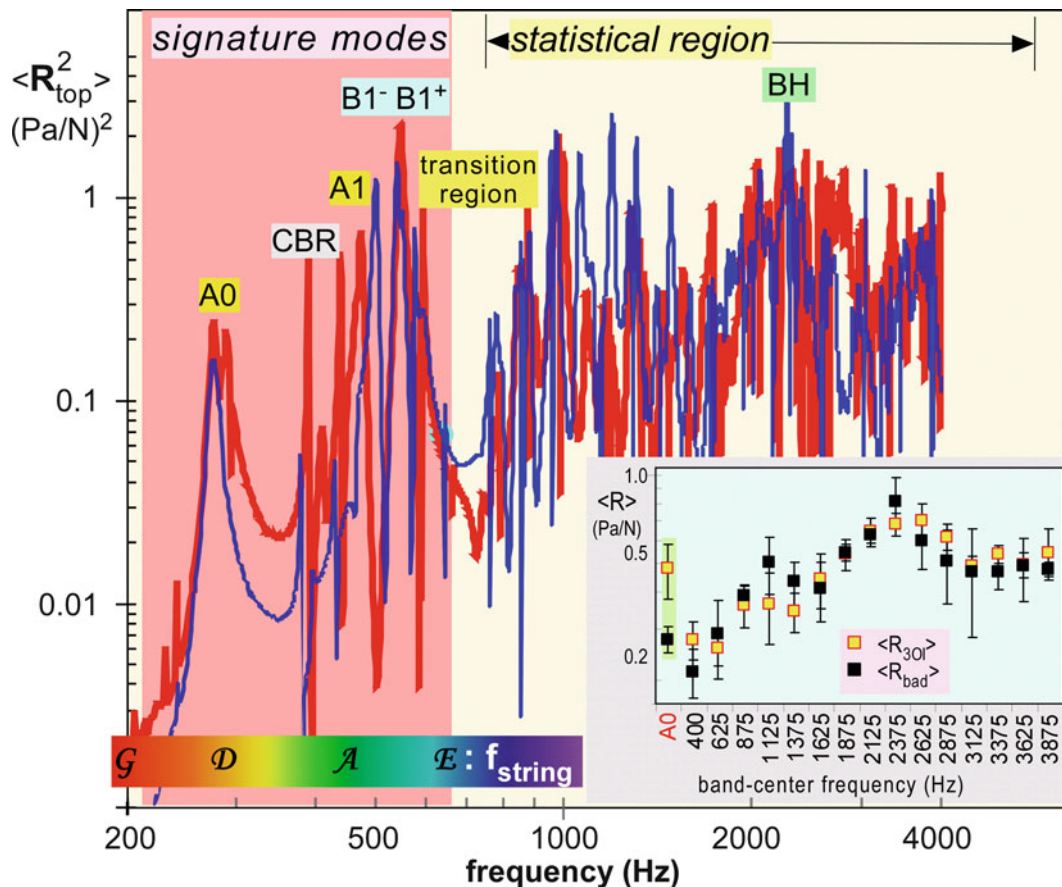


Fig. 32.1 Comparison of top hemisphere “bad” violin radiativity profile (*thinner blue line*) with *Titian* Stradivari (*thicker red line*). *Inset*: band-averaged radiativity profiles (over sphere) for three “bad” violins (black squares) and three “excellent” old Italian violins; error bars are one standard deviation. [Deterministic (“signature” modes) and statistical regions noted, as are open string frequencies.]

Scientific research on violins has been further bedeviled by the fact that the measurable differences between properly setup violins seem far smaller than the perceptual evaluations would indicate, e.g., compare the top hemisphere radiativity profiles in Fig. 32.1 for two violins, a Strad copy “bad” violin, vs. the *Titian* Stradivari (considered one of the world’s great solo violins).

Since no analytic approach seems possible and no two made-of-wood violins can ever be the same, our strategy is to invert the problem: comprehensively characterize the violin experimentally, i.e., let the violin “solve” how it radiates so that we can describe the violin not by what it is—materials-shape-construction, the essential ingredients of a finite element model—but by what it *does*, its dynamics.

The very uniformity of shape, size, materials, and construction inherent to the traditional violin are subsumed into the model; the violin becomes a “filter” inserted between the violinist’s input and the final sound, characterized here by the radiativity “profile”, the far-field, frequency-dependent pressure per unit force, mean-square-averaged over a sphere. Such an experimental characterization can then be interpreted in a modern structural acoustics context with radiation efficiency and damping, total damping, critical frequency, statistical mobility and a simple model for excitation of two low-lying important cavity modes. The surprising simplifications and straightforward simulations of radiativity profiles in this “dynamic filter” model incorporate the two most important adjustments the violinmaker typically makes—plate tuning *pre*-assembly and bridge tuning *post*-assembly. The model can then be extended to simulate the effect of holding the violin and soundpost removal on the radiativity profile filter function.

32.2 Experimental Characterization

Four sets of dynamics measurements—all with zero-mass-loading hammer-impact excitation at the violin bridge—provide the necessary experimental characterization of assembled violin dynamics (free–free suspension):

1. Zero-mass-loading experimental modal analysis EMA mobility $Y(\omega)$ (complex velocity/force, v/F in $m/s/N$) measurements over ~ 550 points on entire violin via scanning laser. Mean-square-averaging over the radiating corpus (top + ribs + back) creates the mobility “profile” $\langle Y_{\text{corp}}^2 \rangle$ for our 14-violin ensemble, most of which had known plate tunings (especially important being plate modes #2 and #5 in the usual ascending-frequency labeling) [1].
2. *Simultaneous* radiativity $R(\omega)$ (complex pressure/force, p/F in Pa/N) at 266 microphone positions over a sphere in an anechoic chamber. Mean-square-averaging over sphere creates total (surface plus ports) radiativity “profile” $\langle R^2 \rangle$.
3. “Patch” near-field acoustical holography NAH radiativity for just the two violin ports (f -holes), mean-square-averaged over a sphere to give *port* radiativity profile $\langle R_f(\omega)^2 \rangle$ [2].
4. Systematic measurements of radiativity and bridge foot motion as bridge rocking frequency f_{rock} was modified [3].

Each of these experiments singly or in combination provides essential information for the model. A brief road map:

1. **EMA** provides (a) mobility “profiles”, (b) mode-by-mode nodal line placements especially important near the bridge feet when investigating mode excitation, (c) total damping power-law trendline $\zeta_{\text{tot}}(f) \propto f^{-0.34}$, and (d) an important, semi-empirical relationship between plate tuning frequencies and first corpus bending modes, $B1^-$ and $B1^+$, for violins with soundpost, bridge, strings and tailpiece in place [1]. (Note: EMA does *not* measure volume flows through the violin’s f -holes, requiring a separate measurement.)
2. **Combining** simultaneous radiativity measurements with EMA leads directly to experimental radiation efficiency R_{eff} for each mode (and for 250 Hz band modal averages), radiation damping $\zeta_{\text{rad}}(f)$, and each violin’s *effective* critical frequency f_{crit} [1].
3. **Structural acoustics** systematics suggest a plate bending mode frequency \leftrightarrow critical frequency relationship in addition to the aforementioned plate \leftrightarrow B1 relation. Hence semi-empirical relationships between plate modes #2 and #5, the B1 frequencies, and f_{crit} expose a crucial link between the low and high ends of the violin’s radiativity profile.
4. **BEM** (boundary element method) calculations using EMA results to compute radiation efficiency R_{eff} for each mode [4]. Since EMA-based BEM calculations neglect crucial port radiation a separate measurement for this was required.
5. **NAH** measurement of f -hole-only radiativity $R_f(\omega)$ for comparison with total radiativity.
6. **Combining** $\langle R_f(\omega)^2 \rangle$ with $\langle R(\omega)^2 \rangle$ provides the fraction of total radiativity from the f -holes. One surprising result: port—not surface—radiation dominates at the lower frequencies, becoming much less important above 1 kHz.
7. **SEA-based mobility profile** $Y_{\text{stat}}^2(\omega)$ for *distributed-over-corpus* excitation in a general structural acoustics framework provides a convenient way to isolate-emphasize bridge filter effects in our *bridge*-excitation mobility profiles. Y_{stat}^2 requires “global” violin parameters such as modal density $n(f)$ and $\zeta_{\text{tot}}(f)$ from EMA, plus total mass M [5].
8. **Systematic f_{rock} bridge tuning** effects were incorporated in a sixth order polynomial scaling function $S(f)$.

32.3 The Dynamic Filter Model

Some surprising conclusions emerge from the EMA-BEM-NAH-SEA approach that, taken all together, provide significant insights into general violin behavior *and* simplifications in the dynamic filter model:

1. Below ~ 600 Hz, our “deterministic” region, there are only three always-strongly-radiating, well-separated, “signature” modes for all violins (14-violin average frequencies used): A0, a cavity mode near 275 Hz, a compliant wall version of the Helmholtz resonator that radiates completely through the f -holes, then the lower of two first corpus (top + ribs + back) bending modes $B1^-$ near 470 Hz and finally the upper $B1^+$ near 545 Hz. Both B1 modes show large volume changes and radiate predominantly through the f -holes. (Important first longitudinal cavity mode A1 near 470 Hz discussed later.)
2. Above ~ 700 Hz individual modes could not be tracked from violin-to-violin, mode overlap increased significantly, suggesting a statistical approach without specific port radiation. Our 250 Hz-band averages were incorporated in Y_{stat}^2 .
3. Bridge filter effects were nil for the 1,375 Hz band, suggesting an important normalization point for *distributed-excitation* mobilities to our *bridge*-excitation $\langle Y_{\text{corp}}^2 \rangle$ in the statistical region.
4. Deterministic and statistical regions can be spliced together at 630 Hz in a “trough” region, where all quality classes had $\langle R \rangle \approx 0.19$ Pa/N.

5. Assuming a mode is best excited at its antinodes at a frequency near its resonant frequency, the nearby B1 modes with their large *in*-phase *f*-hole volume flows (similar to A0) became the best “pump” candidates for A0 (and A1), with B1[−] being more important. Passing all our experimental results through a “logical sieve” leaves *only* the B1 modes as A0 “pumps”. Also implied—the importance of B1 damping, important in understanding free–free → *held* violin transition.

Thus measured violin dynamics lead us to create separate deterministic and statistical regions, each with appropriate models, spliced together at 630 Hz. For A0 and the B1 modes, which primarily radiate through in-phase *f*-hole volume flows, an analytic wall-driven Helmholtz resonator network model is appropriate, with surface and background contributions added. In the statistical region a generalized structural acoustics approach, with Y_{stat}^2 providing global parameters, is key to applying f_{crit} , $\zeta_{\text{rad}}(f)$, $\zeta_{\text{tot}}(f)$ and bridge f_{rock} parameterizations.

32.3.1 Deterministic Region

Edgar Shaw in 1990 created a network model that included A0 *and* A1 in a rigid-wall, violin-shaped cavity [6]; coupling observed between A0 and A1 strongly affected the Helmholtz resonator A0 volume dependence, $V^{-0.5}$, dropping it to $V^{-0.25}$, quite close to actual experimental results [7]. Since two partial volumes connected by a narrower waist are common to all bowed string instruments, all share this reduced volume dependence, with rib height the primary determiner of cavity volume. A0 *and* A1 were incorporated in a new dual-Helmholtz resonator network model using two resonators placed neck to neck with an offset port (dimensions based on actual violin values), with parameters adjusted to return average A0 and A1 frequency and damping values for our 14-violin ensemble. B1 total radiativity $\langle R_{\text{tot}} \rangle$ was computed by adding a surface radiation contribution R_{surf} to the *f*-hole radiation R_f along with a background contribution from higher modes, R_{bgd} . Then the required B1 mode frequencies and total dampings were set to 14-violin ensemble values. B1-induced cavity volume flows were then adjusted to give measured B1 radiativities *and* $\langle R_{\text{tot}} \rangle = R_{\text{surf}} + R_f + R_{\text{bgd}} \approx 0.19$ Pa/N at 630 Hz ($r = 1.2$ m). After setting these B1 parameters A0 radiativity follows directly, giving values in excellent agreement with experiment [5].

32.3.2 Statistical Region

The approach for the statistical region is quite different from the deterministic, starting with the mathematical identity

$$\langle R^2 \rangle = \langle Y^2 \rangle \frac{\langle R^2 \rangle}{\langle Y^2 \rangle} \quad (32.1)$$

In our specific experiment the ratio $\langle R^2 \rangle / \langle Y^2 \rangle$ cancels out the driving force, returning $\langle p^2 \rangle / \langle v^2 \rangle$, which contains all the dynamics needed to compute R_{eff} . Equation (32.1) is transformed in successive stages by substituting structural acoustics equations [8] for R_{eff} , ζ_{rad} and the SEA-based *distributed-over-corpus*-excitation, statistical mobility function Y_{stat}^2 ,

$$Y_{\text{stat}}^2(f_c) \propto \frac{n(f_c)}{f_c \cdot \zeta_{\text{tot}}(f_c) \cdot M^2} \quad (32.2)$$

which has *no* bridge filter effects. Normalizing Y_{stat}^2 to our 14-violin ensemble corpus mobility profile $\langle Y_{\text{corp}}^2 \rangle$ at 1,375 Hz where bridge filter effects are nil defines the shape function $\Phi = \langle Y_{\text{corp}}^2 \rangle / Y_{\text{stat}}^2$; $\Phi = 1$ at 1,375 Hz. Modal density $n(f_c)$ was computed band-by-band over 250 Hz intervals up to 5 kHz (f_c = band-center frequency) for the 14-violin ensemble, and represented by a sixth order polynomial; $\zeta_{\text{tot}}(f) \propto f^{-0.34}$; violin total mass $M \approx 0.40$ kg. Φ displays three broad structures near ~ 1 , ~ 2.3 and ~ 3 kHz. The structures near 1 and 2.3 kHz, little affected by bridge or plate tuning were parameterized in the dynamic filter model by two fixed, constant frequency resonance functions. (Note: plate tuning does change M .)

The third, resonance-like structure near 3 kHz, which reliably followed the f_{rock} changes, was parameterized with a third, f_{rock} -variable resonance function. These three functions combined provide a good parametric representation of the shape function [5]. Setting f_{rock} initially at an intermediate value of 3.0 kHz for the dynamic filter equation for the radiativity profile in the statistical region requires only applying the scaling function $S(f)$. After collecting terms the defining equation for the dynamic filter radiativity “profile” in the statistical region for *free–free* suspension (anechoic chamber) becomes simply

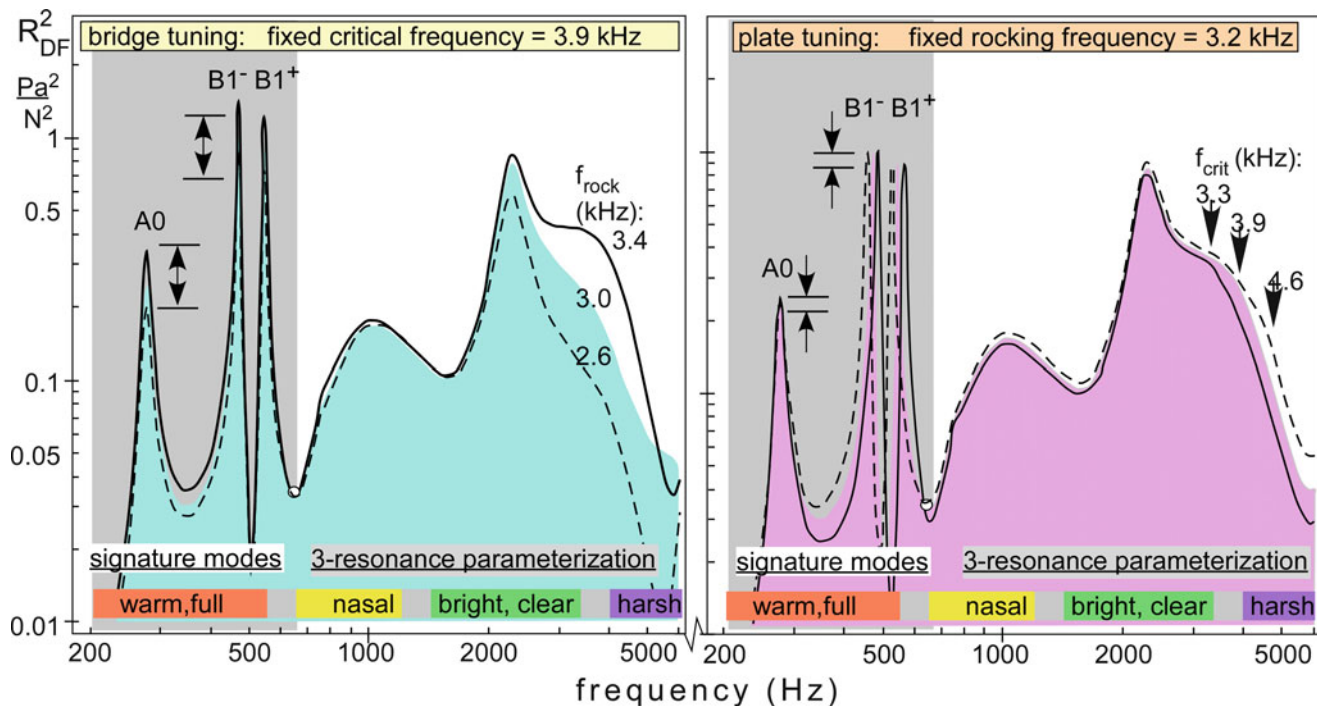


Fig. 32.2 DFM simulations of violin radiativity profiles (common vertical scale) for: (L) variable bridge tuning with fixed critical/plate frequency; (R) variable critical/plate frequency with fixed bridge f_{rock}

$$R_{\text{DF}}^2(f) \propto \left\{ \frac{\Phi(f) \cdot n(f) \cdot S(f)}{M} \right\} F_{\text{RAD}}(f) \quad (32.3)$$

The first $\{\}$ term includes all those matters associated with transferring string energy into the corpus, bridge filter, etc., and becomes the “gatekeeper” filter. The second term, $F_{\text{RAD}}(f) = \zeta_{\text{rad}}(f)/\zeta_{\text{tot}}(f)$ —the “egress” filter—involves only vibrational energy loss via radiation and internal (heat) plus support fixture damping where appropriate. Holding the violin increases support fixture damping greatly, highlighting the importance of the original free–free suspension, which effectively eliminated support fixture damping so as to emphasize *violin-only* properties. Dynamic filter model (DFM) radiativity profile simulations in Fig. 32.2 cover plate/critical frequency and bridge tuning variations over our experiment range. The overall similarity between Figs. 32.1 and 32.2 is now apparent.

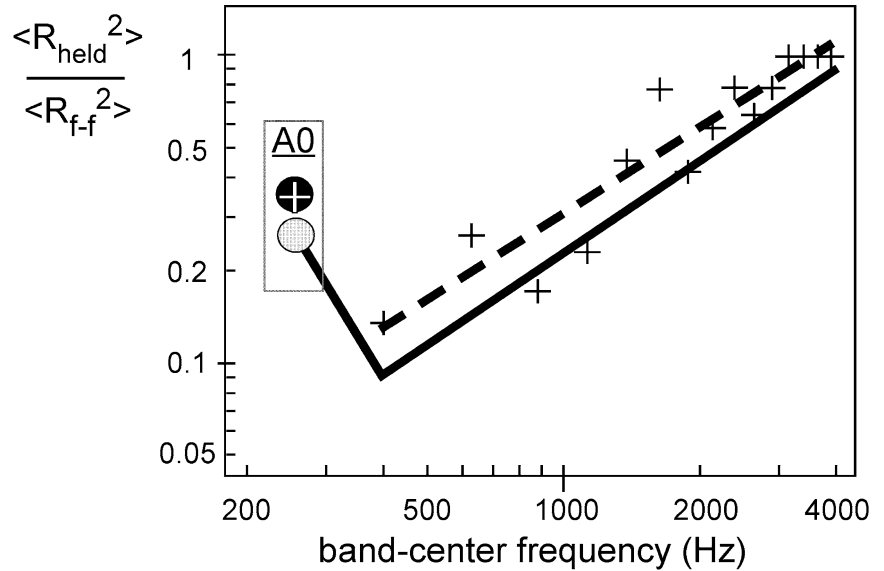
32.4 Dynamic Filter Model Applications

A held violin played in an auditorium obviously differs from the free–free suspension/zero-mass-loading/anechoic chamber violin. The DFM formalism however can be applied to such cases, or even to the traditional violin without soundpost, by adding germane serial filters to the DFM gatekeeper-egress. Two applications of the DFM are presented here: (1) holding the violin and (2) soundpost removal, both represented by decades-old experiments. The basic DFM application procedure will be covered in detail for the *held* violin then somewhat more briefly for the soundpost removal case.

32.4.1 Holding the Violin

In 1986 Marshall tabulated mode-by-mode free–free vs. *held* frequency and total dampings on a violin held by a violinist [9] (but no acoustic measurements). Since the DFM “understands” violins in the free–free state these measurements are really all that are needed to compute the *held* filter, as will become apparent. Holding the violin significantly increases the support fixture damping $\zeta_{\text{fix}}(f)$, lower modes having relatively larger ζ_{tot} , but mode frequencies were hardly affected, hence

Fig. 32.3 Dynamic filter model *held* filter (solid line) including A0 (filled circle; computed relative to DFM B1) compared to band-averaged experimental ratios from Marshall's Fig. 32.3 for corpus modes (+ symbol, with empirical power law trendline (dashed line) and A0 (circled + symbol)



$n(f) \approx \text{constant}$. We can also infer that: (1) without frequency changes mode shapes will not be affected significantly, hence R_{eff} and ζ_{rad} will not change, (2) the bridge filter effect is unchanged, (3) the A0-B1⁻ frequency difference remains constant, and (4) the Φ drop-off as frequency decreases follows ζ_{tot} systematics. Thus $n(f)$, $S(f)$ and M effectively remain unchanged, while F_{RAD} and Φ are affected by the ζ_{tot} increase. Power law fits, $\zeta_{\text{tot}} \propto Af^x$, to Marshall's free-free damping data returned $x = -0.36$, quite close to the 14-violin ensemble $x = -0.34$, while *held* data returned $x = -0.88$; ζ_{tot} values at 4 kHz were nearly equal.

The DFM transition from free-free to *held* violin proceeds by creating a new identity

$$\langle R_{\text{held}}^2 \rangle = \langle R_{\text{f-f}}^2 \rangle \cdot \frac{\langle R_{\text{held}}^2 \rangle}{\langle R_{\text{f-f}}^2 \rangle} \approx R_{\text{DF}}^2 \cdot \frac{\langle R_{\text{held}}^2 \rangle}{\langle R_{\text{f-f}}^2 \rangle} \quad (32.4)$$

where R_{DF}^2 was substituted *only* for the initial $\langle R_{\text{f-f}}^2 \rangle$ term, the rationale being that since the free-free violin is well understood in the DFM all plate-bridge tuning simulations from Fig. 32.2 can be used directly in the first term. The second term—the *held* filter—was determined entirely from Marshall's experimental values.

Since $n(f)$, $S(f)$ and M cancel in the ratio, Marshall's held/free-free ratio reduces to

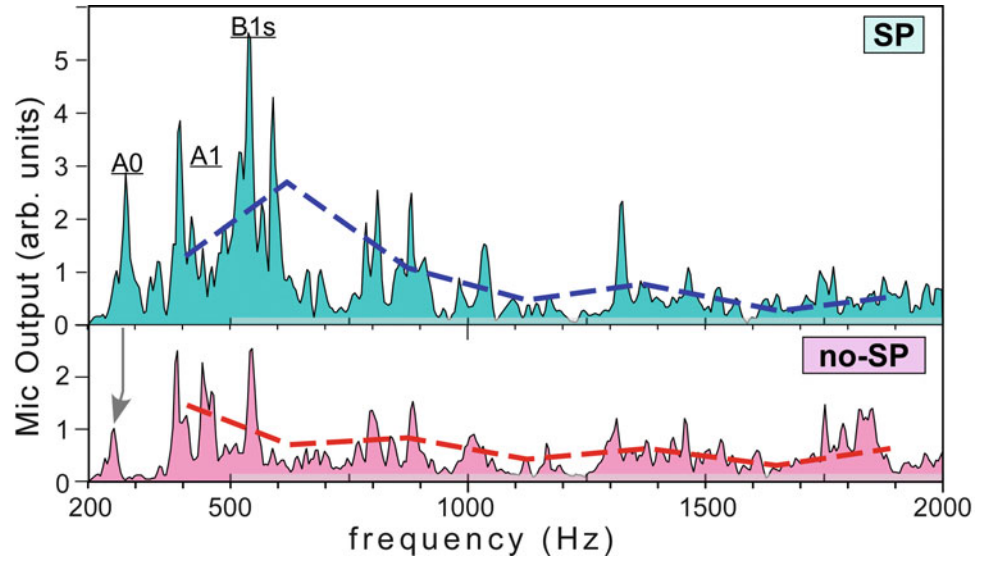
$$\frac{\langle R_{\text{held}}^2 \rangle}{\langle R_{\text{f-f}}^2 \rangle} = \frac{\langle \Phi_{\text{held}}^2 \rangle}{\langle \Phi_{\text{f-f}}^2 \rangle} \cdot \frac{\langle F_{\text{RADheld}}^2 \rangle}{\langle F_{\text{RADf-f}}^2 \rangle} \approx \frac{\zeta_{\text{totf-f}}^2}{\zeta_{\text{totheld}}^2} \approx 2.28 \times 10^{-4} \cdot f^{1.0} \quad (32.5)$$

Equation (32.5) thus reduces to the simple DFM *held* filter result— $2.28 \times 10^{-4} \cdot f^{1.0}$ —that can be compared directly to experimental measurements of violin accelerance response up to 4 kHz in Marshall's Fig. 32.3, free-free vs. *held*. Ratios of responses mode-by-mode taken directly from this figure—A0 response was assumed proportional to induced corpus motions—were then band-averaged and compared with the DFM predictions in Fig. 32.3. As is obvious from this figure the DFM model reliably predicts magnitude and trends seen in Marshall's measured free-free \rightarrow *held* violin responses. Two important points: (1) *held* B1 amplitude was computed directly from the free-free value since the B1 modes were included in the ζ_{tot} power-law damping trendline and (2) A0 actually increased somewhat *relative* to the B1 modes because of the large B1⁻ damping increase, even though B1 mode amplitudes dropped considerably.

32.4.2 Soundpost Removal

Removal of the violin soundpost dramatically degrades violin sound by greatly reducing its radiativity at low frequencies relative to high. This is a much more problematical DFM application since the violin itself has been modified—hence the deterministic region cannot be spliced to the statistical region at 630 Hz—whereas the *held* violin had only a large increase in $\zeta_{\text{fix}}(f)$. Fortunately a much broader information base is available for this situation:

Fig. 32.4 Room-averaged slide-tone pressures for a held violin with a soundpost (*top*) and without (*bottom*). The superimposed 250 Hz band averages (*dashed lines*) indicate similar averaged acoustic outputs above ~ 800 Hz



1. **EMA** pre- and post- soundpost removal up to 2 kHz. Foam supports used in this experiment increased support fixture damping somewhat above free-free results, but $\zeta_{\text{fix}}(f)$ was certainly not a dominant contributor to $\zeta_{\text{tot}}(f)$ and its unknown frequency dependence was common to both measurements.
2. **BEM** R_{eff} calculations for a violin *without* f -holes. R_{eff} values are suspect when a major part of a mode's radiation is due to large volume flows through the f -holes, as for the B1 modes.
3. **Room-averaged, slide-tone acoustic measurements** shown in Fig. 32.4 (after [4]) show how soundpost removal affects the radiativity profile of the violin less in the statistical region than in the deterministic.

EMA revealed significant B1 mode shape changes: comparing pre-/post-removal EMA revealed only one B1⁺-like no-SP mode near 497 Hz (close to the SP-state B1⁻ frequency) that showed the large volume changes *and* rigid-body, bridge-pivot action about a “fixed” soundpost foot that are common to both B1 modes in the SP state. Soundpost removal thus eliminated one of the large volume change A0 “pump” modes *and* increased the frequency difference between A0 and the B1⁺-like mode by ~ 30 Hz. Prior DFM deterministic region simulations incorporating these SP \rightarrow no-SP changes predicted that no-SP $\langle R_{A0}^2 \rangle$ was weaker than SP $\langle R_{A0}^2 \rangle$ by a factor of ~ 6 [5] in good agreement with the drop of ~ 3 —corresponding to a drop of ~ 9 in the radiativity profile—seen in the room-averaged, slide-tone pressure measurements of Fig. 32.4.

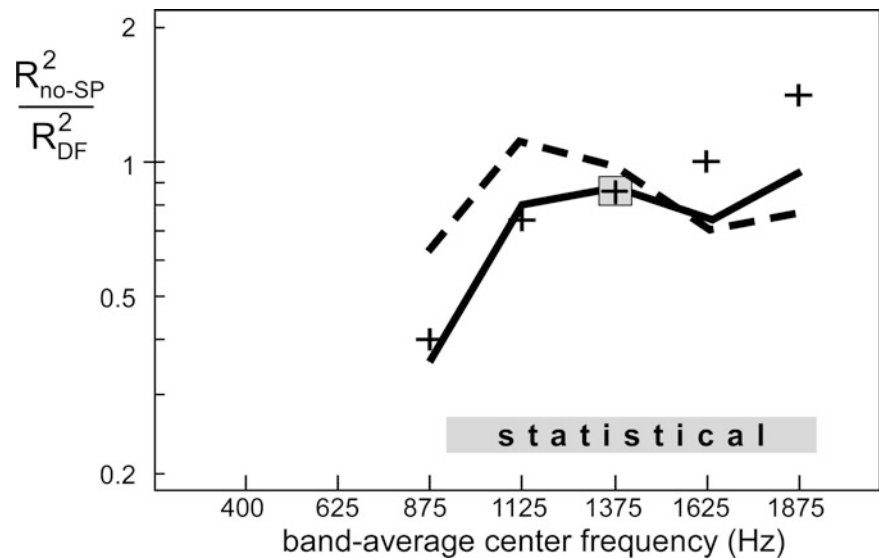
In the statistical region mobility profiles showed a similar number of peaks, similar in frequency, clumped similarly, and similar in amplitude hence $n(f)$ was effectively constant between the SP and no-SP states [4]; total mass $M \sim 0.40$ kg was also mainly unaffected by the removal of the \sim gram soundpost. The ζ_{tot} power-law trendlines fell off slightly more slowly for the no-SP state, $\zeta_{\text{tot}} = 19.2 \cdot f^{-0.50}$, than the SP, $\zeta_{\text{tot}} = 32.9 \cdot f^{-0.58}$, hardly an important difference given the data scatter. Corpus mobility profiles also showed little variance between SP and no-SP states in the band-averages, hence we conclude that the shape function Φ was also approx. constant. Quite similar bridge motions observed in EMA animations for both states in the statistical region, suggest that $S(f)$ should hardly vary in the statistical region up to 2 kHz—unlike the deterministic region.

Φ , $S(f)$, $n(f)$ and M then are all approx. constant and thus cancel in the no-SP/SP ratio, leaving only the ratio of F_{RAD} egress filters in the DFM soundpost removal filter equation. For comparison with band-averaged, room-averaged *held* violin acoustic measurements the *soundpost-removal*, SP \rightarrow no-SP DFM equation in the statistical region is simply

$$\langle R_{\text{no-SPheld}}^2 \rangle = \langle R_{\text{SPf-f}}^2 \rangle \cdot \frac{\langle R_{\text{no-SPf-f}}^2 \rangle}{\langle R_{\text{SPf-f}}^2 \rangle} \cdot \frac{\langle R_{\text{held}}^2 \rangle}{\langle R_{\text{f-f}}^2 \rangle} \approx R_{\text{DF}}^2 \cdot \frac{F_{\text{RADno-SPf-f}}}{F_{\text{RADSPf-f}}} \cdot \frac{\langle R_{\text{held}}^2 \rangle}{\langle R_{\text{f-f}}^2 \rangle} \quad (32.6)$$

SP or no-SP BEM R_{eff} mode calculations up to 2 kHz were used to compute ζ_{rad} in F_{RAD} , with relevant power-law trendline values used for ζ_{tot} , followed by band-averaging of F_{RAD} . BEM R_{eff} calculations can be used in the statistical region with greater validity due to: (a) f -hole radiation falling off relative to surface radiation, (b) R_{eff} increasing as frequency nears the critical frequency, and (c) mobility falling off with frequency. All these should conspire in the no-SP/SP *ratio* to minimize the effect of neglected f -hole radiation [5]. Similarly room acoustic effects common to both SP and no-SP measurements should mostly cancel out in the ratio.

Fig. 32.5 Dynamic filter model predictions in the statistical region for SP \rightarrow no-SP filter (dashed line) and SP \rightarrow no-SP + held filter (solid line), compared to experimental no-SP/SP pressure-squared ratio (+ symbol)



Ratios of the statistical region band-averages of the room-average, slide-tone acoustic pressure measurements shown in Fig. 32.4 for the SP and no-SP states are shown in Fig. 32.5 along with DFM predictions from Eq. (32.6). The comparison includes the *soundpost-removal* filter computed separately for comparison with the *held* filter in Fig. 32.3. The full *soundpost-removal/held* DFM comparison, normalized to experiment at 1,375 Hz where bridge tuning effects are nil, clearly improves agreement with experimental *trends*, dropping the low frequency bands relative to high, but the predicted magnitudes fall lower by a factor of ~ 2 .

Even if the DFM cannot reproduce the magnitude of experimental soundpost removal effects on the room-averaged radiation with the same reliability as for the *held* violin, it does appear to capture the observed trends well, but it cannot splice the deterministic and statistical regions together as in the case of properly set up violins with a soundpost. Still, overall the model offers real insights into how soundpost removal affects the radiation from the violin in each region.

32.5 Conclusions

The dynamic filter model—born of necessity because the vibroacoustic violin is definitely not a candidate for an a priori analytic model of violin radiativity—subsumes all of the violinmaker’s materials-shape-construction craft into a “traditional-violin” black box defined by its systematic *measured* dynamic responses to changes in plate and bridge tuning, all couched in a structural acoustics framework. The serial filter formalism of the model is consistent with the serial nature of the various stages of energy flow through the violin and readily lends itself to broadening the range of application.

Although no single technique in our vibration-radiation toolbox can crack the violin radiativity code EMA gives us fundamental insights into how a violin and its various substructures move although it offers no information on cavity or *f*-hole volume flows. Thus NAH was used to inform us about *f*-hole volume flows and their resultant far-field radiation. BEM calculations based on EMA vibration data can compute the violin’s far-field radiation but requires a complete internal-external formalism for radiation from this hollow, fluid-filled/surrounded structure. The importance of the *distributed-excitation* SEA-based mobility function was actually dual: (1) quite helpful in emphasizing bridge filter effects for simple parameterization, and (2) introducing a quite simple global parameter set that in its turn led to remarkably simple dynamic filter model predictions of violin radiativity trends due to holding and soundpost removal. Perhaps surprising was the importance of understanding violin damping—in all its various forms across the frequency spectrum—to this model’s success.

Generally successful validation of the dynamic filter model on two such disparate, decades-old experiments that were not part of the original model or its foundational database gives one confidence in the generality of this model not just for simulating violin radiativity trends from plate or bridge tuning but also for broadening its scope to estimating the effect of holding the violin, or even to such an extreme case as removal of the soundpost.

References

1. Bissinger G (2008) Structural acoustics model of the violin radiativity profile. *J Acoust Soc Am* 124:1764–1773
2. Bissinger G, Williams EG, Valdivia N (2007) Violin *f*-hole contribution to far-field radiation via patch near-field acoustical holography. *J Acoust Soc Am* 121:3899–3906
3. Bissinger G (2006) The violin bridge as filter. *J Acoust Soc Am* 120:482–491
4. Bissinger G (1995) Some mechanical and acoustical consequences of the violin soundpost. *J Acoust Soc Am* 97:3154–3164
5. Bissinger G (2012) Parametric plate-bridge dynamic filter model of violin radiativity. *J Acoust Soc Am* 132:465–476
6. Shaw EAG (1990) Cavity resonance in the violin: network representation and the effect of damped and undamped rib holes. *J Acoust Soc Am* 87:398–410
7. Bissinger G (1998) A0 and A1 coupling, arching, rib height, and *f*-hole geometry dependence in the 2-degree-of-freedom network model of violin cavity modes. *J Acoust Soc Am* 104:3608–3615
8. Fahy F, Gardonio P (2007) *Sound and structural vibration: radiation, transmission and response*, 2nd edn. Academic, New York
9. Marshall KD (1986) The musician and the vibrational behavior of the violin. *Catgut Acoust Soc J* 45:28–33

Chapter 33

Coupled Vibro-Acoustic Model of the *Titian* Stradivari Violin

Michael A. Pyrkosz and Chuck Van Karsen

Abstract The instruments of Antonio Stradivari (1644–1737) are still considered the finest in the world and have set the standard for violin quality that has yet to be exceeded by a modern luthier. To determine the relationship between the sound of the instrument and its structure and material properties a vibro-acoustic finite element model was developed for the 1715 *Titian* Stradivari violin. The structural model was created by measuring the structural geometry and density from CT scans of the actual instrument. The predicted structural modes were correlated with experimental modal data on the 1715 violin and updated accordingly. The correlated structural modes were then projected onto the acoustic envelope. The vibro-acoustic transfer function between force input at the violin bridge and acoustic pressure response 1.2 m away was predicted. These results were compared to experimental radiativity measurements made on the actual instrument. It was shown that including structural and acoustic damping characteristics are important to accurately predict the vibro-acoustic behavior of the *Titian* Stradivari violin. Predicted structural modal frequencies were all within 5 % of the experimental data, while the main acoustic mode was within 7 %. The predicted radiativity magnitude was within 1.5 dB for all mode peaks. This is the first comprehensive analytical vibro-acoustic model of a Stradivari instrument and can be used to determine how structural modifications effect violin sound quality.

Keywords Vibro-acoustic coupling • Finite element acoustics • Model validation • Violin acoustics • Antonio Stradivari

Nomenclature

c	Speed of sound
k	Wave number
MAC	Modal assurance criterion
p	Acoustic pressure
r	Acoustic field position vector
t _{PML}	Thickness of the perfectly matched layer
V	Mode shape vector
ζ	Damping factor, $\zeta = C/C_c$
η	Loss factor, energy dissipation per cycle
λ	Wave length, $\lambda = 1/f = 2\pi/\omega$
ρ	Mass density

M.A. Pyrkosz (✉)

LMS, A Siemens Business, Engineering Services, LMS North America, 5755 New King Court, Troy, MI 48098, USA
e-mail: Mike.Pyrkosz@lmsintl.com

C. Van Karsen

Dynamic Systems Laboratory, Mechanical Engineering-Engineering Mechanics, Michigan Technological University,
1400 Townsend Drive, Houghton, MI 49931, USA

33.1 Introduction

Today, the instruments made by Antonio Stradivari in the early eighteenth century are considered to be the best in the world. Unfortunately, no one in our generation fully understands how Stradivari crafted his instruments, and no one has ever produced an instrument that has quite the same musical quality of one of his instruments. There are many theories about how Stradivari made his instruments, and why they are superior to other violins. To determine the relationship between the sound of the instrument and its structure and material properties a vibro-acoustic finite element model was developed for the 1715 *Titian* Stradivari violin. The structural model was created by measuring the structural geometry and density from CT scans of the actual instrument [1].

The next step is to bring the dynamic behavior of the structural model in greater agreement with the real test structure through modal correlation and updating. This technique uses correlation of experimental modal data with the modal results of an approximate FE model with initial material properties. The sensitivity of the correlation to the different properties is determined and the material properties are updated accordingly. This process is iterated until the model is a reasonable representation of reality.

The final step in the process was to create an accurate vibro-acoustic model of the instrument. To do this an acoustic finite element mesh was developed based on the existing structural FE model. The predicted structural modes were projected onto this mesh, and a coupled vibro-acoustic analysis was performed to predict the transfer function between acoustic pressure response and force input at the violin bridge. These results were compared to experimental radiativity measurements made on the actual instrument [2–4]. The acoustical model properties were updated accordingly. The structural and acoustic damping properties were both found to play an important role in vibro-acoustic response.

33.2 Methods

33.2.1 Model Methods

The basic modeling methods employed in this project were thoroughly discussed in an earlier publication [1]. The following is a summary. Geometry and density information is taken from CT scans of the actual instrument. The CT images are taken through a CT interpretation program where the various parts are converted into 3D objects and surface meshed. The meshes are exported to a Finite Element (FE) format and edited in a FE preprocessor. These surface meshes envelope the original 3D objects computed by the CT interpretation software. For thin parts, such as the plates and ribs, the surface mesh is reduced to a single layer on the outer surface. For solid parts, such as the blocks, and the neck and scroll, the original surface mesh is filled with solid elements.

The triangular elements generated on the surfaces by the CT interpretation software were upgraded to quadrangular elements for improved performance. Care was taken to match opposing faces of solid components (i.e. blocks, sound post, bass bar, neck and scroll) so that they could be filled with hex-dominant meshes. Figure 33.1 shows a side-by-side comparison of the mid-treble region of the corpus before and after the re-meshing process. Note that the edges around plates and f-holes are now smooth.

Strings were modeled with a series of beam elements between the bridge and the nut (128 elements each) and between the bridge and the tail piece (20 elements each). The windings on the G, D, and A strings were modeled as non-structural mass. Properties for the beam elements were taken from those used in Knott's model [5]. Similarly, the tail loop is modeled as two lines of beam elements between the bottom of the tail piece and the saddle (three elements each).

To apply tension in the strings a static preload subcase was included. At the top of each string a coincident node was added at the string-nut interface and connected with a zero-length rigid bar element (RBE). In this way a local axis system could be created for each string to orient the DOF of the RBE with that of the beams. The constraint in the axial direction was then excluded for each RBE. Initial preloads were applied in the axial direction at each of the beams. After an initial run, these tension preloads were adjusted to “tune” the strings.

The final *Titian* Stradivari violin structural FE mesh contains 74,756 nodes and 117,528 elements. A full description of the *Titian* Stradivari mesh composition is given in Table 33.1. Note that skins are not included in the individual component counts but are included in the full mesh. The plates were attached to the rib structure with a single layer of hexahedral elements. Figure 33.2 shows a screen capture of the final *Titian* Stradivari FE mesh.

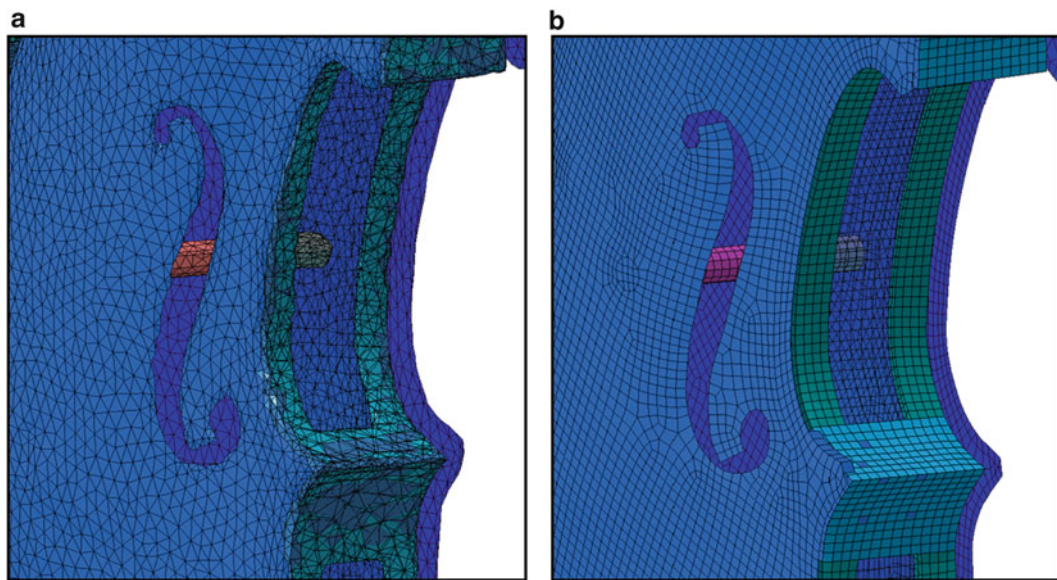


Fig. 33.1 Comparison of the mid-treble region of the corpus (a) before and (b) after the remeshing

Table 33.1 *Titian* Stradivari violin structural FE mesh composition

Component	Beams	TRIA	QUAD	TETRA	PENTA	HEXA	Total elements (no skins)
Back plate	–	62	11,193	–	–	–	11,255
Top plate + bass bar	–	46	10,619	186	18	1,176	12,045
Rib structure	–	–	6,458	–	266	10,724	17,448
Sound post	–	–	–	–	116	348	464
Neck and scroll	–	–	–	27,828	159	7,502	35,489
Fingerboard	–	–	–	–	–	4,032	4,032
Bridge	–	–	–	–	30	1,300	1,330
Tail piece	–	–	–	–	64	4,776	4,840
Nut	–	–	–	–	–	72	72
Saddle	–	–	–	–	–	84	84
Strings + tail loop	598	–	–	–	–	–	598
Full mesh (including skins)	598	438	55,526	28,014	691	32,206	117,528

The thickness graduations of both plates were mapped similarly to the factory violin, using the data collected by Zygmontowicz and mapped by Loen [6]. The published graduation measurements were transferred to the coordinates of the model through a set of transformation vectors estimated from points taken at the corners. The results of the thickness mapping are shown in Figs. 33.3 and 33.4 (color (gray scale) indicates thickness in mm).

33.2.2 Structural Correlation Methods

Ensuring reliable validity of an FE model is essential for realistic noise and vibration simulations of penetrator systems. This requires that component, subsystem, and full-system models be compared to experimental data or to validated models of similar structures. One common tool for comparing and validating an FE model with experimental data is the Modal Assurance Criterion (MAC).

The modal assurance criterion is a statistical indicator that measures the degree of relationship between a pair of vectors [7]. These vectors can be the Modal vectors (normal or complex mode shapes) or Response vectors from a Forced

Fig. 33.2 Final *Titian* Stradivari violin structural FE model with Pre-loaded strings



Response Case for instance. The MAC values are normalized by the magnitude of the vectors, and thus always lie between 0 and 1, where values near 1 indicate consistency between the vectors, while values near 0 indicate the vectors are not consistent [7]. Generally, reasonable values of MAC are 0.7 whereas good correlation is above 0.9 [8].

The MAC formula between two vectors (V_i , V_j) is given in Eq. (33.1).

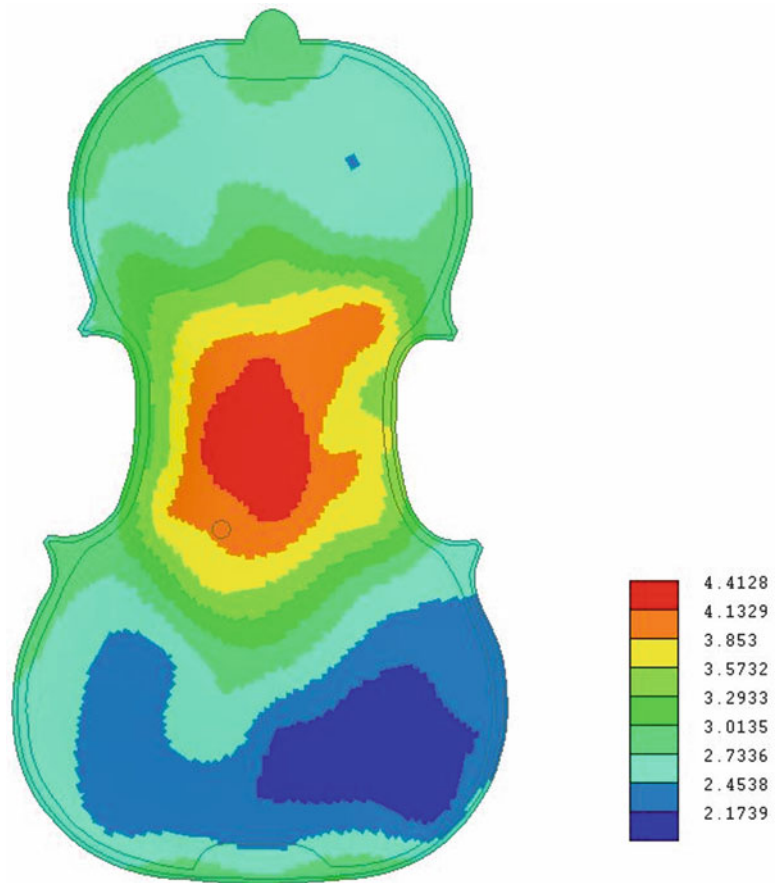
$$MAC_{ij} = \frac{[V_i^T \cdot V_j]^2}{[V_i^T \cdot V_i] \cdot [V_j^T \cdot V_j]} \quad (33.1)$$

Between an FE and test model this results in Eq. (33.2).

$$MAC_{Test_i FE_j} = \frac{[V_{Test_i}^T \cdot V_{FE_j}]^2}{[V_{Test_i}^T \cdot V_{Test_i}] \cdot [V_{FE_j}^T \cdot V_{FE_j}]} \quad (33.2)$$

More details on the modal assurance criterion can be found in [7, 8].

Fig. 33.3 Element thickness of the *Titian* Stradivari violin back plate in mm



33.2.3 Acoustic Methods

33.2.3.1 Sommerfeld Radiation Condition in FEM

Traditionally, the only practical way to handle an interior/exterior acoustic problem (such as a violin with an inner cavity connected to the outside air via the f-holes) was using the Boundary Element Method (BEM). However, technology has been developed in recent years that makes the Finite Element Method (FEM) more practical, and indeed better suited for the violin acoustic problem.

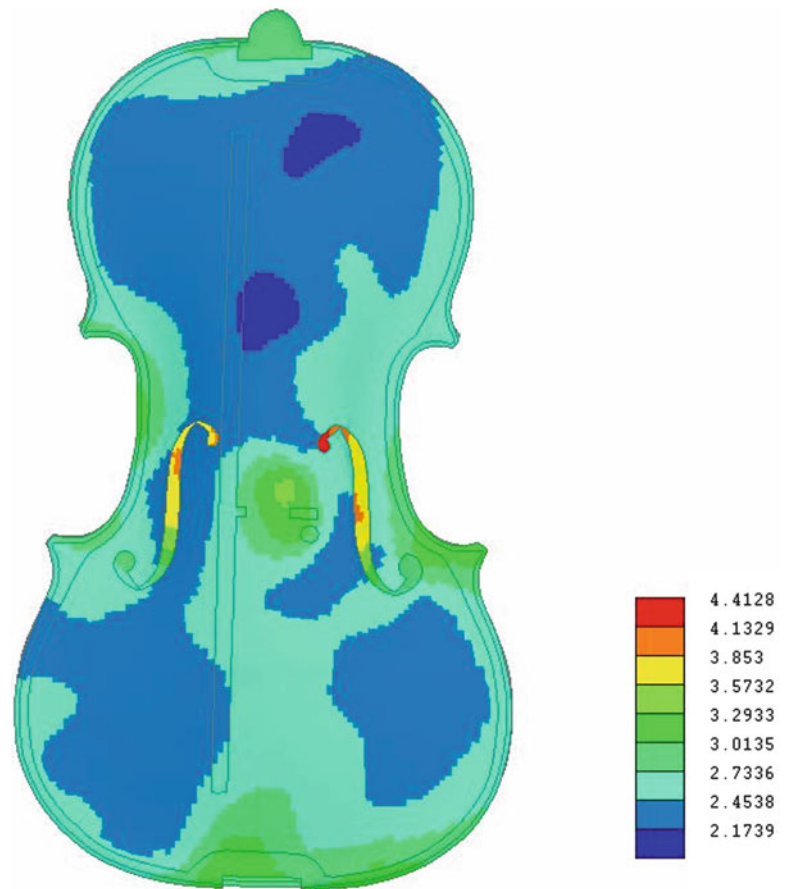
The Sommerfeld radiation condition requires that the boundary surface of the acoustic FEM mesh allows all acoustic waves to propagate freely towards infinity, and that no reflections occur at this boundary [9]. This is represented by Eq. (33.3).

$$\lim_{|\vec{r}| \rightarrow \infty} |\vec{r}| \cdot \left(\frac{\partial p(\vec{r})}{\partial |\vec{r}|} + jkp(\vec{r}) \right) = 0 \quad (33.3)$$

There are currently two methodologies for handling the Sommerfeld radiation condition in exterior FEM problems: the Infinite Element Method (IFEM), and the Perfectly Matched Layer (PML).

IFEM is the older of these two, which requires that the boundary surface of the air be meshed as a canonical shape (such as a sphere or ellipsoid). Special decay shape functions are used on the boundary elements to minimize reflections. The radius of the boundary surface must be at least a full wavelength for the lowest frequency of interest, $R > \lambda$, and up to two full wavelengths away from radiating bodies. This leads to extremely large models with many elements to have a useful dynamic range.

Fig. 33.4 Element thickness of the *Titian* Stradivari violin top plate in mm



With PML a special perfectly matched layer of elements is added to the outer boundary of a convex mesh that is locally-conformal to the structure mesh. This layer utilizes an anti-reflection function to create a coating around the radiating body to absorb the waves. In this case the thickness of the PML only needs to be greater than one fifteenth of the lowest frequency wavelength, $t_{\text{PML}} > (1/15) * \lambda$. Additionally, the distance between the radiating surface and the boundary of the PML only needs to be one to two elements thick.

In both IFEM and PML response points may be placed inside or outside of the FEM boundary. For responses outside the FEM domain the solver will use Kirchoff surface integration to compute the solution for these points once the FEM solution is known.

33.2.3.2 Acoustic Mesh for FEM with AML

LMS Virtual.Lab (R11) software now includes an Automatically Matched Layer (AML) property. This feature constructs the absorbing layer on the solver level by extruding the boundary surface elements automatically [10]. This is similar to PML except that the layer is created on the solver level. This eliminates the need for the user to create the layer manually within the GUI.

For an opened structural mesh, the acoustic medium is present on both sides of the structure, and a volumize mesher was used to create duplicated meshes projected on both sides of the structural shell elements. This is shown in Fig. 33.5. The structure mesh of the violin is shown in green (gray in print version) (lines represent shell elements and filled-in areas represent solid elements). The volumize mesh is shown as a black line enveloping the structure mesh. The convex mesh is then created to wrap around the outside of the volumize mesh with room for at least one or two elements in between. The AML property is applied on this surface. A tetrahedron filler mesh is used to fill the space between the volumize mesh and the convex mesh with tetrahedral elements.

It should be noted that although the structural mesh must be fine to capture the bending waves through the wood materials, the acoustic mesh can be considerably coarser. By coarsening the acoustic mesh, the size of the model was kept small,

Fig. 33.5 Setting up FE meshes for AML property on an opened structural mesh of a violin

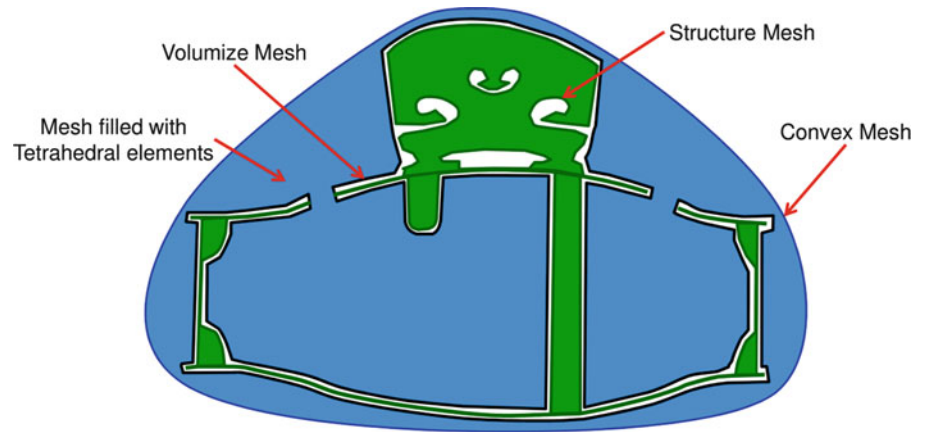
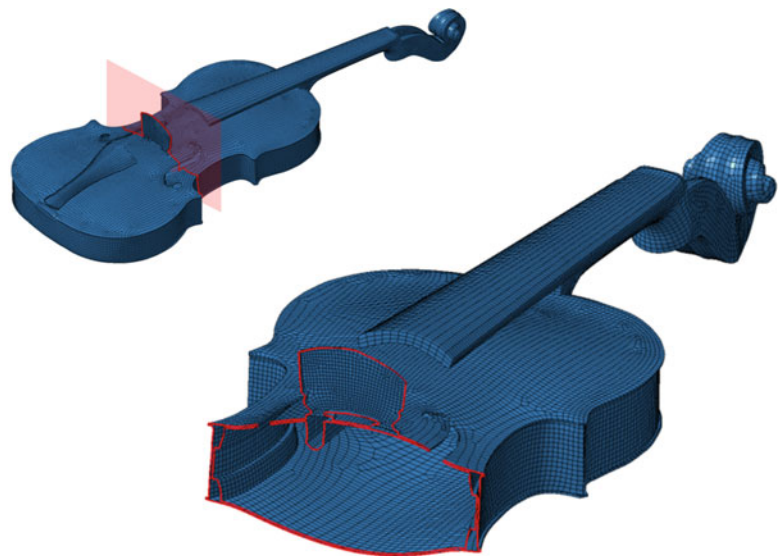


Fig. 33.6 The edges around the f-holes are selected to be maintained



Fig. 33.7 Final volumize mesh of the *Titian* Stradivari violin and cut-plane at bridge location



reducing the solve time. This coarsening is performed before the volumize step. To ensure that the area around the f-holes is not compromised the edges of the f-holes are selected and a mesh group is created to maintain these edges during the coarsening process. This is shown in Fig. 33.6.

The final volumize mesh is shown in Fig. 33.7. This mesh is composed of 56,147 nodes, and 56,234 shell elements (56064 QUAD, and 170 TRIA). A cut-plane view of the final volumize mesh is also shown in Fig. 33.7. This mesh will become the “acoustic envelope” where the structural modes will be transferred to the surrounding air.

Fig. 33.8 Convex mesh around *Titian* Stradivari violin FE model

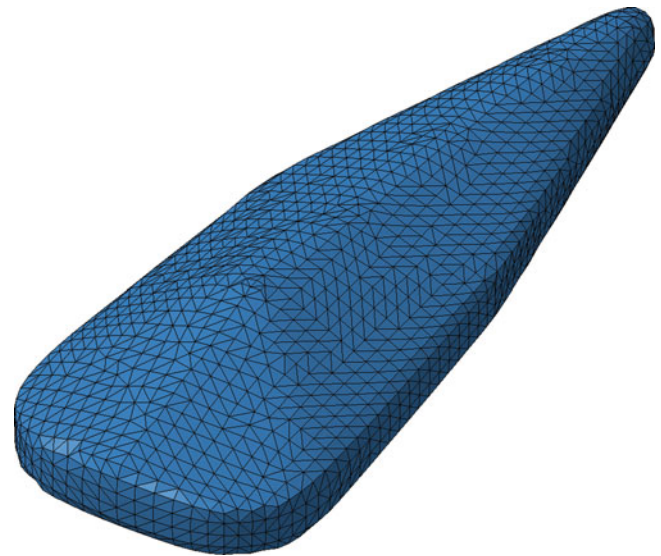


Table 33.2 Mesh compositions for vibro-acoustic FEM analysis of the *Titian* Stradivari violin

Structure mesh	Acoustic mesh
74,756 nodes	226,142 nodes
438 TRIA3 elements	1,191,283 TETRA4 elements
55,526 QUAD4 elements	
28,014 TETRA4 elements	
691 PENTA6 elements	
32,206 HEXA8 elements	
598 beam elements	
55 rigid spider elements	

A convex mesh was created around the volumize mesh. A scaling factor of 1.1 was applied, and the element size was set to 14 mm (this guarantees at least six elements per wavelength up to a frequency of 4,000 Hz, assuming speed of sound 340 m/s). The final convex mesh for the *Titian* Stradivari violin vibro-acoustic model is shown in Fig. 33.8. This mesh defines the point at which the AML property is applied.

Once a convex mesh was wrapped around the outside of volumize mesh the volume between the meshes was filled with tetrahedral elements.

The final mesh compositions of both the structure mesh and acoustic mesh are given in Table 33.2. Figure 33.9 shows the structural mesh inside a cut-away view of the acoustic mesh.

33.2.3.3 Coupled Vibro-Acoustic Set-Up

Once the acoustic mesh was prepared, several pre-processing steps were performed. These include setting the properties for air, defining the AML property on the convex mesh, transferring the structural modes onto the acoustic envelope, and defining input and output locations for the Vibro-acoustic transfer function analysis case.

Properties of air were initially assumed as follows:

$$\begin{aligned} \text{Speed of Sound} &= 340 \text{ m/s} \\ \text{Mass density} &= 1.225 \text{ kg/m}^3 \end{aligned}$$

The parameters used for the AML property are given in Table 33.3.

Response locations for the vibro-acoustic transfer function analysis were selected using field point meshes. These virtual microphones can be placed anywhere in the model. To create results comparable to the available experimental data [2], a spherical field point mesh was placed around the *Titian* Stradivari vibro-acoustic mesh. Like the Bissinger experiment its center point was set on the top plate, midway between the two bridge feet. The radius of the sphere was set to 1.2 m, and the number of equatorial elements was set to 24, creating a response location every 15° along the equator. The resulting sphere contained 218 nodes and is shown in Fig. 33.10.

Fig. 33.9 *Titian* Stradivari structural FE mesh inside a cut-away (coronal) of the acoustic volume mesh

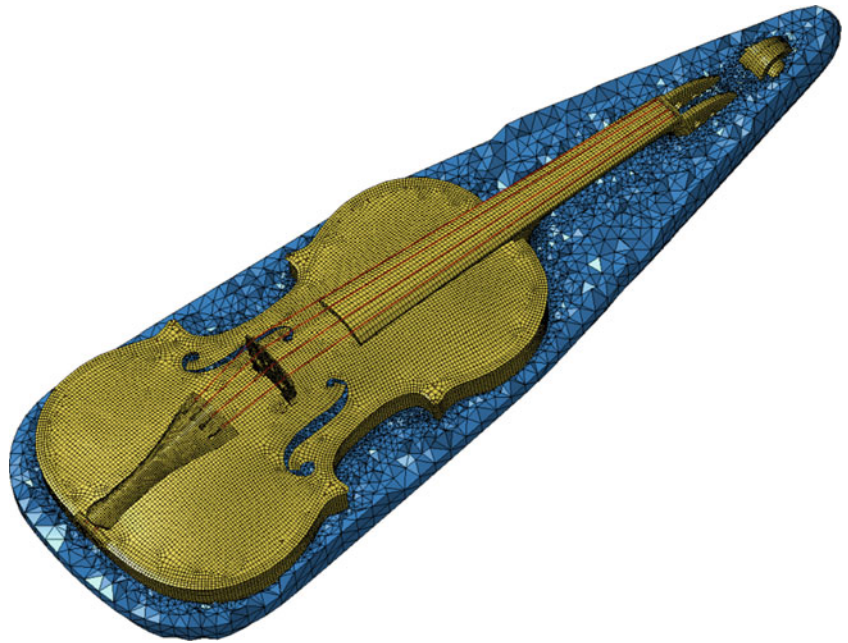


Table 33.3 AML parameters for vibro-acoustic analysis of the *Titian* Stradivari

Number of layers	5
Minimum thickness (as a ratio of wavelength)	0.16
Surface element count	3,728

Fig. 33.10 Field point mesh around the *Titian* Stradivari FE model

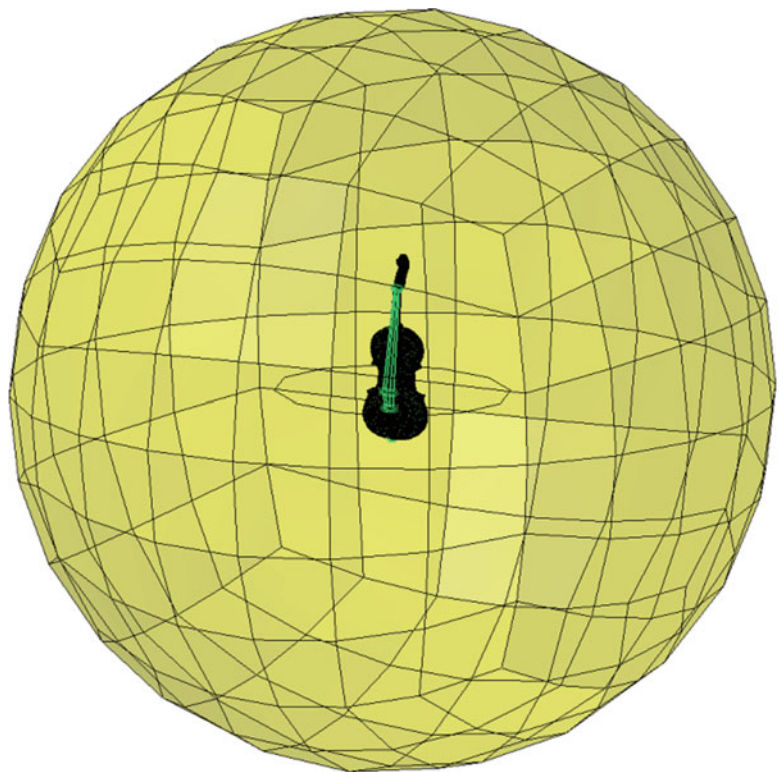
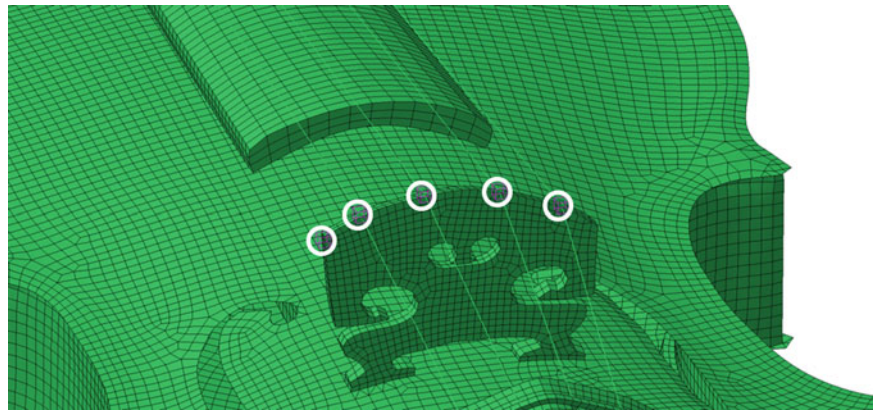


Fig. 33.11 Input locations for the vibro-acoustic transfer function analysis of the *Titian* Stradivari violin



Five input locations were selected for the vibro-acoustic transfer function analysis case, as shown in Fig. 33.11. The first of these was at the upper bass-side corner of the bridge (again to generate results comparable to the Bissinger data [2]). The other four were selected at each of the string-bridge interface points. These were selected to be used in future studies that may include measurements of the forces from the strings being transmitted to the bridge during normal operation (i.e. a musician playing the violin). All three degrees-of-freedom were included for each input point, bringing the total number of inputs to fifteen.

33.3 Results

33.3.1 FE Results for the *Titian* Stradivari Violin

The final results of the *Titian* Stradivari violin structural FE normal modes analysis is given in Table 33.4.

33.3.2 *Corpus Modes (Signature Modes)*

The most important modes of the violin structural FE are the three corpus flexural modes, shown in Figs. 33.12, 33.13, and 33.14. These are the corpus twisting mode known as the CBR (Center-Bout-Rhomboid) mode, and the two corpus bending modes, B1– and B1+. These involve flexure of the plates, and are the efficient radiators of sound in the open string frequency range of the violin (196–659 Hz), and are the structural signature modes [2].

33.3.3 *Correlation Results of the Titian Stradivari Structural Model*

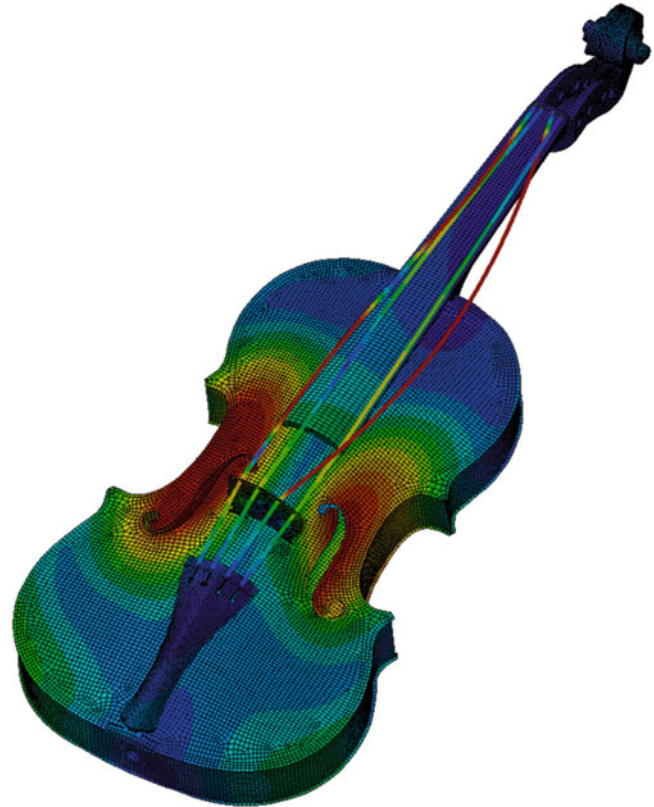
The initial results of the *Titian* violin FE model were correlated with those from test data using the Modal Assurance Criterion (MAC). A plot of the MAC matrix is shown in Fig. 33.15. Note that string frequencies were removed from both sets. The color scale indicates MAC values from 0 (poor correlation, blue (dark in print version)) to 1 (good correlation, red (light in print version)). A magenta (white in print version) box has been added to the figure around the signature modes sub-matrix. These are the main modes of interest as they are the strongest radiators of sound, and are expected to be well captured in the experimental data.

The correlation results were updated to include all modifications and material updates made to the model. The final MAC matrix results are shown in Fig. 33.16. Again, string frequencies have been removed from both sets. The final mode pairs are given in Table 33.5; note that only mode pairs with MAC values greater than 0.6 are included. Overall the final correlation results are excellent. The average absolute percent frequency difference for the signature modes is 3.8%. The average MAC value for the signature modes is 0.873.

Table 33.4 Summary of updated *Titian* Stradivari violin normal modes analysis

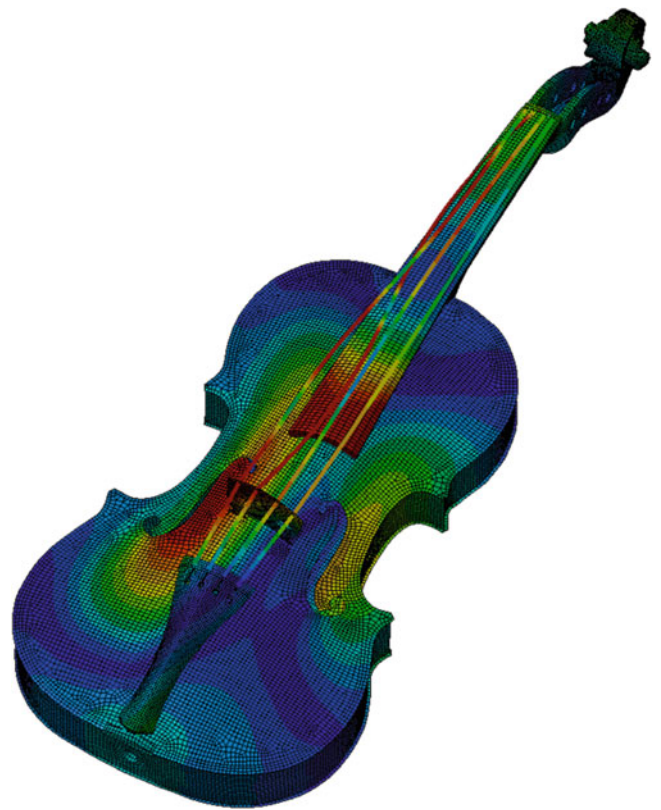
Mode #	Description	Frequency (Hz)
1	B0 (Tail IP)	158.9
2	B0 (Tail OP)	181.1
3	Lateral B0 (Tail IP)	223.5
4	B0 (FB bend)	227.2
5	Lateral B0 (Tail OP)	245.8
6, 7	1st G-string	195.0, 197.0
8, 9	1st D-string	292.2, 294.8
10, 11	2nd G-string	387.9, 393.0
12	CBR	427.3
13, 14	1st A-string	436.2, 442.5
15	B1-	452.5
16	B1+	529.8
17, 18	2nd D-string	587.5, 589.0
19, 20	3rd G-string	590.3, 593.3
21, 22	1st E-string	654.4, 657.5
23	Lateral FB	538.6
24	Neck-FB twist IP	633.6
25	Tail rock	650.8
26	Neck-FB twist OP	661.1

Fig. 33.12 CBR: 427.3 Hz



It is noted that the material properties of the *Titian* Stradivari violin FE model were updated to “tune” the modal frequencies. Updating was performed until the average percent difference for the three signature modes was below 5 %. A summary of the final material properties is given in Table 33.6.

Final mass of the full *Titian* Stradivari violin structural FE model was 323.2 g. The back plate of the model weighed 88.8 g, while the top plate + bass bar of the model weighed 48.1 g.

Fig. 33.13 B1-: 452.5 Hz**Fig. 33.14** B1+: 529.8 Hz

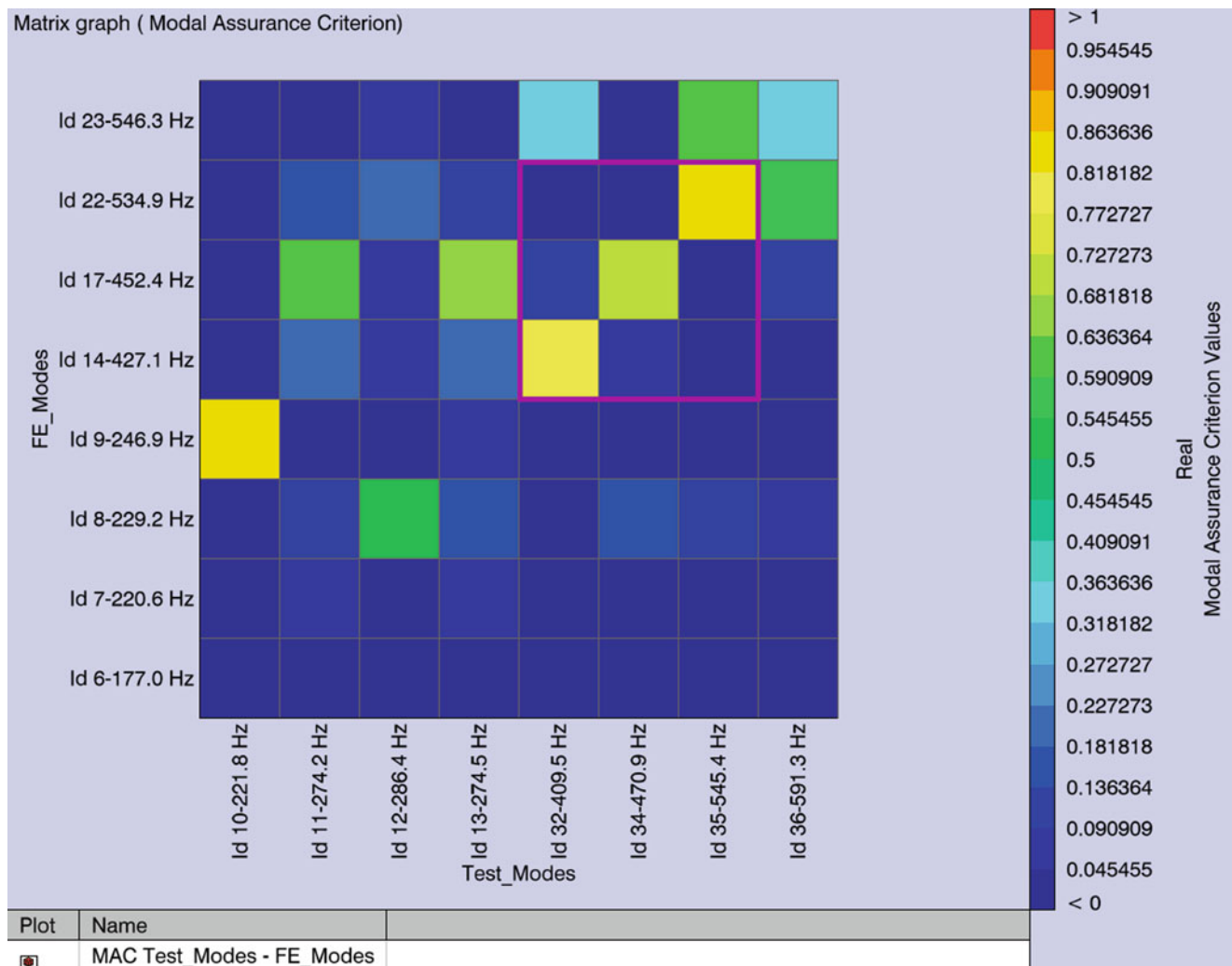


Fig. 33.15 Initial correlation results for the *Titian* violin

33.3.4 FEM Vibro-Acoustic Noise Transfer Function Analysis

The initial modal based vibro-acoustic noise transfer function case was set to calculate the transfer function for frequencies from 100 to 1,000 Hz with a 2 Hz increment. The Direct solver was used, rather than the iterative solver, due to the relatively small size of the model (<700,000 DOFs) and the complexity of a problem involving both interior and exterior domains.

The combined level multi-processing feature utilizes both frequency level and matrix level parallelization. This was used to speed up the solve time and to reduce total memory required. The system used for solving the model had two processor cores with two threads per processor.

The response of the point directly in front of the violin top plate was selected for comparison with the Bissinger test data. The transfer function (radiativity) magnitude for this point with respect to the lateral (X-direction) input at the upper bass-side corner of the bridge was extracted from each run and plotted against that of the Bissinger data [2].

Since the structural FE model was correlated with experimental modal data previously, the frequencies of peaks in the radiativity curve that are associated with structural FE modes are all within 5 % of those of the experimental data. The acoustic modes, A0 (275 Hz) and A1 (464 Hz), are of interest for verification of the vibro-acoustic model. The A1 peak is somewhat obfuscated by the B1– peak making it difficult to use as a reliable verifier. The A0 peak has a split in the experimental data of the *Titian* Stradivari violin, most likely due to a substructure mode. Despite this, the A0 peak is clearly visible, and can be used for updating the acoustic results. For comparison, the experimental peak in radiativity for A0 was 0.396 Pa/N.

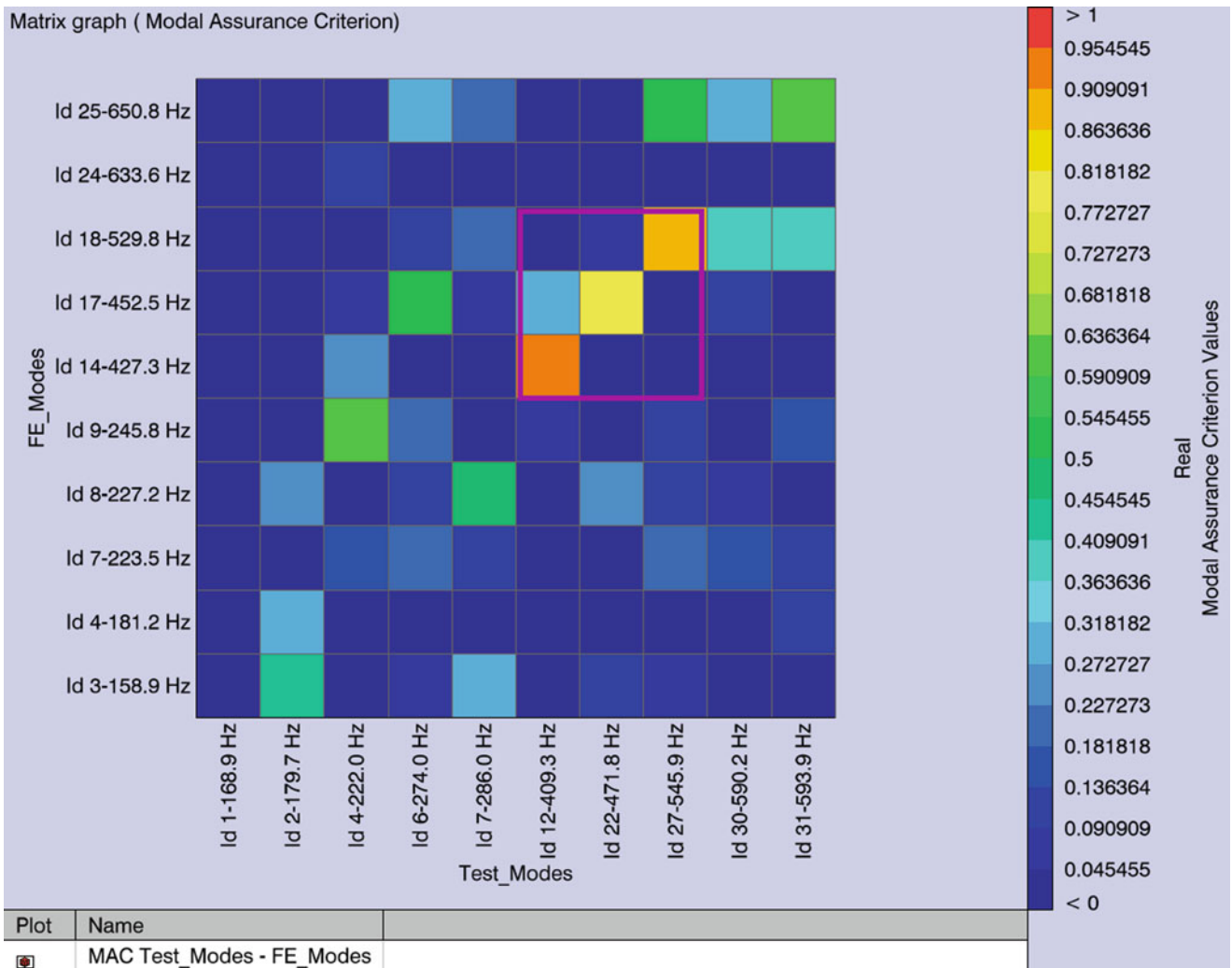


Fig. 33.16 Updated correlation results for the *Titian* violin

Table 33.5 Updated mode pair results for the *Titian* violin

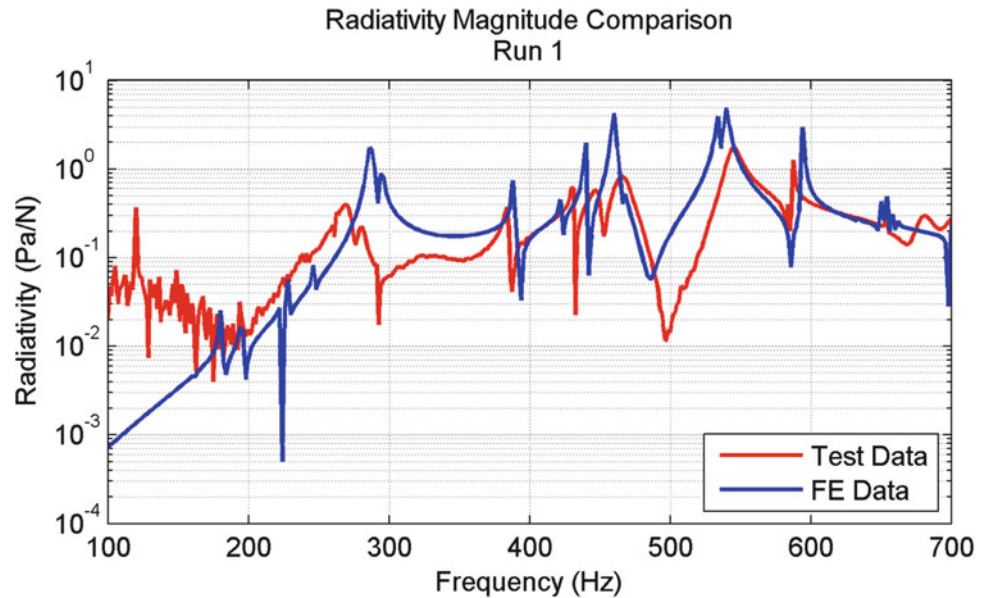
Test id	Test freq (Hz)	FE id	FE freq (Hz)	MAC value	Freq diff (Hz)	Freq diff (% of test)
4	222	9	245.8	0.631	23.71	10.7
12	409.3	14	427.3	0.916	18.02	4.4
22	471.8	17	452.5	0.808	-19.25	-4.1
27	545.9	18	529.8	0.896	-16.08	-2.9
31	593.9	25	650.8	0.634	56.85	9.6

Table 33.6 Summary of final material properties for *Titian* Stradivari FE model

Component	Thickness (mm)	E1 (MPa)	E2 (MPa)	NU12	G12 (MPa)	G1Z (MPa)	G2Z (MPa)	RHO (kg/m ³)
Back plate	Variable	11,730	1,560	0.424	892	505	265	570
Top plate	Variable	9,350	1,190	0.422	786	760	63.7	350

In the initial run the structural modes are left as is; that is, they are real normal modes and have no modal damping. The properties of air were kept as default real constant values, $c = 340$ m/s, $\rho = 1.225$ kg/m³. The comparison of the radiativity result with experiment is given in Fig. 33.17. In almost all cases the peaks of the FE modes are sharper than those of the experiment, indicating that damping is important and needs to be included. The A0 mode is also considerably more prominent in the FE results (6.4 dB higher) than in the test data.

Fig. 33.17 Radiativity results comparison for point directly in front of violin top plate; real normal modes on structural FE; air properties constant real: $c = 340$ m/s, $\rho = 1.225$ kg/m³



The properties of air are adjusted to include a loss factor in media. Skudrzyk shows that a loss factor, η , can be added to the speed of sound to make it complex [11]. This is shown in Eq. (33.4).

$$c = c_0 (1 + j \frac{\eta}{2}) \quad (33.4)$$

Lord also discusses this loss factor in terms of bending waves in a plate, and concludes that for small values of damping ($\zeta \leq 0.1$) this loss factor is approximately proportional to the damping factor, ζ [12]. This proportionality is given in Eq. (33.5).

$$\eta \cong 2\zeta \quad (33.5)$$

In the experimental data of the *Titian* Stradivari violin the radiativity has a split in the A0 peak. This is most likely due to a local structure mode of either the tail piece or fingerboard; however, since no response points were measured on either of these sub-structures, it is difficult to curve fit this area reliably, and the damping factor estimate would be particularly sensitive.

The average damping factor of the A0 mode for all 14 violins in the VIOCADEAS database [4] is 2.12 %. The loss factor in the air property was thus adjusted. In the final run the speed of sound was $c = 340 + j8$ m/s. The structural modal damping, the string modes were undamped, while all others had an estimated modal damping applied.

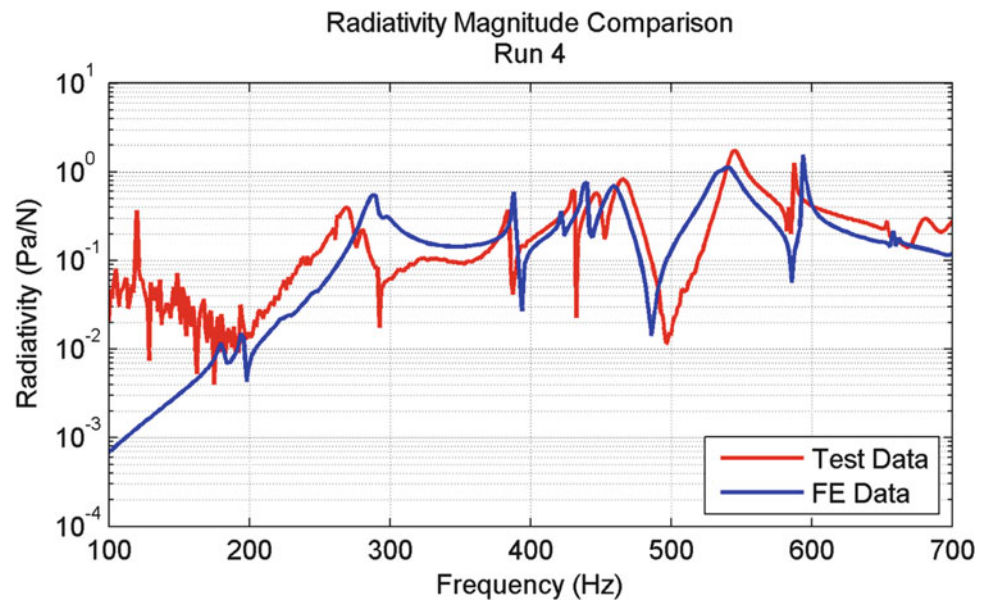
The comparison of the transfer function of the point over the top with respect to the bass-side bridge input for this final analysis run compared to the experimental data is given in Fig. 33.18. The FE and test curves follow the same trend. Structural modes all have approximately the same shape (again, structural damping is realistic). The peak of the predicted A0 mode is now only 1.45 dB above that of the test.

The predicted frequency of the A0 mode is consistently above that of test by 6.8 % for all four runs; this could be a function of the air density, or related to sound post stress loading [13, 14].

33.4 Conclusions

Based on the results of these analyses, the coupled vibro-acoustic FEM model of the *Titian* Stradivari violin is an excellent representation of the real structure. This model was created by measuring the structural geometry and density from CT scans of the actual instrument. Correlation between the experimental data and the initial FE models was used to compare the modal behavior, and the material properties in the models were iterated to determine a set of parameters that reflect the dynamic behavior of the real instruments. The structural model was updated so that the first several modes were within 5 % of the experimental modal frequencies, and all MAC values for mode pairs of interest were above 0.6.

Fig. 33.18 Radiativity results comparison for point directly in front of violin top plate; modal damping added to structural modes (except string modes); air properties complex:
 $c = (340 + j8) \text{ m/s}$,
 $\rho = 1.225 \text{ kg/m}^3$



Most importantly structural and acoustic damping characteristics were taken from a 14 violin experimental study [2]. These were incorporating into a fully coupled vibro-acoustic model of the *Titian* Stradivari violin using the latest acoustic FEM techniques.

It was shown that by including all these details, the vibro-acoustic behavior of the *Titian* Stradivari violin is accurately predicted. Predicted structural mode frequencies were all within 5 % of the experimentally measured modes. The main acoustic mode, A0, of the *Titian* Stradivari was predicted within 7 % of the experimental result, and its associated peak in the radiativity magnitude was within 1.5 dB.

References

1. Pyrkosz M, Van Karsen C, Bissinger G (2010) Converting CT scans of a stradivari violin to a FEM. In: Proceedings of the 28th international modal analysis conference, Jacksonville, February 2010
2. Bissinger G (2008) Structural acoustics of good and bad violins. *J Acoust Soc Am* 124(3):1764–1773
3. Bissinger G (2005) A unified materials-normal mode approach to violin acoustics. *Acustica* 91:214–228
4. Bissinger G (2008) Structural acoustics model of the violin radiativity profile. *J Acoust Soc Am* 124(6):4013–4023
5. Knott GA (1987) A modal analysis of the violin using MSC/NASTRAN and PATRAN. M.S. Thesis, Naval Postgraduate School. Available through NTIS website (March 1987)
6. “Thickness Contour Maps” by Jeffrey Loen with Violin specification and thickness measurements by S. Zyguntowicz, *Strad3D* (2009)
7. Allemang RJ (2002) The modal assurance criterion (MAC): twenty years of use and abuse. In: Proceedings of the international modal analysis conference, Los Angeles, February 2002
8. Heylen W, Lammens S, Sas P (1998) Modal analysis theory and testing. Katholieke Universiteit Leuven, Department of Mechanical Engineering, Division of Production Engineering, Machine Design and Automation, Leuven
9. Desmet W et al (1998) Numerical acoustics – theoretical manual. LMS International
10. Hong K et al (2008) LMS International A next generation solution for functional performance engineering – LMS Virtual.Lab Acoustic Training
11. Skudrzyk E (1972) The foundation of acoustics: basic mathematics and basic acoustics. Springer, New York, pp 319–322
12. Lord H, Gatley W, Evensen H (1980) Noise control for engineers. Krieger Pub. Co., Malabar, pp 258–263
13. Meinel H (1937) On the frequency curves of violins. *Akust Z* 2:22–33. Translated by Fan C (2007)
14. Bissinger G (1995) Some mechanical and acoustical consequences of the violin soundpost. *J Acoust Soc Am* 97:3154–3164

Chapter 34

Vibrational Response of Elastic Membranes Coupled to Acoustic Fluids Using a BEM–BEM Formulation

Jairo Useche and Alexander Narvaez

Abstract In the last two decades, few works have been reported in the literature related to analysis of fluid–structure interaction problems using Boundary Element Method for modeling both structure and fluid. To the author’s knowledge, none of them applied to the dynamic analysis of elastic membranes coupled to acoustic fluids.

In this work a full time-direct Boundary Element Formulation for the dynamic analysis of elastic membranes coupled to acoustics fluid is presented. The elastic membranes is modeled using the classical linear elastic pre-stretched membrane theory. The acoustic fluid is modeled using the acoustic-wave equation for homogeneous, isotropic, inviscid and irrotational fluids. Elastostatic fundamental solution is used in the boundary element formulation for the elastic membrane. The boundary element formulation for the acoustic fluid is based on the fundamental solution of three dimensional Poisson equation. Domain integrals related to inertial terms and those related with distributed pressure on membrane, were treated using the Dual Reciprocity Boundary Element Method. Fluid–structure coupling equations were established considering the continuity of the normal acceleration of the particles and dynamic pressure at fluid–structure interfaces. The time integration is carried out using the Houbolt method. Results obtained shows the accuracy and efficiency of the proposed boundary element formulation.

Keywords Boundary element method • Dual reciprocity boundary element method • Fluid–structure interaction • Acoustic fluid • Elastic membrane

34.1 Introduction

The analysis of fluid–structure coupled systems is a challenging and complex task. In general, the use of experimentation or numerical methods represent the two unique alternatives to obtain approximate solutions for these kind of problems. However, numerical methods based on domain discretization requires refined meshes for high frequency problems, since the length of the elements should be proportional to the size of the wavelength. This means a more time-consuming model.

Since consolidation of the boundary element method (BEM) as reliable numerical method for structural and fluid analysis, linear vibrations of structures coupled with an internal fluid has been carried out using hybrid BEM–FEM formulations. In these formulations BEM is used to model the fluid media and the FEM to model the structural response [2–9, 11, 12, 14, 17, 19, 20, 26]. The main advantage of such formulations lies in a substantial reduction in the number of the degrees of freedom in the discretization of the fluid domain. However, in this formulations is necessary to discretize the entirely structure due to the use of the FEM.

Few BEM–BEM coupled formulations for fluid–structure interaction has been published [1, 15, 16, 21–23]. However, despite the fact that the BEM has been used for dynamic analysis of membrane structures and for analyses of acoustic fluids, to the best of authors knowledge, these formulations do not have been used for the fluid–structure interaction problem analysis using a full boundary element formulation for such purpose.

J. Useche (✉) • A. Narvaez

Department of Mechanical Engineering, Technological University of Bolivar, Cartagena, Colombia
e-mail: juseche@unitecnologica.edu.co; anarvaez@unitecnologica.edu.co

34.2 Structure Subjected to a Fluid Pressure Loading

Consider a partially opened cavity Ω_f with rigid walls and a flexible elastic membrane Ω_s with mass density ρ_s and thickness h (see Fig. 34.1). Cavity contains homogeneous and isotropic acoustic fluid with mass density ρ_f . The membrane vibrations and the acoustic pressure field in the fluid are influenced by the mutual vibro-acoustic coupling interaction. In this work, the vibro-acoustic coupling interaction is modeled using a Eulerian formulation where the acoustic response is described by the pressure, while the membrane response is described by the transversal displacement field.

34.2.1 Acoustic Wave Equation

The dynamic pressure of an ideal inviscid fluid under small perturbations in a spatial region Ω_f confined by the boundary surface $\Gamma_f = \Gamma_f^p + \Gamma_f^q$, is governed by the wave equation [10] (see Fig. 34.2):

$$p_{,\alpha\alpha} = \frac{1}{c_f^2} \ddot{p} \tag{34.1}$$

In this equation p is the fluid pressure, $c_f^2 = \kappa/\rho_f$ stands for wave propagation velocity, κ is the bulk modulus. Above equation can be modified to include the effect of presence of an acoustic source. Double dot represents a second time derivative. Indicial notation is used throughout this work. Greek indices vary from 1 to 2 and Roman indices from 1 to 3.

34.2.2 Dynamic Equation of an Elastic Membrane

Now consider a linear elastic membrane with thickness h and density ρ_s occupying the spatial domain Ω_w confined by the boundary $\Gamma_s = \Gamma_s^w + \Gamma_s^f$, as showed in Fig. 34.3. An initial tension T_0 is uniformly applied to the membrane. In this

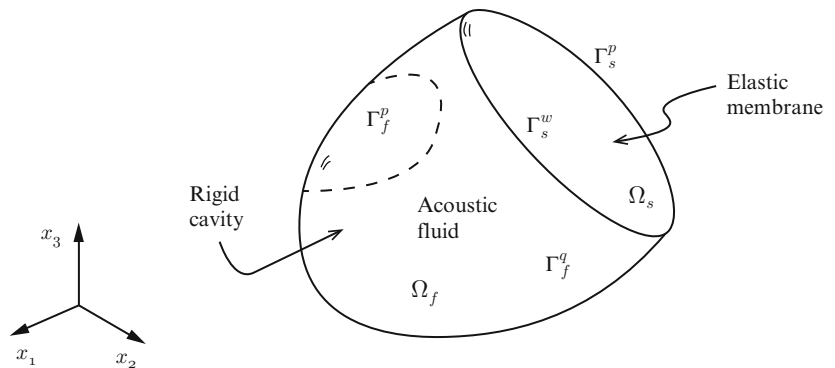


Fig. 34.1 Fluid–structure interaction problem (Ipe 7.1.1)

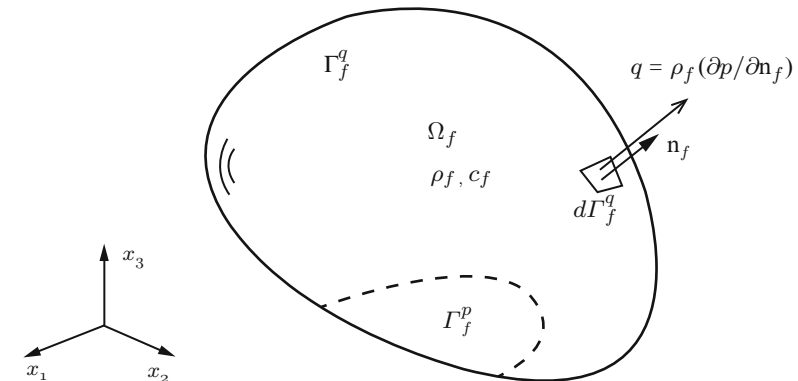
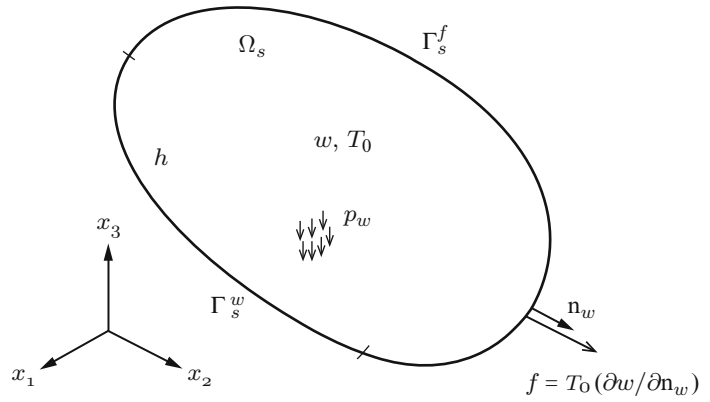


Fig. 34.2 Acoustic fluid domain (Ipe 7.1.1)

Fig. 34.3 Elastic membrane domain (Ipe 7.1.1)



work, the small deflection elastic membrane theory is considered. Thus, differential equation describing the transversal displacement $w(x, t)$ of this membrane in the time interval $[0, t^*]$ is given by:

$$w_{,\alpha\alpha} + \frac{p_w}{T_0} = \frac{1}{c_w^2} \ddot{w} \quad (34.2)$$

where $c_w^2 = T_0/\rho_s$ and $p_w(x, t)$ is a distributed pressure applied over the membrane.

34.3 Boundary Element Equations

34.3.1 Boundary Element Equations for Acoustic Wave Equation

The derivation of the integral formulation for Eq. (34.1) is based on application of the Boundary Element Method to the acoustic wave equation as presented in [25]. Thus, by using the weighted residual method and making use of the Green's identity, the following equation is obtained:

$$c(\mathbf{x}') p(\mathbf{x}') + \int_{\Gamma_f} Q(\mathbf{x}', \mathbf{x}) p(\mathbf{x}) d\Gamma_f = \int_{\Gamma_f} P(\mathbf{x}', \mathbf{x}) q(\mathbf{x}) d\Gamma_f + \frac{1}{c_f^2} \int_{\Gamma_f} Q(\mathbf{x}', \mathbf{x}) \ddot{p}(\mathbf{x}) d\Gamma_f \quad (34.3)$$

In this equation, \mathbf{x}' and \mathbf{x} represent collocation and field points, respectively; $P(\mathbf{x}', \mathbf{x})$ and $Q(\mathbf{x}', \mathbf{x})$ are fundamental solutions for pressure and gradient pressures for three dimensional acoustic problems, respectively, as presented in [25]. The value of $c(\mathbf{x}')$ is equal to $1/2$ when \mathbf{x}' is located on a smooth boundary. In order to treat the domain integral, the Dual Reciprocity Boundary Element Method (DRM) is used as presented in [18]. DRM particular solutions were obtained considering the function $f_j(r) = 1 + r_j$ for the approximation of $\ddot{p}(t)$, as presented in [18]. In order to discretize boundary surfaces of the acoustic medium, N boundary quadrilateral elements were used and $p(\mathbf{x})$ and $q(\mathbf{x})$ were assumed to be constant over each element and equal to their values at the mid-element node. Thus, the discretised form of Eq. (34.3) applied at each collocation point obtaining the following linear system of equations:

$${}^f \mathbf{M} \ddot{\mathbf{p}} + {}^f \mathbf{H} \mathbf{p} = {}^f \mathbf{G} \mathbf{q} \quad (34.4)$$

where ${}^f \mathbf{M}$ is the fluid mass matrix, ${}^f \mathbf{H}$ and ${}^f \mathbf{G}$ are boundary element influence matrices; \mathbf{p} and \mathbf{q} are vectors of nodal pressures and normal derivative of pressure, respectively.

34.3.2 Boundary Element Equations for an Elastic Membrane

The derivation of the integral formulation for Eq. (34.2) is based on the application of the BEM to the membrane equation as presented in [25]. Thus, by using the weighted residual method, and making use of the Green’s identity, the integral formulation for Eq. (34.2) is given by:

$$\begin{aligned}
 c(\mathbf{x}') w(\mathbf{x}', t) + \int_{\Gamma_s} T(\mathbf{x}', \mathbf{x}) w(\mathbf{x}, t) d\Gamma_s - \int_{\Gamma_s} W(\mathbf{x}', \mathbf{x}) f(\mathbf{x}, t) d\Gamma_s \\
 = -\frac{1}{T_0} \int_{\Omega_s} W(\mathbf{x}', \mathbf{x}) p_w(\mathbf{x}, t) d\Omega_s + \frac{1}{c_w^2} \int_{\Omega_s} Q(\mathbf{x}', \mathbf{x}) \ddot{w}(\mathbf{x}) d\Omega_s
 \end{aligned}
 \tag{34.5}$$

where \mathbf{x} and \mathbf{x}' are field and collocation points respectively, $W(\mathbf{x}', \mathbf{x})$ and $T(\mathbf{x}', \mathbf{x})$ are fundamental solutions for displacement and traction, respectively as given in [24]. $c(\mathbf{x}')$ is the jump term arising from the terms of $O(1/r)$ in the kernel $T(\mathbf{x}', \mathbf{x})$. In this work, the DRM was used to transform domain integrals related to inertial terms into boundary integrals. DRM particular solutions were obtained considering the function $f_j(r) = 1 + r_j$ for the approximation of $\ddot{w}(t)$ and $p_w(t)$ terms, as presented in [18]. Applying Eq. (34.5) at each collocation point, the following linear system of equations is obtained:

$${}^s M \ddot{w} + {}^s H w = {}^s G f - {}^s B p_w
 \tag{34.6}$$

Here ${}^s M$ is the membrane mass matrix, ${}^s H$ and ${}^s G$ are the influence matrices, ${}^s B$ is the influence matrix related with distributed pressure p_w applied over the membrane.

34.4 Fluid–Structure Coupling Equations

Fluid–structure coupling equations are given by compatibility considerations about normal pressure and dynamic pressure force acting at fluid–structure interface (see Fig. 34.4). Mathematically, these conditions can be written as follows [13]:

$$\begin{aligned}
 \mathbf{n}_f \nabla p = \mathbf{q}_n = -\rho_w \mathbf{C}_w \ddot{w} \\
 p_w = -\mathbf{C}_f p
 \end{aligned}
 \tag{34.7}$$

That is, pressure gradient acting on the fluid–structure interface Γ_{fs} are related to normal acceleration of the plate and the acoustic pressure is equilibrated with pressure on the membrane (see Fig. 34.2). In these equations, \mathbf{C}_w and \mathbf{C}_f represent connectivity matrices joining fluid and structural degree of freedom at fluid–structure interface.

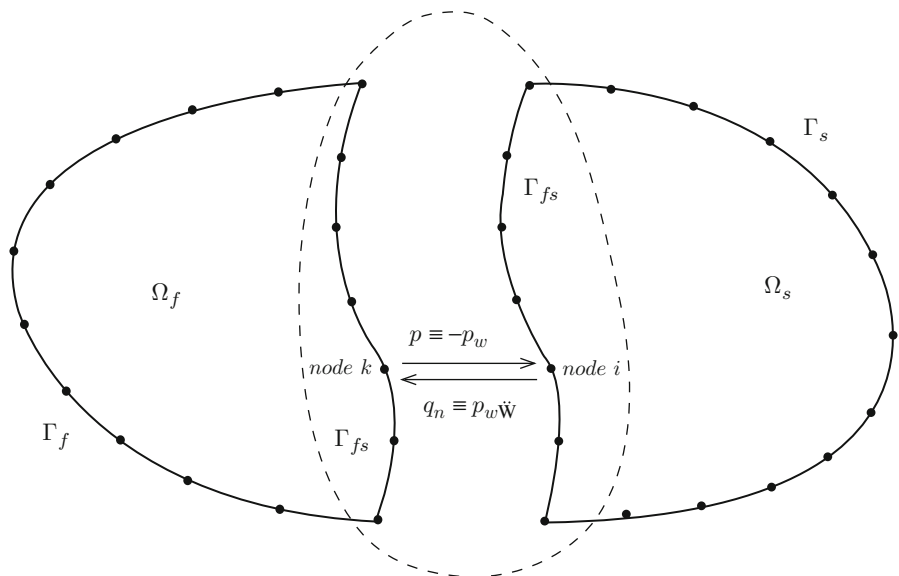


Fig. 34.4 Discretized coupled problem using BEM (Ipe 7.1.1)

Replacing Eqs. (34.7) into Eqs. (34.4) and (34.6) we obtain the coupled fluid–structure equation problem:

$$\begin{bmatrix} {}^s\mathbf{M} & \mathbf{0} \\ \mathbf{S} & {}^f\mathbf{M} \end{bmatrix} \begin{Bmatrix} \ddot{\mathbf{w}} \\ \ddot{\mathbf{p}} \end{Bmatrix} + \begin{bmatrix} {}^s\mathbf{H} & -\mathbf{A} \\ \mathbf{0} & {}^f\mathbf{H} \end{bmatrix} \begin{Bmatrix} \mathbf{w} \\ \mathbf{p} \end{Bmatrix} = \begin{bmatrix} {}^s\mathbf{G} & \mathbf{0} \\ \mathbf{0} & {}^f\mathbf{G}_{ff} \end{bmatrix} \begin{Bmatrix} \mathbf{f} \\ \mathbf{q} \end{Bmatrix} \quad (34.8)$$

In this equation, the off-diagonal sub-matrices $\mathbf{A} = {}^s\mathbf{B}_{fs}\mathbf{C}_f$ and $\mathbf{S} = \rho_w {}^f\mathbf{G}_{fs}\mathbf{C}_w$ are fluid-membrane coupling matrices. ${}^f\mathbf{G}_{fs}$ and ${}^f\mathbf{G}_{ff}$ are submatrices of ${}^f\mathbf{G}$ related with degrees of freedom defined on the interface Γ_{fs} . ${}^s\mathbf{B}_{fs}$ is a sub-matrix of ${}^s\mathbf{B}$ related with pressure terms defined in s. Equations (34.8) can be rewritten in a general way as:

$$\mathbf{M}\ddot{\mathbf{u}} + \mathbf{H}\mathbf{u} = \mathbf{G}\mathbf{r} \quad (34.9)$$

where: $\ddot{\mathbf{u}} = \{\ddot{\mathbf{w}}, \ddot{\mathbf{p}}\}^T$, $\mathbf{u} = \{\mathbf{w}, \mathbf{p}\}^T$ and $\mathbf{r} = \{\mathbf{f}, \mathbf{q}\}^T$. The Houbolt integration scheme is used in order to obtain the time response using Eq. (34.9). The most important aspect of this method when compared to other time integration methods based on central difference approximations or Newmark scheme is the introduction of artificial damping which truncates the influence of higher modes in the response. The Houbolt integration scheme is an explicit unconditionally stable algorithm based on backward-type finite difference formula with error of order $O(\Delta t^2)$.

34.5 Numerical Example: Rigid Channel Containing an Acoustic Fluid Coupled to a Membrane

In this problem, a 50 m long channel containing an acoustic fluid under a transient pressure load and coupled with a homogeneous elastic membrane is analyzed as showed in Fig. 34.5. A distributed sinusoidal pressure load $p(t) = 1.0\sin(0.25t)$ is considered. The fluid has a density $\rho_f = 100 \text{ kg/m}^3$ and a bulk's modulus of $\kappa = 10,000 \text{ Pa}$. The membrane is inclined 53° with respect to the vertical axis and density $c_w = 1.0 \text{ kg/m}^2$.

In this case, fluid boundary was discretized with 618 constant quadrilateral elements and 40 interior collocation points, while membrane boundary was discretized with 12 constant elements and 9 interior collocation points. Again, these collocation points are coincident with fluid collocation points located in the fluid-membrane interface. Membrane tensile load, T_0 , from 125 to 2,000 N/m^2 was considered in the analysis.

The history of the central deflection for time interval 0–75 s is shown in Fig. 34.6, for different values of stretch load. Good results were obtained by choosing $\Delta t = 0.75 \text{ s}$, although results for all time step sizes inside the interval $0.03 \text{ s} < \Delta t < 1 \text{ s}$ were satisfactory. As expected, displacements were getting smaller when membrane tensile load is increased as shown in Fig. 34.7. As presented in Fig. 34.8, normal pressure gradient converges to the rigid wall solution by increasing the membrane tensile load. As shown in Fig. 34.9, displacements and pressures present a delay in time until the wave arrives to the membrane, because the fluid wave velocity is $c_f = 10 \text{ m/s}$ and the channel is approximate 50 m long, so it takes about 5 s to cross it.

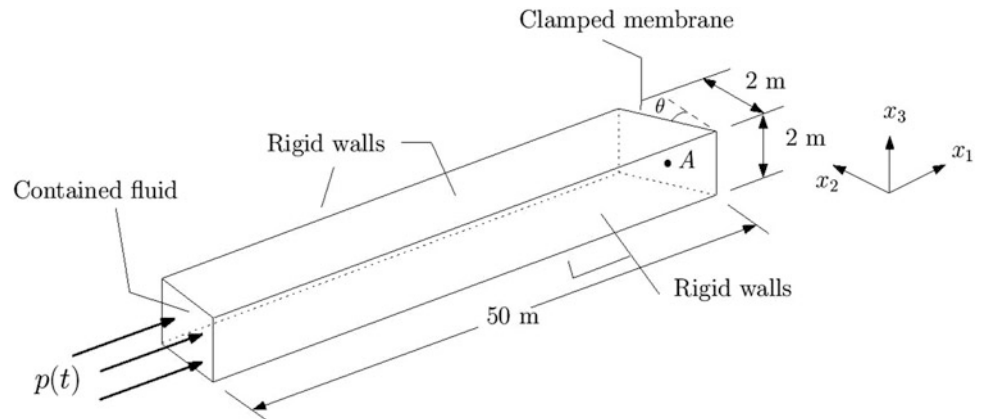


Fig. 34.5 Fluid in a rigid channel coupled to a membrane (Ipe 7.1.1)

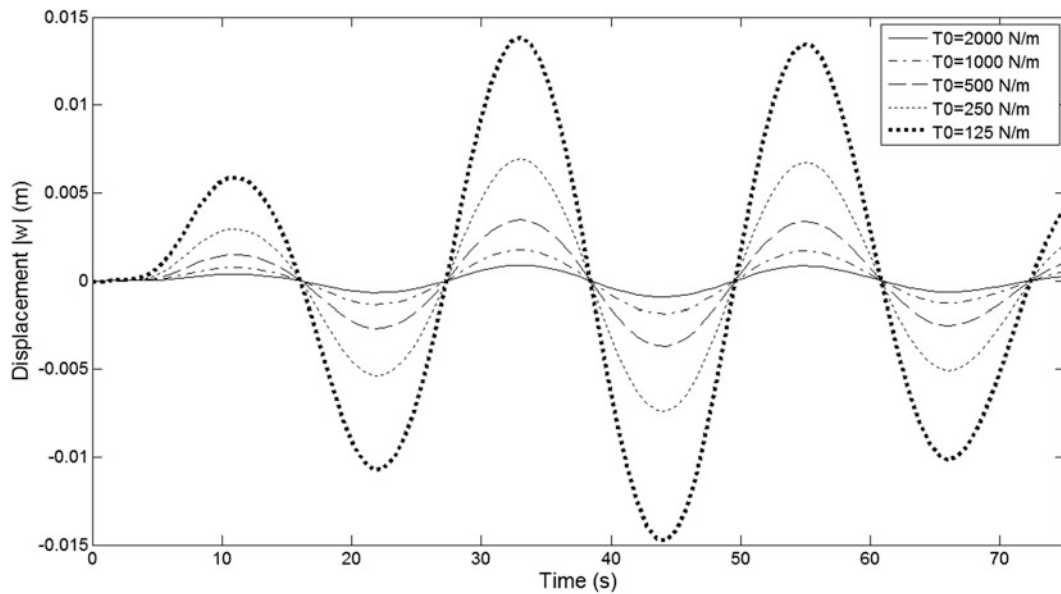


Fig. 34.6 Time history of central deflection for membrane in the channel problem (MATLAB[®] 11)

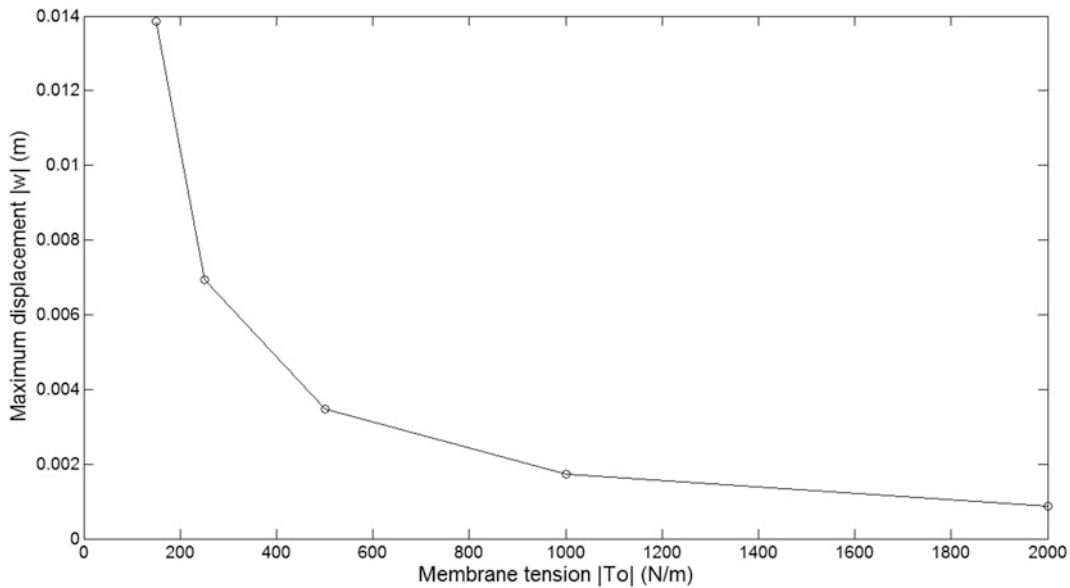


Fig. 34.7 Maximum displacement at membrane as function of membrane stretch tension (MATLAB[®] 11)

34.6 Conclusions

A new full boundary element formulation for the transient dynamic analysis of acoustic fluids coupled to elastic membranes is presented. Membranes were modeled using a boundary element formulation based on the linear elastic membrane theory under small deflection. The acoustic fluid was modeled using a boundary element formulation for the three dimensional acoustic wave equation. Fluid–structure coupling equations were established considering the continuity of the normal acceleration of the particles at fluid–structure interfaces. Domain integrals on both, fluid and structure equations, were treated using the Dual Reciprocity Boundary Element Method. Results show good agreement with those obtained from finite difference models, turning proposed formulation a reliable and an alternative numerical engineering tool for the dynamic analysis of acoustic fluids coupled flexible elastic membranes.

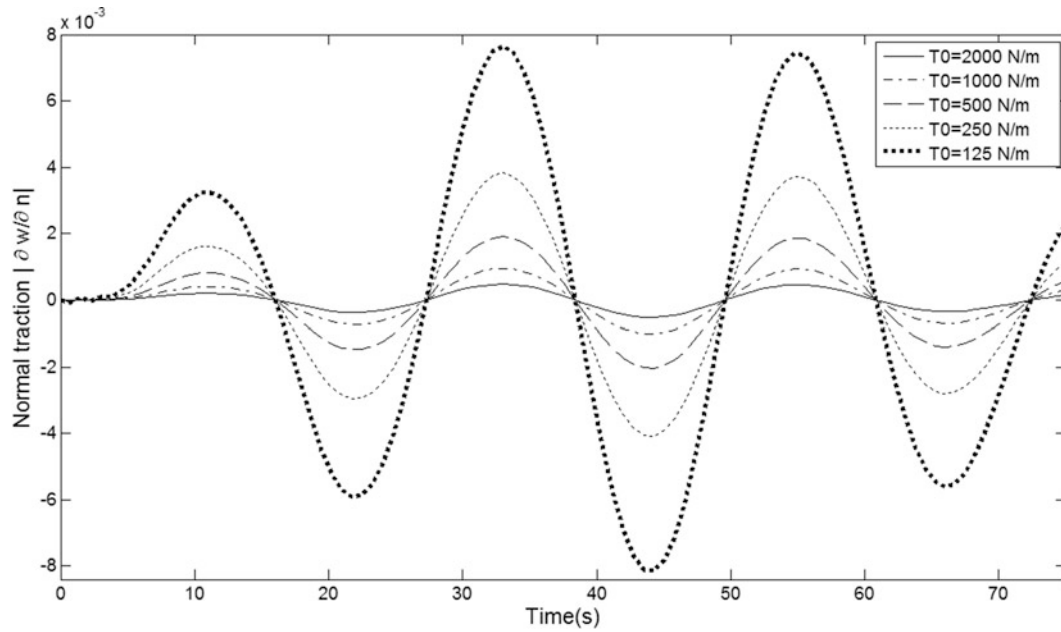


Fig. 34.8 Normal pressure gradient time history at the center of the membrane (MATLAB® 11)

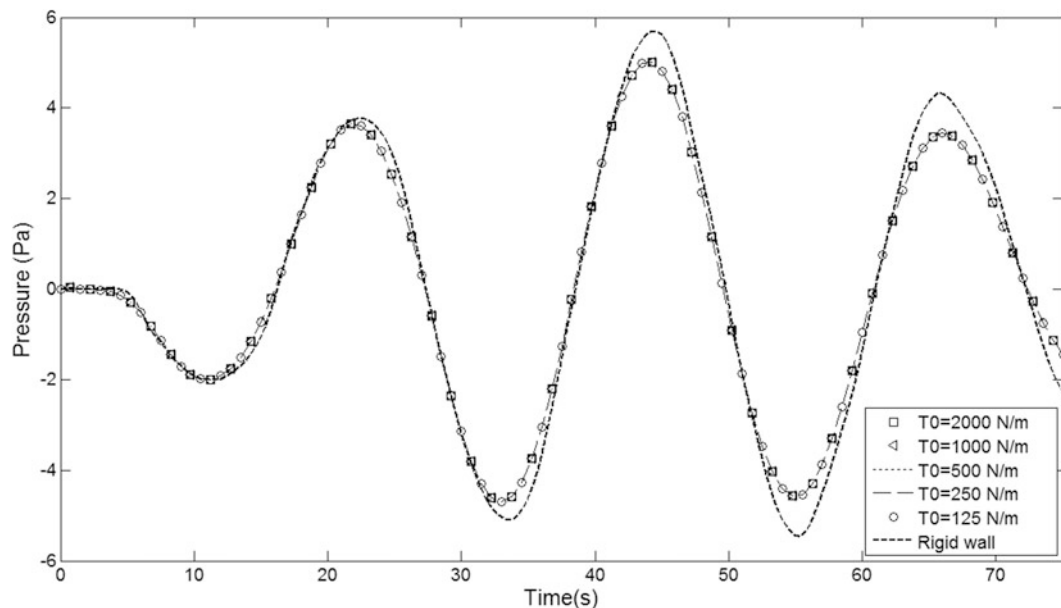


Fig. 34.9 Pressure time history at the center of the membrane (MATLAB® 11)

References

1. Burgschweiger R, Ochmann M, Nolte B (2008) Calculation of the acoustic target strength of elastic objects based on BEM–BEM-coupling. *J Acoust Soc Am* 123:3757
2. Chen P-T, Ju S-H, Cha K-C (2000) A symmetric formulation of coupled BEM/FEM in solving responses of submerged elastic structures for large degrees of freedom. *J Sound Vib* 233:407–422
3. Citarella R, Federico L, Cicatiello A (2008) Modal acoustic transfer vector approach in a FEM–BEM vibro-acoustic analysis. *Eng Anal Bound Elem* 31:248–258
4. Dhandole SD, Modak SV (2005) Review of vibro-acoustics analysis procedures for prediction of low frequency noise inside a cavity. In: IMAC XXV conference and exposition on structural dynamics
5. Everstine GC, Henderson FM (1990) Coupled finite element/boundary element approach for fluid–structure interaction. *J Acoust Soc Am* 87:1938–1947

6. Fritze D, Marburg S, Hardtke H-J (2005) FEM–BEM coupling and structural acoustic sensitivity analysis for shell geometries. *Comput Struct* 83:143–154
7. Gaul L, Wenzel W (2002) A coupled symmetric BEM–FEM method for acoustic fluid–structure interaction. *Eng Anal Bound Elem* 26:629–636
8. He Z, Liu G, Zhong Z, Zhang G, Cheng A (2011) A coupled ES-FEM/BEM method for fluid–structure interaction problems. *Eng Anal Bound Elem* 35:140–147
9. Hwang T, Ting K (1989) Boundary element method for fluid-structure interaction problems in fluid storage tanks. *J Press Vessel Technol* 111(4):435–440
10. Kinsler LE, Frey AR, Coppens AB, Sanders JV (2005) *Fundamental of acoustics*. Wiley-Blackwell, Chichester, New York
11. Mackerle J (1999) Fluid–structure interaction problems, finite element and boundary element approaches: a bibliography (1995–1998). *Finite Elem Anal Des J* 31:231–240
12. Marburg S, Nolte B (2010) *Computational acoustics of noise propagation in fluids—finite and boundary element methods*. Springer, Berlin
13. Morand P, Ohayon R (1995) *Fluid structure interaction*. Wiley-Blackwell, Chichester, New York
14. Naumenkob V, Strelnikovac E, Yeselevac E (2010) Free vibrations of shells of revolution filled with a fluid. *Eng Anal Bound Elem J* 34(10):856–862
15. Nolte B (1998) Fluid–structure-interaction-phenomena on the basis of a BEM–BEM coupling formulation. In: ISMA 23th international conference on noise and vibration engineering, September 1998, Leuven, pp 705–710
16. Nolte B, Gaul L (1999) Fluid–structure interaction with the boundary element method. In: *Proceedings of the 17th IMAC international modal analysis conference*, vol 1, Kissimmee, pp 496–502
17. Of G, Steinbach O (2011) Coupled FE/BE formulations for the fluid–structure interaction. In: Huang Y, Kornhuber R, Widlund O, Xu J (eds) *Domain decomposition methods in science and engineering XIX*, vol 78, *Lecture notes in computational science and engineering*. Springer, Berlin, pp 293–300
18. Partridge P, Brebbia C, Wrobel L (1992) *The dual reciprocity boundary element method*. Computational Mechanics Publications, Southampton
19. Shekari MR, Khaji N, Ahmadi MT (2009) A coupled BE-FE study for evaluation of seismically isolated cylindrical liquid storage tanks considering fluid–structure interaction. *J Fluids Struct* 25(3)
20. Soares D (2009) Acoustic modelling by BEM–FEM coupling procedures taking into account explicit and implicit multi-domain decomposition techniques. *Int J Numer Methods Eng* 78:1076–1093
21. Soares D, Von Estorf O, Mansur WJ (2005) Efficient non-linear solid–fluid interaction analysis by an iterative BEM/FEM coupling. *Int J Numer Methods Eng* 64:1416–1431
22. Soares D, Mansur W (2006) Dynamic analysis of fluid–soil–structure interaction problems by the boundary element method. *J Comput Phys* 219:498–512
23. Tanaka M, Masuda Y (1988) Boundary element method applied to certain structural-acoustic coupling problems. *Comput Methods Appl Mech Eng* 71:225–234
24. Wrobel LC, Aliabadi MH (2002) *The boundary element method volume 2: applications in solid and structures*. Wiley, New York
25. Wrobel LC (2002) *The boundary element method volume 1: applications in thermo-fluids and acoustics*. Wiley-Blackwell, Chichester, New York
26. Young Y (2008) Fluid–structure interaction analysis of flexible composite marine propellers. *J Fluids Struct* 24:799–818

Chapter 35

Parametric Study of a Continuous Scanning Method Used to Characterize an Acoustic Field

V.V.N. Sriram Malladi, Kevin L. Lefeave, and Pablo A. Tarazaga

Abstract A novel approach utilizing the acoustic emissions of a vibrating source is developed to analyze the relationship between the source characteristics and its acoustic field. In previous work, the authors presented a new methodology for sound field characterization based on a Continuous Acoustic Scanning (CAS) approach. As a part of that work, the feasibility of the proposed method was established by validating the theory developed by a roving microphone experiment. The CAS approach utilizes the side bands in a fast Fourier Transform (FFT) of the time-based-data collected by a roving microphone. The present work herein, is an extension and in-depth study of the different parameters affecting these side bands.

The work presented in this paper simulates a continuous acoustic scan of a simple-source dipole. Various parameters affecting the acoustic field characterization are studied. The variables considered in this paper include the distance between the microphone and the sound source, the roving speed of the microphone, the length of the sweep and the amplitude of the dipole velocity.

Keywords Acoustic scanning • Vibro-acoustics • Acoustic field • FFT • Dipole

Nomenclature

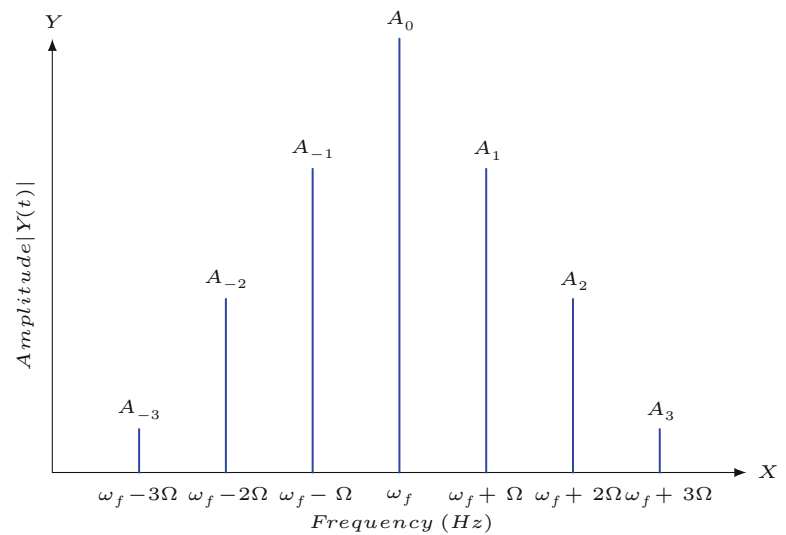
V_s	Amplitude of radial velocity of a pulsating sphere
ω_f	Frequency of the pulsating sphere
Φ	Phase of the dipole
d	Distance between poles of a dipole
L	Sweep length of the microphone
Ω	Sweeping frequency i.e the frequency at which the microphone roves the sweeping trajectory
Ψ	Angle made by the sweeping trajectory with x-axis
h	Vertical distance between the origin and the center of the sweeping trajectory
y	Horizontal distance between the origin and the center of the sweeping trajectory

35.1 Introduction

Experimental investigations have been a crucial step in studies that quantify the physics of a dynamic system. In mechanical systems, which deal with the vibratory features of structures, experimentation is a major method used to evaluate the spatial behavioral patterns of a system. Historically, research has focused on developing techniques that enable engineers/scientists

V.V.N.S. Malladi (✉) • K.L. Lefeave • P.A. Tarazaga
Department of Mechanical Engineering, Center for Intelligent Material Systems and Structures, Virginia Polytechnic Institute and State University, Blacksburg, VA 24061, USA
e-mail: sriram@vt.edu

Fig. 35.1 Characteristics of the monopole and dipole



to quantify vibratory stresses at different operational conditions through mechanical measurements. With today's increased computational power, the last few decades have seen a rapid development of science in multiple disciplines, making it possible to translate physical dynamics into a measurable signal.

An important part in the studies of dynamic systems, has been the consolidation of the tremendous amounts of data acquired through improved transducers. This has facilitated the extraction of meaningful features that are representative of the underlying physics. Simultaneous advancements in hardware architectures and theoretical techniques have a synergetic effect on the development of signal processing techniques. A continual improvement of transformatory and manipulatory techniques has given rise to a wider range of features that characterize time based raw information. Fourier transform is one such widely used mathematical tool which consolidates and demodulates features from temporal data. FFT [1], a computationally facile form of Fourier transform [2], has been a key component of modal testing of structures.

Accelerometers are one of the most widely used sensors that transduce a mechanical vibration into an analog signal. Over the years, many other types of contact and non-contact transducers have emerged in the market. There are inherent advantages to non-contact transducers within structurally delicate and specially constrained applications over traditional transducers. These advantages have attracted research in multiple disciplines, such as acoustics and lasers [3]. The laser displacement sensor and laser Doppler vibrometer (LDV) [4] are products of research in such non-contact methodologies. LDV operates by capturing the back-scattered light from the vibrating surface. The frequency demodulation of the signal received from a photo-detector results in the extraction of the Doppler frequency shift. Information related to the target vibration is embedded as a component in this shift. The Continuous Scanning laser Doppler vibrometer (CSLDV) [5–7], the Tracking Laser Doppler Vibrometer (TLDV) and arrayed microphone techniques [8] are some of the much recent advancements in this field, as compared to the traditional sensing methods. The assembly of a scanning mirrors with an LDV resulted in a faster and automated measurement process, which is capable of capturing both the spatial and dynamic properties in a single time record. The relationship between the operational deflection shape (ODS) [9] of the vibrating structure and the time-resolved component in the spectrum, is developed for the above mentioned techniques.

The aim of this work is to combine features from previously developed microphone array techniques and CSLDV. In this work, the acoustic field is mapped by a scanning microphone over a vibrating surface. When the structure is excited, the Continuous Acoustic Scanning (CAS) time signal, obtained from roving the microphone, presents an amplitude modulation that is given by the amplitude of the deflected structure at the time the microphone passes. This signal, when convolved into a frequency domain, results in a number of sidebands, which are equally spaced, around the excitation frequency. As can be seen in Fig. 35.1, the spacing between these sidebands is an integer multiple of the sweeping frequency. The amplitudes of these sidebands are algebraically related to the coefficients of the polynomial which represents the deflection shape of the structure. This is the concept of CAS. The present work is confined to the parametric study of a handful of factors affecting the sidebands.

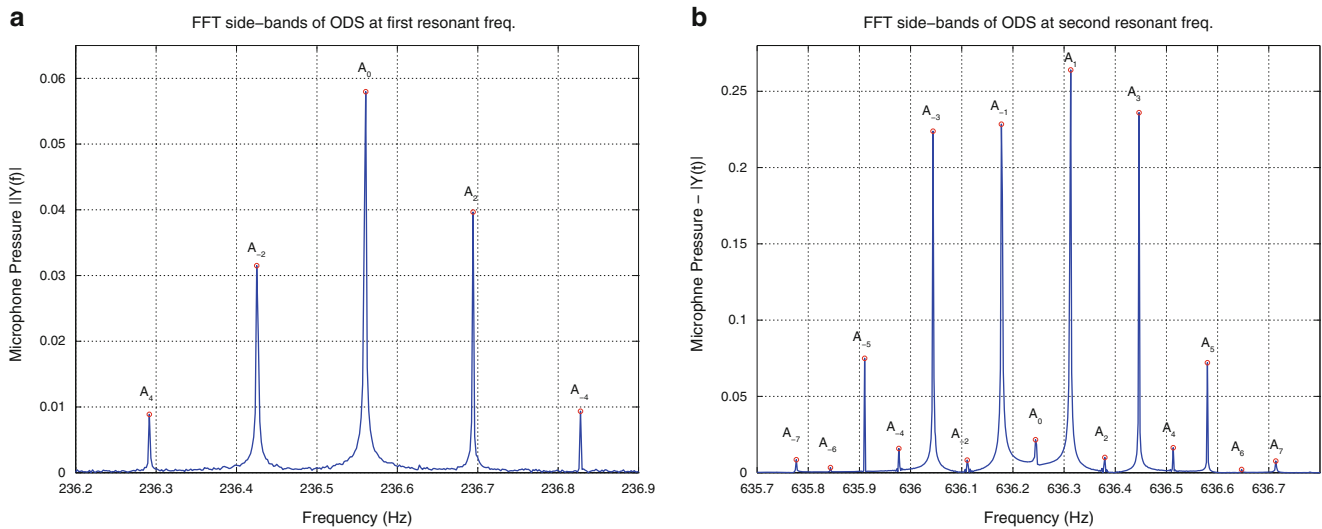


Fig. 35.2 FFT sidebands from a microphone scanning over a clamped-clamped beam vibrating at its first and second resonant frequency. (a) First resonant frequency. (b) Second resonant frequency

35.2 The Simplification of the Field Around a Fixed-Fixed Beam

In previous experimentation [10], the measurement of the acoustic field emitted by the first and second operational deflection shapes of a clamped-clamped beam, has resulted in the sidebands shown in Fig. 35.2. These plots show the FFTs of experimentally obtained acoustic pressure signals at the first two resonant frequencies of a clamped-clamped beam. These figures are symmetrically spaced about the excitation frequency or the resonant frequencies; i.e. at 236.5 Hz and 636.2 Hz. Further observation of these figures show that the larger sideband frequencies are spaced at two times the sweeping frequency (0.063 Hz).

The other noticeable feature is that the central peak is more prominent in Fig. 35.2 as compared to its side peaks, contrary to the central peak in Fig. 35.2. In order to further understand the nature of these peaks, an experimental parametric study is required. Due to physical and time-related constraints, it is not possible to conduct such a large number of experiments and determine the effect of various parameters on sidebands. Therefore, a theoretical approach is developed to study these parametric relationships.

When a clamped-clamped beam is excited at its first resonant frequency, all particles along the length of the beam vibrate at different velocities, but at the same phase. The acoustic field developed above the beam by the dynamics of the first mode shape is similar to the acoustic field developed by a pulsating sphere or monopole. The alternating high and low pressure bands created by this beam at this frequency can be simulated by the acoustic field surrounding a monopole. Similarly, when the beam is excited at its second resonant frequency, the particles of the beam on either sides of the nodal point are out of phase with each other. The resulting acoustics from such structural vibrations, is similar to the field created by a pair of monopoles which are out of phase i.e. a dipole. Simulations of continuous acoustic scanning test on a monopole and dipole has resulted in the FFTs shown in Fig. 35.3. These plots show similar characteristics, like the plots in Fig. 35.2, corresponding to the first and second ODS of the beam. Thus, the paper will show this approach in studying the CAS methodology and how it relates to the acoustic source.

35.3 Acoustic Field Characterization of a Dipole

Although a monopole and a dipole can be used to simulate the acoustic field generated by a clamped-clamped beam at the first two resonant frequencies, the present work is confined to the parametric study of a dipole. A schematic of a dipole and its parameters are considered for this study, as shown in Fig. 35.4. The spheres with radius a pulsates with an amplitude V_s and frequency ω_f , resulting in a velocity profile given by V_1 and V_2 . The phase difference ϕ of 180° between the two monopoles,

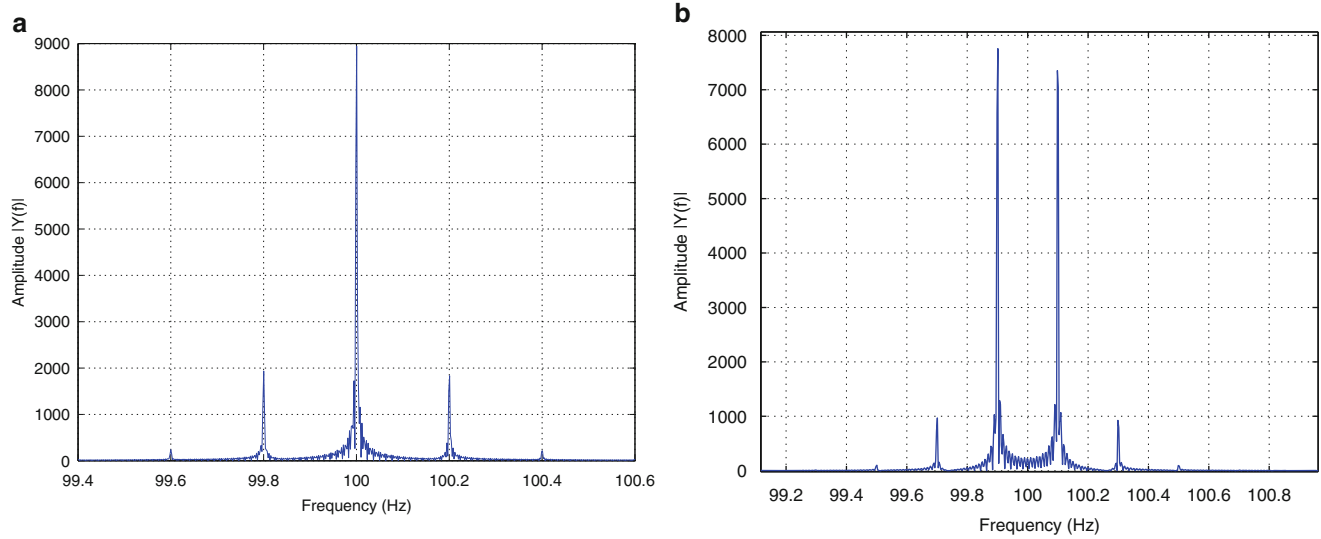
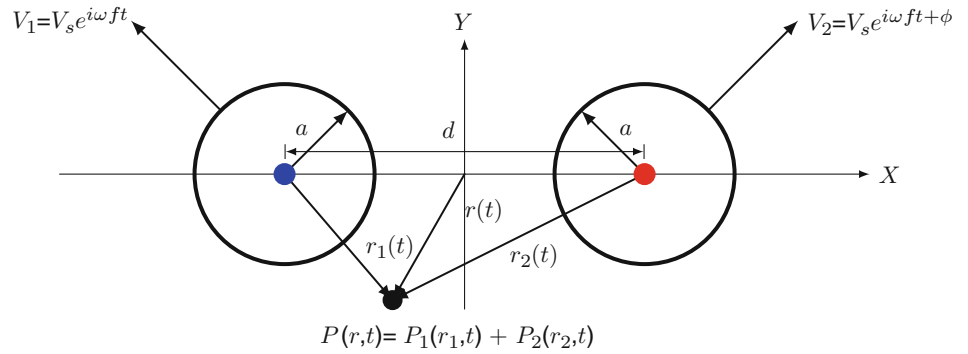


Fig. 35.3 FFT of the acoustic pressure readings. (a) Monopole. (b) Dipole

Fig. 35.4 Schematic of a dipole



develops the dynamics in which one sphere pulsates out, while the other contracts inward. The pressure of a monopole is given by

$$P(r, t) = \frac{V_s \rho c k a^2 (1 + ika) e^{i(\omega_f t - k(r-a))}}{r(1 + k^2 a^2)}, \tag{35.1}$$

where V_s is the velocity of the sphere when its pulsating, ρ is the density of the medium the acoustics are in, c is the speed of sound in that medium, a is the average radius of the sphere, k is the ratio of the forcing frequency over the speed of sound and r is the radius at a given point. Using the principle of superposition the pressure at a distance r from the origin is the sum of the pressure contribution of each monopole. This final pressure of a dipole is

$$P(r, t) = P_1(r_1, t) + P_2(r_2, t), \tag{35.2}$$

where r_1 and r_2 are the distance of this point from the center of the pulsating monopoles.

The representative acoustic field surrounding a dipole is shown in Fig. 35.5a. This figure is not drawn to scale, in order to see the high-pressure and low-pressure bands. At the central axis of this figure, it can be seen that pressures from two out of phase acoustic sources results in a line with zero acoustic pressure due to its cancelling effect. When a microphone sweeps symmetrically across this nodal pressure line, a symmetric pressure distribution is obtained. This is seen in Fig. 35.5b. The trajectory of the microphone is given by

$$x(t) = \frac{L}{2} \cos(\Omega t), \tag{35.3}$$

where L is the full sweep length and Ω is the sweeping frequency.

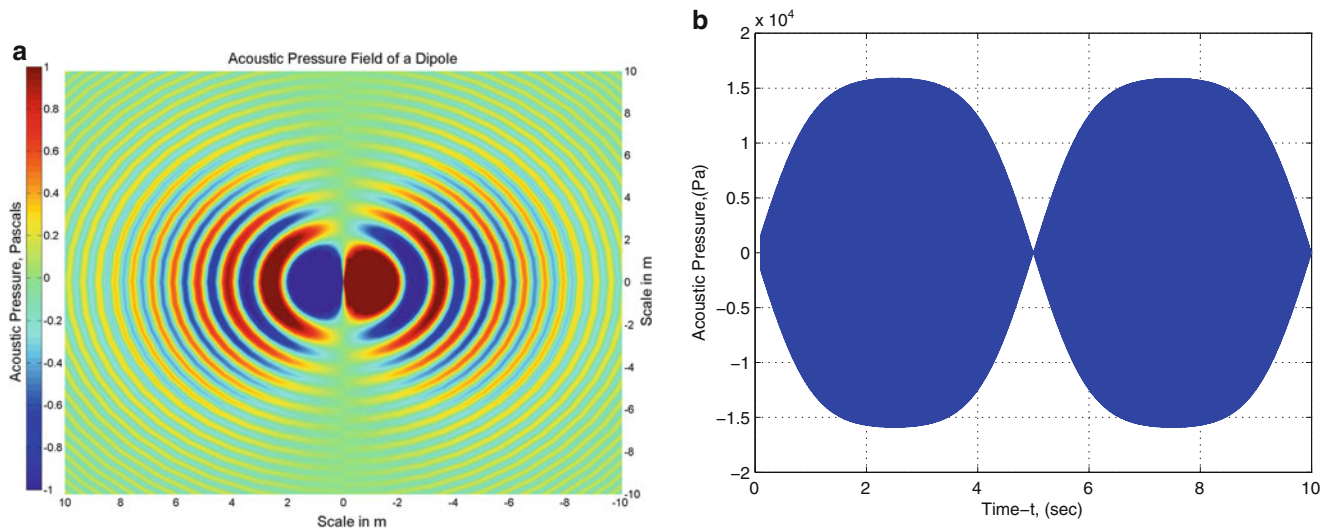


Fig. 35.5 Dipole acoustic pressure characteristics. (a) Sample pressure distribution of a dipole (not to scale). (b) Acoustic pressure readings of the microphone scanning a dipole

The time-based pressure reading of the dipoles are convolved into the frequency domain by the Fourier transform. The FFT of the dipole pressure distribution is shown in Fig. 35.3b. The forcing frequency ω_f is 100 Hz, which accounts for the FFT being symmetric around 100 Hz. The sweeping rate Ω , is 0.1 Hz for this simulation. The largest peaks of this FFT are located 0.1 Hz away from the forcing frequency, and sidebands every 0.2 Hz. The effect of various parameters on these characteristics will be discussed in the next section.

35.4 Parameters Involved in C.A.S. of a Dipole

The schematic of the continuous acoustic scanning of a pressure field around the dipole is shown in Fig. 35.6. All the parameters involved in this simulation are depicted in this figure. The parameters that are involved in the CAS of a dipole are the height above the dipole h , the length of the sweep l , the sweep frequency Ω , and the angle of the sweep ψ . An offset y , of the sweep over the dipole can also be included. The distance between the dipoles d , forcing frequency ω_f , the phase difference ϕ , and the amplitude of velocity of pulsation V_s are the parameters of the dipole.

During the simulation, one of the parameters is varied while the rest are left constant. This allows a study of the effect of that parameter on the FFT characteristics. The default parameters used in the simulation are presented in Table 35.1.

35.5 Results of CAS Simulations

35.5.1 Variation of Amplitude of Dipole Velocity- V_s

The amplitude of the pulsating velocity V_s of a dipole is varied from 1 to 1,000 m/s in steps of 25 m/s. As the microphone roves along its scanning trajectory, it records the time-related acoustic pressure emitted by the dipole. The FFT then converts this data into the frequency domain. The FFTs at different values of V_s are stitched together to obtain the 3D-FFT plotted in Fig. 35.7a. This figure has frequency on the x-axis, amplitude of velocity on the y-axis and amplitude of FFT on the z-axis. It can be seen that any two consecutive peaks are separated by 2Ω . The influence of this parameter on the sidebands can be better seen in Fig. 35.7b. This figure is a side view of the FFT with the peaks for a given frequency. This figure shows that the peaks A_1 and A_{-1} overlap each other. Similarly for other symmetric peaks, it can be seen that the peaks are growing linearly as the velocity increases. The odd peaks are also the only amplitudes present, with the sidebands at low amplitudes. Thus, there is a linear relationship between V_s and the magnitude of the peaks.

Fig. 35.6 Schematic of continuous acoustic scanning of a dipole

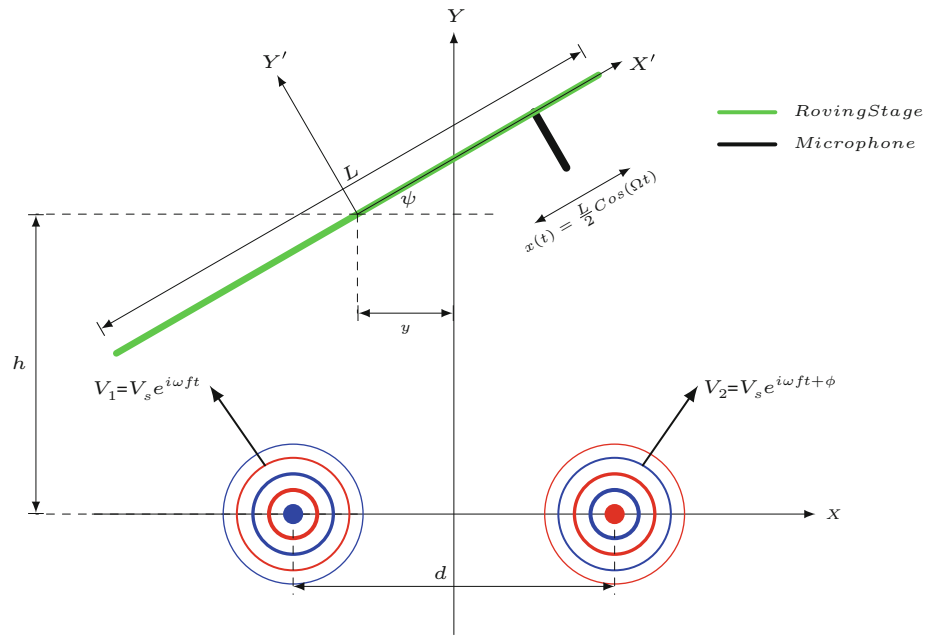


Table 35.1 Default values of parameters for simulations

V_s	L	ϕ	d	h	ψ	Ω	ω_f	y
20 m/s	0.2 m	90°	0.1 m	0.05 m	0°	0.5 Hz	600 Hz	0 m

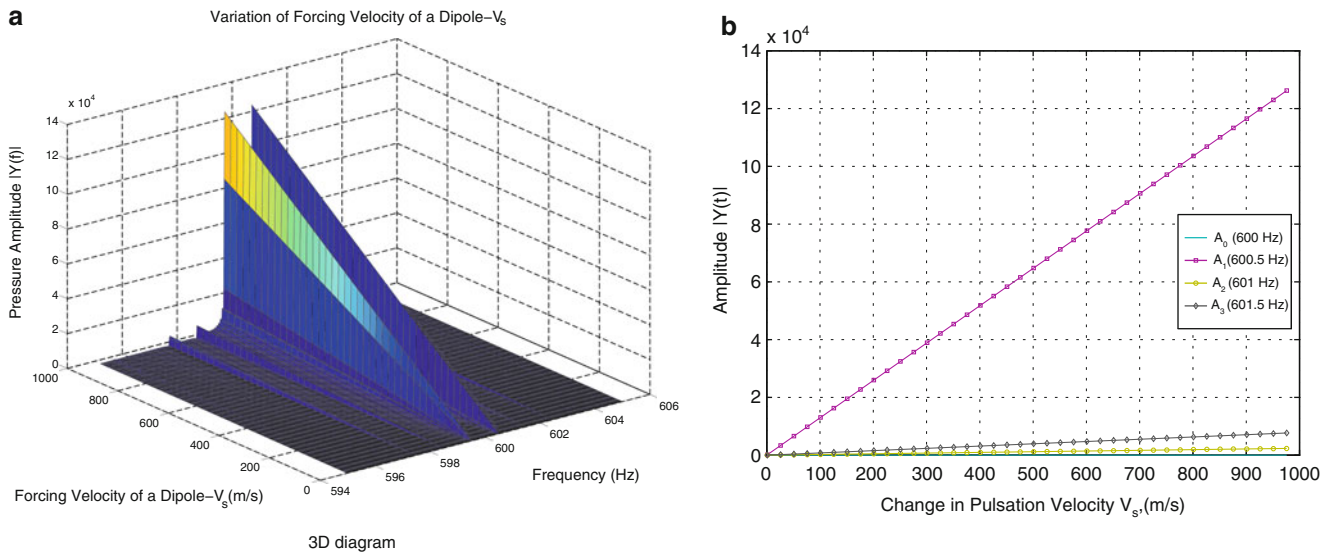


Fig. 35.7 Variation of amplitude of velocity of dipole- V_s . (a) 3D diagram. (b) 2D diagram

35.5.2 Variation of Vertical Height Between the Monopole and Dipole-h

The height above the source is important to characterize as it will have a strong correlation to the acoustic field being measured. The height of the microphone from the dipole is varied from 0.005 to 0.5 m in steps of 0.005 m. The 3D FFT plot and the corresponding 2d FFT plot is presented in Fig. 35.8. The sideband peaks occur symmetrically about the forcing frequency ω_f and are separated by 2Ω Hz. The sideband heights initially increase till a point and then quickly taper off. This trend can be seen more predominantly in the 2D plot shown in Fig. 35.8b. This set of default values results in a maximum

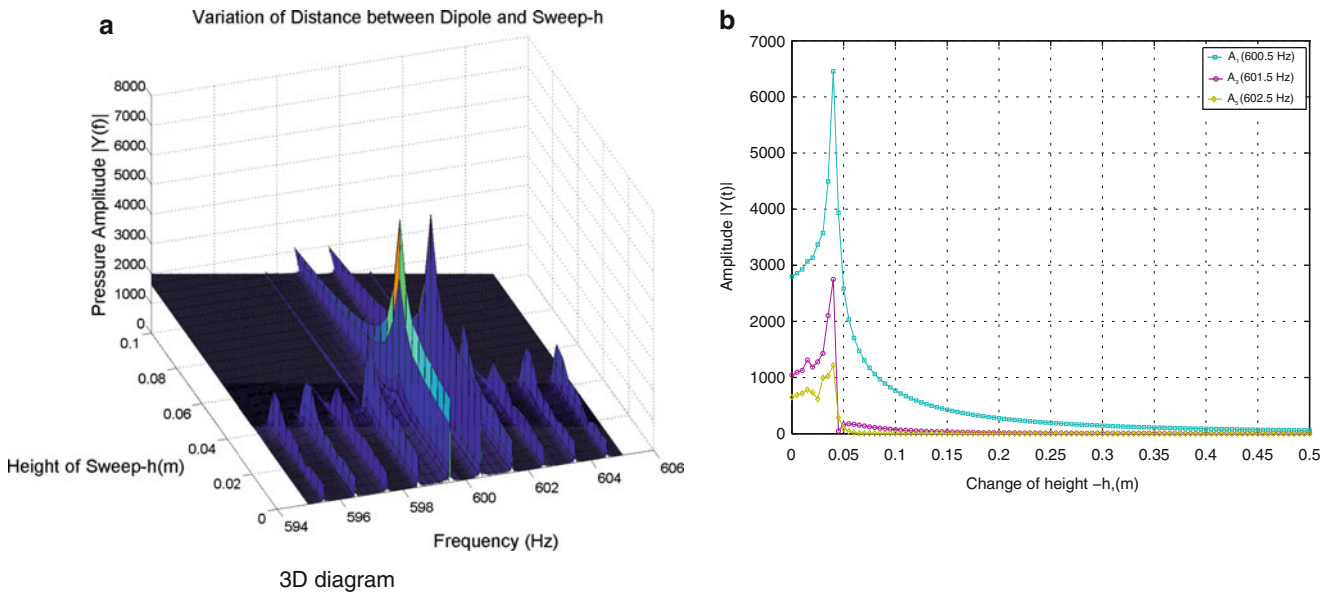


Fig. 35.8 Variation of vertical distance between the dipole and roving trajectory. (a) 3D diagram. (b) 2D diagram

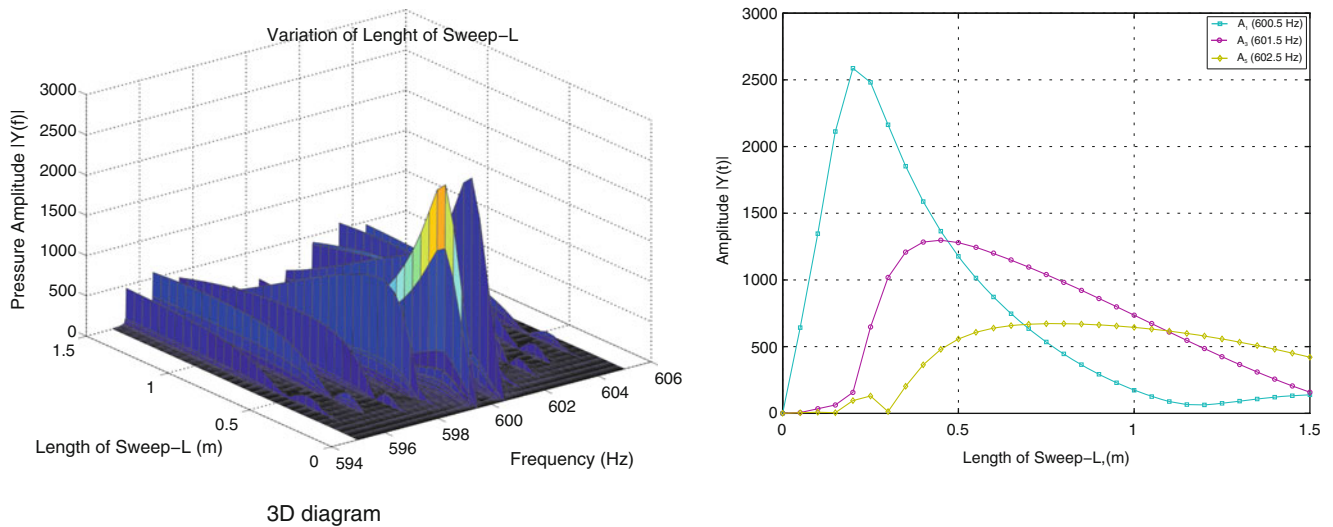


Fig. 35.9 Variation of length of sweep. (a) 3D diagram. (b) 2D diagram

value of side peaks when the height is 0.05 m. All the side peaks achieve their maximum value at this value of the height. Thus, the maximum value of the side peaks occur at a particular value, and the factors influencing this behavior need further investigation.

35.5.3 Variation of Sweep Length-L

The variation of length of the sweep showed interesting results; these can be seen in Fig. 35.9. This figure is developed by changing the length of the sweep from 0.05 to 1.5 m, in steps of 0.05 m. Initially, only two peaks at $\omega_f \pm \Omega$ are present. As the length is increased, more and more peaks tend to appear. Another characteristic feature of this plot is that the side peaks, starting from $\omega_f \pm 3\Omega$, initially increase, then dips back to zero, then increases again. The emergence of the peaks of the first three sidebands occur when the length of the sweep is at 0.2, 0.45 and 0.75 m respectively.

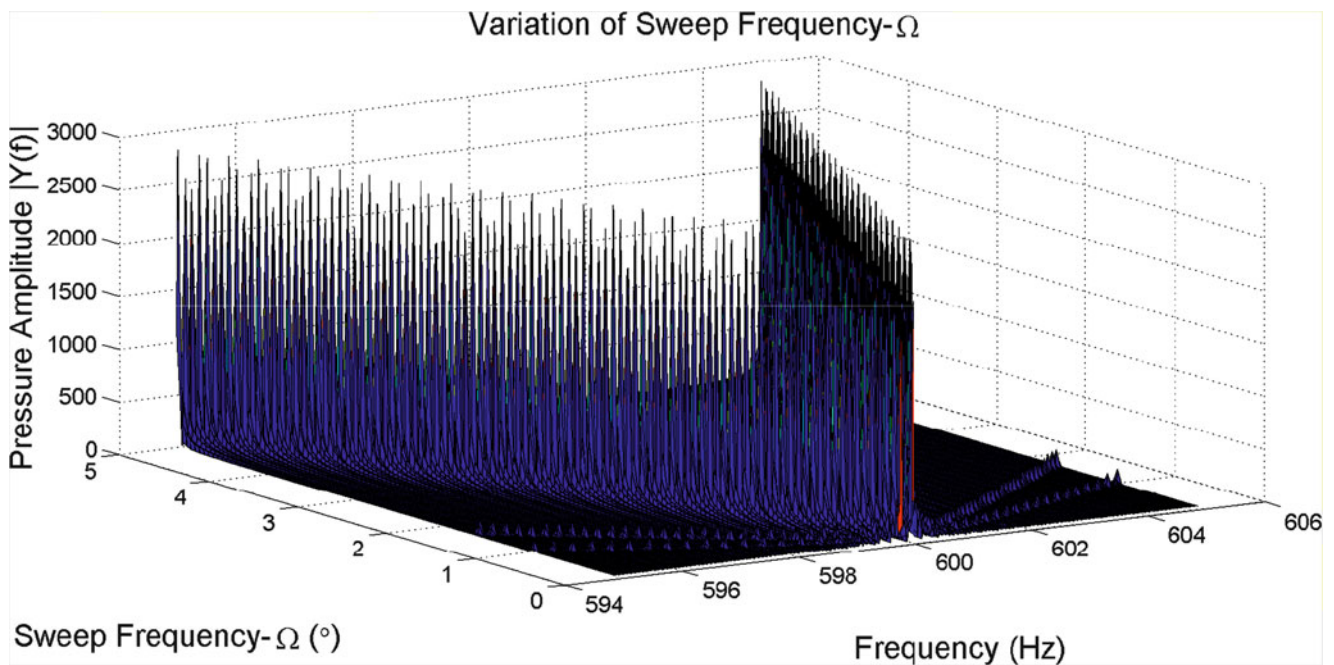


Fig. 35.10 Variation of sweep frequency

35.5.4 Variation of Sweep Frequency- Ω

The sweeping frequency Ω , of the linear stage was then adjusted from 0.1 to 5 Hz in steps of 0.05 Hz; these results can be seen in Fig. 35.10. As the sweeping frequency is increased, the distance between the adjacent peaks is seen to change linearly. On one hand, this shows that sweeping at very high frequencies can interfere with other resonant frequencies of the structure. On the other hand, very low sweeping frequency needs a finer resolution of the FFT. More spectral lines can be achieved when the microphone collect data for a longer period of time. An optimal trade-off has to be achieved in the selection of the sweep frequency.

35.6 Conclusion

Previously, the study of the Continuous Acoustic Scanning (CAS) methods to characterize an acoustic field have been studied by the authors and the feasibility of this technique has been proven. The experimental results for a clamped-clamped beam, by the authors, is now modeled as a pulsating dipole and monopole to understand the influence of various parameters on sidebands. The monopole is an approximation of the ODS at the first natural frequency of the beam and the dipole represents the second mode. The simulation of the dipole sources were used to study variations of parameters effects on a FFT, taken from the acoustic pressure distribution collected from the source. The variables considered in this paper include the distance between the microphone and the sound source, the roving speed of the microphone, length of the sweep and the amplitude of the dipole velocity. In this study, it is observed that for these parameters the sideband peaks in the FFTs are symmetric about the dipole frequency. Each of these parameters have a characteristic effect on the shape, size and number of the peaks present. These variations offered a more accurate way to depict what is governing the outcome found from experimental results and to better evaluate parameter selection in experimentation. In the future, the different parameters of the acoustic source would be extracted by studying the distinctive signatures of these parameters in the FFT.

References

1. Cochran WT, Cooley JW, Favin DL, Helms HD, Kaenel RA, Lang WW, Maling GC Jr, Nelson DE, Rader CM, Welch PD (1967) What is the fast Fourier transform? *Proc IEEE* 55(10):1664–1674
2. Cooley JW, Tukey JW (1965) An algorithm for the machine calculation of complex Fourier series. *Math Comput* 19(90):297–301
3. Ameri N, Tarazaga P, Di Maio D, Ewins D (2012) Non-contact operational modal analysis of an optical membrane for space application. Springer, New York
4. Pickering C, Halliwell N, Wilmshurst T (1986) The laser vibrometer: a portable instrument. *J Sound Vib* 107(3):471–485
5. Di Maio D (2008) SLDV technology for measurement of mistuned bladed disc vibration. Ph.D. thesis, Imperial College London
6. Di Maio D, Ewins D (2011) Continuous scan, a method for performing modal testing using meaningful measurement parameters; Part I. *Mech Syst Signal Process* 25(8):3027–3042
7. Tarazaga PA, Di Maio D, Ameri N, Ewins DJ (2012) Continuous laser scanning of a lightweight membrane with monotone and multi-tone excitation techniques. In: Proceedings, 53rd AIAA/ASME/ASCE/AHS structures, structural dynamics and materials conference (SDM), April 2012, Honolulu, Hawaii
8. Brooks TF, Humphreys WM (2006) A deconvolution approach for the mapping of acoustic sources (DAMAS) determined from phased microphone arrays. *J Sound Vib* 294(4):856–879
9. Richardson MH (1997) Is it a mode shape, or an operating deflection shape? *SV Sound Vib* 31(1):54–61
10. Garcia CE, Malladi S, Tarazaga PA (2014) Continuous scanning for acoustic field characterization, Topics in modal analysis, vol 7, pp 625–636. Springer, New York